MICRO- TO MACRO-SCALE DYNAMICS OF EARTH'S FLANK MAGNETOPAUSE

EDITED BY: Kyoung-Joo Hwang, Hiroshi Hasegawa, Katariina Nykyri, Takuma Nakamura and Simon Wing

PUBLISHED IN: Frontiers in Astronomy and Space Sciences and Frontiers in Physics

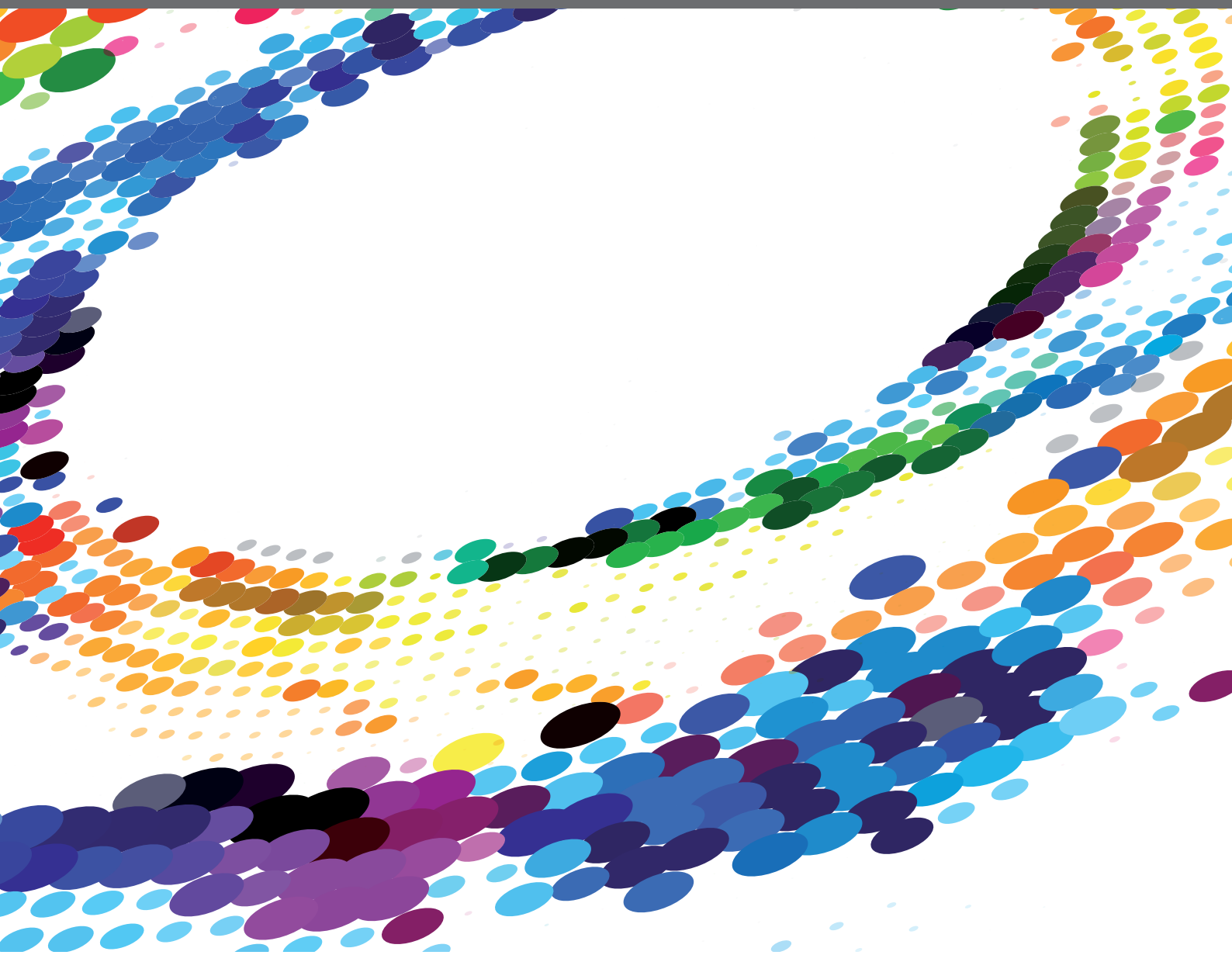

frontiers Research Topics

ISSN 1664-8714
ISBN 978-2-88976-319-1
DOI 10.3389/978-2-88976-319-1

About Frontiers

Frontiers is more than just an open-access publisher of scholarly articles: it is a pioneering approach to the world of academia, radically improving the way scholarly research is managed. The grand vision of Frontiers is a world where all people have an equal opportunity to seek, share and generate knowledge. Frontiers provides immediate and permanent online open access to all its publications, but this alone is not enough to realize our grand goals.

Frontiers Journal Series

The Frontiers Journal Series is a multi-tier and interdisciplinary set of open-access, online journals, promising a paradigm shift from the current review, selection and dissemination processes in academic publishing. All Frontiers journals are driven by researchers for researchers; therefore, they constitute a service to the scholarly community. At the same time, the Frontiers Journal Series operates on a revolutionary invention, the tiered publishing system, initially addressing specific communities of scholars, and gradually climbing up to broader public understanding, thus serving the interests of the lay society, too.

Dedication to Quality

Each Frontiers article is a landmark of the highest quality, thanks to genuinely collaborative interactions between authors and review editors, who include some of the world's best academicians. Research must be certified by peers before entering a stream of knowledge that may eventually reach the public - and shape society; therefore, Frontiers only applies the most rigorous and unbiased reviews.
Frontiers revolutionizes research publishing by freely delivering the most outstanding research, evaluated with no bias from both the academic and social point of view. By applying the most advanced information technologies, Frontiers is catapulting scholarly publishing into a new generation.

What are Frontiers Research Topics?

Frontiers Research Topics are very popular trademarks of the Frontiers Journals Series: they are collections of at least ten articles, all centered on a particular subject. With their unique mix of varied contributions from Original Research to Review Articles, Frontiers Research Topics unify the most influential researchers, the latest key findings and historical advances in a hot research area! Find out more on how to host your own Frontiers Research Topic or contribute to one as an author by contacting the Frontiers Editorial Office: frontiersin.org/about/contact

MICRO- TO MACRO-SCALE DYNAMICS OF EARTH'S FLANK MAGNETOPAUSE

Topic Editors:
Kyoung-Joo Hwang, Southwest Research Institute (SwRI), United States
Hiroshi Hasegawa, Institute of Space and Astronautical Science, Japan Aerospace Exploration Agency, Japan
Katariina Nykyri, Embry–Riddle Aeronautical University, United States
Takuma Nakamura, Austrian Academy of Sciences (OeAW), Austria
Simon Wing, Johns Hopkins University, United States

Citation: Hwang, K.-J., Hasegawa, H., Nykyri, K., Nakamura, T., Wing, S., eds. (2022). Micro- to Macro-Scale Dynamics of Earth's Flank Magnetopause. Lausanne: Frontiers Media SA. doi: 10.3389/978-2-88976-319-1

Table of Contents

frontiers | Frontiers in Astronomy and Space Sciences

EDITORIAL
published: 13 May 2022
doi: 10.3389/fspas.2022.911633

Editorial: Micro- to Macro-Scale Dynamics of Earth's Flank Magnetopause

Kyoung-Joo Hwang[1], Hiroshi Hasegawa[2], Katariina Nykyri[3], Takuma Nakamura[4] and Simon Wing[5]*

[1]Southwest Research Institute, San Antonio, TX, United States, [2]Institute of Space and Astronautical Science, Japan Aerospace Exploration Agency, Sagamihara, Japan, [3]Physical Sciences Department, Embry-Riddle Aeronautical University, Daytona Beach, FL, United States, [4]Austrian Academy of Sciences ÖAW, Space Research Institute, Vienna, Austria, [5]Applied Physics Laboratory, Johns Hopkins University, Baltimore, MD, United States

Keywords: Magnetopause and boundary layers, magnetic reconnection, Kelvin-Helmholtz waves, Kelvin-helmholtz vortices, flux transfer event, wave-particle interaction, ULF activity, field-aligned current (FAC)

Editorial on the Research Topic

Micro- to Macro-Scale Dynamics of Earth's Flank Magnetopause

The Earth's magnetopause is a boundary between the shocked solar wind and the magnetosphere and host to diverse physical processes such as the velocity shear driven Kelvin-Helmholtz instability (KHI), the magnetic shear driven magnetic reconnection, and the excitation of various plasma waves and turbulence. They are fundamental processes that occur within the heliosphere and throughout the Universe. Understanding their generation and effect have been advanced via individual *in-situ* observations and theoretical and numerical modeling on various spatiotemporal scales. Yet, the evolution of these processes along the flank-side magnetopause and corresponding impacts on the solar wind-magnetosphere-ionosphere coupling leave room for enhanced and coherent understanding. This Research Topic serves as a forum to bring existing and new pieces of understanding together to construct the comprehensive picture of those local processes evolving from the dayside magnetopause via the flanks down to the distant tail magnetopause.

Eleven papers published in this Research Topic present the most recent perspectives on the Kelvin-Helmholtz waves or vortices (KHWs/KHVs) and accompanying kinetic processes using new observations or established/advanced models. KHWs/KHVs provide a pathway for energy transfer from the velocity shear layer to the Earth's magnetosphere via the coupling between KHWs and Alfvén waves (Chaston et al., 2007). Kim et al. emphasize the generation of secondary KHWs and their dominancy in energy transfer due to a stronger mode conversion to the shear Alfvén waves than primary KHWs. The energy transfer is also mediated via the excitation of global ULF (ultra-low frequency) waves driven by KHWs, as conceptualized by Zhu and Kivelson (1989). Kronberg et al. and Petrinec et al. using conjunctions of multiple spacecraft or ground magnetometers identify the close linkage between magnetopause KHWs and coincident ULF waves. Additionally, Petrinec et al. use the theory, developed by Johnson et al. (2021), that KHVs at the magnetopause can couple to the ionosphere and generate micro-scale field-aligned currents. They employ KHV observations at the magnetopause to predict micro-scale upward field-aligned current structures in the auroral oval, which are then compared with ionospheric observations.

Five articles among those eleven papers are focused on magnetic reconnection. Hwang et al. report detailed properties of in-plane (velocity-shear plane) reconnection under the combined shear flow, guide field, and density asymmetry. Another in-plane reconnection under such conditions but without being associated with KHWs (Tang et al.) indicate that the flank-magnetopause reconnection recloses the open field lines generated by the primary (dayside) magnetopause

OPEN ACCESS

Edited and reviewed by:
Rudolf A. Treumann, Ludwig Maximilian University of Munich, Germany

****Correspondence:***
Kyoung-Joo Hwang
jhwang@swri.edu

Specialty section:
This article was submitted to Space Physics, a section of the journal Frontiers in Astronomy and Space Sciences

Received: *02 April 2022*
Accepted: *19 April 2022*
Published: *13 May 2022*

Citation:
Hwang K-J, Hasegawa H, Nykyri K, Nakamura T and Wing S (2022) Editorial: Micro- to Macro-Scale Dynamics of Earth's Flank Magnetopause. Front. Astron. Space Sci. 9:911633. doi: 10.3389/fspas.2022.911633

reconnection. This modifies the classical Dungey cycle, where the reclosing occurs near the nightside magnetotail. Ma et al. and Eriksson et al. investigate out-of-velocity-shear-plane reconnection, so-called mid-latitude reconnection (Faganello et al., 2012) that occurs due to a 3D twist of mid-latitude magnetospheric fields and engulfed magnetosheath fields induced by the low-latitude KHVs. Eriksson et al. identify double (northern and southern) mid-latitude reconnection via counter-streaming ion beams. Ma et al. show that the KHV-induced double mid-latitude reconnection leads to significant transport and mixing of multi-species ions. Dokgo et al. investigate the localized energy conversion facilitated by wave-particle interactions observed at the reconnection current sheet inside a KHV-induced flux rope. Their observation supported by linear wave theory shows that the electrostatic beam-mode waves thermalize electrons effectively. Hwang et al. also report that the electrostatic waves may pre-heat a magnetosheath population that is to participate into the reconnection process, leading to two-step energization of the magnetosheath plasma entering into the magnetosphere via KHV-driven reconnection.

While the statistics indicate that KHWs occur most frequently under the northward IMF (interplanetary magnetic field), their occurrence under southward IMF is not rare (Kavosi and Raeder, 2015), as reported by Kronberg et al. and Petrinec et al. in this Topic. Two additional papers, via numerical modelling, address the behavior of the magnetopause or the evolution of KHWs under this condition. The former study by Park et al. shows the result of 3D global MHD simulations of dayside reconnection, KHVs generated in the inner boundary of the magnetopause, and a cross-polar-cap potential increase under weakly southward IMF. Based on 2D and 3D fully kinetic simulations modeling an *in-situ* observation event of KHWs during southward IMF, Nakamura et al. reveal that a turbulent evolution of the lower-hybrid drift instability near the magnetospheric side of the KHW rapidly disturbs the KHW structure and causes an effective transport of plasmas across the magnetopause. These studies suggest collaborative effects of reconnection and KHWs in the solar wind transport, implying that the diffusive transport induced by KHWs may be active at the flank magnetopause during southward IMF.

Four papers in this Topic are dedicated to the evolution and effect of dayside transients including KHWs from the dayside magnetopause along the magnetopause flank down to the distant-tail magnetopause. Wilder et al. compare three KHW events at different locations along the magnetopause flank in the aspect of the occurrence of double layers and electrostatic solitary waves. Both indicative of kinetic-scale activity are most prevalent in the early phase of KHWs and become less common as vortices grow. Mejnertsen et al. use the 3D MHD code to trace dayside flux ropes of a variety of topology that determines the propagation and evolution of flux ropes. Flux ropes containing field lines connected to both hemispheres propagate along flanks and eventually dissipate due to non-local magnetotail reconnection. Wang et al. employ the 3D global hybrid (kinetic ions, fluid electrons) code to analyze the 3D magnetopause distortion driven by foreshock transients propagating anti-sunward. These external transients result in a transient appearance of the magnetosphere as observed by satellites sitting in the flank magnetosheath. The resultant magnetopause distortion also generates compressional magnetic-field perturbations within the magnetosphere and localized field-aligned currents into/out of the ionosphere. Brenner et al. focus on the energy transfer through the magnetopause occurring at dayside, flank, and tail regions during CME-driven storm conditions. According to them, while dayside reconnection is an important process for the energy transfer, the surface fluctuations at flanks dominate the Poynting flux injection, which dominates the energy entry to the magnetosphere.

Němeček et al. statistically analyze the inverse magnetic-field gradient across the magnetopause events whose occurrence rate increases toward flanks and under strong southward IMF. The intensive reconnection during southward IMF drives strong magnetospheric currents that overheat the magnetospheric plasma, which leads to a diamagnetic effect (decrease in the magnetic field) and increases the plasma pressure on the magnetospheric side.

KHWs/KHVs are ubiquitous in planetary magnetospheres. Delamere et al. review these processes on Saturn's magnetopause environment from the perspective of 2D and 3D hybrid simulations that resolve the ion kinetic scale. They also investigate heavy ion effects and find that the heavy ions not only modify the growth rate of KHI but also reduce Alfvén speed which increase the fraction of resonant particles in the wave-particle interaction, thus, affecting mass transport across the magnetopause. These results would be applied to other KH-unstable planetary magnetopause.

As organized in this editorial, articles published in this Research Topic emphasize the role and impact played by the magnetopause dynamics in mass, momentum and energy transfer between the solar wind and magnetosphere. Unprecedented high-resolution *in-situ* observations and analytic/numerical studies are integrated to shed light on how this transfer is facilitated throughout the entire magnetopause over micro-to macro-scales. We believe that articles collected in this Topic present the most active fronts of the magnetospheric research field and promote a comprehensive understanding by filling gaps in the role and importance of flank-magnetopause processes bridging the dayside and distant tail dynamics.

AUTHOR CONTRIBUTIONS

All authors listed have made a substantial, direct and intellectual contribution to the work, and approved it for publication.

ACKNOWLEDGMENTS

The Editors wish to thank all the authors and reviewers of the submitted papers for their work, time, effort, and patience. We gratefully acknowledge the assistance of the people in the Editorial Office of Frontiers in Astronomy and Space Sciences.

REFERENCES

Chaston, C. C., Wilber, M., Mozer, F. S., Fujimoto, M., Goldstein, M. L., Acuna, M., et al. (2007). Mode Conversion and Anomalous Transport in Kelvin-Helmholtz Vortices and Kinetic Alfvén Waves at the Earth's Magnetopause. *Phys. Rev. Lett.*, 99 doi:10.1103/PhysRevLett.99.175004

Faganello, M., Califano, F., Pegoraro, F., and Andreussi, T. (2012). Double Mid-latitude Dynamical Reconnection at the Magnetopause: An Efficient Mechanism Allowing Solar Wind to Enter the Earth's Magnetosphere. *EPL*, 100, 69001. doi:10.1209/0295-5075/100/69001

Johnson, J. R., Wing, S., Delamere, P., Petrinec, S., and Kavosi, S. (2021). Field-Aligned Currents in Auroral Vortices. *J. Geophys. Res. Space Phys.* 126, 1–15. doi:10.1029/2020JA028583

Kavosi, S., and Raeder, J. (2015). Ubiquity of Kelvin-Helmholtz Waves at Earth's Magnetopause. *Nat. Commun.*, 6 doi:10.1038/ncomms8019

Zhu, X., and Kivelson, M. G. (1989). Global Mode ULF Pulsations in a Magnetosphere with a Nonmonotonic Alfvén Velocity Profile, *J. Geophys. Res.*. 94, 1479–1485.doi:10.1029/ja094ia02p01479

Conflict of Interest: The authors declare that the research was conducted in the absence of any commercial or financial relationships that could be construed as a potential conflict of interest.

frontiers in Astronomy and Space Sciences

ORIGINAL RESEARCH
published: 21 September 2021
doi: 10.3389/fspas.2021.751244

Impact of Foreshock Transients on the Flank Magnetopause and Magnetosphere and the Ionosphere

Chih-Ping Wang[1]*, *Xueyi Wang*[2]*, *Terry Z. Liu*[3] and *Yu Lin*[2]

[1]Department of Atmospheric and Oceanic Sciences, University of California, Los Angeles, Los Angeles, CA, United States, [2]Physics Department, Auburn University, Auburn, AL, United States, [3]Department of Earth, Planetary, and Space Sciences, University of California, Los Angeles, Los Angeles, CA, United States

Mesoscale (on the scales of a few minutes and a few R_E) magnetosheath and magnetopause perturbations driven by foreshock transients have been observed in the flank magnetotail. In this paper, we present the 3D global hybrid simulation results to show qualitatively the 3D structure of the flank magnetopause distortion caused by foreshock transients and its impacts on the tail magnetosphere and the ionosphere. Foreshock transient perturbations consist of a low-density core and high-density edge(s), thus, after they propagate into the magnetosheath, they result in magnetosheath pressure perturbations that distort magnetopause. The magnetopause is distorted locally outward (inward) in response to the dip (peak) of the magnetosheath pressure perturbations. As the magnetosheath perturbations propagate tailward, they continue to distort the flank magnetopause. This qualitative explains the transient appearance of the magnetosphere observed in the flank magnetosheath associated with foreshock transients. The 3D structure of the magnetosheath perturbations and the shape of the distorted magnetopause keep evolving as they propagate tailward. The transient distortion of the magnetopause generates compressional magnetic field perturbations within the magnetosphere. The magnetopause distortion also alters currents around the magnetopause, generating field-aligned currents (FACs) flowing in and out of the ionosphere. As the magnetopause distortion propagates tailward, it results in localized enhancements of FACs in the ionosphere that propagate anti-sunward. This qualitatively explains the observed anti-sunward propagation of the ground magnetic field perturbations associated with foreshock transients.

Keywords: foreshock transients, magnetosheath perturbations, flank magnetopause distortion, compressional waves, field-aligned currents

OPEN ACCESS

Edited by:
Simon Wing,
Johns Hopkins University,
United States

Reviewed by:
Brandon Burkholder,
Embry–Riddle Aeronautical University,
United States
Primoz Kajdic,
National Autonomous University of Mexico, Mexico
Lucile Turc,
University of Helsinki, Finland

***Correspondence:**
Chih-Ping Wang
cat@atmos.ucla.edu
Xueyi Wang
wangxue@auburn.edu

Specialty section:
This article was submitted to Space Physics, a section of the journal Frontiers in Astronomy and Space Sciences

Received: *31 July 2021*
Accepted: *08 September 2021*
Published: *21 September 2021*

Citation:
Wang C-P Wang X, Liu TZ and Lin Y (2021) Impact of Foreshock Transients on the Flank Magnetopause and Magnetosphere and the Ionosphere. Front. Astron. Space Sci. 8:751244. doi: 10.3389/fspas.2021.751244

INTRODUCTION

Perturbations in front of the bow shock are more frequently observed in front of the quasi-parallel shock (the foreshock) and the perturbed region extends further upstream, as compared to those in front of the quasi-perpendicular shock. In this paper, the mesoscale perturbations generated in the foreshock are referred to as ion foreshock transients. There are many different types of foreshock transients with their time scales ranging from seconds to minutes and spatial scales ranging from foreshock ion gyroradius up to 10 R_E (Zhang and Zong, 2020). Almost all foreshock transient perturbations include a core with the number density and magnetic field strength lower than the

background solar wind values and compression edge(s) with the density and magnetic field strength higher than the solar wind values. Some foreshock transients may also include flow deflection. Some foreshock transients are generated by the kinetic interaction of energetic ions reflected from the bow shock with interplanetary magnetic field (IMF) discontinuities, such as foreshock bubbles (Omidi et al., 2010; Turner et al., 2013; Liu et al., 2015, 2016; Omidi et al., 2020; Turner et al., 2020), hot flow anomalies (Chu et al., 2017; Lin, 1997, 2002; Liu et al., 2017; Lucek et al., 2004; Omidi and Sibeck, 2007; Schwartz et al., 1985; Schwartz et al., 2018; Thomsen et al., 1986; Zhang et al., 2010; 2017), foreshock cavities (e.g., Sibeck et al., 2002, 2004; Schwartz et al., 2006; Billingham et al., 2008), and traveling foreshock (e.g., Kajdičet al., 2017), while some are formed without IMF discontinuities, such as diamagnetic cavities (Lin, 2003; Lin and Wang, 2005), foreshock cavitons (Omidi, 2007; Blanco-Cano et al., 2011; Kajdičet al., 2013), and spontaneous hot flow anomalies (Omidi et al., 2013; Zhang et al., 2013). The foreshock transients that do not have the density core are foreshock compressional boundary (e.g., Sibeck et al., 2008) and short large-amplitude magnetic structures (e.g., Schwartz, 1991). Some of the above transients, such as HFAs, can also be generated in front the quasi-perpendicular shock. Recent MHD simulations found that the bow shock response to transient density depleted regions in the solar wind can also result in structures that resemble HFAs (Otto and Zhang, 2021).

The density perturbations of foreshock transients result in perturbations in dynamic pressure. As the perturbations propagate into the magnetosheath, they can cause magnetopause distortion. The resulting magnetosheath perturbations and the impact on the dayside magnetopause have been simulated (e.g., Lin and Wang, 2005; Omidi et al., 2016; Sibeck et al., 2021)) and observed (e.g., Archer et al., 2014; 2015; Jacobsen et al., 2009; Kajdičet al., 2021; Sibeck et al., 1999; 2000). Similar to the impact of the solar wind dynamic pressure perturbations, the magnetopause distortion driven by foreshock transients can subsequently generate ultralow frequency (ULF) waves inside the magnetosphere (e.g., Hartinger et al., 2013; Wang et al., 2017; Wang et al., 2018b; Wang et al., 2019; Wang B. et al., 2020; Shi et al., 2021; Wang B. et al., 2021), enhance particle precipitation and the resulting aurora brightness (e.g., Fillingim et al., 2011; Wang et al., 2018a; Wang et al., 2018b; Wang et al., 2019), and enhance field-aligned currents (FACs) and the associated perturbations in ionospheric currents and ground magnetic field (e.g., Kataoka et al., 2002; Murr and Hughes, 2003; Fillingim et al., 2011; Shen et al., 2018).

Recent studies have extended our understanding of the foreshock transients to the nightside. In observations, Liu et al. (2020; 2021) reported foreshock transients observed in the midtail foreshock around X ~ −40 R_E. Using multi-point satellite measurements, Wang et al. (2018) showed that the perturbations driven by foreshock transients can propagate tailward within the flank magnetosheath to the midtail around X ~ −50 R_E and can cause transient flank magnetopause distortion. 3D global hybrid simulations have been conducted to investigate foreshock transients associated with an IMF directional rotational discontinuity (RD) (Wang C. P. et al., 2020) and tangential discontinuity (TD) (Wang C. P. et al., 2021). They showed the evolution of the foreshock transient perturbations as they propagate from the dayside to nightside foreshock and the associated magnetosheath perturbations in the flanks. In this paper, we use the simulation by Wang B. et al. (2021) to show qualitatively the 3D structure of the flank magnetopause distortion caused by foreshock transients and the impact on the magnetosphere and ionosphere. The results presented here should provide a qualitative understanding of the impacts common to the foreshock transients of different types since they all have the same features of density perturbations (low-density core and high-density edge). We also present two observation events to provide qualitative comparisons with the simulated magnetopause distortion and ionospheric perturbations.

SIMULATION

Wang B. et al. (2021) used the AuburN Global hybrId CodE in 3D (ANGIE3D) hybrid code (Lin et al., 2014) to simulate foreshock transients resulting from the interaction of an IMF directional TD (i.e., with direction change only) with the foreshock ions. The simulation model and setup for this simulation is described in *Simulation Model and Setup*. In *Magnetosheath Perturbations and Tailward Propagation*, *Dayside Magnetopause Distortion*, *Dayside Magnetopause Distortion*, *Flank Magnetopause Distortion*, *Impact on the Magnetosphere, Impact on the Ionosphere*, we present the simulation results for the tailward propagating magnetosheath perturbations, the magnetopause distortion on the dayside and the flank, and the impacts on the magnetosphere and the ionosphere.

Simulation Model and Setup

In the ANGIE3D code, the ions (protons) are treated as discrete, fully kinetic particles, and the electrons are treated as a massless fluid. Quasi charge neutrality is assumed. Detailed descriptions of the equations for ion particle motion, electric and magnetic fields and assumptions used in the ANGIE3D code are given in Lin et al. (2014). The code is valid for low-frequency physics with $\omega \sim \Omega_i$ and $k\rho_i \sim 1$ (wavelength $\lambda \sim 6\rho_i$), where ω is the wave frequency, k is the wave number, Ω_i is the ion gyrofrequency, and ρ_i is the ion Larmor radius.

The simulation domain is $25 \geq X \geq -60$, $60 \geq Y \geq -35$, $35 \geq Z \geq -45$ R_E in the geocentric solar magnetospheric (GSM) coordinates. Inflow time-dependent boundary conditions for the solar wind are specified at the sunward boundary and open boundary conditions are used for the rest of the outer boundaries. An inner boundary is assumed at the geocentric distance of $r \approx 3$ R_E. This inner boundary is composed of a zigzag grid line approximating the spherical surface as in global MHD simulations. For the region of the inner magnetosphere, a cold, incompressible ion fluid is assumed to be dominant in $r < 6$ R_E, which coexists with particle ions, since this simulation focuses on the dynamics and ion kinetic physics in the outer magnetosphere. The inclusion of the cold ion fluid in the inner magnetosphere simplifies the conditions for the fluid-dominant low-altitude,

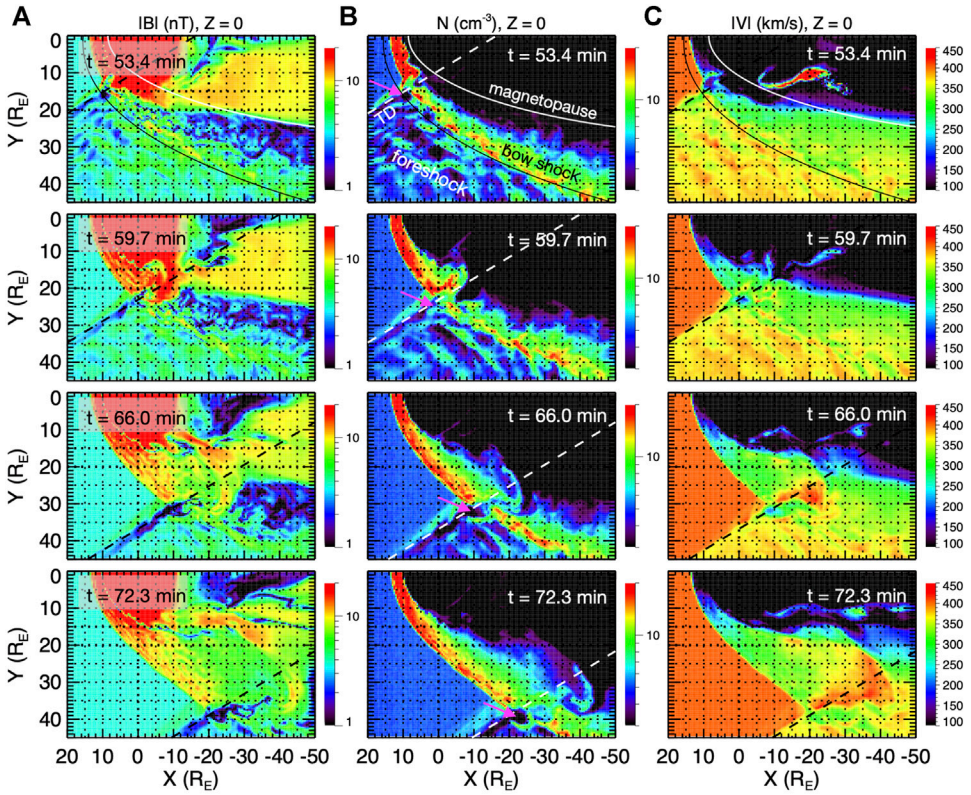

FIGURE 1 | Time sequences of the X-Y distributions from t = 53.4–72.3 min at Z = 0 for **(A)** magnetic field strength, **(B)** number density, and **(C)** ion bulk flow speed. The straight white or black dashed lines indicate the projection of the TD plane. The white curve in the top panel indicates the model magnetopause from Roelof and Sibeck (1993) and the black curve indicates the model bow shock from Peredo et al. (1995). The magenta arrows in **(B)** indicate the low-density core.

inner boundary. A combination of spherical and Cartesian coordinates is used at the inner boundary. We let particles be reflected at exactly r = 3 R_E. This simple reflection of the ion parallel velocity means that loss cone effects are omitted. The **E** and **B** fields at the boundary reside on the Cartesian boundary approximating the spherical boundary, which are extrapolated to an extra grid point inside the r = 3 R_E surface. The **B** field is assumed to maintain the dipole field values at the inner boundary.

The ionospheric conditions (1,000 km altitude) are incorporated into the ANGIE3d code. The FACs, calculated within the inner boundary, are mapped along the geomagnetic field lines into the ionosphere as input to compute ionospheric potential. For this simulation, simplified ionospheric conductance with uniform Pederson conductance of 10 siemens and Hall conductance of 5 siemens is specified.

The TD is specified as a planar IMF discontinuity with a half-width of 0.12 R_E and the normal direction of (−0.5, 0.86, 0). The TD propagates with a velocity of (−400, 0, 33.7) km/s. At t = 0, the TD plane intersects the Y = 0 axis at X = 185 R_E. Unless otherwise noted, downstream (upstream) of the TD in this paper indicates the anti-sunward (sunward) side of the TD. The downstream IMF direction is (3, 1.7, 0) nT and upstream IMF is (0, 0, −3.4) nT. Constant solar wind density of 5 cm^{-3} and isotropic solar wind ion temperature of 10 eV are used. The solar wind velocities are (−370.7, 16.8, 33.7) km/s downstream and (−400, 0, 0) km/s upstream. The average solar wind Alfvén Mach number is M_A = 11.8. These solar wind values are within the typically observed ranges. To accomplish this large-scale simulation with the available computing resources and can still produce physical results, we choose the solar wind d_i to be 0.1 R_E (about 6 times larger than the realistic value) and the cell dimensions to be $n_x \times n_y \times n_z$ = 502 × 507 × 400. Also, we use time-independent nonuniform cell sizes (ranging from ~0.1 to 0.5 R_E) so that we can appropriately assign cell sizes comparable to the d_i values in different key regions from the solar wind to the outer magnetosphere. The bow shock and magnetopause form self-consistently by the interaction of the solar wind with the geomagnetic dipole. Before the arrival of the TD, the bow shock nose is at X ~14 R_E and the magnetopause nose is at X ~10 R_E, similar to the realistic locations.

Magnetosheath Perturbations and Tailward Propagation

Figures 1A–C show the 2D profiles of the magnetic field strength (|B|), ion density (N), and ion bulk flow speed (|V|), respectively, in the X-Y plane at Z = 0 at four different times from t = 53.4–75.3 min (see also **Supplementary Movie S1** in Supplementary Material). The simulated magnetopause and bow shock are disturbed, so we also add in the t = 53.4 min

plots two smooth model boundaries, the magnetopause locations predicted by Roelof and Sibeck (1993) and the bow shock locations predicted by Peredo et al. (1995), as visual references to help readers discern the magnetosheath perturbations. In this stimulation, before the arrival of the TD, the foreshock is mainly on the duskside extending from the dayside to the nightside. Note that there are weak perturbations in the foreshock and the magnetosheath due to the foreshock ULF waves. The TD first encounters the foreshock ions just outside the dayside bow shock at t ~44 min and foreshock transient perturbations are formed (see Wang B. et al. (2021) for more details about the initiation of the foreshock transient). The foreshock transient perturbations consist of a core with lower density, higher temperature, lower magnetic field strength, and lower anti-sunward bulk flow speed than the values of the solar wind. An edge with relatively higher density and higher magnetic field strength is on the upstream side of the core. As the TD (indicated by the black or white dashed straight lines) propagates tailward, it continues to interact with the foreshock ions and generate perturbations around the TD (the low-density core is indicted by magenta arrows in **Figure 1B**). The perturbations newly generated just outside the bow shock subsequently enter the magnetosheath via their anti-sunward flows and continue to propagate anti-sunward. Note that these magnetosheath perturbations associated with the foreshock transients are the focus of this paper, not the pre-existing perturbations associated with the foreshock ULF waves.

Figure 1 shows the tailward propagation of the magnetosheath plasma and magnetic field perturbations resulting from foreshock transients. In the near-Earth region, as shown in the t = 53.4 and 59.7 min plots, the structures of magnetosheath perturbations are approximately aligned with the TD plane (the black or white dashed line). The perturbations seen closer to the magnetopause are associated with the foreshock transient perturbations that are generated and enter the magnetosheath earlier, while those seen closer to the bow shock are associated with the foreshock transient perturbations that are generated and enter the magnetosheath more recently. The newer perturbations coming into the magnetosheath interact nonlinearly with those further inside, leading to changes in the spatial structures of the perturbations across the magnetosheath. In this simulation, the foreshock region extends to the nightside. Thus, as the TD propagates from the near-Earth to the midtail, as shown in the t = 66 and 72.3 min plots, there are still new foreshock transient perturbations being continuously added into the flank magnetosheath. As a result, the magnetosheath perturbations are still strong in the midtail. Compared to the earlier magnetosheath perturbations in the near-Earth flank shown in the t = 59.7 min plots, which are more spatially confined around the TD plane and have well-defined structures, the spatial size of the mid-tail magnetosheath perturbations shown in the t = 72.3 min plots have become larger and their spatial structures become complex because of the nonlinear interaction described above.

Dayside Magnetopause Distortion

Figure 2 compares the dayside magnetosheath and magnetopause before the arrival of the TD at t = 45.6 min with those associated with the magnetosheath perturbations at t = 52.8 min. As shown in **Figures 2A–E** for the X-Y distributions at Z = 0, at t = 45.6 min, there are small and localized perturbations in both the magnetosheath plasma and the magnetopause shape (black or white curves) associated with the foreshock ULF waves. The dayside magnetopause locations are determined by tracing magnetic field lines from Z = 0 and the field lines in the dayside magnetosphere are closed (both ends of the field lines are in the ionosphere). At t = 52.8 min, the low-density core and high-density edge can be seen in the new perturbations forming outside the bow shock as well as in the magnetosheath perturbations that have entered the magnetosheath earlier (**Figure 2B**). The magnetic field strength is lower inside the core and higher at the edge (**Figure 2A**). **Figure 2C** shows different flow speeds and directions for the core and edge, which would later cause the spatial extents of the core and edge regions to change as they propagate tailward. As a result of the lower density and flow speed within the core than at the edge, both the thermal pressure (P_{th}) and the dynamic pressure along the direction normal to the magnetopause ($P_{dyn,n}$) (the magnetopause normal direction in this paper is estimated using the model magnetopause of Roelof and Sibeck (1993)) are relatively lower within the core and higher at the edge. As shown in **Figure 2D**, the dayside magnetopause and magnetosphere intrude locally outward for ~3 R_E into the magnetosheath in response to the lower P_n ($P_n = P_{th} + P_{dyn,n}$) of the core and are distorted locally inward for ~1 R_E by the stronger P_n of the edge. The outward intruding magnetosphere is indicated by the plasma with relatively higher magnetic field strength (**Figure 2A**) and lower density (**Figure 2B**) than the surrounding magnetosheath plasma. **Figure 2E** shows the perpendicular current density. It shows that the magnetosheath perturbations at t = 52.8 min results in strong perpendicular currents along the distorted magnetopause. **Figures 2F,G** show the 2D X(Y)-Z profiles along the white dashed line indicated in **Figure 2A** (the TD plane at t = 52.8 min). The magnetopause outward distortion is seen mainly in the region of $|Z| < \sim 5$ R_E with the maximum distortion near Z = 0. The 1D profiles at Z = 0 along the white dashed line indicated in **Figure 2A** are shown in **Figures 2H–K**. Comparing the 1D profiles between t = 45.6 and 52.8 min clearly show the changes in magnetic field components, flow velocity components, and pressure components outside the magnetopause (vertical magenta dashed lines) associated with the low-density core.

Flank Magnetopause Distortion

Figure 3 compares the X-Y distributions of the nightside magnetosheath and magnetosphere at Z = 0 at t = 45.6 with those at t = 60 min when the magnetosheath perturbations have propagated to the nightside around X = −10 R_E. The magnetosheath perturbations at t = 60 min are seen to be around the TD line (white dashed line). Similar to the dayside magnetopause distortion shown in **Figure 2**, the magnetopause (indicated by white dashed line) intrudes locally outward into the magnetosheath around X = −10 R_E in response to the low-density core of the magnetosheath perturbations while it is distorted inward around X = −7 R_E in response to the high-density edge. In

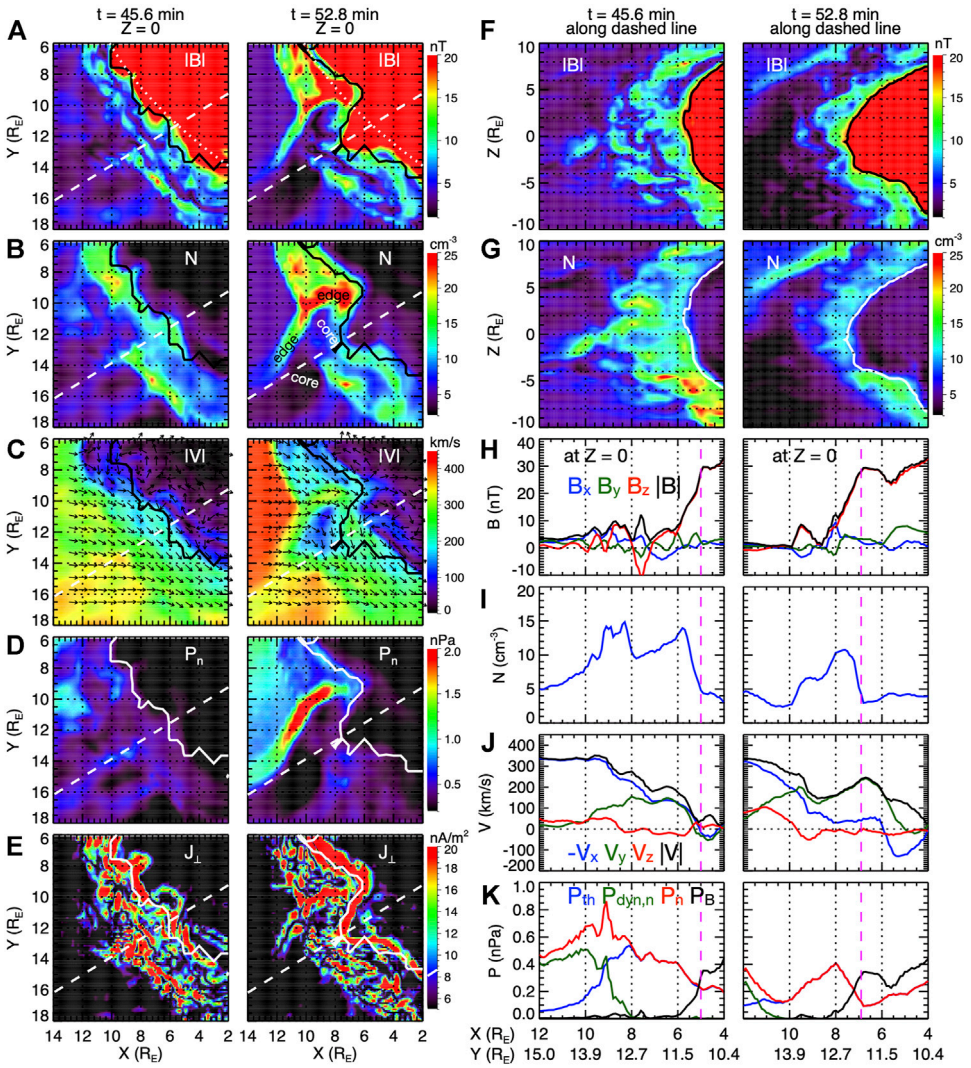

FIGURE 2 | The X-Y distributions at Z = 0 for **(A)** magnetic field strength, **(B)** number density, **(C)** ion bulk flow speed and flow directions (black arrows), **(D)** pressure along the direction normal to the model magnetopause, **(E)** perpendicular current density at t = 45.6 **(left panels)** and 52.8 min **(right panels)**. The straight white dashed lines indicate the projection of the TD plane at t = 52.8 min. The black or white curves in **(A–G)** indicate approximately the simulated magnetopause. The white dotted curves in (a) indicates the model magnetopause based on Roelof and Sibeck (1993). **(F–K)** The 2-D and 1-D profiles at t = 45.6 **(left)** and 52.8 min **(right)** along the TD plane at t = 52.8 min indicated in (a): The 2-D profiles for **(F)** magnetic field strength and **(G)** number density. The 1-D profiles at Z = 0 for **(H)** magnetic field components, **(I)** number density, **(J)** ion bulk flow velocities, and **(K)** pressures. The magenta dashed line in **(H)–(K)** indicate approximately the magnetopause.

determining the nightside magnetopause boundaries shown in **Figure 3** and later in **Figures 4**, **5**, we investigate the magnetosonic Mach number from the magnetosheath to the magnetosphere and use the location of a quick drop in the Mach number values to below a certain threshold as the approximate location for the magnetopause boundary. The outward intruding magnetosphere can be seen by the plasma with relatively higher magnetic field strength (**Figure 3A**), lower density (**Figure 3B**), and higher temperature (**Figure 3C**) than the surrounding magnetosheath plasma. Different from the slow-flowing plasma deep within the magnetosphere, the intruding magnetospheric plasma has a strong tailward flow speed (**Figure 3D**). **Figure 3E** shows the changes in the perpendicular current density within the magnetosphere associated with the distorted magnetopause. This results in FACs flowing into and out of the ionosphere, as described later in *Impact on the Ionosphere*. **Figure 3F** shows the 3D view of the number density distributions at t = 60 min from three different viewing angles together with the magnetic field lines. As indicated by the closed magnetic field lines (red), the plasma sheet is seen within the outward intruding magnetosphere. The field lines in the magnetosheath tailward of the intruding magnetosphere are open field lines (purple, with one end connecting to the Earth) due to open flank magnetopause resulting from the duskward IMF downstream of the discontinuity, while those earthward of the intruding

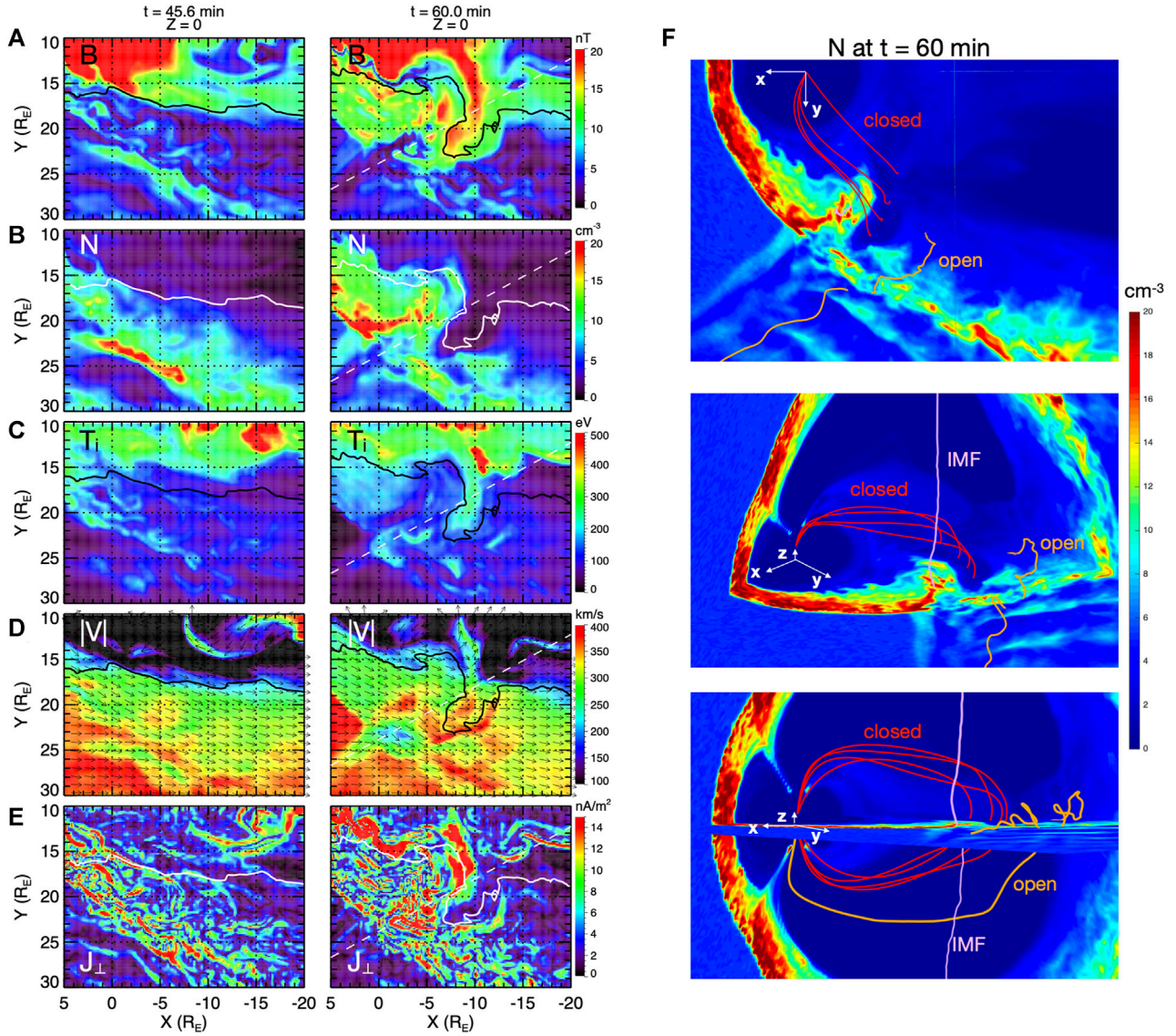

FIGURE 3 | The X-Y distributions at Z = 0 for **(A)** magnetic field strength, **(B)** number density, **(C)** ion temperature, **(D)** ion bulk flow speed and flow directions (black arrows), and **(E)** perpendicular current density at t = 45.6 **(left panels)** and 60 min **(right panels)**. The black or white curves indicate approximately the magnetopause boundary. The straight white dashed lines in the **left panels** indicate the projection of the TD plane at t = 60 min. **(F)** Number density distributions at t = 60 min viewing from three angles. The red curves indicate closed magnetic field lines, the orange lines indicate open magnetic field lines, and light pink lines indicate IMF field lines.

magnetosphere are IMF field lines (light pink) corresponding to the southward IMF upstream of the discontinuity.

The 3D structure of the outward intruding magnetosphere at t = 60 min shown in **Figure 3** can be better constructed with the 2D Y-Z and X-Z distributions cutting through the intrusion shown in **Figures 4A,B,G,H**, respectively (see also **Supplementary Movie S2** in Supplementary Material). The magnetopause is distorted mainly in the region from Z ~ −10 to 10 R_E with the maximum outward distortion at Z ~0 (**Figures 4A,B**) so that the cross-section in the *X* direction is the widest near Z = 0 (**Figures 4G,H**). The Y-profiles of plasma and magnetic field along the cutting plane at Z = 0 are shown in **Figures 4C–F**. As indicated by the vertical magenta dashed line, the magnetopause boundary moves outward from Y ~18 to 24 R_E during the distortion. **Figures 4I–M** show the X-profiles at Z = 0 along Y = 21 R_E. The X scale of the intruding magnetosphere is ~6 R_E.

Figures 5A–C show the time sequence of the flank magnetopause (white solid curves) distortion in the X-Y, X-Z, and Y-Z planes, respectively. The white dotted curves in **Figures 5A,C** indicate the magnetopause at t = 45.6 min. Note that the magnetopause boundary shape can appear filamentary at some locations. This is associated with fine structures of the magnetosheath perturbations in the magnetic field strength and flow speed, which resulting in fine structures in the magnetosonic Mach number distributions used in determining the approximate magnetopause boundary. **Figure 5** shows that as

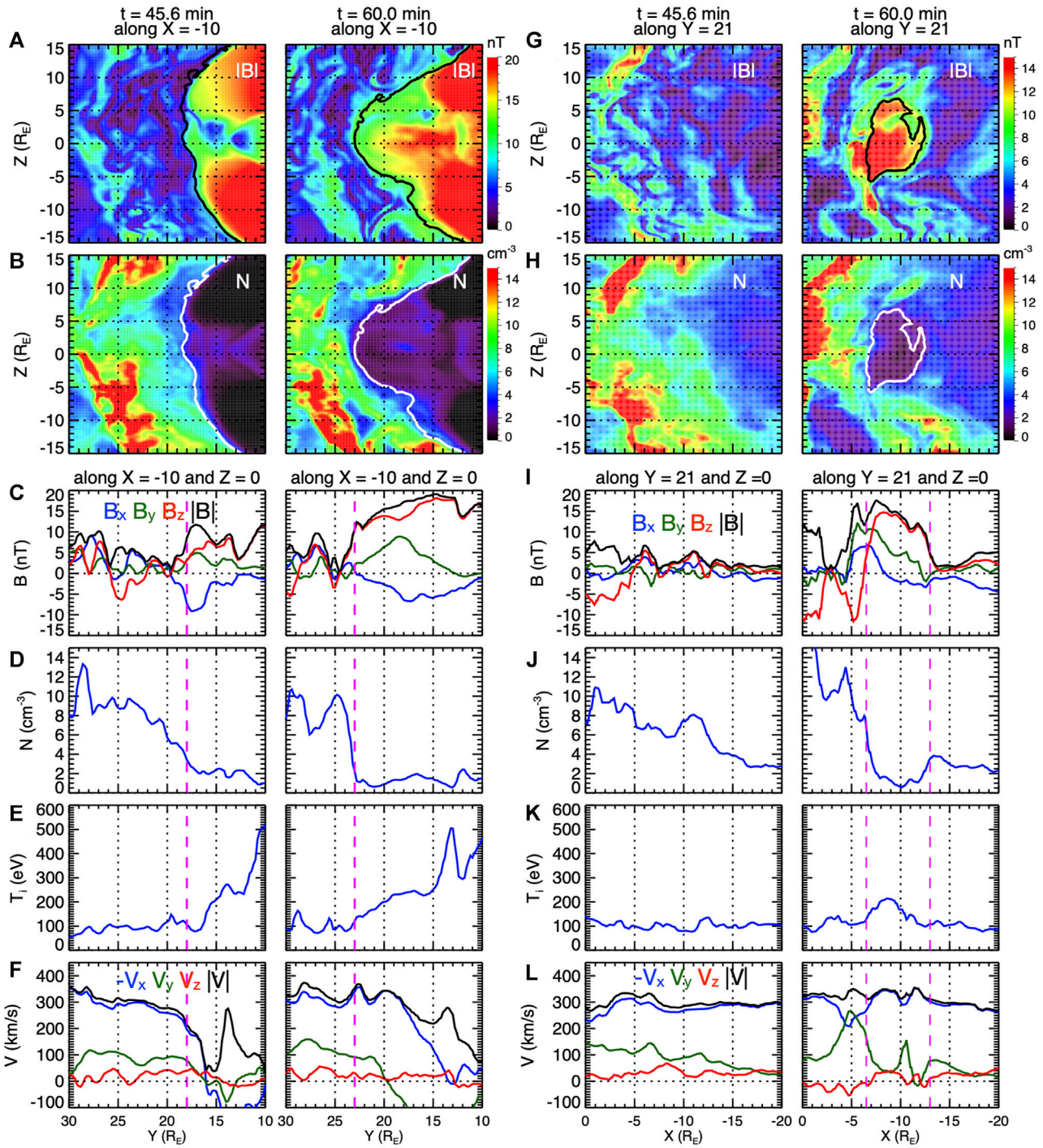

FIGURE 4 | The Y-Z distributions at X = −10 R_E for **(A)** magnetic field strength and **(B)** number density and the Y profiles at X = −10 and Z = 0 R_E for **(C)** magnetic field components, **(D)** number density, **(E)** ion temperature, and **(F)** ion bulk flow velocities at t = 45.6 **(left panels)** and 60 min **(right panels)**. The X-Z distributions at Y = 21 R_E for **(G)** magnetic field strength and **(H)** number density and the X profiles at Y = 21 and Z = 0 R_E for **(I)** magnetic field components, **(J)** number density, **(K)** ion temperature, and **(M)** ion bulk flow velocities at t = 45.6 **(left panels)** and 60 min **(right panels)**. The white or black curves in **(A–B)** and **(G–H)** indicate approximately the magnetopause boundary. The vertical magenta dashed lines in **(C–F)** and **(I–M)** indicate the magnetopause.

the magnetosheath perturbations move tailward from X ~ −10 to X ~ −40 R_E, they continue to distort the magnetopause. As described in *Magnetosheath Perturbations and Tailward Propagation*, the spatial structures of magnetosheath perturbations change substantially as they propagate tailward, thus the 3D structure of the outward intruding magnetosphere in

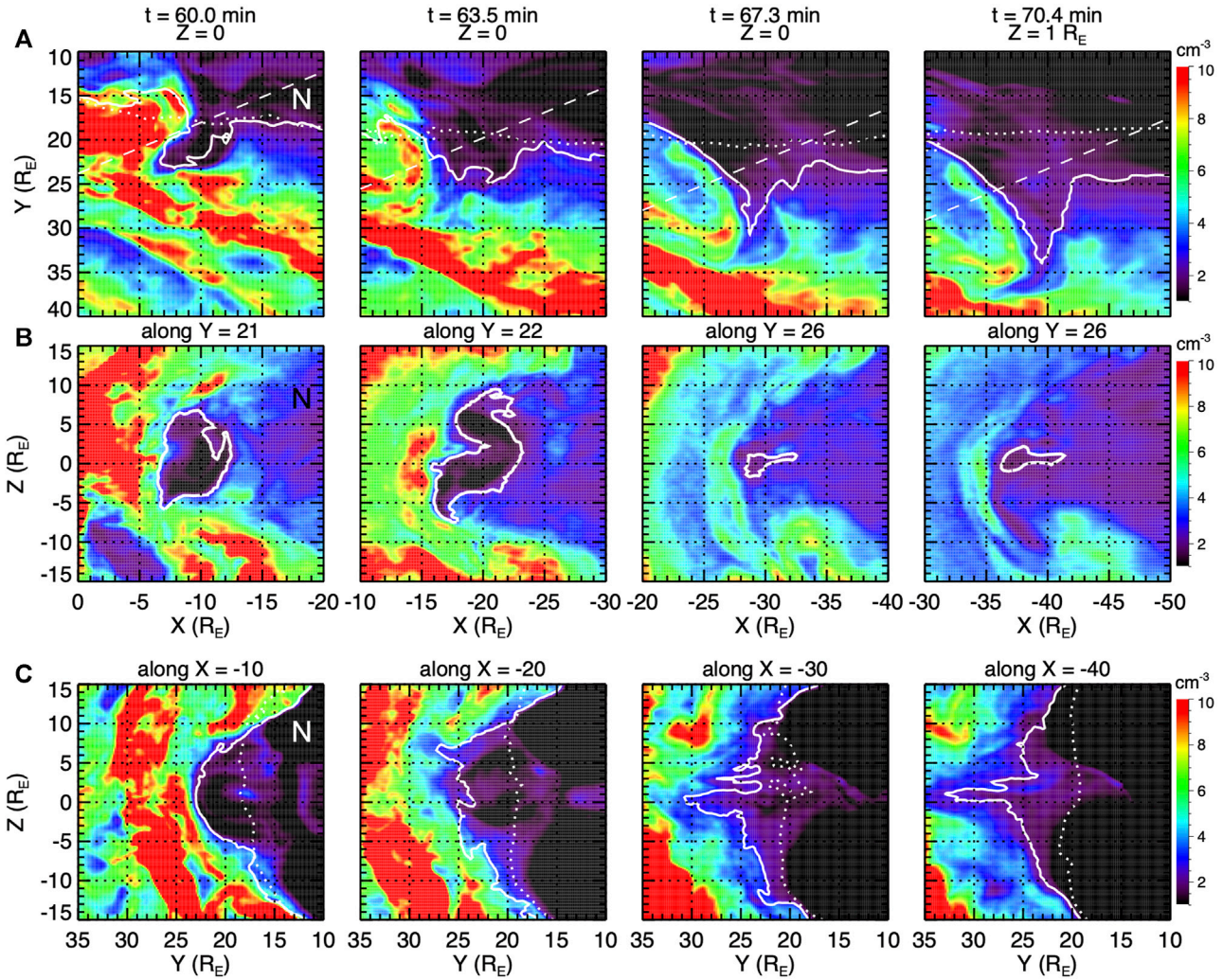

FIGURE 5 | Time sequences of number density distributions in **(A)** X-Y, **(B)** X-Z, and **(C)** Y-Z planes from t = 60–70.4 min. The white solid curves indicate approximately the magnetopause. The white dotted curves in **(A)** and **(C)** indicate the magnetopause at t = 45.6 min. The straight white dashed lines in **(A)** indicate the projection of the TD plane.

the midtail (t = 70.4 min plot) is quite different from the earlier structure in the near-Earth tail (t = 60 min plot). The maximum outward intrusion remains around Z = 0 and it extends farther out in the Y direction with increasing downtail distances. The localized structure of the outward distortion shown in **Figure 5** indicates that a satellite in the magnetosheath may observe the outward intruding magnetosphere with the probability strongly depending on the satellite locations.

Figure 6 shows the temporal profiles of magnetic field components, number density, ion temperature, and ion bulk flow velocities that would be observed by a virtual satellite in the magnetosheath at three downtail distances at Z ~0. Because of the passing of the localized outward magnetopause distortion, the virtual satellite would observe transient appearance of the magnetosphere, as indicated by the magnetic field strength, density, and temperature changing from the magnetosheath values to the magnetospheric values and then return to the magnetosheath values. These temporal profiles are qualitatively similar to the perturbations observed in the midtail magnetosheath at X = −54 R_E reported by Wang et al. (2018). Another observation event in the flank magnetosheath closer to the Earth is shown in *An Event for Flank Magnetopause Distortion*.

Impact on the Magnetosphere

The localized and transient magnetopause distortion affects the magnetic field within the magnetosphere. **Figure 7** shows a time sequence of the Y-Z distributions at X = −10 R_E from the dusk flank to midnight for number density (**Figure 7A**), magnetic field strength (**Figure 7B**), amplitudes of the magnetic field perturbations in the parallel direction (**Figure 7C**), and perpendicular current strength (**Figure 7D**). The magnetic field perturbations shown in **Figure 7C** are obtained by subtracting the 10 min running averages. To better show the

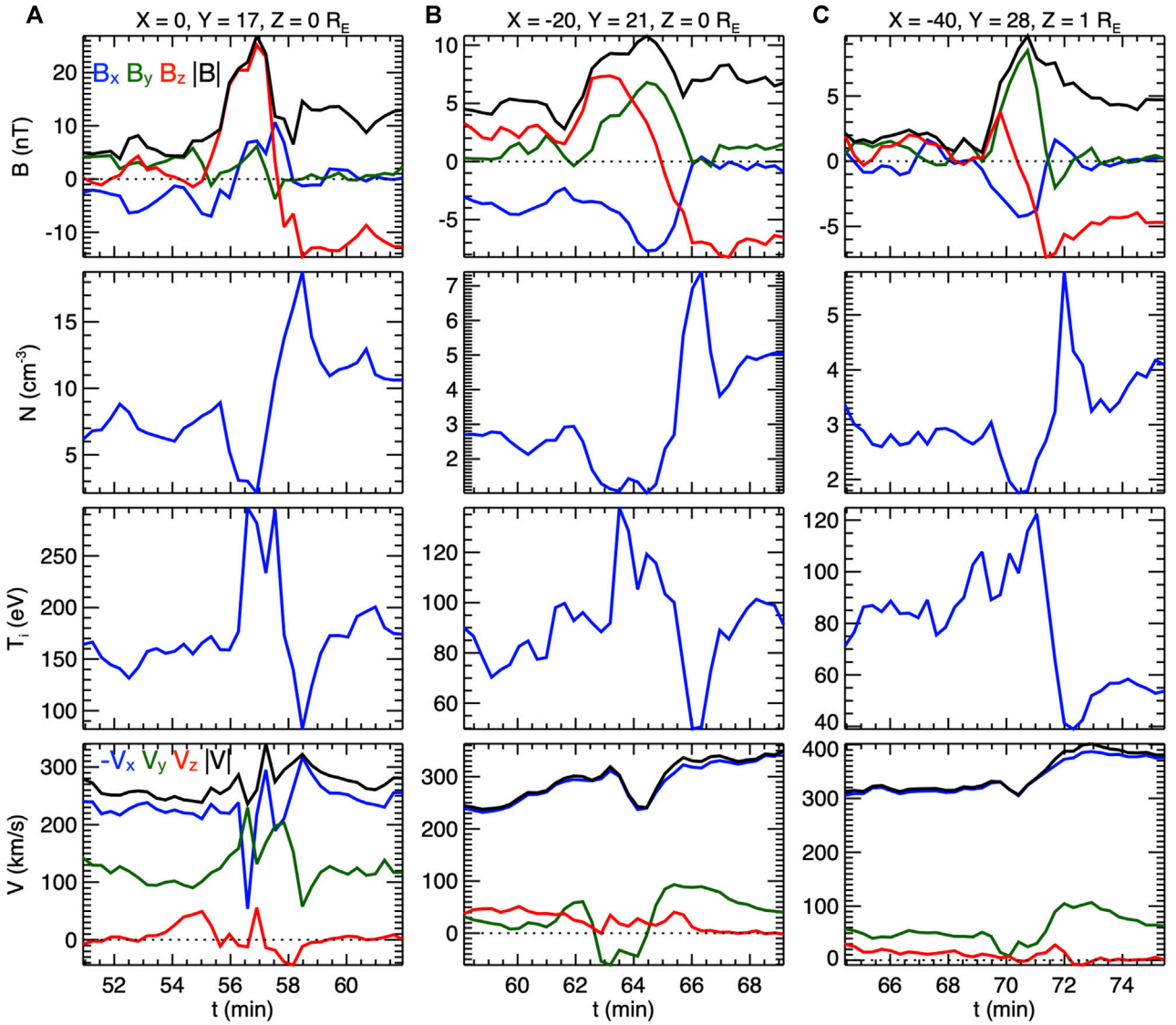

FIGURE 6 | Temporal profiles at **(A)** X = 0, Y = 17, and Z = 0 R_E, **(B)** X = –20, Y = 22, and Z = 0 R_E, and **(C)** X = –40, Y = 28, and Z = 1 R_E. From **top** to **bottom**: Magnetic field components, number density, ion temperature, and ion bulk flow velocities.

perturbations associated with waves propagating through a relatively uniform background, only the perturbations in the northern lobe where B_x >15 nT are plotted in **Figure 7C**. As shown in the t = 45.6 min plot for before the arrival of the magnetopause distortion, there are weak magnetic field perturbations within the magnetosphere. These are due to the small magnetopause disturbances associated with the foreshock ULF waves, like that seen on the dayside as shown in **Figure 2A** for t = 45.6 min. As the magnetopause distortion passes through X = –10 R_E, as shown in the t = 59.7 – t = 61.6 min plots in **Figure 7**, the magnetic field perturbations within the magnetosphere are enhanced. The enhancements are seen to extend from the dusk flank into the magnetosphere. Compared to the enhancements when the magnetopause is distorting outward around t ~60 min, the perturbations generated by the inward magnetopause distortion around t = 61.3 min are stronger and deeper into the magnetosphere. This shows that the magnetopause distortion driven by foreshock transients can launch compressional waves within the magnetosphere, which qualitatively explains the observed enhancements in magnetospheric ULF waves associated with foreshock transients (e.g., Hartinger et al., 2013; Wang et al., 2017; Wang et al., 2018b; Wang et al., 2019; Wang B. et al., 2020).

As shown in **Figure 7B**, the inward and outward motion of the distorted magnetopause alters the magnetospheric magnetic field near the flank in Y >~10 R_E. This causes transient changes in the perpendicular currents in the flank magnetosphere shown

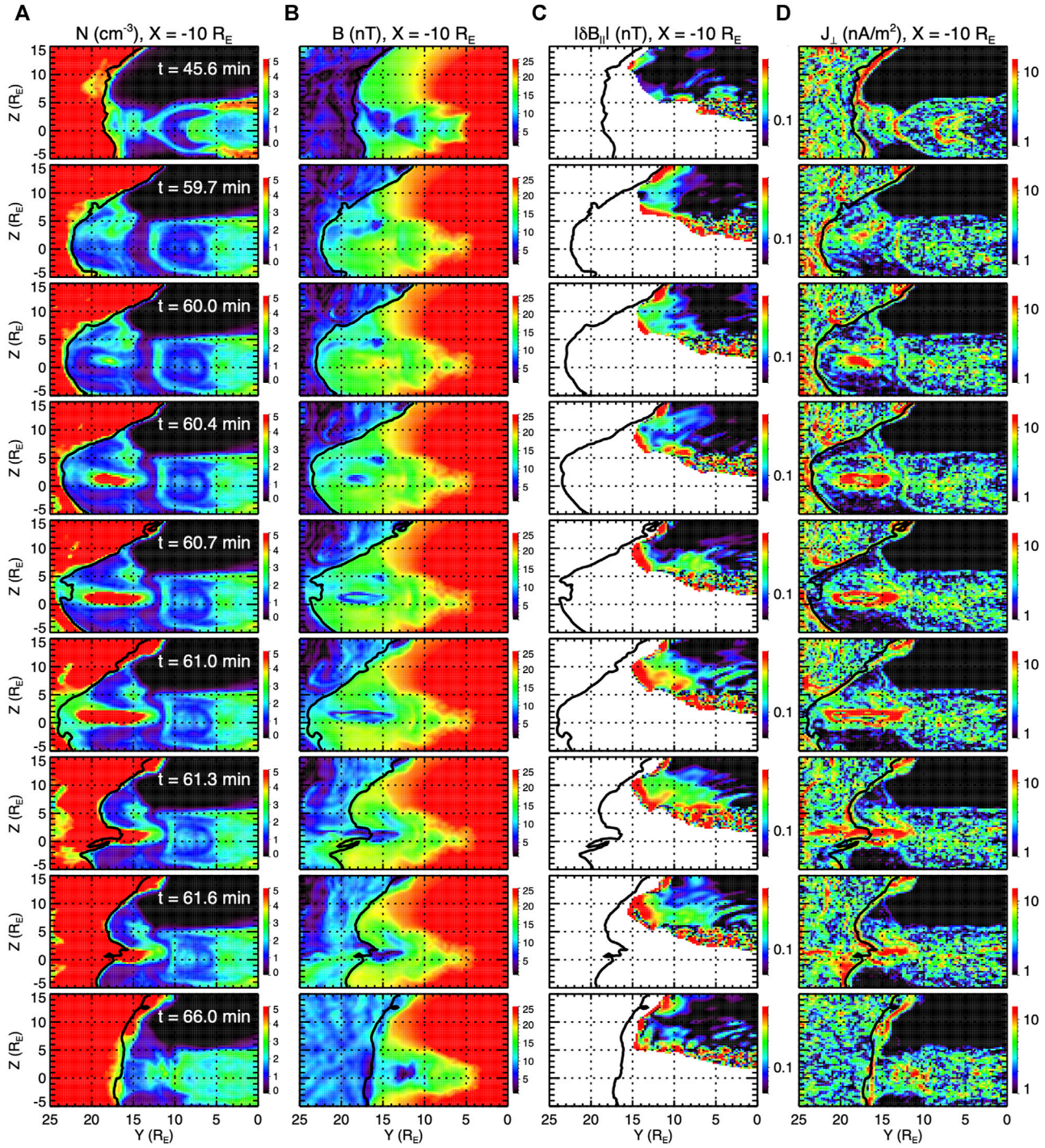

FIGURE 7 | Time sequences of the Y-Z profiles at X = −10 R_E from t = 45.6–66 min for **(A)** number density, **(B)** magnetic field strength, and **(C)** the amplitudes of magnetic field perturbations in the parallel direction in the northern lobe where B_x >15 nT, and **(D)** perpendicular current density. The black curves indicate approximately the magnetopause.

Figure 7D as well as FACs flowing into or out of the ionosphere in order to maintain current continuity, establishing impact on the ionosphere. The resulting FAC perturbations in the ionosphere are shown in *Impact on the Ionosphere*.

Impact on the Ionosphere

Figures 8A,B show the FACs and FAC perturbations at t = 60 min, respectively, in the Northern Hemisphere (N.H.) ionosphere (positive value indicates FACs flowing into the

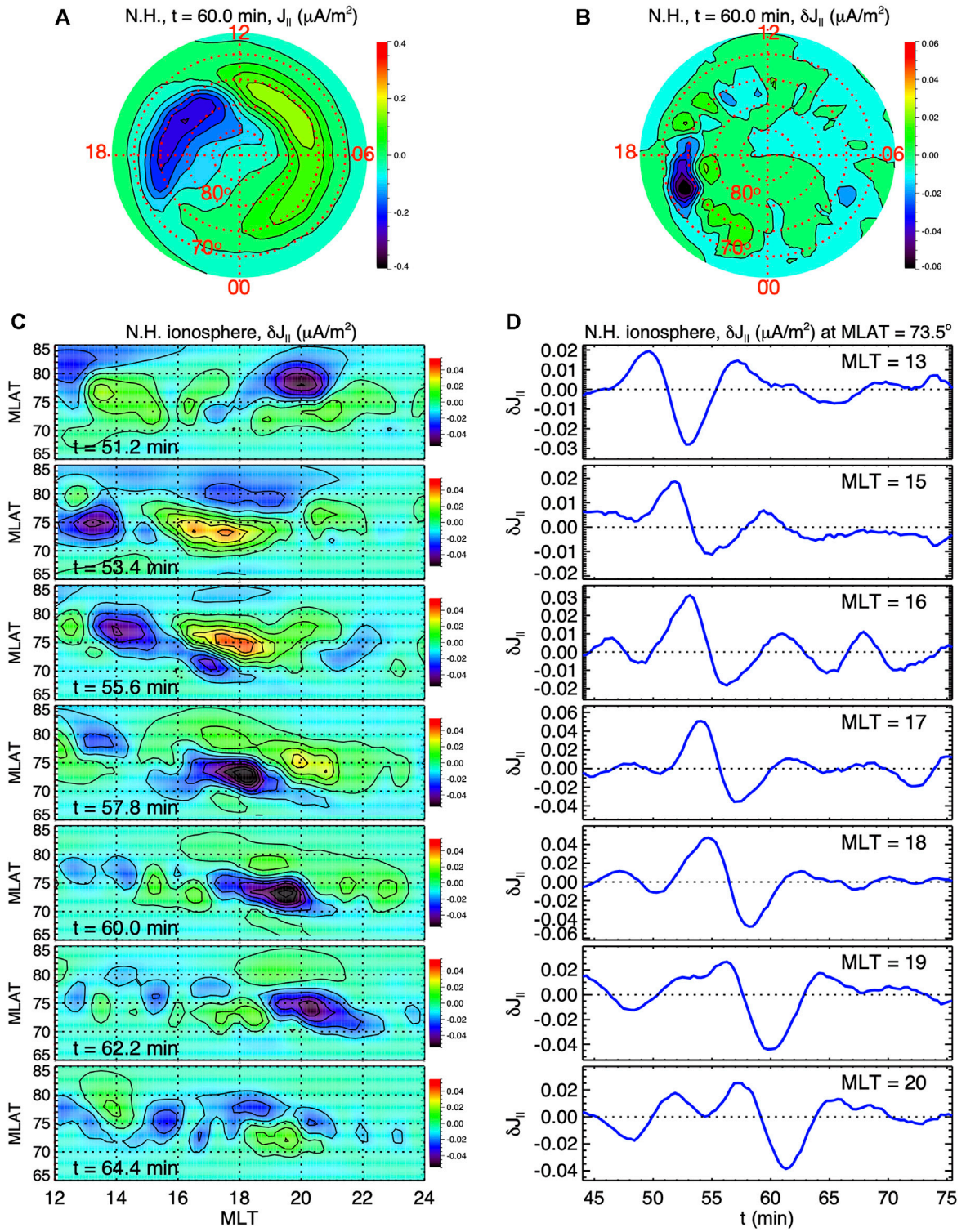

FIGURE 8 | (A) FAC and **(B)** FAC perturbations at t = 60 min in N.H. **(C)** Time sequences of the MLAT-MLT distributions for the FAC perturbations in the ionosphere from t = 51.2–64.4 min **(B)** Time series of the FAC perturbations at different MLTs along MLAT = 73.5°.

N.H. Ionosphere). The FAC perturbations are obtained by subtracting the 10 min averages of the FACs in the ionosphere. The FAC spatial distribution shown in **Figure 8A** has currents flowing into (out of) the ionosphere on the dawnside (duskside), which is the large-scale region-1 FACs connecting to the magnetosphere near the magnetopause. **Figure 8B** shows that

the FAC perturbations are spatially localized. **Figure 8C** shows the time sequence of the ionospheric FAC perturbations in N.H. as a function of MLT and MLAT. **Figure 8D** shows the time series of N.H. FAC perturbations at different duskside MLT locations along MLAT = 73.5. **Figures 8C,D** show that the region of enhanced FAC perturbations moves anti-sunward from near noon toward later MLTs, which is consistent with the tailward propagation of the flank magnetopause distortion. At t = 60 min, FAC perturbations have moved to nightside at ~18–20 MLT when the magnetopause distortion has propagated to nightside at X ~ −10 R_E. The FAC perturbations would result in perturbations in the horizontal currents flowing in the ionosphere due to the current continuity, both would generate magnetic field perturbations on the ground.

Note that simplified and spatially uniform ionospheric conductance is used in this simulation and we do not further evaluate the simulated ionospheric horizontal currents. The spatial distributions of the simulated ionospheric potential pattern and FACs corresponding to this uniform conductance do not have day-night and dawn-dusk asymmetries as realistic as those corresponding to non-uniform conductance that accounts for EUV and aurora contribution (Ridley et al., 2004). We expect that using realistic EUV- and aurora-generated conductance would shift the MLT and MLAT locations as well as the amplitudes of the perturbations in FAC and horizontal currents, but it would not affect their physical connection with the flank magnetopause distortion presented above. The simulated FAC perturbations seen at a fixed ionospheric location shown in **Figure 8D** should still provide a qualitative explanation for the observed ground magnetic field perturbations associated with foreshock transients (e.g., Shen et al., 2018). An observation event for ground magnetic field perturbations propagating to the nightside is shown in *An Event for the Ionospheric Disturbances*.

OBSERVATION EVENTS

In this section, we present two observation events associated with foreshock transients for qualitative comparisons with the simulated flank magnetopause distortion and ionospheric perturbations presented in *Simulation*. The first event shows transient appearance of the magnetosphere observed in the flank magnetosheath. The second event shows simultaneous observations of the magnetosheath perturbations and ground magnetic field perturbations.

An Event for Flank Magnetopause Distortion

We present in **Figure 9** an observation event for transient flank magnetopause distortion driven by a foreshock transient on May 31, 2018. **Figures 9A,B** show that Geotail was in the solar wind, Cluster was in the dawnside magnetosheath at X ~ 0 (data from Cluster C4 probe are used), and MMS was also in the dawnside magnetosheath further down the tail at X ~ −18 R_E (data from MMS-3 probe are used). Both Cluster and MMS were near Z = 0. **Figures 9C,D** show that Geotail observed two IMF directional discontinuities (no change in the IMF strength) at ~21:50 and 21:54 UT (indicated by the two vertical dashed lines), respectively. There were no changes in the solar wind density (**Figure 9D**), temperature (**Figure 9E**), and flow speed (**Figure 9F**) across the discontinuities. The IMF B_x was positive and IMF B_y was negative between the two discontinuities. The same discontinuities were also observed earlier at ~21:05 UT by WIND at X ~ 200 R_E (not shown) and the normal direction of the discontinuities estimated using the WIND-Geotail pair is (−0.85, 0.12, 0.5). This IMF condition would result in a foreshock cavity on the dawnside. The discontinuities later arrived at Cluster at ~22:05 UT (**Figure 9G**). The ~15 min delay from Geotail to Cluster is expected from the propagation of the discontinuities being slowed down after they entered the dayside magnetosheath (for example, see **Figure 3A** of Wang C. P. et al. (2020) for the propagation of an RD in the magnetosheath). Between the discontinuities, Cluster observed perturbations (yellow shaded region) with a core of low density (**Figure 9H**) and low magnetic field strength (**Figure 9G**), slight flow deflection (a slight decrease in $|V_x|$ and increase in $|V_y|$) (**Figure 9I**), and some superthermal ions at ~ 10 keV (**Figure 9J**). An edge of slightly higher magnetic field strength and density was seen next to the core (red shaded region at ~22:08 UT in **Figures 9G,H**). These confirm the magnetosheath perturbations associated with the expected foreshock transient. Even though the type of the foreshock transient in this event is different from that of this simulation, the observed magnetosheath perturbations are qualitatively similar to the simulated perturbations shown in **Figure 2** in the dayside magnetosheath. This is expected since, as described in Introduction, almost all types of foreshock transients exhibit the same characteristics in their density and magnetic field perturbations.

As the discontinuities and the magnetosheath perturbations observed at the Cluster location moved to the MMS location at ~22:13 UT (**Figure 9K**), MMS observed transient appearance of the magnetosphere (yellow shaded region). The magnetosphere is indicated by that the values for the low density (**Figure 9M**) and high temperature (**Figure 9N**) within the yellow shaded region are typical for magnetospheric plasma. This change from the magnetosheath to the magnetosphere can also be seen in the sharp increases of ion fluxes at >10 keV and decreases at <2 keV shown in **Figure 9P**. This magnetospheric plasma seen intruding outward into the magnetosheath has substantial tailward flow speed, which is qualitatively consistent with the simulations shown in **Figure 6B**.

An Event for the Ionospheric Disturbances

We present in **Figure 10** an observation event for ground magnetic field perturbations associated with a foreshock transient on January 20, 2010. This event has been reported by Wang et al. (2018) and they have shown simultaneous satellite observations of the event in the solar wind, foreshock, and flank magnetosheath. For this event, the driver discontinuity was observed by WIND in the solar wind. Geotail was on the dayside in the foreshock (the location is indicated in

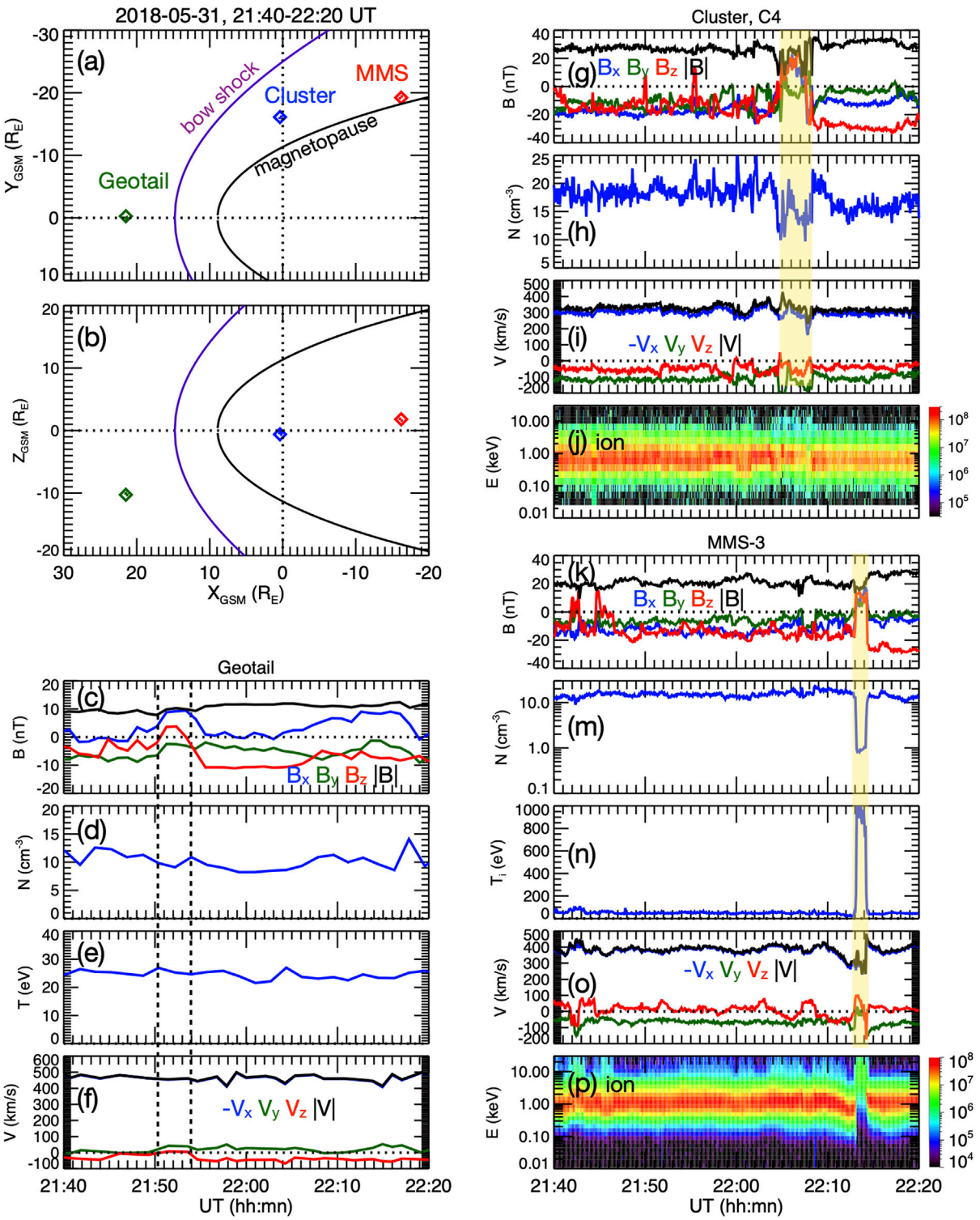

FIGURE 9 | A foreshock transient event on May 31, 2018. The projections of the locations of Geotail, Cluster C4, and MMS-3 on **(A)** X-Y and **(B)** X-Z planes. Geotail observations of **(C)** magnetic field components, **(D)** number density, **(E)** ion temperature, and **(F)** ion bulk flow velocities. The two vertical dashed lines indicate the two discontinuities. Cluster observations of **(G)** magnetic field components, **(H)** number density, **(I)** ion bulk flow velocities, and **(J)** ion energy flux (eV/(s-sr-cm^2-eV)). The shaded yellow and red region indicate the core and edge of the magnetosheath perturbations, respectively. MMS observations of **(K)** magnetic field components, **(M)** number density, **(N)** ion temperature, **(O)** ion bulk flow velocities, and **(P)** ion energy fluxes (eV/(s-sr-cm^2-eV)). The shaded yellow region indicates the magnetosphere.

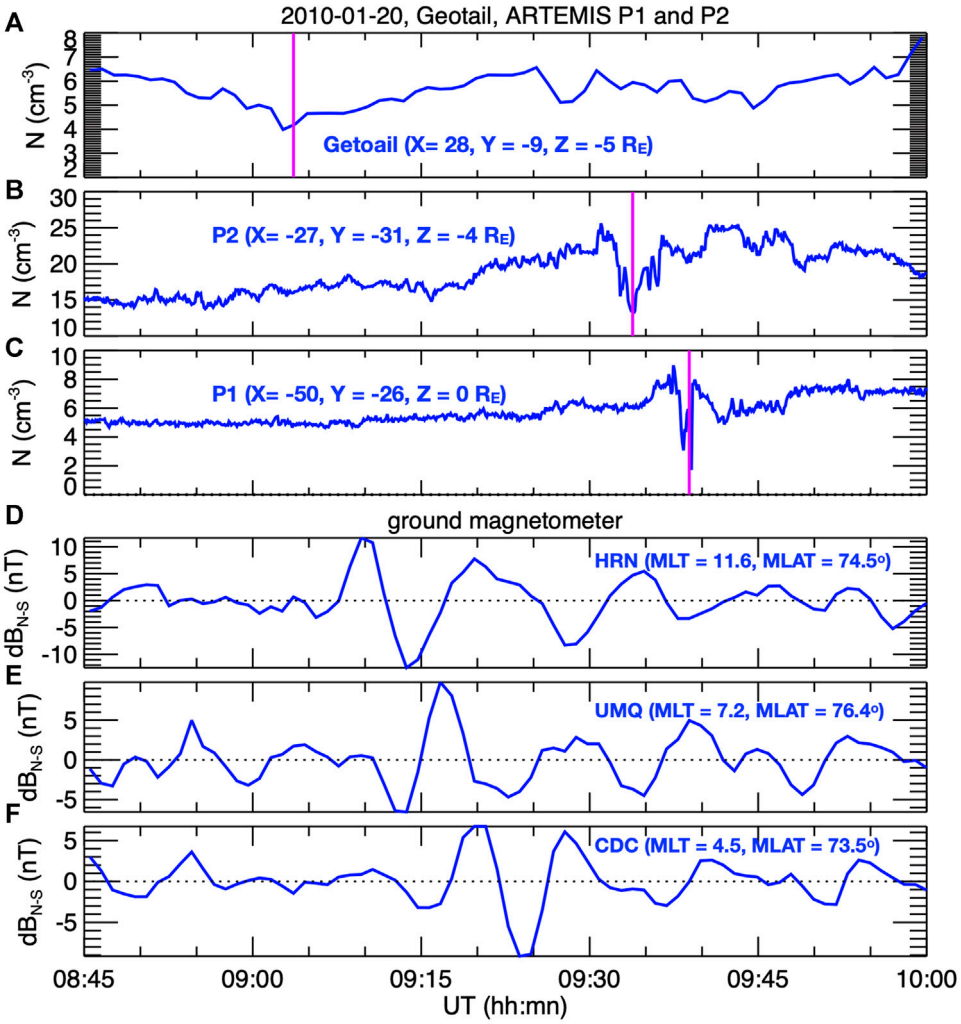

FIGURE 10 | A foreshock transient event on January 20, 2010. The number density observed by **(A)** Geotail, **(B)** artemis P2, and **(C)** AREMIS P1. The vertical magenta line indicates the time when the IMF discontinuity was observed. The ground magnetic field perturbations (perturbations from 10-min running averages) in the north-south direction observed at **(D)** HRN, **(E)** UMQ, and **(F)** CDC stations.

Figure 10A) and observed a transient low-density core with higher temperature and deflected flows (see **Figure 4** of Wang et al. (2018) for the WIND and Geotail observations). The density perturbations observed by Geotail are shown in **Figure 10A** with the time of the discontinuity observed at the Geotail location indicated by the vertical magenta line. As shown in **Figures 10B,C** for P2 and P1, respectively, artemis P1 and P2 were both in the dawnside magnetosheath (their locations are indicated in the plots) with P2 closer to the Earth at X ~ −27 R_E and P1 further down the tail at X ~ −50 R_E. **Figures 10A–C** show that the discontinuity and the associated low-density core observed at the Geotail location at 09:04 UT propagated to P2 at ~09:34 UT then to P1 at ~09:39 UT.

Figures 10D–F show the ground magnetic field perturbations (obtained by subtracting the 10 min running averages) in the north-south direction observed by three magnetometer stations. The three stations were on the dawnside at similar magnetic latitudes (~73°–76°) but at different MLTs from the dayside to the nightside (their MLTs and MLATs at 09:10 UT are indicated in the plots). The aurora image in N.H. from DMSP F17 satellite around 09:11 UT (not shown) indicates that the three stations were within diffuse aurora so that they were mapped to the closed field-line region of the magnetosphere. The ground magnetic field perturbations were enhanced at the three stations within the interval when the foreshock transient perturbations propagated from Geotail on the dayside to P2 and P1 on the nightside. The enhanced perturbations were first observed at ~11 MLT, then at 07 MLT, and then 04 MLT. These simultaneous observations of the tailward propagating magnetosheath perturbations and the anti-sunward propagating ground perturbations are qualitatively consistent with the simulated anti-sunward propagating FAC perturbations in the ionosphere shown in **Figure 8** generated by the simulated tailward propagating magnetopause distortion shown in **Figures 1–5**.

SUMMARY AND DISCUSSION

We use the 3D global hybrid simulation results of foreshock transient perturbations driven by a TD as an example to qualitatively describe the mesoscale (in a time scale of a few minutes and a spatial scale of a few R_E) distortion of the flank magnetopause resulting from the density/pressure perturbations of the foreshock transients. After the foreshock transient perturbations propagate into the magnetosheath, the low-density core contributes to a decrease of the magnetosheath pressure (thermal pressure and dynamic pressure), which causes the magnetopause to distort locally outward. On the other hand, the high-density edge results in an increase in the magnetosheath pressure and localized inward distortion of the magnetopause. The magnetosheath perturbations propagate tailward and continue to distort the flank magnetopause. This tailward-propagating localized outward distortion qualitatively explains the transient appearance of the magnetosphere observed by satellites sitting in the flank magnetosheath. We show that the simulated flank magnetopause distortion can generate compressional magnetic field perturbations within the tail magnetosphere, which can explain the enhancements of magnetospheric ULF waves associated with foreshock transients reported in previous observation studies. As the magnetopause distortion propagates tailward, it generates FAC perturbations in the ionosphere propagating anti-sunward, which can qualitatively account for observed anti-sunward propagation of the ground magnetic field perturbations associated with the tailward propagating magnetosheath perturbations driven by foreshock transients.

The simulated magnetosheath perturbations and magnetopause distortion presented here are associated with foreshock transients generated by specific IMF and discontinuity conditions, nevertheless, we expect that they can provide a generalized and qualitative understanding of the transient and mesoscale nature of the impact on the nightside magnetopause/magnetosphere and the ionosphere since the density core and edge is the common feature to the majority of foreshock transients. In this simulation, $|\text{IMF } B_y|$ is comparable to $|\text{IMF } B_x|$ so that the foreshock region extends from the dayside to the nightside. Thus, as the TD propagates tailward to the nightside, it can still encounter foreshock ions so that new perturbations can be continuously generated and added into the magnetosheath. This process can be important to maintaining the significance of the magnetosheath perturbations and the corresponding flank magnetopause distortion as they propagate to the midtail. We expect that the nightside magnetosheath perturbations might become weaker in different scenarios when the IMF becomes more radial and the foreshock region is limited to the dayside. In that case, the foreshock transients entering the dayside magnetosheath would be the sole perturbations affecting the nightside magnetopause, and decay or diffuse of the perturbations during their tailward propagation would weaken their impact on the nightside. This thought experiment will be further investigated in feature simulations.

DATA AVAILABILITY STATEMENT

The datasets presented in this study can be found in online repositories. The names of the repository/repositories and accession number(s) can be found below:https://doi.org/10.6084/m9.figshare.14058359.v1.

AUTHOR CONTRIBUTIONS

C-PW is responsible for analyzing the simulation results and the two observational events. XW and YL are responsible for conducting the simulations and analysis of the simulation results. TL is responsible for analyzing the two observational events.

FUNDING

C.-P. Wang is supported by NASA 80NSSC19K0840. Xueyi Wang and Yu Lin are supported by NASA 80NSSC19K0840, 80NSSC17K0012, NNX17AI47G, and 80NSSC20K0604.T. Z. L. is supported by the NASA Living With a Star Jack Eddy Postdoctoral Fellowship Program, administered by the Cooperative Programs for the Advancement of Earth System Science (CPAESS). T. Z. L. is partially supported by NSF award AGS-1941012.T. Z. L. is partially supported by NSF award AGS-1941012. Computer resources for the simulations were provided by NASA Advanced Supercomputing (NAS) Division. The simulation data can be found at https://doi.org/10.6084/m9.figshare.14058359.v1.

SUPPLEMENTARY MATERIAL

The Supplementary Material for this article can be found online at: https://www.frontiersin.org/articles/10.3389/fspas.2021.751244/full#supplementary-material

REFERENCES

Archer, M. O., Turner, D. L., Eastwood, J. P., Horbury, T. S., and Schwartz, S. J. (2014). The Role of Pressure Gradients in Driving Sunward Magnetosheath Flows and Magnetopause Motion. *J. Geophys. Res. Space Phys.* 119, 8117–8125. doi:10.1002/2014JA020342

Archer, M. O., Turner, D. L., Eastwood, J. P., Schwartz, S. J., and Horbury, T. S. (2015). Global Impacts of a Foreshock Bubble: Magnetosheath, Magnetopause and Ground-Based Observations. *Planet. Space Sci.* 106, 56–66. doi:10.1016/j.pss.2014.11.026

Billingham, L., Schwartz, S. J., and Sibeck, D. G. (2008). The Statistics of Foreshock Cavities: Results of a Cluster Survey. *Ann. Geophys.* 26, 3653–3667. doi:10.5194/angeo-26-3653-2008

Blanco-Cano, X., Kajdič, P., Omidi, N., and Russell, C. T. (2011). Foreshock Cavitons for Different Interplanetary Magnetic Field Geometries: Simulations and Observations. *J. Geophys. Res.* 116, a–n. doi:10.1029/2010JA016413

Chu, C., Zhang, H., Sibeck, D., Otto, A., Zong, Q., Omidi, N., et al. (2017). THEMIS Satellite Observations of Hot Flow Anomalies at Earth's bow Shock. *Ann. Geophys.* 35 (3), 443–451. doi:10.5194/angeo-35-443-2017

Fillingim, M. O., Eastwood, J. P., Parks, G. K., Angelopoulos, V., Mann, I. R., Mende, S. B., et al. (2011). Polar UVI and THEMIS GMAG Observations of the Ionospheric Response to a Hot Flow Anomaly. *J. Atmos. Solar-Terrestrial Phys.* 73, 137–145. doi:10.1016/j.jastp.2010.03.001

Hartinger, M. D., Turner, D. L., Plaschke, F., Angelopoulos, V., and Singer, H. (2013). The Role of Transient Ion Foreshock Phenomena in Driving Pc5 ULF Wave Activity. *J. Geophys. Res. Space Phys.* 118, 299–312. doi:10.1029/2012JA018349

Jacobsen, K. S., Phan, T. D., Eastwood, J. P., Sibeck, D. G., Moen, J. I., Angelopoulos, V., et al. (2009). THEMIS Observations of Extreme Magnetopause Motion Caused by a Hot Flow Anomaly. *J. Geophys. Res.* 114, a–n. doi:10.1029/2008JA013873

Kajdič, P., Blanco-Cano, X., Omidi, N., Meziane, K., Russell, C. T., Sauvaud, J.-A., et al. (2013). Statistical Study of Foreshock Cavitons. *Ann. Geophys.* 31 (12), 2163–2178. doi:10.5194/angeo-31-2163-2013

Kajdič, P., Blanco-Cano, X., Omidi, N., Rojas-Castillo, D., Sibeck, D. G., and Billingham, L. (2017). Traveling Foreshocks and Transient Foreshock Phenomena. *J. Geophys. Res. Space Phys.* 122, 9148–9168. doi:10.1002/2017JA023901

Kajdič, P., Raptis, S., Blanco-Cano, X., and Karlsson, T. (2021). Causes of Jets in the Quasi-Perpendicular Magnetosheath. *Geophys. Res. Lett.* 48, e2021GL093173. doi:10.1029/2021GL093173

Kataoka, R., Fukunishi, H., Lanzerotti, L. J., Rosenberg, T. J., Weatherwax, A. T., Engebretson, M. J., et al. (2002). Traveling Convection Vortices Induced by Solar Wind Tangential Discontinuities. *J. Geophys. Res.* 107 (A12), 22-1–22-12. doi:10.1029/2002JA009459

Lin, Y. (1997). Generation of Anomalous Flows Near the bow Shock by its Interaction with Interplanetary Discontinuities. *J. Geophys. Res.* 102, 24,265–24, 281. doi:10.21236/ada635320

Lin, Y. (2002). Global Hybrid Simulation of Hot Flow Anomalies Near the bow Shock and in the Magnetosheath. *Planet. Space Sci.* 50, 577–591. doi:10.1016/s0032-0633(02)00037-5

Lin, Y. (2003). Global-scale Simulation of Foreshock Structures at the Quasi-Parallel bow Shock. *J. Geophys. Res.* 108, 1390. doi:10.1029/2003JA009991A11

Lin, Y., Wang, X. Y., Lu, S., Perez, J. D., and Lu, Q. (2014). Investigation of Storm Time Magnetotail and Ion Injection Using Three-Dimensional Global Hybrid Simulation. *J. Geophys. Res. Space Phys.* 119, 7413–7432. doi:10.1002/2014JA020005

Lin, Y., and Wang, X. Y. (2005). Three-dimensional Global Hybrid Simulation of Dayside Dynamics Associated with the Quasi-Parallel bow Shock. *J. Geophys. Res.* 110, A12216. doi:10.1029/2005JA011243

Liu, J., Lyons, L. R., Wang, C. P., Ma, Y., Strangeway, R. J., Zhang, Y., et al. (2021). Embedded Regions 1 and 2 Field-Aligned Currents: Newly Recognized from Low-Altitude Spacecraft Observations. *J. Geophys. Res. Space Phys.* 126, e2021JA029207. doi:10.1029/2021JA029207

Liu, T. Z., Angelopoulos, V., Hietala, H., and Wilson III, L. B. (2017). Statistical Study of Particle Acceleration in the Core of Foreshock Transients. *J. Geophys. Res. Space Phys.* 122, 7197–7208. doi:10.1002/2017JA024043

Liu, T. Z., Turner, D. L., Angelopoulos, V., and Omidi, N. (2016). Multipoint Observations of the Structure and Evolution of Foreshock Bubbles and Their Relation to Hot Flow Anomalies. *J. Geophys. Res. Space Phys.* 121, 5489–5509. doi:10.1002/2016JA022461

Liu, T. Z., Wang, C. P., Wang, B., Wang, X., Zhang, H., and Angelopoulos, Y. V. (2020). ARTEMIS Observations of Foreshock Transients in the Midtail Foreshock. *Geophys. Res. Lett.* 47, e2020GL090393. doi:10.1029/2020GL090393

Liu, Z., Turner, D. L., Angelopoulos, V., and Omidi, N. (2015). THEMIS Observations of Tangential Discontinuity-driven Foreshock Bubbles. *Geophys. Res. Lett.* 42, 7860–7866. doi:10.1002/2015GL065842

Lucek, E. A., Horbury, T. S., Balogh, A., Dandouras, I., and Rème, H. (2004). Cluster Observations of Hot Flow Anomalies. *J. Geophys. Res.* 109, A06207. doi:10.1029/2003JA010016

Murr, D. L., and Hughes, W. J. (2003). Solar Wind Drivers of Traveling Convection Vortices. *Geophys. Res. Lett.* 30, 1354. doi:10.1029/2002GL0154987

Omidi, N., Berchem, J., Sibeck, D., and Zhang, H. (2016). Impacts of Spontaneous Hot Flow Anomalies on the Magne- Tosheath and Magnetopause. *J. Geophys. Res. Space Phys.* 121, 3155–3169. doi:10.1002/2015JA022170

Omidi, N., Eastwood, J. P., and Sibeck, D. G. (2010). Foreshock Bubbles and Their Global Magnetospheric Impacts. *J. Geophys. Res.* 115, A06204. doi:10.1029/2009JA014828

Omidi, N. (2007). Formation of Cavities in the Foreshock. *AIP Conf. Proc.* 932, 181. doi:10.1063/1.2778962

Omidi, N., Lee, S. H., Sibeck, D. G., Turner, D. L., Liu, T. Z., and Angelopoulos, V. (2020). Formation and Topology of Foreshock Bubbles. *J. Geophys. Res. Space Phys.* 125, e2020JA028058. doi:10.1029/2020JA028058

Omidi, N., and Sibeck, D. (2007). Formation of Hot Flow Anomalies and Solitary Shocks. *J. Geophys. Res.* 112, A01203. doi:10.1029/2006JA011663

Omidi, N., Zhang, H., Sibeck, D., and Turner, D. (2013). Spontaneous Hot Flow Anomalies at Quasi-Parallel Shocks: 2. Hybrid Simulations. *J. Geophys. Res. Space Phys.* 118, 173–180. doi:10.1029/2012JA018099

Otto, A., and Zhang, H. (2021). Bow Shock Transients Caused by Solar Wind Dynamic Pressure Depletions. *J. Atmos. Solar-Terrestrial Phys.* 218, 105615. doi:10.1016/j.jastp.2021.105615

Peredo, M., Slavin, J. A., Mazur, E., and Curtis, S. A. (1995). Three-dimensional Position and Shape of the bow Shock and Their Variation with Alfvénic, Sonic and Magnetosonic Mach Numbers and Interplanetary Magnetic Field Orientation. *J. Geophys. Res.* 100 (A5), 7907–7916. doi:10.1029/94JA02545

Ridley, A. J., Gombosi, T. I., and Dezeeuw, D. L. (2004). Ionospheric Control of the Magnetosphere: Conductance. *Ann. Geophys.* 22 (2), 567–584. doi:10.5194/angeo-22-567-2004

Roelof, E. C., and Sibeck, D. G. (1993). Magnetopause Shape as a Bivariate Function of Interplanetary Magnetic Field B_z and Solar Wind Dynamic Pressure. *J. Geophys. Res.* 98 (A12), 21,421–21,450. doi:10.1029/93JA02362

Schwartz, S. J., Avanov, L., Turner, D., Zhang, H., Gingell, I., Eastwood, J. P., et al. (2018). Ion Kinetics in a Hot Flow Anomaly: MMS Observations. *Geophys. Res. Lett.* 45, 11,520–11,529. doi:10.1029/2018GL080189

Schwartz, S. J., Chaloner, C. P., Christiansen, P. J., Coates, A. J., Hall, D. S., Johnstone, A. D., et al. (1985). An Active Current Sheet in the Solar Wind. *Nature* 318, 269–271. doi:10.1038/318269a0

Schwartz, S. J. (1991). Magnetic Field Structures and Related Phenomena at Quasi-Parallel Shocks. *Adv. Space Res.* 11 (9), 231–240. doi:10.1016/0273-1177(91)90039-m

Schwartz, S. J., Sibeck, D., Wilber, M., Meziane, K., and Horbury, T. S. (2006). Kinetic Aspects of Foreshock Cavities. *Geophys. Res. Lett.* 33 (12), 103. doi:10.1029/2005gl025612

Shen, X.-C., Shi, Q., Wang, B., Zhang, H., Hudson, M. K., Nishimura, Y., et al. (2018). Dayside magnetospheric and ionospheric responses to a foreshock transient on 25 June 2008: 1. FLR observed by satellite and ground-based magnetometers. *J. Geophys. Research: Space Phys.* 123, 6335–6346. doi:10.1029/2018JA025349

Shi, F., Lin, Y., Wang, X., Wang, B., and Nishimura, Y. (2021). 3-D Global Hybrid Simulations of Magnetospheric Response to Foreshock Processes. *Earth Planets Space* 73, 138. doi:10.1186/s40623-021-01469-2

Sibeck, D. G., Borodkova, N. L., Schwartz, S. J., Owen, C. J., Kessel, R., and Kokubun, S. (1999). Comprehensive Study of the Magnetospheric Response to a Hot Flow Anomaly. *J. Geophys. Res.* 104, 4577–4593. doi:10.1029/1998JA900021

Sibeck, D. G., Kudela, K., Lepping, R. P., Lin, R., Nemecek, Z., Nozdrachev, M. N., et al. (2000). Magnetopause Motion Driven by Interplanetary Magnetic Field Variations. *J. Geophys. Res.* 105 (A11), 25155–25169. doi:10.1029/2000JA900109

Sibeck, D. G., Kudela, K., Mukai, T., Nemecek, Z., and Safrankova, J. (2004). Radial Dependence of Foreshock Cavities: a Case Study. *Ann. Geophys.* 22, 4143–4151. doi:10.5194/angeo-22-4143-2004

Sibeck, D. G., Lee, S. H., Omidi, N., and Angelopoulos, V. (2021). Foreshock Cavities: Direct Transmission through the bow Shock. *J. Geophys. Res. Space Phys.* 126, e2021JA029201. doi:10.1029/2021JA029201

Sibeck, D. G., Omidi, N., Dandouras, I., and Lucek, E. (2008). On the Edge of the Foreshock: Model-Data Comparisons. *Ann. Geophys.* 26, 1539–1544. doi:10.5194/angeo-26-1539-2008

Sibeck, D. G., Phan, T.-D., Lin, R., Lepping, R. P., and Szabo, A. (2002). Wind Observations of Foreshock Cavities: A Case Study. *J. Geophys. Res.* 107, 4–1. doi:10.1029/2001ja007539

Thomsen, M. F., Gosling, J. T., Fuselier, S. A., Bame, S. J., and Russell, C. T. (1986). Hot, Diamagnetic Cavities Upstream from the Earth's bow Shock. *J. Geophys. Res.* 91, 2961–2973. doi:10.1029/JA091iA03p02961

Turner, D. L., Liu, T. Z., Wilson, L. B., Cohen, I. J., Gershman, D. G., Fennell, J. F., et al. (2020). Microscopic, Multipoint Characterization of Foreshock Bubbles with Magnetospheric Multiscale (MMS). *J. Geophys. Res. Space Phys.* 125, e2019JA027707. doi:10.1029/2019JA027707

Turner, D. L., Omidi, N., Sibeck, D. G., and Angelopoulos, V. (2013). First Observations of Foreshock Bubbles Upstream of Earth's bow Shock: Characteristics and Comparisons to HFAs. *J. Geophys. Res. Space Phys.* 118, 1552–1570. doi:10.1002/jgra.50198

Wang, B., Liu, T., Nishimura, Y., Zhang, H., Hartinger, M., Shi, X., et al. (2020). Global Propagation of Magnetospheric Pc5 ULF Waves Driven by Foreshock Transients. *J. Geophys. Res. Space Phys.* 125, e2020JA028411. doi:10.1029/2020JA028411

Wang, B., Nishimura, Y., Hietala, H., Lyons, L., Angelopoulos, V., Plaschke, F., et al. (2018a). Impacts of Magnetosheath High-Speed Jets on the Magnetosphere and Ionosphere Measured by Optical Imaging and Satellite Observations. *J. Geophys. Res. Space Phys.* 123, 4879–4894. doi:10.1029/2017JA024954

Wang, B., Nishimura, Y., Hietala, H., Shen, X.-C., Lyons, L., Angelopoulos, V., et al. (2019). The 2-D Structure of Foreshock-driven Field Line Resonances Observed by THEMIS Satellite and Ground-based Imager Conjunctions. *J. Geophys. Res. Space Phys.* 124, 6792–6811. doi:10.1029/2019JA026668

Wang, B., Nishimura, Y., Hietala, H., Shen, X.-C., Shi, Q., Zhang, H., et al. (2018b). Dayside Magnetospheric and Ionospheric Responses to a Foreshock Transient on 25 June 2008: 2. 2-D Evolution Based on Dayside Auroral Imaging. *J. Geophys. Res. Space Phys.* 123, 6347–6359. doi:10.1029/2017JA024846

Wang, B., Zhang, H., Liu, Z., Liu, T., Li, X., and Angelopoulos, V. (2021). Energy Modulations of Magnetospheric Ions Induced by Foreshock Transient-Driven Ultralow-Frequency Waves. *Geophys. Res. Lett.* 48, e2021GL093913. doi:10.1029/2021GL093913

Wang, C. P., Liu, T. Z., Xing, X., and Masson, A. (2018). Multispacecraft Observations of Tailward Propagation of Transient Foreshock Perturbations to Midtail Magnetosheath. *J. Geophys. Res. Space Phys.* 123, 9381. doi:10.1029/2018JA025921

Wang, C. P., Thorne, R., Liu, T. Z., Hartinger, M. D., Nagai, T., Angelopoulos, V., et al. (2017). A Multispacecraft Event Study of Pc5 Ultralow-frequency Waves in the Magnetosphere and Their External Drivers. *J. Geophys. Res. Space Phys.* 122, 5132–5147. doi:10.1002/2016JA023610

Wang, C. P., Wang, X., Liu, T. Z., and Lin, Y. (2021). A Foreshock Bubble Driven by an IMF Tangential Discontinuity: 3D Global Hybrid Simulation. *Geophys. Res. Lett.* 48, e2021GL093068. doi:10.1029/2021GL093068

Wang, C. P., Wang, X., Liu, T. Z., and Lin, Y. (2020). Evolution of a Foreshock Bubble in the Midtail Foreshock and Impact on the Magnetopause: 3-D Global Hybrid Simulation. *Geophys. Res. Lett.* 47, e2020GL089844. doi:10.1029/2020GL089844

Zhang, H., Le, G., and Sibeck, D. G. (2017). *MMS Observations of a Hot Flow Anomaly in the Magnetosheath*. American Geophysical Union, Fall Meeting 2017, abstract #SM11B-230.

Zhang, H., Sibeck, D. G., Zong, Q.-G., Gary, S. P., McFadden, J. P., Larson, D., et al. (2010). Time History of Events and Macroscale Interactions during Substorms Observations of a Series of Hot Flow Anomaly Events. *J. Geophys. Res.* 115, A12235. doi:10.1029/2009JA015180

Zhang, H., Sibeck, D. G., Zong, Q.-G., Omidi, N., Turner, D., and Clausen, L. B. N. (2013). Spontaneous Hot Flow Anomalies at Quasi-Parallel Shocks: 1. Observations. *J. Geophys. Res. Space Phys.* 118, 3357–3363. doi:10.1002/jgra.50376

Zhang, H., and Zong, Q. (2020). "Transient Phenomena at the Magnetopause and Bow Shock and Their Ground Signatures," in *Dayside Magnetosphere Interactions*. Editors Q. Zong, P. Escoubet, D. Sibeck, G. Le, and H. Zhang, 11–37. doi:10.1002/9781119509592.ch2

Conflict of Interest: The authors declare that the research was conducted in the absence of any commercial or financial relationships that could be construed as a potential conflict of interest.

Publisher's Note: All claims expressed in this article are solely those of the authors and do not necessarily represent those of their affiliated organizations, or those of the publisher, the editors and the reviewers. Any product that may be evaluated in this article, or claim that may be made by its manufacturer, is not guaranteed or endorsed by the publisher.

frontiers in Physics

ORIGINAL RESEARCH
published: 30 September 2021
doi: 10.3389/fphy.2021.734437

Waves Generated by Electron Beam in a Crater-Shaped Flux Rope

Kyunghwan Dokgo[1]*, *Kyoung-Joo Hwang*[1], *James L. Burch*[1] and *Peter H. Yoon*[2,3]

[1]Southwest Research Institute, San Antonio, TX, United States, [2]Institute for Physical Science and Technology, University of Maryland, College Park, MD, United States, [3]School of Space Research, Kyung Hee University, Yongin, South Korea

Understanding the nature and characteristics of high-frequency waves inside a flux rope may be important as the wave-particle interaction is important for charged-particle energization and the ensuing dissipation process. We analyze waves generated by an electron beam in a crater-shaped magnetic flux rope observed by MMS spacecraft on the dawnside tailward magnetopause. In this MMS observation, a depression of magnetic field, or a crater, of ~100 km is located at the center of the magnetic flux rope of ~650 km. There exist parallel and perpendicular electrostatic wave modes inside the depression of the magnetic field at the center of the flux rope, and they are distinguished by their locations and frequencies. The parallel mode exists at the center of the magnetic depression and its power spectrum peaks below F_{ce} (electron cyclotron frequency). In contrast, the perpendicular mode exists in the outer region associated with the magnetic depression, and its power spectrum peaks near F_{ce}. The linear analysis of kinetic instability using a generalized dispersion solver shows that the parallel mode can be generated by the electron beam of 5,000 km/s. They can thermalize electrons $\lesssim$100 eV effectively. However, the generation mechanism of the perpendicular mode is not clear yet, which requires further study.

Keywords: flux rope, waves, MMS, reconnection, magnetopause

OPEN ACCESS

Edited by:
Rudolf von Steiger,
University of Bern, Switzerland

Reviewed by:
Bogdan Hnat,
University of Warwick,
United Kingdom
Tieyan Wang,
Rutherford Appleton Laboratory,
United Kingdom

***Correspondence:**
Kyunghwan Dokgo
kyunghwan.dokgo@swri.org

Specialty section:
This article was submitted to Space Physics, a section of the journal Frontiers in Physics

Received: *01 July 2021*
Accepted: *17 September 2021*
Published: *30 September 2021*

Citation:
Dokgo K, Hwang K-J, Burch JL and Yoon PH (2021) Waves Generated by Electron Beam in a Crater-Shaped Flux Rope. Front. Phys. 9:734437. doi: 10.3389/fphy.2021.734437

1 INTRODUCTION

Magnetic flux ropes are 3-D helical structures with coherently twisted magnetic field lines winding about a common axis. A typical flux rope features an enhancement of magnetic field intensity in the core region and a reversal of the normal component of the magnetic field line at the center. Such characteristics are employed for the identification of flux ropes. It is known that the generation of flux ropes is closely related to the magnetic reconnection process. Converging reconnection jets in the same plane coming from two distinct reconnection X-lines can form a flux rope [1, 2]. Alternatively, the instability of a single X-line may generate flux ropes as secondary islands [3, 4].

Previous studies have shown that flux ropes can play an important role in the energization of particles during magnetic reconnection. Several acceleration mechanisms associated with flux ropes have been suggested. The *O*-type acceleration explains electron acceleration by contracting flux ropes [3]. A newly reconnected magnetic field becomes contracted due to a tension force. The electrons trapped in the flux rope gain energy through multiple reflections at the converging boundaries (Fermi acceleration). The anti-reconnection, or equivalently, the secondary reconnection describes coalescence of multiple flux ropes [5]. If the central X-line is weaker than the other two adjacent X-lines in a configuration of three sequential magnetic islands, then two flux ropes may emerge by absorbing the central structure. Subsequently, they may further merge into a sinle large flux rope as a consequence of secondary reconnection between two the flux ropes. By employing a

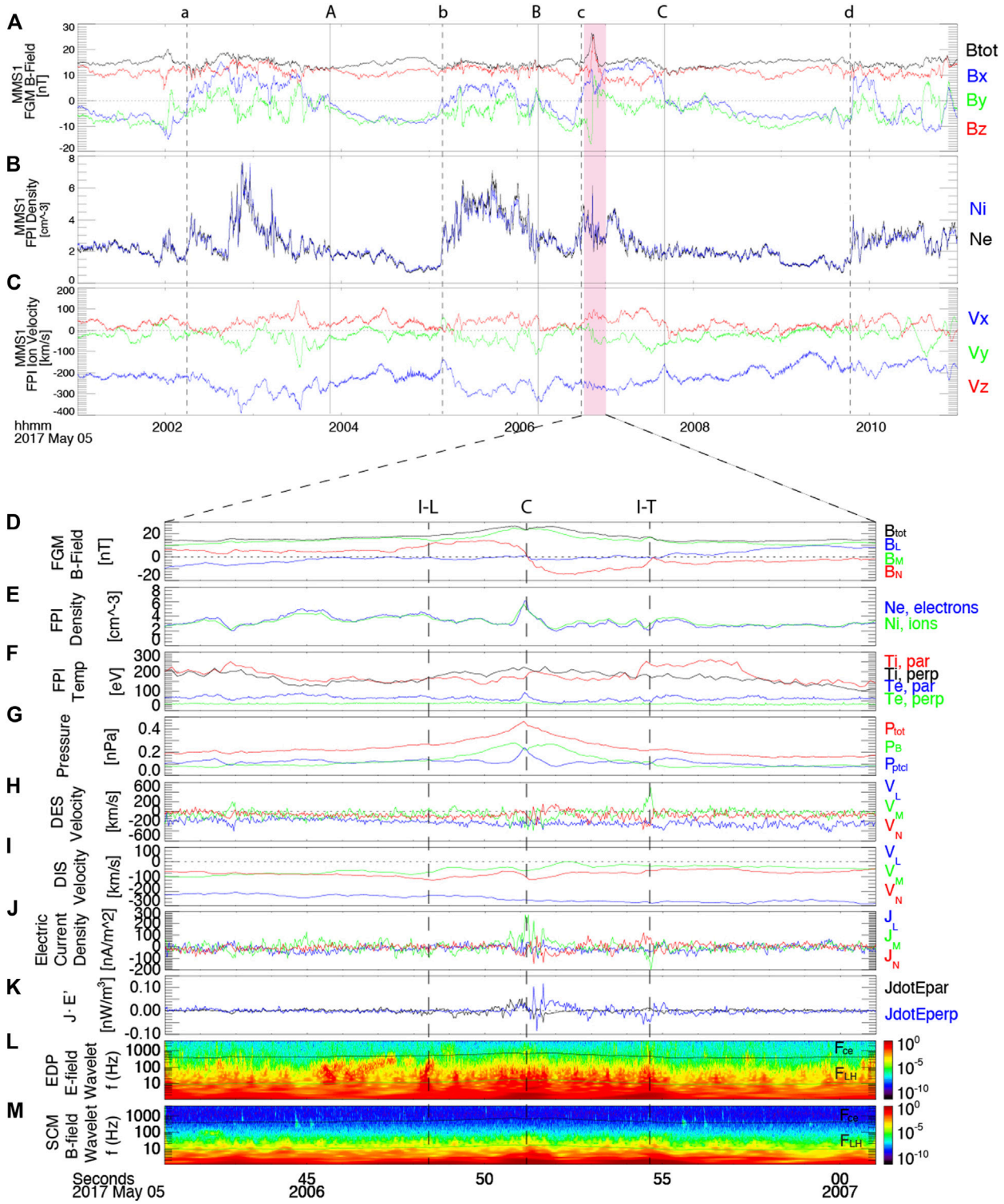

FIGURE 1 | (A–C) Overview of MMS1 observation of May 5. 2017 event. **(A)** Magnetic field, **(B)** particle density, and **(C)** ion velocity in the GSM coordinate. Vertical dashed lines **(A–D)** correspond to trailing edges of nonlinear developed K-H waves, and solid vertical lines **(A–C)** correspond to leading edges. **(D–M)** Enlarged plots showing the crater flux rope in LMN coordinate. **(D)** Magnetic field, **(E)** density, **(F)** temperature, **(G)** pressure, **(H)** electron velocity, **(I)** ion velocity, **(J)** electric current density, **(K)** energy dissipation proxy J·E′, **(L)** electric field power spectrogram, and **(M)** magnetic field power spectrogram.

two-dimensional (2D) Particle-In-Cell (PIC) simulation, Oka et al. [5] showed that energization in the secondary reconnection region is the most important among other processes.

Recent *in-situ* observations have shown that various waves exist in the near vicinity of flux ropes. Flux ropes are made of complex and dynamic structures. Their formation is intimately involved with reconnection jets and gradients of density, temperature, and magnetic field intensity. Consequently, flux ropes contain a variety of free energy sources, which can generate waves. By analyzing data from Cluster spacecraft, Khotyaintsev et al. [6] identified solitary structures associated with the electric field. The observed solitary structures are interpreted as slow electron holes and weak double layers generated by Buneman instability at the center of the flux rope. Jiang et al. [7] studied whistler waves near two sequential flux ropes and compared properties of whistler waves inside and outside of the flux ropes. They report that the frequency range inside ($0.5F_{ce} \sim F_{ce}$) is higher than outside ($0.1F_{ce} \sim F_{ce}$), where F_{ce} is electron cyclotron frequency. Low-frequency waves such as lower-hybrid drift waves (LHDI) and kinetic Alfven waves (KAW) were also studied by Tang et al. [8, 9]. A variety of waves associated with the flux ropes were intensively studied by Øieroset et al. [10], showing an entire picture of wave distribution near the flux rope. Charged particles may efficiently interact with a number of different plasma waves and thus be energized. Moreover, the electrostatic perpendicular mode can modify larger-scale equilibrium or force-balance by changing electric current, temperature, and off-diagonal pressure tensors [11]. Consequently, understanding waves in flux ropes and magnetic reconnection is important, and may provide clues as to the underlying charged-particle acceleration processes.

In this paper, we investigate waves inside the magnetic field depression (crater) at the center of a crater-shaped flux rope on the May 5. 2017 event using observation data from the Magnetospheric Multiscale (MMS) mission [12]. The MMS Mission has provided multi-spacecraft measurements at separations varying from a few electron inertial lengths (d_e) to several ion inertial lengths (d_i). MMS enables investigations of multi-scale structures from electron- to ion-scale by its unprecedented high-resolution data. We use burst mode data from the fluxgate magnetometer [13], the electric field double probes [14, 15], and the fast plasma investigation [16] in this study.

2 DATA ANALYSIS AND RESULTS

The event on May 5. 2017 was analyzed in detail by Hwang et al. [17], but we will briefly describe the event for the sake of completeness. Note here that we present MMS1 data because the MMS4 EDP data, essential for the electric wave analysis, is not available at this event. All of the other three MMS1-3 spacecraft observed similar features of the flux rope and waves, and MMS1 shows the clearest features. **Figure 1** presents an overview of the MMS observation of the event. **Figures 1A–C** show (a) magnetic field, (b) particle density (black: electron, blue: ion), and (c) ion velocity during 10-min time interval in GSM coordinates. All of the quantities show quasi-periodic fluctuations: positive B_x and B_y are accompanied by enhanced particle densities and reduced temperature, and vise versa. On the basis of several approaches, Hwang et al. [17] demonstrated that these large-scale fluctuations are nonlinearly developed Kelvin-Helmholtz waves (KHW). Specifically, they showed that the averaged quantities from the magnetosheath side and the magnetosphere side satisfy the threshold condition for the KHW, $[\mathbf{k}\cdot(\mathbf{V}_{sh}-\mathbf{V}_{sp})]^2 > \mu_0^{-1}(\rho_{sp}^{-1}+\rho_{sh}^{-1})[(\mathbf{B}_{sp}\cdot\mathbf{k})^2+(\mathbf{B}_{sh}\cdot\mathbf{k})^2]$, where subscripts *sp* and *sh* stand for magnetopause and magnetosphere, respectively; **V**, **B**, and ρ, are flow velocity, magnetic field vector, and plasma density, respectively; **k** is the wave vector associated with KHW; and μ_0 denotes the vacuum permeability [18]. They further showed that normal directions of leading (vertical solid lines in 1) and trailing edges (vertical dashed lines) agreed with the PIC simulation results of KHW. In addition, they found that the shapes of fluctuations are attributed to nonlinearly developed KHWs or rolled-up Kelvin-Helmholtz vortices (KHVs). This interpretation is supported by the finding that the particle densities abruptly jump around trailing edges forming compressed layers while slowly decrease around leading edges forming thicker mixed layers, a feature consistent with KH dynamics.

A peak in the magnetic field intensity near 20:06:51 UTC can be identified in relation to KHWs. **Figures 1D–M** are enlarged portion of the red-shaded region showing the details of this peak in LMN coordinates, which are calculated by the MVA method [19] using the magnetic field data ($\hat{\mathbf{m}}$ is the axis of a flux rope, $\hat{\mathbf{n}}$ is outward direction from the magnetopause, and $\hat{\mathbf{l}}$ completes the orthonormal coordinates). We marked three vertical lines for inner-leading edge "I–L", inner-trailing edge "I–T", and core region "C" of the flux rope. In **Figure 1D**, B_N is reversed from positive to negative inside the enhancement of the total magnetic field B_{TOT}. It means that this peak is associated with a flux rope structure. We note that there is a depression of total magnetic strength at the center of the flux rope "C". The magnetic pressure decreases at the depression "C" in **Figure 1G**. However, total pressure increases because plasma pressure increases due to the enhancement of plasma density and electron parallel temperature, as shown in **Figures 1E,F**. As a consequence, Hwang et al. [17] concluded that this is an M-shaped crater flux rope similar to a crater flux transfer event (FTE). Their sizes of the flux rope and the crater measured by the cross-sectional distances of the peak-to-peak B_n component are ~650 km ($\sim 4.3d_i$, d_i: ion inertial length) and ~100 km ($\sim 0.7d_i$), respectively (Δt ~2.6 s, ~0.4 s, and $V_{i,l}$ ~−250 km/s).

Figure 1J shows the electric current around this flux rope that is calculated from electron (**Figure 1H**) and ion bulk velocity (**Figure 1I**). It was found that these currents are related to the electron jet coming from magnetic reconnection under a strong guide field [17]. Ion bulk velocity is not changed significantly in the flux rope; thus, this current is carried by the electrons. The coincidence of nonzero $J\cdot E'$ and wave activities near "I–T" and "C" shown in **Figures 1L, M** is a strong indication that the energy conversion might be mediated by waves inside the flux rope. The frequency of $J\cdot E'$ fluctuation is few Hz which is slightly lower

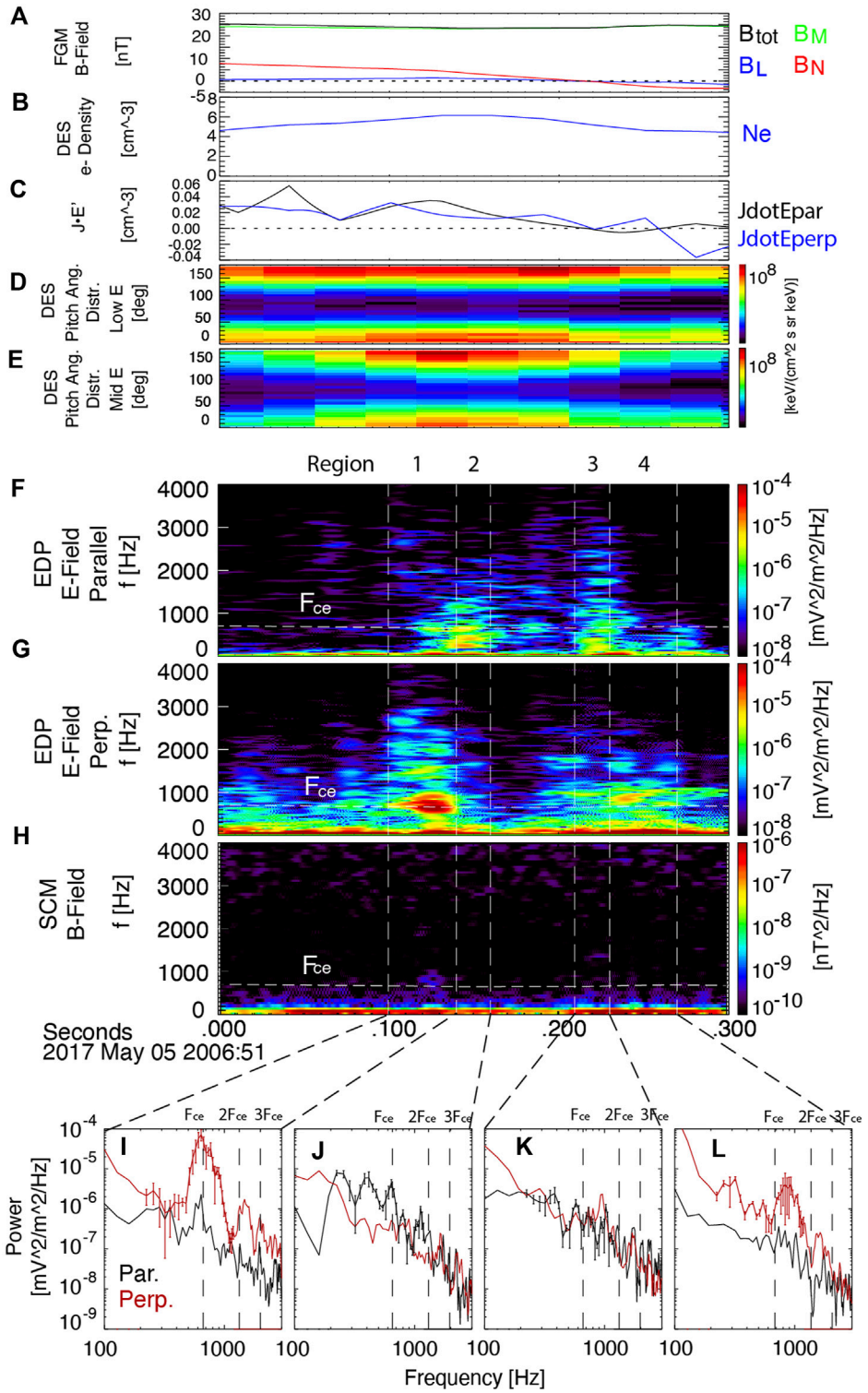

FIGURE 2 | Wave data near the depression of magnetic field at the center of the flux rope. **(A)** Magnetic field in LMN coordinate, **(B)** electron density, **(C)** energy dissipation proxy J·E′, **(D)** electron pitch angle distribution of low energy range, and **(E)** mid energy range, **(F)** power spectrum of the parallel electric field, **(G)** perpendicular electric field, and **(H)** magnetic field. **(I–L)** Averaged power spectrum of electric field in time ranges of **(I)** 20:06:51.100–0.140, **(J)** 0.140–0.160, **(K)** 0.210–0.230, and **(L)** 0.230–0.270 showing the distribution of parallel and perpendicular modes. (Error bars: standard errors).

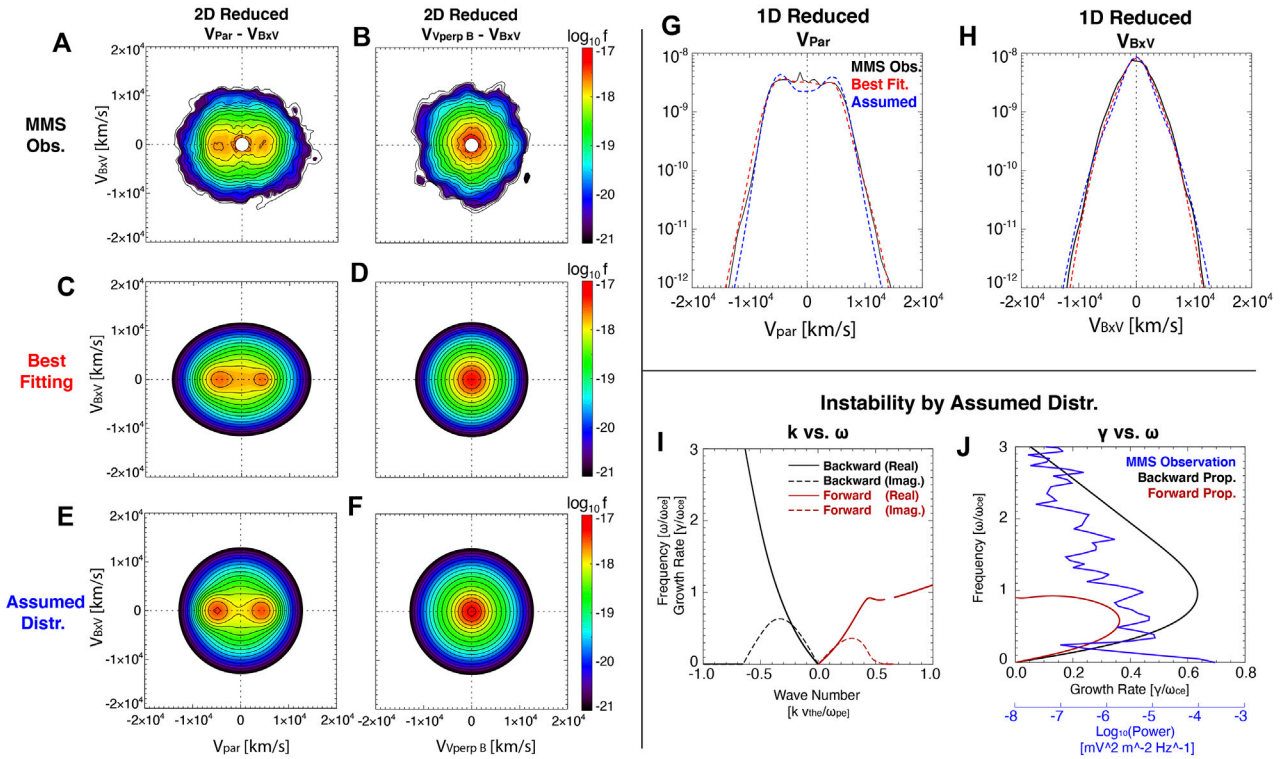

FIGURE 3 | (Left) 2D reduced electron distribution of **(A, B)** MMS observation, **(C, D)** the best fitting, and **(E, F)** an assumed distribution for wave instability in V_{par}-V_{BxV} and $V_{perp\times B}$-V_{BxV} space. **(Right Top)** 1D reduced distribution in **(G)** V_{par}, and **(H)** V_{BxV} space: (black) MMS observation, (red) the best fitting, and (blue) the assumed distribution. **(Right Bottom)** Instability derived from the assumed distribution. **(I)** wave number k vs. frequency ω. (black) the backward-propagating mode, and (red) the forward-propagating mode. Solid lines and dashed lines are real and imaginary parts of solutions. **(J)** Comparison between (red) the forward-, (black) backward-propagating mode, and (blue) power spectrum in MMS observation.

than the lower-hybrid frequency. Thus, it might come from electric field associated with the enhanced lower-hybrid mode as mentioned by Hwang et al. [17].

Figure 2 is an enlarged plot showing the wave spectrum near the depression of magnetic field "C". **Figures 2A,B** present magnetic field in LMN coordinate and electron density, respectively. **Figure 2C** is the parallel and perpendicular energy dissipation proxy J·E′. **Figures 2D,E** are pitch angle distributions of electrons in low and middle energy ranges, which show there are bi-direction (parallel and anti-parallel) beams near "C". **Figures 2F–H** show power spectra of (f) parallel electric field, (g) perpendicular electric field, and (h) magnetic field. The parallel and perpendicular components of the electric field are decomposed using the instantaneous magnetic field. As shown in **Figures 2F, G**, we observe that there are two high-frequency wave modes in this region, one is a parallel mode in **Figure 2F**, and the other is a perpendicular mode in **Figure 2F**. Frequencies of both wave modes are close to the electron cyclotron frequency (F_{ce}) plotted by horizontal dashed lines in each figure. We conclude that both high-frequency modes near F_{ce} are electrostatic or quasi-electrostatic modes because there is no significant signal of the magnetic field near F_{ce} as shown in **Figure 2H**. Moreover, the ratio between amplitudes of electric and magnetic fluctuations E/cB is 5–10 for both modes.

The two modes exist very close to each other but can be distinguished because they have different characteristics. **Figures 2I–L** present averaged power spectra of electric field in the time ranges of 1) 20:06:51.100–140, (j) 0.140–0.160, (k) 0.210–0.230, and (L) 0.230–0.270. These figures show that the two wave modes occur at different locations. We also checked the Lomb-Scargle periodogram [20, 21], and it shows similar peaks with power spectrogram of **Figures 2I–L** (not shown here). Therefore, we concluded that those peaks are significant. Black and red lines denote the power spectra for parallel and perpendicular electric fields, respectively. The enhancement of parallel mode, as displayed in **Figures 2J, K**, occurs in the inner region of the magnetic field depression, while the perpendicular mode (black) locates in the outer region, 1) and (L). Moreover, their frequencies are also different. The frequency of the parallel mode is lower than F_{ce} (vertical dashed lines), but the frequency of the perpendicular mode is almost the same as or is higher than F_{ce}. It is notewothy that the perpendicular mode features harmonics near the integer multiples of F_{ce}.

To understand the generation mechanism of waves, we carry out linear stability analysis based upon observed electron distribution functions. **Figure 3** shows electron distributions and the associated linear stability characteristics. **Figures 3A, B** are the 2D reduced electron distribution obtained from MMS1

spacecraft at the center of the flux rope in velocity space of V_{par} vs. $V_{B\times V}$ for (a), and $V_{V_{perp}\times B}$ vs. $V_{B\times V}$ for (b). **Figure 3A** shows bi-direction electron beams along the magnetic field with a speed of about 5,000 km/s. We note that this electron beam does not exist outside of the magnetic field depression. Therefore, this beam would be a free energy source for waves excited inside the magnetic field depression region.

In order to investigate the possible unstable mode, we model the observed electron distribution as a sum of Maxwellian distributions as shown in **Figures 3C, D**, where the 2D reduced distribution that produces the best fitting is shown. In addition, **Figures 3G,H** show 1D reduced distribution from MMS observation (black solid line) and the best fitting results (red dashed line). The best fitting model is given as follows: n_0 = 2.8 cm^{-3}, $v_{th\|,0}$ = 5,400 km/s, $v_{th\perp,0}$ = 4,000 km/s, $v_{d\|,0}$ = 0.0 km/s, n_1 = 1.05 cm^{-3}, $v_{th\|,1}$ = 2,500 km/s, $v_{th\perp,1}$ = 2,300 km/s, $v_{d\|,1}$ = −5,000 km/s, n_2 = 0.55 cm^{-3}, $v_{th\|,2}$ = $v_{th\perp,2}$ = 1,800 km/s, $v_{d\|,2}$ = 4,500 km/s, where indices 0, 1, and 2 mean core electron, parallel beam in negative direction, and positive direction, respectively. $v_{th\|}$ and $v_{th\perp}$ are parallel and perpendicular thermal speeds, while $v_{d\|}$ is the beam speed in the parallel direction. In these figures, the fitting result agrees with MMS data remarkably. However, we found that there is no instability nor growing mode associated with this distribution. We note that electron distributions from all of the other MMS spacecraft are almost identical when they passed the crater. This can be interpreted either as the waves generated elsewhere and have simply propagated into the observation location, or alternatively, the waves might be generated at an earlier time so the thermalization of electrons has already been completed. In the case of latter, the observed distribution may represent the relaxed state rather than the true initial state that is subject to instability.

We model another electron distribution assuming plasma conditions when the beam is injected into the plasma. We use the parameters of plasma outside of the flux rope for core electrons. Considering the thermalized distribution after the wave generation and thermalization process to become similar to the MMS observation, we calculate the beam density and speeds as follows: n_0 = 1.8 cm^{-3}, $v_{th\|,0}$ = $v_{th\perp,0}$ = 4,600 km/s, v_d = 0.0 km/s, n_1 = 1.4 cm^{-3}, $v_{th\|,1}$ = $v_{th\perp,1}$ = 2,150 km/s, $v_{d\|,1}$ = −5,000.0 km/s, n_2 = 1.2 cm^{-3}, $v_{th\|,2}$ = $v_{th\perp,2}$ = 2,150 km/s, $v_{d\|,2}$ = 4,500.0 km/s. The 2D and 1D reduced distributions of the assumed electron distribution are plotted in **Figures 3E–H** using the same format.

By making use of this assumed distribution, we carried out the linear kinetic instability analysis using BO code [22]. **Figure 3I** shows the solutions by way of plotting the wave number k versus frequency ω, where solid lines and dashed lines are real and imaginary parts, respectively. Wave number k is normalized by electron Debye length ($\lambda_{De} = v_{the}/\omega_{pe}$) and frequency is normalized by electron cyclotron frequency ω_{ce}. We found that there are two growing modes: one is a backward-propagating mode along the negative (−) direction with respect to the ambient magnetic field plotted by black lines, and the other is a forward-propagating mode along the positive (+) direction plotted by red lines, which is consistent with their generation by bi-directional beams. Note that the backward-propagating mode grows faster than the forward-propagating mode. The maximum growth rate of the backward-propagating mode is twice that of the forward-propagating mode, and the frequency range of the backward-propagating mode is much broader than the forward-propagating mode.

We compare MMS observation and two growing modes in **Figure 3J** where x-axis is the wave power and the growth rate γ, while y-axis denotes the frequency. The blue line is the power spectrum of parallel electric field observed by MMS, and red and black lines are the growth rates of forward- and backward-propagating modes, respectively. In the y-axis, it is seen that the growth rate of forward mode is located below ω_{ce} and its peak is ~ 0.6 ω_{ce}. The peak of the backward mode locates slightly higher than the forward mode near ~ 0.9 ω_{ce}, and its range is much broader from 0 to 4 ω_{ce}. The shape of the MMS observation in **Figure 3J** is not exactly matched with the growth rates because MMS observed a highly nonlinear phase of waves as the fully thermalized electron distribution indicates. Even so, the broad frequency range of the observation agrees with the backward mode, and its peak seems to agree with the forward mode. Therefore, we think this MMS observation shows a mixed feature of both modes, and the observed waves were generated by electron beams in the crater. However, we cannot clearly distinguish forward- and backward-propagating modes in the MMS observation.

We note here that the frequency range of beam modes in this event is unusual and extremely low if we consider that beam mode waves are usually generated near or under 1 F_{pe} as a result of beam-plasma interaction. At the center of the flux rope, the electron plasma frequency F_{pe} is ~ 22 kHz, and the electron cyclotron frequency F_{ce} is ~ 640 Hz, thus, $F_{ce} \cong 2.9 \times 10^{-2}$ F_{pe}. This downshift of the frequency range of beam mode from 1 F_{pe} is caused by high beam density [23, 24]. The sum of densities of two beams is higher than that of the core electrons in the assumed electron distribution as shown in **Figures 3E–G**. The agreement of wave analysis appears to indicate that the assumed electron distribution well represents the situation when the beams are injected, and when the beam modes are generated. Despite the good agreement in the parallel direction, no instability in the perpendicular direction was found within the framework of uniform plasma dispersion relation solver. It is possible that agyrotropic crescent-shaped electron distribution or ring-shaped distribution might exist where the perpendicular waves are generated if we consider that the May 5, 2017 event is closely related to magnetic reconnection. The reconstruction of the nonlinear structure of this flux rope using the second-order Taylor expansion showed that the core-field topology of this flux rope indicates two interlinked flux tubes [17]. Thus, the crater "C" could be interpreted as a reconnecting current sheet between two interlinked flux tubes [25, 26] Such electron distributions are known to generate (electrostatic and perpendicular) electron Bernstein waves near integer harmonics of F_{ce} [24, 27]. However, all four MMS spacecraft didn't observe agyrotropic or ring-shaped electron distribution. Therefore, we couldn't clearly verify the generation mechanism of perpendicular mode at this stage. We will discuss this and other possibilities in more detail in the following section.

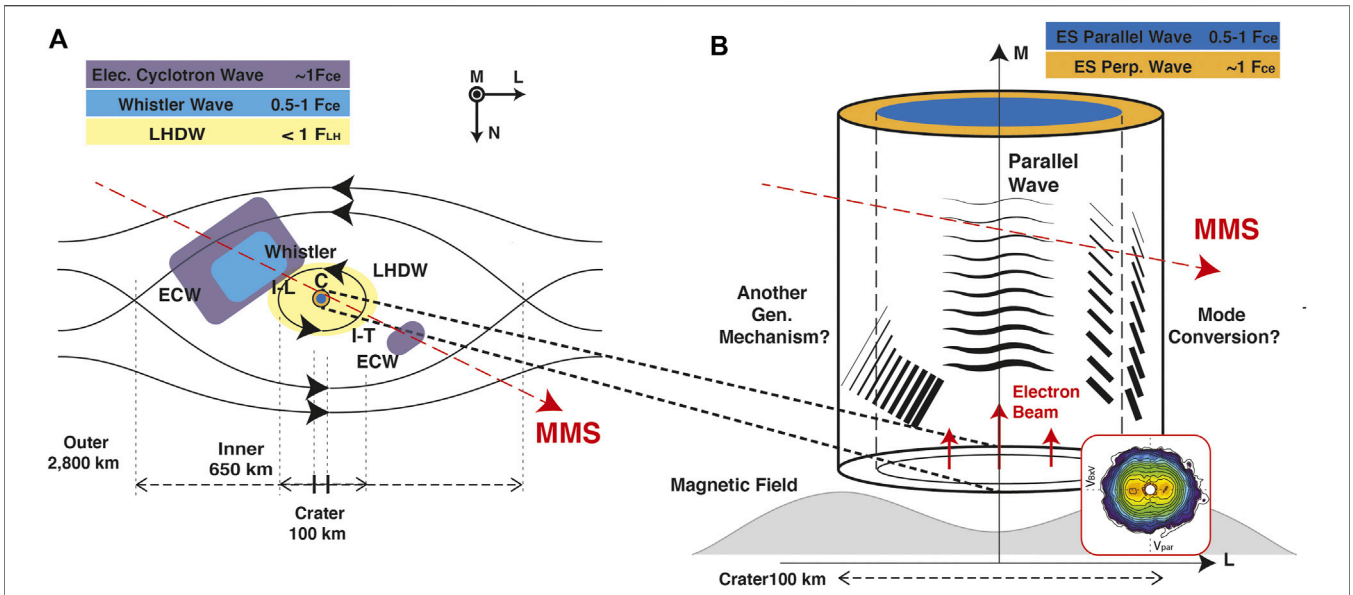

FIGURE 4 | (A) Various waves observed in May 5. 2017 event. Waves observed in **Figure 2** are plotted in a flux rope diagram. Red-dashed line shows the trajectory of MMS spacecraft. **(B)** Waves in the depression of magnetic field at the center of flux rope. Two possibilities of perpendicular wave generation are plotted together.

3 DISCUSSION AND CONCLUSION

In the present manuscript the issue of high-frequency waves measured inside the center of the magnetic field depression in a crater-shaped flux rope is discussed. Upon comparing MMS observation and linear dispersion relation, we found that the characteristics of wave dispersion relation are consistent with the beam mode generated by a counter-streaming electron populations. In particular, it is found that the frequencies of the beam mode are downshifted to the order of F_{ce} because of high beam density.

In this event, other waves are also observed, as mentioned in previous papers. In **Figure 4A**, we schematically plot location where such waves are observed. Electron cyclotron waves (ECW) are observed in **Figures 1L, M**. Although they appear intermittently during the entire event, it seems that they are more frequently observed outside of the inner edge (I–L and I–T) of the flux rope. Those sporadic ECW might be the same branch of waves with the perpendicular beam mode in our study, but they are related to the primary reconnection generating the flux rope. During the time interval of 20:06:45–47 in **Figure 1L**, wave signals in a frequency range of 0.1–0.9 F_{ce} are observed. It might be an oblique whistler wave generated in separatrix or outflow region of magnetic reconnection. Around the flux rope (20:06:48–55), low frequency waves are also observed in **Figures 1L, M**. Their frequency is lower than the lower-hybrid frequency. Thus, it might be a lower-hybrid drift wave (LHDW) generated by the density gradient of the flux rope.

Figure 4B schematically depict the spatial location where high-frequency waves associated with the magnetic field depression are measured. The parallel wave is dominant in the central region, while the perpendicular wave is dominant in the outer region. However, we were not able to identify the generation mechanism of perpendicular waves based upon the uniform plasma theory of wave excitation. We have entertained, however, a possibility of a perpendicular beam, in the location of wave generation. Since the May 5. 2017 event is closely related to magnetic reconnection as investigated by Hwang et al. [17], it is possible that agyrotropic crescent-shaped electron distribution or ring-shaped distribution might exist, which in turn may excite the quasi perpendicular electrostatic electron Bernstein waves near integer harmonics of F_{ce} [24, 27]. Another possible scenario is a mode conversion from parallel waves at the edge of magnetic field depression. In the edge of magnetic field depression, the gradients of magnetic field and density are formed. Moreover, the direction of the magnetic field is drastically changed. Therefore, the parallel mode would not remain an eigenmode of the region. Hence, mode conversion to quasi-perpendicular mode may take place.

Speaking of the density and magnetic field gradient on the edge of the magnetic field depression region, we may entertain further possibilities as well. In the presence of density gradient, warm ions undergoing diamagnetic drift may lead to the electron cyclotron drift instability at the multiple harmonics of F_{ce} [28–30]. Another possibility is that, even in the absence of free energy source, for sufficiently energetic electrons, the spontaneous emission of electrostatic cyclotron harmonics may take place [31, 32]. As a matter of fact, the emission of multiple harmonic cyclotron emission is frequently observed in inner magnetosphere and other planetary magnetopheric environment during active and even quiet periods [33–35]. The analysis of quasi-perpendicular multiple cyclotron harmonic mode by the above-referenced alternative scenarios is, however, beyond the scope of the present paper.

The results of the present study may be summarized as follows. In a crater flux rope, beam-generated waves are observed by MMS spacecraft. At the center of the magnetic field depression, there

exist parallel and perpendicular wave modes near the electron cyclotron frequency F_{ce}. The kinetic linear dispersion analysis shows that the bi-direction electron beam generates the parallel modes. Because the beam density is very high compared to the core electrons, the frequency of the parallel mode is quite low. The peak of the power spectrum locates in the frequency range of 0.6 ~0.9 F_{ce} where $F_{ce} \cong 2.9 \times 10^{-2} F_{pe}$. The generation mechanism of the perpendicular mode is not clear in the observation because MMS spacecraft passed far from where the waves were generated. A mode-conversion from the parallel mode at the outer edge of the magnetic field depression might generate the perpendicular mode, or other instability mechanisms might be operative near the wave generation location. Our study shows that the electron beam inside a flux rope can not only change the flux rope structure making the magnetic field depression but also thermalize electrons inside the magnetic field depression by wave activity.

DATA AVAILABILITY STATEMENT

Publicly available datasets were analyzed in this study. This data can be found here: https://lasp.colorado.edu/mms/sdc/public/.

AUTHOR CONTRIBUTIONS

All authors contributed conception and design of this study. KD and K-JH wrote the first draft of the manuscript. All authors contributed to scientific discussion, manuscripts revision and writing of the manuscript.

FUNDING

This study was supported, in part, by NASA Guest Investigator Grant 80NSSC18K1337. KD and K-JH. were partly supported by NASA 80NSSC18K0693. K-JH was supported, in part, by NSF AGS-1834451 and NASA 80NSSC18K1534 and 80NSSC18K0570. PY acknowledges NSF Grant AGS1842643 and NASA Grant NNH18ZDA001N-HSR to the University of Maryland and BK21 Plus grant to Kyung Hee University, Korea, from NRF.

ACKNOWLEDGMENTS

We acknowledge the use of Pleiades in NASA High-End Computing Program.

REFERENCES

1. Hughes WJ, and Sibeck DG. On the 3-dimensional Structure of Plasmoids. *Geophys Res Lett* (1987) 14:636–9. doi:10.1029/GL014i006p00636
2. Eastwood JP. Observations of Multiple X-Line Structure in the Earth's Magnetotail Current Sheet: A Cluster Case Study. *Geophys Res Lett* (2005) 32:L11105. doi:10.1029/2005GL022509
3. Drake JF, Swisdak M, Che H, and Shay MA. Electron Acceleration from Contracting Magnetic Islands during Reconnection. *Nature* (2006) 443:553–6. doi:10.1038/nature05116
4. Daughton W, Scudder J, and Karimabadi H. Fully Kinetic Simulations of Undriven Magnetic Reconnection with Open Boundary Conditions. *Phys Plasmas* (2006) 13:072101. doi:10.1063/1.2218817
5. Oka M, Phan TD, Krucker S, Fujimoto M, and Shinohara I. Electron Acceleration By Multi-Island Coalescence. *Astrophysical J* (2010) 714: 915–26. doi:10.1088/0004-637X/714/1/915
6. Khotyaintsev YV, Vaivads A, André M, Fujimoto M, Retinò A, and Owen CJ. Observations of Slow Electron Holes at a Magnetic Reconnection Site. *Phys Rev Lett* (2010) 105:165002. doi:10.1103/PhysRevLett.105.165002
7. Jiang K, Huang SY, Yuan ZG, Yu XD, Liu S, Deng D, et al. Observations of Whistler Waves in Two Sequential Flux Ropes at the Magnetopause. *Astrophysics Space Sci* (2019) 364. doi:10.1007/s10509-019-3647-4
8. Tang B, Li W, Wang C, Dai L, Khotyaintsev Y, Lindqvist PA, et al. Magnetic Depression and Electron Transport in an Ion-Scale Flux Rope Associated with Kelvin-Helmholtz Waves. *Ann Geophysicae* (2018) 36:879–89. doi:10.5194/angeo-36-879-2018
9. Tang BB, Li WY, Wang C, Dai L, and Han JP. Effect of Kinetic Alfvén Waves on Electron Transport in an Ion-Scale Flux Rope. *Chin Phys Lett* (2018) 35. doi:10.1088/0256-307X/35/11/119401
10. Øieroset M, Sundkvist D, Chaston CC, Phan TD, Mozer FS, McFadden JP, et al. Observations of Plasma Waves in the Colliding Jet Region of a Magnetic Flux Rope Flanked by Two Active X Lines at the Subsolar Magnetopause. *J Geophys Res Space Phys* (2014) 119:6256–72. doi:10.1002/2014JA020124
11. Dokgo K, Hwang K, Burch JL, Yoon PH, Graham DB, and Li W. The Effects of Upper-Hybrid Waves on Energy Dissipation in the Electron Diffusion Region. *Geophys Res Lett* (2020) 47:e2020GL089778. doi:10.1029/2020GL089778
12. Burch JL, Moore TE, Torbert RB, and Giles BL. Magnetospheric Multiscale Overview and Science Objectives. *Space Sci Rev* (2016) 199:5–21. doi:10.1007/s11214-015-0164-9
13. Russell CT, Anderson BJ, Baumjohann W, Bromund KR, Dearborn D, Fischer D, et al. The Magnetospheric Multiscale Magnetometers. *Space Sci Rev* (2016) 199:189–256. doi:10.1007/s11214-014-0057-3
14. Ergun RE, Tucker S, Westfall J, Goodrich KA, Malaspina DM, Summers D, et al. The Axial Double Probe and Fields Signal Processing for the MMS Mission. *Space Sci Rev* (2016) 199:167–88. doi:10.1007/s11214-014-0115-x
15. Lindqvist PA, Olsson G, Torbert RB, King B, Granoff M, Rau D, et al. The Spin-Plane Double Probe Electric Field Instrument for MMS. *Space Sci Rev* (2016) 199:137–65. doi:10.1007/s11214-014-0116-9
16. Pollock C, Moore T, Jacques A, Burch J, Gliese U, Saito Y, et al. Fast Plasma Investigation for Magnetospheric Multiscale. *Space Sci Rev* (2016) 199: 331–406. doi:10.1007/s11214-016-0245-4
17. Hwang KJ, Dokgo K, Choi E, Burch JL, Sibeck DG, Giles BL, et al. Magnetic Reconnection inside a Flux Rope Induced by Kelvin-Helmholtz Vortices. *J Geophys Res Space Phys* (2020) 125. doi:10.1029/2019JA027665
18. Hasegawa A. *Plasma Instabilities and Nonlinear Effects, Physics and Chemistry in Space*, Vol. 8. Berlin, Heidelberg: Springer Berlin Heidelberg (1975) doi:10.1007/978-3-642-65980-5
19. Sonnerup BUO, and Scheible M. Minimum and Maximum Variance Analysis. *ISSI Scientific Rep* (1998) 1:185–220.
20. Lomb NR. Least-squares Frequency Analysis of Unequally Spaced Data. *Astrophysics Space Sci* (1976) 39:447–62. doi:10.1007/BF00648343
21. Scargle JD. Studies in Astronomical Time Series Analysis. II - Statistical Aspects of Spectral Analysis of Unevenly Spaced Data. *Astrophysical J* (1982) 263:835. doi:10.1086/160554
22. Xie HBO. A Unified Tool for Plasma Waves and Instabilities Analysis. *Comput Phys Commun* (2019) 244:343–71. doi:10.1016/j.cpc.2019.06.014
23. Cairns IH. Electrostatic Wave Generation above and below the Plasma Frequency by Electron Beams. *Phys Fluids B* (1989) 1:204–13. doi:10.1063/1.859088
24. Dokgo K, Hwang KJ, Burch JL, Yoon PH, Graham DB, and Li W. High-Frequency Waves Driven by Agyrotropic Electrons Near the Electron Diffusion Region. *Geophys Res Lett* (2020) 47. doi:10.1029/2020GL087111
25. Kacem I, Jacquey C, Génot V, Lavraud B, Vernisse Y, Marchaudon A, et al. Magnetic Reconnection at a Thin Current Sheet Separating Two Interlaced

Flux Tubes at the Earth's Magnetopause. *J Geophys Res Space Phys* (2018) 123: 1779–93. doi:10.1002/2017JA024537
26. Øieroset M, Phan TD, Drake JF, Eastwood JP, Fuselier SA, Strangeway RJ, et al. Reconnection with Magnetic Flux Pileup at the Interface of Converging Jets at the Magnetopause. *Geophys Res Lett* (2019) 46:1937–46. doi:10.1029/2018GL080994
27. Li WY, Graham DB, Khotyaintsev YV, Vaivads A, André M, Min K, et al. Electron Bernstein Waves Driven by Electron Crescents Near the Electron Diffusion Region. *Nat Commun* (2020) 11:141. doi:10.1038/s41467-019-13920-w
28. Forslund DW, Morse RL, and Nielson CW. Electron Cyclotron Drift Instability. *Phys Rev Lett* (1970) 25:1266–70. doi:10.1103/PhysRevLett.25.1266
29. Wu CS, and Fredricks RW. Cyclotron Drift Instability in the bow Shock. *J Geophys Res* (1972) 77:5585–9. doi:10.1029/JA077i028p05585
30. Janhunen S, Smolyakov A, Sydorenko D, Jimenez M, Kaganovich I, and Raitses Y. Evolution of the Electron Cyclotron Drift Instability in Two-Dimensions. *Phys Plasmas* (2018) 25:082308. doi:10.1063/1.5033896
31. Sentman DD. Thermal Fluctuations and the Diffuse Electrostatic Emissions. *J Geophys Res Space Phys* (1982) 87:1455–72. doi:10.1029/JA087iA03p01455
32. Yoon PH, Hwang J, Kim H, and Seough J. Quasi Thermal Noise Spectroscopy for Van Allen Probes. *J Geophys Res Space Phys* (2019) 124:2811–8. doi:10.1029/2019JA026460
33. Meyer-Vernet N, Hoang S, and Moncuquet M. Bernstein Waves in the Io Plasma Torus: A Novel Kind of Electron Temperature Sensor. *J Geophys Res* (1993) 98:21163–76. doi:10.1029/93JA02587
34. Moncuquet M, Lecacheux A, Meyer-Vernet N, Cecconi B, and Kurth WS. Quasi thermal Noise Spectroscopy in the Inner Magnetosphere of Saturn with Cassini/RPWS: Electron Temperatures and Density. *Geophys Res Lett* (2005) 32:L20S02. doi:10.1029/2005GL022508
35. Kurth WS, De Pascuale S, Faden JB, Kletzing CA, Hospodarsky GB, Thaller S, et al. Electron Densities Inferred from Plasma Wave Spectra Obtained by the Waves Instrument on Van Allen Probes. *J Geophys Res Space Phys* (2015) 120: 904–14. doi:10.1002/2014JA020857

Conflict of Interest: The authors declare that the research was conducted in the absence of any commercial or financial relationships that could be construed as a potential conflict of interest.

Publisher's Note: All claims expressed in this article are solely those of the authors and do not necessarily represent those of their affiliated organizations, or those of the publisher, the editors and the reviewers. Any product that may be evaluated in this article, or claim that may be made by its manufacturer, is not guaranteed or endorsed by the publisher.

frontiers in Astronomy and Space Sciences

ORIGINAL RESEARCH
published: 15 October 2021
doi: 10.3389/fspas.2021.756732

Stormtime Energetics: Energy Transport Across the Magnetopause in a Global MHD Simulation

Austin Brenner[1,2]*, *Tuija I. Pulkkinen*[1,3], *Qusai Al Shidi*[1] and *Gabor Toth*[1]

[1]Department of Climate and Space Sciences and Engineering, University of Michigan, Ann Arbor, MI, United States, [2]Department of Aerospace Engineering, University of Michigan, Ann Arbor, MI, United States, [3]Department of Electronics and Nanoengineering, Aalto University, Espoo, Finland

Coupling between the solar wind and magnetosphere can be expressed in terms of energy transfer through the separating boundary known as the magnetopause. Geospace simulation is performed using the Space Weather Modeling Framework (SWMF) of a multi-ICME impact event on February 18–20, 2014 in order to study the energy transfer through the magnetopause during storm conditions. The magnetopause boundary is identified using a modified plasma β and fully closed field line criteria to a downstream distance of $-20R_e$. Observations from Geotail, Themis, and Cluster are used as well as the Shue 1998 model to verify the simulation field data results and magnetopause boundary location. Once the boundary is identified, energy transfer is calculated in terms of total energy flux **K**, Poynting flux **S**, and hydrodynamic flux **H**. Surface motion effects are considered and the regional distribution of energy transfer on the magnetopause surface is explored in terms of dayside ($X > 0$), flank ($X < 0$), and tail cross section ($X = X_{min}$) regions. It is found that total integrated energy flux over the boundary is nearly balanced between injection and escape, and flank contributions dominate the Poynting flux injection. Poynting flux dominates net energy input, while hydrodynamic flux dominates energy output. Surface fluctuations contribute significantly to net energy transfer and comparison with the Shue model reveals varying levels of cylindrical asymmetry in the magnetopause flank throughout the event. Finally existing energy coupling proxies such as the Akasofu ϵ parameter and Newell coupling function are compared with the energy transfer results.

Keywords: space plasma, magnetopause, energy transfer, magnetosphere, substorm, poynting flux, MHD simulations

OPEN ACCESS

Edited by:
Katariina Nykyri,
Embry–Riddle Aeronautical University,
United States

Reviewed by:
Bogdan Hnat,
University of Warwick,
United Kingdom
Laxman Adhikari,
University of Alabama in Huntsville,
United States

***Correspondence:**
Austin Brenner
aubr@umich.edu

Specialty section:
This article was submitted to Space Physics, a section of the journal Frontiers in Astronomy and Space Sciences

Received: *11 August 2021*
Accepted: *27 September 2021*
Published: *15 October 2021*

Citation:
Brenner A, Pulkkinen TI, Al Shidi Q and Toth G (2021) Stormtime Energetics: Energy Transport Across the Magnetopause in a Global MHD Simulation. Front. Astron. Space Sci. 8:756732. doi: 10.3389/fspas.2021.756732

1 INTRODUCTION

The past decades have greatly advanced our understanding of the dynamics in the space environment. The currently operative fleet termed by NASA as the Heliophysics System Observatory comprises several spacecraft in the solar wind (WIND, ACE, DSCOVR) and in the magnetosphere (Geotail, Cluster, THEMIS, MMS, AMPERE). Multipoint measurements can be made in electron (MMS), ion (Cluster), and mesoscales (THEMIS). Meanwhile, advances in global solar wind—magnetosphere—ionosphere simulations such as the SWMF (Space Weather Modeling Framework, Tóth et al., 2012), LFM (Lyon-Fedder-Mobarry model, Lyon et al., 2004), GAMERA (Grid Agnostic MHD for Extended Research Applications, Zhang et al., 2019), OpenGGCM (Open Geospace General Circulation Model, Raeder et al., 1996), and GUMICS (Grand Unified

Magnetosphere Ionosphere Coupling Simulation model, Janhunen et al., 2012) have increased the level to which we can realistically reproduce dynamic processes in the different scales (Liemohn et al., 2018).

One of the key questions in heliospheric physics is to resolve how the solar wind energy enters the magnetosphere—ionoshere system to drive the dynamic space weather processes. In the solar wind, kinetic energy density ($\frac{1}{2}\rho V^2 \sim 10^{-9}$ J/m^3, where ρ is plasma density and V the solar wind speed) typically exceeds the magnetic energy density ($B^2/2\mu_0 \sim 10^{-11}$ J/m^3, where B is the interplanetary magnetic field (IMF) intensity and μ_0 is the vacuum permeability) under typical conditions. The bow shock reduces the kinetic energy density by a factor of about 4 and increases the magnetic energy density by about a factor of 16, so they become comparable. However, it is the orientation of the IMF that controls the magnetic reconnection process, which allows for energy and plasma transfer from one magnetic topology to another (Akasofu, 1981). Global simulations have shown that the localized magnetic reconnection controls the energy input into the magnetosphere, changing in intensity and location as function of the solar wind density, speed, and IMF magnitude and orientation (Palmroth et al., 2003; Laitinen et al., 2006). However, reconnection has also been found in association with flux transfer events (Chen et al., 2017) and with boundary waves such as those driven by the Kelvin-Helmholtz instability typically observed during northward IMF (Nykyri and Otto, 2001).

While there is general agreement that magnetic reconnection at the magnetopause is the main conduit of energy entry into the magnetosphere—ionosphere system, the complexity of the processes and the multiple scales in which they occur still pose many challenges for producing reliable predictions of the space environment. Even without accounting for the complex inner magnetosphere processes that cannot be represented by pure MHD simulations, Pulkkinen et al. (2006) and Palmroth et al. (2006) explored magnetosphere reconnection under time varying solar wind drivers (solar wind speed and interplanetary magnetic field controlling the magnetospheric activity) and argued that magnetopause reconnection is a function of not only of the solar wind driver, but also depends on the prior level of geomagnetic activity. Furthermore, the magnetosheath electric field downstream of the bow shock is slightly larger in the quasi-parallel flank (Pulkkinen et al., 2016), suggesting that the foreshock waves may contribute to the way the plasma and magnetic field propagate across the bow shock (Pokhotelov et al., 2013). Furthermore, Nykyri et al. (2019) present an interesting case suggesting that a small-scale magnetosheath jet nudging the flank magnetopause can trigger a tail reconnection event leading to a substorm onset. Such sequences demonstrate the power of local disturbances to drive the magnetosphere through a large-scale reconfiguration process (Baker et al., 1999).

In this paper we return to the question of energy transfer into and out of a closed volume of the magnetosphere bounded by the magnetopause and a cross-section of the magnetotail at a given distance (20 R_E). We use the University of Michigan Space Weather Modeling Framework (SWMF) simulation of a storm event on Feb 18–20, 2014, to examine how the energy transfer rates correlate with empirical proxies of energy entry, and how the energy input–output balance is maintained. **Section 2** describes the simulation setup, **Section 3** presents the observations of the event, **Section 4** discusses the simulation analysis methodology, and **Section 5** discusses the analysis results. **Section 6** concludes with discussion.

2 THE SWMF GEOSPACE SIMULATION

We use the SWMF Geospace configuration (Tóth et al., 2012), which consists of the outer magnetosphere, inner magnetosphere and ionosphere electrodynamics components. The Geospace model can run faster than real time and is sufficiently accurate (Pulkkinen et al., 2013) to have been implemented by the NOAA Space Weather Prediction Center for operational use.

The solar wind and the magnetosphere are modeled by the BATS-R-US ideal MHD model (Tóth et al., 2012) with the adaptive grid resolution changing between 0.125 R_E near the Earth and $8R_E$ in the far tail. The simulation box in the Geocentric Solar Magnetospheric (GSM) coordinates extend from 32 R_E to −224 R_E in the X direction and ±128 R_E in the Y and Z directions. The inner boundary is a spherical surface at radial distance R = 2.5 R_E.

The inner magnetosphere's non-Maxwellian plasmas are modeled by the Rice Convection Model (RCM) (Toffoletto et al., 2003), which solves the bounce- and pitch-angle-averaged phase space densities for protons, singly charged oxygen, and electrons in the inner magnetosphere. The MHD based model feeds the outer boundary condition and magnetic field configuration to the RCM, and the RCM plasma density and pressure values are used to modify the inner magnetosphere MHD solution (De Zeeuw et al., 2004). The 2-way coupling of BATS-R-US with RCM is performed every 10s. Including RCM provides a much improved representation of the ring current dynamics (Liemohn et al., 2018).

The ionospheric electrodynamics is described by the Ridley Ionosphere Model (RIM), which solves the Poisson equation for the electrostatic potential distribution at a two-dimensional ionospheric surface (Ridley et al., 2006). BATS-R-US feeds the RIM the field-aligned currents from the simulation inner boundary, and the ionospheric conductances are derived using the incoming field-aligned current intensity and location combined with background dayside and night-side conductances. The potential is set to zero at the lower latitude boundary at 10°. The RIM solves the Vasyliunas (1970) equation for the electric potential and feeds the electric field values back to the MHD simulation, giving a boundary condition for the velocity at the inner boundary. At the same time, the electric field values are fed to the RCM via a one-way coupling for determination of the drift speeds. The ionosphere and magnetosphere models are coupled every 5 s.

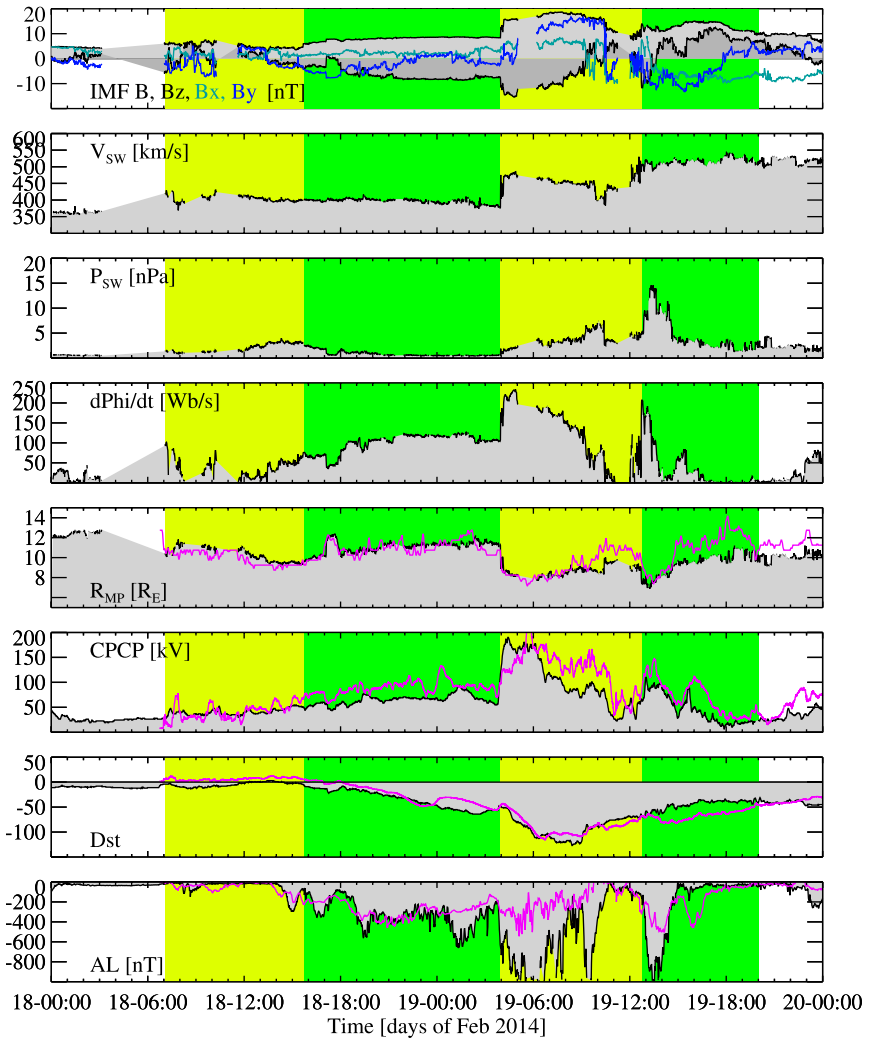

FIGURE 1 | Observations of the solar wind driver and magnetospheric response (black line with shading) compared with SWMF Geospace results (magenta line). From top to bottom: IMF X (green), Y (blue) Z (black) components, total field magnitude (black); solar wind speed; solar wind pressure, Newell coupling function (see text); Magnetopause standoff distance (see text); cross-polar cap potential (see text); SMR (SuperMAG SYM-H index); SML (SuperMAG AL index). The yellow and green shading indicate the ICME sheath and ejecta respectively. The magenta lines in the bottom four panels show the SWMF Geospace simulation results.

3 EVENT OVERVIEW

We focus on a time interval that comprises two interplanetary coronal mass ejections (ICME), which are a subset of a sequence of four that impacted the Earth during Feb 14–22, 2014. The geomagnetic activity that followed caused a complex sequence of depletions and enhancements of the van Allen belt electron populations (Kilpua et al., 2019). Here we focus on two consequtive ICMEs (second and third in the sequence) that were associated with a large geomagnetic storm and strong auroral region activity.

The period of Feb 18–20, 2014 contained two ICMEs that occurred back to back with the sheath region of the second ICME running into the ejecta of the first ICME. The first ICME impact was initiated by a shock at 0706 UT on Feb 18, and the ejecta arrived at 1545 UT. The second ICME shock arrived at 0356 UT, and the ejecta was observed between 1245 UT on Feb 19 and 0309 on Feb 20. **Figure 1** shows the solar wind observations measured by the WIND spacecraft at the first Lagrangian point L1 point about 220 R_E upstream of the Earth, and propagated to the bow shock as documented in the OMNI dataset (https://omniweb.gsfc.nasa.gov/). The yellow and green shading indicate the ICME sheath and ejecta respectively.

The IMF magnitude hovered between 5 and 10 nT until the second shock, when the field magnitude increased to almost 20 nT. IMF B_X was positive and small before the second ICME during which it turned strongly negative. IMF B_Y was close to zero before the second shock, which was associated with first strongly positive and then strongly negative B_Y. The B_Z decreased during the first sheath to negative, but was mostly positive during the second ejecta.

The proton density was generally small at about 2 cm^{-3}, but had a peak reaching above 10 cm^{-3} between about 1,200–1700 UT on Feb 18. The density increased gradually after the second shock, with peaks close to and above 30 cm^{-3} around 1000 and 1300 UT on Feb 19, respectively. The shock at 0356 UT on Feb 19 was also associated with a jump in the solar wind speed, from the nominal value at about 400 km/s during the first ICME, to slightly higher reaching above 500 km/s during the second ICME.

Figure 1 also shows the Newell et al. (2007) coupling parameter, representing the rate of change of magnetic flux at the nose of the magnetopause, and is an often used measure of the energy input from the solar wind into the magnetosphere—ionosphere system. The Newell function can be written in the form

$$\frac{d\Phi_{MP}}{dt} = \alpha\left[\left(\frac{V}{1\,\mathrm{km/s}}\right)^2 \frac{B_T}{1\,\mathrm{nT}} \sin^4\frac{\theta}{2}\right]^{2/3} \tag{1}$$

where $\theta = \tan^{-1}(B_Y/B_Z)$ is the IMF clock angle and $B_T = (B_Y^2 + B_Z^2)^{1/2}$ denotes the transverse component of the magnetic field perpendicular to the Sun-Earth line. As pointed out by Cai and Clauer (2013) and others, a normalizing factor must be included for the coupling function to have units of Wb/s. For this work $\alpha = 10^3$ Wb/s was chosen as a normalizing factor. The periods with largest Newell function values occurred during the ejecta of the first ICME and the sheath region of the second ICME. The ejecta of the second ICME occurred during northward IMF, and the Newell function during that period was small.

The following panels of **Figure 1** show the magnetospheric response to the solar wind driving. A proxy for the subsolar magnetopause standoff distance R_{MP} is given by the empirical Shue et al. (1998) model

$$R_{MP} = \left[10.22R_E + 1.29R_E \cdot \tanh\left(0.184\frac{B_Z}{1\,\mathrm{nT}} + 1.498\right)\right]\left(\frac{P}{1\,\mathrm{nPa}}\right)^{-1/6.6} \tag{2}$$

where P is the solar wind dynamic pressure $P = \rho V^2$, ρ is the plasma mass density, and the factor 1.498 = 0.184 8.14 used in the original paper. While the first ICME did not cause major compression of the magnetopause, the sheath region of the second ICME pushed the magnetopause to near 8 R_E, and the arrival of the ejecta compressed the magnetopause even closer to the Earth.

The sixth panel of **Figure 1** shows an empirical proxy for the cross-polar cap potential (CPCP) given by Ridley and Kihn (2004) as a function of the polar cap index (PCI) measured in the northern polar cap (Thule station) and season. In this formulation, the CPCP is given in the form

$$CPCP = 29.28\,\mathrm{kV} - 3.31\,\mathrm{kV} \cdot \sin(T + 1.49) + 17.81\,\mathrm{kV} \cdot PCI/(1\mathrm{mV/m}), \tag{3}$$

where the time of year is scaled as $T = 2\pi(N_{MONTH}/12)$ and the numbering of months starts from zero (Jan = 0, Jul = 6). The polar cap potential was above 50 kV for the early part of the interval, but peaked at nearly 200 kV following the second shock, reducing to below 50 kV as the IMF turned northward.

The two bottom panels show the storm time index SYM-H and the auroral electrojet index AL, measuring the intensity of the ring current and westward ionospheric current, respectively. The sheath region of the first ICME had no marked effects on the inner magnetosphere or auroral currents, but both intensified strongly during the ejecta passage during the latter part of Feb 18. The second ICME sheath region in the interval was characterized by strongly southward IMF, and consequently drove very strong auroral currents and led to strong enhancement of the SYM-H index. The second ICME ejecta was associated with recovery of the ring current as well as quieting of the auroral currents.

The magenta lines in **Figure 1** show the SWMF results in comparison with the observations. The SWMF Geospace simulation reproduces the subsolar magnetopause position to high accuracy with the exception of a diversion during the latter part of Feb 19th. The polar cap potential agrees quite well with the Ridley and Kihn (2004) empirical proxy. While the SYM-H index is quite well reproduced by the simulation, the simulation AL index does not reach the observed very high intensity during the second ICME sheath region.

4 MAGNETOSPHERIC BOUNDARY MOTION

Several of the Heliophysics System Observatory spacecraft were monitoring the dynamics of the magnetospheric boundaries at the time of the storm. The Cluster 4-spacecraft constellation as well as Geotail were on the dayside, traversing through the bow shock and magnetopause. The three inner THEMIS spacecraft A, D, and E had their apogee on the dayside skimming the dayside magnetopause. THEMIS B and THEMIS C were in the dawn flank, moving outward toward the nominal bow shock location. **Figure 2** shows the spacecraft trajectories in the GSM equatorial plane projection during the 2-day period. The grey shadings indicate a range of magnetopause and bow shock positions that empirical models predict for conditions that were observed during the interval.

In order to examine how well the SWMF Geospace simulation reproduces the magnetospheric boundary locations during this interval, we use observations from all five THEMIS craft, from Geotail, and from Cluster 4. **Figures 3–5** show magnetic field magnitude observations and simulation results. The vertical lines point out key times when there were changes in the solar wind and IMF (shown in black solid lines) or in the ground-based magnetic indices (substorm onsets, shown with dotted lines).

Figure 3 shows the Geotail and Cluster-1 measurements of the magnetic field magnitude (the Cluster craft were close together, and show essentially similar behavior). The top panel repeats the OMNI IMF magnitude for reference. Geotail was in the solar wind, traveling inbound, monitoring the near-shock IMF until entering into the magnetosheath at about 20 UT on Feb 19. Cluster crossed from the magnetopause into the magnetosheath at around 07 UT and into the solar wind at around 12 UT on Feb 18. Cluster showed a brief encounter with

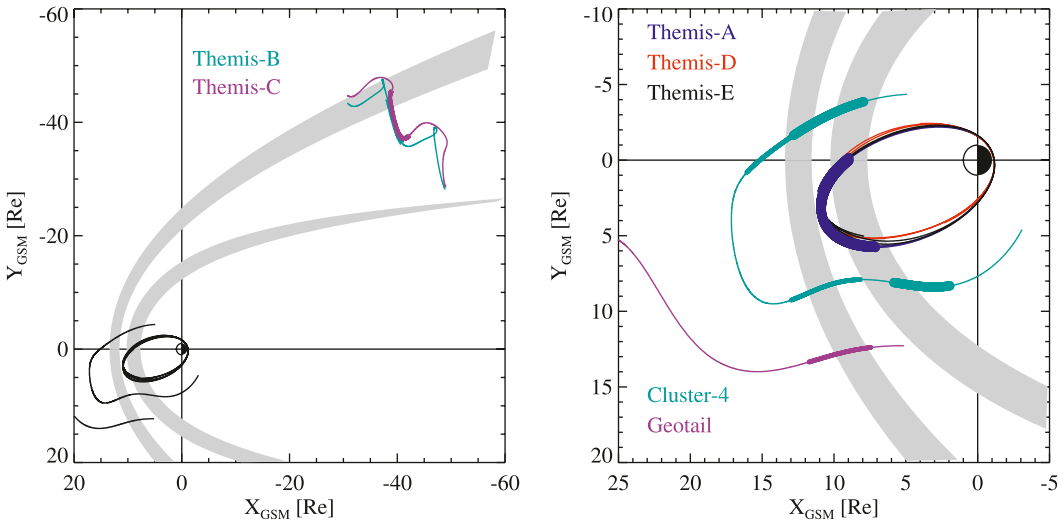

FIGURE 2 | Spacecraft trajectories in the GSM *X*–*Y* plane during Feb 18–20, 2014. The grey shadings show a range of magnetopause and bow shock locations based on the range of solar wind conditions during the period. The thickest line segments show periods when the SCWeb locator places the trajectory within 2 R_E from the magetopause, the medium thick segments show periods when the trajectory is within 2 R_E from the bow shock position.

the magnetosheath around 18 UT, a longer encounter between 20 UT on Feb 18 and 04 UT on Feb 19, and exited to the solar wind with the arrival of the sheath region of the second ICME which was associated with a strong compression of the magnetosphere. On its inbound path, Cluster crossed back to the magnetosheath at about 17 UT and into the magnetosphere at about 20 UT on Feb 19.

Figure 4 shows the THEMIS B and THEMIS C measurements at the dawn flank, close to the bow shock as demonstrated by the field values close to the IMF value combined with foreshock fluctuations. Both craft recorded a strong enhancement of the magnetic field in response to the increased IMF magnitude at about 04 UT on Feb 19 exceeding that of the IMF, indicating that the craft crossed the shock into the magnetosheath. As the IMF magnitude decreased, the THEMIS spacecraft returned to the solar wind.

Figure 5 shows the three inner THEMIS spacecraft observations of the dayside magnetospheric magnetic field. The large changes in IMF magnitude are seen as compression and relaxation in the dayside magnetic field as observed by all three spacecraft. Following the strongest compression period, THEMIS D and E crossed into the magnetosheath and during brief periods even to the pristine solar wind.

In each of the figures, the SWMF simulation results for the spacecraft locations are shown with magenta lines. In general, the boundary crossings associated with the inward motion of the magnetopause as the field magnitude increases are well reproduced by the simulation, while there are some timing differences associated with the boundary crossings.

The Geotail and Cluster virtual spacecraft time series match closely with observations other than brief enhancements, for the Geotail spacecraft around 23 UT on Feb 18 and for Cluster 4 most significantly shortly after 4 UT. Both simulation time series also show an early enhancement of B near the end of the simulation as they approach the magnetopause, indicating that the model magnetopause was slightly further out than the real one.

For THEMIS B and C, the only major difference between the simulation and observations is during the second ICME ejecta, when the simulation shows that the THEMIS location is immersed in the magnetosheath, shown as a strong and rapid increase and decrease of the simulated magnetic field magnitude between about 01 and 05 UT on Feb 19. The fluctuating field magnitude especially observed by THEMIS C is indicative of the spacecraft location very close to the bow shock, indicating that the simulation is likely showing only a minor deviation from the real location of the bow shock. The virtual spacecraft results of for the dayside THEMIS probes A, D, and E show minor timing errors and an overall lack of high-frequency oscillations in the magnetic field magnitude.

In **Figure 5**, times when the spacecraft locator (Staples et al., 2020) predicted magnetopause crossings are marked with red vertical lines (**Figure 2**). The local B magnitude average near the identified magnetopause crossings gives an indication that the magnetopause location is well reproduced with the simulation.

5 BOUNDARY IDENTIFICATION IN THE SIMULATION

In order to quantify the energy transfer into the magnetosphere, we need to identify the magnetopause surface in the simulation. While the magnetopause can be topologically defined as the boundary between open and closed field lines in the dayside, it is often not a practical way to define the surface beyond the (quasi)dipolar region. In this work, the magnetopause identification was done via a field variable iso-surface of a modified plasma β parameter, which includes the MHD ram pressure ($P = \rho V^2$) as part of the plasma pressure,

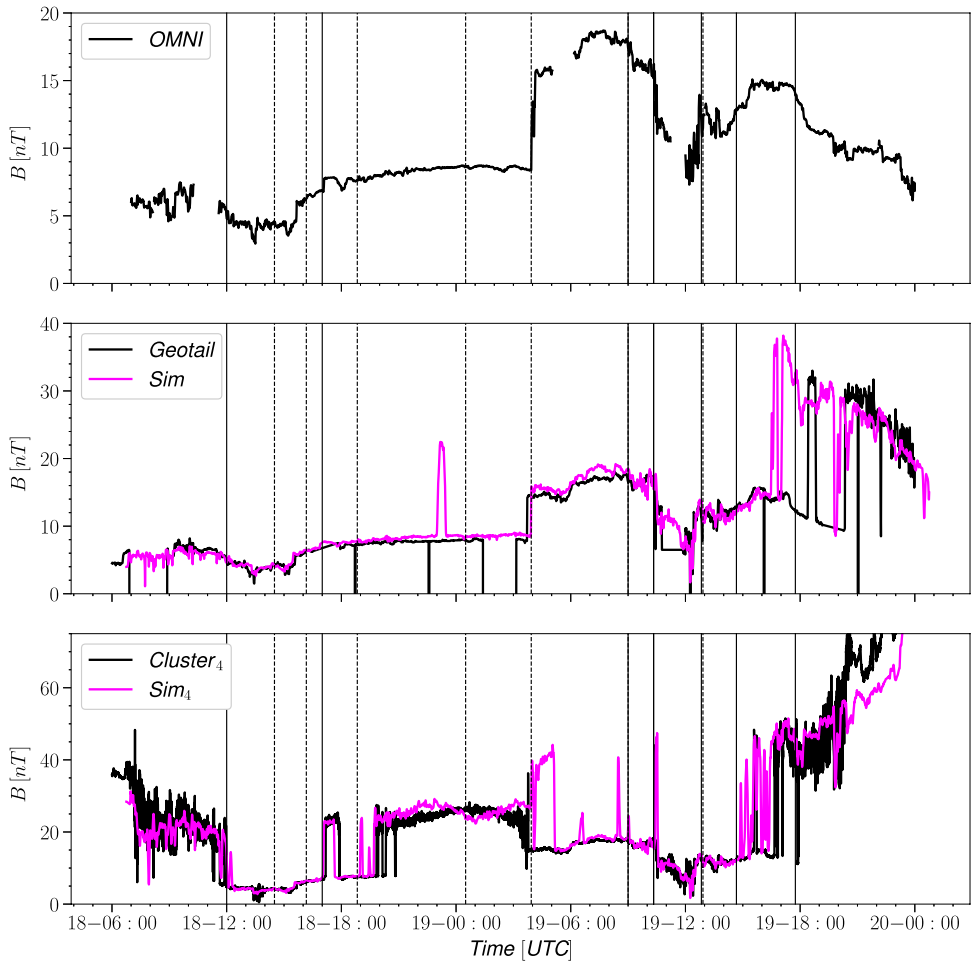

FIGURE 3 | Magnetic field magnitude trace observation (black) vs simulation (magenta) Geotail and Cluster 4.

$$\beta^* = \frac{P_{th} + P}{B^2/2\mu_0} \tag{4}$$

where *Pth* is the plasma thermal pressure. This isosurface was expanded to include the fully closed field line region found by field line tracing techniques during simulation run time. The iso-surface generation technique was that provided by the "all triangles" creation method available in Tecplot software (Tecplot 360 EX 2020 R1, Version 2020.1.0.107285, Jul 13, 2020). The magnetospheric volume is closed by a cross-section of the tail at a constant X-value. Note that high β^* plasma in the plasma sheet that is no longer on fully closed field lines can be found at distances within the constant X closure so the back surface was not always a perfect plane.

Figure 6 shows color contours of β^* in the $Y = 0$ plane, which shows that there is a sharp gradient in the contour around the selected boundary value of 0.7. The sharp gradient demonstrates the insensitivity of the exact β^* iso-surface level to the boundary location results. Indeed, multiple values of β^* were tried and 0.7 was selected in order to push the boundary as far out as possible without pushing the dayside boundary sunward of the last closed fieldline, where β^* can drop significantly. If this effect was compensated for separately, any value between 0.1 and 1.5 should yield similar results.

The complete closed 3D surface was split into dayside, flank, and tail subsections such that the dayside corresponds to the region with $X > 0$, the tail cross-section is defined by $X = X_{min}$ mostly in the YZ_{GSM} plane, and the flank is the remaining magnetopause surface area between the terminator and $X = X_{min}$. The top panels of **Figure 7** show the identified surface with dayside highlighted in light blue, magnetotail lobes in dark blue, and the tail cross section at $X_{min} = -20R_E$ in purple. These surfaces combined form a closed surface that we use to examine energy flow into and out of the (inner part) of the magnetosphere.

6 ENERGY TRANSFER THROUGH A SIMULATION SURFACE

The total energy density U within a plasma volume is given in the MHD limit as

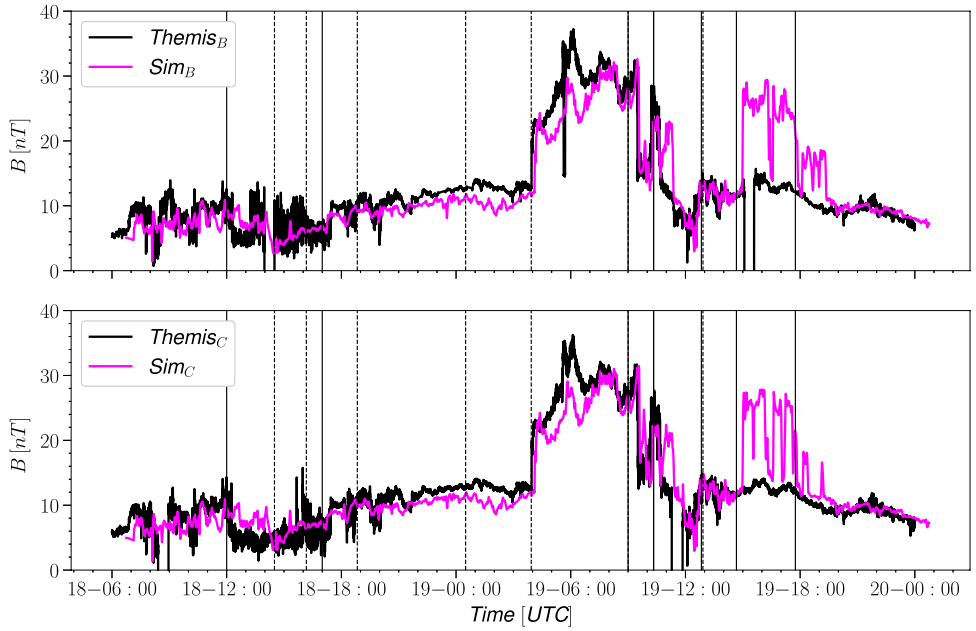

FIGURE 4 | Magnetic field magnitude trace observation (black) vs simulation (magneta) Themis B and C.

$$U = \frac{1}{2}\rho V^2 + \frac{1}{\gamma - 1}P_{th} + \frac{B^2}{2\mu_0} \tag{5}$$

where $\gamma = 5/3$ is the ratio of specific heats. The corresponding total energy flux vector **K** is then given by

$$\mathbf{K} = \left(\frac{1}{2}\rho V^2 + \frac{\gamma}{\gamma - 1}P_{th} + \frac{B^2}{\mu_0}\right)\mathbf{V} - \frac{\mathbf{B}\cdot\mathbf{V}}{\mu_0}\mathbf{B} \tag{6}$$

In order to examine the relative contributions of the plasma and electromagnetic processes, we re-arrange the equation to a sum of hydrodynamic energy flux **H** and Poynting flux $\mathbf{S} = (\mathbf{E}\times\mathbf{B})/\mu_0$ to read

$$\mathbf{K} = \left(\frac{1}{2}\rho V^2 + \frac{\gamma}{\gamma - 1}P_{th}\right)\mathbf{V} + \left(\frac{B^2}{\mu_0}\mathbf{V} - \frac{\mathbf{B}\cdot\mathbf{V}}{\mu_0}\mathbf{B}\right) = \mathbf{H} + \mathbf{S} \tag{7}$$

The energy transfer through the boundary specified in the previous section is given by the component of the energy fluxes normal to the boundary ($\mathbf{K}\cdot\mathbf{n}$), using the convention that the surface normal **n** points outward. The total energy flux rate is then obtained by integration over the entire surface area: $K_{tot} = \int_A \mathbf{K}\cdot\mathbf{dA}$. Using this notation, negative values of the flux through the surface ($\mathbf{K}\cdot\mathbf{n} < 0$) indicate total energy injection through the magnetopause into the magnetosphere. The time rate of change of the total energy enclosed within the boundary is then given as the net transport across the surface.

At times when the solar wind is rapidly changing and the magnetopause undergoes rapid compression or expansion, it is necessary to include the boundary motion into the equation. This can be done using the Reynolds transport theorem that describe the time rate of change of the total energy—the energy that is added to and lost from the volume enclosed by a surface in motion. Using the Reynolds transport theorem, the time rate of change of the total energy density (U) within the volume enclosed by the magnetopause (including the tail cross section closing the surface) can be written in the form

$$\frac{d}{dt}\int_V U dV = -\int_{A(t)} (\mathbf{K} - U\mathbf{q})\cdot\mathbf{dA} \tag{8}$$

where **q** is the surface velocity. Note that only the normal component of the surface velocity $\mathbf{q}\cdot\mathbf{n}$ matters. We also note that this equation does not account for the coupling to the inner magnetosphere module, which will also alter the energy density from the ideal MHD value. However, the right hand side captures all energy transfer effects at the magnetopause boundary, which is the focus of this study.

The surface is determined at discrete times, which means that the surface velocity has to be determined from a discrete approximation. We approximate the energy change associated with the moving boundary as a volumetric integral between the two surfaces:

$$\int_{A(t)} U\mathbf{q}\cdot\mathbf{dA} \approx \frac{1}{\delta t}\int_{\delta V} U dV, \tag{9}$$

where $\delta t = t_{n+1} - t_n$ is the time difference between times t_n and t_{n+1}, and δV is the signed volume between the magnetospheric surfaces at the two times. **Figure 8** illustrates the sign convention for this contribution to the energy transfer. This method allows us to compute energy addition and loss due to the boundary motion separately for the dayside, flank, and tail regions.

The streamlines in **Figure 6** show the total energy transfer vector **K**, and demonstrate that the energy transfer vectors

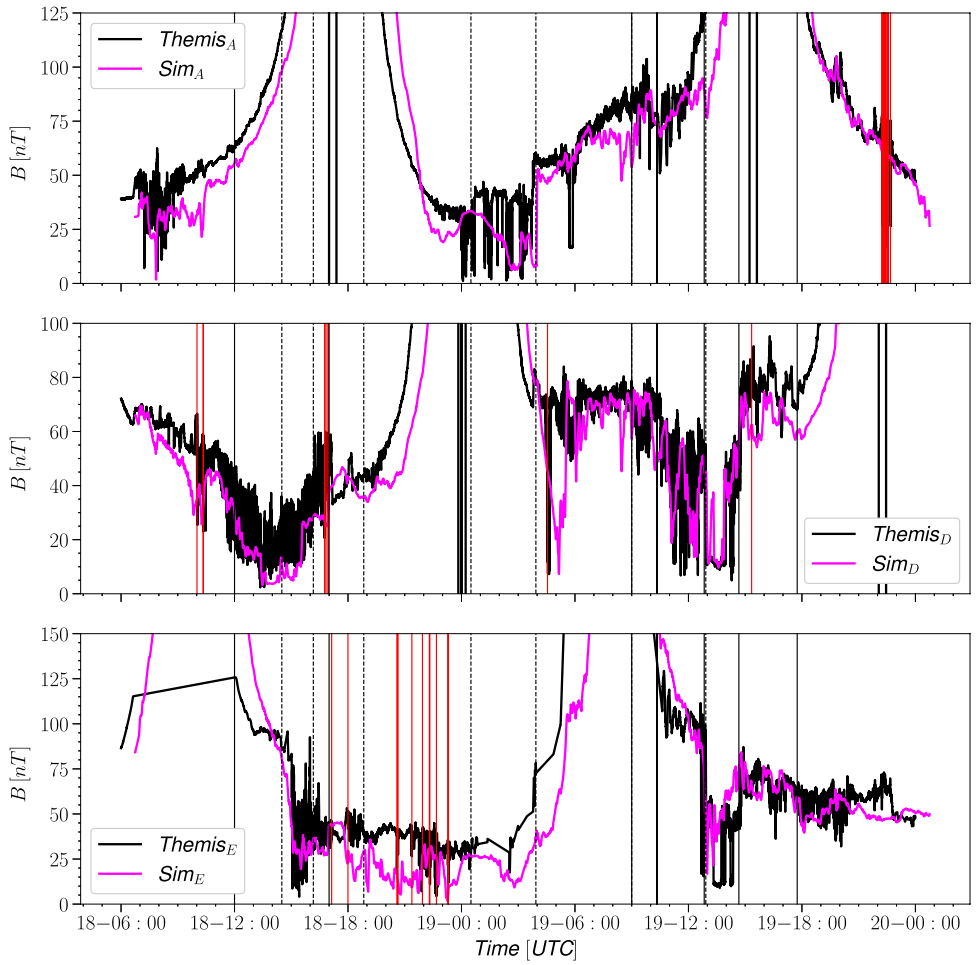

FIGURE 5 | Magnetic field magnitude trace observation vs simulation Themis A, D, and E. Vertical red lines indicate crossings as determined by Staples et al. (2020).

penetrate well into the identified surface before turning, giving further evidence that the determination of energy at the boundary is insensitive to the exact value of β^*. The bottom panels of **Figure 7** show, at one given time instant, the energy flux into the magnetosphere (left) and out of the magnetosphere and through the magnetotail (right).

7 STORMTIME ENERGY TRANSFER

Figure 9 shows integrated energy transfer through the entire magetopause surface broken down by type and sign. The top panel shows the total energy transfer rates, demonstrating that the net injection (brown) and escape (magenta) closely trace each other (with opposite signs). This indicates that there is much more energy flowing through the system than building up or escaping from inside the system. The net energy transfer (grey) shows short (of the order of a few hours) excursions of imbalance, but the average values are smaller than the totals by at least a factor of two.

The next two panels of **Figure 9** show the Poynting flux and hydrodynamic energy components of energy transfer. The energy injection is clearly dominated by the Poynting flux, while the Poynting flux has only a minor effect on the energy escape. On the other hand, hydrodynamic energy dominates the energy escape. Both types of energy as well as the total energy transfer rates clearly increase during the high ram pressure, high IMF magnitude portion of the event.

Figure 10 shows the contribution to the total energy transfer solely from the moving surface, using the right hand side of **Eq. 9**. The net energy transfer from the combined static and motional effects is shown in grey shading for comparison. The motional contributions of energy injection and escape are often unbalanced, which results the surface motion making a major contribution to the net totals. The top panel showing the solar wind ram pressure demonstrates a clear correlation with (changes in) the pressure and the boundary motion contribution to the energy transfer. As expected, during ram pressure spikes the surface volume decreases and energy escapes from the magnetosphere, especially during the oscillating behaviour of

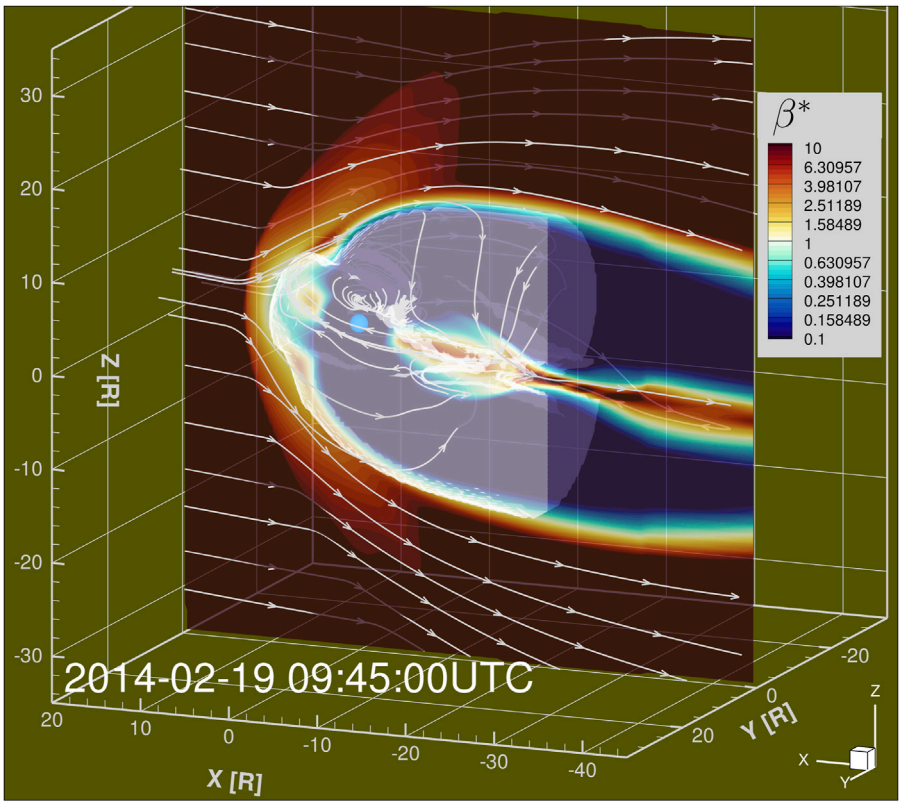

FIGURE 6 | 3D snapshot of total energy transfer vector **K** flowfield with meridional cut showing color contours of β^*. Translucent structure represents identified magnetopause surface out to $-20R_e$ in the x direction.

the volume beginning around 05 UT on the 19th (based on the relation between standoff distance and ram pressure the ram pressure and volume raised to −2.2 should scale about linearly; the Pearson correlation coefficient between the two is about 0.65). The first small enhancement in energy transfer due to the moving surface occurs during the first ICME ejecta and is due to enhanced energy in the flowfield, which cause relatively small fluctuations in surface velocity to transfer significant energy. The next enhancement results in net energy escape and is due to a dramatic shape change in the magnetosphere volume along the closed field line "wings" in the equatorial plane. Similar to the first energy enhancement the latter part of the event contains enhanced IMF magnitude which results in large changes in energy transfers due to the moving surface.

The bottom panel of **Figure 10** shows the volume enclosed by the surface created by the magnetopause and the tail cross section, using the Shue et al. (1998) model (black) and the surface identified from the SWMF Geospace simulation (magenta). While the two volumes generally correlate well, there are differences especially prior to when the strongest storm activity begins.

Figure 11 shows the contributions from the dayside, flank and tail stacked together to equal the total injection (negative) and escape (positive) for each type of energy. The top panel, which shows the total energy transfer indicates that the flank contribution can reach the level of the dayside energy transfer, while the tail cross-section consistently has only a small contribution. The second panel of **Figure 11** shows that the dayside contribution to Poynting flux is quite steady throughout the event and is primarily energy escape, while the flank region contributes more to energy injection throughout the event and contains almost all of the high Poynting flux transfers both into and out of the magnetosphere. The bottom panel shows the breakdown for the total energy transfer by region in terms of percent contribution to better illustrate the tradeoff between the dayside and flank. The times when the flank contribution overtakes the dayside contribution appears to coincide with periods when high energy transfer on the surface is advected along the magnetopause surface from the dayside to the flank. These transient periods can also be seen in the third panel, in the distance between sharp drops in the dayside contribution in light blue and the total energy transfer indicated by the extremes of the curves.

8 DISCUSSION

In this paper, we have developed a method to identify the magnetopause boundary from a global MHD simulation, and

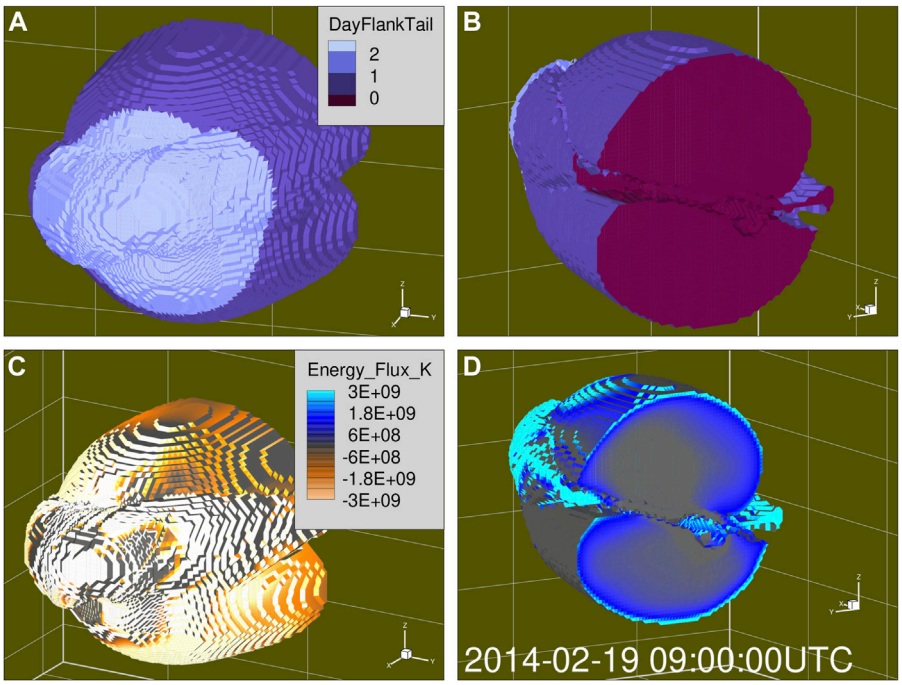

FIGURE 7 | (A,B) show spatial breakdown of Dayside, Flank, and Tail subsections. **(C,D)** show energy flux into and out of the magnetosphere volume normal to the surface.

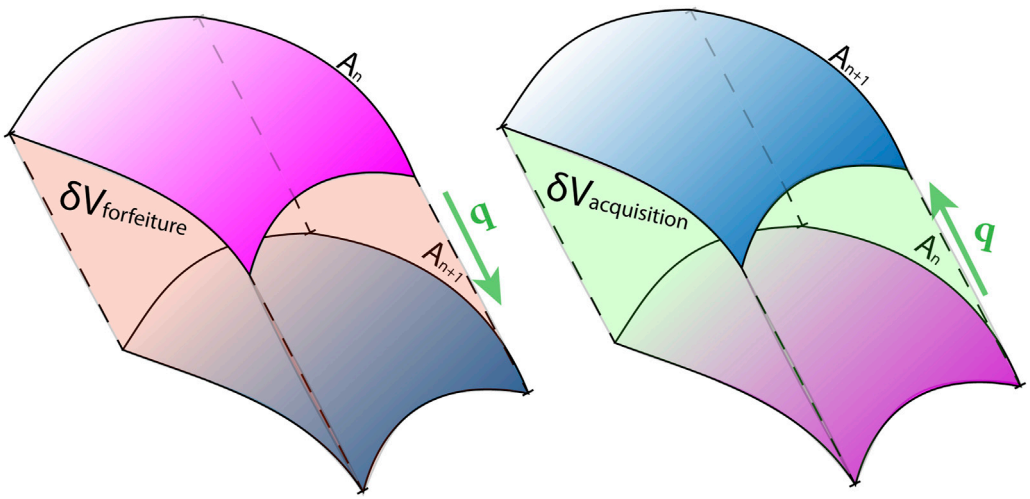

FIGURE 8 | At each time step the energy density is integrated over δV representing the volume that will be acquired and/or lost in the next time step. Acquisitions and forfeitures are included in integrated flux of energy injected or escaped respectively. The local surface velocity is indicated by the vector **q**. The normal distance between the surfaces is $(\mathbf{q} \cdot \mathbf{n})\delta t$ (**Eq. 9**).

calculate the energy transfer through that boundary into and out of the magnetosphere during a large geomagnetic storm. We examined the energy entry and exit separately, integrating the totals over the closed surface. Moreover, we examined contributions from the dayside (Sunward of the terminator), from the flanks (magnetopause between the terminator and $X = -20\ R_E$) and the tail cross section at the $X = -20\ R_E$ plane, and computed the energy components related to the Poynting flux and hydrodynamic energy flux separately.

The most striking conclusion from our study is that most of the time, there is significant energy injection into the magnetosphere, but it is (almost) balanced by energy escaping the system. Our results show that most of the energy enters as

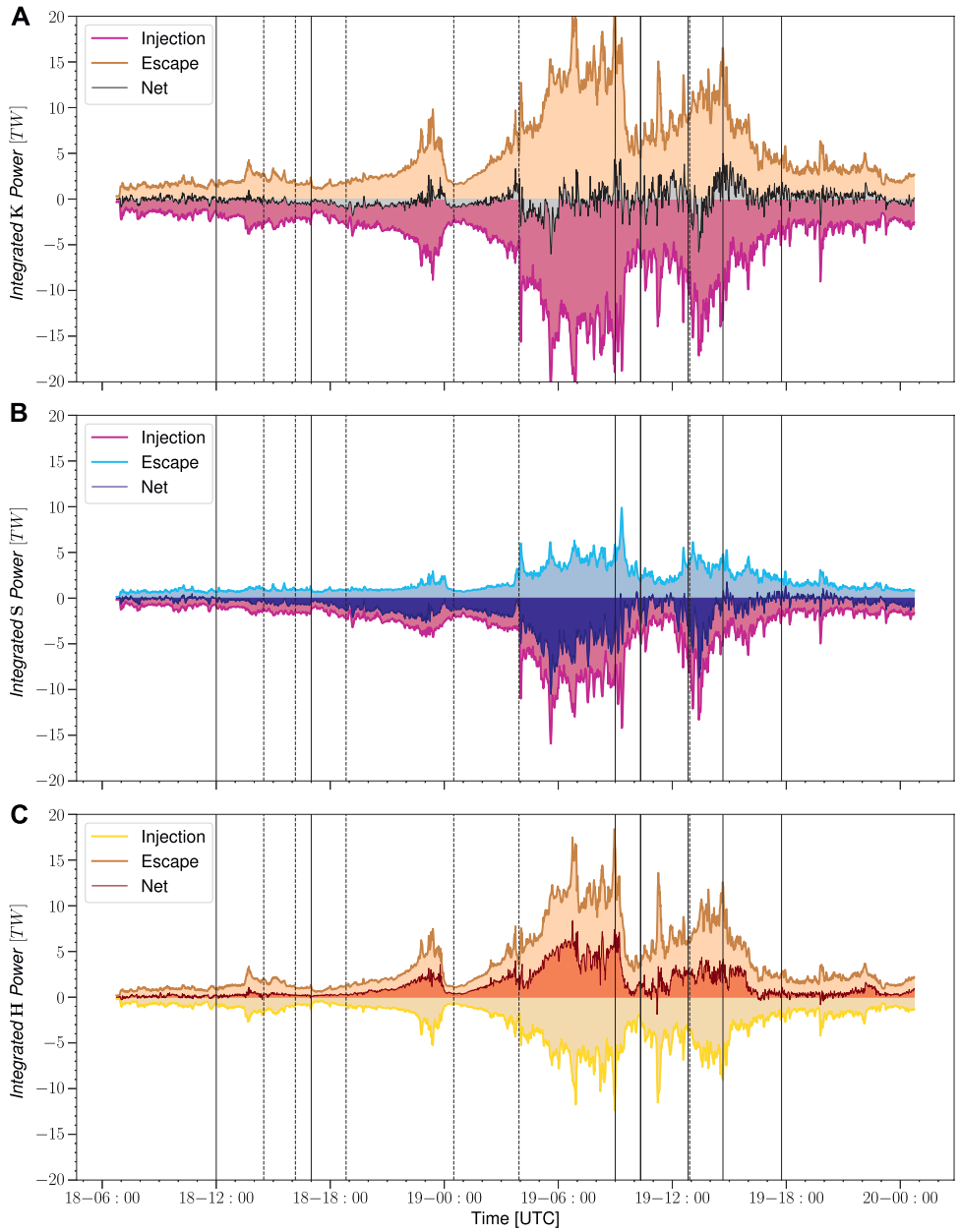

FIGURE 9 | Full surface energy flux integration breakdown by type, **(A)**: **K (B)**: **S (C)**: **H** (**Eq. 7**).

Poynting flux, while the escape is dominated by the hydrodynamic energy flux (**Figure 9**). The energy transfer processes are most active in the dayside region (Sunward of the terminator), while the flank processes can be dominant at times. More events need to be analyzed to distinguish the conditions that dictate where the energy transfer processes take place. A lot of magnetospheric research has focused on processes in the magnetotail and estimating the energy that is associated with plasmoids leaving the system (e.g. Baker et al., 1996; Angelopoulos et al., 2013). However, our analysis shows that, in the large scale, the magnetotail plays only a minor role in the overall energy transfer. More detailed study focusing on substorm periods is needed to assess how important the tail contribution is during the substorm expansion phases.

Earlier work by Palmroth et al. (2003) shows an analogous analysis of magnetopause energy transfer in a global MHD simulation. Their results are based on a different method for magnetopause identification, they did not consider the effects of the boundary motion, and their simulation did not include the inner magnetosphere ring current contribution that in our case is represented via the coupling of the Rice Convection Model to the global MHD model. However, in the large scale, the results are analogous, showing the significant energy transfer along the tail flanks, and strongly and rapidly varying location and intensity of

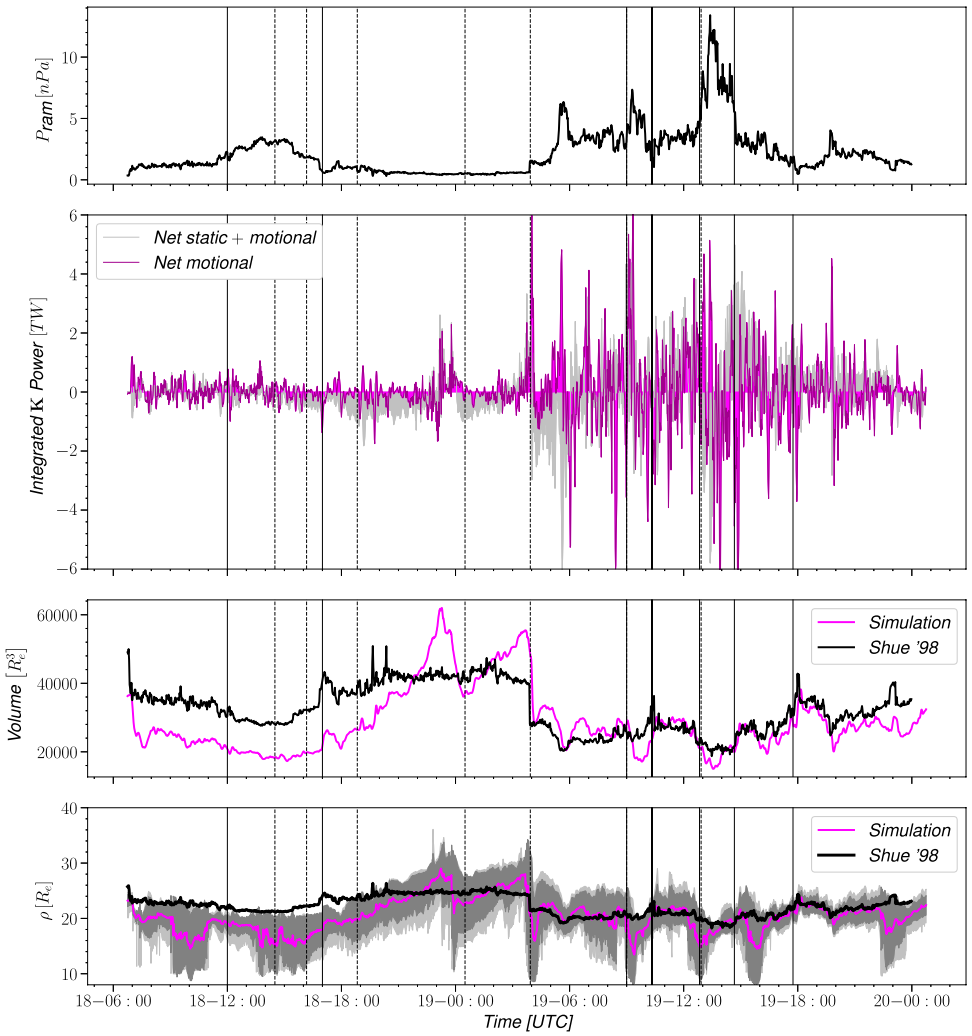

FIGURE 10 | From top to bottom: Solar wind ram pressure; Integrated net power transfer due to surface motion effects only (magenta) compared with static and motion effects (grey); Magnetosphere volume integrated from simulation (magenta) compared with Shue 1998 model (black); Radial distance $\rho = \sqrt{Y^2 + Z^2}$ evaluated at $X = -10R_e$ for the magnetopause from simulation (magenta) with dark and light bars indicating ±1.5 standard deviations and max/min respectively, compared with Shue 1998.

the energy transfer processes. While their tail integration extended out to 30 R_E, and they did not include a magnetotail cross section, the overall magnitudes are comparable (Pulkkinen et al., 2008), which speaks to the robustness of the procedure. A more recent study by Jing et al. (2014) used SWMF with the magnetopause detection technique of Palmroth et al. (2006) and results support their findings, giving further confidence to the tools used for this study.

Observationally, the spaceborne measurements are not sufficient to yield global energy transfer rate estimates, but a significant body of work has assessed the role of the IMF components, the solar wind density and speed, and the solar wind electric field in the efficiency of the energy transfer process. Several coupling parameters relating the solar wind driver to the geomagnetic indices such as AL or Dst have been devised: The most widely used are the solar wind electric field $E_Y = V_X B_Z$ (where V_X is negative) (Burton et al., 1975), the rectified solar wind electric field $E_S = \max(E_Y, 0)$ (so $E_S = 0$ for $B_Z > 0$) (McPherron et al., 2013), or the electric field parallel to the large-scale neutral line at the magnetopause (Pulkkinen et al., 2010). More complicated functions include the epsilon-parameter ($\epsilon = 10^7 \nu B^2 \sin^4(\theta/2)$) introduced by (Akasofu, 1981) and the (Newell et al., 2007) coupling parameter given by **Eq. 1**.

The top panel of **Figure 12** shows a comparison of the energy injection rate integrated over the entire surface compared with the Akasofu epsilon-parameter. While the magnitudes differ (the ϵ-parameter has empirical scaling that originally was matched with the Dst and AL contributions), the shape of the functions agree very well, indicating that the gating function $\sin^4(\theta/2)$ in the ϵ-parameter is quite representative of the energy entry process.

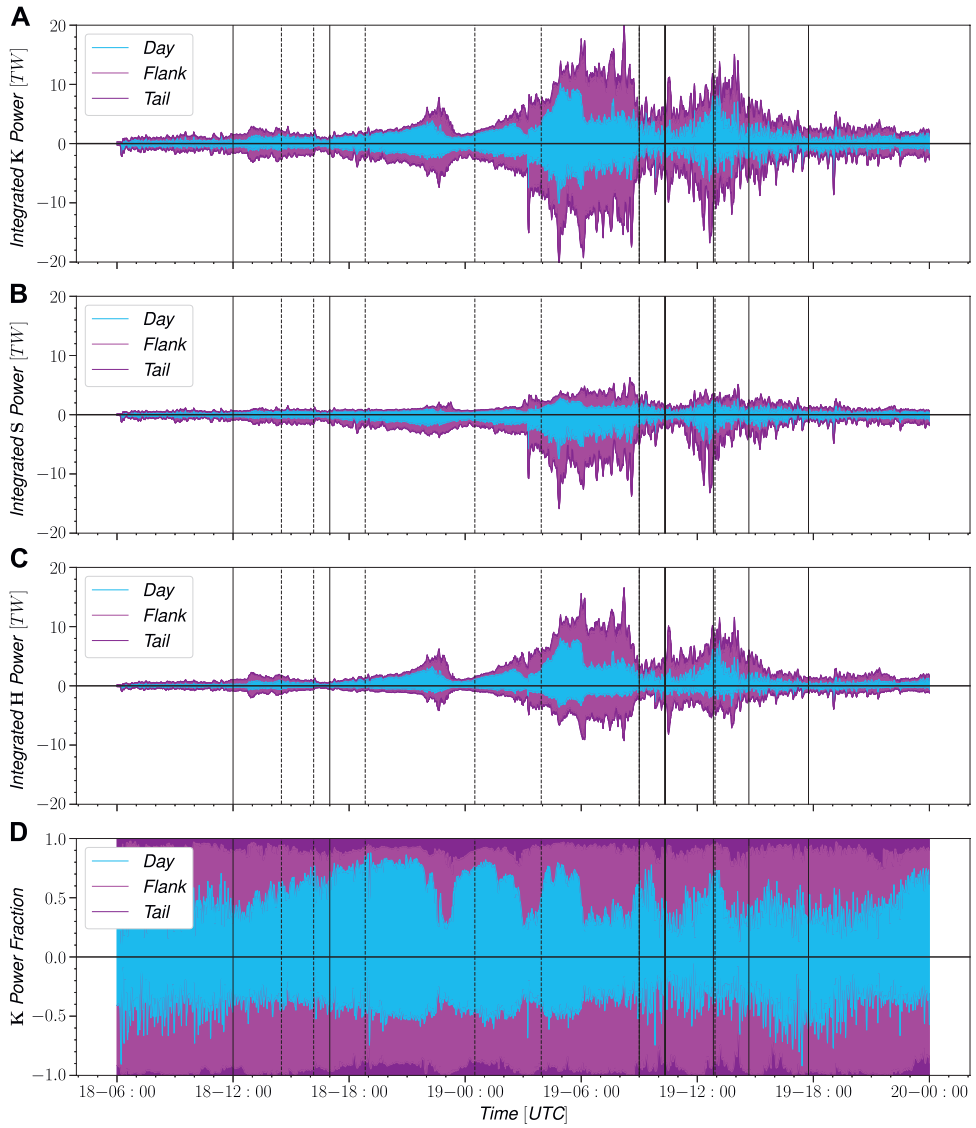

FIGURE 11 | Energy injection and escape stacked by contribution. The first stack represents contribution from the dayside starting from 0. Next is the contribution from the flank starting from the dayside contribution and lastly is the contribution from the tail cap totalling to the injection and escape values found in **Figure 9**. As before the **(A)** represents total energy transfer, the **(B)** is Poynting flux and the **(C)** is the hydrodynamic energy flux. The **(D)** shows the relative contributions.

The second panel of **Figure 12** shows a similar comparison with the Newell coupling function and the polar cap potential in the simulation northern and southern ionosphere. Using the scaling for the Newell coupling parameter introduced by Cai and Clauer (2013), the magnitudes as well as the functional forms agree quite well, indicating that the Newell coupling function is a good proxy for energy that enters the polar ionospheres.

While the focus of this work is on the energy coupling at the magnetopause boundary, the energy density was also integrated over the entire volume to compare with the ground magnetic perturbation. The bottom panel of **Figure 12** shows a high degree of correlation between the total energy and ground magnetic perturbation represented by the Dst index. This correlation is expected considering the theoretical formulation of the Dessler-Parker-Sckopke relation Dessler and Parker (1959) and the more general applications of the virial theorem as reviewed by Carovillano and Siscoe (1973). The clear connection between the total energy and ground magnetic perturbation underlines the importance of studying magnetosphere coupling in terms of energy transport.

The addition of the surface motion makes significant contributions to the energy transfer integrated totals despite having a relatively low amplitude due to the unbalanced contributions to energy injection and escape. Comparisons of the volume to the Shue model reveal a high degree of cylindrical asymmetry as the closed field line regions expand and are then lost, first by an internal process and again corresponding to a solar wind ram pressure spike. This effect can clearly be seen in

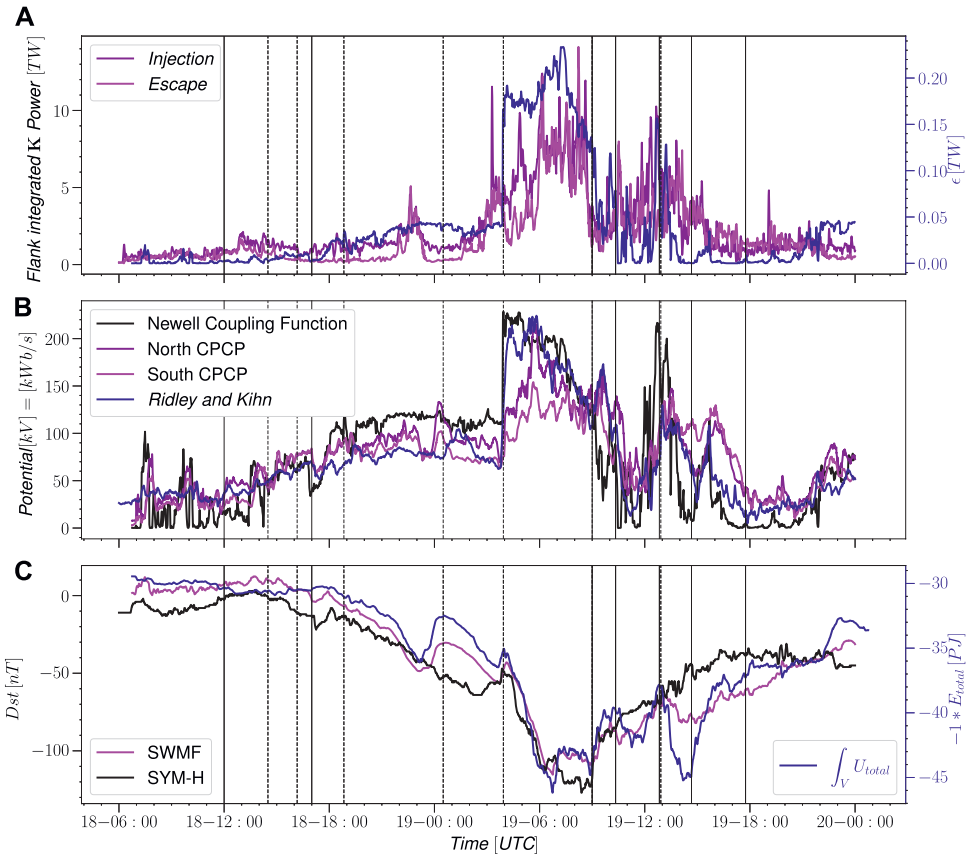

FIGURE 12 | (A): Total energy transfer compared with Akasofu coupling parameter. **(B)**: Cross polar cap potential from simulation and empirical model, compared with solar wind coupling of Newell. **(C)**: Ground magnetic perturbation from simulation (magenta) and observation (black), plotted with energy density integrated over the defined magnetosphere volume.

the observations of ground magnetic perturbation and total energy around 04 UT on the 19th when the second ICME shock impacts. During this time a portion of the lateral closed field line region is lost, the volume undergoes rapid decrease, the simulated total energy sharply decreases in magnitude, and the energy spike is matched by both the simulated and ground based observation. Further studies are needed to understand what takes place in the magnetosphere during these fluctuations, to determine how much of the motion is due to magnetopause boundary oscillations. The results also show that the moving surface contribution is sensitive to the surrounding flowfield properties: When more energy density is contained in the magnetosheath, a relatively small fluctuation in surface position can result in large energy transfer.

9 CONCLUSION

In this work a 3D simulation was used to investigate the magnetosphere solar wind coupling during a very active event. *In situ* observations were combined with ground measurements of magnetic perturbations and empirical models were employed to better understand the expected behavior of the magnetosphere system and to validate the simulation results.

The main conclusions can be summarized as:

1) We have developed a robust method to assess the energy entry through the magnetopause into the magnetosphere. The energy entry is dominated by the Poynting flux, while the energy escapes from the system mainly in the form of hydrodynamic energy flux.
2) While dayside reconnection is an important process for the energy transfer, the energy transfer occurs throughout the magnetopause surface, with the flank contribution often being dominant.
3) Motion of the magnetopause causes an important contribution to the energy transfer rates, and thus cannot be ignored in the energy transfer rate computations.
4) The energy injection rate scales well with the Akasofu epsilon-function, while the total energy integrated within the closed volume defined by the magnetopause and a tail cross section (at $X = -20R_E$) has a very similar functional shape to the Dst index, highlighting the ability of the Dst to capture the energy content within the magnetosphere.

5) The simulation magnetosphere shows significant asymmetry (deviation from rotational symmetry of the magnetopause surface). This leads to significant differences between volume estimates using the true magnetopause surface and empirical models especially during rapid variations in the driver parameters.

DATA AVAILABILITY STATEMENT

The datasets presented in this study can be found at the University of Michigan Deep Blue repository. https://doi.org/10.7302/nxyj-7062.

AUTHOR CONTRIBUTIONS

AB and QA, were responsible for running the simulation. AB, TP, QA, and GT contributed to analysis methodology conception. AB wrote and developed the analysis code. TP was responsible for event selection and initial event analysis. AB and TP were responsible for writing the manuscript. AB, TP, QA, and GT contributed to manuscript revisions leading to submitted version.

FUNDING

This research was funded through NSF grant number 2033563 and as part of the NASA DRIVE Center SOLSTICE (Grant Number 80NSSC20K0600).

ACKNOWLEDGMENTS

This work was carried out using the SWMF and BATS-R-US tools developed at the University of Michigan's Center for Space Environment Modeling (CSEM). The modeling tools described in this publication are available online through the University of Michigan for download and are available for use at the Community Coordinated Modeling Center (CCMC) as well as through Github at https://github.com/MSTEM-QUDA.

REFERENCES

Akasofu, S. (1981). Energy Coupling between the Solar Wind and the Magnetosphere. *Space Sci. Rev.* 28, 121–190. doi:10.1007/bf00218810

Angelopoulos, V., Runov, A., Zhou, X. Z., Turner, D. L., Kiehas, S. A., Li, S. S., et al. (2013). Electromagnetic Energy Conversion at Reconnection Fronts. *Science* 341, 1478–1482. doi:10.1126/science.1236992

Baker, D. N., Pulkkinen, T. I., Angelopoulos, V., Baumjohann, W., and McPherron, R. L. (1996). Neutral Line Model of Substorms: Past Results and Present View. *J. Geophys. Res.* 101, 12975–13010. doi:10.1029/95ja03753

Baker, D. N., Pulkkinen, T. I., Büchner, J., and Klimas, A. J. (1999). Substorms: A Global Instability of the Magnetosphere-Ionosphere System. *J. Geophys. Res.* 104, 14601–14611. doi:10.1029/1999JA900162

Burton, R. K., McPherron, R. L., and Russell, C. T. (1975). An Empirical Relationship between Interplanetary Conditions andDst. *J. Geophys. Res.* 80, 4204–4214. doi:10.1029/ja080i031p04204

Cai, X., and Clauer, C. R. (2013). Magnetospheric Sawtooth Events during the Solar Cycle 23. *J. Geophys. Res. Space Phys.* 118, 6378–6388. doi:10.1002/2013JA018819

Carovillano, R. L., and Siscoe, G. L. (1973). Energy and Momentum Theorems in Magnetospheric Processes. *Rev. Geophys.* 11, 289–353. doi:10.1029/RG011i002p00289

Chen, Y., Tóth, G., Cassak, P., Jia, X., Gombosi, T. I., Slavin, J. A., et al. (2017). Global Three-Dimensional Simulation of Earth's Dayside Reconnection Using a Two-Way Coupled Magnetohydrodynamics with Embedded Particle-in-Cell Model: Initial Results. *J. Geophys. Res. Space Phys.* 122, 10,318–10,335. doi:10.1002/2017JA024186

De Zeeuw, D. L., Sazykin, S., Wolf, R., Gombosi, T., Ridley, A., and Tóth, G. (2004). Coupling of a Global MHD Code and an Inner Magnetospheric Model: Initial Results. *J. Geophys. Res.* 109, 219. doi:10.1029/2003JA010366

Dessler, A. J., and Parker, E. N. (1959). Hydromagnetic Theory of Geomagnetic Storms. *J. Geophys. Res.* 64, 2239–2252. doi:10.1029/JZ064i012p02239

Janhunen, P., Palmroth, M., Laitinen, T., Honkonen, I., Juusola, L., Facskó, G., et al. (2012). The GUMICS-4 Global MHD Magnetosphere-Ionosphere Coupling Simulation. *J. Atmos. Solar-Terrestrial Phys.* 80, 48–59. doi:10.1016/j.jastp.2012.03.006

Jing, H., Lu, J. Y., Kabin, K., Zhao, J. S., Liu, Z.-Q., Yang, Y. F., et al. (2014). Mhd Simulation of Energy Transfer across Magnetopause during Sudden Changes of the Imf Orientation. *Planet. Space Sci.* 97, 50–59. doi:10.1016/j.pss.2014.04.001

Kilpua, E. K. J., Turner, D. L., Jaynes, A. N., Hietala, H., Koskinen, H. E. J., Osmane, A., et al. (2019). Outer Van allen Radiation belt Response to Interacting Interplanetary Coronal Mass Ejections. *J. Geophys. Res. Space Phys.* 124, 1927–1947. doi:10.1029/2018JA026238

Laitinen, T. V., Janhunen, P., Pulkkinen, T. I., Palmroth, M., and Koskinen, H. E. J. (2006). On the Characterization of Magnetic Reconnection in Global Mhd Simulations. *Ann. Geophys.* 24, 3059–3069. doi:10.5194/angeo-24-3059-2006

Liemohn, M., Ganushkina, N. Y., De Zeeuw, D. L., Rastaetter, L., Kuznetsova, M., Welling, D. T., et al. (2018). Real-Time SWMF at CCMC: Assessing the Dst Output from Continuous Operational Simulations. *Space Weather.* 16, 1583–1603. doi:10.1029/2018SW001953

Lyon, J. G., Fedder, J. A., and Mobarry, C. M. (2004). The Lyon-Fedder-Mobarry (LFM) Global MHD Magnetospheric Simulation Code. *J. Atmos. Solar-Terrestrial Phys.* 66, 1333–1350. doi:10.1016/j.jastp.2004.03.020

McPherron, R. L., Baker, D. N., Pulkkinen, T. I., Hsu, T.-S., Kissinger, J., and Chu, X. (2013). Changes in Solar Wind-Magnetosphere Coupling with Solar Cycle, Season, and Time Relative to Stream Interfaces. *J. Atmos. Solar-Terrestrial Phys.* 99, 1–13. Dynamics of the Complex Geospace System. doi:10.1016/j.jastp.2012.09.003

Newell, P. T., Sotirelis, T., Liou, K., Meng, C.-I., and Rich, F. J. (2007). A Nearly Universal Solar Wind-Magnetosphere Coupling Function Inferred from 10 Magnetospheric State Variables. *J. Geophys. Res.* 112, a–n. doi:10.1029/2006JA012015

Nykyri, K., Bengtson, M., Angelopoulos, V., Nishimura, Y., and Wing, S. (2019). Can Enhanced Flux Loading by High-Speed Jets Lead to a Substorm? Multipoint Detection of the Christmas Day Substorm Onset at 08:17 UT, 2015. *J. Geophys. Res. Space Phys.* 124, 4314–4340. doi:10.1029/2018JA026357

Nykyri, K., and Otto, A. (2001). Plasma Transport at the Magnetospheric Boundary Due to Reconnection in Kelvin-Helmholtz Vortices. *Geophys. Res. Lett.* 28, 3565–3568. doi:10.1029/2001GL013239

Palmroth, M., Janhunen, P., and Pulkkinen, T. I. (2006). Hysteresis in Solar Wind Power Input to the Magnetosphere. *Geophys. Res. Lett.* 33, L03107. doi:10.1029/2005GL025188

Palmroth, M., Pulkkinen, T., Janhunen, P., and Wu, C.-C. (2003). Stormtime Energy Transfer in Global MHD Simulation. *J. Geophys. Res.* 108, 1048. doi:10.1029/2002JA009446

Pokhotelov, D., von Alfthan, S., Kempf, Y., Vainio, R., Koskinen, H. E. J., and Palmroth, M. (2013). Ion Distributions Upstream and Downstream of the Earth's bow Shock: First Results from Vlasiator. *Ann. Geophys.* 31, 2207–2212. doi:10.5194/angeo-31-2207-2013

Pulkkinen, A., Rastätter, L., Kuznetsova, M., Singer, H., Balch, C., Weimer, D., et al. (2013). Community-wide Validation of Geospace Model Ground Magnetic Field Perturbation Predictions to Support Model Transition to Operations. *Space Weather* 11, 369–385. doi:10.1002/swe.20056

Pulkkinen, T. I., Dimmock, A. P., Lakka, A., Osmane, A., Kilpua, E., Myllys, M., et al. (2016). Magnetosheath Control of Solar Wind-magnetosphere Coupling Efficiency. *J. Geophys. Res. Space Phys.* 121, 8728–8739. doi:10.1002/2016JA023011

Pulkkinen, T. I., Palmroth, M., Koskinen, H. E. J., Laitinen, T. V., Goodrich, C. C., Merkin, V. G., et al. (2010). Magnetospheric Modes and Solar Wind Energy Coupling Efficiency. *J. Geophys. Res.* 115, A03207. doi:10.1029/2009ja014737

Pulkkinen, T. I., Palmroth, M., and Laitinen, T. (2008). Energy as a Tracer of Magnetospheric Processes: GUMICS-4 Global MHD Results and Observations Compared. *J. Atmos. Solar-Terrestrial Phys.* 70, 687–707. doi:10.1016/j.jastp.2007.10.011

Pulkkinen, T. I., Palmroth, M., Tanskanen, E. I., Janhunen, P., Koskinen, H. E. J., and Laitinen, T. V. (2006). New Interpretation of Magnetospheric Energy Circulation. *Geophys. Res. Lett.* 33, L0701. doi:10.1029/2005GL025457

Raeder, J., Berchem, J., and Ashour-Abdalla, M. (1996). "The Importance of Small Scale Processes in Global MHD Simulations: Some Numerical Experiments," in *The Physics of Space Plasmas*. Editors T. Chang and J. R. Jasperse (Cambridge, Mass.: MIT Cent. for Theoret. Geo/Cosmo Plasma Phys.), 14, 403.

Ridley, A. J., Deng, Y., and Tóth, G. (2006). The Global Ionosphere-Thermosphere Model. *J. Atmos. Solar-Terrestrial Phys.* 68, 839–864. doi:10.1016/j.jastp.2006.01.008

Ridley, A. J., and Kihn, E. A. (2004). Polar Cap index Comparisons with AMIE Cross Polar Cap Potential, Electric Field, and Polar Cap Area. *Geophys. Res. Lett.* 31, a–n. doi:10.1029/2003GL019113

Shue, J.-H., Song, P., Russell, C. T., Steinberg, J. T., Chao, J. K., et al. (1998). Magnetopause Location under Exteme Solar Wind Conditions 103, 17,691–17,700doi:10.1029/98ja01103

Staples, F. A., Rae, I. J., Forsyth, C., Smith, A. R. A., Murphy, K. R., Raymer, K. M., et al. (2020). Do statistical Models Capture the Dynamics of the Magnetopause during Sudden Magnetospheric Compressions? *J. Geophys. Res. Space Phys.* 125, e2019JA027289. doi:10.1029/2019JA027289

Toffoletto, F., Sazykin, S., Spiro, R., and Wolf, R. (2003). Inner Magnetospheric Modeling with the Rice Convection Model. *Space Sci. Rev.* 107, 175–196. doi:10.1023/A:1025532008047

Tóth, G., van der Holst, B., Sokolov, I. V., De Zeeuw, D. L., Gombosi, T. I., Fang, F., et al. (2012). Adaptive Numerical Algorithms in Space Weather Modeling. *J. Comput. Phys.* 231, 870–903. doi:10.1016/j.jcp.2011.02.006

Vasyliunas, V. M. (1970). "Mathematical Models of Magnetospheric Convection and its Coupling to the Ionosphere," in *Particles and fields in the Magnetosphere*. Editor B. M. McCormack (Dordrecht, Holland: D. Reidel Publishing), 60–71. doi:10.1007/978-94-010-3284-1_6

Zhang, B., Sorathia, K. A., Lyon, J. G., Merkin, V. G., Garretson, J. S., and Wiltberger, M. (2019). GAMERA: A Three-Dimensional Finite-Volume MHD Solver for Non-orthogonal Curvilinear Geometries. *ApJS* 244, 20. doi:10.3847/1538-4365/ab3a4c

Conflict of Interest: The authors declare that the research was conducted in the absence of any commercial or financial relationships that could be construed as a potential conflict of interest.

Publisher's Note: All claims expressed in this article are solely those of the authors and do not necessarily represent those of their affiliated organizations, or those of the publisher, the editors and the reviewers. Any product that may be evaluated in this article, or claim that may be made by its manufacturer, is not guaranteed or endorsed by the publisher.

frontiers in Astronomy and Space Sciences

ORIGINAL RESEARCH
published: 15 October 2021
doi: 10.3389/fspas.2021.756563

The Occurrence and Prevalence of Time Domain Structures in the Kelvin-Helmholtz Instability at Different Positions Along the Earth's Magnetospheric Flanks

F. D. Wilder[1], R. E. Ergun[2,3], D. Gove[2,4], S. Eriksson[2], P. Hansel[2], N. Ahmadi[2], D. M. Malaspina[2,3], J. L. Burch[5], R. B. Torbert[6], R. J. Strangeway[7] and B. L. Giles[8]*

[1]Department of Physics, University of Texas at Arlington, Arlington, TX, United States, [2]Laboratory for Atmospheric and Space Physics, University of Colorado Boulder, Boulder, CO, United States, [3]Department of Astrophysical and Planetary Sciences, University of Colorado Boulder, Boulder, CO, United States, [4]Department of Physics, Davidson College, Davidson, NC, United States, [5]Southwest Research Institute, San Antonio, TX, United States, [6]Department of Physics, University of New Hampshire, Durham, NH, United States, [7]Department of Earth, Planetary and Space Sciences, University of California, Los Angeles, Los Angeles, CA, United States, [8]NASA Goddard Space Flight Center, Greenbelt, MD, United States

OPEN ACCESS

Edited by:
Simon Wing, Johns Hopkins University, United States

Reviewed by:
Adam Michael, Johns Hopkins University, United States
Alexei V. Dmitriev, Lomonosov Moscow State University, Russia

***Correspondence:**
F. D. Wilder
frederick.wilder@uta.edu

Specialty section:
This article was submitted to Space Physics, a section of the journal Frontiers in Astronomy and Space Sciences

Received: *10 August 2021*
Accepted: *17 September 2021*
Published: *15 October 2021*

Citation:
Wilder FD, Ergun RE, Gove D, Eriksson S, Hansel P, Ahmadi N, Malaspina DM, Burch JL, Torbert RB, Strangeway RJ and Giles BL (2021) The Occurrence and Prevalence of Time Domain Structures in the Kelvin-Helmholtz Instability at Different Positions Along the Earth's Magnetospheric Flanks. Front. Astron. Space Sci. 8:756563. doi: 10.3389/fspas.2021.756563

The Kelvin-Helmholtz instability (KHI) is thought to be an important driver for mass, momentum, and energy transfer between the solar wind and magnetosphere. This can occur through global-scale "viscous-like" interactions, as well as through local kinetic processes such as magnetic reconnection and turbulence. An important aspect of these kinetic processes for the dynamics of particles is the electric field parallel to the background magnetic field. Parallel electric field structures that can occur in the KHI include the reconnection electric field of high guide field reconnection, large amplitude ion acoustic waves, as well as time domain structures (TDS) such as double layers and electrostatic solitary waves. In this study, we present a survey of parallel electric field structures observed during three Kelvin Helmholtz events observed by NASA's Magnetospheric Multiscale (MMS), each at different positions along the magnetosphere's dusk flank. Using data from MMS's on-board solitary wave detector (SWD) algorithm, we statistically investigate the occurrence of TDS within the KHI events. We find that early in the KHI development, TDS typically occur in regions with strong field-aligned currents (FACs) on the magnetospheric side of the vortices. Further down the flanks, as the vortices become more rolled up, the prevalence of large electric currents decreases, as well as the prevalence of SWDs. These results suggest that as the instability develops and vortices grow in size along the flanks, kinetic-scale activity becomes less prevalent.

Keywords: Kelvin–Helmholtz instability, flank magnetopause, electrostatic solitary waves, satellite observation, magnetospheric multiscale (MMS)

INTRODUCTION

In addition to magnetic reconnection at the dayside magnetopause, viscous-like interactions at magnetospheric flanks are also thought to transfer energy and momentum from the solar wind to the magnetosphere (Axford and Hines, 1961). This viscous-like interaction is also important for the transer of energy and momentum from the solar wind to the magnetospheres of gas giants, such as Jupiter and Saturn (Johnson et al., 2014). Although it was once unclear what these "viscous" interactions were, the main mechanism by which this momentum and energy transfer occurs along the magnetospheric flanks is now thought to be the Kelvin-Helmholtz instability (KHI) (Hasegawa et al., 2004; Johnson et al., 2014; Kavosi and Raeder, 2015). The KHI manifests as surface waves that form on the magnetopause in response to flow shear between the magnetosheath and magnetospheric plasma. In the non-linear phase of the instability, these surface waves roll up and form vortices that propagate anti-sunward down the flanks (Johnson et al., 2014).

The mechanisms by which the KHI transfers energy and momentum from the solar wind to the magnetosphere is a topic of ongoing study. One mechanism that has been suggested to facilitate this transfer is magnetic reconnection. As the KHI grows, converging flows on the edges of the vortices lead to compressed current sheets where magnetic reconnection can occur, facilitating the mixing and transport of plasma across the magnetopause boundary (Nakamura et al., 2013). Additionally, reconnection can occur on current sheets within the vortices (Nykyri and Otto, 2001) and at higher latitudes as the instability twists up the magnetic field (Johnson et al., 2014). Further, in the intervals between the compressed current sheets, simulations show that turbulence can develop within the vortices as they roll up (Karimabadi et al., 2013; Nakamura and Daughton, 2014). Turbulent cascades transfer energy from large to small scales and can lead to a variety of kinetic processes that dissipate the injected energy and can heat particles in the plasma. Additionally, reconnection could occur on intermittent current sheets that develop in a turbulent cascade (Phan et al., 2018; Sharma-Pyakurel et al., 2019).

On September 8, 2015, the NASA Magnetospheric Multiscale mission, which was launched to study the physics of collisionless magnetic reconnection, observed a KHI event in the post-noon sector of the flank magnetopause for a prolonged (~3 h) period during northward interplanetary magnetic field (IMF) conditions. The presence of periodic compressed current sheets in the equatorial plane were confirmed, with reconnection jets observed in ~50% of the current sheets (Eriksson et al., 2016a) Additionally, between the compressed current sheets, the spectra of the magnetic field fluctuations showed a power law indicative of fully developed turbulence, as well as the presence of intermittent currents at small scales (Stawarz et al., 2016). There was also evidence for the mixing of multiple particle populations in the middle of the vortices, leading to strong ion-acoustic-like parallel electric field fluctuations that did not appear to be current-driven (Wilder et al., 2016a; Wilder et al., 2020). The study of another KHI event, on September 27, 2016, suggested that lower hybrid waves that arise during the instability could also facilitate the diffusion of plasma across the flank magnetopause (Tang et al., 2018).

One aspect of the KHI that has not been observed in detail is the role of non-linear plasma structures in dissipating the turbulence. In particular, we focus on broadband electric field solitary structures called "Time Domain Structures" (TDS) (Mozer et al., 2015). These structures are typically on the order of a few to 10°s Debye lengths, and move at speeds ranging from the ion acoustic to the electron thermal speed. Due to their small size, they manifest as short time-duration fluctuations in the electric field, typically in the component of the electric field parallel to the background magnetic field $E_{\parallel}$. These structures include unipolar parallel electric field structures with a net electrostatic potential, such as double layers, as well as bipolar electric field signatures. These bipolar signatures are often referred to as "electrostatic solitary waves" (ESWs), and can refer to several plasma structures such as electron and ion phase space holes (Muschietti et al., 1999; Main et al., 2006), negative potential electron bunching as a result of non-linear whistler waves (Wilder et al., 2016b) and a variety of structures that arise from the mixing of plasmas with differing temperatures (Holmes et al., 2019). One important aspect of TDS, and particularly the readily observable ESWs, is that they are a sign that there is enhanced kinetic activity in plasma. Oftentimes, ESWs are a result of the non-linear evolution of kinetic instabilities, such as the Buneman and two-stream instabilities (Mozer et al., 2015). For example, streaming instabilities on the separatrix in magnetic reconnection can lead to the presence of ESWs (Graham et al., 2016; Wilder et al., 2017). ESWs can also be the sign of nearby double-layers, as the accelerated electrons on one side of the potential drop can become Buneman unstable (Newman et al., 2001) Therefore, because ESWs are self-sustaining beyond the instability that produces them (Muschietti et al., 2000), the presence of ESWs can be viewed as a "smoking gun" for the presence of kinetic instabilities, as well as their drivers, such as plasma beams. Investigating where TDS are most likely to occur within the larger structure of the KHI can therefore provide information on where the "hot spots" are for kinetic activity within the instability. Further, investigating the prevalence of TDS at different stages of the instability can provide information on how the sub-vortex-scale kinetic activity evolves over time.

The NASA MMS mission's on-board digital signal processing (DSP) board includes an algorithm to detect TDS, particularly ESWs (Ergun et al., 2016). This solitary wave detector (SWD) algorithm has been tested on THEMIS electric field burst data and detected 70% of ESWs identified by visual inspection, and had a less than 10% "false positive" rate. Analysis of an event in the Earth's magnetotail observed by MMS suggested comparable success rates for detecting ESWs (Hansel et al., 2021). The SWD algorithm reports a histogram (binned by amplitude) of the total TDS counts detected per reporting period. The reporting period used here is 1s. These data are ideal for studying the occurrence and prevalence of TDS in the KHI, where often, more than an hour of burst observations are available from the MMS spacecraft.

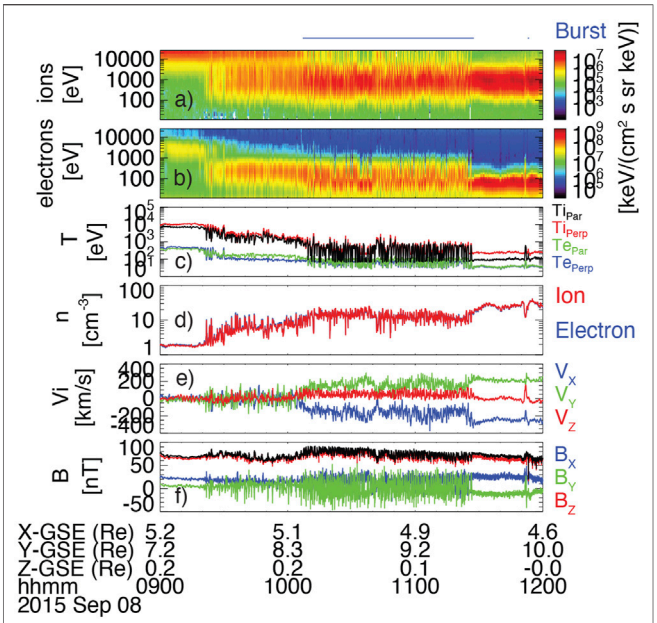

FIGURE 1 | MMS survey data during the September 8, 2015 KHI event: **(A)** Ion omni-directional energy spectra, **(B)** electron omni-directional energy spectra, **(C)** electron and ion temperatures perpendicular (Perp) and parallel (Par) to the background magnetic field, **(D)** ion and electron number density, **(E)** ion bulk velocity in GSE coordinates, **(F)** magnetic field vector in GSE coordinates.

In this study, we investigate three KHI events observed by MMS at different positions along the flanks, and different stages of the instability's development. We use SWD data to investigate the occurrence and prevalence of TDS both within the vortices for each event, as well as cross-event comparisons. We find that TDS are more likely to occur on the magnetospheric side of the vortex intervals between compressed current sheets, particularly in the presence of turbulent magnetic field fluctuations and enhanced field-aligned currents. We also find that at positions of increasing anti-sunward distances along the flanks, the electric currents within the KHI become weaker, and TDS observed by the SWD become less prevalent.

THE 8 SEPTEMBER 2015 KELVIN-HELMHOLTZ EVENT

The study of TDS in the KHI will begin with the September 8, 2015 event. This was the first KHI interval observed by MMS with enough periods to do statistical analysis of the instability. Previous studies of this event have shown magnetic reconnection on compressed current sheets (Eriksson et al., 2016a; Eriksson et al., 2016b), turbulence in the vortex-like intervals between the current sheets (Stawarz et al., 2016), and large-amplitude ion-acoustic waves in the plasma mixing regions on the magnetospheric side of the vortex-like intervals (Wilder et al., 2016a; Wilder et al., 2020).

Event Overview and Time Domain Structure Example

Figure 1 shows an overview of MMS survey data from 9:00–12:00 UT on September 8, 2015. Plasma data is from the MMS Fast Plasma Investigation (FPI) (Pollock et al., 2016), and magnetic field data comes from the fluxgate magnetometers (FGM) (Russel et al., 2016). At the beginning of the interval, MMS observed magnetospheric plasma, as evidenced by hot ions and electrons in the omni-directional spectra shown **Figures 1A,B**. At the end of the interval, cooler ions centered at a few hundred eV suggest MMS was in the magnetosheath. This can also be seen in **Figure 1C** where the ion and electron temperatures are higher at the beginning of the interval, and significantly lower at the end of the interval. **Figure 1D** shows the electron and ion number density, which was near 1 cm^{-3} when the spacecraft was in the magnetosphere, and near 20 cm^{-3} in the magnetosheath. **Figure 1E** shows the ion bulk velocity, $\boldsymbol{V_i}$, in Geocentric Solar Ecliptic (GSE) coordinates. The x-component of $\boldsymbol{V_i}$ begins at 0 km/s at the beginning of the interval and rises to a value near

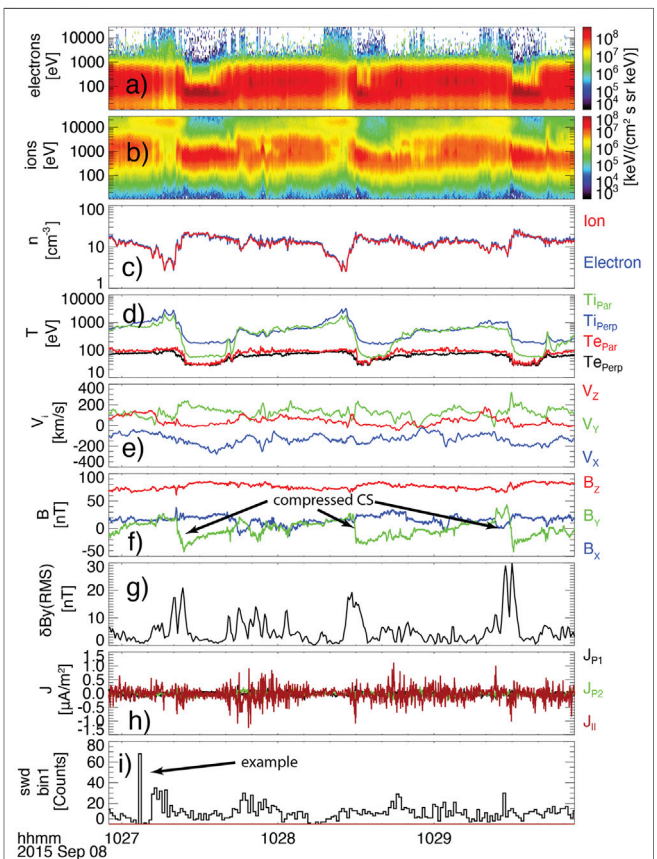

FIGURE 2 | MMS data showing two periods of KHI during the September 8, 2015 event. **(A)** electron omni-directional energy spectra, **(B)** ion omni-directional energy spectra, **(C)** electron and ion number density, **(D)** electron and ion temperature perpendicular and parallel to the background magnetic field, **(E)** ion bulk velocity in GSE coordinates, **(F)** magnetic field vector in GSE coordinates, **(G)** dB_Y(RMS), **(H)** the electric current density in field-aligned coordinates, **(I)** swd bin 1 counts.

−250 km/s (anti-sunward), consistent with magnetosheath plasma. Finally, **Figure 1F** shows the magnetic field vector, ***B***, in GSE coordinates. The positive B_Z component at the end of the interval indicates that the interplanetary magnetic field (IMF) had a northward orientation during this event.

During the slow boundary layer crossing between the magnetosphere and magnetosheath, **Figure 1** shows that the spacecraft periodically crossed back and forth between magnetosphere-like and magnetosheath-like plasma. This is most easily seen in the ion spectra (**Figure 1A**) and ion temperature (**Figure 1C**). This periodic motion becomes especially pronounced after about 10 UT. During this time, there are also periodic reversals in the B_Y component, which are signatures of the compressed current sheets predicted by (Nakamura et al., 2013). Eriksson et al. (2016a) showed that approximately 50% of these reversals observed by MMS exhibited signatures of reconnection ion jets. From the top of **Figure 1**, there was an interval of continuous high rate burst data from MMS between 10:07 and 11:27 UT.

To show the structure of the KHI in more detail, **Figure 2** shows a time series of burst data from MMS for three periods of the KHI from the September 8, 2015 event shown in **Figure 1**. From **Figures 2A,B**, there are three sudden transitions from hotter magnetosphere-like to cooler magnetosheath-like electrons and ions. Coincident with these transitions is a change in density from small (~2–3 cm^{-3}) to larger (~20–30 cm^{-3}) plasma densities, and a sudden change from higher to lower temperature in both the ions and electrons. Coinciding with each of these three temperature drops, there is a sharp reversal in B_Y from positive-to-negative, which are signatures of the compressed current sheets predicted by (Nakamura et al., 2013). On the third reversal, there is a significant increase in the ion bulk velocity V_Y, seen in **Figure 2E** This is one of the reconnection jet intervals reported by (Eriksson et al., 2016a). **Figure 2G** shows the root-mean-square (RMS) amplitude of B_Y, labeled $\delta B_Y(RMS)$. $\delta B_Y(RMS)$ was calculated with a window-length of 1 s, and a shift-length of 0.5 s. From **Figure 2G**, it is apparent that the largest values of $\delta B_Y(RMS)$ (>15 nT) occur on the compressed current sheets, with high variability between the current sheets. **Figure 2H** shows the electric current density $\boldsymbol{J} = ne(\boldsymbol{V}_i - \boldsymbol{V}_e)$, where n is the plasma number density, e is the electron charge, $\boldsymbol{V}_i$ and $\boldsymbol{V}_e$ are the ion and electron bulk velocities, respectively. The current is given in magnetic field-aligned coordinates with $J_\parallel$ being along the background magnetic field as defined by the survey magnetic field data, J_{P1} is along a unit vector in the spin plane of the MMS spacecraft that is perpendicular to the background magnetic field, and J_{P2} completes the right-handed coordinate system. At each of the compressed current sheets, there is a negative $J_\parallel$, which will be important when determining where in the KHI TDS are most likely to occur.

Between the compressed current sheets, there is a slow rotation of B_Y from negative back to positive. From **Figures 2A,B**, magnetosphere-like plasma begins to appear during this rotation. Additionally, there is high variability in $\delta B_Y(RMS)$, though it does not quite reach the large values seen coincident with the compressed current sheets. This region is where the

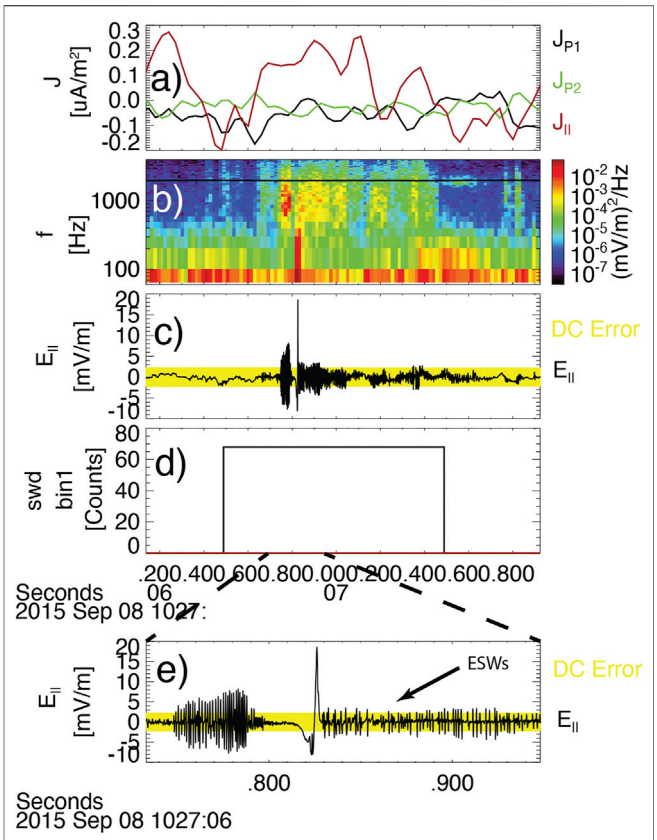

FIGURE 3 | Zoom on burst data for the interval with highest SWD counts from **Figure 2**. **(A)** electric current density in field-aligned coordinates, **(B)** electric field power spectral density, **(C)** parallel electric field at 8,192 Samples/s, **(D)** SWD bin1 counts, **(E)** zoom on the data from **(C)** to showcase ESWs.

"vortex"-like structures in the KHI between the compressed current sheets exist, and has been shown to exhibit turbulent cascades and magnetic field intermittency (Stawarz et al., 2016), as well as the presence of large-amplitude ion acoustic waves where the magnetosphere- and magnetosheath-like plasma populations mix (Wilder et al., 2016a; Wilder et al., 2020).

Figure 2I shows counts from the lowest amplitude bin (0.5–3 mV/m) from the on-board solitary wave detector (SWD) that is designed to detect ESWs in the burst data (up to 256 kSps). The SWD uses one pair of the spin-plane probes and a sliding window of 1/256th of a second, examining the time series electric field data in each window for spikes at least 4x above the pseudo-RMS (Ergun et al., 2016). The number of spike detections are summed over 1s intervals. A version of this algorithm has been checked against THEMIS data and found to detect about 70% of ESWs with a less than 10% false positive rate (Andersson et al., 2009). These spikes are sorted into four amplitude bins: 0.5–3, 3–12, 12–50, and 50 + mV/m, with an instrument saturation at 500 mV/m. In the September 8, 2015 event, the lowest amplitude bin had almost all of the counts, but this is likely due to the fact that the magnetic field has a large Z-GSE component, and therefore, only a small portion of the

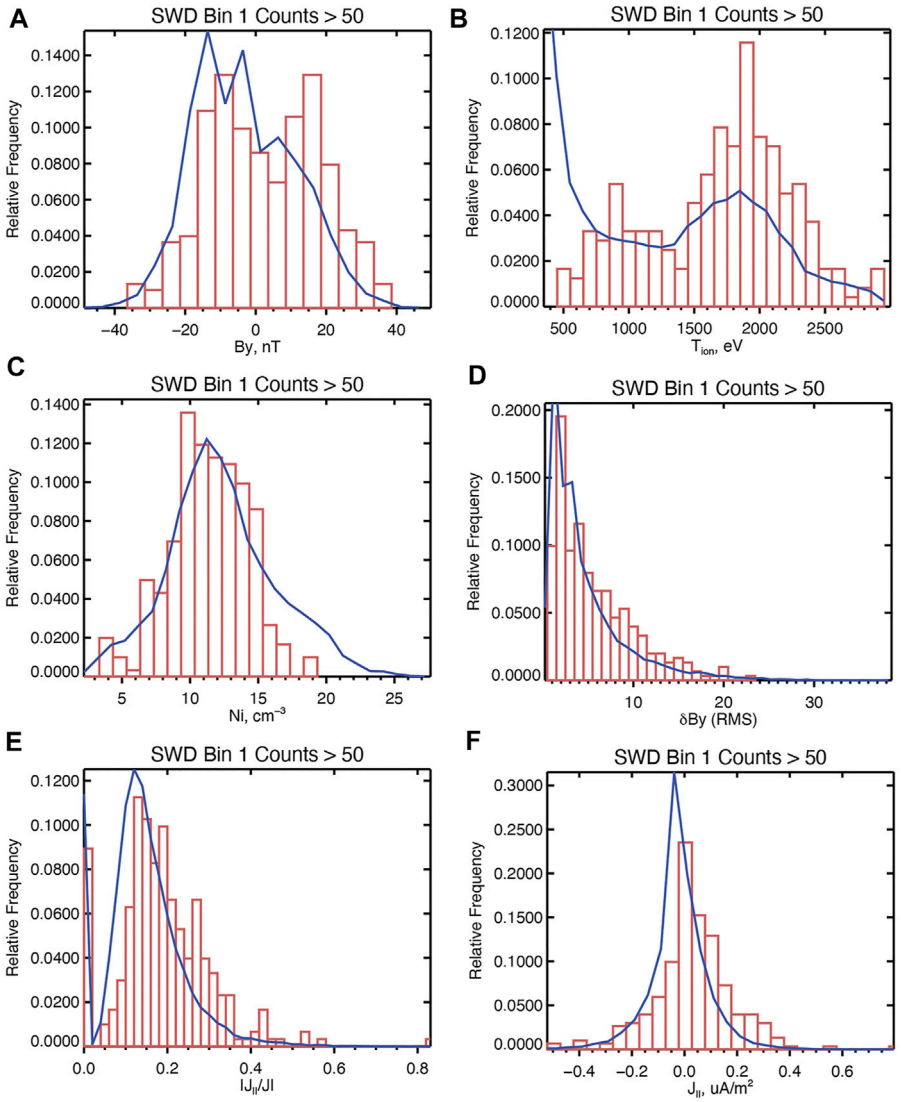

FIGURE 4 | Histograms of magnetic field and plasma quantities during the September 8, 2015 burst interval for (red bars) 1s intervals with SWD bin1 counts greater than 50 and (blue line) all 1s intervals during the burst selections. **(A)** Magnetic field GSE B_Y, **(B)** Ion temperature, T_{ion}, **(C)** Ion number density, N_i, **(D)** $\delta B_{Y,RMS}$, **(E)** $|J_\parallel / J|$, **(F)** $J_\parallel$.

parallel electric field will map to a single spin-plane probe pair that is mostly aligned with the X-Y GSE plane. Therefore, the present study will focus on counts from the SWD algorithm rather than the individual amplitude bins. Throughout the interval there is significant variability in the detection of solitary waves, with many of the largest-count intervals occurring in the "vortex" intervals between the compressed current sheet.

As an example of what the SWD detects, **Figure 3** shows MMS burst data surrounding the interval with the largest number of counts (>60). From **Figure 3A**, it can be seen that during the interval with high counts, the electric current density is dominated by $J_\parallel$. The electric field power spectral density, measured by the electric field double probe (EDP) instrument (Lindqvist et al., 2016; Ergun et al., 2016) shows broadband enhancements during this interval as well. No comparable enhancement was seen in the magnetic field spectra (not shown), suggesting that the broadband signals are electrostatic. **Figure 3C** shows the electric field parallel to the background magnetic field, $E_\parallel$, at 8,192 Samples/s, along with uncertainty in the DC electric field. We see that throughout the interval, the DC $E_\parallel$ is flat, but when the SWD reports enhanced couts, there is significant high frequency activity, as well as spikes. **Figure 3E** zooms in on the waveform shown in **Figure 3C**. From left to right, enhanced wave activity is followed by a large bipolar spike, and then a train of shorter duration bipolar spikes. These bipolar spikes are among the types of TDS that the SWD algorithm looks for, and from visual inspection, there are at least 40 ESWs present in the figure, and at least 100 in the entire 1s interval. It is worth noting that the amplitude of the ESWs are larger than the 2.5 mV/

m maximum of the SWD bin 1, because the magnetic field is dominated by the Z-GSE component, which is roughly normal to the spin plane of the spacecraft. This was consistently observed for events with high SWD counts throughout the September 8, 2015 event.

Solitary Wave Detector Statistics

From **Figure 2**, it is apparent that the SWD detects TDS throughout the three periods of the KHI, with a high variability in count levels. Additionally, the presence of turbulent cascades in the vortex intervals suggests that the behavior of the instability is highly stochastic, therefore, statistical analysis of SWD detections is needed to determine their occurrence with respect to the larger structure of the KHI. To do this, we calculated 1s averages of plasma data which provides information about the position within the KHI to match the cadence of the SWD. All data comes from the burst interval between 10:07 and 11:27 UT in order to ensure that the time cadence of FPI can be reliably interpolated to the SWD cadence. This is also the interval where the compressed current sheets were observed by (Eriksson et al., 2016a). Histograms of these data are shown by the blue lines in **Figure 4**. These data in **Figure 4** include 1) the magnetic field B_Y (GSE) component, 2) the total ion temperature, $T_{ion} = 2T_{iperp} + T_{ipar}$, 3) the ion number density, N_i, 4) $\delta B_Y\,(RMS)$, 5) the ratio of the field-aligned current to total current $\left|J_\parallel/J\right|$, and 6) $J_\parallel$. To determine where TDS were most likely to occur within the instability, 1s events where the SWD counts exceeded 50 were identified. The number 50 was chosen both to ensure there were enough statistics, and also that the 1s intervals would contain significant activity such as shown in **Figure 3**, rather than just stray solitary waves from spatially or temporally distant kinetic instabilities. For example, if we show statistics of events where the counts exceeded 10, we would have 10,631 intervals out of 18,703, which is more than half of the intervals. Conversely, using a threshold of 50, we were more likely to capture events with large trains of ESWs, like those shown in **Figure 3**, and the events were rarer, with only 302 intervals of 18,703, or 1.6% of intervals. Histograms of the previously-identified plasma parameters during these events with enhanced SWD counts are shown in red in **Figure 4**, allowing for comparisons with the "background" distribution of these parameters.

The magnetic field B_Y is helpful in determining where in a given period of the KHI we are likely to see the most ESW activity. From **Figure 4A**, it is clear that for the high SWD count intervals, the B_Y skews more positive with a mean of 2.7 nT, while for the overall KHI event, B_Y skews negative with a mean of −0.8 nT. This suggests that SWD activity is likely to happen on the "magnetosphere-like" side of the vortices, where the B_Y component is positive. This can also be seen in **Figure 4B**, where the largest peak in the distribution for high SWD count intervals is when T_{ion} is around 1900 eV. The mean T_{ion} for high SWD count intervals is 1701 eV, while for the overall KHI event it is 1,259 eV, suggesting TDS are more likely to be observed when there is the presence of hotter magnetosphere-like plasma. A similar picture is shown in **Figure 4C** for N_i, with the mean being 9 cm^{-3} for high SWD count intervals, and 12.8 cm^{-3} for the overall event. All of this suggests that while TDS are seen throughout the KHI, there is a bias towards the portion of each period where magnetosphere-like plasma is present. This is consistent with observations of the reconnecting dayside magnetopause, where the bulk of the plasma wave activity occurred on the magnetospheric side of the current sheet (Wilder et al., 2019). It is also similar to the Ion Acoustic Waves (IAWs) observed in the KHI by (Wilder et al., 2020), which seemed to occur on the magnetospheric side of the "vortex" intervals, though in that case, the waves occurred closer to $B_Y = 0$, in a region referred to as the "turbulent mixing region."

In addition to identifying the presence of compressed current sheets, $\delta B_Y\,(RMS)$ also provides a measure of how strong the turbulent fluctuations in B are. From **Figure 4D**, the distribution of $\delta B_Y\,(RMS)$ for high SWD count intervals largely follows the distribution for the overall event, however, between $\delta B_Y\,(RMS)$ values of 5 and 15 nT, higher SWD counts are present. This suggests that TDS are more likely to be observed in the presence of turbulent fluctuations. This is different from the IAWs in the KHI, which, while also appearing to occur on the magnetospheric side of the "vortex" intervals, did not appear to be correlated with large $\delta B_Y\,(RMS)$ (Wilder et al., 2020). These observations of TDS occurring in more turbulent intervals is consistent with **Figure 4E**, where the histogram for intervals with high SWD counts is skewed towards larger $\left|J_\parallel/J\right|$ than the overall event, confirming the hypothesis that TDS are more likely to be observed in the presence of enhanced field-aligned currents. It is worth noting that intervals where $\left|J_\parallel/J\right| > 0.2$ do not have a bias towards the magnetospheric side of the vortices the way the large SWD counts do. For intervals where $\left|J_\parallel/J\right| > 0.2$, the mean B_Y is −0.78 nT, while the mean B_Y for the entire event was −0.76 nT. Surprisingly, there is a bias towards positive $J_\parallel$ for high SWD intervals apparent in **Figure 4F**. Since the compressed currents are typically intervals with negative $J_\parallel$, this suggests that the most significant ESW activity occurs in the turbulent region. Putting all of this together, the histograms in **Figure 4** suggest that the region of largest ESW activity is on the magnetospheric side of the turbulent interval between the compressed current sheets.

KELVIN-HELMHOLTZ EVENTS FURTHER DOWN THE FLANKS

The KHI event on September 8, 2015 was observed in the post-noon sector, and therefore was likely early in the development of the KHI. In order to understand how the prevalence and location of TDS evolve as the instability evolves, the analysis in *Solitary Wave Detector Statistics* is repeated for events further down the Earth's magnetospheric flank. We introduce two additional KHI events: one on September 27, 2016 and one on September 26, 2017. **Figure 5** shows MMS survey data for the two additional events, given in the same format as **Figure 1**. The September 27, 2016 event was first reported by (Tang et al., 2018). The interval from 19:50–20:06 UT, while shorter in duration than the September 8, 2015 observations, shows similar activity. Specifically, there are periodic boundary crossings apparent in the ion and electron spectra and temperature. There were also

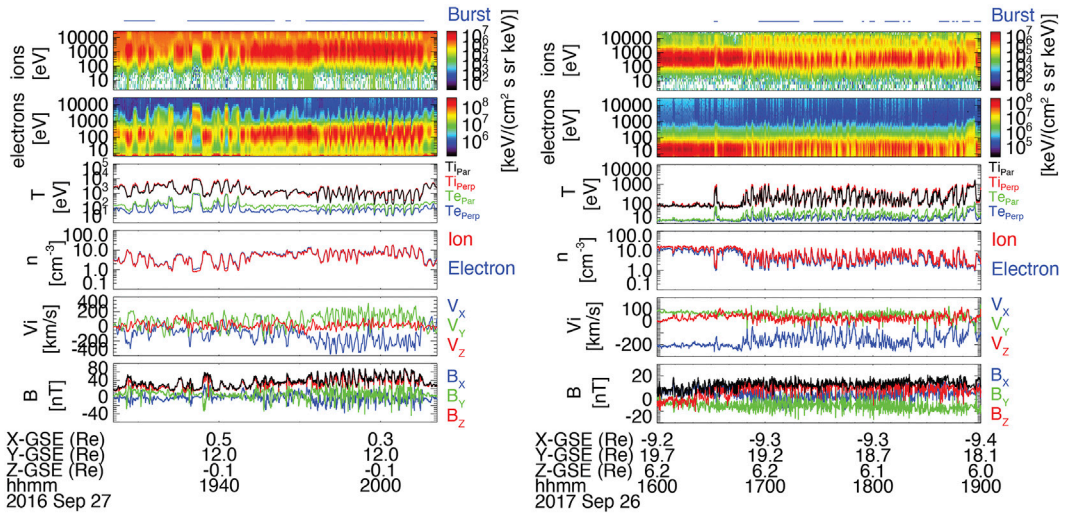

FIGURE 5 | Overview of additional KHI events observed by MMS on **(left)** September 27, 2016 and **(right)** September 26, 2016. Both are given in the same format as **Figure 1**.

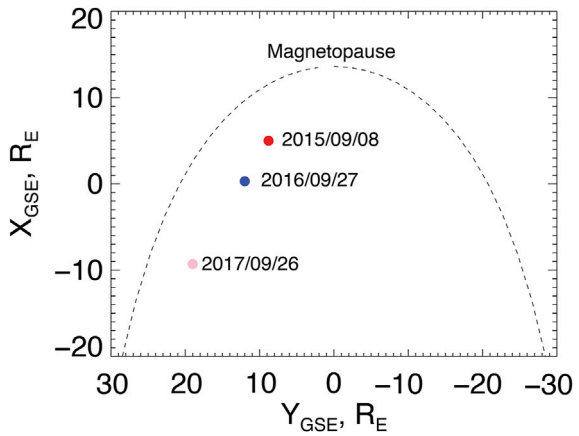

FIGURE 6 | The location of MMS in the X-Y GSE plane during the three KHI events shown in this study. The dashed line shows the nominal magnetopause from Shue et al. (1997).

periodic reversals in the magnetic field GSE B_Y component. One significant difference between the September 27, 2016 event and the September 8, 2015 event was that the periodic fluctuations in the anti-sunward ($-V_X$) component of the flow were much larger compared to the maximum negative value than in the September 8, 2015, suggesting more "rolled up" conditions. This will be investigated further in *Event Comparison*.

The September 26, 2017 event has, to our knowledge, not been previously reported. From **Figure 5**, there are some immediate similarities with the other events. First, between 16:50 and 19:00 UT, there were periodic boundary crossings apparent in the ion and electron spectra and temperature, as well as the plasma density, with a dominant periodicity of 230˚s, which is longer than the terminator event (~45˚s) (Tang et al., 2018) One difference is that the reductions in the anti-sunward flow are even more significant than in the other two events. The challenge in analyzing this event is that immediately after this event is that immediately after the plotted interval in **Figure 5**, the MMS exited fast survey mode, and therefore the complete crossing into the magnetospheric side of the boundary was not recorded. This makes linear growth analysis difficult; however, given the similarities with the other events, as well as behavior consistent with rolled up vortices (*Event Comparison*), the interval is likely a KHI event.

Figure 6 shows the locations of the MMS constellation in the X-Y GSE plane when it observed the three events, with the dashed line being the nominal magnetopause as determined by (Shue et al., 1997). From **Figure 6** it is clear that the magnetosphere was more compressed than usual, since all three spacecraft observed the magnetopause inside the nominal location. Additionally, the three events exist on three different positions along the flanks. The September 8, 2015 event previously discussed is in the post-noon sector but still on the dayside and will be referred to as the "post-noon" event henceforth. The September 27, 2016 event was near the dusk terminator (X ~ 0 Re) and will be referred to as the "terminator" event. Finally, the September 26, 2017 event was approximately −9 Re down the dusk flank and will be referred to as the "down-tail" event. For the terminator and down-tail events, the MMS burst data coverage is less frequent than in the post-noon event; however, the burst selections that were downlinked still managed to capture 16 and 25 periods for the terminator and down-tail events, respectively.

Figure 7 shows solar wind conditions for each event from the OMNI database (King and Papitashvili, 2005). All three events exhibit northward IMF B_Z conditions, although the downtail exhibits a brief southward turning of the IMF. The relative strength of B_X, B_Y, and B_Z also varies between events, with the September 8, 2015 being the most IMF B_Z-dominant. The solar wind was fastest during the post-noon event, and slowest during

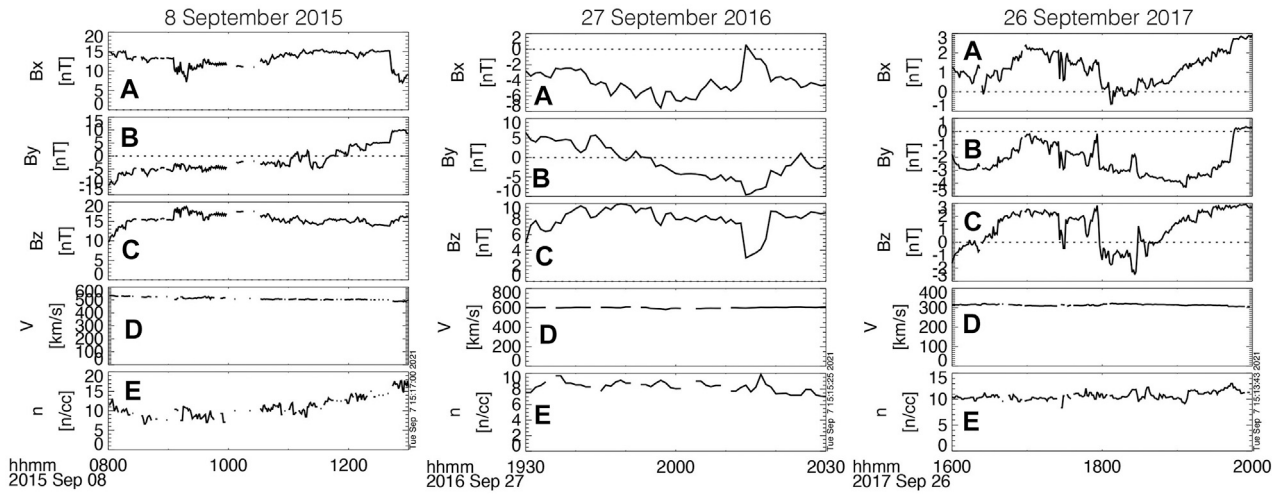

FIGURE 7 | Solar wind conditions from OMNI during the **(left)** September 8, 2015 **(center)** September 27, 2016, and **(right)** September 26, 2017 events. Panels include **(A)** interplanetary magnetic field (IMF) B_X GSE component, **(B)** IMF B_Y GSE component, **(C)** IMF B_Z GSE component, **(D)** solar wind bulk speed, **(E)** solar wind proton number density.

the downtail event. Because each event is occurring during a different year and under different solar wind conditions, it is impossible to do a one-to-one comparison, however, it is worth comparing events at different positions and under different IMF conditions to determine how the behavior of TDS in the KHI varies. One thing that can be quantified is the state of vortex rollup for each event, which is discussed in *Event Comparison*.

Event Comparison

From **Figure 5**, there are some similarities between the post-noon event and the two events further down the flank. In all three, there are periodic crossings of the boundary as seen in the spectra, temperature and density plots. Additionally, both events show frequent reversals of the B_Y component. One striking difference is that for the terminator and down-tail events, there are larger oscillations in V_X, suggesting that the instabilities were at a later stage in the development of the KHI. To test this, the method for identifying rolled up vortices given by (Hasegawa et al., 2004) was used. To do this, the velocity along the flow shear direction, V_M, vs. ion number density, N_i is plotted, shown in **Figure 8** for all three events. Coordinates were chosen so that V_M is approximately sunward along the flanks. From **Figure 8A**, which shows data from the post-noon event, there is an approximately linear relationship between the velocity and density, with the lower density (magnetosphere-like) plasma being roughly stationary and the higher density (magnetosheath-like) plasma flowing anti-sunward. This is consistent with the early stages of the instability where the vortices have not fully rolled up (Hasegawa et al., 2004). From **Figure 8B**, which shows data from the terminator event, there is an increasingly non-linear relationship between velocity and density, with more of the lower density population moving anti-sunward along with the high-density population. The rolled-up state for the terminator event has already been reported by (Tang et al., 2018). The data from the down-tail event, shown in **Figure 8C**, shows an even more nonlinear relation, with a significant portion of the lowest density plasma moving at the same anti-sunward speed as the high-density population. This suggests an increasing state of roll-up for the instability as it is observed at different positions down the flanks, with the post-noon event not having rolled up vortices, and the down-tail exhibiting the most non-linear "rollup" (Hasegawa et al., 2004).

Since the three events at different positions along the flanks exhibit different amounts of "rollup" in the vortices, they can be used to study the occurrence and prevalence of TDS at different stages of the instability. **Figure 9** shows histograms of SWD bin 1 counts for all three events. The time interval used for the post-noon event was the 10:07–11:27 UT burst interval studied by (Eriksson et al., 2016a). For the terminator event, the time period from 19:50–20:06 UT was used, which was the most similar in behavior to the post-noon event. For the downtail event, times from 16:50–19:00 UT were used, which was when periodic boundary crossings comparable to the other two events were observed. From **Figure 5**, contiguous burst data was not available, and so only times when burst selections were made were used. Comparing **Figures 9A,B**, the post-noon and terminator events show comparable prevalence of SWDs. One difference with the terminator event is that there are significantly more counts found in bin 2 (not shown) than in the post-noon event. This suggests that there was more ESW activity in the terminator event, which could point to the presence of more kinetic instabilities in the non-linear stage in this event. This can also be seen in the number of 1s intervals where the SWD counts exceeded 50, which were 358 out of 3,280, or ~11% of intervals. For the down-tail event, shown in **Figure 9C**, the SWD counts were much lower. There were no intervals where the counts exceeded 50. Using a much smaller threshold of 10 counts, we found 41 out of the 11,200 1s intervals, or 0.3%. This suggests that TDS activity was extremely rare during the event.

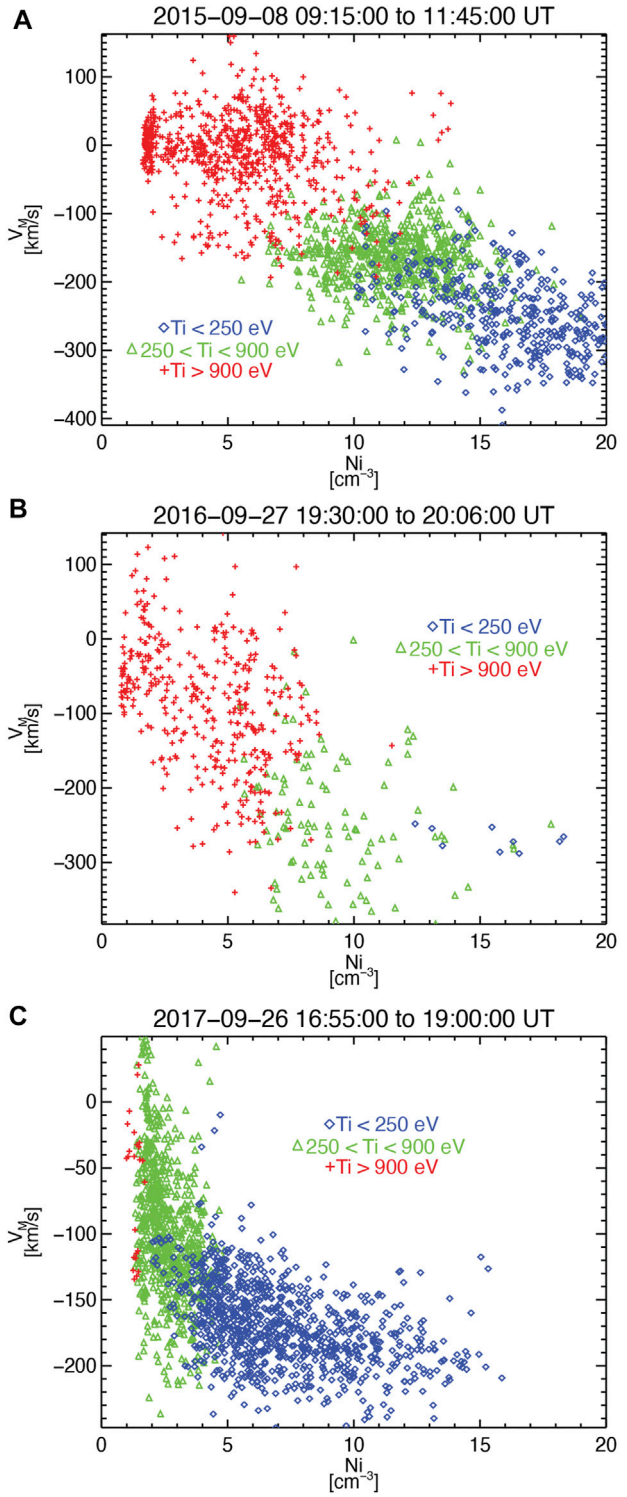

FIGURE 8 | V_M vs. plasma number density color coded by ion temperature, for three K-Helmholtz intervals on **(A)** 2015-09-08, **(B)** 2016-09-27, and **(C)** 2017-09-26.

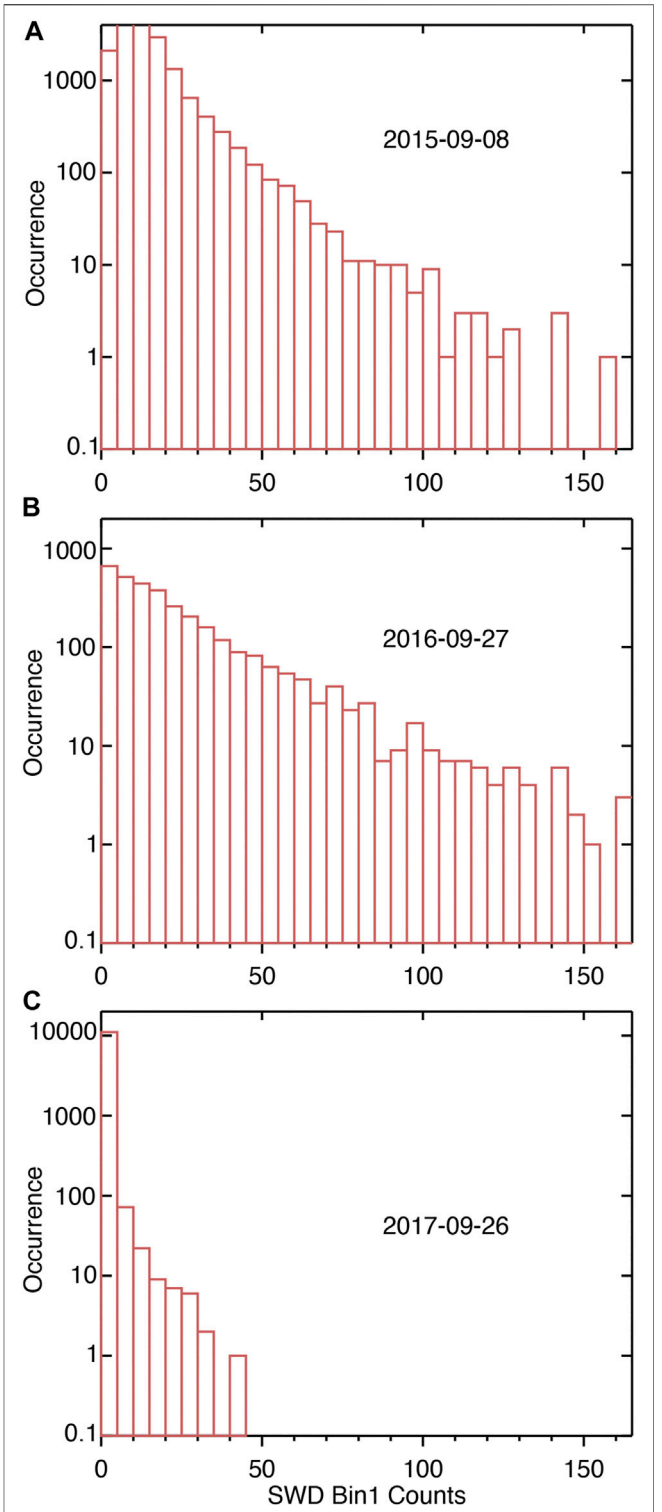

FIGURE 9 | Histograms of SWD bin 1 counts for the three KHI intervals on **(A)** 2015-09-08, **(B)** 2016-09-27, and **(C)** 2017-09-26.

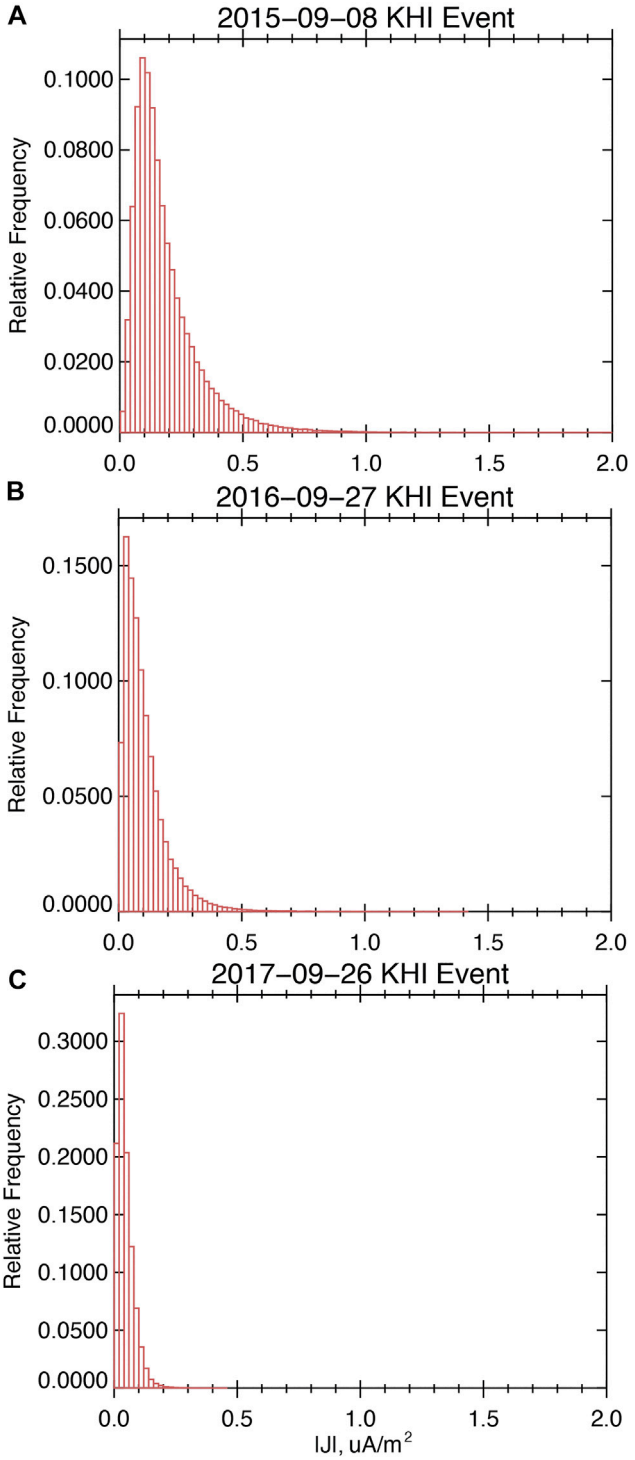

FIGURE 10 | Histograms of electric current density, measured using data from the Fast Plasma Investigation (FPI) for the three KHI intervals on **(A)** 2015-09-08, **(B)** 2016-09-27, and **(C)** 2017-09-26.

Figure 10 shows histograms of the magnitude of electric current density measured by FPI for all three events using the same time ranges as **Figure 9**. From **Figure 10**, the post-noon event exhibits the strongest currents and the electric current density on average becomes weaker for observations at increasing anti-sunward distances along the flank. Since from **Figures 4E,F**, high SWD counts tend to occur in the presence of large field-aligned current, one expects the SWD counts to be lower for the down-tail event, and this could be one explanation of the low prevalence of solitary waves shown in **Figure 8C**. One possible explanation for this is that as one moves further down the flanks, the vortices may grow in size. Additionally, the magnetic field on the magnetospheric side becomes weaker. These two conspire to reduce $\nabla \times \boldsymbol{B}$, and therefore the current.

Solitary Wave Detector Statistics

In order to compare the occurrence of solitary waves in the terminator and down-tail event with the post-noon event, the analysis from *Solitary Wave Detector Statistics* is repeated for each event. **Figure 11** shows histograms of plasma parameters during the post-noon event, given in the same format as **Figure 4**, using the burst interval from 19:50 to 20:06 UT. This burst interval was chosen because it was when the periodicity was most apparent, as well as the presence of reversals in the B_Y. This allows for more ready comparison to the September 8, 2015 event. From **Figure 11**, several similarities between the post-noon event and the terminator event are apparent. First, from **Figure 11A**, there is still a bias in the high SWD count events towards positive B_Y in comparison to the histograms for the overall event. This bias is not as apparent as in the post-noon event, however. Additionally, high SWD count intervals are still more likely to occur in the presence of field-aligned currents, although the bias towards positive currents is no longer as strong. Further, the high SWD count histograms are more spread in temperature and density in the terminator event than in the post-noon event, suggesting SWDs are more evenly distributed throughout the interval. One reason for this may be the increase "rolled up" state of the vortices in the terminator event versus the post-noon event, leading to the plasma being more mixed.

Figure 12 shows histograms for the down-tail event given in the same format as **Figures 4**, **11**, using all burst data between 16:50 to 18:20 UT. For **Figure 12**, the threshold for "high SWD counts" for bin 1 was reduced to 10, given the reduced prevalence in solitary wave activity shown in **Figure 9**. Several similarities and several differences are immediately apparent. First, for the overall event, the temperatures were significantly lower and the B_Y was most likely negative, suggesting most of the observations during this event occurred on the magnetosheath side of the vortices. This may be a possible explanation for the reduced SWD counts shown in **Figure 9** for the down-tail event, since in the post-noon and terminator events, higher SWD count events were more likely to be seen on the magnetospheric side. However, in the post-noon and terminator event, there were still high SWD count events even on the magnetosheath side. Therefore, the event seems to simply just have less activity that would lead to the presence of TDS. One similarity between all three events is seen in **Figure 12E**, where the high SWD count intervals are biased towards intervals with enhanced field-aligned currents.

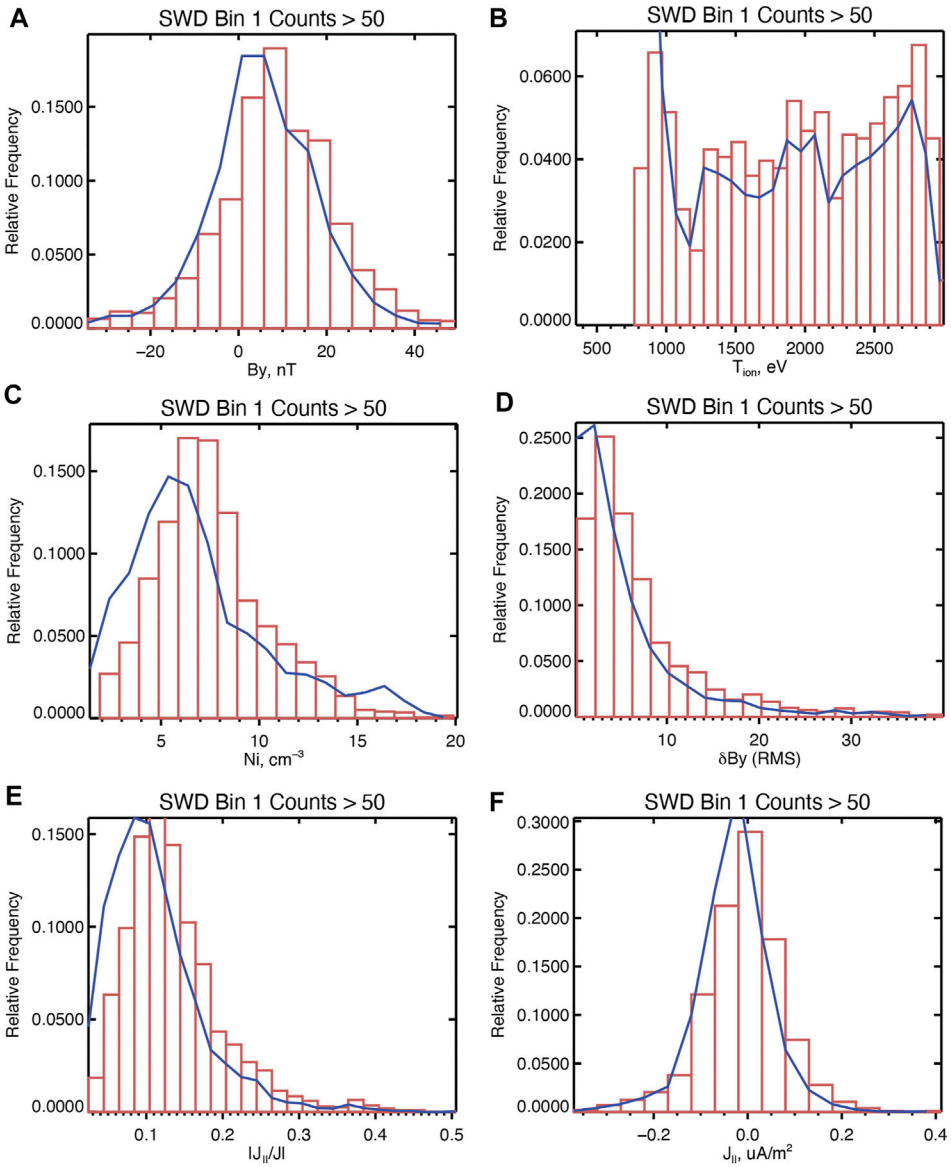

FIGURE 11 | Histograms of magnetic field and plasma quantities during the September 27, 2016 burst interval, given in the same format as **Figure 4**. **(A)** Magnetic field GSE B_Y, **(B)** Ion temperature, T_{ion}, **(C)** Ion number density, N_i, **(D)** $\delta B_{Y,RMS}$, **(E)** $|J_\parallel / J|$, **(F)** $J_\parallel$.

SUMMARY AND CONCLUSION

In this study, we investigated the occurrence and prevalence of time domain structures (TDS) in the Kelvin-Helmholtz instability (KHI) observed by MMS at different positions along the dusk magnetospheric flank. The events investigated included an event observed in the post-noon sector on September 8, 2015, one near the dusk terminator on September 27, 2016 and one further down the magnetospheric flanks on September 26, 2017. In each event, a different stage of the instability's development were observed, with the post-noon event including the least rolled up vortices, and the down-tail event having the most. To investigate the location of TDS in the vortices for each event, we used data from the MMS mission's on-board solitary wave detector (SWD) algorithm (Ergun et al., 2016). For each event, we identified 1s intervals where the SWD counts exceeded a threshold, and then investigated the plasma parameters where these intervals were most likely to occur.

In the post-noon event, it was shown that intervals with high SWD counts were more likely to be on the magnetospheric side of the "vortex" intervals between the compressed current sheets. This was similar to the observations of ion-acoustic waves during the post-noon event, which found the waves were most likely to occur on the magnetospheric side (Wilder et al., 2020). One difference between the prevalence of TDS and ion-acoustic waves is that the latter did not appear to have any correlation with the

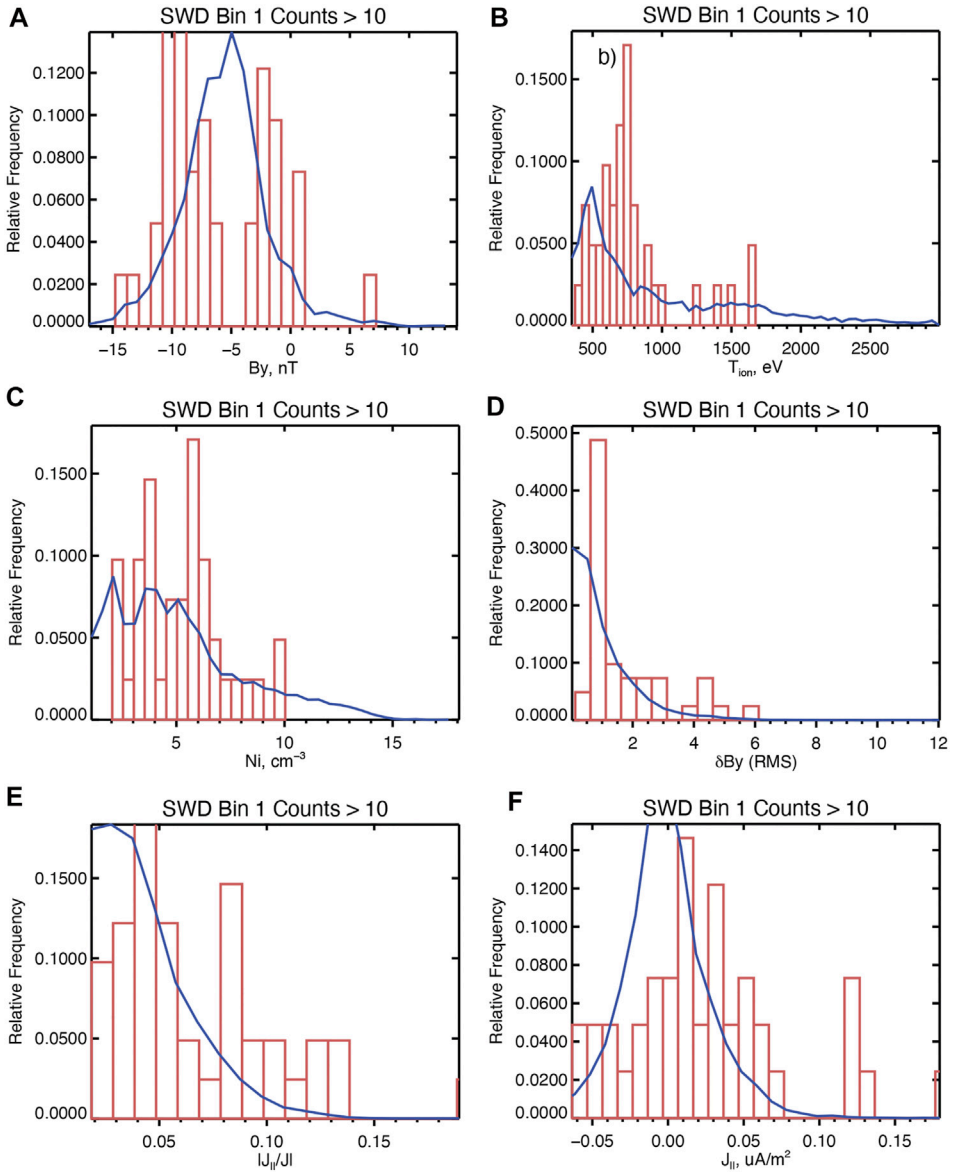

FIGURE 12 | Histograms of magnetic field and plasma quantities during the September 26, 2017 burst interval, given in the same format as **Figure 4**. **(A)** Magnetic field GSE B_Y, **(B)** Ion temperature, T_{ion}, **(C)** Ion number density, N_i, **(D)** $\delta B_{Y,RMS}$, **(E)** $|J_{\parallel}/J|$, **(F)** $J_{\parallel}$.

presence of magnetic fluctuations, while in the present study, intervals with high SWD counts were more likely to be seen when moderate-to-large (10–20 nT) RMS fluctuations in the magnetic field normal to the magnetopause boundary. It was also shown that high SWD count intervals were more likely to be observed during times when the field-aligned current was significant compared to the total current density. This is consistent with the idea that the instabilities and processes that can drive TDS (e.g., double layers, streaming instabilities) are likely to occur in the presence of strong FACs (Ergun et al., 2001; Mozer et al., 2014). One surprising result was that the intervals with high SWD counts were more likely to occur on positive field-aligned currents, while the compressed current sheets are negative. This suggests that the processes that drive TDS in the KHI are more likely to occur inside the vortices rather than on the compress current sheets on the edge. Also—since the TDS seem to occur in the presence of currents, while the previously-reported ion-acoustic waves do not, the present study supports the hypothesis by (Wilder et al., 2016a, Wilder et al., 2020) that the ion-acoustic waves in the KHI are driven by plasma mixing rather than being current-driven.

One immediate difference between the three events was that the down-tail event had significantly less SWD counts than the post-noon and terminator. Consistent with this, MMS also observed increasingly weak electric current densities as the KHI evolved towards more rolled up vortices. It is unclear why this happens, but one hypothesis is that as the KHI evolves along the flank, the smaller-scale turbulent features

largely dissipate by the time the vortices reach an anti-sunward distance of −10 Re from the terminator. Another hypothesis is that the vortices may grow in size as they propagate down the flanks, and since the magnetic field also becomes weaker at increasing distance from Earth, the electric current densities become smaller by way of Ampere's law. This is consistent with the reduced SWD counts in the down-tail event, as for all three events, the intervals with higher SWD counts were more likely to occur in the presence of field-aligned currents. More events along the flanks need to be studied to understand the difference in electric current density between observations of the KHI at different positions along the flanks.

The importance of the KHI for magnetospheric physics is that it is thought to be one of the mechanisms by which energy and momentum are transferred from the solar wind to the magnetosphere Axford and Hines, 1961; Kavosi and Raeder, 2015. Exactly how this transfer is facilitated is a topic of ongoing research. Suggested mechanisms include magnetic reconnection (Nykyri and Otto, 2001; Nakamura et al., 2013, Eriksson et al., 2016a) and diffusion via particles interacting with waves, such as lower hybrid waves (Tang et al., 2018). Turbulent cascades have also been observed within the vortices (Stawarz et al., 2016), and it is unclear how they impact the overall mass-energy transfer in the KHI. It has long been suggested that time domain structures and parallel electric fields may be a mechanism by which turbulent cascades can be dissipated. For example, electron phase space holes and double layers have been observed in the bursty bulk flow braking region, where magnetic field spectra consistent with a turbulent cascade were observed (Ergun et al., 2014; Stawarz et al., 2015) The present study shows that TDS tend to occur on the magnetospheric side of the vortices near strong fluctuations in the magnetic field and field-aligned currents, which suggests that the processes that lead to their occurrence are also likely to happen there. Future studies should investigate what these processes and instabilities that lead to the presence of TDS are, and what role they play in the overall mass/energy transfer between the solar wind and magnetosphere, as well as the dissipation of turbulence on the flanks.

DATA AVAILABILITY STATEMENT

Publicly available datasets were analyzed in this study. This data can be found here: https://lasp.colorado.edu/mms/sdc/public/.

AUTHOR CONTRIBUTIONS

FW performed the bulk of the analysis and wrote the paper, RE developed the SWD algorithm, DG and SE identified KHI events for study, PH and DM assisted in validating the SWD algorithm, NA calibrated the electric field booms, JB and RT confirmed appropriate use of MMS data and worked as scientist in the loop to identify events, RS calibrated the magnetometer, BG calibrated the fast plasma investigation.

FUNDING

This work was funded by the NASA MMS project and NASA Grant 80NSSC18K1359.

REFERENCES

Andersson, L., Ergun, R. E., Tao, J., Roux, A., LeContel, O., Angelopoulos, V., et al. (2009). New Features of Electron Phase Space Holes Observed by the THEMIS mission. *Phys. Rev. Lett.* 102, 225004. doi:10.1103/PhysRevLett.102.225004

Axford, W. I., and Hines, C. O. (1961). A Unifying Theory of High-Latitude Geophysical Phenomena and Geomagnetic Storms. *Can. J. Phys.* 39, 1433–1464. doi:10.1139/p61-172

Ergun, R. E., Goodrich, K. A., Stawarz, J. E., Andersson, L., and Angelopoulos, V. (2015). Large-amplitude Electric fields Associated with Bursty Bulk Flow Braking in the Earth's Plasma Sheet. *J. Geophys. Res. Space Phys.* 120, 1832–1844. doi:10.1002/2014JA020165

Ergun, R. E., Su, Y.-J., Andersson, L., Carlson, C. W., McFadden, J. P., Mozer, F. S., et al. (2001). Direct Observation of Localized Parallel Electric fields in a Space Plasma. *Phys. Rev. Lett.* 87, 045003. doi:10.1103/PhysRevLett.87.045003

Ergun, R. E., Tucker, S., Westfall, J., Goodrich, K. A., Malaspina, D. M., Summers, D., et al. (2016). The Axial Double Probe and Fields Signal Processing for the MMS Mission. *Space Sci. Rev.* 199, 167–188. doi:10.1007/s11214-014-0115-x

Eriksson, S., Lavraud, B., Wilder, F. D., Stawarz, J. E., Giles, B. L., Burch, J. L., et al. (2016a). Magnetospheric Multiscale Observations of Magnetic Reconnection Associated with Kelvin-Helmholtz Waves. *Geophys. Res. Lett.* 43, 5606–5615. doi:10.1002/2016GL068783

Eriksson, S., Wilder, F. D., Ergun, R. E., Schwartz, S. J., Cassak, P. A., Burch, J. L., et al. (2016b). Magnetospheric Multiscale Observations of the Electron Diffusion Region of Large Guide Field Magnetic Reconnection. *Phys. Rev. Lett.* 117, 1. doi:10.1103/PhysRevLett.117.015001

Graham, D. B., Khotyaintsev, Y. V., Vaivads, A., and André, M. (2016). Electrostatic Solitary Waves and Electrostatic Waves at the Magnetopause. *J. Geophys. Res. Space Phys.* 121, 3069–3092. doi:10.1002/2015JA021527

Hansel, P., Wilder, F., Malaspina, D., Ergun, R., Ahmadi, N., Holmes, J., et al. (2021). Mapping MMS Observations of Solitary Waves in Earth's Magnetic Field. *J. Geophys. Res.* 1, 1, 2021. Under Review.

Hasegawa, H., Fujimoto, M., Phan, T.-D., Rème, H., Balogh, A., Dunlop, M. W., et al. (2004). Transport of Solar Wind into Earth's Magnetosphere through Rolled-Up Kelvin-Helmholtz Vortices. *Nature* 430, 755–758. doi:10.1038/nature02799

Holmes, J. C., Ergun, R. E., Nakamura, R., Roberts, O., Wilder, F. D., and Newman, D. L. (2019). Structure of Electron-Scale Plasma Mixing along the Dayside Reconnection Separatrix. *J. Geophys. Res. Space Phys.* 124, 8788–8803. doi:10.1029/2019JA026974

Johnson, J. R., Wing, S., and Delamere, P. A. (2014). Kelvin Helmholtz Instability in Planetary Magnetospheres. *Space Sci. Rev.* 184, 1–31. doi:10.1007/s11214-014-0085-z

Karimabadi, H., Roytershteyn, V., Wan, M., Matthaeus, W. H., Daughton, W., Wu, P., et al. (2013). Coherent Structures, Intermittent Turbulence, and Dissipation in High-Temperature Plasmas. *Phys. Plasmas* 20 (1), 012303. doi:10.1063/1.4773205

Kavosi, S., and Raeder, J. (2015). Ubiquity of Kelvin-Helmholtz Waves at Earth's Magnetopause. *Nat. Commun.* 6, 7019. doi:10.1038/ncomms8019

Lindqvist, P.-A., Olsson, G., Torbert, R. B., King, B., Granoff, M., Rau, D., et al. (2016). The Spin-Plane Double Probe Electric Field Instrument for MMS. *Space Sci. Rev.* 199, 137–165. doi:10.1007/s11214-014-0116-9

Main, D. S., Newman, D. L., and Ergun, R. E. (2006). Double Layers and Ion Phase-Space Holes in the Auroral Upward-Current Region. *Phys. Rev. Lett.* 97, 185001. doi:10.1103/PhysRevLett.97.185001

Mozer, F. S., Agapitov, O., Krasnoselskikh, V., lejosne, S., Reeves, G. D., and Roth, I. (2014). Direct Observation of Radiation-Belt Electron Acceleration from Electron-Volt Energies to Megavolts by Nonlinear Whistlers. *Phys. Rev. Lett.* 113, 035001. doi:10.1103/PhysRevLett.113.035001

Mozer, F. S., Agapitov, O. V., Artemyev, A., Drake, J. F., Krasnoselskikh, V., Lejosne, S., et al. (2015). Time Domain Structures: What and where They Are, what They Do, and How They Are Made. *Geophys. Res. Lett.* 42, 3627–3638. doi:10.1002/2015GL063946

Muschietti, L., Ergun, R. E., Roth, I., and Carlson, C. W. (1999). Phase-space Electron Holes along Magnetic Field Lines. *Geophys. Res. Lett.* 26, 1093–1096. doi:10.1029/1999GL900207

Muschietti, L., Roth, I., Carlson, C. W., and Ergun, R. E. (2000). Transverse Instability of Magnetized Electron Holes. *Phys. Rev. Lett.* 85, 94–97. doi:10.1103/PhysRevLett.85.94

Nakamura, T. K. M., Daughton, W., Karimabadi, H., and Eriksson, S. (2013). Three-dimensional Dynamics of Vortex-Induced Reconnection and Comparison with THEMIS Observations. *J. Geophys. Res. Space Phys.* 118, 5742–5757. doi:10.1002/jgra.50547

Nakamura, T. K. M., and Daughton, W. (2014). Turbulent Plasma Transport across the Earth's Low-latitude Boundary Layer. *Geophys. Res. Lett.* 41 (24), 8704–8712. doi:10.1002/2014gl061952

Newman, D., Goldman, M., Ergun, R., and Mangeney, A. (2001). Formation of Double Layers and Electron Holes in a Current-Driven Space Plasma. *Phys. Rev. Lett.* 87, 255001. doi:10.1103/PhysRevLett.87.255001

Nykyri, K., and Otto, A. (2001). Plasma Transport at the Magnetospheric Boundary Due to Reconnection in Kelvin-Helmholtz Vortices. *Geophys. Res. Lett.* 28, 3565–3568. doi:10.1029/2001GL013239

Phan, T. D., Eastwood, J. P., Shay, M. A., Drake, J. F., Sonnerup, B. U. Ö., Fujimoto, M., et al. (2018). Electron Magnetic Reconnection without Ion Coupling in Earth's Turbulent Magnetosheath. *Nature* 557, 202–206. doi:10.1038/s41586-018-0091-5

Pollock, C., Moore, T., Jacques, A., Burch, J., Gliese, U., Saito, Y., et al. (2016). Fast Plasma Investigation for Magnetospheric Multiscale. *Space Sci. Rev.* 199, 331. doi:10.1007/s11214-016-0245-4

Russell, C. T., Anderson, B. J., Baumjohann, W., Bromund, K. R., Dearborn, D., Fischer, D., et al. (2016). The Magnetospheric Multiscale Magnetometers. *Space Sci. Rev.* 1, 1. doi:10.1007/s11214-014-0057-3

Sharma Pyakurel, P., Shay, M. A., Phan, T. D., Matthaeus, W. H., Drake, J. F., TenBarge, J. M., et al. (2019). Transition from Ion-Coupled to Electron-Only Reconnection: Basic Physics and Implications for Plasma Turbulence. *Phys. Plasmas* 26, 082307. doi:10.1063/1.5090403

Shue, J.-H., Chao, J. K., Fu, H. C., Russell, C. T., Song, P., Khurana, K. K., et al. (1997). A New Functional Form to Study the Solar Wind Control of the Magnetopause Size and Shape. *J. Geophys. Res.* 102 (A5), 9497–9511. doi:10.1029/97JA00196

Stawarz, J. E., Ergun, R. E., and Goodrich, K. A. (2015). Generation of High-Frequency Electric Field Activity by Turbulence in the Earth's Magnetotail. *J. Geophys. Res. Space Phys.* 120, 1845–1866. doi:10.1002/2014JA020166

Stawarz, J. E., Eriksson, S., Wilder, F. D., Ergun, R. E., Schwartz, S. J., Pouquet, A., et al. (2016). Observations of Turbulence in a Kelvin-Helmholtz Event on 8 September 2015 by the Magnetospheric Multiscale mission. *J. Geophys. Res. Space Phys.* 121, 021–111. doi:10.1002/2016JA023458

Tang, B., Li, W., Wang, C., Dai, L., Khotyaintsev, Y., Lindqvist, P.-A., et al. (2018). Magnetic Depression and Electron Transport in an Ion-Scale Flux Rope Associated with Kelvin-Helmholtz Waves. *Ann. Geophys.* 36, 879–889. doi:10.5194/angeo-36-879-2018

Wilder, F. D., Ergun, R. E., Eriksson, S., Phan, T. D., Burch, J. L., Ahmadi, N., et al. (2017). Multipoint Measurements of the Electron Jet of Symmetric Magnetic Reconnection with a Moderate Guide Field. *Phys. Rev. Lett.* 118 (26), 1. doi:10.1103/PhysRevLett.118.265101

Wilder, F. D., Ergun, R. E., Goodrich, K. A., Goldman, M. V., Newman, D. L., Malaspina, D. M., et al. (2016b). Observations of Whistler Mode Waves with Nonlinear Parallel Electric fields Near the Dayside Magnetic Reconnection Separatrix by the Magnetospheric Multiscale mission. *Geophys. Res. Lett.* 43, 5909–5917. doi:10.1002/2016GL069473

Wilder, F. D., Ergun, R. E., Hoilijoki, S., Webster, J., Argall, M. R., Ahmadi, N., et al. (2019). A Survey of Plasma Waves Appearing Near Dayside Magnetopause Electron Diffusion Region Events. *J. Geophys. Res. Space Phys.* 124, 7837–7849. doi:10.1029/2019JA027060

Wilder, F. D., Ergun, R. E., Schwartz, S. J., Newman, D. L., Eriksson, S., Stawarz, J. E., et al. (2016a). Observations of Large-Amplitude, Parallel, Electrostatic Waves Associated with the Kelvin-Helmholtz Instability by the Magnetospheric Multiscale mission. *Geophys. Res. Lett.* 43, 8859–8866. doi:10.1002/2016GL070404

Wilder, F. D., Schwartz, S. J., Ergun, R. E., Eriksson, S., Ahmadi, N., Chasapis, A., et al. (2020). Parallel Electrostatic Waves Associated with Turbulent Plasma Mixing in the Kelvin-Helmholtz Instability. *Geophys. Res. Lett.* 47, e2020GL087837. doi:10.1029/2020GL087837

Conflict of Interest: The authors declare that the research was conducted in the absence of any commercial or financial relationships that could be construed as a potential conflict of interest.

frontiers in Astronomy and Space Sciences

ORIGINAL RESEARCH
published: 04 November 2021
doi: 10.3389/fspas.2021.760885

MMS Observations of Double Mid-Latitude Reconnection Ion Beams in the Early Non-Linear Phase of the Kelvin-Helmholtz Instability

Stefan Eriksson[1], Xuanye Ma[2], James L. Burch[3], Antonius Otto[4], Scot Elkington[1] and Peter A. Delamere[4]*

[1]Laboratory for Atmospheric and Space Physics, University of Colorado, Boulder, CO, United States, [2]Department of Physical Sciences, Embry-Riddle Aeronautical University, Daytona Beach, FL, United States, [3]Department of Physics and Astronomy, University of Texas, San Antonio, TX, United States, [4]Department of Physics, Geophysical Institute, University of Alaska, Fairbanks, AK, United States

OPEN ACCESS

Edited by:
Takuma Nakamura, Austrian Academy of Sciences (OeAW), Austria

Reviewed by:
Julia E. Stawarz, Imperial College London, United Kingdom
Rungployphan Om Kieokaew, UMR5277 Institut de recherche en astrophysique et planétologie (IRAP), France

***Correspondence:**
Stefan Eriksson
eriksson@lasp.colorado.edu

Specialty section:
This article was submitted to Space Physics, a section of the journal Frontiers in Astronomy and Space Sciences

Received: *19 August 2021*
Accepted: *08 October 2021*
Published: *04 November 2021*

Citation:
Eriksson S, Ma X, Burch JL, Otto A, Elkington S and Delamere PA (2021) MMS Observations of Double Mid-Latitude Reconnection Ion Beams in the Early Non-Linear Phase of the Kelvin-Helmholtz Instability. Front. Astron. Space Sci. 8:760885. doi: 10.3389/fspas.2021.760885

The MMS satellites encountered a Kelvin-Helmholtz instability (KHI) period in the early non-linear phase at the post-noon flank magnetopause on 8 Sep 2015. The adjacent magnetosheath was characterized by a pre-dominantly northward Bz > 0 magnetic field with weakly positive in-plane components in a GSM coordinate system. Ion velocity distribution functions indicate at least 17 KH vortex intervals with two typically D-shaped ion beam distributions, commonly associated with reconnection exhausts, that stream in both directions along a mostly northward magnetic field at 350–775 km/s with a median 525 km/s ion beam speed. The counter-streaming ion beams are superposed on a core population of slowly drifting magnetosheath ions with a field-aligned 50–200 km/s speed. Each interval lasted no more than 5.25 s with a median duration of 1.95 s corresponding to in-plane spatial scales $3 < \Delta S < 22$ di assuming a constant 1 di = 61 km ion inertial scale and a tailward V_{KH}~258 km/s KH vortex propagation speed along the MMS trajectory. The counter-streaming ions are predominantly observed in the warm KH vortex region between the cold magnetosheath proper and the hot isotropic ion temperature of a low-latitude boundary layer as the MMS constellation traverses a KH vortex. The in-plane spatial scales and the locations of the observed counter-streaming ion beams generally agree with the predictions of twice-reconnected magnetic fields at two mid-latitude reconnection (MLR) regions in a two-fluid three-dimensional numerical simulation previously reported for this KH event. MMS typically recorded a higher phase space density of the fast parallel ion beam that we associate with a tailward reconnection exhaust from the southern MLR (SMLR) and a lower phase space density of the fast anti-parallel ion beam that we associate with a tailward reconnection exhaust from the northern MLR (NMLR) of similar speed. This is either consistent with MMS being closer to the SMLR region than the NMLR region, or that the KHI conditions may have favored reconnection in the SMLR region for the observed in-plane magnetosheath magnetic field as predicted by a two-fluid three-dimensional numerical simulation.

Keywords: KHI, mid-latitude reconnection, ion beams, MMS satellite observations, flank magnetopause

INTRODUCTION

A fast magnetosheath flow around the Earth's magnetosphere can trigger a Kelvin-Helmholtz (KH) instability (Chandrasekhar, 1961; Miura and Pritchett, 1982) when the stabilizing interplanetary magnetic field (IMF) is mostly perpendicular to the shear flow across the magnetopause surface (Kokubun et al., 1994). The most KH unstable regions thus tend to occur in the equatorial plane of the flank magnetopause (Farrugia et al., 1998; Foullon et al., 2008; Vernisse et al., 2020) during northward IMF conditions that typically results in well-developed KH waves of the magnetopause surface as observed by *in-situ* spacecraft [e.g., (Chen and Kivelson, 1993; Fairfield et al., 2000; Hasegawa et al., 2004; Hasegawa et al., 2006; Nykyri et al., 2006; Nishino et al., 2007; Eriksson et al., 2016a)]. The KH wave amplitude grows as the shear-flow disturbance propagates from a dayside source region along the flank magnetopause in a general magnetosheath flow direction. This wave amplitude growth eventually causes the magnetopause KH wave to roll up on itself in a non-linear phase of the KH evolution that typically occurs near the dawn-dusk terminator and beyond (Otto and Fairfield, 2000; Nakamura et al., 2013).

Developing KH waves support the formation of thin current sheets as the magnetic field on the two sides of the magnetopause evolves with the KH plasma vortex motion. Two-dimensional numerical simulations (Otto and Fairfield, 2000; Nykyri and Otto, 2001; Nakamura et al., 2008) suggest that magnetic field reconnection (Sonnerup, 1979; Schindler et al., 1988; Birn et al., 2001) may proceed at such current sheets inside KH vortices, involving a small in-plane component of a predominantly northward directed magnetic field in the magnetosheath that folds up on itself. Low-shear magnetic reconnection may also proceed along the equatorial spine region of the compressed magnetopause current sheet (CS) that connects a pair of KH vortices (Pu et al., 1990; Knoll and Chacón, 2002; Hasegawa et al., 2009; Nakamura et al., 2013; Eriksson et al., 2016a; Eriksson et al., 2016b; Vernisse et al., 2016). Reconnection in the spine region creates new open magnetic fields as it merges a small in-plane component of the magnetic field in the magnetosheath with an anti-parallel component of the in-plane magnetic field in the magnetosphere consistent with electron observations (Vernisse et al., 2016).

Otto (2008) first proposed that a KH vortex motion of the equatorial plane magnetic field will support magnetic reconnection off the equator to relax twisted magnetic fields in a northern mid-latitude region and a southern mid-latitude region of the three-dimensional KH vortex. The mid-latitude reconnection (MLR) concept was further refined in Faganello and Califano (2017) to suggest that it typically involves a shearing of KH-vortex associated magnetic fields along the direction of KH propagation at the two off-equator magnetopause locations rather than a well-developed vortex motion also in the mid-latitude region. The mid-latitude shearing results from a closed magnetic field earthward of the magnetopause being pulled tailward in the equatorial plane by the KH vortices and an open magnetic field in the adjacent magnetosheath being slowed down in the equatorial plane as it gets entrained in a KH vortex flow pattern. Faganello et al. (2014) explored the proposed off-equatorial reconnection process in a three-dimensional (3-D) Hall-MHD numerical model and suggested that reconnection proceeds nearly simultaneously off the equator in the northern and southern mid-latitude regions of the KH vortex to form new, closed field lines consisting of high-latitude magnetosphere field-line segments off the equator (north and south) and an embedded magnetosheath field-line segment between the two MLR regions. Faganello et al. (2014) also reported a short-duration interval of 100–500 eV counter-streaming electrons as observed by the THEMIS-C satellite at 0916:20 UT on 15 April 2008 in the equatorial low-latitude boundary layer (LLBL) region (Mitchell et al., 1987) of a KH wave, and beyond the dusk flank terminator at $(x,y,z)_{GSM} = (-7.1, 18.0, -1.9)$ R_E. Faganello et al. (2014) argued that the short-duration, counter-streaming electrons may be interpreted as accelerated magnetosheath electrons along recently closed field lines at two MLR regions.

Ma et al. (2017) analyzed a 3-D MHD simulation of the KH instability (KHI) for northward IMF conditions to demonstrate that non-linear, rolled-up KH waves may result in a significant amount of double-reconnected closed magnetic flux and a highly efficient plasma transport mechanism across the flank magnetopause. However, Ma et al. (2017) also predicted that a finite in-plane component of the magnetic field along the XY_{GSM}-shear flow direction should cause an important north-south asymmetry with a lower probability of forming newly closed magnetic flux in the KH vortex due to double mid-latitude reconnection (DMLR). In other words, an in-plane magnetic field component is more likely to favor an off-equator magnetic reconnection process in only one mid-latitude region (north or south) to form new, open magnetic flux within the KH vortex. Fadanelli et al. (2018) and Sisti et al. (2019) explored this asymmetric MLR concept that we associate with KH vortices numerically using a two-fluid 3-D simulation, and discussed the importance of "once-reconnected" open field lines and "twice-reconnected" closed field lines due to MLR, and the predicted location of the more active MLR region relative the most KH-unstable location on the flank magnetopause. Sisti et al. (2019) simulated the 8 Sept 2015 KH event observed by MMS to predict a more active MLR region in the southern hemisphere. Indirect evidence of this single MLR process, as acquired by a satellite in the equatorial region, would consist of accelerated electrons and ions in only one direction along the magnetic field, and a loss of particles streaming in the opposite direction of this open magnetic field. Vernisse et al. (2016) confirmed this signature in the electron observations obtained by MMS on 8 Sept 2015.

There are some early reports of beams in ion velocity distribution functions (VDFs) as obtained by the Cluster and the Geotail satellites in a non-linear phase of the KHI near the flank magnetopause terminator and beyond. Geotail recorded 12-s cadence ion observations during a KH period in a non-linear phase (Nishino et al., 2007) well beyond the dusk flank at $(x,y,z)_{GSM} = (-14.9, 19.2, 2.9)$ R_E in close proximity to CSs characterized by changes in the magnetic field direction. It was concluded (Nishino et al., 2007) that the ion beams were in agreement with vortex-induced magnetic reconnection (VIR) in

the equatorial plane (Otto and Fairfield, 2000; Nakamura et al., 2006; Nakamura et al., 2013) inside a KH-vortical structure rather than associated with a source at one or two MLR regions.

The Cluster satellites recorded a dawnside KH event at $(x,y,z)_{GSM}$ = (−9.1, −16.5, 4.3) R_E on 3 Jul 2001 (Nykyri et al., 2006) including a well-resolved single ion beam with an anti-parallel V_B = −500 km/s speed in a northward Bz > 0 magnetic field with a sunward Bx > 0 component. The anti-parallel ion beam was superposed on a magnetosheath ion population in an ion VDF that the Cluster-1 satellite observed at 0547:55 UT as it transitioned from a cold and high-density magnetosheath into a warm KH-vortex region. That single anti-parallel ion beam could be associated with one northern MLR region considering the Cluster-1 location at Z_{GSM} = 4.3 R_E and the direction of the local magnetic field rather than direct evidence of magnetic reconnection associated with KH-induced CSs in the equatorial plane of the KH vortex.

"Multiple field-aligned ion populations" were reported in 4-s cadence Cluster satellite observations (Bavassano Cattaneo et al., 2010) throughout the rolled-up vortex regions of a non-linear KHI on 25 Nov 2001 near the dusk terminator at $(x,y,z)_{GSM}$ = (−4.5, 16.8, 3.8) R_E including an apparent single anti-parallel ion beam at 0223:11 UT. In the absence of local magnetic reconnection exhausts in the equatorial plane of the Cluster satellites, and a presence of field-aligned electrons streaming in both directions along the northward magnetic field, Bavassano Cattaneo et al. (2010) proposed a source near a southern cusp, high-latitude reconnection (HLR) region. However, it is possible that the ion VDF collected by the Cluster satellite at 0223:11 UT, and the discussion in Bavassano Cattaneo et al. (2010), may support a presence of an anti-parallel ion beam associated with a "once-reconnected" MLR process to the north of Cluster in this northward-directed magnetic field rather than a single, southern hemisphere HLR region.

Here we report a signature of two typically D-shaped (Cowley, 1982) counter-streaming ion beams as recorded at the fast 150-ms cadence of the MMS ion observations (Burch et al., 2015; Burch et al., 2016; Pollock et al., 2016) in a well-documented KHI event on the post-noon flank magnetopause on 8 Sept 2015 [e.g., (Eriksson et al., 2016a; Eriksson et al., 2016b; Li et al., 2016; Stawarz et al., 2016; Vernisse et al., 2016; Wilder et al., 2016; Nakamura et al., 2017; Sorriso-Valvo et al., 2019; Vernisse et al., 2020)] as MMS moved from $(x,y,z)_{GSM}$ = (5.1, 7.2, −4.4) R_E at 1007:30 UT to $(x,y,z)_{GSM}$ = (4.8, 8.1, −5.1) R_E at 1123:30 UT. The phase space density (PSD) of the two ion beams is typically two orders of magnitude lower than the PSD of a slowly drifting ion core distribution of magnetosheath ions measured along the same magnetic field. The well-resolved counter-streaming ion beams are not observed throughout the KH vortex region. They are rather observed in short <6 s bursts in the warm leading edge of the post-noon KH vortices, and typically by all four MMS satellites, far from the intense CSs at the trailing edges of the KH waves associated with vortex-induced reconnection of the spine region (Eriksson et al., 2016a; Eriksson et al., 2016b).

The paper is organized as follows. **Section 2** presents an overview of the KH wave observations by MMS in GSM coordinates. **Section 3** presents detailed ion observations from the Fast Plasma Instrument (FPI) instrument (Pollock et al., 2016) for a few example periods as ion pitch-angle (PA) information in the 2–3 keV energy range, 2-D ion VDFs in V_B-V_{BxV} space, and as 1-D cuts of the ion VDFs along the field-aligned V_B direction. **Section 4** provides a discussion of the MMS observations and their comparison with numerical simulation predictions during the KHI evolution. Finally, **section 5** provides a summary and conclusions on the proposed origin of the two counter-streaming ion beams that MMS observed within the warm leading edges of this KHI period in its early non-linear stage (Nakamura et al., 2017).

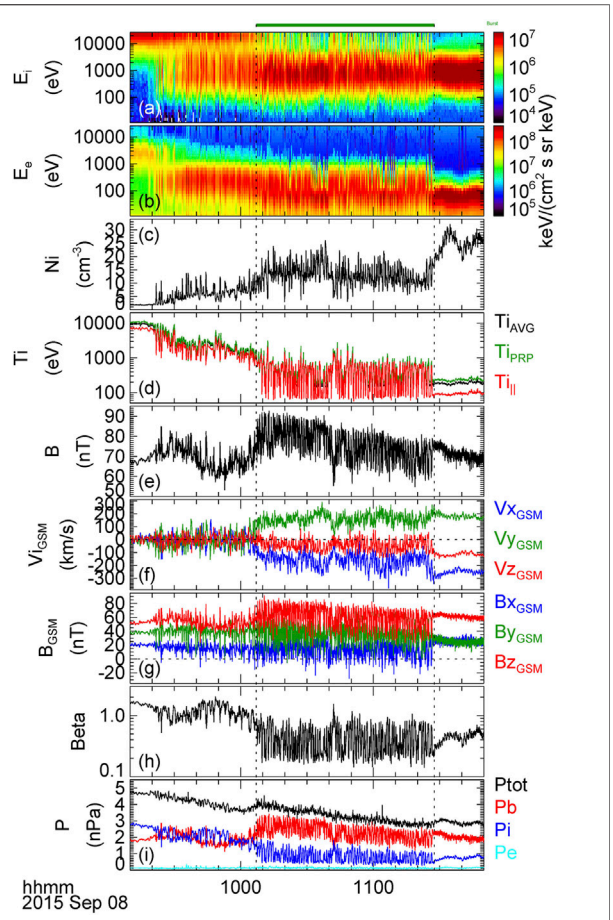

FIGURE 1 | MMS-1 observations in fast survey mode from 0910 UT to 1150 UT on 8 Sept 2015: **(A)** ion omni-directional energy-time spectrogram; **(B)** electron omni-directional energy-time spectrogram; **(C)** ion plasma number density; **(D)** ion temperature; **(E)** magnetic field strength; **(F)** ion velocity in the GSM coordinate system; **(G)** magnetic field GSM components; **(H)** plasma β; **(I)** magnetic field pressure (red), ion plasma pressure (blue), electron plasma pressure (cyan) and their sum (black).

MMS OVERVIEW OBSERVATIONS OF KELVIN-HELMHOLTZ WAVES ON 8 SEPT 2015

NASA launched the four identical MMS satellites into a 12 R_E apogee elliptical orbit near the equatorial plane on 12 Mar 2015. In this study, we examine the MMS burst mode observations of the KHI waves on 8 Sept 2015 as recorded 10.1 R_E from Earth in

the 15.7 magnetic local time sector with a particular focus on the 150-ms ion measurements of the Dual Ion Spectrometer (DIS) top hat electrostatic analyzer (ESA) and the 30-ms electron measurements of the Dual Electron Spectrometer (DES) of the FPI suite of instruments (Pollock et al., 2016). We also take advantage of magnetic field observations of the fluxgate magnetometer instrument (Russell et al., 2016) at 7.8 ms cadence, and parallel electric field observations measured at 8192 Hz cadence by the Axial Double Probe (ADP) instrument (Ergun et al., 2016).

Figure 1 shows an overview of the MMS measurements, sampled in fast survey mode from 0910 UT to 1150 UT with FPI plasma observations recorded at 4.5 s. The continuous interval of burst mode data is indicated by the green horizontal bar above the top panel at 1007:04–1127:34 UT. The omni-directional ion energy-time spectrogram (**Figure 1A**) and the omni-directional electron energy-time spectrogram (**Figure 1B**) show how MMS traversed this post-noon magnetopause region from the low-density (N~2 cm^{-3}, **Figure 1C**) and high-temperature (Ti_{AVG}~10 keV, **Figure 1D**) outer magnetosphere, as observed prior to ~0920 UT, to the high-density and low-temperature magnetosheath that MMS sampled after ~1128 UT. During the intervening period, MMS recorded an interval with much more variable observations in all the measured quantities as shown in **Figure 1**. The periodic behavior, which is particularly clear during the burst mode interval, is consistent with a KH instability with a maximum sustained KHI wave growth on the order $\gamma/k > 131$ km/s (Eriksson et al., 2016a) between a pre-existing inner LLBL region and the adjacent magnetosheath. A global MHD analysis was performed (Vernisse et al., 2020) to suggest that MMS was very close to a region of maximum KHI wave growth in latitude with similar KHI growth rates as that reported by Eriksson et al. (2016a). The MMS measurements were further proposed to satisfy an early non-linear phase of the KHI (Nakamura et al., 2017; Sisti et al., 2019). The initial period between ~0920 UT and 1007 UT reflect periodic KH waves of the inner LLBL region, while the 1 h 20 min of MMS burst mode observations rather reflect KH waves of the outer LLBL region with MMS sampling the periodic magnetopause KH surface waves between the outermost LLBL and the adjacent magnetosheath.

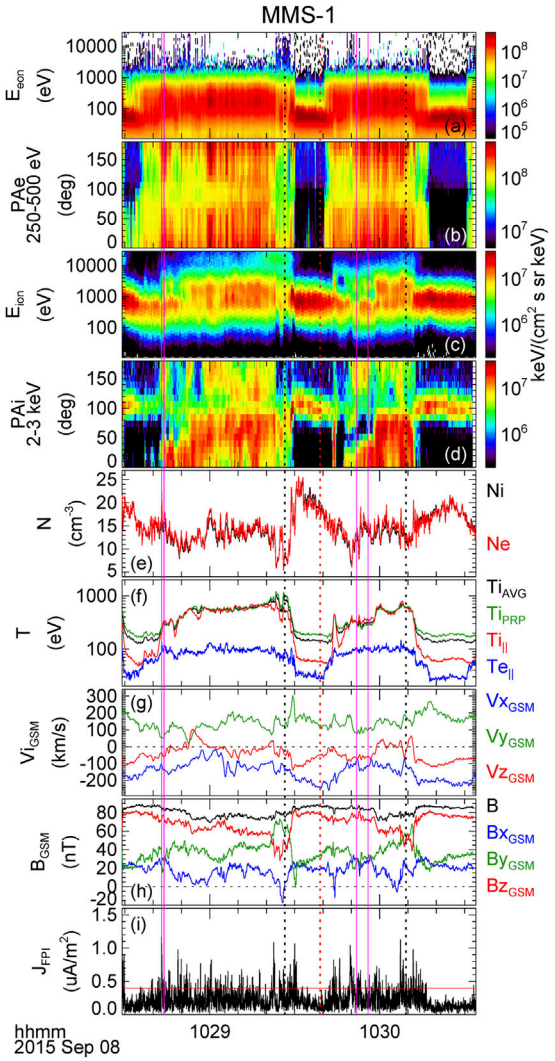

FIGURE 2 | MMS-1 observations in burst mode from 1028:29 UT to 1030:34 UT on 8 Sept 2015: **(A)** electron omni-directional energy-time spectrogram; **(B)** electron pitch-angle distribution in the 250–500 eV energy range; **(C)** ion omni-directional energy-time spectrogram; **(D)** ion pitch-angle distribution in the 2–3 keV energy range; **(E)** plasma number density for electrons (red) and ions (black); **(F)** electron parallel temperature ($Te_{||}$, blue), ion parallel temperature ($Ti_{||}$, red), ion perpendicular temperature (Ti_{perp}, green), and the ion average temperature $Ti_{AVG}=(Ti_{||}+2Ti_{perp})/3$; **(G)** ion velocity in the GSM coordinate system; **(H)** magnetic field GSM components and their magnitude (black); **(I)** magnitude of the current density GSM vector as measured by the FPI instruments. Three dotted vertical lines mark the times of 150-ms ion VDFs sampled at 1029:26.500 UT (black), 1029:39.000 UT (red), and 1030:09.299 UT (black). Four solid vertical lines in pink color mark two sustained periods of distinct counter-streaming ion beams in the ion VDFs at 1028:42.950–1028:43.849 UT and 1029:51.849–1029:55.900 UT.

MMS KINETIC OBSERVATIONS

We performed a thorough survey of burst-mode ion velocity distribution functions (VDFs) that the MMS satellites obtained on 8 Sept 2015 for distinct evidence of sustained periods of two counter-streaming ion beams during an early non-linear phase of the KH waves on the dusk flank magnetopause (Nakamura et al., 2017) and relatively close in latitude to a region of maximum KHI growth (Vernisse et al., 2020). The study was directly motivated following some tantalizing new evidence of two ion beams in a time averaged ion velocity distribution centered at 1044:54.164 UT as first reported by Vernisse et al. (2016) that we discuss in more detail in **section 4**, and to explore whether DMLR may actually be active this early in the KH vortex evolution as predicted by Sisti et al. (2019) for this KH event by using a two-fluid 3D numerical simulation.

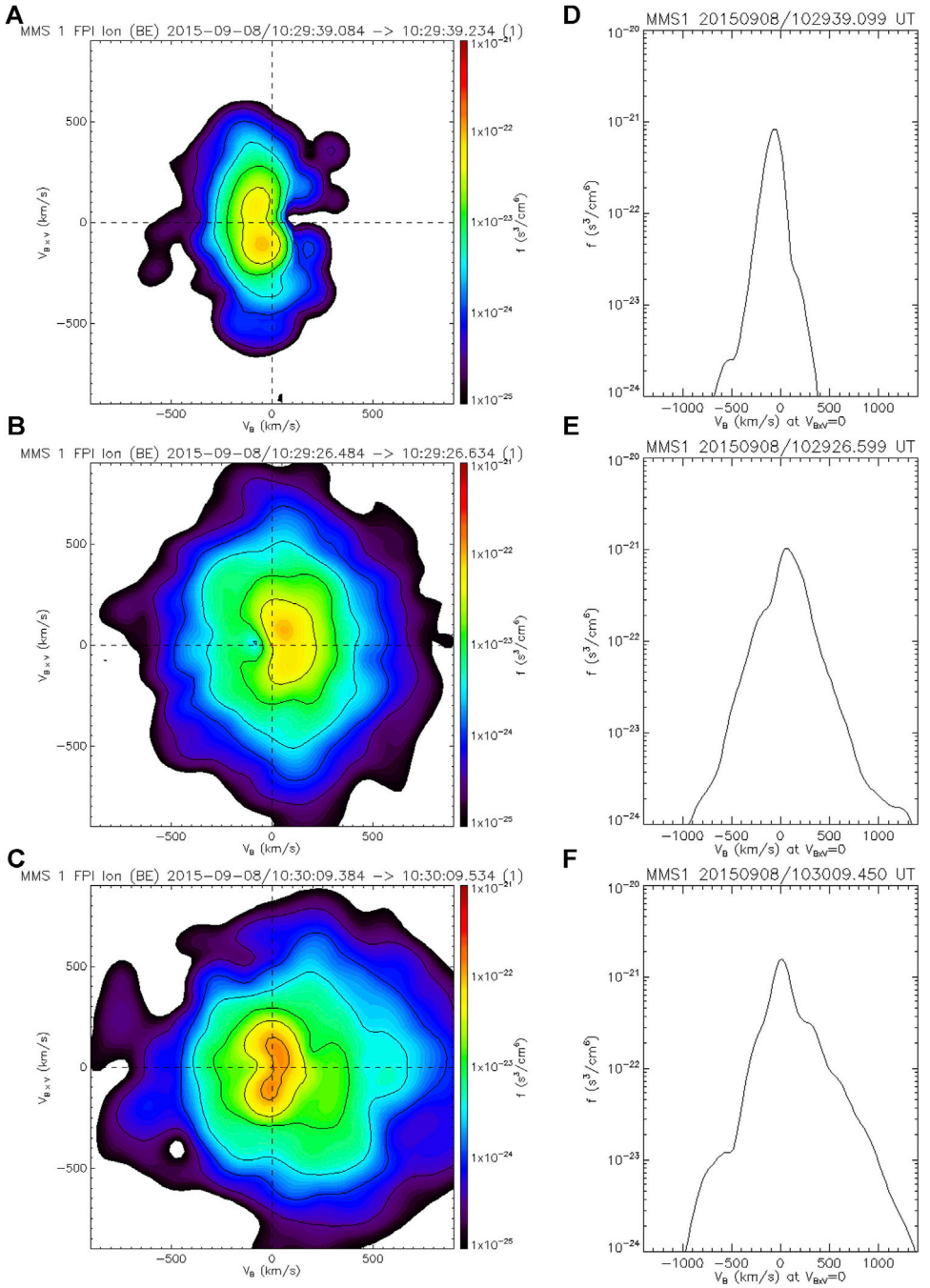

FIGURE 3 | (A) MMS-1 ion VDF at 1029:39.099 UT; **(B)** MMS-1 ion VDF at 1029:26.599 UT; **(C)** MMS-1 ion VDF at 1030:09.450 UT; **(D)** 1-D cut of the MMS-1 ion VDF at 1029:39.099 UT; **(E)** 1-D cut of the MMS-1 ion VDF at 1029:26.599 UT; **(F)** 1-D cut of the MMS-1 ion VDF at 1030:09.450 UT. The 2-D ion phase space density of the VDFs **(A–C)** are shown in V_{BxV} vs V_B space. The 1-D cuts along V_B are taken along V_{BxV} = 0 km/s.

Ion Beam Observations

Figure 2 displays MMS-1 burst mode observations at 1028: 29–1030:34 UT when the MMS satellites were located at $(x,y,z)_{GSM}$ = (5.0, 7.5, −4.6) R_E. These data cover two complete KH wave periods consisting of three short intervals in a cold magnetosheath plasma and two longer intervals in a KH vortex region, where MMS typically measured a more isotropic ion temperature (**Figure 2F**). The magnetosheath plasma is characterized by a very low energy flux of electrons in the 250–500 eV energy range (**Figures 2A,B**) that corresponds to anti-parallel strahl electrons from the Sun (Feldman et al., 1975; Vernisse et al., 2016). The higher-density (**Figure 2E**) magnetosheath periods are also characterized by a high ion energy flux below 2 keV with a core ion distribution at

90–110° pitch-angle (**Figures 2C,D**) and $Ti_{perp} > Ti_{||}$ (**Figure 2F**) in agreement with a tailward magnetosheath flow deflected along the dusk flank magnetopause, Vx < 0 and Vy > 0 (**Figure 2G**), with the ions gyrating about a pre-dominantly northward (Bz > 0) magnetic field with weaker in-plane components generally displaying Bx > 0 and By > 0 (**Figure 2H**). The trailing edges of the two KH vortex regions are associated with more intense CSs, characterized by significant rotations of the By component. **Figure 2I** displays the magnitude of the GSM current density vector **J** = Ne(**V**i-**V**e), measured by the FPI ion and electron instruments. Here, N is the plasma number density, **V**i the ion velocity and **V**e the electron velocity. The trailing KH regions support some of the strongest CSs of this ~2-min interval with J~1 μA/m^2. In fact, one such CS encountered just before 1029:30 UT also supports a local, vortex-induced "type-I" reconnection exhaust (Nakamura et al., 2013) with a measured Vy~100 km/s flow enhancement in the positive Y_{GSM} direction relative the Vy~200 km/s external flow (Eriksson et al., 2016a; Li et al., 2016; Vernisse et al., 2016). The adjacent magnetosheath does not support many intense CSs, where MMS typically measured J < 0.4 μA/m^2. The two KH vortex regions support localized CSs with typical magnitudes 0.5 < J < 1 μA/m^2.

Figure 3 displays three ion VDFs in a plane that consists of a vertical axis along one of the two ion velocity components perpendicular to the magnetic field (V_{BxV}) and a horizontal axis that shows the ion velocity along the magnetic field (V_B). MMS-1 sampled the 150-ms ion VDF of **Figure 3A** in the magnetosheath-proper at 1029:39.084–1029:39.234 UT, which is marked as a red, vertical dotted line between the two KH vortex intervals of **Figure 2**. The core magnetosheath population shows up as a slow, mostly negative 50–200 km/s drift in a direction opposite the magnetic field direction. The ion VDF thus reflects the fast tailward (Vx < 0) ion flow with a southward (Vz < 0) flow deflection (**Figure 2G**) in a magnetic field with a positive Bx > 0 component and a stronger Bz > 0 component (**Figure 2H**) that MMS measured in a southern hemisphere location at Z_{GSM} = −4.6 R_E. **Figure 3** compares this ion VDF of the magnetosheath proper with two ion VDFs measured by MMS-1 in two LLBL regions, which are marked as the black vertical dotted lines in **Figure 2**. MMS-1 measured the two ion VDFs just Earthward of the two intense trailing edge CSs of the two tailward-propagating KH vortices with **Figure 3B** showing the 150-ms ion VDF at 1029:26.599 UT, and **Figure 3C** showing the ion VDF at 1030:09.450 UT. This side-by-side comparison shows how the LLBL ion velocity distributions are hot and more isotropic as compared with a cold anisotropic magnetosheath ion VDF, which is also reflected in the corresponding 1-D cuts taken along the magnetic field V_B direction at V_{BxV} = 0 km/s and shown in **Figures 3D–F**.

The left-side column of **Figure 4** presents the 2-D plane ion VDFs as observed by all four MMS satellites at approximately the same time with MMS-1 recording the ion VDF at 1029:55.284–1029:55.434 UT. This time is embedded within a 4.1-s long interval as displayed in **Figure 2** between the two, pink vertical lines at 1029:51.849 UT and 1029:55.900 UT. The corresponding 1-D field-aligned cuts at V_{BxV} = 0 km/s are shown in the right-side column of **Figure 4**. There are two very distinct ion beams that propagate both parallel and anti-parallel to the local magnetic field at this time. The MMS-1 satellite (**Figures 4A,E**) measured a parallel D-shaped ion beam with a PSD peak around V_B = 550 km/s and a roughly D-shaped anti-parallel ion beam with a PSD peak near V_B = −525 km/s. The kinetic energy $W_K = m_p V_B^2/2$ corresponding to protons traveling southward at this fast field-aligned V_B speed is W_K~1.4 keV for the anti-parallel ions, and W_K~1.6 keV for the parallel ions traveling northward. The PSD of the two parallel beams is similar, and roughly two orders of magnitude lower than the PSD of the slowly drifting ion core distribution. The MMS-2 satellite (**Figures 4B,F**) observed two very similar counter-propagating ion beams as MMS-1 along this local magnetic field with a similar PSD and V_B magnitude, but obtained in a more southward location with a separation $(\Delta X,\Delta Y,\Delta Z)_{GSM}$=(−43,−85,−119) km from the MMS-1 satellite. The MMS-4 satellite (**Figures 4D,H**) also observed the two counter-propagating ion beams of similar PSD as MMS-1 and MMS-2, despite a more tailward separation $(\Delta X,\Delta Y,\Delta Z)_{GSM}$ = (−178,−24,−42) km from MMS-1. However, MMS-4 measured a positive ion beam with a faster V_B = 600 km/s speed (W_K~1.9 keV) and a negative ion beam that peaked at a slower V_B = −500 km/s speed (W_K~1.3 keV) as compared with the MMS-1 ion observation. Finally, the MMS-3 satellite (**Figures 4C,G**) observed a strikingly different ion VDF as compared with the other MMS satellites with a much diminished PSD in velocity phase space, where the other satellites had recorded a distinct anti-parallel ion beam. Moreover, the parallel ion beam displayed the lowest PSD and the fastest V_B = 700 km/s (W_K~2.6 keV) at MMS-3 as compared with the other locations in the MMS tetrahedron at this same time. Interestingly, this MMS-3 observation was obtained in a much more northward location $(\Delta X,\Delta Y,\Delta Z)_{GSM}$ = (−17,−78,164) km relative MMS-2, and in a more earthward location $(\Delta X,\Delta Y,\Delta Z)_{GSM}$ = (−60,−162,45) km from MMS-1.

The 4.1-s long interval marked in **Figure 2** consists of 27 separate MMS-1 ion VDFs that displayed structurally very similar ion distributions as the ones illustrated in **Figure 4A** with two ion beams streaming up and down the local magnetic field, and superposed on a third, slowly drifting core population typically opposite the magnetic field. **Figure 2** shows that the ion VDFs of **Figure 4** were sampled well inside the leading edge of one KH vortex as MMS moved from the cold magnetosheath proper into a warmer section of the KH vortex, but before the satellites entered the hot, isotropic ion temperature region of the KH vortex that we associate with the LLBL-proper (**Figures 3C,F**). A closer examination of the ion VDF observations across the entire MMS tetrahedron through this particular KH vortex shows how MMS-2 measured two counter-propagating ion beams during a continuous ~4.4 s period at 1029:51.299–1029:55.650 UT, while the MMS-4 satellite observed the two ion beams in two separate intervals; first as a short 0.70 s "burst" (1029:51.900–1029:52.599 UT) and then again as a longer ~3.6 s period (1029:52.950–1029:56.500 UT). In contrast to the other satellites, the most earthward MMS-3 satellite recorded the two clearly resolved ion beams in three

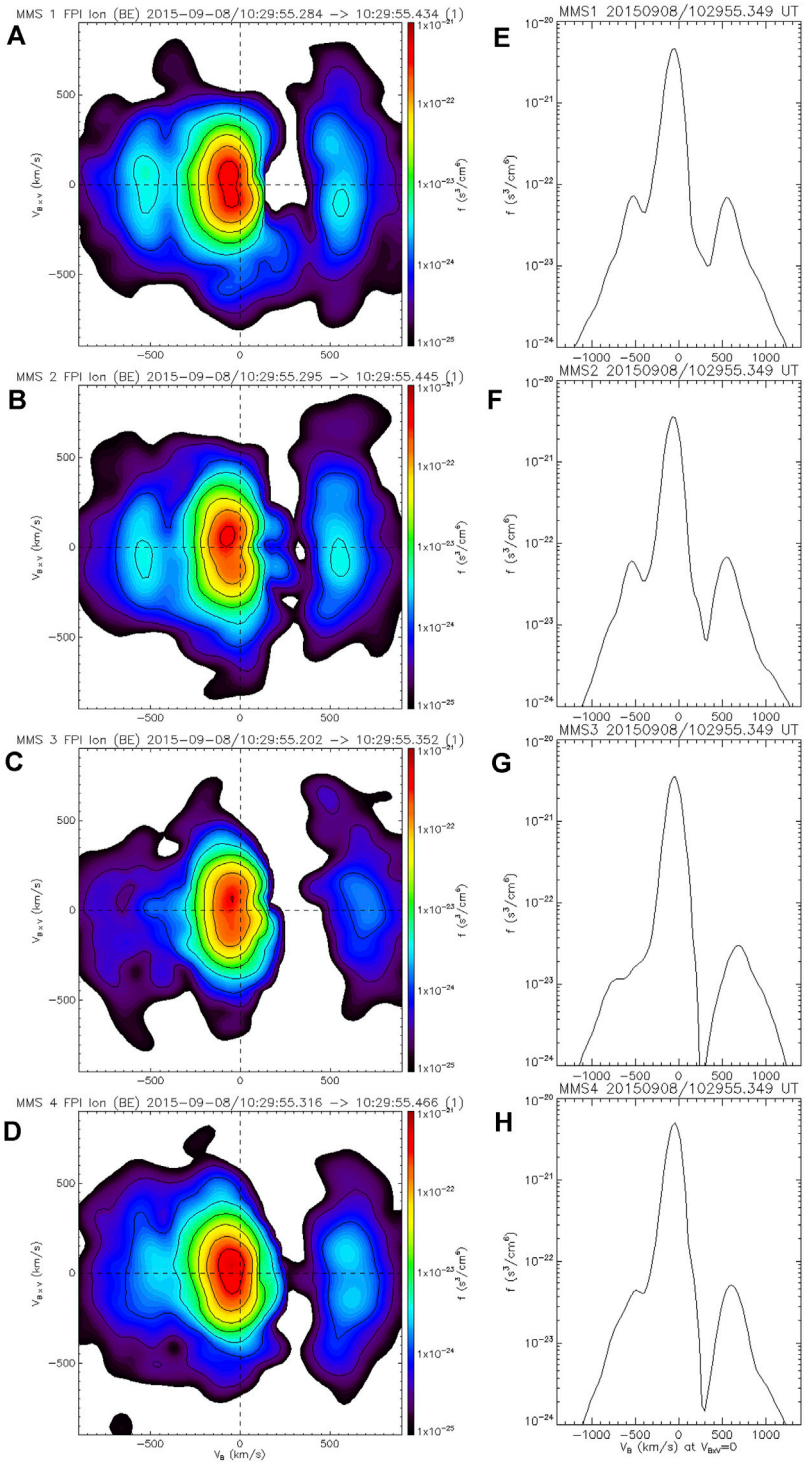

FIGURE 4 | Ion velocity distribution functions at 1029:55.349 UT: **(A)** 2-D ion phase space density at MMS-1; **(B)** 2-D ion phase space density at MMS-2; **(C)** 2-D ion phase space density at MMS-3; **(D)** 2-D ion phase space density at MMS-4; **(E)** 1-D cut at MMS-1; **(F)** 1-D cut at MMS-2; **(G)** 1-D cut at MMS-3; **(H)** 1-D cut at MMS-4.

separate "bursts" with durations 0.30 s (1029:51.099–1029:51.400 UT), 0.95 s (1029:52.150–1029:53.099 UT), and 0.80 s (1029:54.099–1029:54.900 UT).

Figure 5 shows all four MMS satellite observations of parallel ion temperature and ion velocity through this KH-vortex encounter with **Figure 5A** showing the MMS-1 omni-directional ion energy-time

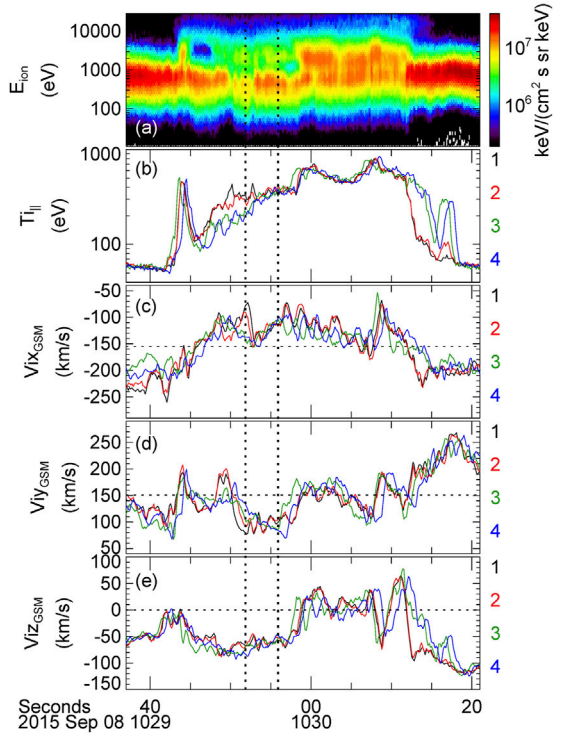

FIGURE 5 | MMS observations in burst mode from 1029:37 UT to 1030:21 UT on 8 Sept 2015: **(A)** MMS-1 ion omni-directional energy-time spectrogram; **(B)** ion parallel temperature; **(C–E)** ion velocity components in the GSM coordinate system. Panels **(B–E)** display MMS-1 observations in black, MMS-2 observations in red, MMS-3 observations in green, and MMS-4 observations in blue color. The two vertical dotted lines mark a time period 1029:51.849–1029:55.900 UT with two counter-propagating ion beams in MMS-1 ion VDFs. The horizontal dotted lines mark the average Vx_{GSM} = −155.37 km/s (panel **C**) and the average Vy_{GSM} = 150.68 km/s (panel **D**).

spectrogram for reference. A cold $Ti_{||}$<100 eV ion temperature (**Figure 5B**) clearly displays a faster tailward Vix<0 (**Figure 5C**) and a fast southward Viz<0 (**Figure 5E**) magnetosheath flow before and after the KH vortex encounter, while a $Ti_{||}$>400 eV plasma corresponds with an LLBL domain characterized by slower Viz > −20 km/s. The two vertical, dotted lines again mark the 4.1 s interval when MMS-1 recorded the two ion beams. Interestingly, the MMS satellites remained within a Viz < −40 km/s magnetosheath-like flow regime at this time of interest with an intermediate $Ti_{||}$ between that of a cold magnetosheath proper and the subsequent hotter LLBL plasma.

We can display the time intervals of the two ion beams by converting the temporal information of **Figure 5** into four MMS trajectories along a $\mathbf{M}_{GSM}$ = [0.717852, −0.696196, 0.0] in-plane direction that we define as $\mathbf{M}_{GSM} = -\mathbf{Vi}_{GSM}/|\mathbf{Vi}_{GSM}|$. Here, $\mathbf{Vi}_{GSM}$ = [−155.37, 150.68, 0.0] is the average in-plane ion velocity that MMS-1 measured during the entire 1029:37–1030:21 UT KH-vortex time interval of **Figure 5** with a magnitude $V_{KH} = |\mathbf{Vi}_{GSM}|$ = 216.4 km/s. The two components of the average in-plane speed (Vx = −155.4 km/s, Vy = 150.7 km/s) are shown as the dotted, horizontal lines of **Figures 5C,D**, respectively. The estimated propagation velocity of this KH vortex ($\mathbf{V}_{KH} = \mathbf{Vi}_{GSM}$) is corroborated using a timing boundary normal analysis (Schwartz, 1998), since there are measurable time delays of a sudden increase of $Ti_{||}$ at the 1029:43.5 UT beginning of this KH vortex encounter at the three MMS satellites (Δt_2 = −0.01 s, Δt_3 = 0.29 s, Δt_4 = −0.53 s) relative the MMS-1 satellite. These time delays and the other MMS satellite positions relative MMS-1 at this time, with MMS-2 at $\mathbf{R}_2$ = [−43.05, −84.85, −118.73] km, MMS-3 at $\mathbf{R}_3$ = [−59.55, −162.51, 45.28] km, and MMS-4 at $\mathbf{R}_4$ = [−177.65, −24.35, −42.05] km, resulted in a V = 219 km/s boundary normal speed along a boundary normal direction $\mathbf{U}_{GSM}$ = [−0.654991, 0.748380, −0.104472]. This local $\mathbf{U}_{GSM}$ direction is only separated 7.6° from $-\mathbf{M}_{GSM}$ with a comparable speed. This means that $-\mathbf{M}_{GSM}$ and V_{KH}~216 km/s represent a realistic, single KH vortex propagation direction and speed for the data displayed in **Figure 5**. The local V_{KH}~216 km/s KH vortex speed is only somewhat slower than the mean V_{KH}~258 km/s KH propagation speed of the many vortices that MMS traversed during the entire KH event (Eriksson et al., 2016a).

Figure 6 illustrates the four MMS satellite observations of the XY_{GSM}-plane ion velocity as shown in **Figure 5** in the KH vortex co-moving frame of reference. Each MMS trajectory is aligned with the sunward-directed $\mathbf{M}_{GSM}$ satellite propagation direction through this tailward-moving KH vortex with the horizontal $\mathbf{M}_{GSM}$-projections of the ion velocity vectors showing $\Delta V_M = V_M$+216 km/s. The vertical axis displays the projection of the measured ion velocity along $\mathbf{N}_{GSM} = \mathbf{L}_{GSM} \times \mathbf{M}_{GSM}$ = [0.696196, 0.717852, 0.0], where $\mathbf{L}_{GSM} \equiv$[0,0,1]. The horizontal axis of **Figure 6** also shows the distance, $M = V_{KH} \cdot t$, that each satellite travelled along the $\mathbf{M}_{GSM}$ direction in time (t) from their start positions relative MMS-1, $\mathbf{R}_1$ = [0,0], at 1029:37 UT (t = 0) using V_{KH}~216 km/s. At time t = 0, MMS-2 started at [M,N] = [28.13, −90.86] km, MMS-3 started at [M,N] = [70.40, −158.12] km and MMS-4 started at [M,N] = [-110.57, −141.19] km. The MN-plane ion velocity vectors are also color-coded using the individually measured $Ti_{||}$ (*see* **Figure 5B**) with a deep red color corresponding to a maximum $Ti_{||}$~800 eV and a deep blue color corresponding to a minimum $Ti_{||}$~52 eV. **Figure 6** shows that all satellites recorded an earthward V_N<0 flow in the cold magnetosheath (M < 1250 km) prior to entering the warmer mixing region of the KH vortex. **Figure 6** also confirms that all satellites measured an accelerated, counter-clockwise ion flow around the downstream KH vortex after M > 8250 km and until 1030:21 UT.

Figure 6 marks the individual times of two counter-streaming ion beams that we listed above as colored dots along each separate MMS trajectory. MMS-1 (black dots) observed the two ion beams at 3214 < M < 4091 km and MMS-2 (red dots) observed the same beams at 3095 < M < 4037 km. MMS-4 (blue dots) encountered the first instance of two ion beams at 3225 < M < 3376 km, and then again at 3452 < M < 4221 km. The most earthward MMS-3 satellite (pink dots) first came across the two ion beams at M = 3052 km, and it exited a more "filamentary" region of two ion beams at M = 3874 km. Note that MMS-2 was located at a distance Rz = −119 km from MMS-1 at 1029:37 UT, with MMS-3

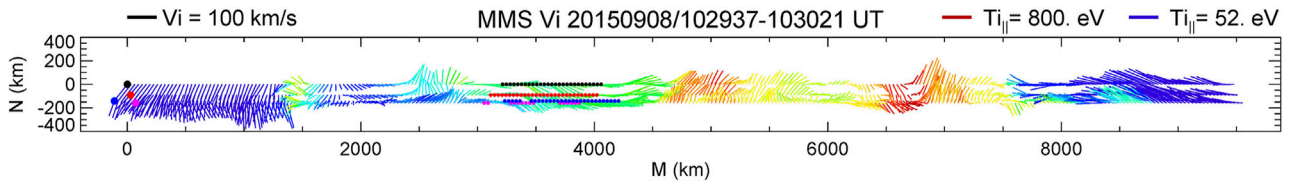

FIGURE 6 | XY_{GSM}-plane ion velocity vectors (150 ms cadence) are displayed along the four MMS satellite propagation directions $\mathbf{M}_{GSM}$ = [0.717852, −0.696196, 0.0] with $\mathbf{N}_{GSM}$ = [0.696196, 0.717852, 0.0] as a direction orthogonal to the MMS tetrahedron trajectory. Time (t) is converted into distance M = $|\mathbf{V}_{KH}|\cdot$t for the time period 1029:37–1030:21 UT and $\mathbf{V}_{KH} = -216.4\cdot\mathbf{M}_{GSM}$ km/s. The vectors are color-coded using a linear color scale that corresponds to the measured parallel ion temperature at each satellite with $Ti_{||}$~800 eV (red) and $Ti_{||}$~52 eV (blue). The M-component of the ion GSM velocity is shown in a tailward KH-vortex moving system with $\Delta V_M = V_M-(-216.4)$ km/s. The [0,0] coordinate defines the t = 0 start position of the MMS-1 satellite (black dot) in this MN-plane at 1029:37 UT with the start positions of MMS-2 (red), MMS-3 (pink) and MMS-4 (blue) shown with their tetrahedron positions relative MMS-1 (*see* text for detailed positions). The colored, smaller dots near 3000 < M < 4250 km mark the spatial coordinates where the four MMS satellites recorded two counter-streaming ion beams (*see* text for detailed times).

at Rz = 45 km and MMS-4 at Rz = −42 km from MMS-1. However, despite the individual $\mathbf{Z}_{GSM}$ separations from MMS-1, it appears that all four satellites came across a region of similar dimension and location when two ion beams were present. Moreover, although the KH-vortex region mostly reflected an outward $V_N>0$ flow deflection from M~2500 km to M~7500 km, as typically expected in a KH co-moving frame of reference, it appears that the region of the two opposite ion beams displayed a more V_M-aligned ion flow direction with occasional earthward deflections ($V_N<0$).

Figure 2 marks another, 0.9-s period of similar counter-streaming ion beams at the very leading ion edge of the preceding KH vortex, which is marked between the two, pink vertical lines at 1028:42.950 UT and 1028:43.849 UT. An ion VDF example of the counter-streaming ion beam nature in this shorter time period is shown in **Figures 7A,D** with a clear D-shaped ion beam streaming in a parallel direction, while the anti-parallel beam appears as a shoulder in a 1-D cut of the 2-D ion VDF at a similar PSD and peak $|V_B|$~500 km/s velocity as the parallel beam.

The two intervals of sustained, counter-streaming ion beams that we highlighted in the MMS-1 observations of **Figure 2** also coincide with bi-directional electrons in the 250–500 eV energy range as shown in **Figure 2B**. However, it is clear from this electron measurement that such bi-directional electrons are prevalent in most of the two KH-vortex regions. In order to appreciate these ion DIS and electron DES measurements, for both intervals of distinctly counter-streaming ion beams inside the leading edges of the two KH vortices, we now compare the field-aligned energy fluxes of electrons in the 250–500 eV energy range at pitch-angles 0–10° and 170–180° with the pitch-angle observations of 2–3 keV ion energy fluxes in the immediate surroundings of the two intervals of distinctly counter-streaming ion beams.

Figure 8 displays the 16-s interval of observations in a region surrounding the first interval of counter-streaming ion beams at the very leading ion edge of the first KH vortex. We note how MMS-1 observed a sudden increase of the electron energy fluxes in both directions along the magnetic field at ~1028:43 UT (*see* **Figure 8E**), near the onset time of the two ion beams. The DES instrument then recorded a second energy flux enhancement of electrons at the end of the period of the two ion beams at ~1028:44 UT. The electron energy fluxes were essentially balanced in both directions along the magnetic field. In contrast, MMS-1 recorded a starkly different electron signature after the counter-streaming ion period between ~1028:46.0 UT and ~1028:47.5 UT when the anti-parallel electron energy flux suddenly decreased, while the parallel streaming electrons essentially maintained a similar energy flux level until decreasing as well toward the end of this ~1.5-s period. In comparison, **Figure 8D** shows how the pitch-angle of the 2–3 keV ion energy flux displayed a dominant parallel component at ~1028:44.5–1028:47.5 UT that overlaps with the 1.5-s period of unbalanced electron energy flux. **Figure 7B** shows an ion VDF example from this overlapping period at 1028:47.000 UT, which is characterized by a single D-shaped parallel ion beam with a peak V_B = 600 km/s velocity (W_K~1.9 keV) along the magnetic field, superposed on a slowly drifting ion core population and a much reduced PSD of ions propagating opposite the magnetic field at speeds V_B < −350 km/s.

Figure 8D indicates another period of apparently counter-streaming ion beams in the pitch-angle distribution of the 2–3 keV ion energy flux at ~1028:52–1028:53 UT deep inside this first KH vortex. This period coincides with a presence of weak energy fluxes of high-energy 3–10 keV electrons as shown in **Figure 8A**, indicating that MMS-1 sampled magnetic fields deeper in the magnetosphere at this time. The 2-D ion VDFs and the 1-D cuts along V_{BxV} = 0 km/s at this time do not display a distinct counter-streaming ion beam distribution of the nature displayed in **Figure 4**. The ion VDFs (not shown) rather suggest a heated magnetosphere-like ion population in a direction opposite the magnetic field, similar to that displayed along the magnetic field in **Figure 3C**, and a potentially diffuse ion beam propagating along the magnetic field.

Figure 9 displays a 19-s period of observations in a region surrounding the second interval of counter-streaming ion beams well inside the warm leading edge (**Figure 9G**) of the subsequent KH vortex. **Figure 9E** shows how the energy flux (E_f) of 250–500 eV electrons gradually increased by 85% in both directions along the magnetic field across the period of counter-streaming ion beams from $<E_f>\sim 2.0\cdot10^8$ keV/(cm^2·s·sr·keV) at 1029:47–1029:49 UT to $<E_f>\sim 3.7\cdot10^8$ keV/(cm^2·s·sr·keV) at 1029:55–1029:56 UT. The MMS-1 DES

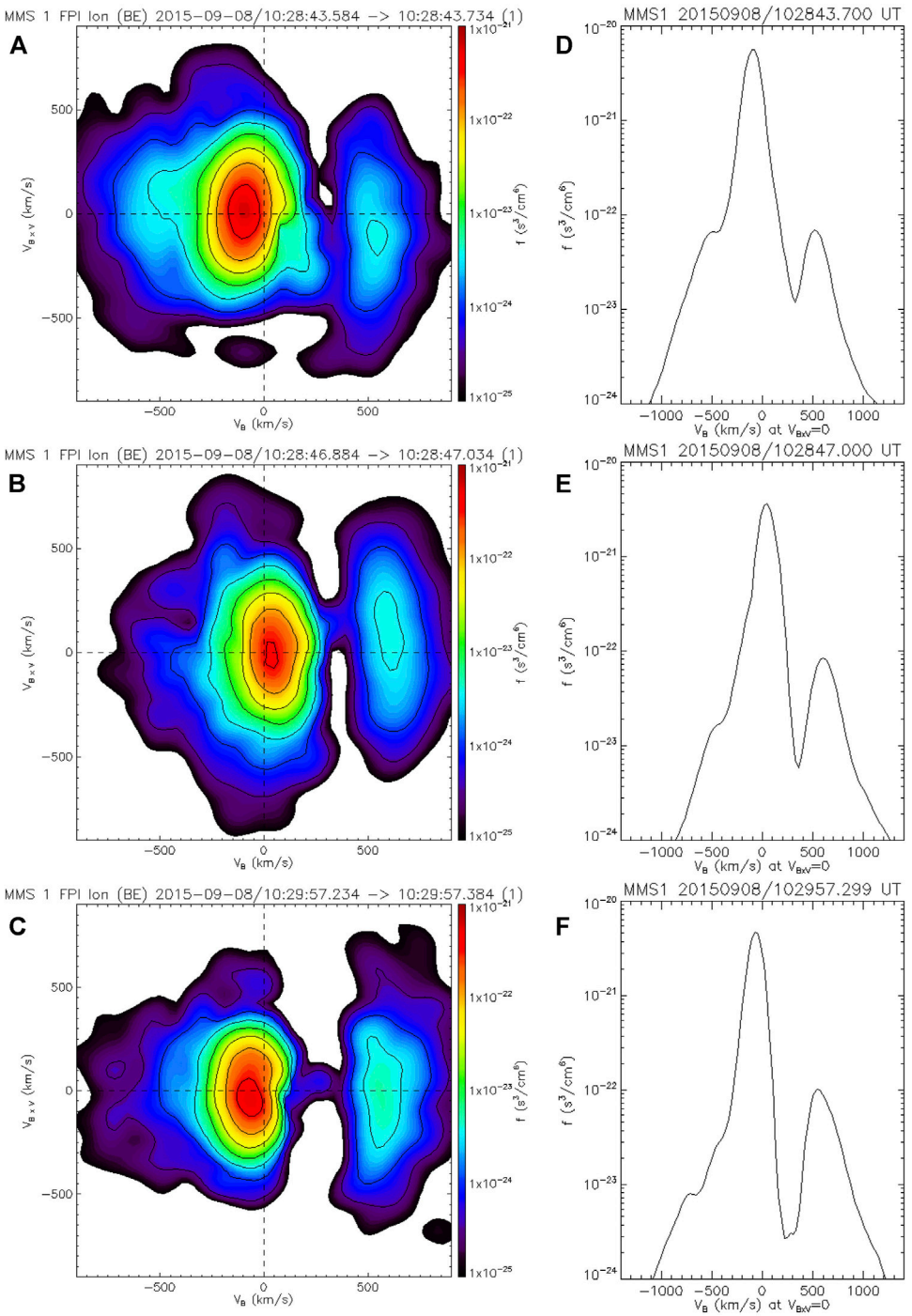

FIGURE 7 | MMS-1 ion velocity distributions: **(A)** Ion VDF at 1028:43.700 UT; **(B)** ion VDF at 1028:47.000 UT; **(C)** ion VDF at 1029:57.299 UT; **(D)** 1-D cut of ion VDF in panel **(A)**; **(E)** 1-D cut of ion VDF in panel **(B)**; **(F)** 1-D cut of ion VDF in panel **(C)**. The 2-D ion phase space density of the VDFs **(A–C)** are shown in V_{BxV} vs V_B space. The 1-D cuts along V_B are taken along V_{BxV} = 0 km/s.

instrument also recorded three periods of localized E_f depletions in the immediate vicinity of the ion beam interval. The first period, centered near 1029:50 UT, is associated with substantial E_f depletions in both directions along the magnetic field. The second E_f depletion, centered near 1029:52.5 UT, is embedded with the counter-streaming ion beams. A third E_f depletion is observed again at ~1029:56–1029:58 UT. In the first and second E_f depletions, **Figure 9F** shows how the electron plasma density (Ne) also decreased substantially at these times and relative the average Ne = 13.5 cm^{-3} of this 19-s period, with localized minima

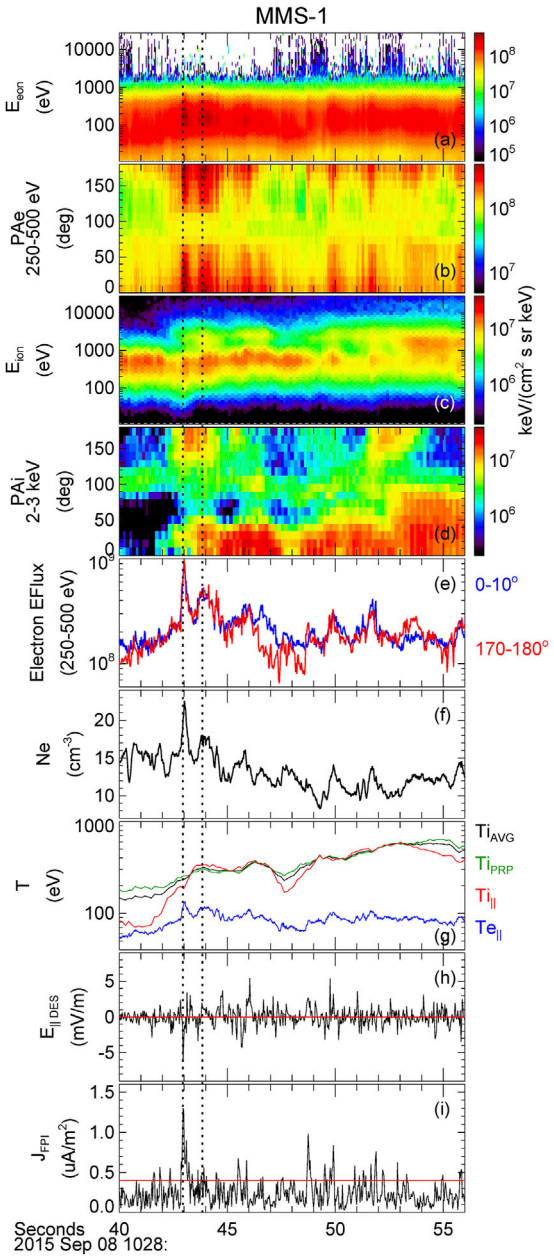

FIGURE 8 | MMS-1 burst observations from 1028:40 UT to 1028:56 UT. Panels display **(A)** electron omni-directional energy-time spectrogram; **(B)** electron pitch-angle distribution in the 250–500 eV energy range; **(C)** ion omni-directional energy-time spectrogram; **(D)** ion pitch-angle distribution in the 2–3 keV energy range; **(E)** electron energy flux for 250–500 eV energy range parallel to the magnetic field (0–10°, blue) and anti-parallel to the magnetic field (170–180°, red); **(F)** electron plasma number density; **(G)** electron parallel temperature ($Te_{||}$, blue), ion parallel temperature ($Ti_{||}$, red), ion perpendicular temperature (Ti_{perp}, green), and the ion average temperature $Ti_{AVG}=(Ti_{||}+2Ti_{perp})/3$; **(H)** Parallel electric field from the ADP instrument interpolated to the 30-ms DES instrument cadence; **(I)** magnitude of the current density GSM vector as measured by the FPI instruments. Vertical dotted lines mark the time period 1028:42.950–1028:43.849 UT associated with counter-streaming ions.

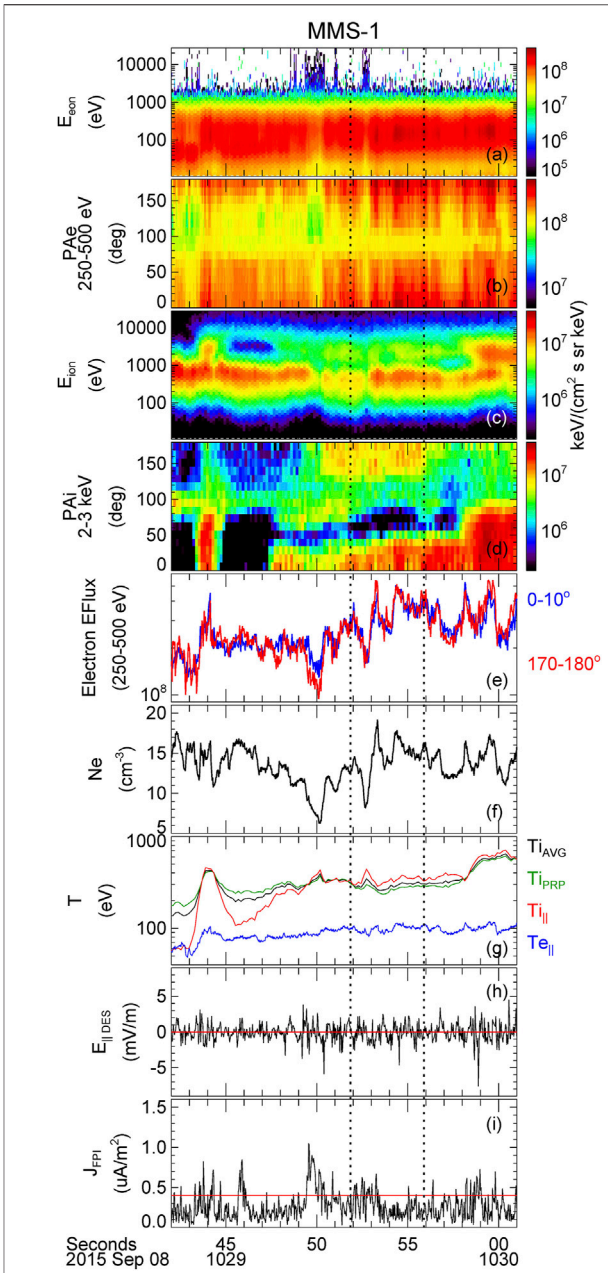

FIGURE 9 | MMS-1 burst observations from 1029:42 UT to 1030:01 UT. Panels show the same parameters as in **Figure 8**. The vertical dotted lines mark the time period from 1029:51.849 UT to 1029:55.900 UT associated with counter-streaming ions.

of Ne = 6.2 cm^{-3} (54% reduction) and Ne = 8.2 cm^{-3} (39% reduction), respectively. In fact, Ne correlates very well with the energy flux of bi-directional 250–500 eV electrons across most of the 19-s period. **Figure 9A** indicates a presence of 3–10 keV high-energy electrons centered at both E_f depletions. These observations suggest how the first two depletions of the bi-directional electron energy flux may be associated with a

temporary region of embedded closed magnetic fields that connect much deeper into a low-density magnetosphere, where the 250–500 eV electron population is less prominent (**Figure 1B**). The third depletion of the 250–500 eV electron energy flux at ~1029:57 UT is different in several aspects with a parallel electron energy flux that dropped to $<E_f>=2.6\cdot10^8$ keV/(cm^2·s·sr·keV) and an anti-parallel electron energy flux that dropped to $<E_f>=2.3\cdot10^8$ keV/(cm^2·s·sr·keV) relative the preceding 1029:54.849–1029:55.929 UT period of a balanced $<E_f>=3.6\cdot10^8$ keV/(cm^2·s·sr·keV). First, there are no high-energy electrons in the 3–10 keV energy range. Second, the plasma density Ne~12 cm^{-3} remained close to the mean value with no significant density reduction as compared with the first two E_f depletions. Finally, the 2–3 keV ion energy flux displayed a significant drop in the anti-parallel direction, with a dominant ion component streaming parallel to the magnetic field at 1029:56–1029:58 UT (**Figure 9D**). **Figures 7C,F** demonstrate how the anti-parallel ion beam that MMS-1 measured with a speed $V_B < -350$ km/s at 1029:55.349 UT (**Figures 4A,E**) had essentially disappeared by this time, as shown in an example ion VDF at 1029:57.299 UT, which rather consists of a single D-shaped parallel ion beam with a PSD peak at $V_B = 550$ km/s (W_K~1.6 keV) and a slowly drifting ion core population.

Parallel Electric Field Observations

Figure 8H shows the parallel electric field measurement by the ADP electric field instrument, but interpolated from 8192 Hz to the 30-ms cadence of the DES electron observations during the 16-s interval associated with a leading edge region of the KH vortex at 1028:40–1028:56 UT. MMS-1 observed a large $E_{||} = -6$ mV/m at this 30-ms cadence near the onset-time of the counter-streaming ion beams at 1028:43 UT. It should accelerate electrons northward along the Bz > 0 magnetic field, and it could accelerate some ions in a southward direction. This $E_{||}<0$ is nearly 50% the surprisingly large $E_{||} = -14$ mV/m that MMS-3 recorded inside a confirmed electron diffusion region (Eriksson et al., 2016b) associated with an intense $J_{||} = -2$ μA/m^2 trailing-edge CS in this same KH event. However, whereas the DES instrument measured a large energy flux increase of the parallel 0–10° electrons in the 250–500 eV energy range at this time (**Figure 8E**), it also recorded an immediate and equal energy flux response in the 170–180° anti-parallel direction at the same time. **Figure 8D** shows how the ion energy flux first increased in a southward, anti-parallel direction at the time of the $E_{||}<0$ as might be expected from a local $E_{||}$ acceleration. However, the subsequent increase of the parallel ion energy flux toward the end of this 0.9-s interval of counter-streaming ion beams is not associated with a positive $E_{||}$ of any significant magnitude.

Figure 9H displays a variable $E_{||}$ with a magnitude below 2 mV/m throughout the 1029:51.8–1029:55.9 UT period of counter-streaming ion beams inside the warm leading edge of a subsequent KH vortex. However, there is no obvious correlation between the locally measured $E_{||}$ and the field-aligned energy flux of 250–500 eV electrons in this region, or between $E_{||}$ and the field-aligned ion energy flux in the 2–3 keV range.

Current Density Observations

Figure 8I indicates a very intense current density layer with a maximum J~1.3 μA/m^2 at the time of the $E_{||}<0$ observation at 1028:43 UT. This intense current layer, which is primarily associated with a very localized decrease of the in-plane magnetic field from By = 40 nT to By = 15 nT (**Figure 2H**) and a $Jz_{GSM} = -1.1$ μA/m^2 component of the FPI current density (not shown), cannot be supported by the enhancement of bi-directional electrons in the 250–500 eV range alone, due to the well-balanced nature of the energy flux in both directions along this magnetic field at this time. The 250–500 eV electrons have a different source than the Jz < 0 current itself. Moreover, the intriguing ~1.5-s period of parallel electrons and ions at 1028:46.0–1028:47.5 UT is not associated with any significant current density or $E_{||}$, despite a significant decrease of the anti-parallel electron energy flux and the disappearance of the anti-parallel ion beam. The current density measured across the leading edge of the subsequent KH vortex period, as shown in **Figure 9I**, is rather benign and mostly weaker than ~0.5 μA/m^2 when the two distinct ion beams are observed streaming in opposite directions along the magnetic field.

Statistical Properties

The detailed energy flux descriptions of ions at 2–3 keV and electrons at 250–500 eV as observed inside the warm leading edges of two adjacent KH vortex regions are not unique to this pair of KH vortices at 1028:29–1030:34 UT on 8 Sept 2015. The signature of fast counter-streaming ions along the magnetic field, although not clearly present in the ion VDFs of all the KH vortices, have been confirmed using the ion VDF observations for 17 such KH vortex regions of this post-noon event. Each KH vortex may also be associated with several individual bursts of sustained counter-streaming ion beam signatures in an uninterrupted series of 150-ms ion VDFs, as seen along the MMS-3 and MMS-4 example trajectories of **Figure 6**, as the MMS satellites travel across the initial, warm ion temperature region of any given KH vortex. **Table 1** lists a total of 26 such MMS-1 periods distributed across the 17 KH vortices, with durations ranging from Δt = 0.75-s to Δt = 5.25-s (column 3, **Table 1**) and a median Δt = 1.95-s. The focused bursts of two ion beams are almost exclusively present in a warm $Ti_{||}$~490 eV, intermediate density Ne ~ 12 cm^{-3} (**Table 1** median values) leading edge of the KH vortex region of this post-noon event, and before MMS moved into the high-temperature LLBL section of the KH vortex, which is mostly characterized by isotropic ion temperatures (**Figures 2C,F**). In contrast, the 26 intervals of two ion beams analyzed here typically reflect very anisotropic ion temperatures due to a presence of these field-aligned beams with an average $T_R = Ti_{||}/Ti_{perp}$ that ranges from 0.94 to 1.62 with a median $T_R = 1.24$ value (**Table 1**). In using the ion VDF observations recorded by the MMS-1 and MMS-2 satellites, which are essentially aligned along the northward-pointing magnetic field, it is clear that the maximum PSD of the parallel ion beam is higher than the maximum PSD of the anti-parallel ion beam in 16 of the 26 intervals. These intervals are indicated using a "+" symbol in the last column of **Table 1**. There were only four periods when MMS-1 and MMS-2 indicated a higher PSD in the anti-parallel ion beam than in the PSD of the parallel ion beam (c.f. "–" symbol in last

TABLE 1 | Time periods when MMS-1 observed two distinct, counter-streaming ion beams in a continuous series of DIS measurements of ion VDFs, superposed on a slowly drifting core of cold magnetosheath ions.

UT1	UT2	Δt	<Ne>	<$Te_{||}$>	<$Ti_{||}$>	<T_R>	<B_{GSM}>	<V_{GSM}>	<J_{FPI}>	Jz_{GSM}	<$E_{||DES}$>	Ef [0°]	Ef [180°]
		s	cm^{-3}	eV	eV		nT	km/s	$\mu A/m^2$	$\mu A/m^2$	mV/m	$\times 10^8$	$\times 10^8$
10:07:43.150	10:07:46.450	3.30	10.9	107	544	1.00	9,32,77	−127,109,−50	0.27	−0.46,1.02	0.08	4.9	5.5 +
10:07:47.049	10:07:48.849	1.80	14.0	112	738	1.12	4,35,68	−85,157,−3	0.26	−0.36,0.70	−0.16	5.6	7.7 +
10:28:42.950	10:28:43.849	0.90	16.9	106	274	1.00	29,20,76	−124,53,−47	0.45	−1.14,0.45	−0.38	9.5	9.6
10:29:51.849	10:29:55.900	4.05	14.4	99	340	1.25	25,30,75	−120,95,−61	0.26	−0.52,0.60	−0.18	5.0	5.4
10:32:16.299	10:32:17.799	1.50	10.6	88	577	0.97	12,36,69	−169,154,−4	0.30	−0.42,0.55	−0.21	2.7	2.7 −
10:35:55.000	10:35:56.950	1.95	12.6	107	631	1.25	9,45,67	−116,152,−11	0.36	−0.82,0.63	−0.09	6.4	5.5 +
10:41:19.049	10:41:20.400	1.35	11.6	82	636	1.24	11,43,60	−103,83,−10	0.16	−0.22,0.30	0.02	2.7	1.9 −
10:42:57.299	10:42:59.250	1.95	14.3	86	310	1.18	0,51,65	−119,127,−51	0.19	−0.31,0.25	−0.12	3.7	3.4 +
10:43:01.500	10:43:02.849	1.35	17.9	76	217	0.99	6,31,73	−137,96,−57	0.35	−0.70,0.57	−0.06	4.0	3.2 +
10:47:45.450	10:47:49.950	4.50	14.2	82	422	0.97	0,46,56	−188,170,−28	0.27	−0.49,0.76	−0.01	3.4	3.1 −
10:47:53.700	10:47:54.450	0.75	11.7	77	694	1.21	10,38,59	−184,163,26	0.31	−0.45,0.61	−0.24	2.1	1.7 +
10:49:04.549	10:49:07.849	3.30	11.6	93	487	1.37	11,39,61	−80,180,−80	0.24	−0.42,0.51	−0.25	3.3	3.4 −
10:51:19.400	10:51:20.750	1.35	11.1	92	468	1.25	6,32,67	−112,144,−26	0.18	−0.33,0.22	0.14	3.0	3.6 +
10:51:22.099	10:51:24.049	1.95	11.4	87	460	1.44	8,31,69	−138,142,−22	0.26	−0.87,0.62	−0.09	5.5	4.4 +
10:51:29.900	10:51:32.150	2.25	12.6	101	759	1.32	9,45,50	−111,202,−15	0.22	−0.35,0.38	−0.09	4.5	4.2 +
10:55:46.250	10:55:48.049	1.80	10.6	89	415	1.24	13,37,66	−89,114,−28	0.21	−0.46,0.53	0.00	2.6	2.3
10:55:55.250	10:55:57.950	2.70	11.0	103	588	1.62	13,37,65	−117,49,24	0.21	−0.46,0.57	0.18	10.4	11.8 +
10:56:46.743	10:56:49.893	3.15	12.4	108	476	1.16	23,25,63	−142,163,−53	0.30	−0.60,0.63	−0.21	10.7	17.3 +
11:05:14.500	11:05:16.599	2.10	8.2	90	831	1.23	−11,51,49	−227,238,−14	0.27	−0.10,0.38	0.11	2.6	2.2 +
11:08:12.750	11:08:15.299	2.55	10.1	98	428	1.25	17,28,66	−115,87,−37	0.27	−0.48,0.67	0.09	3.6	2.8 +
11:08:16.950	11:08:19.950	3.00	10.4	110	465	1.13	16,32,62	−119,135,−38	0.31	−0.73,0.91	−0.08	6.3	6.2 +
11:13:07.950	11:13:09.750	1.80	8.7	81	367	0.94	12,32,63	−163,169,−98	0.35	−0.14,0.82	0.01	1.7	1.9
11:15:55.549	11:15:58.250	2.70	10.9	89	365	1.48	30,19,64	−100,92,−57	0.23	−0.49,0.42	−0.03	2.6	3.8
11:16:00.349	11:16:05.599	5.25	12.5	106	528	1.44	15,37,56	−140,136,−58	0.29	−0.42,0.64	−0.13	5.8	7.6 +
11:22:09.650	11:22:11.599	1.95	9.7	106	549	1.17	21,31,57	−112,131,−60	0.21	−0.30,0.45	−0.13	3.1	4.2
11:22:14.900	11:22:15.799	0.90	7.5	101	610	1.52	16,28,62	−139,108,−27	0.22	−0.43,0.21	0.32	2.5	3.2 +

The symbols of the last column indicates "−" if f1>f2 or "+" if f1<f2, with no symbol if f1~f2, where f1 is the PSD at the peak of the anti-parallel ion beam and f2 is the PSD at the peak of the parallel ion beam. Burst data are time-averaged, indicated <. . .> for the duration of each interval and $T_R \equiv Ti_{||}/Ti_{perp}$. The exceptions are the 250–500 eV electron energy flux (Ef, in units keV/cm²·s·sr·keV) for 0–10° and 170–180° that display the maximum values of each period, and the Jz_{GSM} column displays the minimum and maximum values of the period.

column of **Table 1**), and in six intervals (no symbols in last column of **Table 1**), the PSDs were essentially of equal magnitude in the two ion beams. The energy flux of bi-directional electrons often display a clear enhancement in the 250–500 eV energy range when the ion VDFs display the two counter-streaming ion beams. Moreover, when one of the two ion beams, with observed speeds in a range $350 < V_B < 775$ km/s (**Table 2**), is absent or displaying a highly suppressed PSD before or after the times listed in **Table 1**, resulting in one single ion beam, then so too does the energy flux of the bi-directional electron signature tend to change, and often in such a way that more electron energy flux will be observed in the same direction along the magnetic field as the remaining field-aligned ion beam.

DISCUSSION

In comparing the slow, dense ion population of **Figure 4** with the ion VDFs of **Figure 3**, it can be argued that it corresponds to a magnetosheath ion population (**Figure 3A**) captured onto closed magnetic fields inside the KH vortex, in general agreement with a presence of bi-directional electrons in the 250–500 eV energy range (**Figure 2**) to support a closed magnetic field topology (Faganello et al., 2014; Vernisse et al., 2016). The observation of a dense core population of magnetosheath ions with a slow drift along a closed magnetic field suggests that a magnetic reconnection process likely occurred at two locations along this northward pointing magnetic field that MMS sampled in an equatorial KH vortex region. However, in a general absence of intense CSs associated with a local reconnection exhaust, or any significant parallel electric fields in the plane of the MMS satellites near $Z_{GSM} = -4.6\ R_E$ in this warm leading edge of the KH vortex regions (**Figures 8**, **9**; **Table 1**), it appears that the two reconnection regions were present at some distance to the north and to the south of the MMS satellites. The simultaneous observation of two typically D-shaped ion beams, streaming in both directions along this same magnetic field that captured ~1 keV magnetosheath ions, but with a much lower PSD and a faster field-aligned speed than this ion core population, also support a presence of two reconnection regions along this northward magnetic field as we shall discuss in more detail below.

The isotropic LLBL ion distributions of **Figure 3** are very different from the ion VDFs of **Figure 4**. In fact, **Figures 2C,D** demonstrate a clear difference of the ion burst measurements during the period of counter-streaming ion beams in a warm leading region of the second KH vortex, as compared with a subsequent period of much hotter and isotropic ion temperatures at 1029:57–1030:12 UT (c.f. **Figures 2D,F**) when a representative LLBL ion VDF (**Figures 3C,F**) was recorded without distinct ion beams. This hot, parallel LLBL ion temperature is also reflected as a wide 0–90° pitch-angle ion distribution as compared with the 0–30° field-aligned ion beams, which makes it difficult to identify similar ion beam features in the LLBL. Considering the simultaneous presence of a slow

TABLE 2 | Times of individual ion VDFs as recorded by MMS-1 that displayed two distinct counter-streaming ion beams and superposed on a slowly drifting magnetosheath ion core population.

VDF	$-V_{B1}$	W_{K1}	V_{B2}	W_{K2}	R_{GSM1}
	km/s	keV	km/s	keV	R_E
10:07:45.400	575	1.73	600	1.88	5.1,7.2,–4.4
10:07:47.650	575	1.73	350	0.64	5.1,7.2,–4.4
10:28:43.700	500	1.30	525	1.44	5.0,7.5,–4.6
10:29:55.349	525	1.44	550	1.58	5.0,7.5,–4.6
10:32:16.450	400	0.84	775	3.14	5.0,7.5,–4.6
10:35:55.549	425	0.94	600	1.88	5.0,7.5,–4.7
10:41:20.299	375	0.73	575	1.73	4.9,7.6,–4.7
10:42:57.450	750	2.94	550	1.58	4.9,7.6,–4.7
10:43:01.650	675	2.38	525	1.44	4.9,7.6,–4.7
10:47:46.049	525	1.44	700	2.56	4.9,7.7,–4.8
10:47:54.150	500	1.30	500	1.30	4.9,7.7,–4.8
10:49:07.000	500	1.30	650	2.21	4.9,7.7,–4.8
10:51:20.200	675	2.38	550	1.58	4.9,7.7,–4.8
10:51:23.349	725	2.74	475	1.18	4.9,7.7,–4.8
10:51:30.349	575	1.73	450	1.06	4.9,7.7,–4.8
10:55:46.650	550	1.58	650	2.21	4.9,7.8,–4.9
10:55:55.950	500	1.30	525	1.44	4.9,7.8,–4.9
10:56:49.049	575	1.73	450	1.06	4.9,7.8,–4.9
11:05:15.950	350	0.64	500	1.30	4.8,7.9,–4.9
11:08:14.549	500	1.30	500	1.30	4.8,7.9,–5.0
11:08:19.950	475	1.18	400	0.84	4.8,7.9,–5.0
11:13:08.549	375	0.73	500	1.30	4.8,8.0,–5.0
11:15:56.349	675	2.38	700	2.56	4.8,8.0,–5.0
11:16:04.000	525	1.44	600	1.88	4.8,8.0,–5.0
11:22:10.849	550	1.58	500	1.30	4.8,8.1,–5.1
11:22:15.500	500	1.30	450	1.06	4.8,8.1,–5.1

V_{B1} is the anti-parallel ion beam speed and V_{B2} is the parallel ion beam speed along the magnetic field at their respective local maximum of the PSD. W_{K1} and W_{K2} are the corresponding proton kinetic energy values for the respective V_B value. R_{GSM1} is the MMS-1 GSM location (R_E = 6378 km) from a 30-s cadence satellite ephemeris product.

magnetosheath source-population, and the general absence of high-energy electrons from the magnetosphere proper, it is unlikely that the two beams of ions streaming in both directions along this northward magnetic field with a fast (median) 525 km/s speed and a corresponding field-aligned kinetic energy $0.6 < W_K < 3.1$ keV (**Table 2**) with a median W_K = 1.4 keV may be associated with a source in the plasma sheet or the isotropic outer LLBL plasma domain. A more straightforward explanation, in the absence of local reconnection exhausts, is that the two ion beams, which typically displayed a D-shaped ion beam velocity distribution (Cowley, 1982; Smith and Rodgers, 1991; Fuselier et al., 2014), are associated with an **ExB**-acceleration of a cold ~1 keV magnetosheath ion source population into the magnetosphere at a more remote location from MMS to parallel speeds $350 < V_B < 775$ km/s (**Table 2**). The parallel component of the captured magnetosheath ion population at the location of MMS, in contrast, is typically centered between $V_B \sim -200$ km/s and V_B~75 km/s along the magnetic field (**Figures 3A**, **4A**).

On the Remote Ion Beam Source Regions: High-Latitude Versus Mid-Latitude

A pair of two off-equatorial magnetic reconnection regions, which may capture a significant volume of magnetosheath plasma onto newly closed magnetic fields [e.g., (Faganello and Califano, 2017; Ma et al., 2017; Ma et al., 2021)], may also be associated with accelerated field-aligned ions and accelerated bi-directional electrons [e.g., (Nykyri et al., 2006; Nishino et al., 2007; Bavassano Cattaneo et al., 2010; Faganello et al., 2014; Vernisse et al., 2016)]. The two numerically predicated magnetopause reconnection regions have either been proposed to be located very far from the KH wave observations near the equatorial plane, such as a high-latitude lobe region tailward of the cusp (Bavassano Cattaneo et al., 2010), or located in a relatively closer mid-latitude region to the KH vortices from a reported presence of field-aligned electron observations [e.g., (Faganello et al., 2014; Vernisse et al., 2016)].

Let us first assume a presence of two mid-latitude reconnection (MLR) regions following some recent numerical advances (Faganello and Califano, 2017; Ma et al., 2017; Fadanelli et al., 2018; Sisti et al., 2019). The two MLR regions may be expected at a minimum λ_{KH}-distance from the region of maximum KHI growth (Ma et al., 2014). In the KHI case of 8 Sept 2015, Eriksson et al. (2016a) estimated λ_{KH}~2.6 R_E and Vernisse et al. (2020) obtained a maximum KHI growth region near the GSM latitude location of the MMS satellites. We, therefore, assume two symmetrically located MLR regions at an equal distance $L = \lambda_{KH}$ to the south of MMS, and $L = \lambda_{KH}$ to the north of MMS at $(x,y,z)_{GSM} = (5.0, 7.5, -4.6)$ R_E. This MMS location corresponds to a polar $\theta = -24.4^o$ angle at radius R_{GSM} = 10.1 R_E, while the distance $L = \lambda_{KH}$ along an assumed circular field-line segment translates to a polar angle separation of only $\theta = 14.7^o$ from MMS. The two assumed MLR regions would then be located at polar angles $\theta_N = -9.7^o$ and $\theta_S = -39.2^o$ corresponding to $Z_{GSM} = -1.7$ R_E for the NMLR region and $Z_{GSM} = -6.4$ R_E for the SMLR region. An ion moving at a field-aligned speed V_B = 525 km/s, which corresponds to the median of the observed distribution (**Table 2**), would cover this $L = \lambda_{KH}$ distance in ~32 s. This corresponds to $0.50T_{KH}$, where T_{KH} = 63.3 s is the estimated KH time period (Eriksson et al., 2016a). A very fast field-aligned ion travelling at the maximum V_B = 775 km/s speed observed at a peak PSD in any of these ion beams, would cover that same distance in only ~21 s or $0.33T_{KH}$. The slowest V_B = 350 km/s field-aligned ions observed here would reach MMS in ~47 s or $0.75T_{KH}$.

A similar exercise for a northern HLR region, assumed to be present in a cusp region [e.g., (Song and Russell, 1992; Fuselier et al., 2014)] at $\theta = 80^o$ on the same post-noon side as MMS (Luhmann et al., 1984), and consistent with the observed IMF By > 0 and IMF Bz > 0 (Nakamura et al., 2017), would result in a polar angle $\theta = 104^o$ separation from MMS. This separation translates into an 18.4 R_E field-aligned distance from MMS if we assume a circular magnetic field line through the location of the MMS satellites. In comparison, one would obtain a ~20.2 R_E distance to the surface of the Earth from the MMS satellite along an unperturbed dipole magnetic field line (Schulz and Lanzerotti, 1974) assumed to exist in this KH region. A more realistic field-aligned distance of the perturbed closed field line through the KH region could be longer still, since it is also associated with a stressed, tailward-extended geomagnetic field, as shown in **Figure 10**. If we assume a northern HLR region ~2 R_E off the

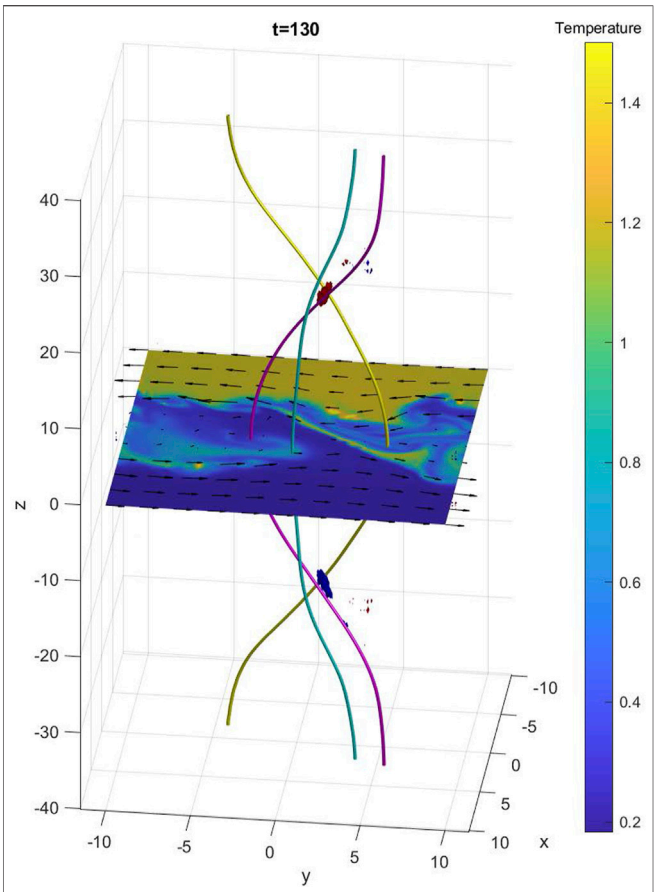

FIGURE 10 | A 3-D MHD simulation rendering for the conditions at time t = 130 in a nonlinear stage of the KHI corresponding to MMS observations on 8 Sept 2015 (Ma et al., 2021). A red patch marks a volume of positive field-aligned current density $J_{||}$ > 0.56 U, where 1 U = 0.087 uA/m^2. A blue patch marks a volume of negative $J_{||}$ < −0.56 U. The magnitudes of the most intense $J_{||}$ ~ 1.5 U in each patch at this time. A yellow-colored field line is a closed field line traced from (Xs, Ys, Zs) = (−0.9, 1.5, 19.0) corresponding to the magnetosphere (MSP) side of current layer. A magenta colored field line is an open field line traced from (Xs, Ys, Zs) = (0.9, 1.5, 19.0) corresponding to the magnetosheath (MSH) side of current layer. A cyan-colored field line is a newly closed field-line traced from (Xs, Ys, Zs) = (2.0, 0.0, 0.0) such that it crosses the plane at the leading edge of the in-plane KH vortex region. A background color index represents the plasma temperature in simulation units. Black arrows show the bulk flow velocity on the equatorial plane. Here, the coordinate system is such that Y is positive along the cold MSH tailward flow direction, Z is positive northward, and X is positive along the non-perturbed magnetopause CS normal direction.

surface of the Earth along this dipole field, we obtain a ~18.2 R_E distance in general agreement with the simplistic, circular field line. A field-aligned ion travelling at V_B = 525 km/s would cover a 18.4 R_E circular field-line distance in 3.5T_{KH}, assuming that it will not pitch-angle scatter off that field line before reaching MMS. The fast V_B = 775 km/s ions would reduce that travel time to 2.4T_{KH}. We note that an assumed HLR in the southern cusp region is expected in a pre-noon sector for the observed IMF conditions (Luhmann et al., 1984), thus requiring more involved modeling analysis to estimate rough ion travel times from a southern HLR region to MMS.

The probability appears to be low for a double HLR process to explain why two mostly D-shaped ion beams would be measured almost exclusively in a warm leading region of the KH vortex as suggested from **Table 1**. The typical, much longer travel times T > 3T_{KH} expected from a northern HLR as compared with T < T_{KH} from two symmetric MLR regions clearly suggest that two counter-streaming ion beams associated with two HLR regions, even if they remain well-collimated along the field, would be more distributed throughout the closed field region of the entire KH vortex. One would also expect a more banana-shaped ion velocity distribution about V_{BxV} = 0 for ions measured by MMS this far from a HLR entry region due to a conservation of the first adiabatic moment of ions, if we also assume that the ions entered the magnetosphere in a region of lower magnetic field strength near the two cusps compared with a higher magnetic field strength measured in an equatorial region (Fuselier et al., 2014). A double HLR process, which is independent from a KHI process near the equator, does not appear to explain the presence of the two counter-streaming ion beams with a mostly D-shaped distribution in a warm leading region of the KH vortices.

Concerning Enhanced Electron Energy Fluxes and Electron Bounce Times

Direct ion-beam evidence in support of one or two KH-related MLR regions has not commonly been discussed in the literature, which is rather focused on electron observations at different energies to deduce the magnetic field topologies that may be present across the dynamic KH vortex region in its various phases of temporal evolution [e.g., (Faganello et al., 2014; Vernisse et al., 2016)]. However, ion observations may be less challenging to utilize in understanding the immediate domain around the KH vortices due to the lower speed of accelerated ions along the magnetic field as compared with accelerated 250–500 eV electrons. A 250 eV electron would travel between a magnetic mirror point at R_M = 1.1 R_E in the northern ionosphere at 72.92° latitude to the mirror point in the southern ionosphere along a closed dipole magnetic field through the MMS location at $(x,y,z)_{GSM}$ = (5.0, 7.5, −4.6) R_E in only $T_B/2$ = 7.25 s (Schulz and Lanzerotti, 1974). Here, T_B is the full bounce period of that electron on a closed field line for an estimated L = 12.75 drift-shell MMS location. A fast 500 eV electron would travel that distance in $T_B/2$ = 5.25 s. A one-way travel time from one HLR region to the MMS location would be shorter still for 250–500 eV electrons. This means that 250–500 eV electrons could sample several important geomagnetic domains as compared with 2–3 keV ions along the magnetic field in the same time, including two double HLR regions. In assuming that the two D-shaped ion beams are associated with accelerated magnetosheath ions in two MLR ion exhaust regions, then it is also likely that the enhanced energy flux of 250–500 eV electrons, as often recorded by MMS in the same time periods, correspond to accelerated magnetosheath electrons from the same MLR regions. However, due to their fast speed, it is possible that the

background of bi-directional 250–500 eV electrons, existing nearly throughout the KH vortex regions on 8 Sept 2015 (**Figure 2B**) may have a different source farther from the MLR regions, such as magnetosheath electrons entering onto new closed field lines formed by two HLR regions.

Comparing MMS Ion Beam Observations and Two-Fluid Numerical Simulation Results

Sisti et al. (2019) performed a two-fluid 3-D numerical simulation for the observed MMS conditions of the 8 Sept 2015 event to suggest (their **Figure 3**) how the warm leading KH vortex region and the associated vortex "arm" are both expected to support once-reconnected field-lines (open field topology) and twice-reconnected field-lines (newly closed field topology) in very limited regions of the KH vortex in the early nonlinear phase of the KH evolution encountered by MMS. The results in Sisti et al. (2019) with spatially limited regions of twice-reconnected fields in the warm leading edge of the KH vortex support a MLR process closer to the KH vortex rather than double-reconnected magnetic fields associated with HLR near the cusps. However, we note that the predictions by Sisti et al. (2019) should be viewed as the expected locations of field-lines associated with one or two active reconnection regions in close proximity to the 3-D KH vortex due to the absence of any HLR regions in their fluid simulation that we understand to be present in a real system for similar conditions of a northward interplanetary magnetic field [e.g., (Gosling et al., 1991; Song and Russell, 1992; Øieroset et al., 2005; Fuselier et al., 2014)].

The time durations of the counter-streaming ion beams of **Table 1** may be used together with an average tailward V_{KH}~258 km/s velocity of the KH vortices (Eriksson et al., 2016a) to estimate a range of in-plane spatial scales (ΔS) that we associate with twice-reconnected magnetic fields connecting two MLR regions. The statistical widths for the 26 events of **Table 1** would correspond to a range of spatial scales 3<ΔS<22 di along the trajectory of MMS with an in-plane median 8 di dimension, if we assume a constant di = 61 km ion inertial scale for the average plasma density N~14 cm^{-3} that MMS-1 measured at the time of the two periods of counter-streaming ion beams in **Figure 2**. This spatial dimension compares well with the narrow regions that Sisti et al. (2019) predicted for this MMS KH event. A straight path through a simulated KH vortex, taken along the *y*-axis of their **Figure 3** (right) and consistent with a tailward KH vortex propagation, also suggests that a region of twice-reconnected MLR fields should be narrower at the very first ion leading edge of the warm KH vortex region as compared with a thicker such region along the vortex arm that stretches in toward the KH vortex center at the boundary between a pre-existing LLBL of hot, isotropic ion temperature and the inner-most region of the warm plasma domain of the KH-mixing region. This is also consistent with the two examples of counter-streaming ion beams measured by MMS and shown in **Figures 2**, **8**, **9** with a narrow ΔS~4 di layer present at the very leading ion edge of the first KH vortex, starting at 1028:42.950 UT (**Table 1**), and a thicker ΔS~17 di layer of counter-streaming ion beams starting at 1029:51.849 UT near the inner edge with the isotropic LLBL. In this second, warm inner region event of the subsequent KH vortex, MMS actually observed a short-duration layer with a single D-shaped parallel ion beam (*see* **Figure 7C** and **Figures 9C,D**) sandwiched between this region of twice-reconnected fields and the LLBL-proper. In contrast, Sisti et al. (2019) predicts that such once-reconnected open magnetic fields (their **Figure 3**, right) associated with just one MLR region to the south of MMS should be present before the twice-reconnected fields, suggesting that KH events may be more complicated. The presence of two or three individual bursts of sustained counter-streaming ion beam signatures in a given warm KH-vortex region (**Table 1**) also suggests a more layered structure of magnetic field topologies with "twice-reconnected" (DMLR) regions occurring not just at the very leading edge and at the subsequent inner vortex arm as predicted by Sisti et al. (2019). However, this does not change the overall agreement between these MMS observations and the Sisti et al. (2019) predictions of expected widths and locations of "twice-reconnected" magnetic fields that we associate with two active MLR regions to generate new closed fields in a KH vortex.

On a Possible Mid-Latitude Magnetosheath Ion Entry Mechanism

Eriksson et al. (2020) reported similar ion VDFs observed by the THEMIS satellites that also consisted of two counter-propagating magnetosheath ion populations, but in a region between two converging dayside magnetopause reconnection exhausts in the early flux rope formation stage. Eriksson et al. (2020) also performed a two-dimensional particle-in-cell numerical simulation for the THEMIS conditions to show how the ion particles of the two ion beams originated as colder upstream particles in the adjacent magnetosheath that drifted toward the magnetopause, where they were picked-up by the magnetic fields and accelerated up to the **ExB** drift of the reconnection exhausts near the two reconnection X-lines. This well-known entry mechanism of magnetosheath ions associated with magnetic reconnection at the magnetopause was first predicted by Cowley (1982), whereby a parallel cutoff-velocity forms below which no magnetosheath ions may enter onto the open magnetic fields earthward of the magnetopause. This cutoff velocity is clearly present in the D-shaped ion VDFs of **Figure 4**. A similar ion entry process likely accelerated a cold magnetosheath ion population, as observed by MMS on the same field-lines as the two counter-streaming ions, in two mid-latitude regions to the north and south of MMS. A difference between the 8 Sept 2015 KH-case and the sub-solar observations reported by Eriksson et al. (2020) is the magnetic topology with the latter case displaying $Bz_{GSM} < 0$ in the adjacent dayside magnetosheath and a north-south directed pair of Vz_{GSM} jets. The KH-case, however, displayed a significant $Bz_{GSM} > 0$ guide magnetic field and weaker $Bx_{GSM} > 0$ and $By_{GSM} > 0$ components of the magnetic field (**Table 1**) when the two ion beams were observed. A similar $\mathbf{B}_{GSM}$ was also observed in the magnetosheath-proper after 1130 UT. Indeed, **Figure 1G** demonstrates how MMS observed a generally positive

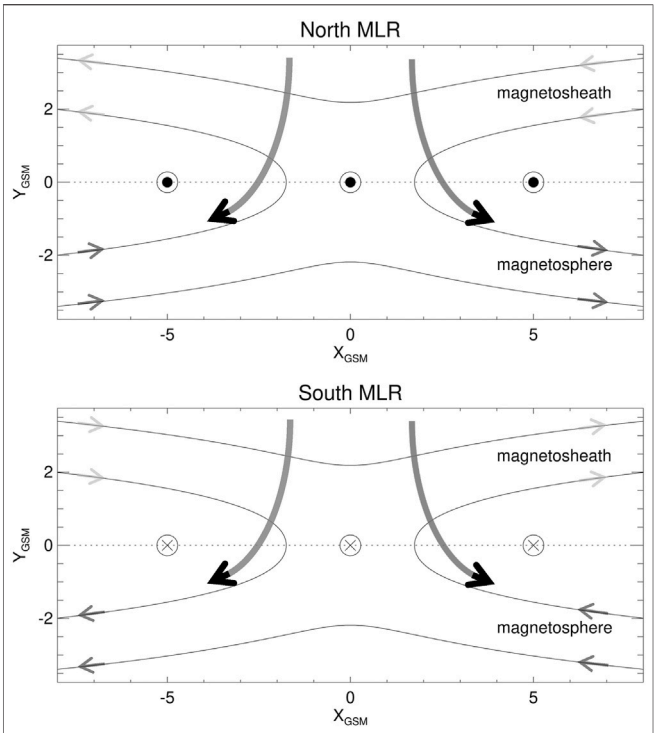

FIGURE 11 | Schematic ion entry from the magnetosheath into the magnetosphere of cold magnetosheath ions associated with KH-sheared magnetic fields in the adjacent magnetosphere and magnetosheath. Thin solid lines and associated arrows mark the direction of the in-plane component of the magnetic field around the ion diffusion regions of a northern MLR region (top) and a southern MLR (bottom) region consistent with a presence of a $Jz_{GSM} > 0$ current (encircled dots at $Y_{GSM} = 0$) in the north and $Jz_{GSM} < 0$ current (encircled crosses at $Y_{GSM} = 0$) in the south. A few proposed ion trajectories are shown.

$By_{GSM} > 0$ at nearly twice the magnitude of a mostly positive $Bx_{GSM} > 0$ throughout this KHI period, including in the tenuous and hot magnetosphere before 0920 UT. In considering two MLR regions roughly 15° north and south of MMS, it would seem plausible that similar $By_{GSM} > Bx_{GSM} > 0$ conditions may have existed adjacent the two MLR regions. However, a KH-dynamic shearing-motion of magnetic fields associated with a tailward propagation of the KH vortex against the stress of the geomagnetic field is likely more important to sustain a MLR process (Faganello and Califano, 2017) than the in-plane components of a magnetic field direction in a nearby magnetosheath. This shearing-process of magnetic fields in the magnetosphere and in the adjacent magnetosheath is clearly illustrated in **Figure 10** for a dedicated 3-D MHD simulation that we performed for this MMS KH event (Ma et al., 2021). The simulated NMLR CS is directed northward ($Jz > 0$) and the SMLR CS is directed southward ($Jz < 0$) as a result of this KH-shearing action on the magnetic fields. **Figure 10** implies that two mostly in-plane (XY_{GSM}) ion exhaust regions will form in the vicinity of both MLR regions, with the ion jets directed typically sunward and tailward from each X-line reconnection region.

The mostly in-plane ion **ExB** reconnection exhausts thus predicted by numerical simulations to be present near the two remote mid-latitude regions will be dominated by their in-plane Vx_{GSM} and Vy_{GSM} components of the ion outflow, and perpendicular to a dominant $Bz_{GSM} > 0$ guide magnetic field. However, in considering individual gyrating ion particles, one must consider the total magnetic field, including this dominant $Bz_{GSM} > 0$ guide magnetic field observed on 8 Sept 2015. A cold magnetosheath proton above some cutoff velocity (Cowley, 1982) may enter the locally opened magnetic field (either MLR, north or south) and, in the case of a plasma density asymmetry with a higher density in the adjacent magnetosheath and a lower density earthward of the MLR magnetopause, the cold magnetosheath ions will most likely cross the mid-plane of the Jz CS onto the geomagnetic field (Cassak and Shay, 2007; Birn et al., 2008; Pritchett, 2008). That is, we assume that most of the ion reconnection outflow supports a significant velocity component along the geomagnetic field direction on the earthward side of the remote MLR magnetopause regions, as we suggest in the **Figure 11** schematic with a few ion trajectories from a high-density magnetosheath into a low-density magnetosphere with thin lines and associated arrows displaying the directions of the in-plane components of the KH-sheared magnetic field in agreement with **Figure 10**. MMS measured a magnetic field strength B_2~85 nT and plasma density N_2~20 cm^{-3} in the adjacent magnetosheath (**Figures 2E,H**). The dynamic equatorial LLBL region supported a similar field strength B~75 nT and a density N~12 cm^{-3} (**Figure 2**), while MMS sampled an outer magnetosphere plasma sheet before ~0920 UT characterized by a field strength B_1~70 nT and a density N_1~2 cm^{-3} (**Figure 1**). If we assume that similar plasma sheet conditions existed earthward of the two MLR regions at a small 15° separation to the north and south of MMS, and with similar conditions expected in an adjacent remote magnetosheath as those measured at MMS, we may estimate a magnetic field ratio B_1/B_2~0.8 and a plasma density ratio N_2/N_1~10 across the remote MLR regions. A similar case ($B_1/B_2 = 0.7$ and $N_2/N_1 = 10$) was simulated by Birn et al. (2008) with a region 2 corresponding to our magnetosheath and a region 1 corresponding to our magnetosphere. This case predicts a bulk exhaust outflow on a magnetosphere-side with higher Alfvén speed, in basic agreement with the **Figure 11** schematic, with this outflow primarily aligned with the magnetic field direction earthward of the magnetopause.

The **Figure 11** schematic ion entry process is viewed from above the NMLR region, and from above the SMLR region, with a dominant $Bz_{GSM} > 0$ pointing outward and the symbols at $Y_{GSM} = 0$ indicating the direction of the Jz_{GSM} CSs, again consistent with **Figure 10**. We also note that the two X-lines of the schematic may be associated with a tailward deHoffmann-Teller drift along this flank magnetopause location. This means that the bulk of the adjacent magnetosheath ion velocity population, which supports a finite field-aligned drift centered near $V_B \sim -75$ km/s (**Figure 3A**), may experience a shift toward V_B~0 km/s in the assumed tailward moving frame of reference of the schematic with magnetosheath ions expected to move in both directions of the magnetic field in **Figure 11**.

There are four cases to consider for a possible explanation of the two counter-streaming, accelerated magnetosheath ion beams

along the magnetic field that we propose that MMS observed on 8 Sept 2015. In Case 1 (NMLR sunward jet), a cold magnetosheath ion is assumed to enter the magnetosphere along the open magnetic field onto a sunward-directed in-plane component of a KH-sheared magnetic field on the earthward side of the $Jz_{GSM} > 0$ CS. However, we note that the locally open magnetic field earthward of the MLR magnetopause is directed mostly northward (Bz > 0 dominant guide-field) with a smaller sunward tilt. The guiding-center of this cold gyrating ion is accelerated by the drift of the reconnected field lines, and it will be measured along that magnetic field as a faster parallel ion beam, but only in a region to the north of the NMLR jet. In Case 2 (NMLR tailward jet), a cold magnetosheath ion enters the magnetosphere and it obtains a fast exhaust speed directed along the geomagnetic field, but this time opposite the open magnetic field onto a sunward-directed (KH tilted) in-plane component of the magnetic field earthward of the $Jz_{GSM} > 0$ CS. The cold gyrating ion is accelerated tailward by the reconnected field lines, and it will be measured as a faster anti-parallel ion beam along this mostly northward magnetic field line with a sunward tilt, but only in a region to the south of this tailward NMLR jet. In Case 3 (SMLR sunward jet), a cold magnetosheath ion enters the magnetosphere opposite the open magnetic field onto a tailward-directed (KH-tilted) in-plane component of the magnetic field earthward of the $Jz_{GSM} < 0$ CS. The guiding-center of this cold gyrating ion is accelerated sunward by the reconnected field lines, and it will be measured along that mostly northward-directed magnetic field line as a fast anti-parallel ion beam, but only in a region to the south of the SMLR jet. Finally, in Case 4 (SMLR tailward jet), a cold magnetosheath ion enters the magnetosphere along the open magnetic field onto a tailward-directed (KH tilted) in-plane component of the field earthward of the $Jz_{GSM} < 0$ CS. As before, the locally open magnetic field is directed mostly northward with a tailward tilt. The guiding-center of the cold ion is accelerated tailward by the reconnected field lines, and it will be measured along that geomagnetic field line as a faster parallel ion beam as compared with its initial magnetosheath speed, but only in a region to the north of the SMLR jet.

The proposed incoming magnetosheath ion particles on 8 Sept 2015 will only be guided toward the equatorial plane of the KH-vortex from the tailward exhaust of the SMLR region, and from the tailward exhaust of the NMLR region, by the dominant $Bz_{GSM} > 0$ magnetic field upon entering the locally open magnetopause. We emphasize the expected importance of a higher Alfvén speed on the earthward side of the MLR regions (Birn et al., 2008) to align the ion exhaust with the geomagnetic field. If the conditions of a given KH case are such that the higher Alfvén speed shifts to the magnetosheath-side of the MLR CSs, then the primary difference should be two counter-streaming magnetosheath ion beams associated with two sunward exhausts in the tailward moving MLR X-line frame of reference, assuming a northward $Bz_{GSM} > 0$ guide-field on the magnetosheath-side and a DMLR process that captures magnetosheath plasma onto newly closed magnetic field lines. A rotation of the in-plane exhausts about the $Bz_{GSM} > 0$ guide-field of the X-line by local KH-vortex action will not affect this simple scenario. What matters is the direction of the normal magnetic field across the magnetopause in the vicinity of the X-line, and that the geomagnetic field is stretched tailward (sunward) near the SMLR (NMLR) X-line, while the KH-entrained mostly northward-directed magnetosheath magnetic field is tilted sunward (tailward) near the SMLR (NMLR) X-line in agreement with

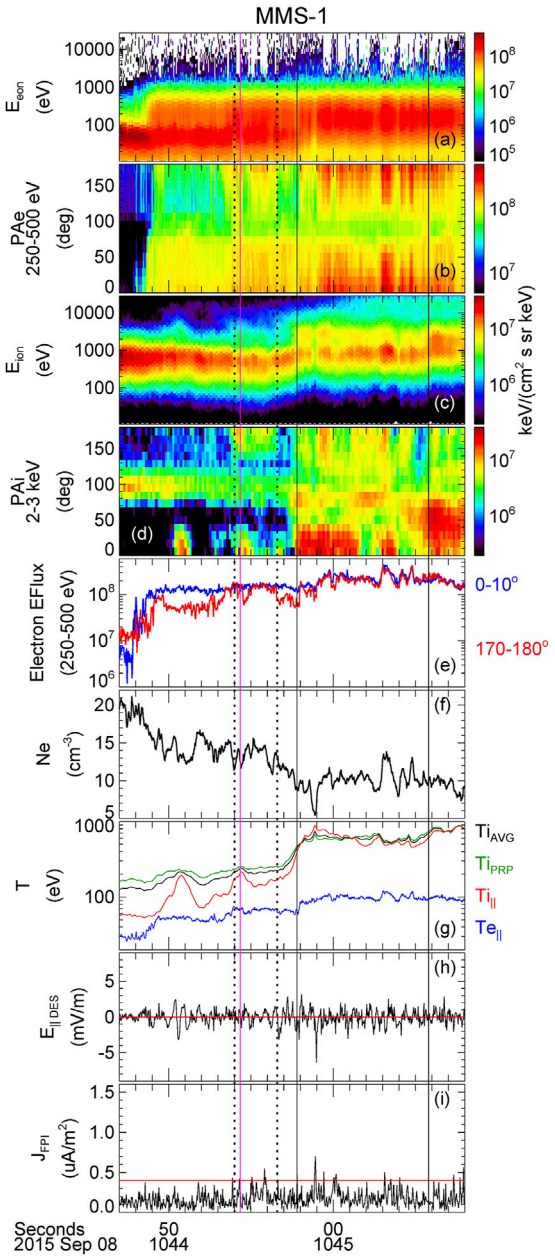

FIGURE 12 | MMS-1 burst observations from 1044:47 UT to 1045:08 UT. Same panel format as described in **Figure 8**. Two vertical dotted lines mark the time period from 1044:54.000 UT to 1044:56.600 UT when (Vernisse et al., 2016) indicated a presence of two counter-streaming ion beams. A pink solid vertical line marks the time 1044:54.349 UT of the MMS-1 ion VDF displayed in **Figures 13A,D**. The two black solid vertical lines at 1044:57.800 UT and 1045:05.800 UT marks an interval with a characteristic warm ion temperature 450 eV < Ti_{AVG} < 800 eV.

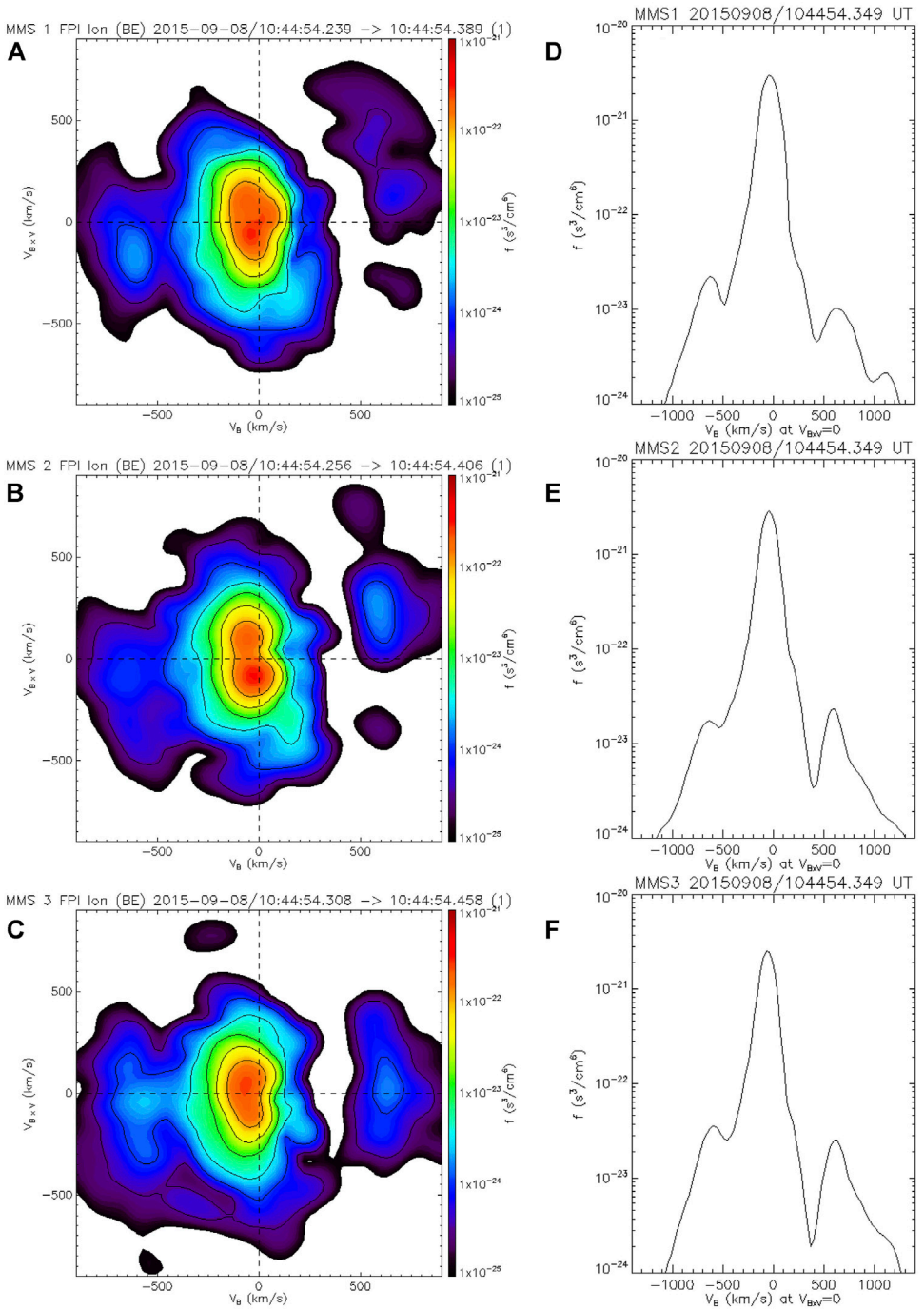

FIGURE 13 | Ion velocity distribution functions at 1044:54.349 UT: **(A)** 2-D ion phase space density at MMS-1; **(B)** 2-D ion phase space density at MMS-2; **(C)** 2-D ion phase space density at MMS-3; **(D)** 1-D cut at MMS-1; **(E)** 1-D cut at MMS-2; **(F)** 1-D cut at MMS-3.

Figure 10. We should note that individual ion particles upon entering the two MLR exhaust regions will also experience a small reconnection electric field $\mathbf{E}_r = -\mathbf{V}\mathrm{x}\mathbf{B}$ as, e.g., associated with a guiding-center outflow motion on the order of $|\mathbf{V}|$~100 km/s in an in-plane (normal) magnetic field on the order of $|\mathbf{B}|$~5 nT that would correspond to an electric field E_r~0.5 mV/m. This E_r electric field is directed away from the equatorial plane at both MLR regions with Ez < 0 at the SMLR X-line and exhaust, and Ez > 0 at the NMLR X-line and exhaust, such that $\mathbf{J}\cdot\mathbf{E} > 0$ associated with the strong Jz currents of **Figure 10**. However, the two poleward diverging Ez electric fields will unlikely affect the bulk population of the incoming magnetosheath ion particles in their attempt to reach the guiding-center ion exhaust speed before they exit the tailward exhaust regions along the dominant

Bz_{GSM} > 0 guide magnetic field near the two MLRs and travel toward the equator.

Revisiting Initial Ion Beam MMS Observations

Vernisse et al. (2016) presented a statistical study focused on MMS observations of field-aligned, heated electrons in the magnetosheath adjacent to the trailing magnetopause CSs of the KH spine region that we associate with "type-I" vortex-induced magnetic reconnection ion exhaust signatures on 8 Sept 2015 (Eriksson et al., 2016a). However, Vernisse et al. (2016) also displayed one important MMS-1 ion velocity distribution averaged over a 1.5-s period at 1044:53.500–1044:55.000 UT near the leading edge of one KH vortex that appears to show two weak ion beams. They concluded that "additional electron and ion populations are shown to be present in the magnetosheath, and those are suggested to come from mid-latitude reconnection driven by the twisting of the field lines away from the KH waves in the northern and southern hemispheres." In the next several paragraphs, we review the MMS observations in and around this single ion VDF measurement using the same format that we employed in **Figures 4**, **8**, **9** to further our understanding of these important ion observations in the immediate 3-D spatial domain of the KH vortex region.

Figure 12 shows a 21-s period around this leading edge region. The 2.6-s interval at 1044:54.000–1044:56.600 UT (two dotted vertical lines) marks the time that Vernisse et al. (2016) associated with a presence of two counter-streaming ion beams in MMS-1 observations, and possibly due to a remote presence of two MLR regions. They referred to this region as an ion boundary layer (IBL) (Gosling et al., 1990; Onsager et al., 2001) in an "interval where the spacecraft is in the magnetosheath."

Figure 13 displays the 150-ms ion VDFs as recorded by MMS-1, MMS-2 and MMS-3 around the same time at 1044:54.349 UT and in the same 2-D plane format as shown in **Figure 4**. We marked this time in **Figure 12** as a pink, solid vertical line inside the 2.6-s interval. The chosen time is close to a local maximum of the parallel ion temperature ($Ti_{||}$). The corresponding 1-D ion cuts at V_{BxV} = 0 in **Figure 13** appear to show two ion beams, but with a significantly lower PSD than the ion beams shown in **Figure 4**. The average $<Ti_{||}>$ = 164 eV during this 2.6-s interval within the IBL region is correspondingly lower as compared with the values listed in **Table 1**. The $Ti_{||}/Ti_{perp}$ ratio only reached a 0.84 maximum with an average $<Ti_{||}/Ti_{perp}>$ = 0.67 ratio in this same period. These ion temperature signatures, together with an average <Ne> = 13.5 cm^{-3} electron plasma density, are consistent with a magnetosheath-like domain adjacent to the ion leading edge of the KH vortex. In comparing the MMS-1 ion observations of **Figures 12C,D** with the corresponding ion observations of the two events of counter-streaming ion beams shown in **Figures 8**, **9**, it is clear that MMS-1 recorded these weaker ion beam signatures in a magnetosheath-like region farther from the warm ion temperature domain of the KH vortex region itself as shown between two solid vertical lines at 1044:57.8–1045:05.8 UT in **Figure 12**.

We note how both MMS-1 and MMS-2, which were located nearly along the same magnetic flux tubes, did not display a D-shaped ion beam distribution in either a parallel or anti-parallel direction. The two MMS satellites rather measured fast parallel and anti-parallel ions with a significant drift in one perpendicular **BxV**-direction as compared with the ion VDFs of **Figure 4**. This finite V_{BxV} drift of the beam ions may reflect a magnetosheath-like domain of the ions, or ion entry potentially farther from the MMS satellites, whereby some parallel motion at the entry location may have changed into perpendicular motion at the satellite due to a conservation of the first adiabatic invariant (Fuselier et al., 2014). Hardly any of the 17 individual ion VDFs that MMS-1 sampled at 150-ms cadence at 1044:54.000–1044:56.600 UT displayed a D-shape distribution of the parallel and anti-parallel streaming ions in contrast with the ion VDFs of **Figure 4** and most of the individual counter-streaming ion beam events listed in **Table 1**. However, **Figures 13C,F** show that MMS-3, with an earthward $\Delta Y_{GSM} \sim -156$ km displacement from MMS-1 and with only a small earthward $\Delta Y_{GSM} \sim -71$ km separation from MMS-2, in fact recorded a mostly D-shaped parallel ion beam and an anti-parallel ion beam with a much smaller V_{BxV} drift at the same time as the two ion VDFs at MMS-1 and MMS-2. MMS-3 measured very similar D-shaped distributions of the parallel ion beam mostly throughout this 2.6-s period inside a variable IBL region adjacent to the KH vortex (not shown). This more earthward MMS-3 location was also associated with relatively warmer ion temperatures during this same 2.6-s period with a higher average $<Ti_{||}>$ = 208 eV and a higher $Ti_{||}/Ti_{perp}$ ratio that peaked at 0.97 with an average $<Ti_{||}/Ti_{perp}>$ = 0.78 ratio.

The presence of two D-shaped ion beams with very weak PSD as observed by MMS-3 in a magnetosheath-like IBL region, and just before it entered a KH vortex region, could indicate a reflection of earthward-drifting magnetosheath ions (Onsager et al., 2001) along the open magnetic field near two MLR regions to the south and to the north of the satellite, and on the magnetosheath-side of the two MLR CSs (**Figure 11**). Another possibility is a leakage of magnetosphere ions, and electrons, from two MLR regions as suggested in Vernisse et al. (2016). The simultaneous presence of a dominant magnetosheath ion core population and a general absence of hot LLBL ions (**Figures 3**, **13C**,F) would seem to support a magnetosheath ion reflection scenario. The D-shaped nature of the ion beam distributions at MMS-3 also supports a more local MLR region and an open magnetopause as, e.g., compared with more banana-shaped ion distributions associated with a more distant ion entry location relative the satellite (Fuselier et al., 2014).

An Ion Velocity Filter Effect?

Figure 4 shows how MMS-3 recorded a faster parallel ion beam speed V_B for a lower PSD as compared with the V_B speed and PSD of the parallel ion beams measured by the other MMS satellites at the same time. This appears to be a typical trend in terms of the field-aligned ion speed at the maximum PSD when these ion

beams are observed on 8 Sept 2015, whereby a lower PSD of the ion beam is often reflected in a faster ion speed along the magnetic field (**Table 2**). That is, fewer and fewer ions are measured the faster the ions are observed to move. This observation suggests the presence of a velocity filter effect for the DMLR process that may be explained in terms of the actual distance to the proposed MLR ion exhaust source region (Eriksson et al., 2020) with only the very fastest ions being able to cover a longer distance as compared with slower ions of a similar ion velocity distribution.

Let us assume as a baseline scenario that two symmetric MLR locations exist at nearly equal latitude distances from a region of maximum KHI growth, which is not far from the predicted locations of the MMS satellites on 8 Sept 2015 (Vernisse et al., 2020). The observation of a typically higher PSD associated with the parallel ion beam of the **Table 1** events, as compared with a lower PSD in the anti-parallel ion beam, would then indicate a more active or steady reconnection process near the SMLR region, perhaps accelerating more ions in a parallel direction than a less-active NMLR region producing fewer ions in the anti-parallel direction. This appears to be consistent with the north-south asymmetry prediction in Sisti et al. (2019) for the observed in-plane magnetic fields of this KH event whereby the number of SMLR regions tends to dominate over the number of NMLR regions. The alternative scenario of two asymmetrically located MLR regions of similar reconnection activity relative a region of maximum KH growth would suggest that MMS could have been closer to the SMLR region than the NMLR region to explain the larger number of ions collected from that direction. Either scenario appears to explain the observed PSD differences with 62% of the 26 cases in **Table 1** typically favoring a higher PSD in the parallel direction than the anti-parallel direction of the two ion beams, with the opposite PSD observation seen in only 15% of the 26 cases.

The Warm KH Vortex Region

MMS mostly observed the counter-streaming ion beams in the warm, intermediate ion temperature region (Ti_w) of the KH vortex, which is defined as the KH-mixing region where $Ti_{MSH} < Ti_w < Ti_{MSP}$. Here, Ti_{MSP} corresponds to the high-temperature region of the pre-existing LLBL-proper and Ti_{MSH} is the cold ion temperature of the adjacent magnetosheath. Sisti et al. (2019) reproduced these three regions in their **Figure 3** on the basis of the plasma density, where Ti_{MSP} corresponds to the highest-density LLBL region of their simulated KH vortex. However, there is not much of a difference in the observed plasma density of the two KH vortex regions (**Figure 2**) that we associate with Ti_w and Ti_{MSP}. Moreover, the regions of two distinct counter-streaming ion beams in individual ion VDFs typically correspond to $Ti_{||} > Ti_{prp}$. This is very rarely, if ever, observed in the LLBL-proper, where the characteristic ion temperature is mostly isotropic $Ti_{||} \sim Ti_{prp}$.

On KH Plasma Turbulence and Mid-Latitude Reconnection

Sorriso-Valvo et al. (2019) explored the MMS observations of the 8 Sept 2015 KH event and reported a presence of bi-directional ion beams with an ion VDF example presented at 1007:45.820 UT. This ion VDF is part of a longer 3.3-s period of 22 individual 150-ms cadence ion burst measurements with sustained counter-streaming ion beams (**Table 1**). The pair of two coherent ion beams presented in Sorriso-Valvo et al. (2019) was proposed to be a result of the observed plasma turbulence first reported in Stawarz et al. (2016) of this same KH vortex region. However, it remains unclear how an extended region of plasma turbulence in the KH vortex region of this event would result in such organized and focused periods of counter-streaming ion beams, and only toward the warm leading edge of the KH vortices. One would expect much more extended intervals of such bi-directional ion beams throughout the KH vortex region, as also expected from a double HLR source discussed earlier, if they were a direct result of plasma turbulence. Indeed, it appears that the two-fluid 3-D numerical simulation (Sisti et al., 2019), which is able to reproduce the observed loci and dimensions of two distinct counter-streaming ion beams reported here, provides a more straightforward explanation of the origin of the two ion beams in terms of twice-reconnected MLR magnetic field lines to the north and south of MMS during the early non-linear phase of the KH instability at the Earth's flank magnetopause.

Finally, we should mention that is not impossible that MMS may have sampled a $Jz < 0$ CS region of one SMLR region at 1028:43 UT when it observed the intense $J \sim 1.3\ \mu A/m^2$ current layer with a dominant $Jz_{GSM} = -1.1\ \mu A/m^2$ component and $E_{||} = -6$ mV/m at the start of the 0.90-s interval of counter-streaming ions (**Figure 8**) that we associate with "twice-reconnected" fields and a presence of two MLRs to the south and north of the region of maximum KHI growth. However, the equal energy flux of bi-directional 250–500 eV electrons did not support this current per se. It is very likely that the ~1.5-s period of parallel 250–500 eV electrons and parallel 2–3 keV ions at 1028:46.0–1028:47.5 UT inside the warm region of this first KH vortex (**Figure 8**) may be explained as magnetosheath particles still entering a tailward reconnection exhaust from one active MLR to the south of MMS, while the decrease of the anti-parallel flux of said electrons and ions at this time suggests that MMS was no longer connected to a northern MLR. Either it ceased to be active, or MMS simply moved away from it onto fields with a different topology.

SUMMARY AND CONCLUSIONS

The KH event recorded by MMS on 8 Sept 2015 in an early non-linear phase of the KHI evolution is examined for a presence of counter-streaming ion beams along the magnetic field as recorded in individual ion VDFs. The commonly observed D-shaped nature of the two ion beams (Cowley, 1982), which are superposed on a slowly drifting magnetosheath population and typically without a hot LLBL population, suggests that the beams are associated with magnetosheath ion particle transmission at a more distant magnetopause reconnection region from the MMS satellites along the

magnetic field due to the absence of local reconnection exhausts.

The typical $T < T_{KH}$ ion travel times for a field-aligned V_B = 525 km/s (median) ion speed and a field-aligned distance $L \sim \lambda_{KH}$ from an assumed nearby MLR region, as compared with $T > 3T_{KH}$ for ions at this same speed between a northern high-latitude region and MMS at a ~18 R_E field-aligned distance, suggest that the two D-shaped ion beams observed by MMS are probably associated with two nearby MLR magnetopause reconnection regions, or else MMS would have likely measured a more common banana-shaped counter-streaming ion beam distribution (Fuselier et al., 2014) associated with the closed magnetic fields of a double HLR region, and across most of the closed field regions of the entire KH vortex.

The in-plane spatial dimensions of the sustained periods of two counter-streaming ion beams show a very good agreement with the similar dimensions of twice-reconnected magnetic field lines reported for this same KH event in a two-fluid, 3-D numerical simulation domain (Sisti et al., 2019) that surrounds the immediate 3-D KH vortex. A proposed plasma turbulence-generated ion beam explanation (Sorriso-Valvo et al., 2019) does not appear to be consistent with the localized MMS observations of counter-streaming ion beams in the warm temperature region of the KH vortex leading edge as reproduced by Sisti et al. (2019).

Vernisse et al. (2016) presented a possible ion leakage-scenario associated with two distant magnetopause reconnection regions to explain the presence of an ion boundary layer with two counter-streaming ion beams with very low PSD in a magnetosheath-like region adjacent to a KH vortex as observed by MMS on 8 Sept 2015. It is possible that the very low PSD of these ion beams may be explained in terms of a magnetosheath ion reflection mechanism (Smith and Rodgers, 1991; Onsager et al., 2001) at the locally open MLR magnetopause. In contrast, we reported new counter-streaming ion beam MMS observations on 8 Sept 2015 with a mostly D-shaped distribution and a much higher PSD inside the warm leading-edge KH vortex region. We propose a magnetosheath ion injection hypothesis in the presence of a plasma density gradient at the mid-latitude magnetopause to explain these remote observations, whereby cold magnetosheath ions are accelerated tailward by a transverse **ExB** drift near two MLR regions, with this **ExB** outflow becoming mostly aligned with the magnetic field on that side of the local MLR magnetopause which is also associated with a higher Alfvén speed (Birn et al., 2008). The accelerated, mostly field-aligned exhaust ions are subsequently guided along a dominant $Bz_{GSM} > 0$ magnetic field toward the equator and the MMS satellites in a direction away from the magnetosheath in general agreement with the mostly D-shaped ion beam observations [e.g., (Cowley, 1982), (Fuselier et al., 2014), (Eriksson et al., 2020)].

MMS frequently observed in-plane reconnection exhausts at the trailing, intense CSs of this same KH event associated with "type-I" vortex-induced reconnection of the magnetopause spine region [e.g., (Eriksson et al., 2016a), (Vernisse et al., 2016)] that connects two neighboring KH vortices. In contrast, the occurrence frequency of "type-II" reconnection exhaust observations appear to be very rare indeed inside this KH-vortex region on 8 Sept 2015. We conclude, therefore, that the observation of two counter-streaming ion beams inside the warm leading layers of the KH vortex, far removed from the trailing CSs, is most likely associated with magnetosheath ion injection in the tailward exhaust regions at two nearby MLR regions, above and below the MMS satellites, as first proposed by Otto (2008) to exist in a 3-D KH vortex regime.

DATA AVAILABILITY STATEMENT

The datasets presented in this study can be found in online repositories. The names of the repository/repositories and accession number(s) can be found below: https://lasp.colorado.edu/mms/sdc/public/.

AUTHOR CONTRIBUTIONS

SE analyzed MMS data and interpreted the observations including generating a schematic of the proposed ion entry process from the magnetosheath in the vicinity of two mid-latitude reconnection regions associated with KHI. XM provided MHD simulation results of field-line topology for the KHI event. JB provided IDL codes to analyze the electron energy flux for a given pitch-angle and energy range of DES observations. AO provided detailed insights on mid-latitude reconnection dynamics. SE analyzed dipole field-line lengths and bounce times of electrons at selected electron energy. PD provided expertise on KHI dynamics.

ACKNOWLEDGMENTS

SE acknowledges primary support from NASA grant award 80NSSC18K1108 to the Embry-Riddle Aeronautical University, Florida and the Laboratory for Atmospheric and Space Physics (LASP) with the University of Colorado Boulder. XM acknowledges support from NASA grants 80NSSC18K1108 and 80NSSC18K1381. MMS observations are publically available *via* NASA CDAWeb resources and the Science Data Center at University of Colorado/LASP. The MMS data analysis performed here employed the SPEDAS V3.1 as described in (Angelopoulos et al., 2019). We thank the entire MMS team for their accomplishments that made this data set available to the entire Heliophysics community.

REFERENCES

Angelopoulos, V., Cruce, P., Drozdov, A., Grimes, E. W., Hatzigeorgiu, N., King, D. A., et al. (2019). The Space Physics Environment Data Analysis System (SPEDAS). *Space Sci. Rev.* 215, 9. doi:10.1007/s11214-018-0576-4

Bavassano Cattaneo, M. B., Marcucci, M. F., Bogdanova, Y. V., Rème, H., Dandouras, I., Kistler, L. M., et al. (2010). Global Reconnection Topology as Inferred from Plasma Observations Inside Kelvin-Helmholtz Vortices. *Ann. Geophys.* 28, 893–906. doi:10.5194/angeo-28-893-2010

Birn, J., Borovsky, J. E., and Hesse, M. (2008). Properties of Asymmetric Magnetic Reconnection. *Phys. Plasmas* 15, 032101. doi:10.1063/1.2888491

Birn, J., Drake, J. F., Shay, M. A., Rogers, B. N., Denton, R. E., Hesse, M., et al. (2001). Geospace Environmental Modeling (GEM) Magnetic Reconnection Challenge. *J. Geophys. Res.* 106, 3715–3719. doi:10.1029/1999JA900449

Burch, J. L., Moore, T. E., Torbert, R. B., and Giles, B. L. (2015). Magnetospheric Multiscale Overview and Science Objectives. *Space Sci. Rev.* 199, 5–21. doi:10.1007/s11214-015-0164-9

Burch, J. L., Torbert, R. B., Phan, T. D., Chen, L.-J., Moore, T. E., Ergun, R. E., et al. (2016). Electron-scale Measurements of Magnetic Reconnection in Space. *Science* 352, aaf2939. doi:10.1126/science.aaf2939

Cassak, P. A., and Shay, M. A. (2007). Scaling of Asymmetric Magnetic Reconnection: General Theory and Collisional Simulations. *Phys. Plasmas* 14, 102114. doi:10.1063/1.2795630

Chandrasekhar, S. (1961). *Hydrodynamic and Hydromagnetic Stability*. New York, NY: Oxford Univ. Press.

Chen, S.-H., and Kivelson, M. G. (1993). On Nonsinusoidal Waves at the Earth's Magnetopause. *Geophys. Res. Lett.* 20, 2699–2702. doi:10.1029/93GL02622

Cowley, S. W. H. (1982). The Causes of Convection in the Earth's Magnetosphere: A Review of Developments during the IMS. *Rev. Geophys.* 20, 531–565. doi:10.1029/rg020i003p00531

Ergun, R. E., Tucker, S., Westfall, J., Goodrich, K. A., Malaspina, D. M., Summers, D., et al. (2016). The Axial Double Probe and Fields Signal Processing for the MMS Mission. *Space Sci. Rev.* 199, 167–188. doi:10.1007/s11214-014-0115-x

Eriksson, S., Lavraud, B., Wilder, F. D., Stawarz, J. E., Giles, B. L., Burch, J. L., et al. (2016a). Magnetospheric Multiscale Observations of Magnetic Reconnection Associated with Kelvin-Helmholtz Waves. *Geophys. Res. Lett.* 43, 5606–5615. doi:10.1002/2016GL068783

Eriksson, S., Wilder, F. D., Ergun, R. E., Schwartz, S. J., Cassak, P. A., Burch, J. L., et al. (2016b). Magnetospheric Multiscale Observations of the Electron Diffusion Region of Large Guide Field Magnetic Reconnection. *Phys. Rev. Lett.* 117, 015001. doi:10.1103/PhysRevLett.117.015001

Eriksson, S., Souza, V. M., Cassak, P. A., and Hoilijoki, S. (2020). Nascent Flux Rope Observations at Earth's Dayside Magnetopause. *J. Geophys. Res. Space Phys.* 125, e2020JA027919. doi:10.1029/2020JA027919

Fadanelli, S., Faganello, M., Califano, F., Cerri, S. S., Pegoraro, F., and Lavraud, B. (2018). North-South Asymmetric Kelvin-Helmholtz Instability and Induced Reconnection at the Earth's Magnetospheric Flanks. *J. Geophys. Res. Space Phys.* 123, 9340–9356. doi:10.1029/2018JA025626

Faganello, M., and Califano, F. (2017). Magnetized Kelvin-Helmholtz Instability: Theory and Simulations in the Earth's Magnetosphere Context. *J. Plasma Phys.* 83, 535830601. doi:10.1017/S0022377817000770

Faganello, M., Califano, F., Pegoraro, F., and Retinò, A. (2014). Kelvin-Helmholtz Vortices and Double Mid-latitude Reconnection at the Earth's Magnetopause: Comparison Between Observations and Simulations. *Epl* 107, 19001. doi:10.1209/0295-5075/107/19001

Fairfield, D. H., Otto, A., Mukai, T., Kokubun, S., Lepping, R. P., Steinberg, J. T., et al. (2000). Geotail Observations of the Kelvin-Helmholtz Instability at the Equatorial Magnetotail Boundary for Parallel Northward Fields. *J. Geophys. Res.* 105, 21159–21173. doi:10.1029/1999JA000316

Farrugia, C. J., Gratton, F. T., Bender, L., Biernat, H. K., Erkaev, N. V., Quinn, J. M., et al. (1998). Charts of Joint Kelvin-Helmholtz and Rayleigh-Taylor Instabilites at the Dayside Magnetopause for Strongly Northward Interplanetary Magnetic Field. *J. Geophys. Res.* 103, 6703–6727. doi:10.1029/97JA03248

Feldman, W. C., Asbridge, J. R., Bame, S. J., Montgomery, M. D., and Gary, S. P. (1975). Solar Wind Electrons. *J. Geophys. Res.* 80, 4181–4196. doi:10.1029/JA080i031p04181

Foullon, C., Farrugia, C. J., Fazakerley, A. N., Owen, C. J., Gratton, F. T., and Torbert, R. B. (2008). Evolution of Kelvin-Helmholtz Activity on the Dusk Flank Magnetopause. *J. Geophys. Res.* 113, A11203. doi:10.1029/2008JA013175

Fuselier, S. A., Petrinec, S. M., Trattner, K. J., and Lavraud, B. (2014). Magnetic Field Topology for Northward IMF Reconnection: Ion Observations. *J. Geophys. Res. Space Phys.* 119, 9051–9071. doi:10.1002/2014JA020351

Gosling, J. T., Thomsen, M. F., Bame, S. J., Elphic, R. C., and Russell, C. T. (1990). Cold Ion Beams in the Low Latitude Boundary Layer During Accelerated Flow Events. *Geophys. Res. Lett.* 17, 2245–2248. doi:10.1029/GL017i012p02245

Gosling, J. T., Thomsen, M. F., Bame, S. J., Elphic, R. C., and Russell, C. T. (1991). Observations of Reconnection of Interplanetary and Lobe Magnetic Field Lines at the High-Latitude Magnetopause. *J. Geophys. Res.* 96, 14097–14106. doi:10.1029/91JA01139

Hasegawa, H., Fujimoto, M., Phan, T.-D., Rème, H., Balogh, A., Dunlop, M. W., et al. (2004). Transport of Solar Wind into Earth's Magnetosphere Through Rolled-Up Kelvin-Helmholtz Vortices. *Nature* 430, 755–758. doi:10.1038/nature02799

Hasegawa, H., Fujimoto, M., Takagi, K., Saito, Y., Mukai, T., and Rème, H. (2006). Single-spacecraft Detection of Rolled-Up Kelvin-Helmholtz Vortices at the Flank Magnetopause. *J. Geophys. Res.* 111, A09203. doi:10.1029/2006JA011728

Hasegawa, H., Retinò, A., Vaivads, A., Khotyaintsev, Y., André, M., Nakamura, T. K. M., et al. (2009). Kelvin-Helmholtz Waves at the Earth's Magnetopause: Multiscale Development and Associated Reconnection. *J. Geophys. Res.* 114, A12207. doi:10.1029/2009JA014042

Knoll, D. A., and Chacón, L. (2002). Magnetic Reconnection in the Two-Dimensional Kelvin-Helmholtz Instability. *Phys. Rev. Lett.* 88 (21), 215003. doi:10.1103/physrevlett.88.215003

Kokubun, S., Kawano, H., Nakamura, M., Yamamoto, T., Tsuruda, K., Hayakawa, H., et al. (1994). Quasi-periodic Oscillations of the Magnetopause During Northward Sheath Magnetic Field. *Geophys. Res. Lett.* 21 (25), 2883–2886. doi:10.1029/94GL02103

Li, W., André, M., Khotyaintsev, Y. V., Vaivads, A., Graham, D. B., Toledo-Redondo, S., et al. (2016). Kinetic Evidence of Magnetic Reconnection Due to Kelvin-Helmholtz Waves. *Geophys. Res. Lett.* 43, 5635–5643. doi:10.1002/2016GL069192

Luhmann, J. G., Walker, R. J., Russell, C. T., Crooker, N. U., Spreiter, J. R., and Stahara, S. S. (1984). Patterns of Potential Magnetic Field Merging Sites on the Dayside Magnetopause. *J. Geophys. Res.* 89, 1739–1742. doi:10.1029/JA089iA03p01739

Ma, X., Otto, A., and Delamere, P. A. (2014). Interaction of Magnetic Reconnection and Kelvin-Helmholtz Modes for Large Magnetic Shear: 1. Kelvin-Helmholtz Trigger. *J. Geophys. Res. Space Phys.* 119, 781–797. doi:10.1002/2013JA019224

Ma, X., Delamere, P., Otto, A., and Burkholder, B. (2017). Plasma Transport Driven by the Three-Dimensional Kelvin-Helmholtz Instability. *J. Geophys. Res. Space Phys.* 122 (10), 10382–10395. doi:10.1002/2017JA024394

Ma, X., Delamere, P., Nykyri, K., Burkholder, B., Eriksson, S., and Liou, Y.-L. (2021). Ion Dynamics in the Meso-scale 3-D Kelvin–Helmholtz Instability: Perspectives From Test Particle Simulations. *Front. Astron. Space Sci.* 8, 758442. doi:10.3389/fspas.2021.758442

Mitchell, D. G., Kutchko, F., Williams, D. J., Eastman, T. E., Frank, L. A., and Russell, C. T. (1987). An Extended Study of the Low-Latitude Boundary Layer on the Dawn and Dusk Flanks of the Magnetosphere. *J. Geophys. Res.* 92, 7394–7404. doi:10.1029/JA092iA07p07394

Miura, A., and Pritchett, P. L. (1982). Nonlocal Stability Analysis of the MHD Kelvin-Helmholtz Instability in a Compressible Plasma. *J. Geophys. Res.* 87, 7431–7444. doi:10.1029/JA087iA09p07431

Nakamura, T. K. M., Fujimoto, M., and Otto, A. (2006). Magnetic Reconnection Induced by Weak Kelvin-Helmholtz Instability and the Formation of the Low-Latitude Boundary Layer. *Geophys. Res. Lett.* 33, L14106. doi:10.1029/2006GL026318

Nakamura, T. K. M., Fujimoto, M., and Otto, A. (2008). Structure of an MHD-Scale Kelvin-Helmholtz Vortex: Two-Dimensional Two-Fluid Simulations Including Finite Electron Inertial Effects. *J. Geophys. Res.* 113, A09204. doi:10.1029/2007JA012803

Nakamura, T. K. M., Daughton, W., Karimabadi, H., and Eriksson, S. (2013). Three-dimensional Dynamics of Vortex-Induced Reconnection and Comparison with THEMIS Observations. *J. Geophys. Res. Space Phys.* 118, 5742–5757. doi:10.1002/jgra.50547

Nakamura, T. K. M., Eriksson, S., Hasegawa, H., Zenitani, S., Li, W. Y., Genestreti, K. J., et al. (2017). Mass and Energy Transfer across the Earth's Magnetopause Caused by Vortex-Induced Reconnection. *J. Geophys. Res. Space Phys.* 122, 11505–11522. doi:10.1002/2017JA024346

Nishino, M. N., Fujimoto, M., Ueno, G., Mukai, T., and Saito, Y. (2007). Origin of Temperature Anisotropies in the Cold Plasma Sheet: Geotail Observations Around the Kelvin-Helmholtz Vortices. *Ann. Geophys.* 25, 2069–2086. doi:10.5194/angeo-25-2069-2007

Nykyri, K., and Otto, A. (2001). Plasma Transport at the Magnetospheric Boundary Due to Reconnection in Kelvin-Helmholtz Vortices. *Geophys. Res. Lett.* 28, 3565–3568. doi:10.1029/2001GL013239

Nykyri, K., Otto, A., Lavraud, B., Mouikis, C., Kistler, L. M., Balogh, A., et al. (2006). Cluster Observations of Reconnection Due to the Kelvin-Helmholtz Instability at the Dawnside Magnetospheric Flank. *Ann. Geophys.* 24, 2619–2643. doi:10.5194/angeo-24-2619-2006

Øieroset, M., Raeder, J., Phan, T. D., Wing, S., McFadden, J. P., Li, W., et al. (2005). Global Cooling and Densification of the Plasma Sheet During an Extended Period of Purely Northward IMF on October 22-24, 2003. *Geophys. Res. Lett.* 32, L12S07. doi:10.1029/2004GL021523

Onsager, T. G., Scudder, J. D., Lockwood, M., and Russell, C. T. (2001). Reconnection at the High-Latitude Magnetopause during Northward Interplanetary Magnetic Field Conditions. *J. Geophys. Res.* 106 (25), 25467–25488. doi:10.1029/2000JA000444

Otto, A., and Fairfield, D. H. (2000). Kelvin-Helmholtz Instability at the Magnetotail Boundary: MHD Simulation and Comparison with Geotail Observations. *J. Geophys. Res.* 105, 21175–21190. doi:10.1029/1999JA000312

Otto, A. (2008). Three-dimensional Simulation of Kelvin-Helmholtz Modes at the Magnetospheric Boundary. *Eos Trans. AGU* 89 (23).

Pollock, C., Moore, T., Jacques, A., Burch, J., Gliese, U., Saito, Y., et al. (2016). Fast Plasma Investigation for Magnetospheric Multiscale. *Space Sci. Rev.* 199, 331–406. doi:10.1007/s11214-016-0245-4

Pritchett, P. L. (2008). Collisionless Magnetic Reconnection in an Asymmetric Current Sheet. *J. Geophys. Res.* 113, A06210. doi:10.1029/2007JA012930

Pu, Z. Y., Yei, M., and Liu, Z. X. (1990). Generation of Vortex-Induced Tearing Mode Instability at the Magnetopause. *J. Geophys. Res.* 95, 10559–10566. doi:10.1029/JA095iA07p10559

Russell, C. T., Anderson, B. J., Baumjohann, W., Bromund, K. R., Dearborn, D., Fischer, D., et al. (2016). The Magnetospheric Multiscale Magnetometers. *Space Sci. Rev.* 199 (1-4), 189–256. doi:10.1007/s11214-014-0057-3

Schindler, K., Hesse, M., and Birn, J. (1988). General Magnetic Reconnection, Parallel Electric fields, and Helicity. *J. Geophys. Res.* 93 (A6), 5547–5557. doi:10.1029/JA093iA06p05547

Schulz, M., and Lanzerotti, L. J. (1974). "Particle Diffusion in the Radiation Belts," in *Physics and Chemistry in Space*. Editors J. G. Roederer (New York, NY: Springer), 215. doi:10.1007/978-3-642-65675-0

Schwartz, S. J. (1998). "Shock and Discontinuity Normals, Mach Numbers, and Related Parameters," in *Analysis Methods for Multi-Spacecraft Data*. Editors G. Paschmann and P. W. Daly (ISSI Scientific Reports Series, ESA/ISSI), Vol. 1, 249–270. Available at: https://ui.adsabs.harvard.edu/abs/1998ISSIR...1..249S/abstract.

Sisti, M., Faganello, M., Califano, F., and Lavraud, B. (2019). Satellite Data-Based 3-D Simulation of Kelvin-Helmholtz Instability and Induced Magnetic Reconnection at the Earth's Magnetopause. *Geophys. Res. Lett.* 46, 11597–11605. doi:10.1029/2019GL083282

Smith, M. F., and Rodgers, D. J. (1991). Ion Distributions at the Dayside Magnetopause. *J. Geophys. Res.* 96, 11617–11624. doi:10.1029/91JA00676

Song, P., and Russell, C. T. (1992). Model of the Formation of the Low-Latitude Boundary Layer for Strongly Northward Interplanetary Magnetic Field. *J. Geophys. Res.* 97, 1411–1420. doi:10.1029/91JA02377

Sonnerup, B. U. Ö. (1979). "Magnetic Field Reconnection," in *Solar System Plasma Physics*. Editors C. F. Kennel, L. J. Lanzerotti, and E. N. Parker (Amsterdam: North-Holland Pub.), Vol. 3, 45–108.

Sorriso-Valvo, L., Catapano, F., Retinò, A., Le Contel, O., Perrone, D., Roberts, O. W., et al. (2019). Turbulence-driven Ion Beams in the Magnetospheric Kelvin-Helmholtz Instability. *Phys. Rev. Lett.* 122, 035102. doi:10.1103/PhysRevLett.122.035102

Stawarz, J. E., Eriksson, S., Wilder, F. D., Ergun, R. E., Schwartz, S. J., Pouquet, A., et al. (2016). Observations of Turbulence in a Kelvin-Helmholtz Event on 8 September 2015 by the Magnetospheric Multiscale Mission. *J. Geophys. Res. Space Phys.* 121, 11021–11034. doi:10.1002/2016JA023458

Vernisse, Y., Lavraud, B., Eriksson, S., Gershman, D. J., Dorelli, J., Pollock, C., et al. (2016). Signatures of Complex Magnetic Topologies from Multiple Reconnection Sites Induced by Kelvin-Helmholtz Instability. *J. Geophys. Res. Space Phys.* 121, 9926–9939. doi:10.1002/2016JA023051

Vernisse, Y., Lavraud, B., Faganello, M., Fadanelli, S., Sisti, M., Califano, F., et al. (2020). Latitudinal Dependence of the Kelvin-Helmholtz Instability and Beta Dependence of Vortex-Induced High-Guide Field Magnetic Reconnection. *J. Geophys. Res. Space Phys.* 125, e2019JA027333. doi:10.1029/2019JA027333

Wilder, F. D., Ergun, R. E., Schwartz, S. J., Newman, D. L., Eriksson, S., Stawarz, J. E., et al. (2016). Observations of Large-Amplitude, Parallel, Electrostatic Waves Associated with the Kelvin-Helmholtz Instability by the Magnetospheric Multiscale Mission. *Geophys. Res. Lett.* 43, 8859–8866. doi:10.1002/2016GL070404

Conflict of Interest: The authors declare that the research was conducted in the absence of any commercial or financial relationships that could be construed as a potential conflict of interest.

Publisher's Note: All claims expressed in this article are solely those of the authors and do not necessarily represent those of their affiliated organizations, or those of the publisher, the editors and the reviewers. Any product that may be evaluated in this article, or claim that may be made by its manufacturer, is not guaranteed or endorsed by the publisher.

frontiers in Astronomy and Space Sciences

ORIGINAL RESEARCH
published: 05 November 2021
doi: 10.3389/fspas.2021.782924

Bifurcated Current Sheet Observed on the Boundary of Kelvin-Helmholtz Vortices

K-J. Hwang[1], K. Dokgo[1], E. Choi[1], J. L. Burch[1], D. G. Sibeck[2], B. L. Giles[2], C. Norgren[3], T. K. M. Nakamura[4,5], D. B. Graham[6], Y. Khotyaintsev[6], Q. Q. Shi[7], D. J. Gershman[2], C. J. Pollock[8], R. E. Ergun[9], R. B. Torbert[10], C. T. Russell[11] and R. J. Strangeway[11]*

[1]Southwest Research Institute, San Antonio, TX, United States, [2]NASA Goddard Space Flight Center, Greenbelt, MD, United States, [3]Department of Physics and Technology, University of Bergen, Bergen, Norway, [4]Institute of Physics, University of Graz, Graz, Austria, [5]Austrian Academy of Sciences ÖAW, Space Research Institute, Graz, Austria, [6]Swedish Institute of Space Physics, Uppsala, Sweden, [7]School of Earth and Space Sciences, Peking University, Peking, China, [8]Denali Scientific, LLC, Fairbanks, AK, United States, [9]Laboratory for Atmospheric and Space Physics, University of Colorado at Boulder, Boulder, CO, United States, [10]Space Science Center, University of New Hampshire, Durham, NH, United States, [11]Institute of Geophysics and Planetary Physics, University of California, Los Angeles, CA, United States

OPEN ACCESS

Edited by:
Christopher H. K. Chen, Queen Mary University of London, United Kingdom

Reviewed by:
Arnaud Masson, European Space Astronomy Centre (ESAC), Spain
Xuanye Ma, Embry–Riddle Aeronautical University, United States

***Correspondence:**
K-J. Hwang
jhwang@swri.edu

Specialty section:
This article was submitted to Space Physics, a section of the journal Frontiers in Astronomy and Space Sciences

Received: *25 September 2021*
Accepted: *22 October 2021*
Published: *05 November 2021*

Citation:
Hwang K-J, Dokgo K, Choi E, Burch JL, Sibeck DG, Giles BL, Norgren C, Nakamura TKM, Graham DB, Khotyaintsev Y, Shi QQ, Gershman DJ, Pollock CJ, Ergun RE, Torbert RB, Russell CT and Strangeway RJ (2021) Bifurcated Current Sheet Observed on the Boundary of Kelvin-Helmholtz Vortices. Front. Astron. Space Sci. 8:782924. doi: 10.3389/fspas.2021.782924

On May 5, 2017 MMS observed a bifurcated current sheet at the boundary of Kelvin-Helmholtz vortices (KHVs) developed on the dawnside tailward magnetopause. We use the event to enhance our understanding of the formation and structure of asymmetric current sheets in the presence of density asymmetry, flow shear, and guide field, which have been rarely studied. The entire current layer comprises three separate current sheets, each corresponding to magnetosphere-side sunward separatrix region, central near-X-line region, and magnetosheath-side tailward separatrix region. Two off-center structures are identified as slow-mode discontinuities. All three current sheets have a thickness of ~0.2 ion inertial length, demonstrating the sub-ion-scale current layer, where electrons mainly carry the current. We find that both the diamagnetic and electron anisotropy currents substantially support the bifurcated currents in the presence of density asymmetry and weak velocity shear. The combined effects of strong guide field, low density asymmetry, and weak flow shear appear to lead to asymmetries in the streamlines and the current-layer structure of the quadrupolar reconnection geometry. We also investigate intense electrostatics waves observed on the magnetosheath side of the KHV boundary. These waves may pre-heat a magnetosheath population that is to participate into the reconnection process, leading to two-step energization of the magnetosheath plasma entering into the magnetosphere *via* KHV-driven reconnection.

Keywords: magnetic reconnection, Kelvin-Helmholtz wave, bifurcated current sheet, magnetopause, Kelvin-Helmholtz vortex

INTRODUCTION

About sixty years ago Dungey (1961) and Axford and Hines (1961) proposed two different models of the solar wind-magnetosphere interaction. The former was based on the concept of magnetic reconnection under large magnetic field shear. The latter was on quasi-viscous interaction in the boundary layer powered by large flow velocity shear. Since then two most important physical

processes that lead and regulate the solar wind-Earth's magnetosphere coupling are thought to be magnetic reconnection and the Kelvin-Helmholtz instability (KHI).

Both processes exhibit multi-scale features and either compete or enhance each other. Magnetic reconnection is initiated on the electron-scale size, i.e., in the electron diffusion region (EDR) and then entails dynamics in the ion diffusion region (IDR), and ultimately propagates its effect to the macroscopic region where magnetohydro-dynamics (MHD) governs. On the other hand, Kelvin-Helmholtz waves (KHWs) occurring on the Earth's magnetopause are often generated on the macroscopic scales, i.e., ~1 R_E (Earth radii) (Hasegawa et al., 2004) and then involve kinetic processes occurring on the ion and electron scales as the waves nonlinearly grow into Kelvin-Helmholtz vortices (KHVs). The vortex motion facilitates the formation of thin current sheets between stretched magnetosheath and magnetospheric field lines at the edge of KHVs where magnetic reconnection can occur (Nykyri and Otto, 2001, 2004). Observations (Fairfield et al., 2000; Nykyri et al., 2006; Eriksson et al., 2009, 2016; Hasegawa et al., 2009; Li et al., 2016; Hwang et al., 2020; Kieokaew et al., 2020) have reported ongoing reconnection in such a thin current sheet developed along the boundary of KHVs or a magnetic island as predicted by simulations (Nakamura et al., 2013, 2017). Magnetic reconnection at the edge of KHVs and/or a wave packet inside KHVs (Moore et al., 2016) result in cross-scale energy transport.

Cassak and Otto (2011) showed that a flow shear across the symmetric reconnection current sheet decreases the efficiency of the reconnected field line to drive the outflow, similarly to the suppression of reconnection by the diamagnetic effect (Swisdak et al., 2003, 2010). They used the full particle simulation to derive that the reconnection-cutoff velocity shear is the upstream Alfvén speed. Doss et al. (2015) studied the effect of the flow shear in asymmetric reconnection, analytically and numerically predicting that the asymmetric effect allows reconnection to continue even for super-Alfvénic upstream velocity shear. Tanaka et al. (2010) further considered the effect of a guide field as well as a flow shear in asymmetric reconnection, reporting that both an initial upstream flow and the Lorentz force acting inflowing plasmas in the presence of a guide field produce a slanted inflow to the current sheet. Resulting asymmetries in the quadrupolar reconnection current layer is qualitatively similar to the MHD simulation by La Belle-Hamer et al. (1995).

The 2-D MHD simulation for the current sheet across which substantial velocity shear and density jump exist (La Belle-Hamer et al., 1995) indicates that depending on either the competition (occurring on the tailward exhaust region) or the enhancement (sunward exhaust) of the two velocity-shear and densty-asymmetry effects, the structure of the current sheet is often different from the simple 1-D Harris model, showing double off-center peaks in current, i.e., current bifurcation. The bifurcated current sheet has been understood as the Petschek-type reconnection layer, where the reconnection outflow jets ejected from the X-line are bounded by two rotational discontinuities or slow mode shock structures, which split a single reconnecting current sheet.

On the other hand, bifurcated current sheets observed in Earth's magnetotail are often not necessarily associated with fast flows (Asano et al., 2003). Numerous studies have been put forth to understand the formation of such bifurcated magnetotail current-sheets, attributing its cause to flapping of the current sheet (Sergeev et al., 2003), magnetic turbulence (Greco et al., 2002), Kelvin-Helmholtz instability (Nakagawa and Nishida, 1989; Yoon, Drake and Lui, 1996), Ion-ion kink instability (Karimabadi et al., 2003), temperature anisotropy (Sitnov et al., 2004; Zelenyi et al., 2004) or relaxation processes of a disequilibrated current sheet, in particular, during current sheet thinning or quasi-steady compression (Schindler and Hesse, 2008; Jiang and Lu, 2021; Yoon et al., 2021).

The formation and structure of asymmetric current sheets in the presence of flow shear, density asymmetry, and guide field have been much less studied. In particular, despite the prediction by La Belle-Hamer et al. (1995), evidence of bifurcated current sheets in KHW/KHV-induced reconnecting layers is rarely reported to this day. The only observation by Cluster (Hasegawa et al., 2009) showed that each of the two current sheets constituting the bifurcated layer had a thickness less than the ion inertial length and that the current was likely supported by electrons.

To enhance our understanding of the properties of the magnetic reconnection layer under the combined sheared plasma flow, guide field, and density asymmetry, i.e., typically occurring on the flank-side magnetopause, we use the data from MMS on May 5, 2017. In this paper, we present the observation of a bifurcated current sheet identified on the boundary of KHVs. The following paragraph briefly describes the MMS instruments and data analysis techniques used for the present study (*Methods* Section). We then investigate plasma and field properties associated with the bifurcated and central current sheets and show that the electrons drifting under both the diamagnetic effect and the magnetic curvature with large temperature anisotropy significantly contribute to the current (*The Structure of Current Sheets* Section). We also investigate intense electrostatics waves that are predominantly observed on the magnetosheath side of the central current layer (*Wave Observation and Analysis* Section). Discussion of the formation and structure of the observed current sheet in the presence of flow shear, density asymmetry, and guide field, and the implied cause and effect of the enhanced waves follow in *Discussion* Section.

METHODS

The four MMS spacecraft (Burch et al., 2016a) fly in low-inclination and highly elliptical orbits. We used the magnetic field data with a time resolution of 10-ms in burst mode, the electric field data with a 0.122-ms time resolution in burst mode, and ion and electron data in burst mode with a 150-ms and 30-ms time resolution, respectively, a 11.25° angular resolution, and an energy range of ~10 eV–26 keV.

We determined boundary normal coordinates (LMN) by performing minimum directional derivative (MDD) analysis (Shi et al., 2005): three eigenvectors corresponding to the medium, minimum, and maximum eigenvalues (λ) of the matrix, $(\nabla \mathbf{B})(\nabla \mathbf{B})^{\mathrm{T}}$ constitute the *l*, *m*, and *n* axes, respectively, in the LMN coordinates. To determine the propagation velocity of the

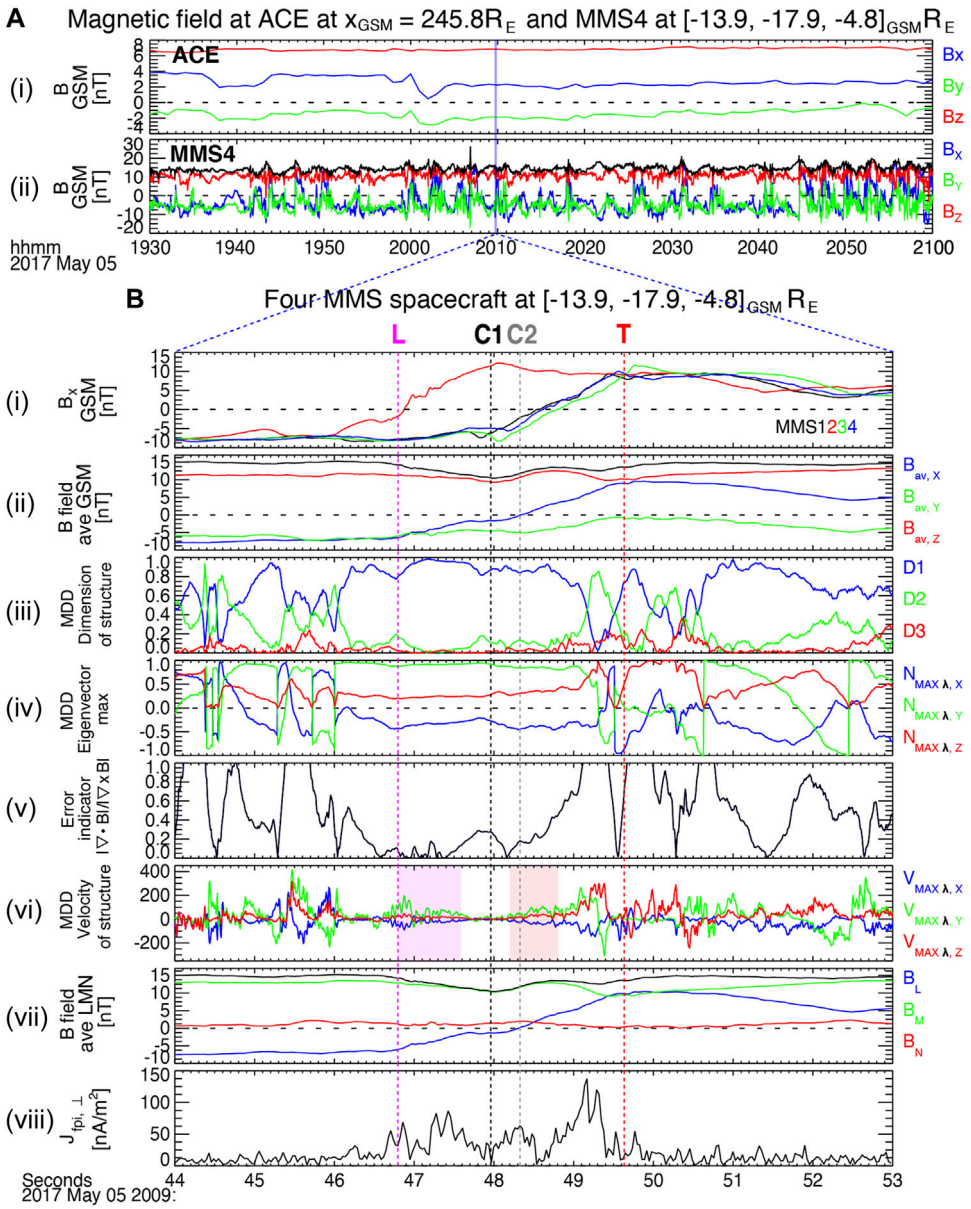

FIGURE 1 | (A) (i) the interplanetary magnetic field obtained from ACE OMNI-HRO 1-min data and **(ii)** the magnetic field at dawnside tailward magnetopause encountered by MMS4 (*x*, *y*, and *z* components in blue, green, and red with the magnetic strength in black) during 1930–2100 UT on May 5 2017 in Geocentric Solar Magnetospheric (GSM) coordinates. **(B)** The four MMS observations on May 5 2017 during 2009:44–53 UT: **(i)** the *x* component of the magnetic field **(B)** in GSM measured at MMS1 (black), 2 (red), 3 (green), and 4 (red); **(ii)** the tetrahedral-averaged **B** in GSM; MDD (Shi et al., 2005; 2006)-derived **(iii)** dimensionality of the structure, **(iv)** the eigenvector corresponding to the maximum eigenvalue of the matrix, $(\nabla \mathbf{B})(\nabla \mathbf{B})^T$, **(v)** error indicator $|\nabla \cdot \mathbf{B}|/|\nabla \times \mathbf{B}|$, **(vi)** the structure's velocity along the eigenvector shown in **(iv)**; **(vii)** the tetrahedral-averaged **B** in LMN; **(viii)** the tetrahedral-averaged current density perpendicular to **B** calculated from the plasma moments.

current layer, we performed spatio-temporal difference (STD) analysis (Shi et al., 2006). The current-sheet-normal propagation velocity is consistent with the value calculated from a four-spacecraft timing analysis (Paschmann et al., 1998). To investigate the wave propagation of the electrostatic waves, we used the maximum variance analysis (Sonnerup and Scheible, 1998; Siscoe and Suey 1972) of the electric field. To further investigate the wave mode, frequency, and growth rate, we performed the linear kinetic instability analysis using BO code (Xie, 2019) with input parameters obtained by fitting the observed ion and electron distributions functions to a sum of multi-component Maxwellian distributions.

THE STRUCTURE OF CURRENT SHEETS

From 1920 to 2320 UT on May 5, 2017, MMS observed quasi-periodic perturbations of the dawnside tailward magnetopause, as

reported by Hwang et al. (2020). **Figure 1A** shows (i) the interplanetary magnetic field obtained from ACE OMNI-HRO 1-min data and (ii) the magnetic field at dawnside tailward magnetopause encountered by MMS4 (x, y, and z components in blue, green, and red with the magnetic strength in black) during 1930–2100 UT in Geocentric Solar Magnetospheric (GSM) coordinates. The ACE HRO data provide the time-shifted IMF (interplanetary magnetic field) at a model bow shock nose location (Russell et al., 1983).

The event occurred within a period of mainly northward and slightly sunward/dawnward IMF (**Figures 1Ai**). MMS4 observed quasi-periodic fluctuations with a period of ~2.5–6 min (**Figures 1Aii**). Hwang et al. (2020) showed via boundary-normal analyses that the fluctuations were likely to be attributed to nonlinear KHWs. During this internal, we identified a thin current sheet formed at the boundary of the KHV at ~2009:49 UT (the vertical blue line in **Figure 1A**) when MMS traversed the boundary from the magnetospheric side to the magnetosheath side.

Figures 1Bi shows the x component of the magnetic field (**B**) in GSM coordinates. The negative-to-positive reversal of B_x observed by MMS1, 2, 3, and 4 (black, red, green, and blue) indicates a current sheet. The B_x profiles are, however, different from a Harris-sheet hyperbolic tangent profile, displaying local dip and peak and plateau (MMS2) or gentle slope (MMS134) between them, indicative of a bifurcated current sheet.

Figures 1Bii shows a 4-spacecraft tetrahedral-averaged **B**, which emphasizes the plateau around the center of the current sheet, marked by "C1" at the top of **Figures 1Bi** and the vertical dashed black line. MDD and STD analyses (*Methods* Section) derive the dimensionality and motional velocity of the structure and its boundary-normal direction (**Figures 1Biii–vi**). The overall current-sheet structure between the leading ("L" on the top of **Figures 1Bi** and vertical dashed magenta line) and trailing ("T" and vertical dashed red line) edges is mostly 1-D (**Figures 1Biii**), but significantly 2-D toward the trailing edge.

The current-sheet-normal vector is mainly along y_{GSM} (**Figures 1Biv**), as expected for the flank-side magnetopause. The three eigenvectors of $(\nabla \mathbf{B})\,(\nabla \mathbf{B})^{T}$ at ~2009:48 UT close to the center of the plateau and when the error is low (**Figures 1Bv**) point l = (0.97, 0.22, 0.13), m = (−0.06, −0.28, 0.96), and n = (0.24, −0.94, −0.26) in GSM. The medium-to-minimum (maximum-to-medium) eigenvalue ratio is ~14.6 (6.4), indicating a reliable calculation. The MDD-derived LMN coordinates are consistent with the LMN coordinates derived from minimum variance analysis (MVA) (Sonnerup and Scheible, 1998; Siscoe and Suey 1972) within 12.5°, 10.9°, and 6.7° differences along l, m, and n for all four spacecraft. We use the LMN coordinates throughout following figures and analyses.

Figure 2A shows the tetrahedral configuration of the four MMS spacecraft in LMN around its barycenter at $(-13.9, -17.9, -4.8)_{GSM}$ Earth radii (R_E). The notable difference in B_x between MMS2 and MMS134 (**Figures 1Bi**) most likely came from the n-directional separation, as seen in their LN-plane projections. About 179 km separation along n as well as the average spacecraft separation of ~156 km/s are comparable to the ion inertial length (d_i) based on the magnetosheath values (d_i = ~185 km).

Figures 1Bvii shows the tetrahedral-averaged **B** in LMN. The negative-to-positive B_l reversal is denoted by "C2" and the vertical dashed gray line. The tetrahedral-averaged electric current calculated from particle moments perpendicular to **B** (**Figures 1Bviii**) shows three overall peaks between "L" and "T". They comprise two larger peaks before and after "C2" and a smaller peak at ~"C2". Using the STD-driven current-sheet normal velocity (**Figures 1Bvi**), we estimate the thickness of each current sheet. The averaged normal velocity during 2009: 46.8–47.5 UT and during 2009:48.2–48.8 UT (with an error indicator less than 0.5) (magenta and red shades in **Figures 1Bvi**) is (−8.6, −1.0, −64.5) km/s and (−11.6, 8.2, −67.8) km/s in LMN, respectively. This is relatively consistent with the result derived from a four-spacecraft timing analysis based on the time difference in the B_x reversal among the four spacecraft (**Figures 1Bi**): (−21.5, −1.68, −68.0) km/s. We assume the overall current-sheet-normal velocity to be 67 km/s along -n. Then, the three current sheets before, at/around, and after "C2" with a duration of ~0.65, 0.50, and 0.65 s (**Figures 1Bviii** and **Figure 4B**) has a thickness of ~43.6, 33.5, and 43.6 km. Since these values correspond to ~0.24, 0.18, and 0.24 d_i (~9.7, 7.4, and 9.7 electron inertial length, d_e ~ 4.5 km in this event) similar to Hasegawa et al. (2009), the current in these sub-ion scale current sheets is expected to be supported by electrons.

Due to the large spacecraft separation compared to the current sheet thickness, investigation of the detailed structure of the current layer should be made using an individual spacecraft. We use the data from MMS1 (**Figure 3** with all vector parameters in LMN). **Figures 3A,B** shows the l (blue), m (green), and n (red) components of the magnetic (**B**) and electric (**E**) fields. The leading and trailing edges ("L" and "T", magenta and red dashed lines) denote dip and hump in B_l, decreases in B_m, and increase (ΔE_n~8.5 mV/m) and decrease (ΔE_n~−2.0 mV/m) in E_n at "L" and "T", respectively. (The latter two signatures correspond to the Hall features as illustrated in **Figure 2B** to be discussed in the following paragraphs) The reversals in B_l and B_n are marked by "C" and "C*" (black and gray dashed lines), respectively.

Variations of the ion density and ion/electron temperatures (**Figures 3C,D**) together with ion/electron energy spectrograms (**Figures 3H,I**) show that MMS1 crossed the current sheet from the more magnetospheric region (prior to "C") to the more magnetosheath region (after "C"). Intense electric field fluctuations (marked by "TB" and two vertical dashed cyan lines) are seen in the magnetosheath side of the current sheet (to be discussed in *Wave Observation and Analysis* Section).

The ion velocity between "L" and "T" varies from slower tailward flow (smaller $-V_{i,l}$) to faster tailward flow (larger $-V_{i,l}$) across "C" (marked by the blue arrow in **Figure 3E**) around $V_{i,l}$ = −154 km/s (the blue dotted line). This indicates the sunward exhaust region (before "C") to the antisunward exhaust region (after "C") of the current sheet, which was convecting antisunward along with the KHV propagation.

Therefore, MMS most likely crossed the overall current sheet from the sunward magnetospheric quadrant to the antisunward magnetosheath quadrant of the reconnection plane with a large guide field, B_g (B_m) ~ 1.5 $|B_l|$ (at 2009:46.0 UT; **Figure 3A**) out of the plane. The trajectory of MMS is denoted by the dashed orange

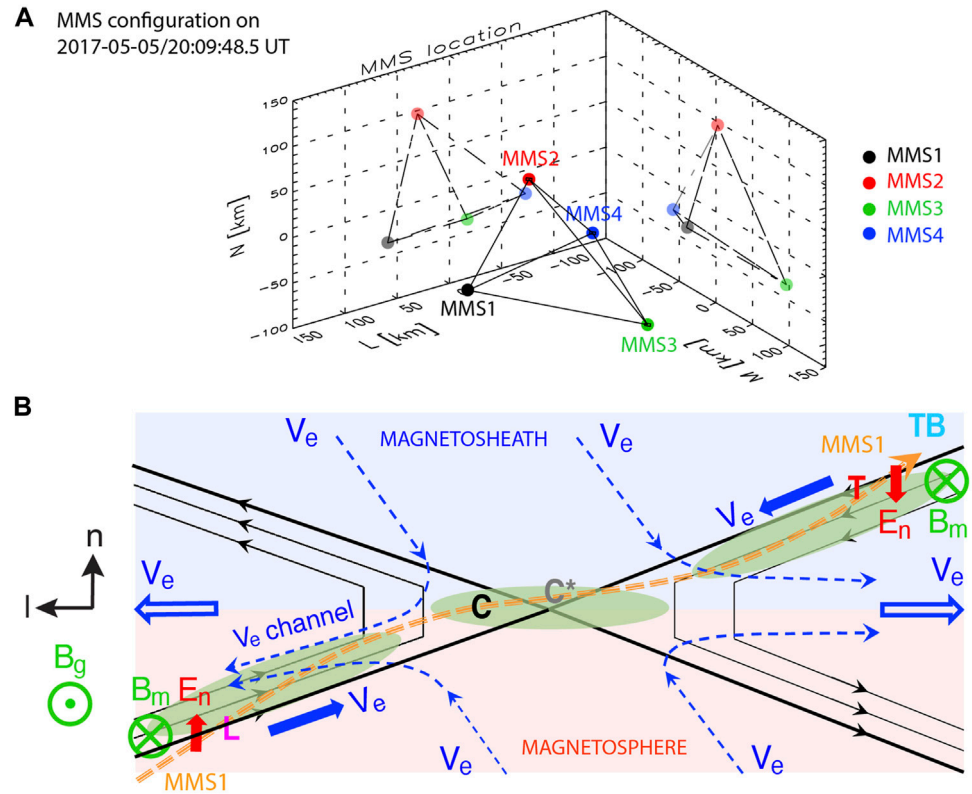

FIGURE 2 | (A) The tetrahedral configuration of the four MMS spacecraft around its barycenter at $(-13.9, -17.9, -4.8)_{GSM}$ Earth radii (R_E) on 2009:48/5 UT; **(B)** the illustration of the trajectory of MMS1 (the dashed orange arrow) across the reconnection plane, where "L", "C", "C*", and "T" correspond to those shown at the top of **Figure 3**.

arrow in **Figure 2B**, where "L", "C", "C*", and "T" correspond to those shown at the top of **Figure 3A**. The aforementioned Hall magnetic and electric field signatures are illustrated in green and red, respectively, around "L" and "T".

The electron velocity shows more complicated patterns than the ion velocity. Beyond the same variation of the slower-to-faster tailward outflow jets across "C" (blue arrow in **Figure 3F**), the slower tailward flow between "L" and "C" includes a short duration of the sunward flow ($+V_{e,l}$) during 2009:47.9–48.1 UT (magenta arrow). This indicates the existence of a narrow (~13.4 km, ~3 d_e) electron-current layer embedded in the outflow region (marked by "V_e channel" in **Figure 2B**). Its counterpart may exist in the tailward exhaust region (between "C" and "T") with a faster tailward jet before "T" (magenta arrow in **Figure 3F**). **Figure 2B** shows possible electron flow streamlines in dashed blue arrows that may explain the observed flow channels.

Around "L" and "T", $V_{e,l}$ sharply changes its sign. The enhanced tailward flow before/at 'L' and the sunward flow at/after "T" (black arrows in **Figure 3F**) are associated with electrons streaming toward an X-line in the separatrix region (see solid blue arrows in **Figure 2B**) (Egedal et al., 2005, 2008; Hwang et al., 2017, 2018). Pitch-angle distributions of the low- (<200 eV) and mid- (200 eV < energy <2 keV) energy electrons support this, showing the enhancement of the parallel flux at/around "L" and "T" (red arrows in **Figures 3J,K**). These counter-streaming electron flows ($\pm V_{e,l}$) across ~"L" and ~"T" sustain the Hall field along the separatrix.

These electron populations carry the electric current (current density, **J**) around "L" and "T". **Figure 4B** shows the *l*, *m*, and *n* components of **J** calculated from both ion and electron moments (solid blue, green, and red profiles). Overplotted are the ion current (dot-dashed light blue, light green, and orange) and the electron current (dotted blue, dark green, and red). The current (in particular, J_m) is mostly carried by electrons. Both J_l and J_m between "L" and "T" show the three-peak structure with two larger peaks before/after "C" and a smaller peak located at the B_n reversal ("C*"), as demonstrated in $J_{||}$ (black arrows in **Figure 4C**). Thus, we speculate that the two larger peaks correspond to one of each pair of a bifurcated current sheet and the central peak is associated with an X-line (**Figure 2B**).

In the sub-ion scale current layers such as this event, ion velocities perpendicular to **B** can be different from the **E** × **B** drift while electrons mostly follow **E** × **B**. **Figures 4D–F** shows ion (red) and electron (blue) velocities perpendicular to **B** compared with the **E** × **B** drift (black). Ion perpendicular velocities relatively agree with the **E** × **B** trend, but showing a substantial deviation

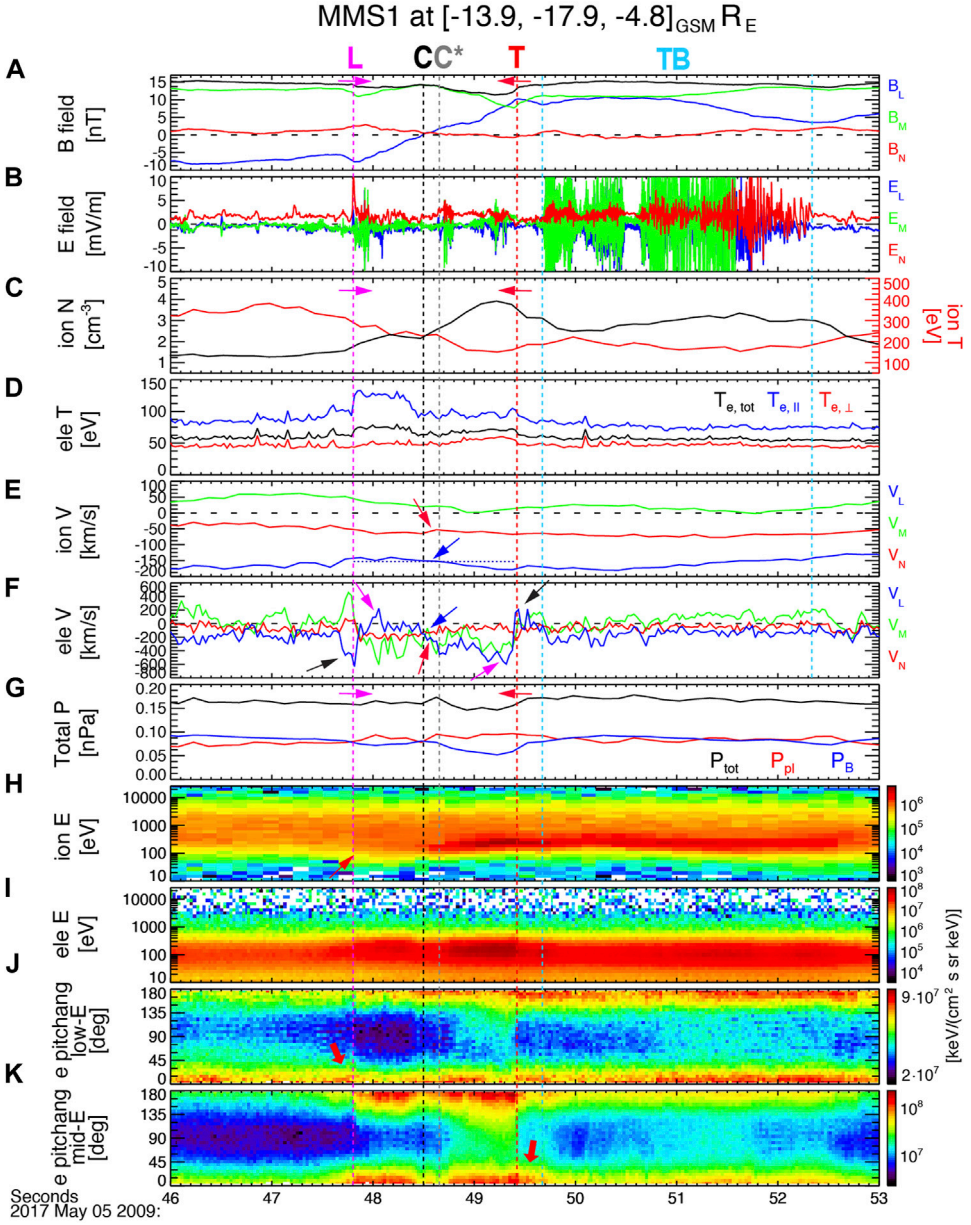

FIGURE 3 | MMS1 observation on May 5,2,017 during 2009:46–53 UT: **(A,B)** the *l* (blue), *m* (green), and *n* (red) components of the magnetic field (**B**) and the electric field (**E**) in LMN; **(C)** the ion density (black) and temperature (red); **(D)** the electron total (black), parallel (bule), and perpendicular (red) temperature; **(E)** the ion velocity; **(F)** the electron velocity; **(G)** the plasma (red) and magnetic (blue) pressures, and the sum (black) of these pressures; **(H)** the ion energy spectrogram; **(I)** the electron energy spectrogram; **(J,K)** pitch angle distributions of the low- (~10 eV ≤ energy <200 eV; **J**), mid- (200 eV ≤ energy <2 keV; **K**) energy electrons.

from $\mathbf{E} \times \mathbf{B}$ around "L" and "T". Electrons show a more notable deviation from $\mathbf{E} \times \mathbf{B}$ during "L"– 'T' as denoted by yellow arrows in **Figures 4D–F**. This can result from a certain level of electron agyrotropy or other perpendicular drifts such as diamagnetic and/or magnetic curvature drifts (Norgren et al., 2018).

To see the level of electron agyrotropy, we use $\sqrt{Q}$ that quantifies the level of agyrotropy (Swisdak, 2016) as shown in green in **Figure 4G**: 0 for gyrotropy and 1 for maximal agyrotropy. In general, the agyrotropy is weak, showing a bit higher level of $\sqrt{Q}$ in the magnetospheric side than the magnetosheath side, as predicted by a higher temperature and lower density for magnetospheric electrons (**Figures 3C,D**). Local peaks around "L", "C" and "T" are insignificant. On the other hand, Joule dissipation in the electron frame, $\mathbf{J} \cdot (\mathbf{E} + \mathbf{V}_e \times \mathbf{B})$ shown in black, blue, and red profiles representing the total, parallel, and perpendicular components to **B**, shows fluctuating or positive values between "L" and "T". The dissipation (mostly along **B**) is enhanced during a later half of "TB", where intense wave activities are found.

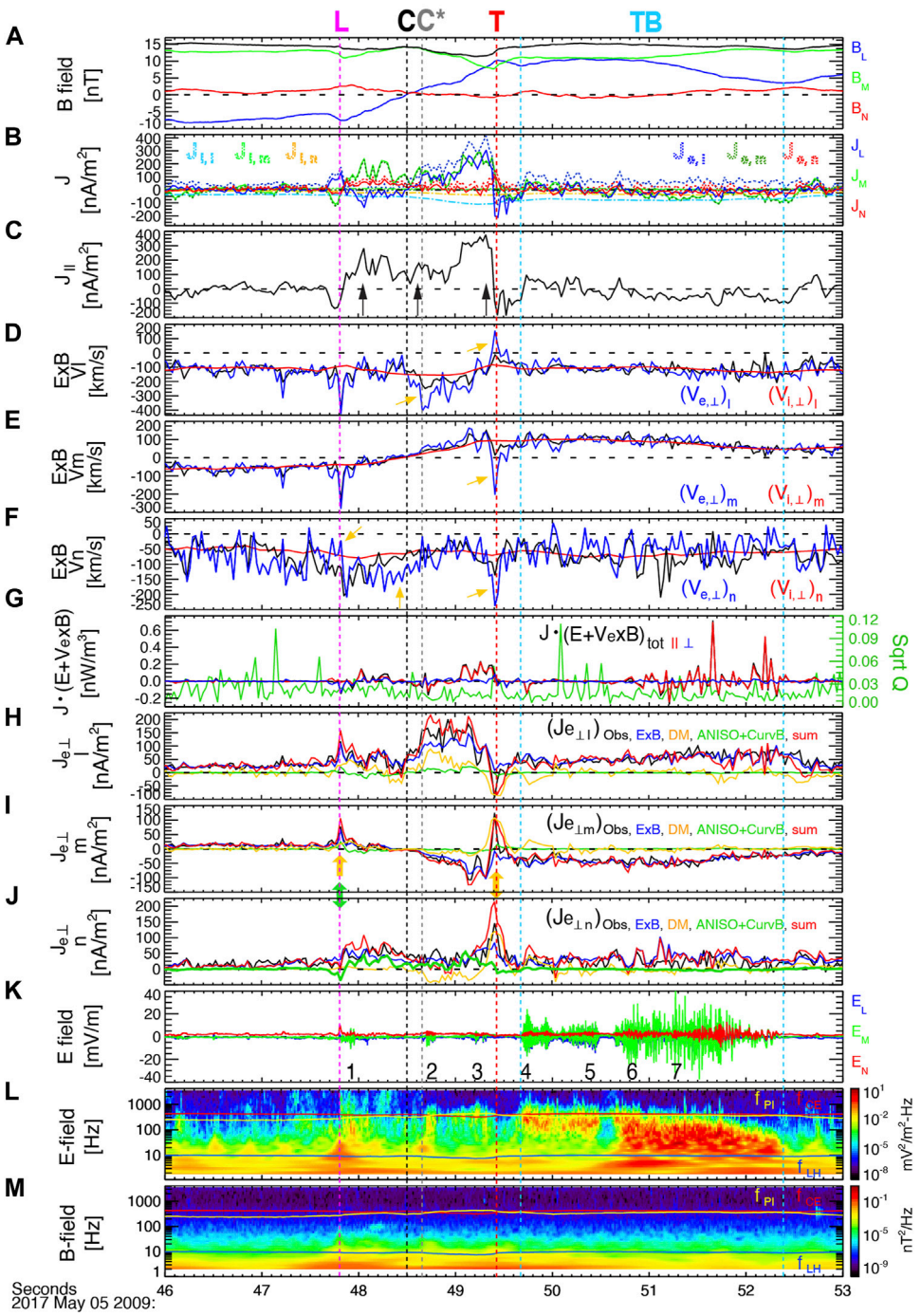

FIGURE 4 | MMS1 observation on May 5 2017 during 2009:46–53 UT: **(A)** the *l* (blue), *m* (green), and *n* (red) components of **B**; **(B)** the *l*, *m*, and *n* components of the current density **(J)** calculated from both ion and electron moments (solid blue, green, and red profiles), the ion current (dot-dashed blue, green, and orange), and the electron current (dotted blue, darkgreen, and orange); **(C)** the current density parallel to **B**; **(D–F)** the *l*, *m*, and *n* components of the $\mathbf{E} \times \mathbf{B}$ drift (black) together with the ion (red) and electron (blue) velocities perpendicular to **B**; **(G)** Joule dissipation in the electron frame, $\mathbf{J} \cdot (\mathbf{E} + \mathbf{V_e} \times \mathbf{B})$shown in black, blue, and red profiles representing the total, parallel, and perpendicular components to **B**, and $\sqrt{Q}$ (green) quantifying the level of departures from gyrotropy using electron pressure tensors (Swisdak, 2016); **(H–J)** the *l*, *m*, and *n* components of the electron perpendicular current, $\mathbf{J}_{e,\perp}$ (black), compared with those of the electron $\mathbf{E} \times \mathbf{B}$ current ($-en_e\frac{\mathbf{E}\times\mathbf{B}}{B^2}$, blue), the electron diamagnetic current ($\frac{\mathbf{B}\times\nabla\mathbf{P}_{e,\perp}}{B^2}$, orange), and the electron anisotropy current taking into account the influence of curvature drifts ($P_{e,\parallel} - P_{e,\perp}$)$\frac{\mathbf{B}\times(\mathbf{B}\cdot\nabla)\mathbf{B}}{B^4}$, green; **(K)** the *l*, *m*, and *n* components of **E**; **(L,M)** the power spectral density (PSD) of **E (L)** and **B (M)**.

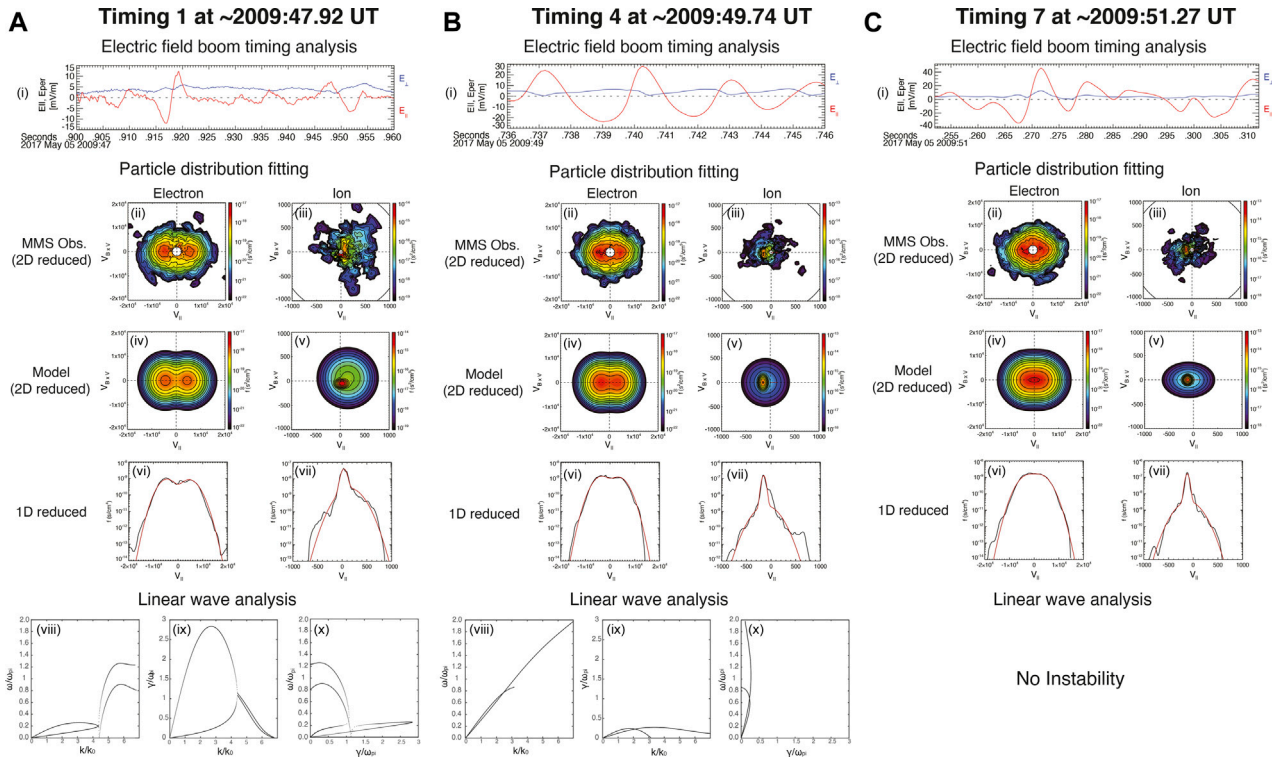

FIGURE 5 | Analysis of the waves observed at timing, 1 **(A)**, 4 **(B)**, and 7 **(C)** marked in **Figure 4K**: **(i)** the electric field decomposed into the parallel (red) and perpendicular (blue) components to **B**; **(ii,iii)** MMS observations of 2-D reduced electron **(ii)** and ion **(iii)** distributions in the $V_{||}$ and $V_{\perp} = \mathbf{B} \times (V_i \times \mathbf{B})$ plane; **(iv,v)** 2-D reduced model distributions in the $V_{||}$ and $V_{\perp} = \mathbf{B} \times (V_i \times \mathbf{B})$ plane, by fitting the observed distribution to a sum of two Maxwellian distributions; **(vi,vii)** 1-D reduced distributions in the $V_{||}$ axis for comparisons between model (red) and observation (black). These modeled distributions are used to perform the linear kinetic instability analysis using BO code (Xie, 2019). The results are shown in **(viii,ix)** the real and imaginary parts of the growing mode in $\omega - k$ space, where the frequency ω and the growth rate γ are normalized to the ion plasma frequency ω_{pi}, and the wave number k is normalized to $k_0 = \omega_{pi}/(10^3 \mathrm{km/s})$. The $\omega - \gamma$ plot **(x)** shows in which frequency range waves are generated.

To understand the electron deviation from $\mathbf{E} \times \mathbf{B}$ and the origin of a pair of off-centered (bifurcated) currents, we plot the l, m, and n components of the measured electron perpendicular current, $\mathbf{J}_{e,\perp}$ (black profiles in **Figures 4H–J**), compared with those of the electron $\mathbf{E} \times \mathbf{B}$ current ($-en_e\frac{\mathbf{E}\times\mathbf{B}}{B^2}$, blue), the electron diamagnetic current ($\frac{\mathbf{B}\times\nabla\mathbf{P}_{e,\perp}}{B^2}$, orange), and the electron anisotropy current taking into account the influence of curvature drifts $(P_{e,||} - P_{e,\perp})\frac{\mathbf{B}\times(\mathbf{B}\cdot\nabla)\mathbf{B}}{B^4}$, green, where n_e is the electron density, and $P_{e,||}$ and $P_{e,\perp}$ are the electron pressures parallel and perpendicular to **B** (Zelenyi et al., 2004). Due to the large spacecraft separation ($\sim d_i$), we cannot calculate gradient terms using four-spacecraft measurements. Instead, we use $\nabla \approx 1/(dt\ \mathbf{V}_{\mathrm{MMS\ across\ structure}}) = -1/(dt\ \mathbf{V}_{\mathrm{structure}})$, where dt is a sampling cadence of the electron data. The normal component of $\mathbf{V}_{\mathrm{structure}}$ was derived from MDD as described earlier. The tangential (l and m) components of $\mathbf{V}_{\mathrm{structure}}$ are, however, largely uncertain for the 1-D structure (**Figures 1Biii**). We use the l and m components of the background ion bulk velocity before "L" (averaged for 2009:46.0–47.5 UT), giving rise to $\mathbf{V}_{\mathrm{structure}} = (-173, 61, -67)$ km/s in LMN. The red profiles in **Figures 4H–J** are the sum of the $\mathbf{E} \times \mathbf{B}$, diamagnetic, and anisotropy currents, and show better agreements with the measured $\mathbf{J}_{e,\perp}$ than each of the three contributions. We find that both the diamagnetic and anisotropy currents significantly contribute to the current at/around "L". The diamagnetic current predominantly supports the current at/around "T" or between "C*" and "T". The anisotropy effect is most dominant in the n component of $\mathbf{J}_{e,\perp}$ and between "L" and "C" (Note a large electron temperature anisotropy between "L" and "C" in **Figure 3D**).

WAVE OBSERVATION AND ANALYSIS

We investigate the intense waves observed intermittently within the current layer (marked by 1, 2, and 3 in **Figure 4K** and stronger wave activities (throughout 4–7) observed during "TB". **Figures 4L,M** show the power spectral density (PSD) of **E** and **B**. The waves are mostly electrostatic and enhanced near or below the electron cyclotron frequency (f_{CE}) or the ion plasma frequency (f_{PI}) and above the lower-hybrid frequency (f_{LH}).

Figure 5i shows the waveform of **E** decomposed into parallel (red) and perpendicular (blue) components with respect to **B** for timing 1, 4, and 7 (**Figure 4K**). To estimate the propagation direction ($\hat{k}$) of the electrostatic waves, we use maximum variance analysis of **E** for each interval. Results shown in **Table 1** (a)

TABLE 1 | Parameters of modeled distributions used for linear analysis, where n_0 is total density and c is the speed of light. Each distribution is modeled as a sum of two Maxwellian distributions.

	(a) $\hat{k}$ in LMN, angle between ($\hat{k}$, B), max-to-mid eigenvalue ratio of MVA	(b) n_1 electron ion	(c) v_{th1} electron ion	(d) v_{d1} electron ion	(e) n_2 electron ion	(f) v_{th2} electron ion	(g) v_{d2} electron ion
Timing 1	± (–0.51, 0.85, 0.12)	$0.5n_0$	$1.33 \times 10^{-2}c$	$1.5 \times 10^{-2}c$	$0.5n_0$	$1.23 \times 10^{-2}c$	$-1.5 \times 10^{-2}c$
~2009:47.92 UT	6.63°, 4.41	$0.8n_0$	$2.33 \times 10^{-4}c$	$1.12 \times 10^{-4}c$	$0.2n_0$	$8.33 \times 10^{-4}c$	$5.0 \times 10^{-4}c$
Timing 4	± (0.64, 0.76, –0.04)	$0.47n_0$	$1.23 \times 10^{-2}c$	$1.17 \times 10^{-2}c$	$0.53n_0$	$1.23 \times 10^{-2}c$	$-1.17 \times 10^{-2}c$
~2009:49.74 UT	8.12°, 38.4	$0.93n_0$	$1.67 \times 10^{-4}c$	$-5.0 \times 10^{-4}c$	$0.07n_0$	$8.33 \times 10^{-4}c$	$-3.33 \times 10^{-4}c$
Timing 7	± (0.40, 0.91, 0.07)	$0.5n_0$	$1.33 \times 10^{-2}c$	$9.0 \times 10^{-3}c$	$0.5n_0$	$1.33 \times 10^{-2}c$	$-9.0 \times 10^{-3}c$
~2009:51.27 UT	12.8°, 118	$0.9n_0$	$1.67 \times 10^{-4}c$	$-4.0 \times 10^{-4}c$	$0.1n_0$	$8.33 \times 10^{-4}c$	$-3.33 \times 10^{-4}c$

demonstrate that these waves propagated parallel or anti-parallel to **B**.

To understand the generation of theses waves, we perform linear instability analysis using the electron and ion distribution functions at timing 1, 4, and 7. Each particle distribution is modeled by a sum of two Maxwellian distributions, and the best fitting parameters (density, thermal speed, and beam drift speed) are listed in **Table 1** (b–g). **Figure 5ii–v** shows MMS observations of 2-D reduced electron (ii) and ion (iii) distributions and their 2-D reduced model distributions (iv, v) in the $V_{||}$ and $V_{\perp} = \mathbf{B} \times (V_i \times \mathbf{B})$ plane. **Figures 5vi–vii** show 1-D reduced distributions in the $V_{||}$ axis for detailed comparisons between model (red) and observation (black). The modeled distributions agree well with the MMS observation for all timing 1, 4, and 7. We note that a cold ion population exists throughout these times and bi-directional electron beams exist in timing 1 and 4, but are flattened at timing 7.

By making use of these modeled-distribution parameters (**Table 1** b–g), we perform the linear kinetic instability analysis using BO code (Xie, 2019). **Figures 5viii–ix** show real and imaginary parts of the growing mode in $\omega - k$ space. The frequency ω and the growth rate γ are normalized to the ion plasma frequency ω_{pi}, and the wave number k is normalized to $k_0 = \omega_{pi}/(10^3\text{km/s})$. The $\omega - \gamma$ plot in **Figure 5x** shows more clearly in which frequency range waves are generated.

At timing 1, a low-frequency mode is generated in the range of $0.2 - 0.3\omega_{pi}$ as well as a broader spectrum in the range of $0 - 1.2\omega_{pi}$. The low-frequency mode is the fastest growing mode, which is observed only at/around timing 1 (**Figure 4L**). The phase speed of the fastest growing mode is ~130 km/s at the maximum growth rate, less than the ion acoustic speed (~250 km/s).

At timing 4, the frequency range of wave generation is much broader than timing 1. Two distinct modes are derived. One locates below ω_{pi} with a peak at $\sim 0.6\omega_{pi}$. The other locates in the range of $0 - 2.0\omega_{pi}$ and peaks at $\sim 1.0\omega_{pi}$. Their phase speeds are ~300 km/s and ~420 km/s, respectively. Because the frequency ranges of the two modes are overlapped as well as their growth rates are comparable to each other, the two wave modes may not be distinguished in the observation. The superposition of these waves might explain that the waveforms (**Figure 5Bi**) slightly deviate from sinusoidal.

At timing 7, the modeled distribution produces no growing mode most likely due to the flattened electron distribution. This indicates that the bi-directional electron beams are a major free-energy source for the generation of the observed electrostatic waves.

DISCUSSION

In this paper, we report a bifurcated current sheet developed on the boundary of KHVs propagating along the flank-side magnetopause, across which both plasma flow shear and density asymmetry exist under a large guide field, $B_g \sim 1.0\ |B_l|$ (on the magnetosheath side) to $1.5\ |B_l|$ (on the magnetospheric side). Via discussion on *The Structure of Current Sheets* Section, we speculate the trajectory of MMS that followed the dashed orange arrow in **Figure 2B** across the reconnection plane.

The overall current density profiles show three peaks (**Figures 4K,L**; green shades in **Figure 2B**), each observed in the proximity to the magnetospheric-side, sunward separatrix region (around "L"), the central, near-X-line region ("C-C*"), and the magnetosheath-side, tailward separatrix region (around "T"). The slower-tailward to faster-tailward jets across the central current sheet, i.e., reconnection outflows, demonstrate that the two off-centered signatures are corresponding to two rotational discontinuities or slow mode shocks in the Petschek reconnection geometry. 1) Tangential (B_l) and normal (B_n) components of **B** are non-zero at/around "L" and "T". 2) Decrease in $|B_l|$ from upstream (inflow region) to downstream (outflow region) of "L" and "T" (along magenta and red arrows in **Figure 3A**) indicates that the magnetic field bends toward *n*. 3) The magnetic field strength or pressure decrease from upstream to downstream (magenta and red arrows in **Figures 3A,G**). 4) The plasma density and pressure increase (magenta and red arrows in **Figures 3C,G**) across "L" and "T". All 1–4) features support that the two discontinuities are identified as slow modes.

For the two periods between "L" and ~"C" and between ~"C" and "T", we performed a Walén test separately for ions and electrons (Scudder et al., 1999; Hwang et al., 2016). The ion flow in the deHoffmann-Teller frame ($\mathbf{V_{HT}}$) showed a linear correlation with the ion Alfvén velocity with a correlation coefficient of ~0.8 for both intervals, but only 0.1–0.2 of the ion Alfvén speed; electrons did neither satisfy the Walén relation

nor display a correlation (not shown). This indicates that 1) the reconnection layer has not been fully developed (equivalently, the MMS orbit was too close to the X-line) or 2) other accelerations exerted on the current sheet. The sub-ion scale current sheet (*The Structure of Current Sheets* Section) and the significant contribution from the diamagnetic drift and/or the electron anisotropy drift (**Figures 4H–J**) indicate these possibilities 1–2), respectively.

Lin and Lee (1994), for asymmetric guide-field reconnection with no velocity shear, predicted the formation of different discontinuities between on the magnetosheath-side separatrix region (a time-dependent intermediate shock and a slow expansion wave, which evolves to a slow shock with time) and the magnetospheric-side separatrix region (a time-dependent intermediate shock and a weak slow shock). Such multiple discontinuities were not observed in this event, where the whole current layer is on a sub-ion scale, i.e., possibly due to the MMS trajectory being too close to the X-line. Further comparison is hindered since MMS did not traverse the entire exhaust region either side of X. The MHD simulation (La Belle-Hamer et al., 1995) for asymmetric no-B_g reconnection with a flow shear also predicted the formation of an intermediate shock on the magnetosheath-side, sunward separatrix region (the upper-left quadrant of **Figure 2B**), which was, again, not traversed by MMS.

We note a short duration of the sunward electron jet between "L" and "C". $V_{e,n}$ and $V_{i,n}$ are more negative and less negative across "C" (red arrows in **Figure 3F**). Thus, the plasma streamlines between "L"–"C" and "C"–"T" might not be symmetric (dashed blue arrows in **Figure 2B**).

La Belle-Hamer et al. (1995) and Tanaka et al. (2010), indeed, predicted such asymmetry in the reconnection geometry under the density gradient and velocity shear. In the tailward exhaust region (i.e., between "C*" and "T"), the outflow ($-L$) is in the same direction as the upstream magnetosheath flow ($-L$). Thus, a smaller force is required to drive the outflow. On the other hand, the larger density/inertia on the magnetosheath side requires a larger accelerating force to drive the outflow. As a result, the effects of shear flow and density gradient compete with each other, which results in the streamlines less deformed (blue dashed arrows in **Figure 2B**) and makes the field transition layer broader (note that the structure was significantly 2-D toward "T" in **Figures 1Biii**) as predicted by Figure 4 of La Belle-Hamer et al. (1995) and Figure 7 of Tanaka et al. (2010).

In the sunward magnetosheath-side exhaust region, the outflow ($+L$) is opposite to the upstream magnetosheath flow ($-L$), requiring a larger accelerating force to drive the outflow. The shear-flow and density-gradient effects enhance each other, forming a narrow field reversal region and putting the accelerated flow on the magnetospheric side of the field reversal (Figure 4 of La Belle-Hamer et al., 1995; Figure 7 of Tanaka et al., 2010). We speculate that the observed narrow sunward electron jet on the sunward, magnetospheric quadrant (between "L" and "C") is consistent with this prediction.

It may be notable that although such asymmetric streamlines are indicated by ion flows in the MHD (La Belle-Hamer et al., 1995) and particle-in-cell (Tanaka et al., 2010) simulations, the electron velocity appears to mostly represent the asymmetry in the present event. This implies that the aforementioned combined effects of the shear flow and density asymmetry are valid for the electron streamlines, in particular, in this sub-ion scale current layer.

We also note that the upstream flow difference across the current sheet is quite weak in this event (~6% of the parallel Alfvén speed on either side of the current sheet) while B_g is strong. Tanaka et al. (2010) showed that the combination of density gradient and guide field led to the similar effect obtained by the combination of density gradient and flow shear. Thus, we conclude that the combined effects of strong guide field, low density asymmetry (ρ_{sh}/ρ_{sp} ~2.2), and weak flow shear appear to derive asymmetries in the streamlines and the current-layer structure of the quadrupolar reconnection geometry, as illustrated in **Figure 2B**.

We estimate how these asymmetries would modify the reconnection rate, using the formula derived by Doss et al. (2015):

$$E_{shear,\,asym} \sim E_{0,\,asym}\left(1 - \frac{\Delta V_{e,l}{}^2}{V_A{}^2}\,\frac{\rho_{sh}B_{sp}\rho_{sp}B_{sh}}{\left(\rho_{sh}B_{sp} + \rho_{sp}B_{sh}\right)^2}\right) \quad (1)$$

where $E_{0,\,asym}$ is the asymmetric reconnection rate in the absence of upstream shear flow (Cassak and Shay, 2007), and V_A is the hybrid Alfvén speed, $V_A = \sqrt{B_{sh}B_{sp}\left(B_{sh}+B_{sp}\right)/\left[\mu_0\left(\rho_{sh}B_{sp}+\rho_{sp}B_{sh}\right)\right]}$ where ρ_{sh} and ρ_{sp} (B_{sh} and B_{sp}) represent the magnetosheath and magnetospheric mass density (magnetic field intensity). We use the magnetospheric and magnetosheath (upstream) values obtained at ~2009:47.0 UT and at ~2009:50.2 UT, respectively, which give the velocity difference, $\Delta V_{e,l}$ ~124 km/s across the current sheet and the density ratio, ρ_{sh}/ρ_{sp} ~2.2. Our estimate of the second term in the parenthesis of **Eq. 1** is ~ −0.003. Thus, the effect of the combined velocity shear and density asymmetry will have little influence in the asymmetric reconnection rate in this event. At the magnetotail flanks, the current sheet developed along the KHV boundary will mainly move with the bulk tailward velocity of the KHV. The velocity shear ($\Delta V_{e,l}$) is expected to be small, significantly reduced from the initial upstream velocity shear, which is the case as shown in **Figures 3E,F**.

Electrons mainly carried the current for the present event, and ion contribution to the currents is limited up to ~27% of the total current (**Figure 4B**), which is expected for the sub-ion scale current sheet. The three current density humps have a thickness of ~43.6, 33.5, and 43.6 km, i.e., ~0.24, 0.18, and 0.24 d_i (~9.7, 7.4, and 9.7 d_e), respectively, demonstrating the sub-ion scale current layer.

Numerous theoretical and simulation studies for the magnetotail (i.e., symmetric) environment have been performed to understand the formation of the current sheet bifurcation. Among various mechanisms proposed, one important factor is temperature anisotropy. Sitnov et al. (2004) suggested that the bifurcation is caused by weak ion temperature anisotropy with $T_{i,\perp}$ = 1.1–1.2 $T_{i,||}$. Zelenyi et al. (2004) and Jiang and Lu (2021) suggested that the bifurcation can be caused by the electron

pressure anisotropy ($P_{e,\perp} > P_{e,||}$), which decreases the current sheet density at the center of the current sheet, via the electron anisotropy drift contribution. Schindler and Hesse (2008) also showed $P_{e,\perp} > P_{e,||}$during the formation of a bifurcated current sheet (with a half-thickness of ~d_i) embedded in an initially wider (~$5d_i$) current sheet under quasisteady compression.

In our observation, we note the opposite electron anisotropy, $P_{e,||} > P_{e,\perp}$ throughout the current layer and most enhanced in the magnetospheric-side, sunward-exhaust region. This results in a significant contribution of the electron anisotropy current in supporting the bifurcated current along *n* direction (**Figure 4J**). A larger contribution from the diamagnetic current was observed in the magnetosheath-side, tailward-exhaust region (**Figures 4H–J**). Therefore, both the diamagnetic and electron anisotropy currents substantially support the bifurcated currents in the presence of density asymmetry and velocity shear.

A statistical study of the bifurcated current sheets using Cluster data (Thompson et al., 2006) indicated that the narrower the current sheets are, the more likely they are bifurcated. This, together with our present study, may suggest that the electrons play a major role in the formation of the bifurcated current sheet in both symmetric and asymmetric environment.

We investigated intense electrostatics waves that were predominantly observed on the magnetosheath side of the central current layer using linear kinetic analysis for selected timings, 1, 4, and 7 (**Figure 4K**). At timing 1 and 4, the electron distributions contain clear bi-directional beams with growing wave modes produced, while at timing 7 they show a plateau distribution with no growing mode wave. Still, large differences in the wave generation between timing 1 and 4 imply that various types of waves could be generated by the bi-directional beams that are ubiquitous in the KHV-induced reconnection sites (Wilder et al., 2016; Hwang et al., 2020).

Unlike the linear kinetic instability theory, we observed the electrostatic wave at timing 7. The waveforms at timing 7 (**Figures 5Ci**), however, indicate highly nonlinear waves. They are possibly propagated to the MMS location, after having been generated remotely. We also note that the first wave signature observed near "L" or 1 in **Figure 4K** corresponds to the location where the low-energy (cold) magnetosheath ion reaches after penetrating into the magnetospheric side, as indicated by the plasma density (black in **Figure 3C**) and the red arrow in **Figure 3H**.

Therefore, we speculate that ion may play an important role in generating different types of waves. According to Omura et al. (1996), ions could change types of generated waves depending on the ion temperature and the ion drift by interacting resonantly with waves generated by electrons or scattering electrons. As a result, various types of waves could be generated such as ion acoustic wave, electron solitary wave, electron hole, and Langmuir wave. Nonlinear wave mode and its evolution cannot be studied by linear analysis. Further study using kinetic simulation is required for understanding how ion dynamics affect nonlinear wave mode.

This observation, however, implies that the electrostatic waves observed predominantly in the magnetospheath side of the KHV boundary may pre-heat the cold magnetosheath population that is to participate into the reconnection process moving toward an X-line via/along the inflow/separatrix region. This may explain the higher-energy (200 eV < energy <2 keV) electrons streaming toward X along the magnetosheath-side separatrix region (red arrow in **Figure 3K**). Large Joule dissipation during the period of the enhanced wave activity (**Figure 4G**) also supports this two-step energization of the magnetosheath plasma entering into the magnetosphere *via* KHV-driven reconnection.

DATA AVAILABILITY STATEMENT

The datasets presented in this study can be found in online repositories. The names of the repository/repositories and accession number(s) can be found in the article/ Supplementary Material.

AUTHOR CONTRIBUTIONS

K-JH led the investigation including data analysis and interpretation, and produced the manuscript with Figures. KD, EC, LB, DS, CN, KN, and DBG participated in the data analysis. BG, YK, DJG, CP, RE, RT, CT, and RS provided the data, assisting the validation of the data use and interpretation. QS and DBG provided the analysis tool.

FUNDING

This study was supported, in part, by NASA's MMS project at SwRI, NSF AGS-1834451, NASA 80NSSC18K1534, 80NSSC18K0570, 80NSSC18K0693, and 80NSSC18K1337, and ISSI program: MMS and Cluster observations of magnetic reconnection. The MMS data used for the present study are accessible through the public link provided by the MMS science working group teams: http://lasp.colorado.edu/mms/sdc/public/. TN was supported by the Austrian Research Fund (FWF): P32175-N27.

ACKNOWLEDGMENTS

We acknowledge MMS FPI and Fields teams for providing data.

REFERENCES

Asano, Y., Mukai, T., Hoshino, M., Saito, Y., Hayakawa, H., and Nagai, T. (2003). Evolution of the Thin Current Sheet in a Substorm Observed by Geotail. *J. Geophys. Res.* 108. doi:10.1029/2002JA009785

Axford, W. I., and Hines, C. O. (1961). A Unifying Theory of High-Latitude Geophysical Phenomena and Geomagnetic Storms. *Can. J. Phys.* 39, 1433–1464. doi:10.1139/p61-172

Cassak, P. A., and Otto, A. (2011). Scaling of the Magnetic Reconnection Rate with Symmetric Shear Flow. *Phys. Plasmas* 18, 074501. doi:10.1063/1.3609771

Cassak, P. A., and Shay, M. A. (2007). Scaling of Asymmetric Magnetic Reconnection: General Theory and Collisional Simulations. *Phys. Plasmas* 14, 102114. doi:10.1063/1.2795630

Doss, C. E., Komar, C. M., Cassak, P. A., Wilder, F. D., Eriksson, S., and Drake, J. F. (2015). Asymmetric Magnetic Reconnection with a Flow Shear and Applications to the Magnetopause. *J. Geophys. Res. Space Phys.* 120, 7748–7763. doi:10.1002/2015JA021489

Dungey, J. W. (1961). Interplanetary Magnetic Field and the Auroral Zones. *Phys. Rev. Lett.* 6, 47–48. doi:10.1103/PhysRevLett.6.47

Egedal, J., Fox, W., Katz, N., Porkolab, M., Øieroset, M., Lin, R. P., et al. (2008). Evidence and Theory for Trapped Electrons in Guide Field Magnetotail Reconnection. *J. Geophys. Res.* 113, a–n. doi:10.1029/2008JA013520

Egedal, J., Øieroset, M., Fox, W., and Lin, R. P. (2005). In SituDiscovery of an Electrostatic Potential, Trapping Electrons and Mediating Fast Reconnection in the Earth's Magnetotail. *Phys. Rev. Lett.* 94. 025006. doi:10.1103/PhysRevLett.94.025006

Eriksson, S., Hasegawa, H., Teh, W.-L., Sonnerup, B. U. Ö., McFadden, J. P., Glassmeier, K.-H., et al. (2009). Magnetic Island Formation between Large-Scale Flow Vortices at an Undulating Postnoon Magnetopause for Northward Interplanetary Magnetic Field. *J. Geophys. Res.* 114, a–n. doi:10.1029/2008JA013505

Eriksson, S., Lavraud, B., Wilder, F. D., Stawarz, J. E., Giles, B. L., Burch, J. L., et al. (2016). Magnetospheric Multiscale Observations of Magnetic Reconnection Associated with Kelvin-Helmholtz Waves. *Geophys. Res. Lett.* 43, 5606–5615. doi:10.1002/2016GL068783.Received

Fairfield, D. H., Otto, A., Mukai, T., Kokubun, S., Lepping, R. P., Steinberg, J. T., et al. (2000). Geotail Observations of the Kelvin-Helmholtz Instability at the Equatorial Magnetotail Boundary for Parallel Northward fields Cm -3) with a Very Steady Northward Magnetic Experienced Multiple Crossings of a Boundary between a Dense. *J. Geophys. Res. Space Phys.* 105, 21159–21173. doi:10.1029/1999ja000316

Greco, A., Taktakishvili, A. L., Zimbardo, G., Veltri, P., and Zelenyi, L. M. (2002). Ion Dynamics in the Near-Earth Magnetotail: Magnetic Turbulence versus normal Component of the Average Magnetic Field. *J. Geophys. Res.* 107, 1–16. doi:10.1029/2002JA009270

Hasegawa, H., Fujimoto, M., Phan, T.-D., Rème, H., Balogh, A., Dunlop, M. W., et al. (2004). Transport of Solar Wind into Earth's Magnetosphere through Rolled-Up Kelvin-Helmholtz Vortices. *Nature* 430, 755–758. doi:10.1038/nature02799

Hasegawa, H., Retinò, A., Vaivads, A., Khotyaintsev, Y., André, M., Nakamura, T. K. M., et al. (2009). Kelvin-Helmholtz Waves at the Earth's Magnetopause: Multiscale Development and Associated Reconnection. *J. Geophys. Res.* 114, a–n. doi:10.1029/2009JA014042

Hwang, K.-J., Sibeck, D. G., Giles, B. L., Pollock, C. J., Gershman, D., Avanov, L., et al. (2016). The Substructure of a Flux Transfer Event Observed by the MMS Spacecraft. *Geophys. Res. Lett.* 43, 9434–9443. doi:10.1002/2016GL070934

Hwang, K. J., Dokgo, K., Choi, E., Burch, J. L., Sibeck, D. G., Giles, B. L., et al. (2020). Magnetic Reconnection inside a Flux Rope Induced by Kelvin-Helmholtz Vortices. *J. Geophys. Res. Space Phys.* 125, 1–16. doi:10.1029/2019JA027665

Hwang, K. J., Sibeck, D. G., Burch, J. L., Choi, E., Fear, R. C., Lavraud, B., et al. (2018). Small-Scale Flux Transfer Events Formed in the Reconnection Exhaust Region between Two X Lines. *J. Geophys. Res. Space Phys.* 123, 8473–8488. doi:10.1029/2018JA025611

Hwang, K. J., Sibeck, D. G., Choi, E., Chen, L. J., Ergun, R. E., Khotyaintsev, Y., et al. (2017). Magnetospheric Multiscale mission Observations of the Outer Electron Diffusion Region. *Geophys. Res. Lett.* 44, 2049–2059. doi:10.1002/2017GL072830

Jiang, L., and Lu, S. (2021). Externally Driven Bifurcation of Current Sheet: A Particle-In-Cell Simulation. *AIP Adv.* 11, 015001. doi:10.1063/5.0037770

Karimabadi, H., Pritchett, P. L., Daughton, W., and Krauss-Varban, D. (2003). Ion-ion Kink Instability in the Magnetotail: 2. Three-Dimensional Full Particle and Hybrid Simulations and Comparison with Observations. *J. Geophys. Res.* 108. doi:10.1029/2003JA010109

Kieokaew, R., Lavraud, B., Foullon, C., Toledo-Redondo, S., Fargette, N., Hwang, K. J., et al. (2020). Magnetic Reconnection inside a Flux Transfer Event-Like Structure in Magnetopause Kelvin-Helmholtz Waves. *J. Geophys. Res. Space Phys.* 125, e2019JA027527, 2020 . Available at:. doi:10.1029/2019JA027527

La Belle-Hamer, A. L., Otto, A., and Lee, L. C. (1995). *Magnetic Reconnection in the Presence of Sheared Flow and Density Asymmetry: Applications to the Earth's Magnetopause*.

Li, W., André, M., Khotyaintsev, Y. V., Vaivads, A., Graham, D. B., Toledo-Redondo, S., et al. (2016). Kinetic Evidence of Magnetic Reconnection Due to Kelvin-Helmholtz Waves. *Geophys. Res. Lett.* 43, 5635–5643. doi:10.1002/2016GL069192.Received

Lin, Y., and Lee, L. C. (1994). Structure of Reconnection Layers in the Magnetosphere. *Space Sci. Rev.* 65, 59–179. doi:10.1007/bf00749762

Moore, T. W., Nykyri, K., and Dimmock, A. P. (2016). Cross-scale Energy Transport in Space Plasmas. *Nat. Phys* 12, 1164–1169. doi:10.1038/nphys3869

Nakamura, T. K. M., Daughton, W., Karimabadi, H., and Eriksson, S. (2013). Three-dimensional Dynamics of Vortex-Induced Reconnection and Comparison with THEMIS Observations. *J. Geophys. Res. Space Phys.* 118, 5742–5757. doi:10.1002/jgra.50547

Nakamura, T. K. M., Hasegawa, H., Daughton, W., Eriksson, S., Li, W. Y., and Nakamura, R. (2017). Turbulent Mass Transfer Caused by Vortex Induced Reconnection in Collisionless Magnetospheric Plasmas. *Nat. Commun.* 8, 1–8. doi:10.1038/s41467-017-01579-0

Norgren, C., Graham, D. B., Khotyaintsev, Y. V., André, M., Vaivads, A., Hesse, M., et al. (2018). Electron Reconnection in the Magnetopause Current Layer. *J. Geophys. Res. Space Phys.* 123, 9222–9238. doi:10.1029/2018JA025676

Nykyri, K., and Otto, A. (2004). Influence of the Hall Term on KH Instability and Reconnection inside KH Vortices. *Ann. Geophys.* 22, 935–949. doi:10.5194/angeo-22-935-2004

Nykyri, K., Otto, A., Lavraud, B., Mouikis, C., Kistler, L. M., Balogh, A., et al. (2006). Cluster Observations of Reconnection Due to the Kelvin-Helmholtz Instability at the Dawnside Magnetospheric Flank. *Ann. Geophys.* 24, 2619–2643. doi:10.5194/angeo-24-2619-2006

Nykyri, K., and Otto, A. (2001). *Plasma Transport at the Magnetospheric Boundary Due to Reconnection in KelvimHe*. mholtz Vortices.

Omura, Y., Matsumoto, H., Miyake, T., and Kojima, H. (1996). Electron Beam Instabilities as Generation Mechanism of Electrostatic Solitary Waves in the Magnetotail. *J. Geophys. Res.* 101, 2685–2697. doi:10.1029/95ja03145

Paschmann, G., Daly, P. W., Robert, P., Roux, A., Harvey, C. C., Dunlop, M. W., et al. (1998). *Reprinted from Analysis Methods for Multi-Spacecraft Data Tetrahedron Geometric Factors 13.1 Introduction*.

Russell, C. T., Mellott, M. M., Smith, E. J., and King, J. H. (1983). Multiple Spacecraft Observations of Interplanetary Shocks: Four Spacecraft Determination of Shock Normals. *J. Geophys. Res.* 88, 4739–4748. doi:10.1029/ja088ia06p04739

Schindler, K., and Hesse, M. (2008). Formation of Thin Bifurcated Current Sheets by Quasisteady Compression. *Phys. Plasmas* 15, 042902. doi:10.1063/1.2907359

Scudder, J. D., Puhl-Quinn, P. A., Mozer, F. S., Ogilvie, K. W., and Russell, C. T. (1999). *Generalized Wal(n Tests through Alfvfn Waves and Rotational Discontinuities Using Electron Flow Velocities*.

Sergeev, V., Runov, A., Baumjohann, W., Nakamura, R., Zhang, T. L., Volwerk, M., et al. (2003). Current Sheet Flapping Motion and Structure Observed by Cluster. *Geophys. Res. Lett.* 30. doi:10.1029/2002GL016500

Shi, Q. Q., Shen, C., Dunlop, M. W., Pu, Z. Y., Zong, Q.-G., Liu, Z. X., et al. (2006). Motion of Observed Structures Calculated from Multi-point Magnetic Field Measurements: Application to Cluster. *Geophys. Res. Lett.* 33. doi:10.1029/2005GL025073

Shi, Q. Q., Shen, C., Pu, Z. Y., Dunlop, M. W., Zong, Q.-G., Zhang, H., et al. (2005). Dimensional Analysis of Observed Structures Using Multipoint Magnetic Field Measurements: Application to Cluster. *Geophys. Res. Lett.* 32, a–n. doi:10.1029/2005GL022454

Sitnov, M. I., Swisdak, M., Drake, J. F., Guzdar, P. N., and Rogers, B. N. (2004). A Model of the Bifurcated Current Sheet: 2. Flapping Motions. *Geophys. Res. Lett.* 31, a–n. doi:10.1029/2004GL019473

Sonnerup, B., and Scheible, M. (1998). Minimum and Maximum Variance Analysis. Anal. Methods Multi-Spacecr. Data 001, 185–220. Available at: http://www.issibern.ch/forads/sr-001-08.pdf%0Ahttp://ankaa.unibe.ch/forads/sr-001-08.pdf.

Swisdak, M., Opher, M., Drake, J. F., and Alouani Bibi, F. (2010). The Vector Direction of the Interstellar Magnetic Field outside the Heliosphere. *ApJ* 710, 1769–1775. doi:10.1088/0004-637X/710/2/1769

Swisdak, M. (2016). Quantifying Gyrotropy in Magnetic Reconnection. *Geophys. Res. Lett.* 43, 43–49. doi:10.1002/2015GL066980

Swisdak, M., Rogers, B. N., Drake, J. F., and Shay, M. A. (2003). Diamagnetic Suppression of Component Magnetic Reconnection at the Magnetopause. *J. Geophys. Res.* 108, 1–10. doi:10.1029/2002JA009726

Tanaka, K. G., Fujimoto, M., and Shinohara, I. (20102010). Physics of Magnetopause Reconnection: A Study of the Combined Effects of Density Asymmetry, Velocity Shear, and Guide Field. *Int. J. Geophys.* 2010, 1–17. doi:10.1155/2010/202583

Thompson, S. M., Kivelson, M. G., El-Alaoui, M., Balogh, A., Réme, H., and Kistler, L. M. (2006). Bifurcated Current Sheets: Statistics from Cluster Magnetometer Measurements. *J. Geophys. Res.* 111, 1–26. doi:10.1029/2005JA011009

Wilder, F. D., Ergun, R. E., Schwartz, S. J., Newman, D. L., Eriksson, S., Stawarz, J. E., et al. (2016). Observations of Large-Amplitude, Parallel, Electrostatic Waves Associated with the Kelvin-Helmholtz Instability by the Magnetospheric Multiscale mission. *Geophys. Res. Lett.* 43, 8859–8866. doi:10.1002/2016GL070404.Received

Xie, H.-s. (2019). BO: A Unified Tool for Plasma Waves and Instabilities Analysis. *Comp. Phys. Commun.* 244, 343–371. doi:10.1016/j.cpc.2019.06.014

Yoon, P. H., Drake, J. F., and Lui, A. T. (1996). Theory and Simulation of Kelvin-Helmholtz Instability in the Geomagnetic Tail. *J. Geophys. Res.* 101, 27 327–27 339. doi:10.1029/96ja02752

Yoon, Y. D., Yun, G. S., Wendel, D. E., and Burch, J. L. (2021). Collisionless Relaxation of a Disequilibrated Current Sheet and Implications for Bifurcated Structures. *Nat. Commun.* 12, 1–8. doi:10.1038/s41467-021-24006-x

Zelenyi, L. M., Malova, H. V., Popov, V. Y., Delcourt, D., Sharma, A. S., and Foss, S. (2004). Nonlinear Equilibrium Structure of Thin Currents Sheets: Influence of Electron Pressure Anisotropy. *Nonlin. Process. Geophys.* 11, 579–587. doi:10.5194/npg-11-579-2004

Conflict of Interest: CP was employed by company Denali Scientific, LLC.

The remaining authors declare that the research was conducted in the absence of any commercial or financial relationships that could be construed as a potential conflict of interest.

The handling editor declared a past co-authorship with several of the authors DG, YK, and RE.

Publisher's Note: All claims expressed in this article are solely those of the authors and do not necessarily represent those of their affiliated organizations, or those of the publisher, the editors and the reviewers. Any product that may be evaluated in this article, or claim that may be made by its manufacturer, is not guaranteed or endorsed by the publisher.

frontiers in Astronomy and Space Sciences

ORIGINAL RESEARCH
published: 05 November 2021
doi: 10.3389/fspas.2021.758312

Control of Magnetopause Flux Rope Topology by Non-local Reconnection

Lars Mejnertsen[1]*, *Jonathan P. Eastwood*[1] *and Jeremy P. Chittenden*[2]

[1]*Space and Atmospheric Physics Group, Blackett Laboratory, Imperial College London, London, United Kingdom,* [2]*Plasma Physics Group, Blackett Laboratory, Imperial College London, London, United Kingdom*

Dayside magnetic reconnection between the interplanetary magnetic field and the Earth's magnetic field is the primary mechanism enabling mass and energy entry into the magnetosphere. During favorable solar wind conditions, multiple reconnection X-lines can form on the dayside magnetopause, potentially forming flux ropes. These flux ropes move tailward, but their evolution and fate in the tail is not fully understood. Whilst flux ropes may constitute a class of flux transfer events, the extent to which they add flux to the tail depends on their topology, which can only be measured *in situ* by satellites providing local observations. Global simulations allow the entire magnetospheric system to be captured at an instant in time, and thus reveal the interconnection between different plasma regions and dynamics on large scales. Using the Gorgon MHD code, we analyze the formation and evolution of flux ropes on the dayside magnetopause during a simulation of a real solar wind event. With a relatively strong solar wind dynamic pressure and southward interplanetary magnetic field, the dayside region becomes very dynamic with evidence of multiple reconnection events. The resulting flux ropes transit around the flank of the magnetosphere before eventually dissipating due to non-local reconnection. This shows that non-local effects may be important in controlling the topology of flux ropes and is a complicating factor in attempts to establish the overall contribution that flux ropes make in the general circulation of magnetic flux through the magnetosphere.

Keywords: flux rope, reconnection, flux transfer events, magnetosphere (magnetospheric configuration and dynamics), global modelling

OPEN ACCESS

Edited by:
Xochitl Blanco-Cano, National Autonomous University of Mexico, Mexico

Reviewed by:
Huishan Fu, Beihang University, China
Tieyan Wang, Rutherford Appleton Laboratory, United Kingdom

***Correspondence:**
Lars Mejnertsen
lars.mejnertsen10@imperial.ac.uk

Specialty section:
This article was submitted to Space Physics, a section of the journal Frontiers in Astronomy and Space Sciences

Received: *13 August 2021*
Accepted: *04 October 2021*
Published: *05 November 2021*

Citation:
Mejnertsen L, Eastwood JP and Chittenden JP (2021) Control of Magnetopause Flux Rope Topology by Non-local Reconnection. Front. Astron. Space Sci. 8:758312. doi: 10.3389/fspas.2021.758312

INTRODUCTION

Magnetic reconnection is an important process in driving the dynamics of the Earth's magnetosphere (*e.g.* Eastwood et al., 2017 and references therein). When the interplanetary magnetic field (IMF) is southward (IMF $B_z < 0$), it allows for enhanced plasma entry into the magnetosphere by opening up magnetic field lines on the dayside and closing on the nightside (Dungey, 1961). In reality, reconnection is inherently three-dimensional and non-steady (Fu et al., 2015; Wang et al., 2020), causing the formation of Flux Transfer Events (FTEs). They are thought to transfer magnetic flux and hence energy into the magnetosphere when they are "open": connected to either of the planet's poles and to the IMF. Though the origin and evolution of FTEs are not fully understood, they have been observed to have a significant effect on magnetospheric dynamics and space weather.

FTEs are identified in spacecraft observations by their characteristic bipolar signature in magnetic field data, typically in the component normal to the magnetopause surface (Farrugia et al., 2016; Russell & Elphic, 1978). This signature may be indicative of rotational magnetic field structures called

flux ropes. While flux ropes exist in a variety of locations, such as on the solar surface or within coronal mass ejections, FTEs are specifically flux ropes generated on at the Earth's magnetopause, and range from $0.6R_E$ to $4.4R_E$ in size (Fear et al., 2007) They consist of twisted magnetic field structures which can persist due to their force-free nature. Furthermore, they typically contain plasma features due to reconnection (hot and high velocity plasma populations), variation in the magnetic field strength (Fear et al., 2008; Paschmann et al., 1982), and force-free magnetic fields (Farrugia et al., 2016).

With the majority of FTEs observed on the dayside, little is known about their transition around the magnetosphere. The prevailing theory is that once reconnection forms an FTE, it is accelerated along the magnetopause surface towards the cusps by the $\vec{J} \times \vec{B}$ force (Fedder et al., 2002; Russell & Elphic, 1978). However, FTEs have been observed far into the magnetotail ($x \simeq 67\ R_E$), where their axis has been rotated from aligned in the azimuthal direction (parallel to the $x_{GSE} - y_{GSE}$ plane) to aligned with the z_{GSE} axis (Eastwood et al., 2012).

One of the main difficulties in understanding FTEs and their impact is due to the relative sparseness of spacecraft observations. Multi-spacecraft missions such as the Magnetospheric Multiscale Mission (MMS), Time History of Events and Macro-scale Interactions during Substorms (THEMIS), and Cluster have improved our understanding of FTE size and motion (Farrugia et al., 2016; Fear et al., 2005, Fear et al., 2008). In an FTE observed by MMS, it was found that there were two distinct electron populations within the FTE: one characteristic of originating from the magnetosphere, and the other from the magnetosheath, suggesting a single FTE can have a complex magnetic topology (Kacem et al., 2018). Whilst auroral signatures of FTEs have been observed, they are rarely accompanied with a spacecraft in the correct position to observe the FTE structure. Hence, global simulations of the magnetosphere, which capture the magnetosphere as a whole, can be very useful in understanding a number of FTE features, giving insights into their formation, evolution, topology and impact on the magnetosphere.

A number of papers have used global simulations to study FTEs and flux ropes. Though it is known that MHD cannot capture the full physics required for reconnection, it has been shown that global simulations do capture the location of reconnection at the dayside magnetopause relatively well (Komar et al., 2015). Raeder (2006) used OpenGGCM to investigate the effect of dipole tilt on the generation of FTEs. Under a strongly southward IMF, the FTEs were formed by multiple x-line reconnection, and was modulated by the dipole tilt. Cardoso et al. (2013)'s simulation of a steady, strong South- and duskward IMF, found elbow-shaped flux tubes. Other flux tubes were found to be interlinked with field lines of different topology. Perez et al. (2018) further reported a study showing a number of flux ropes spontaneously forming under constant solar wind parameters.

The majority of simulations studying this problem have used idealized solar wind events, with inflow parameters usually kept constant. In this article, the Gorgon code (Ciardi et al., 2007; Mejnertsen et al., 2016, 2018) is used to simulate flux ropes that are formed in response to a real interval of strongly southward IMF solar wind as observed by ACE and Cluster on March 31, 2001 (Maksimovic et al., 2003). By using a global simulation approach, the full three-dimensional structure of different flux ropes are found as a function of time. This allows their properties to be established, and their generation, transport and fate to be studied. Furthermore, their magnetic topology can be calculated, from which the amount of flux transferred into the magnetosphere can be inferred. The manuscript is organized as follows. In *Methodology*, we discuss the methodology, including the Gorgon MHD code and the properties of the solar wind on the day of interest. *Overview of the Event Simulation* provides an overview of the Simulation, and *Identification of Flux Ropes Through Field Line Tracing and Topology Mapping* describes in detail the methodology used to identify and study flux ropes at the magnetopause. *Results* presents the results of the flux rope analysis, and conclusions are summarized in *Conclusion*.

METHODOLOGY

The Gorgon MHD Code

In this work, we simulate the magnetosphere using the Gorgon 3D magnetohydrodynamic code. Gorgon was initially developed for studying high energy, collisional plasma interactions such as Z-pinches (Chittenden et al., 2004; Jennings, 2006; Jennings et al., 2010), laser-plasma interactions (Smith et al., 2007) and magnetic tower jets (Ciardi et al., 2007), but has recently been adapted to simulate planetary magnetospheres and their interaction with the solar wind (Desai et al., 2021; Eggington et al., 2020; Mejnertsen et al., 2016, 2018).

Gorgon uses a fully explicit, Eulerian formulation of the resistive MHD equations for a fully ionized hydrogen plasma, as given by **Equations 1 to 6**:

$$\frac{\partial \rho}{\partial t} + \vec{\nabla} \cdot \left(\rho \vec{v}\right) = 0, \tag{1}$$

$$\frac{\partial}{\partial t}\rho\vec{v} + \left(\vec{v} \cdot \vec{\nabla}\right)\rho\vec{v} = -\vec{\nabla}\left(P_e + P_p\right) + \vec{J} \times \vec{B}, \tag{2}$$

$$\frac{\partial \varepsilon_p}{\partial t} + \vec{\nabla} \cdot \left(\varepsilon_p \vec{v}\right) = -P_p \vec{\nabla} \cdot \vec{v} - \Delta_{pe}, \tag{3}$$

$$\frac{\partial \varepsilon_e}{\partial t} + \vec{\nabla} \cdot \left(\varepsilon_e \vec{v}\right) = -P_e \vec{\nabla} \cdot \vec{v} + \eta\left|\vec{J}\right|^2 - \Lambda + \Delta_{pe}, \tag{4}$$

$$\frac{\partial^2 \vec{A}}{\partial t^2} = -c^2 \vec{\nabla} \times \vec{\nabla} \times \vec{A} + \frac{\vec{J}}{\epsilon_0}, \tag{5}$$

$$\text{where } \eta\vec{J} = -\frac{\partial \vec{A}}{\partial t} + \vec{v} \times \vec{B}. \tag{6}$$

These equations describe the conservation of mass (1), momentum (2), proton energy (3), electron energy (4), the magnetic induction equation (5) and Ohms law (6), where ρ is the mass density, $\vec{v}$ is the bulk plasma flow, $P_{p,e}$ is the proton and electron pressure, $\vec{J}$ is the current density, $\vec{B}$ is the magnetic field, $\varepsilon_{p,e}$ is the ion and electron energy density and η is the plasma resistivity.

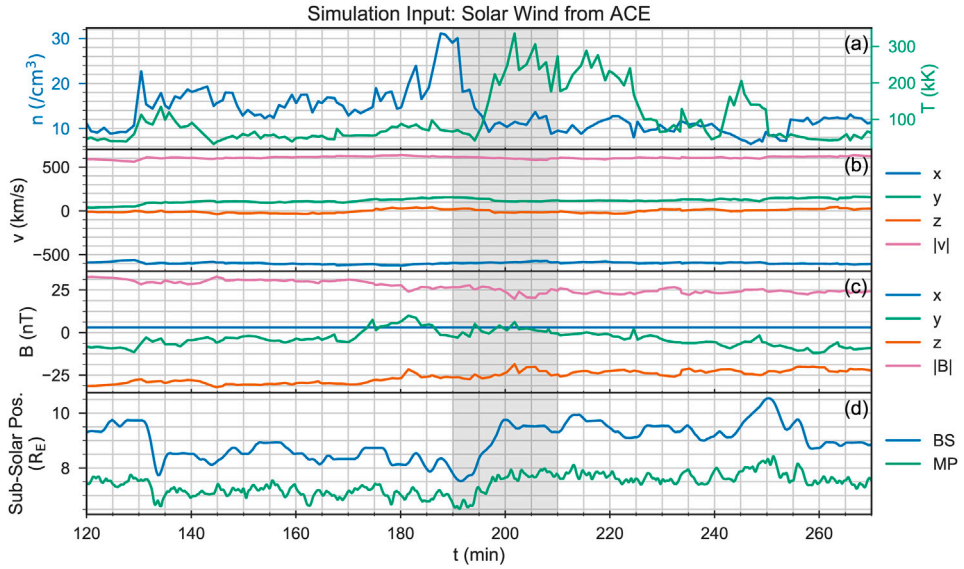

FIGURE 1 | The solar wind input to the simulation, and the position of the bow shock and magnetopause in response. The shaded region denotes the region of interest during this chapter.

Because of its roots in high energy plasma physics, the MHD formulation in Gorgon is atypical. Firstly, it treats the electron and proton energy equations separately (**Equations 3**, **4**), allowing them to be out of thermodynamic equilibrium. These equations include terms for Ohmic heating $\eta|\vec{J}|^2$, optically thin radiation losses Λ, and electron-proton energy exchange Δ_{pe}. In the parameter regime of magnetospheric space plasmas, these terms are negligible, and hence have been disabled in the code or are also negligibly small. The pressure is calculated using the ideal gas law, with $\gamma = 5/3$. It makes use of second Order Van Leer advection to solve the advection terms in **Equations 1**-**6**. It also employs a variable timestep which automatically satisfies the relevant Courant conditions.

Secondly, the magnetic field solver uses the vector potential representation of the magnetic field, on a staggered grid (Yee, 1966). This allows the magnetic divergence condition to be satisfied automatically to machine accuracy, without using divergence cleaning algorithms. It also allows the electromagnetic fields to propagate through a vacuum. In the code, a vacuum is defined by a threshold density, below which plasma properties forces are set to zero. Here, the fields propagate as vacuum solutions to Maxwell's Equations.

Space plasmas are in general collisionless, meaning they have a very small resistivity and a broad applicability of the "frozen-in" flux theorem. Under ideal MHD, a process such as reconnection should not occur, as the fields cannot disassociate from the plasma. In numerical simulations, there is a numerical resistivity which allows the magnetic field to reconnect. This is dependent on the size of the grid. Whilst Gorgon is a resistive MHD code, this resistivity has been set to the Spitzer resistivity, which is lower than the numerical resistivity. A common approach in reconnection studies in global MHD simulations is to apply an anomalous resistivity (Komar et al., 2015), and has been found necessary when simulating substorms (Raeder et al., 2001). However, numerous simulations (Raeder, 2006; Cardoso et al., 2013; Perez et al., 2018) have shown that flux ropes can form with numerical resistivity, and anomalous resistivity has no impact on dayside reconnection (Raeder, 2006).

In this work, we use the same simulation as in Mejnertsen et al. (2018). We simulate a region spanning $x_{GSE} = (-50, 30)R_E$, $y_{GSE} = (-20, 20)R_E$ and $z_{GSE} = (-30, 30)R_E$, with a uniform grid resolution of $0.2\,R_E$. The solar wind is applied on the sunward boundary of simulation domain, with von-Neumann conditions on all other boundaries.

MARCH 31, 2001

The work in this article also uses the same solar wind parameters as in Mejnertsen et al. (2018), from March 31, 2001 17:14:00 – 19:34:00 UT. This interval was the subject of a case study by Maksimovic et al. (2003), who used four spacecraft Cluster observations to characterize the motion of the bow shock in response to variation in the solar wind inflow. Whereas Mejnertsen et al. (2018) focused on the motion of the outer boundaries over the whole 2 hour period, but reduced to the ecliptic and noon-midnight plane, in this chapter the focus is on the formation of FTEs over a shorter 20 min timeframe. For this, the full three-dimensional state of the simulation is sampled at 10 s intervals.

The full solar wind input to the simulation is shown in **Figure 1**. However, now the focus is on the analysis interval from $t = 190$ min to 210 min as is indicated by the grey shaded region. The start of the simulated period (t = 0) is 15:14:00 UTC,

and so this corresponds to 18:24:00 – 18:44:00 UTC. During this time, the solar wind number density drops from 30 /cm^3 to 10 /cm^3, as seen in panel (a). The solar wind speed stays constant at approximately 600 km/s (panel b). However, there is a significant v_y component, averaging approximately 100 km/s. The strength of the IMF (panel 3) was larger than typical IMF strength, ranging between 20 nT and 25 nT. The dominating IMF component is the B_z component, with B_z starting at approximately −30 nT and reducing in magnitude slightly near the end. During this interval, the B_y component drops to approximately zero. With a negligibly small constant B_x, the IMF is predominantly southward, with no dawn-dusk component. The final panel 4) shows the sub-solar magnetopause and bow shock positions, as calculated by the methods in Mejnertsen et al. (2018). As expected, the reduction of solar wind number density causes the magnetopause distance to increase, from approximately 6.5 R_E to 7.5 R_E. This causes the bow shock position to also increase in distance. The magnetopause position is much more variable than the bow shock position (Mejnertsen et al., 2018).

OVERVIEW OF THE EVENT SIMULATION

We first discuss the overall dynamics of the magnetopause during the 20 min interval of interest. The plasma number density in the ecliptic plane is shown in **Figure 2** at 1.5 min intervals from t = 190 min to 206.5 min. The solar wind streaming in from the left of each subplot first passes through the bow shock, shown by the increase in mass density. It flows around the magnetopause, which corresponds to the sharp cut-off in mass density. The magnetopause and bow shock are approximately conical, but oriented at an angle to the Sun-Earth line: this is due to the significant v_y component in the solar wind. At t = 190 min (panel 1), the magnetopause appears relatively smooth: there are only a few small structures, indicated by the bulges in the sharp density cut-off corresponding to the magnetopause. At this time, the solar wind number density is also at its highest, leading to the bow shock and magnetopause being most compressed, with a relatively thin magnetosheath. As time increases, the solar wind number density decreases, as can be seen by the decreasing magnitude of the color bar scales. This increases the magnetopause and bow shock standoff distances, and increases the magnetosheath width, which is most easily seen by comparing panels 1, 4, 7 and 10. As the number density decreases, more coherent structure forms on the magnetopause. On the dawn side, $y_{GSE} < 0$, there is a rippling of the magnetopause surface (indicated by the white dotted ellipse on **Figure 2**) which persists throughout each panel in **Figure 2** with varying amplitude. On the dusk side, $y_{GSE} > 0$, distinct bulges in the plasma can be seen propagating down the flanks of the magnetopause; an example of one is shown in **Figure 2** by the white dotted ellipse. These bulges are much more sporadic and intermittent than on the dawn side. An example of these bulges can be seen at t = 193 min, at position x = 5 R_E, y = 10 R_E, which propagates along the magnetopause surface before disappearing in the tail.

This same variability in the structure of the magnetosphere can also be seen in the current density magnitude, as shown in **Figure 3**. The magnetopause current density magnitude is largest in the sub-solar region, and decreases down the flanks. Many of the structures seen in the number density (**Figure 2**) are also visible here. On the dawn side, the same oscillatory feature can be seen (indicated by the white dotted circle on **Figure 3**), as well as the bulges moving down the dusk-side flank. More structure can also be seen on the sub-solar magnetopause. For example, at t = 194.5 min (panel 4), the magnetopause current sheet exhibits local variations in current density strength.

Figure 2 and **Figure 3** show that there are dynamic processes occurring on the magnetopause surface, which propagate down the flanks of the magnetosphere. We now discuss these features in more detail, finding that they are in fact caused by flux ropes associated with magnetic reconnection on the dayside magnetopause. We now describe the methodology used to identify flux ropes in the simulation before examining their properties in more detail.

IDENTIFICATION OF FLUX ROPES THROUGH FIELD LINE TRACING AND TOPOLOGY MAPPING

In order to visualize magnetic field lines and understand the features of the magnetopause, in particular to identify flux ropes, streamlines are calculated from the magnetic field vector field. This is performed for two reasons. The first is to establish the existence of flux ropes based on identifying twisted field line structures, and the second is to examine flux rope topology. Flux ropes may be open (connected at one end to the ionosphere with the other end in the solar wind), closed (connected at both ends to either the ionosphere), or entirely contained within the solar wind.

The quality of stream-tracing is heavily dependent on its starting (seed) point. By under-sampling the magnetic field, visualizations can miss vital structure and dynamics. Ideally, there would be multiple seed points for every grid cell to ensure that every flux rope of interest is captured. In typical simulation grid sizes, this is computationally prohibitive. To render stream-tracing feasible, it is only performed in regions of interest, such as on the dayside or the nightside flank, as is shown in **Figure 4**.

Since global simulations provide the full three-dimensional path of field lines, their topology can be found by categorizing the field line according to their end point location. In cases where both ends of the field line reaches the outer boundary, the field line is said to be part of the IMF, and is colored red. When both ends of the field line touch the inner boundary, it is said to be closed, and is colored blue. Open field lines occur when one end connects to the inner boundary, and the other to the outer boundary. Open field lines are further classified by which pole they reach: North (magnetic South) is purple, and South (magnetic North) is green. The final type of field line identified by the algorithm are so-called incomplete field lines, where one or both ends do not reach a simulation boundary. Computationally, the stream-tracer assign a finite number of

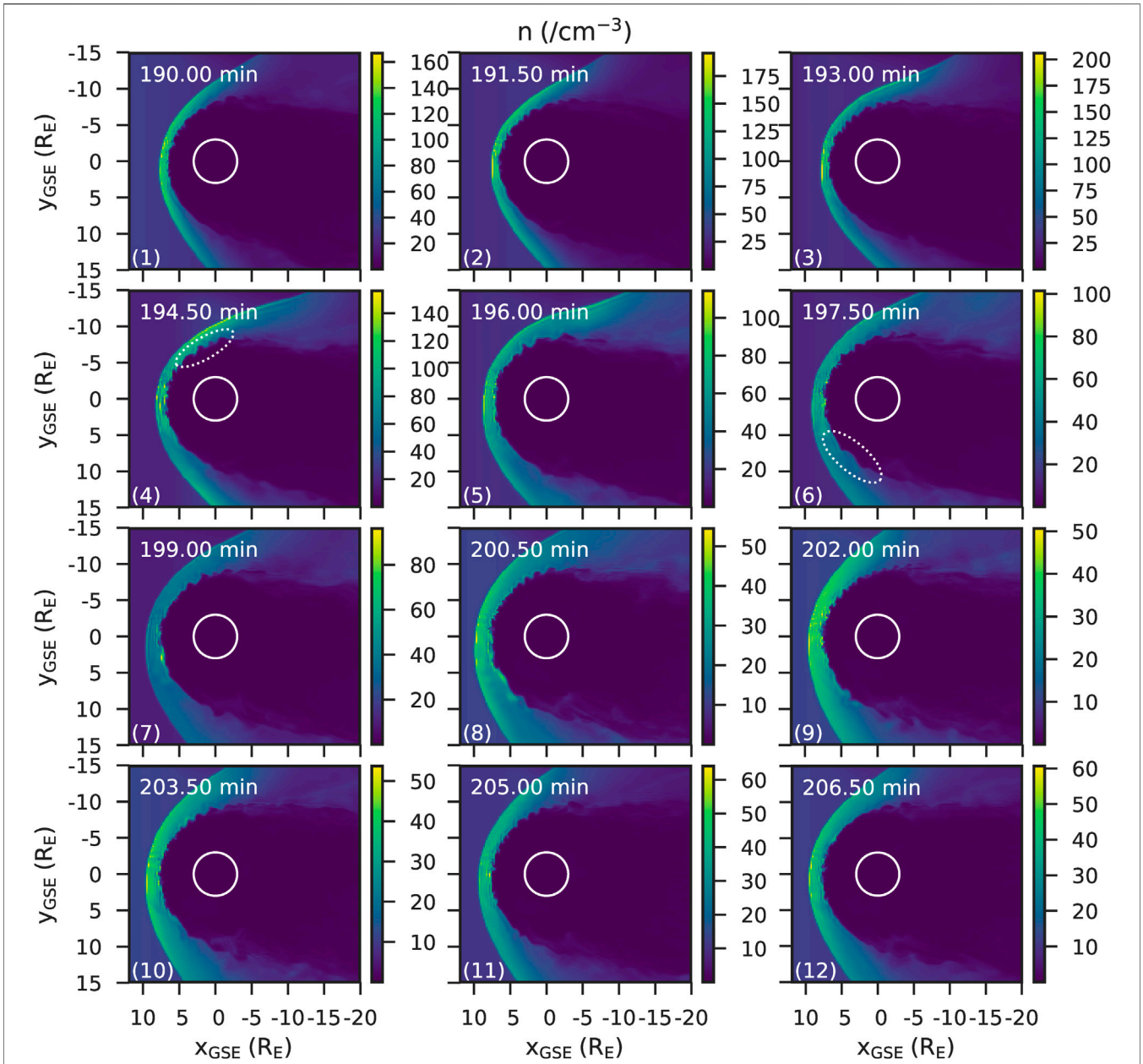

FIGURE 2 | The number density in the ecliptic plane every 1.5 min from t = 190 min to t = 206.5 min. The number density color bar scale changes every timestep. With the solar wind streaming from the left, the sharp increase in number density to the left denotes the bow shock. The brightly colored region after it is the magnetosheath. The subsequent sharp decrease moving to the right is the magnetopause. The white circle is the inner boundary of the simulation, of radius 3 R_E.

steps to the streamline, so when the field line has not reached a boundary, it has likely run out of steps.

In order to filter out flux ropes from background magnetic field lines, the amount a field line twists or rotates is also computed. This measure of twist provides a way to isolate the twisted flux rope fields. The total rotation, Λ, is given by the angle between subsequent magnetic field directions along a field line,

$$\Lambda = \sum_i \cos^{-1}\Big(- \hat{B}(s_i) \cdot \hat{B}(s_i + \Delta s)\Big),$$

where s is the path along the field line and Δs is the stream-tracer step size. A perfectly straight field line will thus have $\Lambda = 0$. A perfectly circular field line will have $\Lambda = 2\pi = 360°$ after completing one revolution.

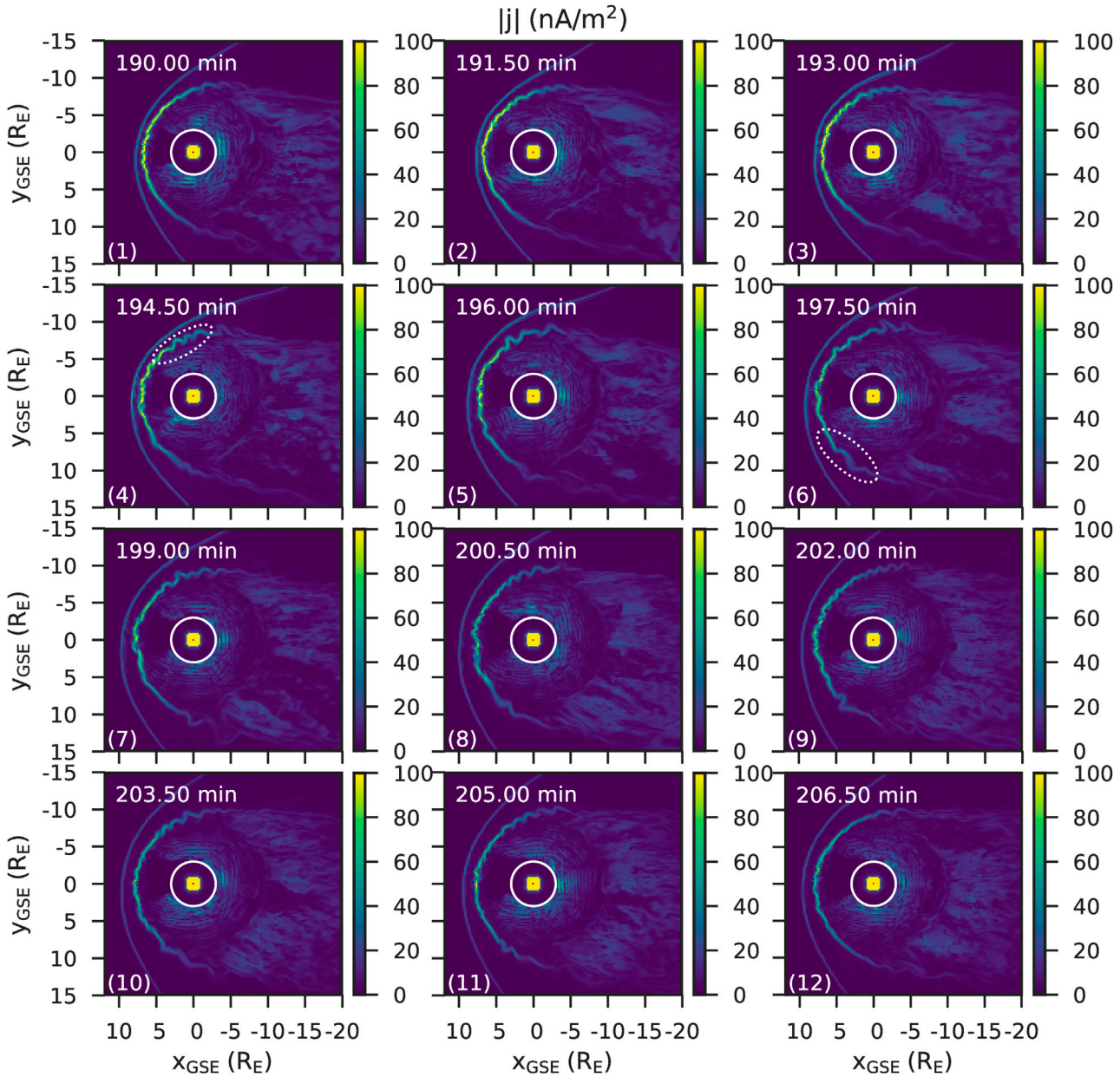

FIGURE 3 | The magnitude of the current density in the ecliptic plane every 1.5 min from t = 190 min to 206.5 min. As with **Figure 2**, the solar wind streams from the left. The compression of the magnetic field through the bow shock is shown as the left most current density peak. The magnetopause current sheet follows shortly after. Rather than a simple conical shape, it has oscillatory and transient structures. In the magnetotail, the white circle is the inner boundary of the simulation, of radius 3 R_E. The subsequent sharp decrease moving to the right is the magnetopause.

We note that the computation time can be decreased even further by removing the need to store every point in the field line and saving only the large-scale properties of each field line. This is used in topology mapping, where, for every seed point of interest, the field line is calculated to determine where it is connected to. An example of this is shown by the slice shown in **Figure 4**: a streamline is calculated from every position on that slice, and its topology is saved. This is then visualized on the slice.

By combining the topology mapping algorithm with calculations of the total rotation, Λ, regions where flux ropes have formed can be identified. Visualizing only field lines which exhibit flux rope characteristics gives a clearer picture of flux rope dynamics, whilst also finding all the flux ropes which meet the rotation criterion. The general method in plotting these flux ropes is as follows. For every timestep, the total rotation is calculated at cells in the simulation grid in the region of interest (e.g. the dayside). For each seed point where

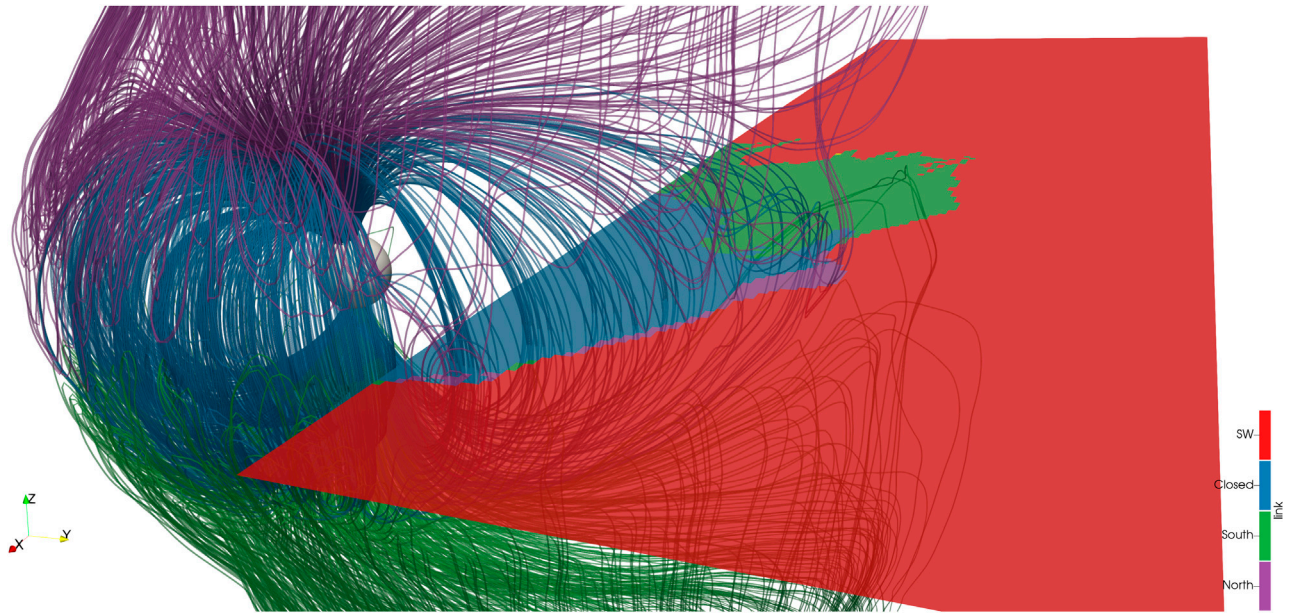

FIGURE4 | An example of field line tracing and topology mapping. The magnetic field lines are colored by their topology: red for solar wind, blue for closed, green for open field lines connected to the South pole (magnetic North) and purple for open field lines connected to the North pole (magnetic South). The solar wind (red) field lines, which would dominate the view, have been filtered out. The slice shows the magnetic topology of cells along the ecliptic plane ($\boldsymbol{z}_{GSE} = 0$): i.e. field lines connected to the red region are solar wind field lines, and map to the outer boundary of the simulation.

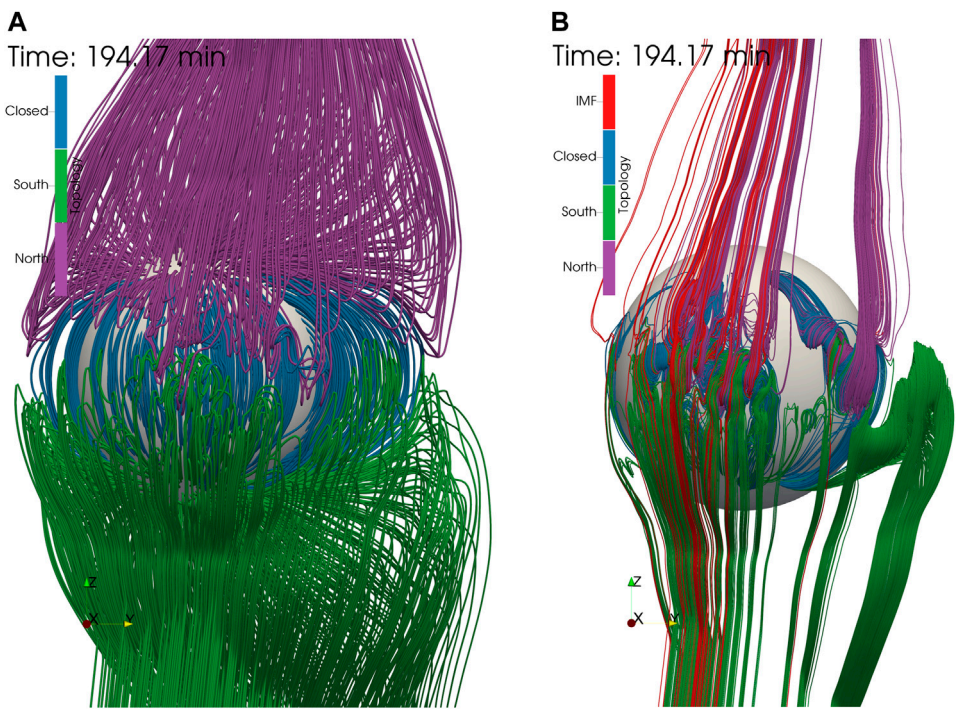

FIGURE 5 | By filtering field lines by rotation, flux rope structure can more easily be seen. Panel **(A)** shows field lines drawn from a regular spherical grid. Panel **(B)** shows field lines drawn from positions on the simulation grid with a high enough rotation, $\Lambda > 8\pi$.

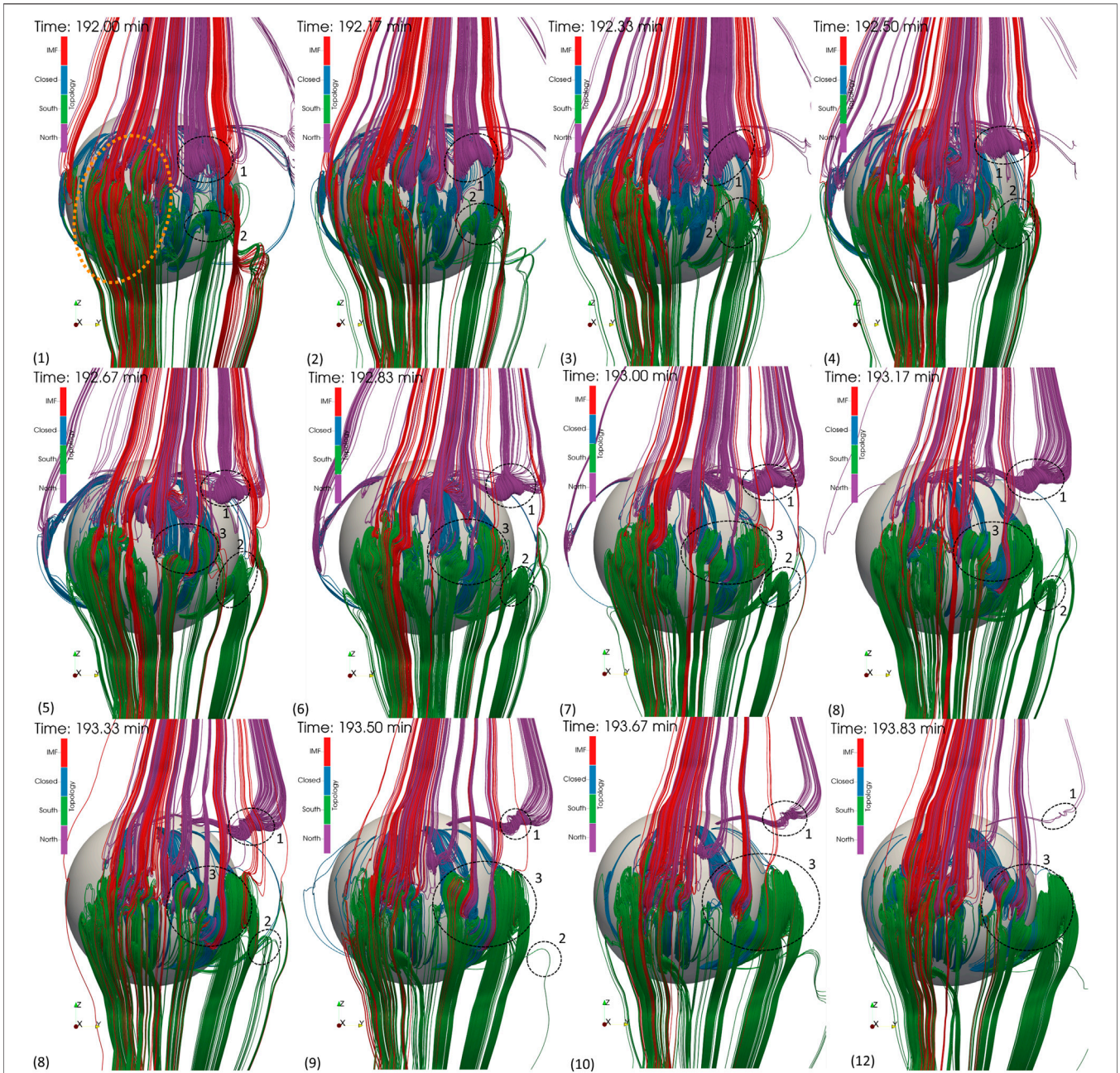

FIGURE 6 | Flux Ropes generated on the dayside magnetopause. With each panel, time increases by 10 s field lines are filtered by their total rotation, showing only flux rope like structures on the magnetopause surface. Behind the flux ropes is a 6 R_E reference sphere. The dayside reconnection region (shown in orange in panel 1), creates a complicated mix of flux ropes. Out of this, a number of distinct flux rope like structures emerge, as denoted by the ellipses marked 1, 2 and 3, which travel down the dusk flank.

the Λ is large enough, usually $\Lambda > 8\pi$, their field line is drawn and its topology calculated. The threshold value of 8π was chosen through trial-and-error, as it allowed for effective filtering of non flux rope like field lines (e.g. draped field lines in the magnetosheath), whilst still including flux rope structures.

An illustration of the method is shown in **Figure 5**. In panel a, the field lines are drawn using seeds spread on a uniform spherical grid. Whilst it does show some structure - for example, the magnetic separator can be inferred by the region separating the South (green) from the North (purple) field lines, it is difficult to see flux ropes, and the IMF has been filtered out as otherwise it would obscure the view of the magnetopause. In contrast, panel b shows the field lines filtered by the rotation method. Flux ropes can more easily be seen, and since the IMF field is not filtered out, examples of all four field topologies is visible.

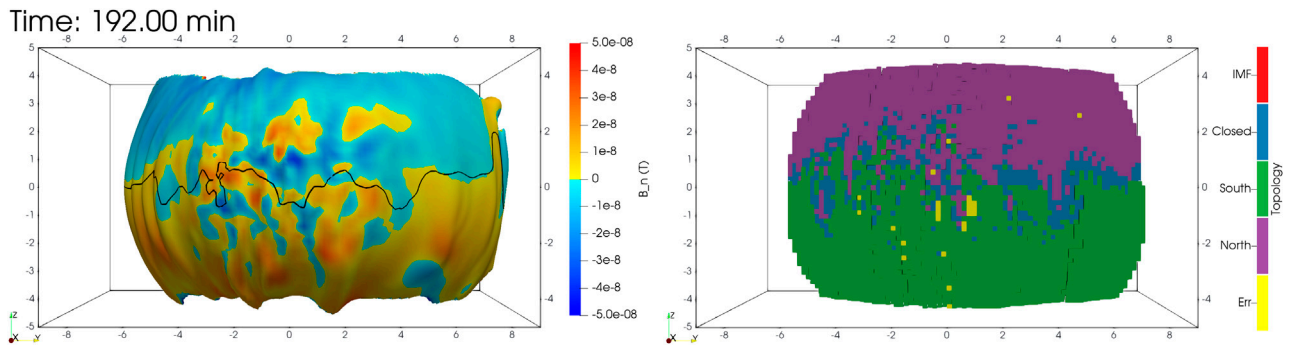

FIGURE 7 | A view of the magnetopause from the magnetosheath, showing its magnetic field properties and plasma motion, and potential regions of reconnection and plasma. The left panel **(A)** shows the $\boldsymbol{B_z} = 0$ contour, coloured by the magnetic field strength normal to the surface, $\boldsymbol{B_n}$. The black line denotes the $\boldsymbol{v_z} = 0$ line: above the line, $\boldsymbol{v_z} > 0$, below $\boldsymbol{v_z} < 0$. The right panel **(B)** shows the magnetic topology of each simulation cell. IMF field lines (red) have been filtered out.

RESULTS

Generation of Flux Ropes on the Dayside Magnetopause

Using the flux rope identification method described previously, **Figure 6** shows the existence of flux ropes on the dayside magnetopause during the interval of interest. As in *Identification of Flux Ropes Through Field Line Tracing and Topology Mapping*, magnetic field lines are colored by their topology: red for IMF, blue for closed, purple for open and connected to the North pole, and green for open and connected to the South pole. The reconnection region, approximately denoted by the orange ellipse in **Figure 6**, shows a complex entanglement of open, closed and IMF field lines, which can vary significantly over the 10 s time period. Out of the tangled reconnection region, distinct flux ropes propagate out along the magnetopause surface, predominantly along the dawn and dusk directions. They are generated with the flux rope axis parallel to the azimuthal direction, as is expected. These flux ropes start off relatively small, approximately 2 R_E long in the azimuthal direction, and $\sim 1\ R_E$ wide.

From the first timestep at $t = 192$ min (panel **Figure 6**), two flux ropes have already formed (flux ropes 1 and 2), indicated by the black dashed ellipses. These are on opposite sides of the ecliptic plane: flux rope 1 is predominantly purple, indicating it is connected to the Northern pole, whilst flux rope two is predominantly green and is connected to the Southern pole. At $t > 192.33$ min (panels 1–3), both flux ropes are intertwined with closed field lines. This can best be seen in flux rope two in panel 2, which shows a blue strip wrapping around the green field lines. As time progresses, the closed field line region disappears, and the flux ropes move around the dusk flank toward higher latitudes.

At a later time $t = 192.67\ min$ (panel 5) a large-scale magnetic structure emerges from the dayside reconnection region, labelled as flux rope 3. This flux rope is complex in structure: it consists of a core of closed field lines (blue), around which open field lines are wrapped. The flux rope core magnetic field of closed magnetic field strength bends in a "U" shape, which is due to a velocity shear in the z direction which kinks the flux rope. Eventually, the "U" shape breaks, forming two flux ropes of different connectivity (**Figure 6**). As it travels toward the dusk flank, the South connected flux rope increases in azimuthal extent, whereas the North connected flux rope stays relatively small, and trails the South connected flux rope. Both flux ropes still have a core of closed magnetic field.

To make sense of the magnetopause reconnection region, the magnetopause surface is plotted in **Figure 7**. In panel (a), a three-dimensional iso-contour at $B_z = 0$ denotes the magnetopause surface. It is coloured by the magnetic field strength normal to the iso-contour surface, with the black line showing where $v_z = 0$. The $v_z = 0$ line is highly warped. Panel 2) shows the magnetic topology, filtering out the IMF field. Regions of closed field lines (blue) denotes places where reconnection could occur, since these have direct contact with the IMF. These regions tend to be clustered together in multiple lines, suggesting the multiple x-line reconnection is occurring.

Flux Rope Evolution

Figure 8 shows a three-dimensional view of the dusk flank of the magnetopause. Two flux ropes are tracked, flux ropes 3 and 4, which due to their differing topology evolve differently as they travel down the flanks.

Flux rope 3, first seen in **Figure 6**, moves down the flank for approximately 6 min until it begins to dissipate at $t \sim 198$ min between **Figure 8** and **Figure 8** reaches the tail reconnection region. As it travels down the flank, it increases in size along the flux rope axis. The axis of flux rope three for both North- and South-open sections remains parallel to the ecliptic plane throughout the simulation.

Flux rope four can be seen being generated in **Figure 8**, and contains a mix of all types of topology: closed, IMF, North- and South-open. Unlike flux rope 3, the two regions of opposite open topology do not separate, but remain as one flux rope. As flux rope four travels down the flank, its axis rotates from being in the ecliptic plane, to parallel to the z axis. It also increases in size along the flux rope axis. At the end, **Figure 8**, flux rope four is seen to only consist of IMF, and becomes less twisted.

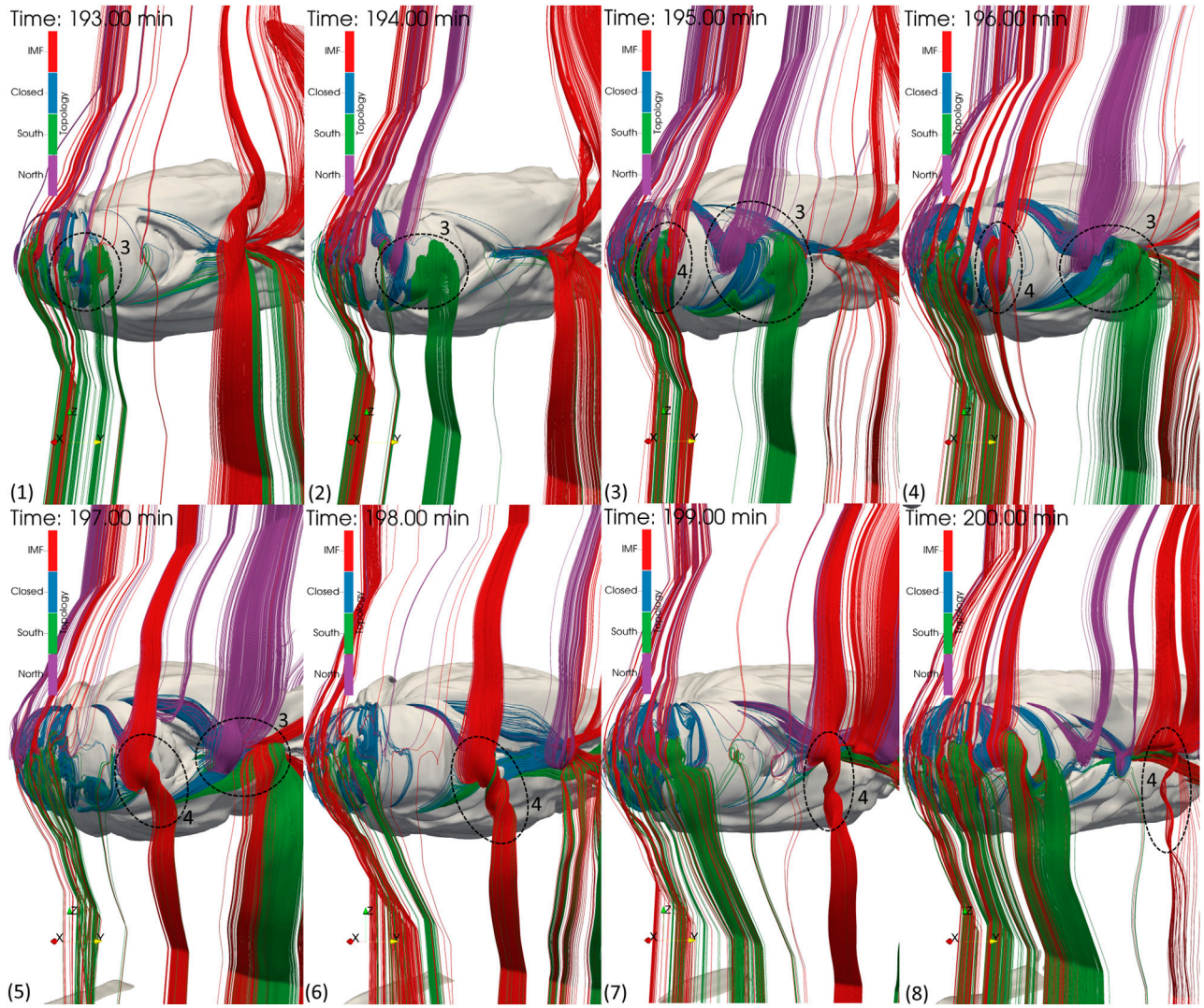

FIGURE 8 | Flux ropes travelling down the dusk flank. With each panel, time increases by 1 min. Magnetic field lines are filtered by their total rotation, showing only flux rope like structures on the magnetopause surface. To filter out the inner magnetosphere, a number density contour of $1/cm^3$ is shown. The dayside reconnection region (shown in orange in panel 1), creates a complicated mix of flux ropes. Flux ropes three and four are tracked as they propagate down the dusk flank.

Both flux ropes three and four behave differently as they travel down the flank due to their differing magnetic topology. However, both flux ropes dissipate shortly after reaching the nightside reconnection region. This can be seen in **Figure 9**, which shows slices of the simulation in the ecliptic plane as flux ropes three and four reach the tail reconnection region, with each row increasing in time by 30 s. The first column 1) shows current density magnitude, the middle 2) shows the total rotation of the magnetic field, and the right 3) shows the magnetic topology of the slice. In the topology plots (column c), the closed field line region can be seen by the blue region. The green region, connected to the South pole, essentially shows the tail reconnection region. The flank magnetopause is the region duskward of the blue and green regions, which coincides with the current sheet shown in column (a). Flux ropes three and four are shown as islands of purple, North connected, magnetic field lines, marked with circles.

Row 1 shows flux rope four just approaching the tail reconnection region, where blue meets green (panel 1c). 30 s later, in row 2, the purple region has disappeared replaced by red. However, the flux rope is still there, as seen by the structure in the current (2a), as the high amount of rotation (2b). As time increases (rows three–5), flux rope four remains connected to the IMF, but continues to be twisted, as shown in column b be its enhanced total rotation. Its total rotation does decrease with time, suggesting the flux rope is unravelling.

A similar process occurs with flux rope 3, except that the open field line region persists long after the reconnection region. In the

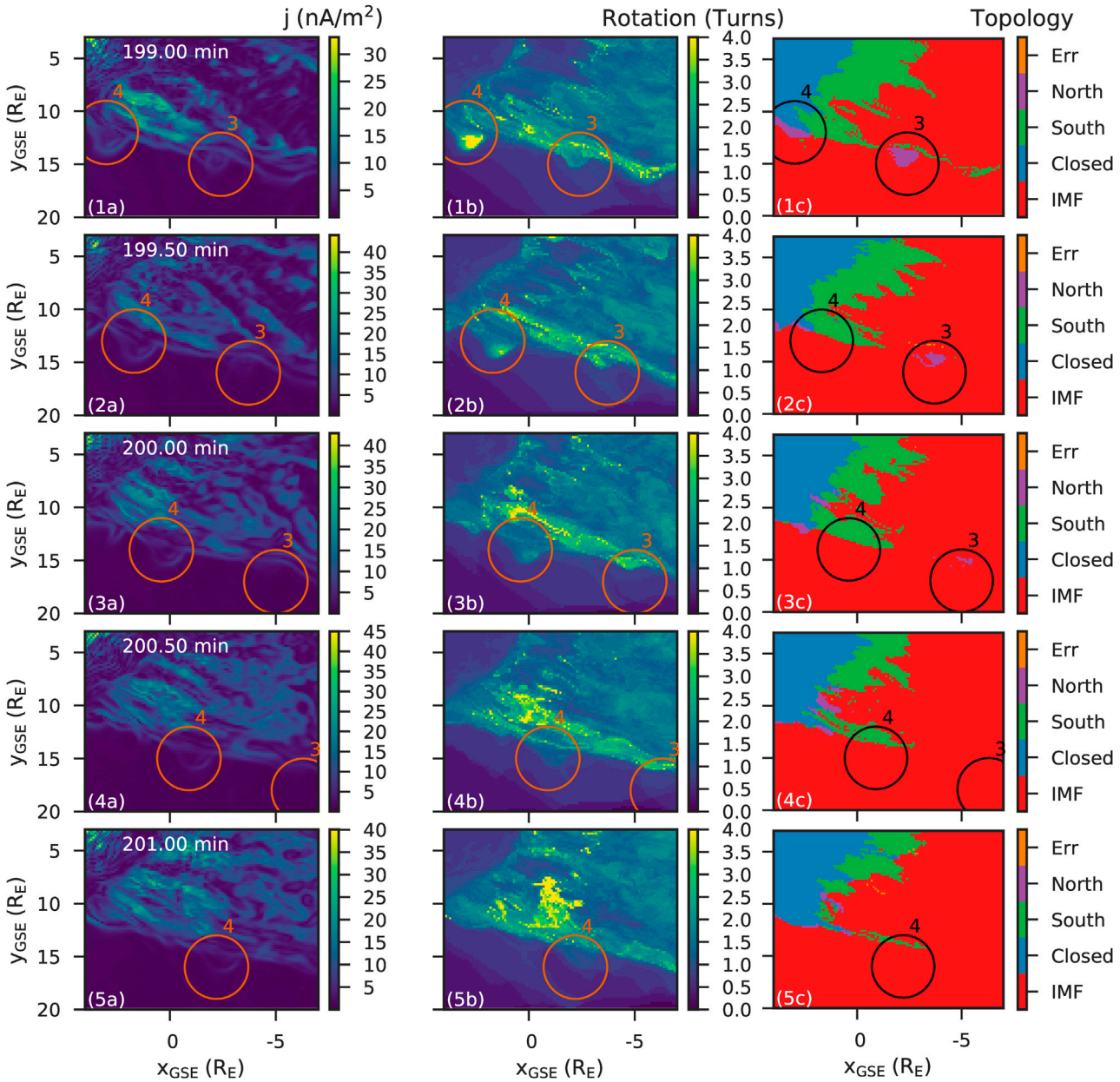

FIGURE 9 | The dissipation of flux ropes past the nightside reconnection region. Each panel shows a slice in the ecliptic plane $\boldsymbol{z}_{GSE} = 0$. With each row, time increases by 30 s. The left column **(A)** shows current density magnitude, the middle **(B)** the total rotation of the magnetic field, and the right **(C)** the magnetic topology.

first timestep shown in **Figure 9**, the purple, open field region has already passed the reconnection region. In subsequent time-steps, the purple region appears to dissipate, converting to red (IMF). This is due to the same reason as flux rope 4: reconnection occurs in the tail reconnection region, upstream of the flux rope rather than at the flux rope.

This process is shown in **Figure 10**. Viewing the dusk magnetotail from the $+x_{GSE}$, $+y_{GSE}$, $+z_{GSE}$ direction, the field lines from flux rope three are shown, as well as closed field lines near the Earth. These field lines have not been filtered by total rotation. Flux rope three is manually tracked through the simulation and seed points chosen which encompass flux rope 3, denoted by the circles labelled three in **Figure 9**. In order to see the open field lines in the flux rope, the IMF field lines (red) start off transparent, but become opaque at $t = 200$ min when the flux rope contains no more open field lines. The closed field lines are generated from a grid in the $y_{GSE} - z_{GSE}$ plane, at $x = -5\ R_E$, and only show the closed field lines (open and IMF field lines have been filtered out).

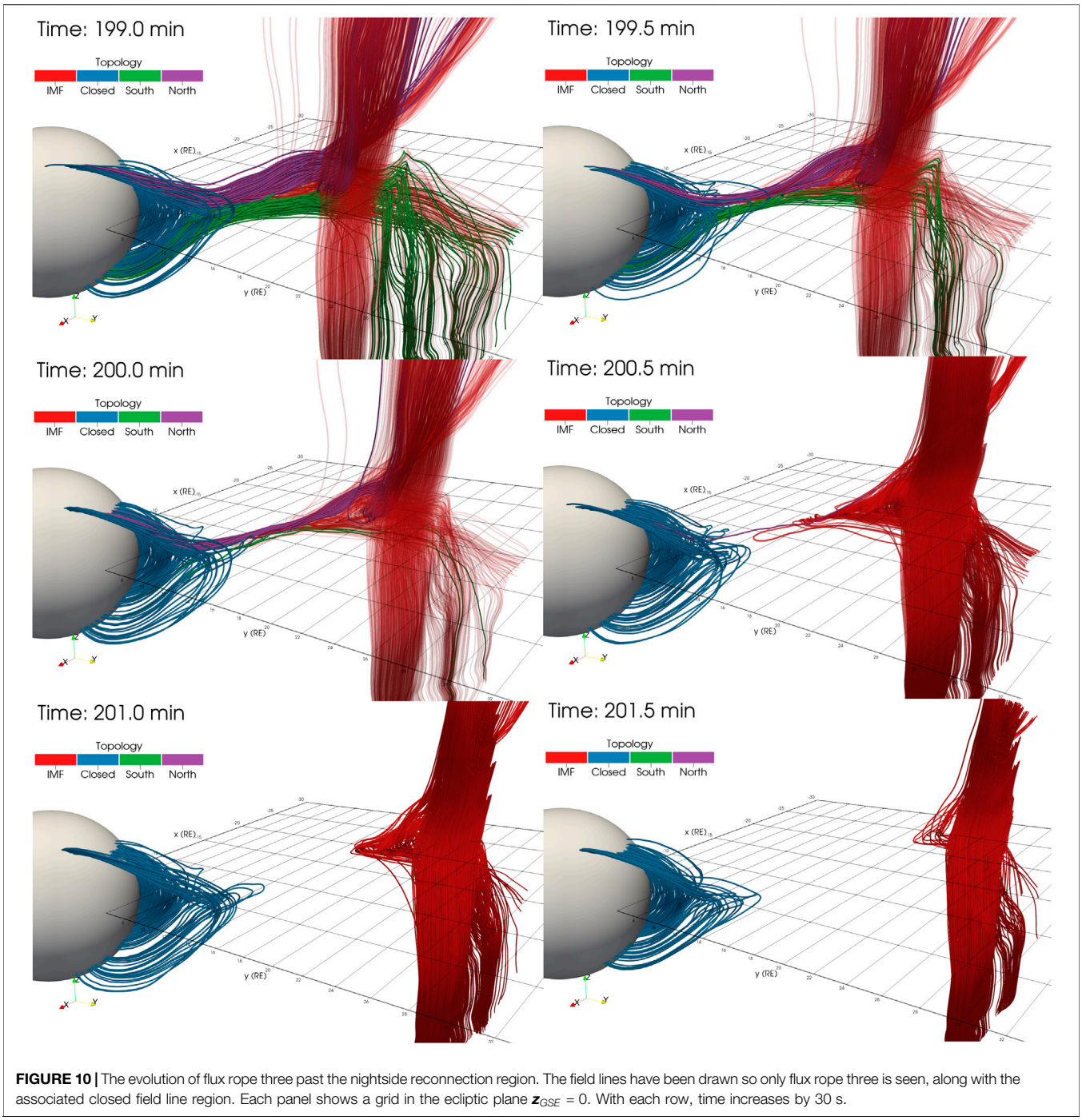

FIGURE 10 | The evolution of flux rope three past the nightside reconnection region. The field lines have been drawn so only flux rope three is seen, along with the associated closed field line region. Each panel shows a grid in the ecliptic plane $\boldsymbol{z}_{GSE} = 0$. With each row, time increases by 30 s.

In **Figure 10**, two main field line regions are shown: the flux rope and the closed field line region. In between there are elongated field lines with a large B_x component, containing both open (green and purple), closed (blue) and IMF (red) field lines. As time progresses from $t = 199$ min to $t = 200.5$ min, the number of field lines in this region decreases, making the region thinner. At the same time, the amount of open field lines in the flux rope is decreasing. This indicates that the flux rope is changing topology, reconnecting in between the flux rope and the closed field line region. This is supported in **Figure 9** which shows field line rotation (9.4b) but open topology (9.4c) at flux rope 3. At $t = 200.5$ min, the flux rope detaches completely from the planetary field, as is indicated by the now red field lines. These field lines still stretch from the flux rope, back to the reconnection site indicating the reconnection site occurred far from the actual flux rope.

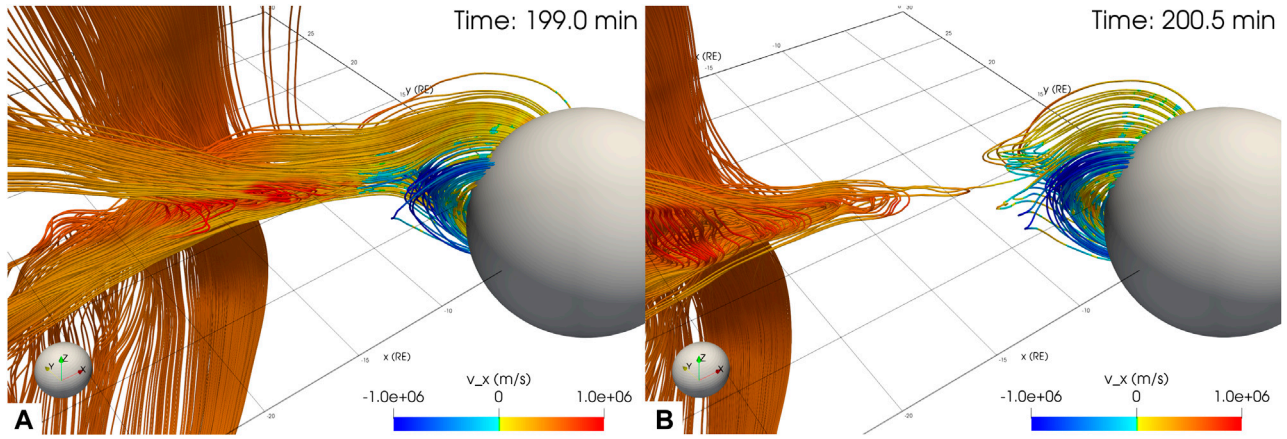

FIGURE 11 | The dissipation of flux ropes past the nightside reconnection region. Each panel is 1.5 min apart, and shows a view onto the dusk magnetotail of flux rope three.

Figure 11 shows the same field lines and sphere as **Figure 10**, except that they are colored by the plasma v_x and the view is onto dusk magnetotail from the $-x_{GSE}$, $-y_{GSE}$, $+z_{GSE}$. At the earlier time, t = 199 min, the flux rope is still attached to the planet. However, there is an enhanced v_x component in the $-x_{GSE}$ direction on the field lines in ellipse 1, and similarly, enhanced positive v_x on the closed field line region in ellipse 2. This suggests that reconnection is occurring, accelerating the plasma *via* the $\vec{J} \times \vec{B}$ force. At the later time, t = 200.5 min, the flux rope has completely reconnected, losing connectivity with the planet, with the same signature in v_x as the earlier time.

CONCLUSION

In this work, we have studied the evolution of flux ropes generated by a real solar wind event using the Gorgon global MHD simulation. The event, observed by Cluster on 2001-03-31, creates several flux ropes on the dayside, which propagate along magnetopause flanks. These flux ropes were identified using a novel magnetic field line filtering method based on computing their total rotation. While the method allowed for effective identification of tightly wound flux ropes, it may miss smaller flux ropes.

The flux ropes are formed on the dayside magnetopause surface, where the strongly southward IMF reconnects with the magnetospheric field. Overlapping the highly warped magnetopause current layer, there exists a complex interlaced set of field lines whose topologies vary from closed to open to completely IMF. This is due to time-dependent reconnection along multiple x-lines on the magnetopause. Out of this complex interwoven dayside field region emerge stand-alone flux ropes which propagate along the magnetopause surface. However, the latitude of their path is dependent on their topology. Flux ropes which are completely open - they are solely connected to a single pole (North/purple or South/green) - tend to move along the magnetopause at high latitudes. These flux ropes would be the equivalent to the classic flux rope evolution picture where they move towards the cusps. No flux ropes were observed to go directly over the cusps.

Flux ropes containing both closed and open field lines connected to both the North and South poles were also generated on the dayside and remain along the ecliptic plane at low latitudes throughout their evolution. In the classic cusp flux rope picture, the $\vec{J} \times \vec{B}$ force acts to move the flux rope over the poles. Since this flux rope is connected to both poles, the two opposite curvature forces cancel out, carrying it along ecliptic plane in the direction of the magnetosheath plasma flow. The flux ropes were found to be force free, with the thermal pressure balancing the $\vec{J} \times \vec{B}$ force. These flux ropes move along the duskward flanks toward the tail, with their axis remaining parallel to the z direction as they move along the flank. However, once they move past the terminator, field lines present in the flux rope begin to reconnect non-locally in the nightside magnetotail current sheet. This alters the topology of the flux rope, detaching it from the magnetosphere. The flux rope-like structure then persists until unravelling ~1 min later.

This behavior is interesting because it shows that flux rope topology can change during its lifetime as a consequence of reconnection at locations far from the flux rope itself. It may also suggest that flux ropes on the flanks of the magnetopause may be more likely to be topologically disconnected from the ionosphere, (although this is tensioned against a possibly shorter lifetime). FTEs have previously been shown to create ionospheric signatures (e.g. Sandholt et al. (1986); Milan et al. (1999); Wild et al. (2001); Fear *et al.* (2009)), and so these ionospheric signatures may only partially represent the magnetopause dynamics, particularly away from the dayside. This behavior has further implications for the amount of flux that flux ropes transfer into the magnetosphere. Further work is required to establish how common these changes in topology are for different solar wind conditions, so as to better constrain the extent to which flux rope topologies observed on the dayside correspond to those subsequently found on the nightside.

In the simulated event, no flux ropes were found to transit along the dawnward flank. One potential reason for this is that the flux ropes on the dawnside magnetopause exhibit a total rotation of less than the threshold 8π, and were filtered out. The other reason could be due to the specific solar wind conditions, whose combination of solar wind and IMF parameters could predispose the flux ropes to transit along the duskward flanks. To fully determine the impact of solar wind and IMF parameters on the direction of transit, a thorough study of different solar wind conditions should be performed.Resistivity is an important aspect in simulating reconnection events and flux rope dynamics. In the Gorgon code, a low resistivity is inherent in the simulation due to numerical resistivity caused by the grid resolution. Previous studies of reconnection in Global MHD simulations have found that enhanced resistivity, either through coarse grid resolutions or an artificial resistivity, prevents the formation of FTEs and causes them to diffuse away rapidly (Komar et al., 2013; Raeder, 2006). With the introduction of an artificial resistivity in the Gorgon code, we would expect similar results with fewer flux ropes generated. Those that do generate are likely to dissipate due to resistive diffusion: this is likely unphysical due to the collisionless nature of magnetospheric plasmas.

One potentially fruitful avenue for future work may be to focus on comparing multi-spacecraft observations of flux ropes (e.g. MMS, THEMIS and Cluster) with global simulations using the same solar wind input, particularly where the local topology can be measured. This would allow the evolution of flux rope topology to be explored experimentally. These results may also be relevant for the SMILE mission, where imaging of the dayside magnetopause is expected to shed new light on the role of flux ropes and FTEs in global magnetospheric dynamics.

DATA AVAILABILITY STATEMENT

The raw data supporting the conclusions of this article will be made available by the authors, without undue reservation.

AUTHOR CONTRIBUTIONS

LM generated the data using the simulation code and analysed the data to produce the results presented. JE provided valuable insight into the direction of the work and its impact. JC is one of the authors of the Gorgon simulation code and provided valuable insight into the validity of the results within the context of the simulation.

FUNDING

The authors acknowledge support from UKRI Natural Environment Research Council (NERC) Grants NE/P017142/1 (SWIGS) and NE/P017347/1 (Rad-Sat). LM also acknowledges the support of UKRI Science and Technology Facilities Council (STFC) Studentship ST/M503538/1.

ACKNOWLEDGMENTS

This work used the Imperial College London High Performance Computing Service (doi: 10.14469/hpc/2232).

REFERENCES

Cardoso, F. R., Gonzalez, W. D., Sibeck, D. G., Kuznetsova, M., and Koga, D. (2013). Magnetopause Reconnection and Interlinked Flux Tubes. *Ann. Geophys.* 31 (10), 1853–1866. doi:10.5194/angeo-31-1853-2013

Chittenden, J. P., Lebedev, S. V., Jennings, C. A., Bland, S. N., and Ciardi, A. (2004). X-ray Generation Mechanisms in Three-Dimensional Simulations of Wire Array Z-Pinches. *Plasma Phys. Control Fusion* 46 (12B), B457–B476. doi:10.1088/0741-3335/46/12B/039

Ciardi, A., Lebedev, S. V., Frank, A., Blackman, E. G., Chittenden, J. P., Jennings, C. J., et al. (2007). The Evolution of Magnetic tower Jets in the Laboratory. *Phys. Plasmas* 14 (5), 056501. doi:10.1063/1.2436479

Desai, R. T., Freeman, M. P., Eastwood, J. P., Eggington, J. W. B., Archer, M. O., Shprits, Y. Y., et al. (2021). Interplanetary Shock-Induced Magnetopause Motion: Comparison between Theory and Global Magnetohydrodynamic Simulations. *Geophys. Res. Lett.* 48. doi:10.1029/2021GL092554

Dungey, J. W. (1961). Interplanetary Magnetic Field and the Auroral Zones. *Phys. Rev. Lett.* 6 (2), 47–48. doi:10.1103/PhysRevLett.6.47

Eastwood, J. P., Nakamura, R., Turc, L., Mejnertsen, L., and Hesse, M. (2017). The Scientific Foundations of Forecasting Magnetospheric Space Weather. *Space Sci. Rev.* 212 (3–4), 1221–1252. doi:10.1007/s11214-017-0399-8

Eastwood, J. P., Phan, T. D., Fear, R. C., Sibeck, D. G., Angelopoulos, V., Øieroset, M., et al. (2012). Survival of Flux Transfer Event (FTE) Flux Ropes Far along the Tail Magnetopause. *J. Geophys. Res.* 117 (A8), a–n. doi:10.1029/2012JA017722

Eggington, J. W. B., Eastwood, J. P., Mejnertsen, L., Desai, R. T., and Chittenden, J. P. (2020). Dipole Tilt Effect on Magnetopause Reconnection and the Steady-State Magnetosphere-Ionosphere System: Global MHD Simulations. *J. Geophys. Res. Space Phys.* 125 (7). doi:10.1029/2019JA027510

Farinas Perez, G., Cardoso, F. R., Sibeck, D., Gonzalez, W. D., Facskó, G., Coxon, J. C., et al. (2018). Generation Mechanism for Interlinked Flux Tubes on the Magnetopause. *J. Geophys. Res. Space Phys.* 123 (2), 1337–1355. doi:10.1002/2017JA024664

Farrugia, C. J., Lavraud, B., Torbert, R. B., Argall, M., Kacem, I., Yu, W., et al. (2016). Magnetospheric Multiscale Mission Observations and Non-force Free Modeling of a Flux Transfer Event Immersed in a Super-alfvénic Flow. *Geophys. Res. Lett.* 43 (12), 6070–6077. doi:10.1002/2016GL068758

Fear, R. C., Fazakerley, A. N., Owen, C. J., and Lucek, E. A. (2005). A Survey of Flux Transfer Events Observed by Cluster during Strongly Northward IMF. *Geophys. Res. Lett.* 32 (18), a–n. doi:10.1029/2005GL023811

Fear, R. C., Milan, S. E., Fazakerley, A. N., Fornaçon, K.-H., Carr, C. M., and Dandouras, I. (2009). Simultaneous Observations of Flux Transfer Events by THEMIS, Cluster, Double Star, and SuperDARN: Acceleration of FTEs. *J. Geophys. Res.* 114 (10), a–n. doi:10.1029/2009JA014310

Fear, R. C., Milan, S. E., Fazakerley, A. N., Lucek, E. A., Cowley, S. W. H., and Dandouras, I. (2008). The Azimuthal Extent of Three Flux Transfer Events. *Ann. Geophys.* 26 (8), 2353–2369. doi:10.5194/angeo-26-2353-2008

Fear, R. C., Milan, S. E., Fazakerley, A. N., Owen, C. J., Asikainen, T., Taylor, M. G. G. T., et al. (2007). Motion of Flux Transfer Events: a Test of the Cooling Model. *Ann. Geophys.* 25 (7), 1669–1690. doi:10.5194/angeo-25-1669-2007

Fedder, J. A., Slinker, S. P., Lyon, J. G., and Russell, C. T. (2002). Flux Transfer Events in Global Numerical Simulations of the Magnetosphere. *J. Geophys. Res.* 107 (A5), 1–11. doi:10.1029/2001JA000025

Fu, H. S., Vaivads, A., Khotyaintsev, Y. V., Olshevsky, V., André, M., Cao, J. B., et al. (2015). How to Find Magnetic Nulls and Reconstruct Field Topology with MMS Data?. *J. Geophys. Res. Space Phys.* 120 (5), 3758–3782. doi:10.1002/2015JA021082

Jennings, C. A., Cuneo, M. E., Waisman, E. M., Sinars, D. B., Ampleford, D. J., Bennett, G. R., et al. (2010). Simulations of the Implosion and Stagnation of

Compact Wire Arrays. *Phys. Plasmas* 17 (9), 092703. doi:10.1063/1.3474947

Jennings, C. A. (2006). *Radiation Transport Effects in Wire Array Z Pinches and Magneto-Hydrodynamic Modelling Techniques*. Doctoral dissertation. Imperial College London.

Kacem, I., Jacquey, C., Génot, V., Lavraud, B., Vernisse, Y., Marchaudon, A., et al. (2018). Magnetic Reconnection at a Thin Current Sheet Separating Two Interlaced Flux Tubes at the Earth's Magnetopause. *J. Geophys. Res. Space Phys.*, 1–15. doi:10.1002/2017JA024537

Kane Yee, K. (1966). Numerical Solution of Initial Boundary Value Problems Involving maxwell's Equations in Isotropic media. *IEEE Trans. Antennas Propagat.* 14 (3), 302–307. doi:10.1109/TAP.1966.1138693

Komar, C. M., Cassak, P. A., Dorelli, J. C., Glocer, A., and Kuznetsova, M. M. (2013). Tracing Magnetic Separators and Their Dependence on IMF Clock Angle in Global Magnetospheric Simulations. *J. Geophys. Res. Space Phys.* 118 (8), 4998–5007. doi:10.1002/jgra.50479

Komar, C. M., Fermo, R. L., and Cassak, P. A. (2015). Comparative Analysis of Dayside Magnetic Reconnection Models in Global Magnetosphere Simulations. *J. Geophys. Res. Space Phys.* 120 (1), 276–294. doi:10.1002/2014JA020587

Maksimovic, M., Bale, S. D., Horbury, T. S., and André, M. (2003). Bow Shock Motions Observed with CLUSTER. *Geophys. Res. Lett.* 30 (7), 41–46. doi:10.1029/2002GL016761

Mejnertsen, L., Eastwood, J. P., Chittenden, J. P., and Masters, A. (2016). Global MHD Simulations of Neptune's Magnetosphere. *J. Geophys. Res. Space Phys.* 121 (8), 7497–7513. doi:10.1002/2015JA022272

Mejnertsen, L., Eastwood, J. P., Hietala, H., Schwartz, S. J., and Chittenden, J. P. (2018). Global MHD Simulations of the Earth's Bow Shock Shape and Motion under Variable Solar Wind Conditions. *J. Geophys. Res. Space Phys.* 123 (1), 259–271. doi:10.1002/2017JA024690

Milan, S. E., Lester, M., Greenwald, R. A., and Sofko, G. (1999). The Ionospheric Signature of Transient Dayside Reconnection and the Associated Pulsed Convection Return Flow. *Ann. Geophys.* 17 (9), 1166–1171. doi:10.1007/s00585-999-1166-2

Paschmann, G., Haerendel, G., Papamastorakis, I., Sckopke, N., Bame, S. J., Gosling, J. T., et al. (1982). Plasma and Magnetic Field Characteristics of Magnetic Flux Transfer Events. *J. Geophys. Res.* 87 (A4), 2159. doi:10.1029/JA087iA04p02159

Raeder, J. (2006). Flux Transfer Events: 1. Generation Mechanism for strong Southward IMF. *Ann. Geophys.* 24 (1), 381–392. doi:10.5194/angeo-24-381-2006

Raeder, J., Wang, Y. L., Fuller-Rowell, T. J., and Singer, H. J. (2001). Global Simulation of Magnetospheric Space Weather Effects of the Bastille Day Storm. *Solar Phys.* 204 (1/2), 323–337. doi:10.1023/A:1014228230714

Russell, C. T., and Elphic, R. C. (1978). Initial ISEE Magnetometer Results: Magnetopause Observations. *Space Sci. Rev.* 22 (6), 681–715. doi:10.1007/BF00212619

Sandholt, P. E., Deehr, C. S., Egeland, A., Lybekk, B., Viereck, R., and Romick, G. J. (1986). Signatures in the Dayside aurora of Plasma Transfer from the Magnetosheath. *J. Geophys. Res.* 91 (A9), 10063. doi:10.1029/JA091iA09p10063

Smith, R. A., Lazarus, J., Hohenberger, M., Marocchino, A., Robinson, J. S., Chittenden, J. P., et al. (2007). High Resolution Imaging of Colliding Blast Waves in Cluster media. *Plasma Phys. Control Fusion* 49 (12B), B117–B124. doi:10.1088/0741-3335/49/12B/S11

Wang, Z., Fu, H. S., Vaivads, A., Burch, J. L., Yu, Y., and Cao, J. B. (2020). Monitoring the Spatio-Temporal Evolution of a Reconnection X-Line in Space. *ApJ* 899 (2), L34. doi:10.3847/2041-8213/abad2c

Wild, J. A., Cowley, S. W. H., Davies, J. A., Khan, H., Lester, M., Milan, S. E., et al. (2001). First Simultaneous Observations of Flux Transfer Events at the High-Latitude Magnetopause by the Cluster Spacecraft and Pulsed Radar Signatures in the Conjugate Ionosphere by the CUTLASS and EISCAT Radars. *Ann. Geophys.* 19 (10/12), 1491–1508. doi:10.5194/angeo-19-1491-2001

Conflict of Interest: The authors declare that the research was conducted in the absence of any commercial or financial relationships that could be construed as a potential conflict of interest.

frontiers in Astronomy and Space Sciences

ORIGINAL RESEARCH
published: 17 November 2021
doi: 10.3389/fspas.2021.778234

Magnetic Field Gradient Across the Flank Magnetopause

Zdeněk Němeček[1], Kostiantyn Grygorov[1], Jana Šafránková[1], Jiří Šimůnek[2] and Gilbert Pi[1]*

[1]Charles University, Faculty of Mathematics and Physics, Prague, Czechia, [2]Institute of Atmospheric Physics, Czech Academy of Sciences, Prague, Czechia

Magnetic pressure inside the magnetopause is usually balanced with a sum of thermal plasma and magnetic pressures on the magnetosheath side. However, observations reveal that the magnetosheath magnetic field can be frequently larger than that in the magnetosphere (inverse magnetic field gradient across the magnetopause), and thus, the enhanced pressure from the magnetosheath side seems to be uncompensated. Such events are rare in the subsolar region, but their occurrence rate increases toward flanks. The analysis, based on statistical processing of about 35,000 THEMIS magnetopause crossings collected in the course of the years 2007–2017, shows that these events are more frequently observed under enhanced geomagnetic activity that is connected with a strong southward IMF. Case studies reveal that such a state of the magnetopause boundary layers can persist for several hours. This study discusses conditions and mechanisms keeping the pressure balance across the magnetopause under these conditions.

Keywords: magnetosphere, magnetopause, magnetosheath, pressure balance, magnetic field gradient, inverse gradient, geomagnetic indices

OPEN ACCESS

Edited by:
Hiroshi Hasegawa, Japan Aerospace Exploration Agency, Japan

Reviewed by:
Anton Artemyev, Space Research Institute (RAS), Russia
Emilia Kilpua, University of Helsinki, Finland

****Correspondence:***
Zdeněk Němeček
zdenek.nemecek@mff.cuni.cz

Specialty section:
This article was submitted to Space Physics, a section of the journal Frontiers in Astronomy and Space Sciences

Received: *16 September 2021*
Accepted: *13 October 2021*
Published: *17 November 2021*

Citation:
Němeček Z, Grygorov K, Šafránková J, Šimůnek J and Pi G (2021) Magnetic Field Gradient Across the Flank Magnetopause. Front. Astron. Space Sci. 8:778234. doi: 10.3389/fspas.2021.778234

1 INTRODUCTION

The magnetopause is a current sheet forming the boundary between the magnetic pressure of the Earth's dipole on the one side and the shocked supersonic solar wind with an embedded interplanetary magnetic field (IMF) on the other side. However, the total pressure even at the subsolar magnetopause is not exactly equal to the solar wind dynamic pressure (e.g., Spreiter et al., 1966; Samsonov et al., 2012), and the total magnetospheric magnetic field is a superposition of the magnetic field of the Earth's dipole field and the field of several magnetospheric current systems (e.g., Tsyganenko and Andreeva, 2015). Since the magnetopause position is given by the total pressure balance of plasmas and fields on either side, the magnetopause is constantly moving back and forth due to solar wind pressure variations at all timescales. The motion is controlled by a combination of direct solar wind variations (predominantly by changes in the solar wind dynamic pressure) and surface waves such as Kelvin-Helmholtz (Haaland et al., 2019). At the flanks, the latter probably plays a larger role because some theories (e.g., Kavosi and Raeder, 2015; Fadanelli et al., 2018) suppose that waves are excited by local instabilities at the dayside and propagate toward the flanks. At present, there does not seem to be a clear consensus about whether surface waves are more frequent on the dawn or dusk flanks; nevertheless, a dawndusk asymmetry of the macroscopic parameters was a subject of the study by Haaland et al. (2020), and they found, based on MMS data, that the dawn magnetopause is thicker than at dusk, while the dusk flank is more dynamic, with a higher average normal velocity.

The magnetopause is one of the most complex boundaries in space because its formation involves electrical currents, gradients of the plasma density and pressure, flow shear, and/or anisotropy of velocity distributions of particles (Němeček et al., 2020). Therefore, different forms of free energy are accessible at and around the magnetopause, and a variety of instabilities such as current-driven (e.g., magnetic reconnection (Paschmann et al., 1979; Sonnerup et al., 1981)), flow shear-driven (e.g., nonlinear Kelvin-Helmholtz waves (Hasegawa et al., 2004, 2009)), and/or anisotropy-driven (e.g., mirror) instabilities can be excited there (Hasegawa, 2012), but also diffusion (e.g., Treumann et al., 1995) and impulsive penetration (e.g., Lemaire et al., 1979) have been suggested to enable transport across the magnetopause. In addition, the magnetopause is curved on a large scale, and thus, when the upstream flow is super-magnetosonic, it is exposed to a highly time-varying and inhomogeneous plasma of the magnetosheath, the region of a shocked solar wind situated between the magnetopause and bow shock (Berchem and Russell, 1982). Moreover, when the magnetopause thickness is comparable to (or less than) the ion Larmor radius, the boundary structure could also be affected by kinetic effects (Cai et al., 1990; Nakamura et al., 2010).

Due to the focus on processes responsible for the transfer of momentum and energy across the magnetopause and the associated impact on magnetospheric dynamics, much attention has been paid to the dayside magnetopause near the SunEarth line. The interaction between the IMF and geomagnetic field at the dayside magnetopause has a direct consequence on the large-scale plasma circulation in the magnetosphere and magnetically connected ionosphere. The magnetopause flanks and possible dawndusk asymmetries have received less attention, partly because interactions along the flanks probably have a smaller effect on the geomagnetic activity and partly due to results of observations in this region which demonstrate a small difference of boundary layer characteristics between dayside and flanks. A study of Artemyev et al. (2017) showed that plasma and magnetic field characteristics are very similar for boundary layers observed at the lunar orbit ($\approx 55\,R_E$) and farther downtail as far as $\approx 200\,R_E$ and that the dynamical magnetosheath pressure does not contribute to the pressure balance across the boundary layer at these distances. Furthermore, Lukin et al. (2020) compared the characteristics of magnetic field and plasma populations during simultaneous magnetopause crossings, which are separated by about 50 R_E (dayside vs night sides), and found that the magnetosheath current sheet profiles are similar at these two locations. Nevertheless, a flank magnetopause configuration and dynamics are critical for understanding the transport of magnetosheath plasma toward the magnetotail (Wing et al., 2014; Haaland et al., 2019).

Němeček et al. (2002), Zastenker et al. (2002), and Šafránková et al. (2002) compared the magnetosheath measurements with calculations using the Spreiter gasdynamic models of the magnetosheath plasma flow (Spreiter et al., 1966) and IMF modification (Spreiter and Stahara, 1980). They have shown that an average behavior of magnetosheath parameters is predicted rather well by these models. However, they noted that large variations of the ion flux and magnetic field magnitude in the magnetosheath are not always predicted by these models because their variations originated in the magnetosheath itself (or in the foreshock). Such structures are moving tailward along the magnetopause together with the plasma flow (Shevyrev et al., 2003). A suggested explanation for these structures (using the similarity of plasma and magnetic field variation levels) is that they are created near the bow shock as compressional waves.

On the sunward side, the Earth's magnetic field has mainly compressed dipolar structure, whereas the field is stretched out and forms the magnetotail that consists of the northern and southern lobes separated by the plasma sheet on the night side. Due to lower densities and temperatures in lobes than in the plasma sheet, a force imposed on the magnetotail toward its center is balanced by the plasma pressure in the plasma sheet (Coroniti and Kennel, 1972). While the pressure equilibrium exists most of the time, the plasma sheet can also be highly dynamic because the lobes and plasma sheet store energy, which is often released in explosive events during substorms and storms (McPherron et al., 2011).

Both the solar wind and ionosphere can be sources of the plasma sheet plasma. Wing et al. (2014) and later Kistler (2020) have summarized knowledge on the solar wind entry and transport to the plasma sheet for different IMF orientations. Generally, during a northward IMF, the plasma sheet ion spectrum is well-described by two populations. The colder component ($< \approx 1$ keV) is identified as being the solar wind origin because it is only slightly hotter than in the adjacent magnetosheath plasma. This cold and dense plasma sheet occurs after several hours of northward IMF and is observed predominantly along the flanks and at high magnetic latitudes (e.g., Fujimoto et al., 1998) as a result of double cusp or lobe reconnection at the dayside (e.g., Song and Russell, 1992; Sandholt et al., 1999; Lavraud et al., 2006) or enters from the flanks through Kelvin-Helmholtz instability (Sorathia et al., 2019). According to Yu et al. (2020), the cold and dense plasma sheet probably contributes to the production of storm-time energetic particles (Borovsky et al., 1997) and can result in stronger ring currents during the main phase of storms (e.g., Lavraud et al., 2006) and can also lead to the mass loading of the magnetotail. Therefore, it may have effects on substorms (e.g., Fu et al., 2012) and reduction of the reconnection rate (e.g., Toledo-Redondo et al., 2016).

On the other hand, the source of the hotter component ($> \approx 3$ keV) could either be from the ionosphere or from the solar wind plasma that enters farther down the tail and is heated during its transport; however, the cusp entry leads also to a hotter population. The ionospheric plasma has access to the plasma sheet through ion outflow over a wide range of energies that occur throughout the auroral oval and in the polar cap (Li et al., 2013). In the polar cap, the ion escape is mainly due to the ambipolar electric field, and in the auroral regions, local wave acceleration energizes ionospheric plasma to higher energies. During storms, O^+ from both the nightside auroral region and dayside cusp regions enters the plasma sheet (Kistler et al., 2019). Statistical studies have shown that the O^+ content in the plasma sheet

increases with both geomagnetic activity (*Kp*) and solar EUV (F10.7) (Mouikis et al., 2010), and investigations of the storm-time ring current (e.g., Mouikis et al., 2019) have identified a significant fraction of the energy density that is carried by O^+, indicating the importance of the ionospheric source. Němeček et al. (2016) studied the influence of these effects on the magnetopause location and showed that increased ionospheric conductivity leads to its inward motion.

During southward IMF conditions, reconnection occurs at the magnetopause on the dayside at low latitudes. The cold and dense plasma can also be observed along both flanks, but the density is smaller than during northward IMF. Thomsen et al. (2003) and Lavraud and Jordanova (2007) investigated the transition when a period of northward IMF is followed by a strongly southward IMF, driving a storm. They have suggested that this dense plasma can load the near-Earth plasma sheet and then get driven into the inner magnetosphere when the IMF turns southward, creating a strong ring current. This would imply that at least at the beginning of a storm, the ring current is formed by solar wind plasma (Kistler, 2020).

Magnetic pressure inside the magnetopause is usually balanced with a sum of thermal plasma pressure and magnetic pressure on the magnetosheath side, but at about 9% of magnetopause crossings, the THEMIS spacecraft encounter the situation when the magnetosheath magnetic field is larger than that in the magnetosphere, and therefore, the enhanced pressure from the magnetosheath side seems to be uncompensated. We call this effect an inverse magnetic gradient across the magnetopause. We investigate the magnetic gradient across the magnetopause and discuss conditions favorable for the creation of an inverse magnetic gradient. An extensive statistical study reveals a large southward IMF in connection with enhanced geomagnetic activity as necessary conditions.

2 DATA PROCESSING

The analysis is based on observations of all THEMIS probes (Angelopoulos, 2008) and covers a half of the solar cycle (2007–2017). The available plasma (McFadden et al., 2008a) and magnetic field (Auster et al., 2008) data were surveyed by an automated routine based on a determination of scanned regions (solar wind, magnetosheath, and magnetosphere). The identification of regions is based on ion and electron densities and temperatures and magnetic field strength. We are using spin resolution ground moments whenever available, otherwise we apply the onboard moments. The solar wind parameters from the OMNI database were lagged on the expected propagation time from the bow shock nose. The identification method is analogous to that suggested by Jelínek et al. (2012), but it is applied on the search for individual magnetopause crossings.

The routine provided about 36,000 magnetopause crossing candidates. We have calculated the location predicted by the Lin et al. (2010) model for them, and all candidates exhibiting difference between predicted and observed distances from the Earth larger than 1.5 R_E were checked by a visual inspection of corresponding plots of the plasma and magnetic field, and events under doubt were discarded. The set includes single crossings as well as a series of multiple crossings that were usually observed close to the apogee of a particular spacecraft. The visual inspection left 34,699 crossings for a further processing.

The time and location of each crossing were complemented with the upstream magnetic field and plasma parameters. We are using wind data lagged on the expected propagation time as a proxy of upstream conditions. Five-minute averages of the spin resolution magnetic field strength, B_{MSH}, the ion density, N_{MSH}, velocity, V_{MSH}, and ion temperature, T_{MSH}, measured by THEMIS just outbound the magnetopause in the magnetosheath and the magnetic field strength just inbound the magnetopause, B_{MSP}, were added for the later processing. In order to account for the uncertainty of the identification of the exact time of magnetopause crossings by our automated routine, we have skipped 1 min on both sides of a particular crossing.

3 MAGNETIC GRADIENT ACROSS THE MAGNETOPAUSE

A distribution of THEMIS crossings projected onto the XY GSM plane is shown in the top left panel of **Figure 1**. Note that we limited our study to $X_{GSE} > -5\ R_E$ because the number of crossings behind this limit is very low. We also did not analyze crossings observed by THEMIS B and C at the lunar orbit because the magnetopause is formed in a different way at these distances. Whereas the ram pressure of the solar wind is principal for the formation of the dayside magnetopause, the solar wind flow is nearly parallel with the magnetopause at far flank locations. We have further divided the crossings into three subsets according to the angle, α, between the radius vector and *X*-axis: subsolar ($|\alpha| < 30^\circ$), near flank ($30^\circ < |\alpha| < 60^\circ$), and distant flank ($|\alpha| > 60^\circ$) that are distinguished by colors in **Figure 1**. We further selected events satisfying a condition $B_{MSH}/B_{MSP} > 1$ that are a dominant subject of the present study. They are indicated by blue crosses, and their number is sufficient to exclude a possibility that they can be attributed to measuring errors. We can note that a relative number of these crossings increases toward the flanks with no apparent dawndusk asymmetry. For this reason, we combine data from dawn and dusk sectors in further analysis.

A portion of events exhibiting an inverse magnetic gradient is illustrated in the bottom panel of **Figure 1**, where the B_{MSH}/B_{MSP} ratio is plotted as a function of α. The gray crosses stand for individual crossings, and the red bars show medians in the angle bins. We can see that this median is about constant and equal to ≈ 0.65 in the subsolar region and then starts to increase toward unity at flanks, but it does not reach the blue dashed line standing for $B_{MSH}/B_{MSP} = 1$. These observations are quantified in **Table 1**. The first row in the table presents the number of events in $|\alpha|$ subsets that decrease toward the flank because an apogee of the THEMIS A, D, and E spacecraft is insufficient to cross the flank magnetopause when the solar wind pressure is low. On the other hand, the number of crossings satisfying a condition of $B_{MSH} >$

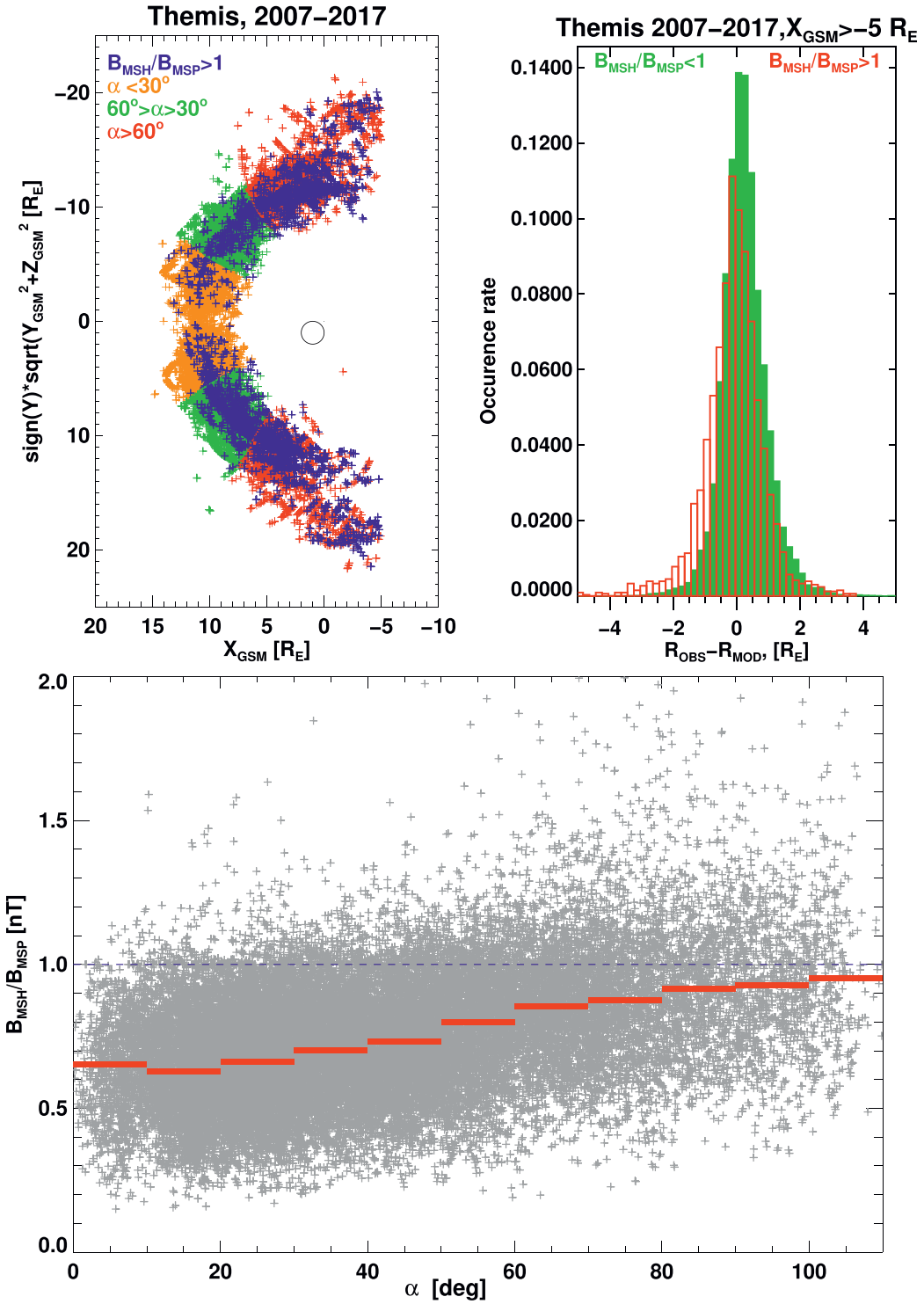

FIGURE 1 | Left—Projections of observed magnetopause crossings onto the *X*–*Y* plane. Colors indicate a division of crossings into particular subsets (subsolar—yellow, near flank—green, distant flank—red). The crossings exhibiting $B_{MSH} > B_{MSP}$ are shown as blue crosses. Right—Distributions of differences between observed R_{obs} and modeled R_{mod} (Lin et al., 2010) magnetopause stand-off distances for the subsets of crossings with $B_{MSH}/B_{MSP} < 1$ (green) and $B_{MSH}/B_{MSP} > 1$ (red). Bottom—Dependence of the B_{MSH}/B_{MSP} ratio on the angle α between the radius vector of a particular crossing and the *X*-axis.

TABLE 1 | Longitudinal distribution of the magnetopause crossings projected onto the equatorial plane.

	All events	$\alpha < 30^\circ$	$30^\circ < \alpha < 60^\circ$	$\alpha > 60^\circ$
All events	34, 699	13, 215	13, 933	7, 551
$B_{MSH} < B_{MSP}$	28, 988	12, 092	11, 845	5, 051
$B_{MSH} > B_{MSP}$	3, 041	216	979	1, 846

B_{MSP} increases with increasing α and reaches 25% of all crossings in the far flank region.

The top right-hand panel in **Figure 1** shows the distribution of differences between observed and modeled magnetopause stand-off distances. We have checked several empirical magnetopause models, but we decide to use the Lin et al. (2010) model because it explicitly contains the effect of the IMF strength on the magnetopause location. The histograms are plotted for $B_{MSH} < B_{MSP}$ (green) and $B_{MSH} > B_{MSP}$ (red) events separately. One can note that $B_{MSH} > B_{MSP}$ events are generally located closer to the Earth than the "standard" events with a larger magnetic field on the magnetospheric side. We also plotted similar histograms for our subsets and fitted them with Gaussian distributions. The parameters of distributions (full width at half maximum (FWHM) and center) are surveyed in **Table 2**.

Table 2 shows that the Lin et al. (2010) model describes the position of the magnetopause rather well, and the deviations of model locations from observations are lower than 0.2 R_E with an exception of the near-flank region. The shift of crossings with $B_{MSH}/B_{MSP} > 1$ toward the Earth by about 0.2 R_E can be observed in all regions. Since B_{MSH} is actually IMF compressed at the bow shock and the IMF strength is included in the model, it indicates that the effect of the IMF strength on the magnetopause location is not limited by the pressure but influences the whole interaction process. On the other hand, we can see only a slight enlargement of the prediction uncertainty described by FWHM for the crossings with $B_{MSH}/B_{MSP} > 1$, but we are operating with a small number of events (**Table 1**) for an ultimate conclusion.

3.1 Upstream Conditions

The previous section has shown that the observations of an inverse magnetic gradient across the magnetopause are rather frequent; the probability of its observations increases with the distance from the subsolar point and reaches nearly 25% at the terminator. In search for the conditions favorable for its formation, we started with an analysis of upstream conditions. We have plotted distributions of the ion density, velocity, and dynamic pressure separately for events with $B_{MSH} > B_{MSP}$ and $B_{MSH} < B_{MSP}$, but we did not find any systematic difference among them, thus we are not showing these plots. The only clear dependence of B_{MSH}/B_{MSP} on upstream conditions was found for the IMF strength and IMF cone angle (the angle between the IMF and solar wind velocity vectors) as **Figure 2** demonstrates.

The gray points stand for values corresponding to individual crossings, and color bars show medians in IMF or cone angle bins for the subsolar (yellow), near flank (green), and distant (red) flank. Consistently with the bottom panel in **Figure 1**, the median B_{MSH}/B_{MSP} ratio increases with the distance from the subsolar point, but the left panel shows that it also increases with an increasing IMF strength (left panel) in a monotonic way, and it exceeds unity even in the subsolar region if the IMF strength is sufficiently high. We should note that we made plots like those in **Figure 2** for the IMF B_Y and B_Z components, and the results were similar to the B_{MSH}/B_{MSP} dependence on the IMF strength.

The clear increase of B_{MSH}/B_{MSP} with the cone angle (right panel) starts at about 30° in all magnetopause segments. It is hard to say whether a little larger median ratio observed for a nearly radial field is the real physical effect or a product of limited statistics in this cone angle bin. Nevertheless, it is observed in all three magnetopause regions. The number of points above the blue dashed line (events exhibiting the inverse gradient) increases with the cone angle, but the medians are below unity in all magnetopause segments.

A larger value of the B_{MSH}/B_{MSP} can be caused either by too large B_{MSH} or too low B_{MSP}. Let us first check B_{MSH} that is actually a compressed IMF. The left-hand panel in **Figure 3** shows B_{MSH} as a function of the IMF strength. The format and color coding are the same as in the previous figures; the full colored bars are medians in IMF bins, and the dotted colored bars present medians computed for events with $B_{MSH} > B_{MSP}$. All individual points as well as all medians roughly correspond to a compression factor of about 4 that is consistent with IMF compression at the supercritical quasi-perpendicular bow shock (Spreiter and Stahara, 1980). Since the red medians in each IMF bin are the lowest, we can conclude that the compression factor decreases with the distance from the subsolar point that is consistent with early magnetosheath models (Spreiter and Stahara, 1980). Comparing the medians computed from all data (full lines) and medians corresponding to events with $B_{MSH} > B_{MSP}$ (dotted lines), we can note that both medians are about equal at the distant flank (red). It means that 1) the number of events with $B_{MSH} > B_{MSP}$ prevails and 2) the inverse gradient is not connected with an enhanced IMF compression in this region. The same is true for the near-flank (green) events with an exception of IMF below 5 nT, and thus, we can conclude that the formation of an enlarged magnetic gradient across the flank magnetopause is not

TABLE 2 | Distributions of differences between observed R_{obs} and modeled R_{mod} magnetopause stand-off distances. Parameters of Gaussian fits (center and FWHM) are given for three magnetopause regions.

	All events		$\alpha < 30^\circ$		$30^\circ < \alpha < 60^\circ$		$\alpha > 60^\circ$	
	Center	FWHM	Center	FWHM	Center	FWHM	Center	FWHM
$B_{MSH} < B_{MSP}$	0.18	1.33	0.14	1.28	0.23	1.3	0.12	1.54
$B_{MSH} > B_{MSP}$	− 0.04	1.6	− 0.06	1.08	0.11	1.46	− 0.16	1.75

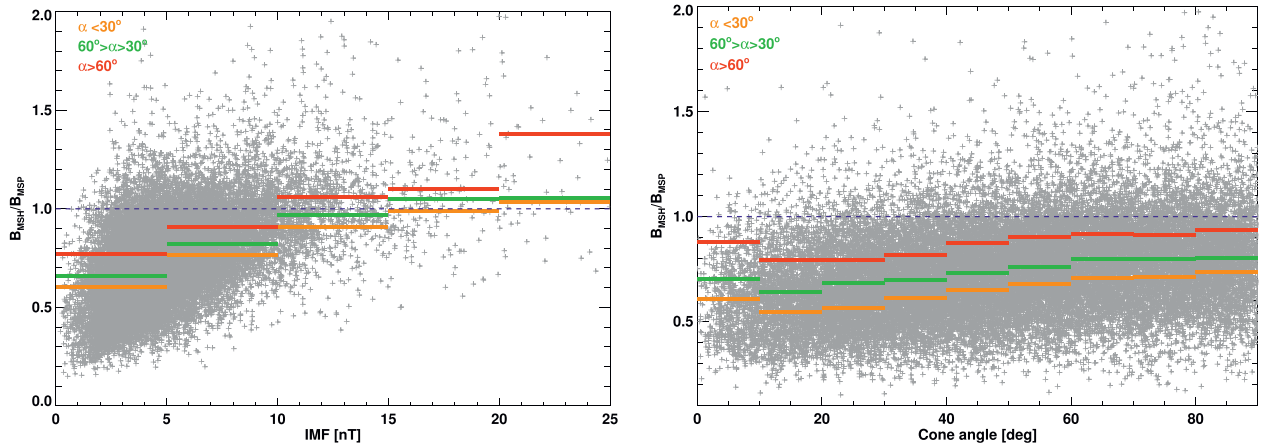

FIGURE 2 | B_{MSH}/B_{MSP} ratio as a function of the IMF strength **(left)** and IMF cone angle **(right).** The gray points mark all MP crossings, and the color bars stand for median values of B_{MSH}/B_{MSP} in particular subsets of crossings. Color coding is explained in the top left corners.

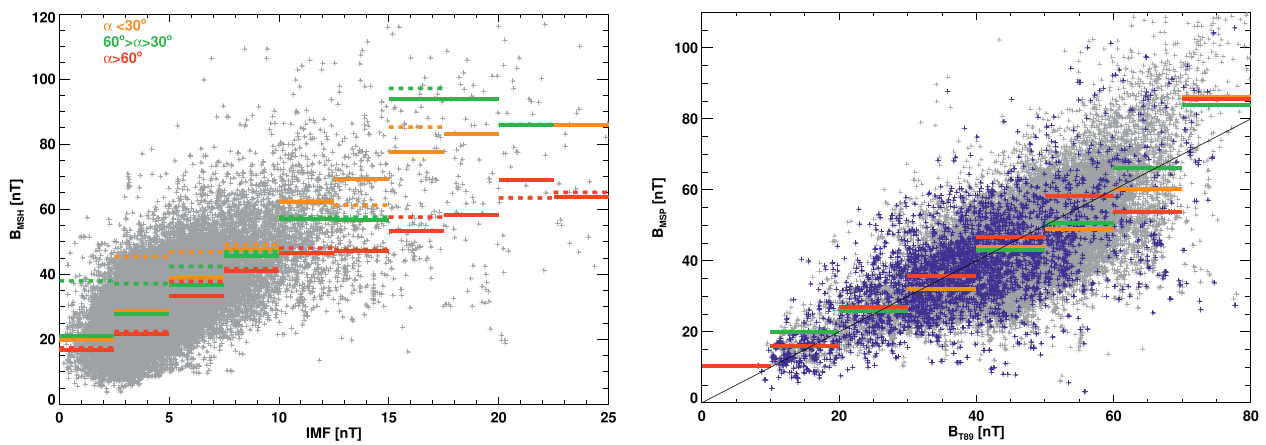

FIGURE 3 | Left—The magnetic field in the magnetosheath as a function of the IMF strength; right—the relation between observed B_{MSP} at the magnetopause and modeled magnetic field according to T89 at the same location. The color-coding follows **Figure 2**; the blue crosses stand for crossings with $B_{MSH}/B_{MSP} > 1$; the straight line in the right-hand panel signifies an identity of both fields.

connected with larger than usual IMF compression at the bow shock.

In order to check the conditions in the magnetosphere, we have applied the Tsyganenko (1989) model (T89 model) of the magnetic field that takes into account variations of the geomagnetic activity and computed a prediction of the magnetic field strength at the point of each magnetopause crossing. The model is parameterized with the *Kp* index that covers geomagnetic activity in a broad range of latitudes, and thus, it would reflect the influence of the ring current as well as auroral electrojects on the magnetospheric magnetic field. A comparison of observed and predicted magnetic fields is shown in the right-hand panel in **Figure 3**. Since the model is relatively simple and does not include the influence of upstream conditions on the magnetospheric field, the spread of points is rather large, but the medians shown by colored bars lie approximately on the black line that signifies the identity of the predicted and measured magnetic fields. It is especially true at the small fields at flanks (green and red bars) where a great majority of events with $B_{MSH} > B_{MSP}$ (blue crosses) were observed.

3.2 Geomagnetic Activity

A combination of conclusions following from the previous figures with the fact that the magnetopause is only slightly compressed (**Figure 1**) suggests that the excess of the magnetic pressure on the magnetosheath side would be compensated by the plasma pressure on the magnetospheric side and thus a link with the geomagnetic activity. In order to check it, the B_{MSH}/B_{MSP} ratio as a function of two basic geomagnetic indices, *SYM-H* and *AE*, is shown in **Figure 4**.

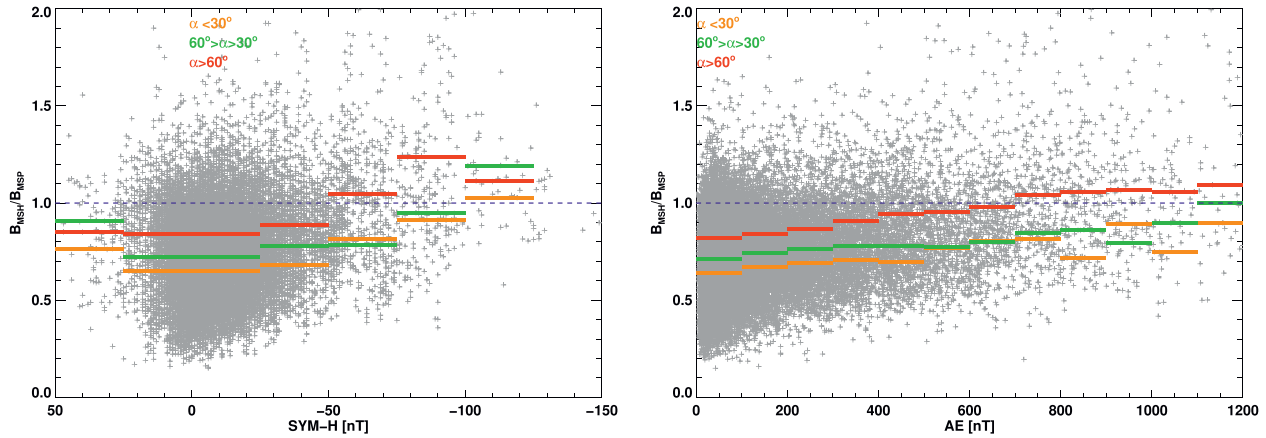

FIGURE 4 | B_{MSH}/B_{MSP} ratio as a function of *SYM-H* **(left)** and *AE* **(right)** indices of the geomagnetic activity. The color bars follow the coding in **Figure 2**.

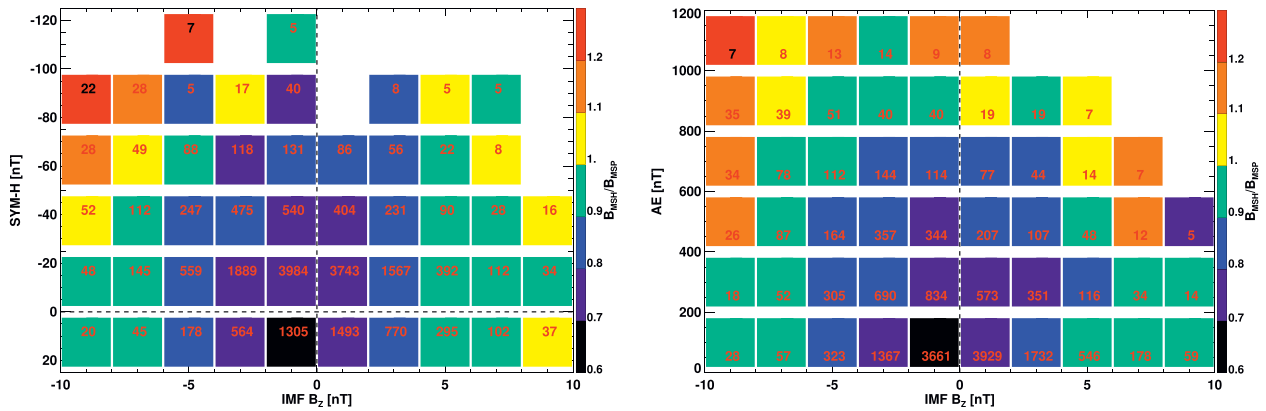

FIGURE 5 | B_{MSH}/B_{MSP} ratio in bins of IMF B_Z and *SYM-H* **(left)** or *AE* **(right)** indices. The color scale shows median values of the ratio in a particular bin, and a number of events in a particular bin are given inside the bin. Note that only crossings of the flank magnetopause (green and red sectors in **Figure 1**) are used.

Since the THEMIS orbits cover predominantly the low-latitude magnetopause, *SYM-H* seems to be more appropriate, and the medians shown by color bars in the left panel reveal that the B_{MSH}/B_{MSP} ratio is about constant and does not depend on a value of the index if the magnetosphere is quiet (*SYM-H* $> -30\,nT$), but it increases with increasing geomagnetic activity. The same conclusion follows from the right-hand panel that presents a dependence of B_{MSH}/B_{MSP} on the *AE* index. It is interesting to note that although THEMIS moves basically in the low-latitude magnetopause, the correlation of the *AE* index describing the auroral activity with the B_{MSH}/B_{MSP} ratio is slightly larger (0.17) than that with *SYM-H* index (0.12) that is predominantly affected by ring current changes, thus processes at low latitudes.

A combination of **Figures 2**–**4** suggests that the conditions for the creation of an inverse magnetic gradient across the flank magnetopause are large IMF dominated by perpendicular (B_Y and B_Z) components and/or enhanced geomagnetic activity. An additional analysis has shown that the correlation of the B_{MSH}/B_{MSP} ratio with IMF B_Z is 0.43 while it is only 0.30 for IMF B_Y, and thus, we focus on *SYM-H*, *AE*, and IMF B_Z. To find which of these factors are more important, **Figure 5** combines these parameters.

We binned data into 2 *nT* wide bins of IMF B_Z and then into 25 *nT* wide bins of *SYM-H* (left panel) and 200 *nT* wide bins of *AE* (right panel), respectively. For each of these bins, we counted the number of events, and if it exceeded 5, we further calculated the median of the B_{MSH}/B_{MSP} ratio. The number of events is given in each bin, and the value of the B_{MSH}/B_{MSP} median is shown by color. To be more illustrative, we use discrete colors instead of a continuous color palette. The scale is shown on the right-hand side of each panel, and numbers stand for rounded medians.

A brief look at the panels of **Figure 5** reveals that low B_{MSH}/B_{MSP} medians (blue color) require a combination of small IMF B_Z, regardless of its polarity, and a low geomagnetic activity. On the other hand, $B_{MSH}/B_{MSP} > 1.1$ (orange and red colors) can be observed nearly exceptionally during intervals of strong (< -4) negative IMF B_Z and enhanced geomagnetic activity. There are several exceptions from these rules in our statistics, but all of them

TABLE 3 | Statistics of inverse gradient observations under different solar wind driving. The first line shows a number of MP crossings under specified conditions, the second line marks a number of crossings exhibiting inverse gradient, and the third line, their ratio.

SW type	SLOW	FAST	HCS	CIR	EJECTA	MC	IS + ISA
No. of events	12,783	10,087	2,178	3,414	1857	455	412
Inv. gradient	837	655	92	733	312	183	61
Occurrence rate	0.06	0.06	0.04	0.21	0.17	0.40	0.04

are connected with a small number of events in the bins, and thus, their statistical significance is low. Although the analysis covers predominantly the magnetopause at low geomagnetic latitudes, it seems that auroral activity (*AE* index) is an important factor for the creation of an inverse magnetic gradient because it is observed always if $AE > 1000$.

3.3 Relation to Solar Wind Categories

Yermolaev et al. (2009) suggested a scheme for a classification of the solar wind into several categories. They use hourly averaged OMNI solar wind and IMF data and attribute each hour to one of nine solar wind types—slow wind (SLOW), fast wind (FAST), heliospheric current sheet (HCS), co-rotating interaction region (CIR), interplanetary coronal mass ejection that does not exhibit magnetic cloud features (EJECTA), magnetic cloud (MC), and two categories of interplanetary shocks (IS and ISA). Although the authors originally processed the 1976–2000 years, they continue with the classification till present, and a list of intervals attributed to mentioned categories are available at ftp://ftp.iki.rssi.ru/pub/omni/catalog/. Since the statistics presented in **Figure 5** suggest a connection of an inverse magnetic gradient with geomagnetic activity, and solar wind geomagnetic effectiveness varies with the category, we have used their classification and checked a possible relation. The results are presented in **Table 3**. Note that we combined IS and ISA categories because the number of intervals in these categories was too low. Looking at **Table 3**, we can note that the occurrence rate of the inverse magnetic gradient agrees well with the results in **Figure 5**. It is not surprising because MCs are typical drivers of large geomagnetic storms, and they often bring a large southward IMF toward the magnetopause. On the other hand, standard upstream conditions (slow or fast solar winds) lead to the inverse gradient only exceptionally.

4 SUMMARY OF STATISTICAL RESULTS

We report a statistics of observations of the magnetic gradient across the dayside magnetopause with an emphasis on the situation when the magnetosheath magnetic field magnitude is larger than the field just inbound the magnetopause, i.e., $B_{MSH} > B_{MSP}$. Since this configuration contradicts to a general understanding of the magnetopause formation, we use the term inverse magnetic gradient for briefness. The statistics compare three regions—subsolar, near, and distant flanks. We can summarize our statistical findings as follows:

1. Median magnitudes of the B_{MSH}/B_{MSP} ratio are 0.65 at the subsolar region, 0.7 at the near flank, and 0.9 at the distant flank, respectively (**Figure 1**). The inverse gradient is observed more frequently across the flank magnetopause, and the occurrence rate strongly rises with the departure of the crossing local time from the noon; it is 1.5% in the subsolar region, 7% at the near flank, and 20% at the distant flank (**Table 1**).
2. A presence of the inverse magnetic gradient across the magnetopause is not exceptional because it is observed at about 9% of all magnetopause crossings. Moreover, the inverse magnetic gradient is a natural continuation of the trends of the B_{MSH}/B_{MSP} ratio dependence on factors such as the IMF strength, cone angle (**Figure 2**), and geomagnetic activity (**Figures 4**, **5**).
3. The magnetosheath magnetic field strength corresponds to its upstream source (**Figure 3**); the compression ratio does not depend on the B_{MSH}/B_{MSP} value (not shown).
4. The magnetopause location is well predicted by the Lin et al. (2010) model; the crossings exhibiting the inverse magnetic gradient are observed slightly closer to the Earth than the model predicts (**Figure 1**; **Table 1**).
5. The B_{MSH}/B_{MSP} ratio > 1 is observed for both polarities of IMF B_Z, but the occurrence rate and median values of this ratio are larger for southward IMF (**Figure 5**).
6. The inverse gradient is observed preferentially during intervals of an enhanced geomagnetic activity described by *AE* and *SYM-H* indices (**Figure 5**).
7. The inverse gradient is not connected with lower than average magnetospheric magnetic field strength just inbound of the magnetopause that is well modeled by the T89 model (**Figure 3**).
8. Correlation coefficients between the B_{MSH}/B_{MSP} ratio and B_{MSP} are 0.06 only, whereas it is 0.70 for B_{MSH}.

The preferential observations of the inverse magnetic gradient during enhanced geomagnetic activity are consistent with a classification of corresponding upstream conditions in **Table 3**—the largest probability of its creation occurs when the magnetosphere is affected by MCs, CMEs, or CIRs, and these structures are responsible for major geomagnetic storms (Richardson et al., 2021). The storm-time magnetosphere is characterized by an enhanced ring current that decreases the magnetic field at the Earth surface (*SYM-H* index becomes negative) and increases the magnetic field at the magnetopause. The enhancement of eastward and westward auroral electrojects during storm times leads to increase/decrease of the surface magnetic field described by *AL*/*AU* indices, and it again would lead to corresponding changes of the magnetic field strength at the magnetopause. Nevertheless, all these effects are implemented in the T89 model, and **Figure 3**

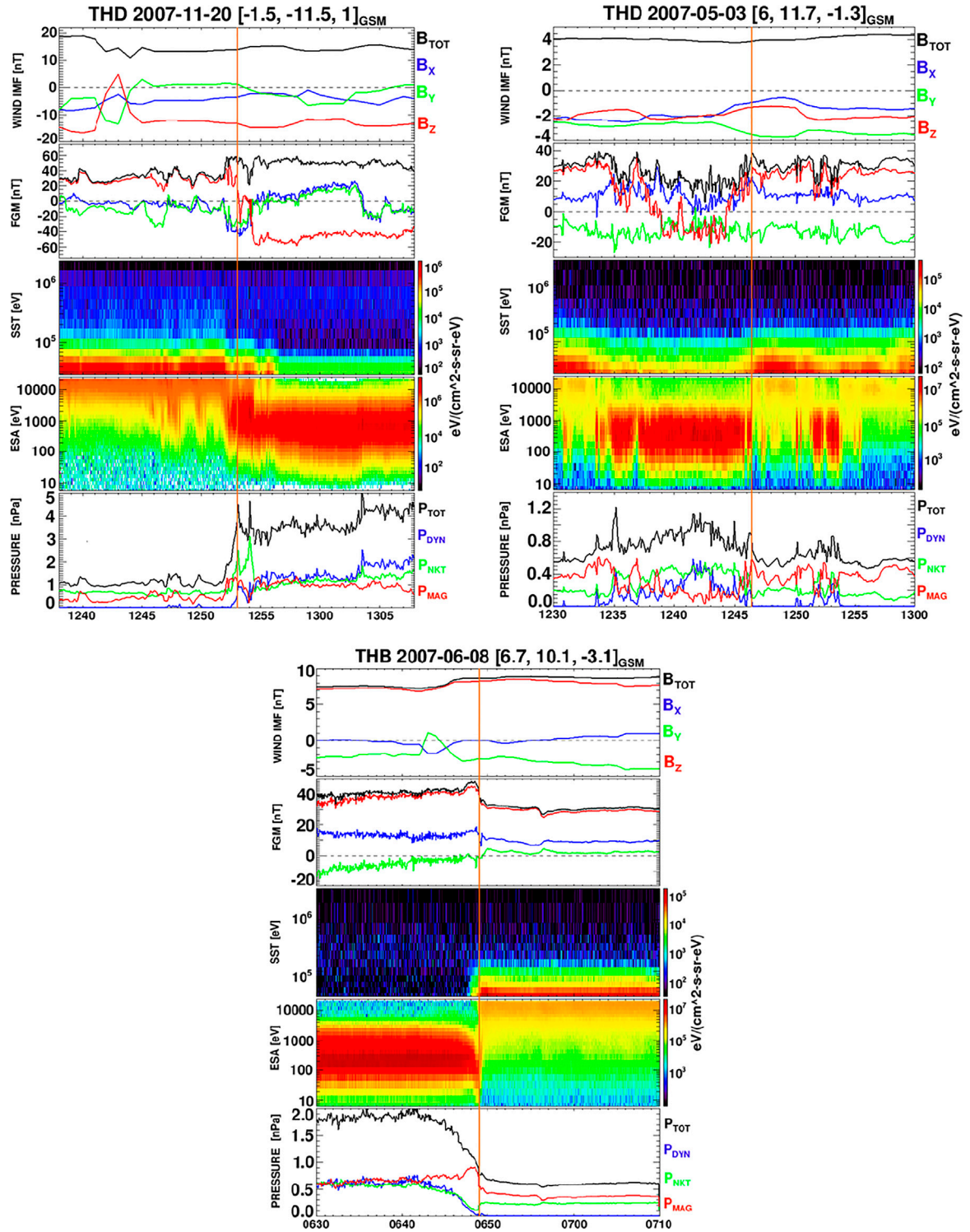

FIGURE 6 | Examples of magnetopause crossings. Left—the crossing exhibiting a strong inverse gradient under southward IMF and enhanced geomagnetic activity (*SYM-H* $\approx -51\,nT$, *AE* $\approx 212\,nT$); right—the crossing with a standard gradient under southward IMF (*SYM-H* $\approx -6\,nT$, *AE* $\approx 162\,nT$); bottom—the crossing exhibiting an inverse gradient under northward IMF (*SYM-H* $\approx 3\,nT$, *AE* $\approx 30\,nT$). The panels in each section show from top to bottom: the IMF strength and components propagated from the wind; the magnetic field measured by THEMIS; the energy flux of energetic ions from the SST instrument; the ion energy flux from the ESA instrument; and the total pressure, P_{TOT}, (black) and its particular components: P_{DYN} (blue)—the dynamic pressure perpendicular to the model magnetopause surface, P_{NKT} (green)—a sum of ion and electron thermal pressures, and P_{MAG} (red)—the magnetic pressure. Note that P_{NKT} was computed from the ESA ground moments, and the contribution of SST represents less than 1% of the total pressure.

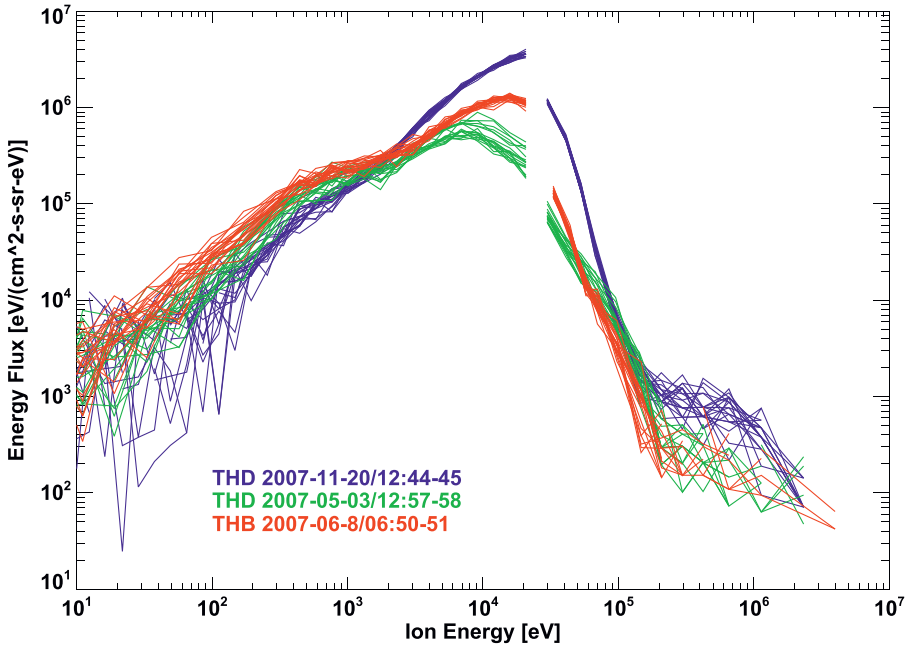

FIGURE 7 | Energetic distributions of the ion energy flux in the magnetosphere just inbound the magnetopause for events in **Figure 6**. The parts of distributions below 30 keV were determined from the ESA spectrometer and the high-energy parts from the SST detector.

shows that the distribution of the measured magnetic field around the value predicted by a model does not depend on the B_{MSH}/B_{MSP} ratio. Moreover, a comparison of T89 predictions for *Kp* index 1 and 6 at different locations shows that the storm effect on the magnetic field at the magnetopause can be as large as + 10 *nT* in the near flank region, but it decreases to + 2 *nT* at the far flank, and these values cannot explain a presence of the inverse gradient because the storm currents increase B_{MSP}, but we observe $B_{MSH} > B_{MSP}$. Weigel (2010) argue that the solar wind density amplifies the geomagnetic response to the solar wind activity, but we did not find any notable effect of the upstream density on the formation of the inverse gradient; the correlation of the B_{MSH}/B_{MSP} ratio with the upstream density is only 0.08.

A common understanding of the pressure balance across the magnetopause is that the sum of magnetic and plasma pressures at the magnetosheath side is balanced by a stronger magnetic field in the magnetosphere, but we are discussing events with an excess of the magnetic pressure on the magnetosheath side. The fact that the magnetopause is approximately at the position predicted by the empirical model (**Figure 1**) suggests an enhanced contribution of the magnetospheric plasma to the total pressure in a comparison with typical conditions. However, determination of plasma parameters at the magnetopause is difficult because the boundary layers on both sides of the magnetopause often contain a mix of magnetosheath and magnetospheric populations (Němeček et al., 2015), and even low-energy plasma from a plasmasphere (McFadden et al., 2008b) can be observed at the magnetopause during storm-time intervals. For this reason, we will demonstrate the conditions leading to the creation of the inverse gradient for several cases.

5 SUPPORTING CASE STUDY

In accord with the above statistical study, we have chosen three events. First of them occurred during the geomagnetic storm under a strong southward IMF and represents a typical example of the inverse gradient, $B_{MSH} \approx 2.2\, B_{MSP}$. This event is contrasted with another crossing observed under similar conditions but with a standard gradient, $B_{MSH} < B_{MSP}$. The third example is a representative of a group of crossings exhibiting the inverse gradient under a northward IMF. The basic data for these three crossings are shown in three sections of **Figure 6**.

Comparison of the figure sections reveals that both magnetopause crossings observed under southward IMF exhibit relatively thick boundary layer characterized by staircase like (left-hand section) or smooth (right-hand section) transition of the B_Z component from the negative value in the magnetosheath to the positive value on the magnetospheric side and mixed plasma populations on both sides of the magnetopause. On the other hand, the northward IMF (bottom section) leads to a sharp MP crossing with abrupt changes of the ion density and temperature, as it can be seen in the bottom section of the figure. These features distinguish the flank and subsolar magnetopause because Němeček et al. (2015) presented statistically that a thick boundary layer is a consequence of cusp reconnection, and thus, it is formed by northward IMF.

The formation of the boundary layer at the low-latitude flanks for strong southward IMF is affected by the presence of dayside extension of the plasma sheet that is supplied by intensive reconnection. This reconnection increases cross-tail potential driving magnetospheric current systems that modify the

magnetic field at the magnetopause. Enhanced current heats the magnetospheric plasma and brings new charge carriers to the boundary layer. As a result, the magnetospheric plasma pressure is enhanced, balances the magnetosheath magnetic pressure, and keeps the magnetopause in an equilibrium state in the southward events with inverse magnetic gradient. We plot the energy distributions of magnetospheric ions just inbound of the magnetopause in **Figure 7** for events shown in **Figure 6**. The figure shows a merged ion energy flux distribution from ESA and SST analyzers. Although there is an energy gap between the two analyzers, one can see that the maximum of the ion energy flux is above the range of the ESA analyzer ($\approx$ 30 keV) for the blue distribution that belongs to the event exhibiting a strong inverse gradient (**Figure 6**, left-hand section).

Consequently, we can suppose that the temperature of the ion population is larger than that calculated as the moment of the ESA distribution, and it causes an apparent lack of the magnetospheric pressure demonstrated in the bottom panels in all sections of **Figure 6**. When the southward IMF is not so strong (right-hand section) of **Figure 6**, the magnetospheric currents are weaker, and density and temperature in the magnetosphere are lower (green distribution in **Figure 7**), and we observe a standard magnetic gradient across the magnetopause. This explanation expects a large cross-tail potential for events with the inverse magnetic gradient, and it is consistent with the *PCN* index being 7 *mV/m* for the example in the left section of **Figure 6**, whereas it is only 1.5 *mV/m* for the event with the standard magnetic gradient shown in the middle section.

The northward crossing (bottom section of **Figure 6**) exhibits a clear plasma depletion layer at the magnetosheath side (Zwan and Wolf, 1976) characterized by an enhancement of the magnetic field complemented with a density depletion in front of the magnetopause. Nevertheless, the magnetosheath magnetic field outside this layer is still larger than that in the magnetosphere in spite of the fact that the geomagnetic activity is low, and it was low within preceding 12 h. The pressure balance calculated using the plasma moments from the ion spectrometer shows a lack of the pressure in the magnetosphere (last panel), but, similarly to the southward event, the ion density and temperature are underestimated because the maximum of the ion distribution is at the upper edge of the spectrometer energy range (red curve in **Figure 7**). However, mechanisms leading to such hot and dense plasma in the magnetosphere layer adjacent to the magnetopause should be further investigated.

6 CONCLUSION

We present a statistical study of the magnetic field gradient across the magnetopause with an emphasis on the flank magnetopause and events when the magnetospheric magnetic field was lower than that in the adjacent magnetosheath. Based on the above discussion, we can believe that we understand the formation of magnetopause layers that can lead to an inverse magnetic gradient across the magnetopause for southward IMF. The intensive reconnection caused by a large southward IMF increases cross-tail potential driving strong magnetospheric currents that overheat the magnetospheric plasma and bring it to the magnetopause. The presence of such plasma leads to a diamagnetic effect (decrease of the magnetospheric magnetic field) and increases the plasma pressure on the magnetospheric side. We have shown that the intensity of these processes increases with the IMF strength, and thus, we can conclude that IMF strength influences the processes in the magnetosphere much more than we expected so far.

DATA AVAILABILITY STATEMENT

Publicly available datasets were analyzed in this study. This data can be found here: http://cdaweb.gsfc.nasa.gov/

AUTHOR CONTRIBUTIONS

The article is a result of efforts of all authors, and their particular contributions are as follows: Data processing—THEMIS, KG and JS; methodology, ZN; data analysis and interpretation, ZN and JS; software and visualization, KG and JS; original draft preparation, ZN; contribution to data interpretation and enhanced discussion, GP.

FUNDING

The work was supported by the Czech Science Foundation under Contract 21-26463S.

ACKNOWLEDGMENTS

The authors thank the Wind and THEMIS teams for the magnetic field and plasma data available *via* http://cdaweb.gsfc.nasa.gov/. They also thank professor Vitek for his continuous support.

REFERENCES

Angelopoulos, V. (2008). The THEMIS mission. *Space Sci. Rev.* 141, 5–34. doi:10.1007/s11214-008-9336-1

Artemyev, A. V., Angelopoulos, V., Runov, A., Wang, C.-P., and Zelenyi, L. M. (2017). Properties of the Quatorial Magnetotail Flanks ~ 50–200 R_E downtail. *J. Geophys. Res. Space Phys.* 122, 11917–11930. doi:10.1002/2017JA024723

Auster, H. U., Glassmeier, K. H., Magnes, W., Aydogar, O., Baumjohann, W., Constantinescu, D., et al. (2008). The THEMIS Fluxgate Magnetometer. *Space Sci. Rev.* 141, 235–264. doi:10.1007/s11214-008-9365-9

Berchem, J., and Russell, C. T. (1982). The Thickness of the Magnetopause Current Layer: ISEE 1 and 2 Observations. *J. Geophys. Res.* 87, 2108–2114. doi:10.1029/ja087ia04p02108

Borovsky, J. E., Elphic, R. C., Funsten, H. O., and Thomsen, M. F. (1997). The Earth's Plasma Sheet as a Laboratory for Flow Turbulence in High-β MHD. *J. Plasma Phys.* 57, 1–34. doi:10.1017/s0022377896005259

Cai, D., Storey, L. R. O., and Neubert, T. (1990). Kinetic Equilibria of Plasma Shear Layers. *Phys. Fluids B: Plasma Phys.* 2, 75–85. doi:10.1063/1.859541

Coroniti, F. V., and Kennel, C. F. (1972). Changes in Magnetospheric Configuration during the Substorm Growth Phase. *J. Geophys. Res.* 77, 3361–3370. doi:10.1029/ja077i019p03361

Fadanelli, S., Faganello, M., Califano, F., Cerri, S. S., Pegoraro, F., and Lavraud, B. (2018). North-South Asymmetric Kelvin-Helmholtz Instability and Induced Reconnection at the Earth's Magnetospheric Flanks. *J. Geophys. Res. Space Phys.* 123, 9340–9356. doi:10.1029/2018JA025626

Fu, H. S., Khotyaintsev, Y. V., Vaivads, A., André, M., and Huang, S. Y. (2012). Occurrence Rate of Earthward-Propagating Dipolarization Fronts. *Geophys. Res. Lett.* 39, L10101. doi:10.1029/2012gl051784

Fujimoto, M., Terasawa, T., Mukai, T., Saito, Y., Yamamoto, T., and Kokubun, S. (1998). Plasma Entry from the Flanks of the Near-Earth Magnetotail: Geotail Observations. *J. Geophys. Res.* 103, 4391–4408. doi:10.1029/97JA03340

Haaland, S., Paschmann, G., Øieroset, M., Phan, T., Hasegawa, H., Fuselier, S. A., et al. (2020). Characteristics of the Flank Magnetopause: MMS Results. *J. Geophys. Res. Space Phys.* 125, e2019JA027623. doi:10.1029/2019JA027623

Haaland, S., Runov, A., Artemyev, A., and Angelopoulos, V. (2019). Characteristics of the Flank Magnetopause: THEMIS Observations. *J. Geophys. Res. Space Phys.* 124, 3421–3435. doi:10.1029/2019JA026459

Hasegawa, H., Fujimoto, M., Phan, T.-D., Rème, H., Balogh, A., Dunlop, M. W., et al. (2004). Transport of Solar Wind into Earth's Magnetosphere through Rolled-Up Kelvin-Helmholtz Vortices. *Nature* 430 (7001), 755–758. doi:10.1038/nature02799

Hasegawa, H., Retinò, A., Vaivads, A., Khotyaintsev, Y., André, M., Nakamura, T. K. M., et al. (2009). Kelvin-Helmholtz Waves at the Earth's Magnetopause: Multiscale Development and Associated Reconnection. *J. Geophys. Res.* 114, 12207. doi:10.1029/2009JA014042

Hasegawa, H. (2012). Structure and Dynamics of the Magnetopause and its Boundary Layers. *Monogr. Environ. Earth Planets* 1 (2), 71–119. doi:10.5047/meep.2012.00102.0071

Jelínek, K., Němeček, Z., and Šafránková, J. (2012). A New Approach to Magnetopause and bow Shock Modeling Based on Automated Region Identification. *J. Geophys. Res.* 117, A05208. doi:10.1029/2011JA017252

Kavosi, S., and Raeder, J. (2015). Ubiquity of Kelvin-Helmholtz Waves at Earth's Magnetopause. *Nat. Commun.* 6, 7019. doi:10.1038/ncomms8019

Kistler, L. M. (2020). Ionospheric and Solar Wind Contributions to the Storm-Time Near-Earth Plasma Sheet. *Geophys. Res. Lett.* 47, e2020GL090235. doi:10.1029/2020GL090235

Kistler, L. M., Mouikis, C. G., Asamura, K., Yokota, S., Kasahara, S., Miyoshi, Y., et al. (2019). Cusp and Nightside Auroral Sources of O + in the Plasma Sheet. *J. Geophys. Res. Space Phys.* 124, 10036–10047. doi:10.1029/2019JA027061

Lavraud, B., and Jordanova, V. K. (2007). Modeling the Effects of Cold-Dense and Hot-Tenuous Plasma Sheet on Proton Ring Current Energy and Peak Location. *Geophys. Res. Lett.* 34, L02102. doi:10.1029/2006GL027566

Lavraud, B., Thomsen, M. F., Wing, S., Fujimoto, M., Denton, M. H., Borovsky, J. E., et al. (2006). Observation of Two Distinct Cold, Dense Ion Populations at Geosynchronous Orbit: Local Time Asymmetry, Solar Wind Dependence and Origin. *Ann. Geophys.* 24, 3451–3465. doi:10.5194/angeo-24-3451-2006

Lemaire, J., Rycroft, M. J., and Roth, M. (1979). Control of Impulsive Penetration of Solar Wind Irregularities into the Magnetosphere by the Interplanetary Magnetic Field Direction. *Planet. Space Sci.* 27, 47–57. doi:10.1016/0032-0633(79)90146-6

Li, K., Haaland, S., Eriksson, A., André, M., Engwall, E., Wei, Y., et al. (2013). Transport of Cold Ions from the Polar Ionosphere to the Plasma Sheet. *J. Geophys. Res. Space Phys.* 118, 5467–5477. doi:10.1002/jgra.50518

Lin, R. L., Zhang, X. X., Liu, S. Q., Wang, Y. L., and Gong, J. C. (2010). A Three-Dimensional Asymmetric Magnetopause Model. *J. Geophys. Res.* 115, A04207. doi:10.1029/2009JA014235

Lukin, A. S., Panov, E. V., Artemyev, A. V., Petrukovich, A. A., Haaland, S., Nakamura, R., et al. (2020). Comparison of the Flank Magnetopause at Near-Earth and Lunar Distances: MMS and ARTEMIS Observations. *J. Geophys. Res. Space Phys.* 125, e2020JA028406. doi:10.1029/2020JA028406

McFadden, J. P., Carlson, C. W., Larson, D., Bonnell, J., Mozer, F. S., Angelopoulos, V., et al. (2008b). Structure of Plasmaspheric Plumes and Their Participation in Magnetopause Reconnection: First Results from THEMIS. *Geophys. Res. Lett.* 35, L17S10. doi:10.1029/2008gl033677

McFadden, J. P., Carlson, C. W., Larson, D., Ludlam, M., Abiad, R., Elliott, B., et al. (2008a). The THEMIS ESA Plasma Instrument and In-Flight Calibration. *Space Sci. Rev.* 141, 277–302. doi:10.1007/s11214-008-9440-2

McPherron, R. L., Hsu, T.-S., Kissinger, J., Chu, X., and Angelopoulos, V. (2011). Characteristics of Plasma Flows at the Inner Edge of the Plasma Sheet. *J. Geophys. Res.* 116, A00133. doi:10.1029/2010JA015923

Mouikis, C. G., Bingham, S. T., Kistler, L. M., Farrugia, C. J., Spence, H. E., Reeves, G. D., et al. (2019). The Storm-Time Ring Current Response to ICMEs and CIRs Using Van Allen Probe Observations. *J. Geophys. Res. Space Phys.* 124, 9017–9039. doi:10.1029/2019JA026695

Mouikis, C. G., Kistler, L. M., Liu, Y. H., Klecker, B., Korth, A., and Dandouras, I. (2010). H+ and O+ content of the Plasma Sheet at 15-19 Re as a Function of Geomagnetic and Solar Activity. *J. Geophys. Res.* 115, A00J16. doi:10.1029/2010JA015978

Nakamura, T. K. M., Hasegawa, H., and Shinohara, I. (2010). Kinetic Effects on the Kelvin-Helmholtz Instability in Ion-To-Magnetohydrodynamic Scale Transverse Velocity Shear Layers: Particle Simulations. *Phys. Plasmas* 17, 042119. doi:10.1063/1.3385445

Němeček, Z., Šafránková, J., Kruparova, O., Přech, L., Jelínek, K., Dušík, Š., et al. (2015). Analysis of Temperature versus Density Plots and Their Relation to the LLBL Formation under Southward and Northward IMF Orientations. *J. Geophys. Res. Space Phys.* 120, 3475–3488. doi:10.1002/2014JA020308

Němeček, Z., Šafránková, J., Lopez, R. E., Dušík, Š., Nouzák, L., Přech, L., et al. (2016). Solar Cycle Variations of Magnetopause Locations. *Adv. Space Res.* 58, 240–248. doi:10.1016/j.asr.2015.10.012

Němeček, Z., Šafránková, J., and Šimůnek, J. (2020). An Examination of the Magnetopause Position and Shape Based upon New Observations. *Geophys. Monogr. Ser.* 248, 135–151. doi:10.1002/9781119509592.ch8

Němeček, Z., Šafránková, J., Zastenker, G. N., Pišoft, P., and Jelínek, K. (2002). Low-frequency Variations of the Ion Flux in the Magnetosheath. *Planet. Space Sci.* 50, 567–575. doi:10.1016/S0032-0633(02)00036-3

Paschmann, G., Sonnerup, B. U. Ö., Papamastorakis, I., Sckopke, N., Haerendel, G., Bame, S. J., et al. (1979). Plasma Acceleration at the Earth's Magnetopause: Evidence for Reconnection. *Nature* 282, 243–246. doi:10.1038/282243a0

Richardson, I. G., Cliver, E. W., and Cane, H. V. (2021). Sources of Geomagnetic Storms for Solar Minimum and Maximum Conditions during 1972–2000. *Geophys. Res. Lett.* 28, 2569–2572.

Šafránková, J., Přech, L., Němeček, Z., and Sauvaud, J. A. (2002). Density Profile in the Magnetosheath Adjacent to the Magnetopause. *Adv. Space Res.* 30, 1693–1703. doi:10.1016/S0273-1177(02)00438-6

Samsonov, A. A., Němeček, Z., Šafránková, J., and Jelínek, K. (2012). Why Does the Subsolar Magnetopause Move Sunward for Radial Interplanetary Magnetic Field? *J. Geophys. Res.* 117, A05221. doi:10.1029/2011JA017429

Sandholt, P. E., Farrugia, C. J., Cowley, S. W. H., Denig, W. F., Lester, M., Moen, J., et al. (1999). Capture of Magnetosheath Plasma by the Magnetosphere during Northward IMF. *Geophys. Res. Lett.* 26, 2833–2836. doi:10.1029/1999gl900600

Shevyrev, N. N., Zastenker, G. N., Nozdrachev, M. N., Němeček, Z., Šafránková, J., and Richardson, J. D. (2003). High and Low Frequency Large Amplitude Variations of Plasma and Magnetic Field in the Magnetosheath: Radial Profile and Some Features. *Adv. Space Res.* 31, 1389–1394. doi:10.1016/S0273-1177(03)00008-5

Song, P., and Russell, C. T. (1992). Model of the Formation of the Low-Latitude Boundary Layer for Strongly Northward Interplanetary Magnetic Field. *J. Geophys. Res.* 97, 1411. doi:10.1029/91ja02377

Sonnerup, B. U. O., Paschmann, G., Papamastorakis, I., Sckopke, N., Haerendel, G., Bame, S. J., et al. (1981). Evidence for Magnetic Field Reconnection at the Earth's Magnetopause. *J. Geophys. Res.* 86, 10049. doi:10.1029/ja086ia12p10049

Sorathia, K. A., Merkin, V. G., Ukhorskiy, A. Y., Allen, R. C., Nykyri, K., and Wing, S. (2019). Solar Wind Ion Entry into the Magnetosphere during Northward IMF. *J. Geophys. Res. Space Phys.* 124, 5461–5481. doi:10.1029/2019JA026728

Spreiter, J. R., and Stahara, S. S. (1980). A New Predictive Model for Determining Solar Wind-Terrestrial Planet Interactions. *J. Geophys. Res.* 85, 6769. doi:10.1029/ja085ia12p06769

Spreiter, J. R., Summers, A. L., and Alksne, A. Y. (1966). Hydromagnetic Flow Around the Magnetosphere. *Planet. Space Sci.* 14, 223–253. doi:10.1016/0032-0633(66)90124-3

Thomsen, M. F., Borovsky, J. E., Skoug, R. M., and Smith, C. W. (2003). Delivery of Cold, Dense Plasma Sheet Material into the Near-Earth Region. *J. Geophys. Res.* 108, 1151. doi:10.1029/2002JA009544

Toledo-Redondo, S., André, M., Khotyaintsev, Y. V., Vaivads, A., Walsh, A., Li, W., et al. (2016). Cold Ion Demagnetization Near the X-Line of Magnetic Reconnection. *Geophys. Res. Lett.* 43, 6759–6767. doi:10.1002/2016gl069877

Treumann, R. A., Labelle, J., and Bauer, T. M. (1995). "Diffusion Processes: An Observational Perspective," in *Geophysical Monograph Series*. Editor D. Chiang (Washington DC: American Geophysical Union), 90, 331.

Tsyganenko, N. A. (1989). A Magnetospheric Magnetic Field Model with a Warped Tail Current Sheet. *Planet. Space Sci.* 37, 5–20. doi:10.1016/0032-0633(89)90066-4

Tsyganenko, N. A., and Andreeva, V. A. (2015). A Forecasting Model of the Magnetosphere Driven by an Optimal Solar Wind Coupling Function. *J. Geophys. Res. Space Phys.* 120, 8401–8425. doi:10.1002/2015ja021641

Weigel, R. S. (2010). Solar Wind Density Influence on Geomagnetic Storm Intensity. *J. Geophys. Res.* 115, A09201. doi:10.1029/2009JA015062

Wing, S., Johnson, J. R., Chaston, C. C., Echim, M., Escoubet, C. P., Lavraud, B., et al. (2014). Review of Solar Wind Entry into and Transport within the Plasma Sheet. *Space Sci. Rev.* 184, 33–86. doi:10.1007/s11214-014-0108-9

Yermolaev, Y. I., Nikolaeva, N. S., Lodkina, I. G., and Yermolaev, M. Y. (2009). Catalog of Large-Scale Solar Wind Phenomena during 1976-2000. *Cosmic Res.* 47, 81–94. doi:10.1134/S0010952509020014

Yu, Y., Chen, Z., and Chen, F. (2020). Cold and Dense Plasma Sheet Caused by Solar Wind Entry: Direct Evidence. *Atmosphere* 11, 831. doi:10.3390/atmos11080831

Zastenker, G. N., Nozdrachev, M. N., Němeček, Z., Šafránková, J., Paularena, K. I., Richardson, J. D., et al. (2002). Multispacecraft Measurements of Plasma and Magnetic Field Variations in the Magnetosheath: Comparison with Spreiter Models and Motion of the Structures. *Planet. Space Sci.* 50, 601–612. doi:10.1016/S0032-0633(02)00039-9

Zwan, B. J., and Wolf, R. A. (1976). Depletion of Solar Wind Plasma Near a Planetary Boundary. *J. Geophys. Res.* 81, 1636–1648. doi:10.1029/ja081i010p01636

Conflict of Interest: The authors declare that the research was conducted in the absence of any commercial or financial relationships that could be construed as a potential conflict of interest.

frontiers in Astronomy and Space Sciences

ORIGINAL RESEARCH
published: 17 November 2021
doi: 10.3389/fspas.2021.758442

Ion Dynamics in the Meso-scale 3-D Kelvin–Helmholtz Instability: Perspectives From Test Particle Simulations

Xuanye Ma[1]*, *Peter Delamere*[2], *Katariina Nykyri*[1], *Brandon Burkholder*[1], *Stefan Eriksson*[3] *and Yu-Lun Liou*[1]

[1]Center for Space and Atmospheric Research, Embry–Riddle Aeronautical University, Daytona Beach, FL, United States, [2]Geophysical Institute, University of Alaska Fairbanks, Fairbanks, AK, United States, [3]Laboratory for Atmospheric and Space Physics, University of Colorado, Boulder, CO, United States

OPEN ACCESS

Edited by:
Luca Sorriso-Valvo, Institute for Space Physics (Uppsala), Sweden

Reviewed by:
Adriana Settino, University of Calabria, Italy
Silvio Sergio Cerri, Princeton University, United States

***Correspondence:**
Xuanye Ma
max@erau.edu

Specialty section:
This article was submitted to Space Physics, a section of the journal Frontiers in Astronomy and Space Sciences

Received: *14 August 2021*
Accepted: *04 October 2021*
Published: *17 November 2021*

Citation:
Ma X, Delamere P, Nykyri K, Burkholder B, Eriksson S and Liou Y-L (2021) Ion Dynamics in the Meso-scale 3-D Kelvin–Helmholtz Instability: Perspectives From Test Particle Simulations. Front. Astron. Space Sci. 8:758442. doi: 10.3389/fspas.2021.758442

Over three decades of *in-situ* observations illustrate that the Kelvin–Helmholtz (KH) instability driven by the sheared flow between the magnetosheath and magnetospheric plasma often occurs on the magnetopause of Earth and other planets under various interplanetary magnetic field (IMF) conditions. It has been well demonstrated that the KH instability plays an important role for energy, momentum, and mass transport during the solar-wind-magnetosphere coupling process. Particularly, the KH instability is an important mechanism to trigger secondary small scale (i.e., often kinetic-scale) physical processes, such as magnetic reconnection, kinetic Alfvén waves, ion-acoustic waves, and turbulence, providing the bridge for the coupling of cross scale physical processes. From the simulation perspective, to fully investigate the role of the KH instability on the cross-scale process requires a numerical modeling that can describe the physical scales from a few Earth radii to a few ion (even electron) inertial lengths in three dimensions, which is often computationally expensive. Thus, different simulation methods are required to explore physical processes on different length scales, and cross validate the physical processes which occur on the overlapping length scales. Test particle simulation provides such a bridge to connect the MHD scale to the kinetic scale. This study applies different test particle approaches and cross validates the different results against one another to investigate the behavior of different ion species (i.e., H+ and O+), which include particle distributions, mixing and heating. It shows that the ion transport rate is about 10^{25} particles/s, and mixing diffusion coefficient is about 10^{10} m^2 s^{-1} regardless of the ion species. Magnetic field lines change their topology *via* the magnetic reconnection process driven by the three-dimensional KH instability, connecting two flux tubes with different temperature, which eventually causes anisotropic temperature in the newly reconnected flux.

Keywords: Kelvin-Helmholtz instability, test particle simulation, ion acceleration, magnetopause, MHD simulation

1 INTRODUCTION

The Kelvin–Helmholtz (KH) instability is one of the most common physical processes at the magnetopause boundary of the Earth (Fairfield et al., 2000; Hasegawa et al., 2004; Nykyri et al., 2006; Eriksson et al., 2016; Li et al., 2016) as well as other planets (e.g., Jupiter and Saturn) (Johnson et al., 2014; Ma et al., 2015; Burkholder et al., 2017). It is driven by a large sheared flow, and it can be stabilized by the magnetic field along the sheared flow direction (Chandrasekhar, 1961), compressibility, and a broad initial shear flow width (Miura and Pritchett, 1982). Therefore, KH instability can occur under north, south, and Parker-spiral interplanetary magnetic field (IMF) conditions in the vicinity of the equatorial plane (Hwang et al., 2011; Kavosi and Raeder, 2015; Henry et al., 2017), as well as at high latitudes during the dawn or dusk-ward IMF condition (Hwang et al., 2012; Ma et al., 2016; Nykyri et al., 2021a).

As a macro-scale dissipation process, the KH instability alone can transport momentum and energy from solar wind into the magnetosphere (Pu and Kivelson, 1983a; Pu and Kivelson, 1983b). It has been shown that the anomalous (eddy) viscosity is about $0.02V_0a$ in the nonlinear stage of the KH instability, where a is the half width of the initial velocity shear layer, and V_0 is total velocity jump (Miura, 1984), which is about 10^9 m^2 s^{-1} for a typical Earth's magnetopause condition. This value is consistent with the requirement by the "viscous-like" interaction (Axford and Hines, 1961; Sonnerup, 1980). Furthermore, during the nonlinear stage, the KH instability can strongly modify the boundary, generating a thin current sheet, which triggers magnetic reconnection (Otto and Fairfield, 2000; Nakamura et al., 2008; Nakamura and Fujimoto, 2008) and other kinetic physics [e.g., kinetic Alfvén wave, magnetosonic wave, see detailed discussion in (Masson and Nykyri, 2018)]. These secondary processes will break the frozen-in condition which allows the plasma transport between the magnetosheath and the magnetosphere (Otto and Fairfield, 2000; Nakamura et al., 2008; Ma et al., 2017). In two-dimensional (2-D) geometry, there are two types of KH driven reconnection (Nakamura et al., 2008; Nakamura and Fujimoto, 2008). "Type I" operates if the initial magnetic field component along the sheared flow direction is anti-parallel across the sheared flow layer (i.e., a pre-existing large current layer case). In this condition, the pre-existing current layer will be further compressed in the spine region (i.e., the region connecting two neighboring vortices) during the growth of the KH instability, and this process will eventually trigger magnetic reconnection. This reconnection process allows the magnetosheath magnetic field to connect to magnetospheric magnetic field. The "type II" operates without a pre-existing current layer, meaning the magnetic field components across the sheared flow layer are mostly along the same direction. In such a condition, the well developed KH vortices can fold the magnetic field line in the KH plane (Otto and Fairfield, 2000). This process can change the magnetic field directions and form thin current layers in the vortices. If the width of the current layer is comparable to the ion inertial length, then magnetic reconnection occurs between the magnetosheath field lines or the magnetospheric field lines, which generates a large magnetic island detached from the original field line which moves to the other side of the original boundary layer. Two-dimensional MHD and Hall MHD estimated that this type of plasma transport process can transport plasma at a speed of several km s^{-1}, equivalent to a diffusion coefficient of about 10^9 m^2 s^{-1} for Earth's typical magnetopause conditions (Nykyri and Otto, 2001; Nykyri and Otto, 2004). Although hybrid simulations show similar overall dynamical properties (e.g., growth rate, anomalous (eddy) viscosity, and the size of mixed region), magnetic reconnection occurs in a more patchy manner, which forms a series of smaller magnetic islands (Ma et al., 2019). In order to quantify the diffusion caused by the nonlinear KH instability, hybrid simulations define mixing region based on the percentage of the particles from both side of the boundary in a given cell (Terasawa et al., 1992), or calculate the standard deviation of the normal direction displacement of the particles in the activity region (Cowee et al., 2009; Cowee et al., 2010). For hybrid simulation, the mixing diffusion coefficient is about 10^8—10^9 m^2 s^{-1} for typical Earth's environment (Cowee et al., 2009; Cowee et al., 2010) and 10^{10} m^2 s^{-1} for Saturn (Delamere et al., 2011).

The observed KH instability at the 3-D magnetopause boundary is often localized in the vicinity of the equatorial plane due to the magnetic field curvature. For northward IMF condition, the well developed KH vortex will drag low-latitude magnetosheath magnetic field lines in the sun-ward direction and low-latitude magnetospheric magnetic field lines in the tail-ward direction, reminiscent of a "candy wrapper." This process will generate anti-parallel magnetic field components at mid-latitude, and eventually will trigger a pair of mid-latitude reconnection sites, which is often referred as double-mid-latitude-reconnection (DMLR) (Otto, 2006; Faganello et al., 2012). Detailed discussions of type-I, type-II, and DMLR can be found in recent papers by Faganello and Califano (Faganello and Califano, 2017) and Ma et al. (Ma et al., 2017). The net effect of this process exchanges the low-latitude magnetosheath and magnetospheric flux tubes, and therefore transports the mass and flux tube entropy between the magnetosheath and the magnetosphere. It has been estimated that the mass transport rate is about 10^{10} m^2 s^{-1} (Ma et al., 2017) for Earth's typical magnetopause condition. For southward IMF condition, the KH instability can occur on the equatorial plane, while the meridian is tearing mode unstable. Thus, both KH instability and magnetic reconnection can operate simultaneously. The nonlinear interaction between these two processes leads to a fast reconnection growth rate which is close to the Petschek reconnection rate without including kinetic physics. However, the total reconnected flux is limited by the KH instability, since the KH instability diffuses the boundary current layer (Ma et al., 2014a; Ma et al., 2014b).

It is also useful to consider the KH instability as a cross-scale process. The typical KH wavelength at the Earth's magnetopause is about 2–6 Earth's radii (R_E), (i.e., about 50–500 ion inertial lengths for the magnetopause density around 1–10 cm^{-3}), and the localization along the z direction is comparable to the KH wavelength (Ma et al., 2014a). However, the different types of secondary instabilities triggered by the nonlinear KH instability often occur at sizes comparable to ion inertial scales (Nykyri et al.,

2021b). Thus, it would be ideal to use hybrid or even fully kinetic simulation to systematically investigate the KH instability and its secondary instability. For instance, Karimabadi et al. (Karimabadi et al., 2013) used kinetic PIC code VPIC to demonstrate the formation of coherent structures in the form of current sheets that steepen to electron scales through turbulent cascade during the KH instability, which triggers strong localized heating of the plasma. However, it is often computationally expensive and the non-periodic boundary conditions along the non-wave-direction are not trivial to incorporate in particle simulations.

One compromise is the test particle simulation approach based on the electromagnetic field provided by fluid simulation. This approach does not provide a feedback mechanism from particles to the field, such that a significant part of the kinetic physics aspect is excluded. However, it still reproduces the anisotropic temperature and particle mixing in a two-dimensional geometry (Ma et al., 2019). Furthermore, Henri et al. (Henri et al., 2013) carefully compared simulation of 2-D KH instability by using MHD, Hall-MHD, two-fluid, hybrid kinetic, and full kinetic codes, showing that the feedback from small, kinetic scales to large, fluid scales is negligible in the nonlinear regime despite differences in the small scale processes between the different models. Thus, the motivation of this paper is to further explore the application of the test particle simulation in a 3-D KH instability.

2 NUMERICAL METHOD

2.1 MHD Simulation

In this study, all physical quantities are normalized by their typical values, which are given by length scale L_0 = 640 km, density n_0 = 10 cm^{-3}, magnetic field magnitude B_0 = 70 nT, and the typical value of other quantities can be derived from these three quantities. The full set of normalized resistive MHD equations are solved by the leap-frog scheme, which has a long heritage of investigating mesoscale MHD instabilities (Birn, 1976; Otto, 1990; Otto and Fairfield, 2000; Nykyri and Otto, 2001; Ma et al., 2014a; Ma et al., 2014b; Ma et al., 2017). The whole set of simulations are carried out in a rectangular cuboid domain (i.e., $[-L_x, L_x] \times [-L_y, L_y] \times [-L_z, L_z]$), in which $L_x = 20$, $L_y = 10$, and $L_z = 40$. Here the x direction is the normal direction of the unperturbed magnetopause boundary, pointing from the magnetosphere to the magnetosheath. The z direction points to the North, which is mostly along the magnetic field direction. The y direction is determined by the right hand rule, which is also mostly along the sheared flow direction. The y direction uses periodic boundary conditions. The x direction uses closed boundary conditions (i.e., $B_x = v_x = 0$ and $\partial_x = 0$ for other quantities), however, the dimension along the x direction is sufficiently large, that the reflection from x boundary is negligible to the end of the simulation. The z direction uses open boundary conditions (i.e., $\partial_z = 0$ for all quantities, except B_z is determined by the zero-divergence of the magnetic field), however quantities on these boundaries remain at their initial value due to the artificial friction term we applied to the top and bottom boundaries (see below).

The initial steady state configuration is a one-dimensional transition layer, which is given by $\mathbf{F} = \bar{\mathbf{F}} + \delta\mathbf{F} \tanh(x/D)$, where $D = 1$ is the width of the transition layer, $\mathbf{F} = [\rho, v_y, B_y, B_z]$, $\bar{\mathbf{F}} = \mathbf{F}_1 + \mathbf{F}_2$, and $\delta\mathbf{F} = \mathbf{F}_1 - \mathbf{F}_2$. Here, the subscripts 1 and 2 represent the value on the magnetosheath side (i.e., $x > 0$) and the magnetospheric side (i.e., $x < 0$), respectively. The other components of the vector quantities are set to be zero (i.e., $v_x = v_z = B_x = 0$). Two different initial conditions are used in this study. The first case is given by $\mathbf{F}_1$ = [1.54, 0.42, 0, 1.02] and $\mathbf{F}_2$ = [0.46, 0.42, 0, 0.98], which is referred to as the symmetric case since $B_y = 0$. In this situation, the bulk velocity is perpendicular to the magnetic field. In a 2-D geometry, the dynamics in the xy-plane decouple from the z direction, which eliminates the onset of magnetic reconnection in the MHD and hybrid description (Otto and Fairfield, 2000; Settino et al., 2020). In the 3-D geometry, the system maintains north-south symmetry, meaning the magnetic field is always perpendicular to the bulk flow in the equatorial plane. Thus, there is no low-latitude reconnection (Ma et al., 2017). However, the localized perturbation and boundary condition (see below) break the translational symmetry along the z direction, which locally twists the magnetic field to generate DMLR (Faganello et al., 2012; Faganello and Califano, 2017; Ma et al., 2017). The second case is given by $\mathbf{F}_1$ = [1.54, 0.42, −0.35, 1.02] and $\mathbf{F}_2$ = [0.46, 0.42, −0.08, 0.98], which is referred to as the asymmetric case and low-latitude KH driven reconnection can occur. The initial conditions for the asymmetric case are approximately the same as those observed by the MMS satellites on 8 Sept 2015 (Eriksson et al., 2016). Notice, this event has been simulated by several numerical models, which mostly use a constant B_z [e.g., (Nakamura et al., 2017; Franci et al., 2020)]. Due to the flexility of the MHD model, we can include a tiny B_z variation in this study to make the model closer to the real event. However, such a tiny variation is not expected to bring a significant impact on the overall dynamics compared to the constant B_z.

The KH instability is triggered by a velocity perturbation, which is given by $\mathbf{v} = \nabla\Phi(x, y) \times \mathbf{e}_z f(z)$. Here, the stream function is $\Phi(x, y) = \delta v \cos(x/l_x) \cosh^{-1}(k_y y)$, $l_x = 2$, $k_y = \pi/L_y$ and $\delta v = v_y/20$. In this study, the simulation assumes the high-latitude magnetic field lines move with the solar wind or are tied to the ionosphere. Thus, the KH perturbation is localized in the vicinity of the equatorial plane, in which the localization function $f(z)$ is given by $f(z) = 0.5\{\tanh[(z + z_d)/D_z] - \tanh[(z - z_d)/D_z]\}$, $z_d = 0.5L_z$, and $D_z = 3$. Furthermore, an artificial friction term $-\nu(z)(\mathbf{v} - \mathbf{v_0})$ is applied to the right-hand side of the momentum equation. Here, $\mathbf{v_0}$ is the unperturbed bulk velocity, which also represents the solar wind or ionosphere speed. The friction term tends to force the plasma to move at its initial velocity, or equivalently it absorbs perturbations, maintaining the initial boundary layer away from the equatorial plane. Therefore, the friction coefficient is given by $\nu(z) = 0.5\{2 - \tanh[(z + z_\nu)/D_\nu] + \tanh[(z - z_\nu)/D_\nu]\}$, $z_\nu = 0.75L_z$, and $D_\nu = 3$, which has been switched on only near the top and bottom boundaries (Ma et al., 2017).

In the MHD simulation, for any given point at any given time, a magnetic field line can be traced from this point to the top and bottom boundaries. Notice, the top and bottom boundaries in this

simulation represent the unperturbed region. Thus, if the x-component of the spatial location of the magnetic field line's footprint on the top (X_{top}) or bottom boundaries (X_{bot}) is smaller than zero, then it means this end of the magnetic field line is connecting to the magnetospheric side at that moment. Similarly, if the X_{top} or X_{bot} is larger than zero, then it means this end of the magnetic field line is connecting to the magnetosheath side. In this study, we refer to the magnetic field line with both top and bottom footprints on the magnetosheath (magnetospheric) side as magnetosheath (magnetospheric) field lines. Magnetic field line with one end connecting to the magnetosheath side and the other end connecting to the magnetospheric side is referred to as open field line.

2.2 Test Particle Simulation

The full set of non-relativistic Lorentz equations are solved using the traditional Boris method (Boris, 1970), which has been used to investigate high-energy particles in the cusp diamagnetic cavity (Nykyri et al., 2012), and KH instability (Ma et al., 2019). The symmetric treatment of the time derivative in the Boris method maintains the temporal reversibility of the Lorentz equation. Thus, this code can reverse trace the test particles to reconstruct particle distributions based on Liouville's theory (Birn et al., 1997; Birn et al., 1998).

For the forward tracing simulation, we launch particles with shifted Maxwellian distributions ($\max v < 4$ in simulation unit or 2000 km s^{-1}) inside of the MHD simulation domain (i.e., [−15, 15] × [−10, 10] × [−40, 40]) with 150 × 200 × 200 cells at $t = 0$, which covers most of the KH active region. Notice, we did not launch the particles outside of $|x| = 15$ to save on computational effort, since the thermal particles there merely reach to the KH active region toward the end of the simulation. The number of particles in each cell is proportional to the plasma density in the middle of the cell (i.e, 50 particles/cell ~ $\rho = 0.46$), which gives a total 6,51,320,000 particles within the MHD simulation domain. The number of particles on the magnetospheric side is about 1/3 of the particles on the magnetosheath side. Maintaining particle numbers in the simulation domain is an important aspect of particle simulations (i.e., PIC, hybrid, and test particle simulation), in which periodic boundary conditions are often used. However, the 3-D KH instability processes, which involves middle latitude reconnection or nonlinear interaction between the KH instability and reconnection processes have no periodicity along the third direction (i.e., z-direction). Therefore, the often used periodic boundary conditions may not be appropriate for these types of simulations. This study uses extended boundary conditions. This type of boundary condition adds additional domains ($[-dL_z - L_z, L_z + dL_z]$) along the top and bottom of the fluid simulation domains ($[-L_z, L_z]$), in which density, pressure, magnetic field, and bulk velocity are set to be the same as the value at the fluid simulation top and bottom boundaries. Consequently, the particle distribution is initialized in the same way as it is inside of the fluid simulation domain. For computational efficiency, we only trace the particles that can reach the simulation domain during the test particle simulation time. Those particles can be easily identified by their initial location z_0 and velocity v_0. Assuming that the total test particle simulation interval is τ and the charged particles are mostly moving along the magnetic field line (at least in the buffer region), then by the time of τ, the z component of the particle location will be within $z_e = z_0 + v_{0\parallel}\tau \pm g_r = z_e' \pm g_r$, where $v_{0\parallel}$ is the initial parallel velocity, and g_r is the gyro-radius, which is dependent on the initial perpendicular velocity. Notice, if $B_y \neq 0$, the gyro motion has a component along the z direction, which is the reason why we have to take the gyro-radius in to account. Thus, we only need to trace particles with $|z_e'| < L_z + \delta z$, where δz is an arbitrary value greater than $\max g_r$. During this study, this boundary condition leads to the total number of particles inside of the simulation box $[-L_z, L_z]$ changing less than 0.4% of the initial number.

For the backward tracing, we only focus on the KH active region in the equatorial plane (i.e., [−6, 6] × [−10, 10] resolved by 61 × 101 grid points) in the nonlinear stage for the symmetric case. For each individual grid point, we traced 51^3 particles backward to $t = 0$, covering a range of $[-3v_{th}, 3v_{th}]^3$ in velocity space. Here, v_{th} is the thermal velocity at the grid point. Then, the weight of each particle, w, is estimated based on the phase space density of the shifted Maxwellian distribution at $[\mathbf{x},\mathbf{v}]_{t=0}$ with the assumption that Liouville's theory is satisfied. Thus, the number density, velocity, and pressure can be obtained through the zeroth to second order moments of w integrated over the whole $[-3v_{th}, 3v_{th}]^3$ velocity space.

3 RESULTS

Figure 1 shows a fully developed KH vortex in the equatorial plane ($z = 0$) at $t = 130$ for the symmetric case (top) and the asymmetric case (bottom). The black arrows are the bulk velocity. The color index represents the plasma density, ρ, (left) and mixing rate, r_M, (right). Here, the high and low density regions indicate the magnetosheath plasma and the magnetospheric plasma, respectively. The mixing rate is defined as $r_M = 1–2|0.5 - p|$, where $1 \geq p \geq 0$ is the probability of magnetosheath particles for a given cell (Matsumoto and Hoshino, 2006). Thus $r_M = 1$ means fully mixed, $r_M = 0$ means no mixing. The magenta line represents the magnetosheath-magnetosphere boundary based on magnetic field topology (i.e., the x-component of the magnetic field line footprints on the top or bottom boundaries are zero). Thus, for the symmetric case all the magnetic field lines on left side of the magenta line are closed magnetospheric field lines, which also includes regions with magnetosheath-like, high-density plasma. Magnetic field lines in these regions have experienced the DMLR process, changing their connection from the magnetosheath to the magnetosphere, which are referred to as "newly connected magnetospheric magnetic field lines." Similarly, magnetospheric-like, low-density plasma also observed on the right side of the magenta line, indicating that magnetic field lines in these regions are "newly connected magnetosheath magnetic field lines." For the asymmetric case, a single magnetic field line may not experience DMLR simultaneously, which will generate open flux regions (e.g., $y \in [2,4]$ region). The right panels of mixing rate r_M show that the majority of the mixed region is along the

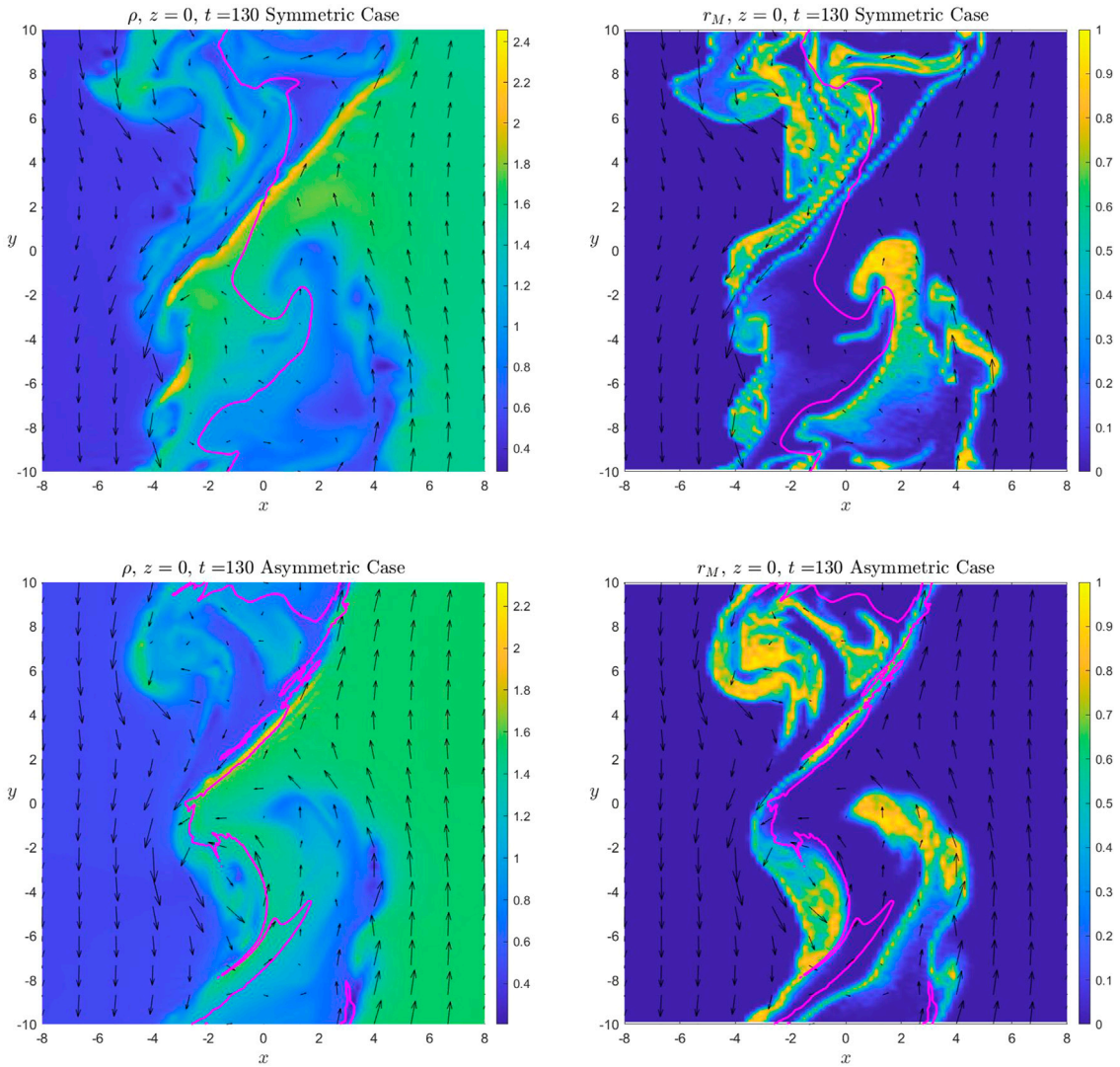

FIGURE 1 | A fully developed KH vortex in the equatorial plane ($z = 0$) at $t = 130$ for the symmetric case (top) and the asymmetric case (bottom). The color index represents the plasma density **(left)** and mixing rate **(right)**. The black arrows represent the x and y components of the bulk velocity. The magenta line represents the magnetosheath-magnetosphere boundary based on magnetic field topology.

density boundary layer. Note, some newly connected magnetospheric magnetic field lines do not involve any mixing. This means the mixing in the low latitude is mostly *via* the finite gyroradius effect. Although the DMLR process provides the connection between magnetosheath and magnetospheric field lines, it takes time for ion particles moving from high latitudes to lower latitudes to influence the mixing rate in the equatorial plane.

Figure 2 shows the overall dynamic properties for the symmetric case (left) and the asymmetric case (right). The top to bottom panels plot the growth of the KH instability (the range of the bulk velocity v_x component), the change of mass on the magnetosheath side (blue) and magnetospheric side (red), and the total mixed volume $V_m = \int r_M(x, y, z)dxdydz$, respectively. This demonstrates that the perturbation grows exponentially before $t = 80$ (i.e., the linear stage) and saturates after $t = 80$ (i.e., the nonlinear stage) for the symmetric case. Stabilized by the magnetic B_y component, the asymmetric case has a relatively lower growth rate. During the nonlinear stage, a significant amount of mass is transported from the magnetosheath into the magnetosphere *via* the DMLR process for the symmetric case. We estimated that the maximum transport rate (i.e., dM/dt) is about 10^{25} particles/s, or the transport diffusion coefficient of 9×10^9 m^2 s^{-1}, which is given by dL_M^2/dt, where $L_M = M/(4L_yL_z\rho_{\mathrm{msh}})$. For the asymmetric case, the plasma lost from the magnetosheath side moves to the magnetospheric side as well as to open flux regions. Thus, the magnetosheath mass decrease rate is comparable to the symmetric case, while the magnetosphere mass increase rate is lower than it is in the symmetric case. Actually, at the early stage, the magnetosphere loses mass into the

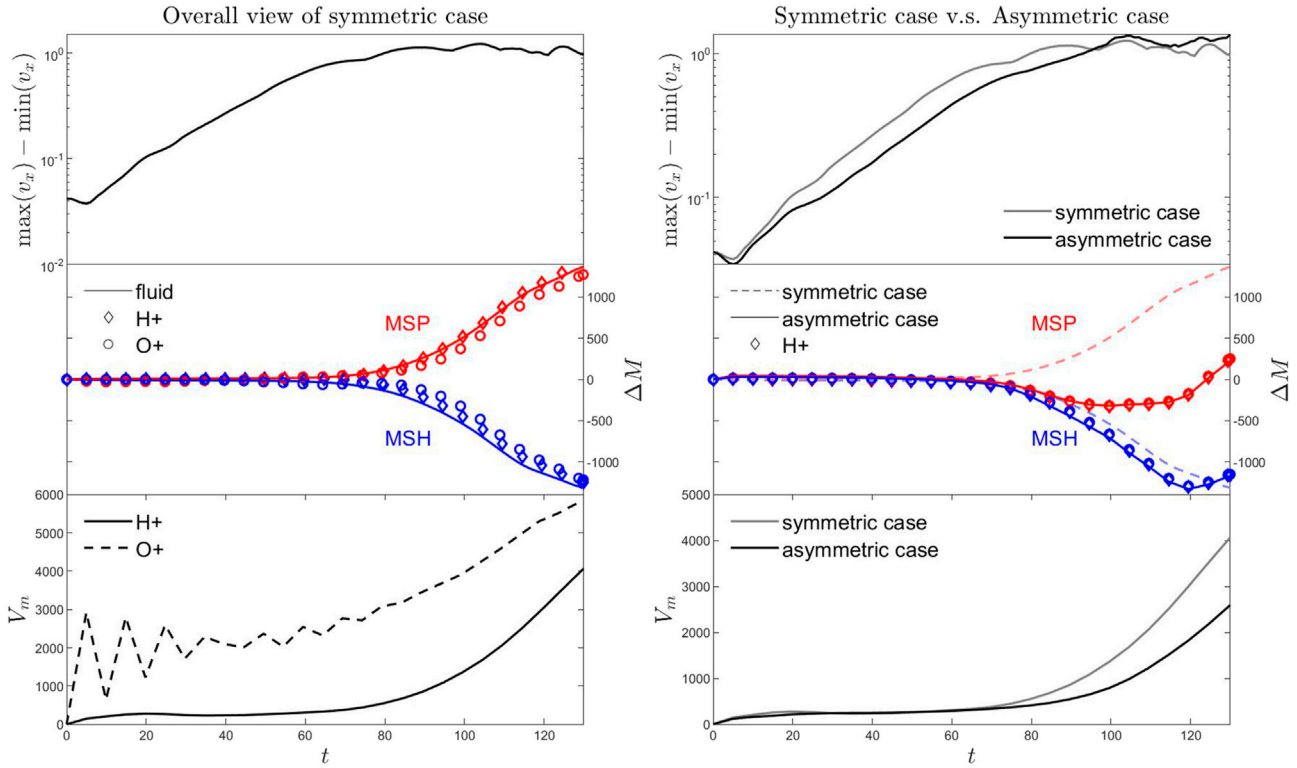

FIGURE 2 | The overall dynamical properties for the symmetric case **(left)** and the asymmetric case **(right)**. The top to bottom panels show the growth of the KH instability (the range of the bulk velocity v_x component), the change of mass on the magnetosheath side (blue) and magnetospheric side (red), and the total mixed volume V_m, respectively. In the left-middle panel, the fluid approach is represented by the solid lines and test particle approaches based on H+ and O+ are represented by diamonds and circles, respectively. In the left-bottom panel the total mixed volume is shown based on H+ (solid line) and O+ (dashed line). In the right panels, the results from symmetric case are in light gray lines or dashed lines for reference.

open flux region, due to the DMLR process operating nonsimultaneously. The total mixed volume, V_m, also shows a significant increase during the nonlinear stage, which is due to the elongation of the magnetosheath-magnetosphere boundary layer *via* the KH vortex as well as magnetic field line topology change *via* the mid-latitude reconnection process. While the asymmetric case shows a much smaller total mixed volume than the symmetric case by the time $t = 130$, it could be simply due to the asymmetric case reaching the nonlinear stage a bit later than the symmetric case. The maximum mixing diffusion rate for the symmetric case is about 1010 m^2 s^{-1}, given by dL_m^2/dt, where $L_m = V_m/(4L_zL_y)$.

In this study, we apply both fluid and particle approaches to evaluate the total mass on the magnetosheath side and the magnetospheric side. For the fluid approach, one can trace the magnetic field lines from the top of the MHD simulation domain, and calculate the flux tube content $\eta(x, y) = \int \rho/Bds$ along the magnetic field line, then integrate the flux tube content on the top boundary on the magnetosheath (i.e., $M_{msh} = \int_{msh}\eta(x, y)B_z dxdy$) and magnetospheric sides ($M_{msp} = \int_{msp}\eta(x, y)B_z dxdy$). This method is computationally inexpensive, however it may incur a large error if the boundary is not perfectly unperturbed. A more accurate method is to integrate the plasma density in the magnetosphere, magnetosheath, and open flux regions (i.e., $M = \int \rho dxdydz$), which can be achieved *via* identification of the connection of each grid point (magnetosphere, magnetosheath or open flux) by tracing the field lines to the top and bottom boundaries. A dense grid is needed in the KH active region to increase the accuracy, which requires a relatively higher computational cost. For the particle approach, one can count the total number of particles with different connections. However, this is a computationally expensive. A more practical approach is to identify the x-component of footprints on the top (X_{top}) and bottom (X_{bot}) boundary for each individual grid point of a dense grid covering the KH active region, and then interpolate the X_{top} and X_{bot} to the guiding center of the particle to identify the connection of each individual particle. One can also redistribute the particles to the eight neighboring grid points to get a smoother statistical count. However, with a large number of particles, these two methods give almost identical results. As long as we know the total mass each particle represents, we can easily covert the particle approach (number of particles) into the fluid approach (mass). The middle panel of **Figure 2** shows the results from the fluid approach (solid lines) and particle approach (diamond) are identical, indicating the zeroth order moment of the particle distribution is consistent with the fluid description.

In this study, we launch two different ion species (i.e., H+ and O+) with the same velocity distribution for the symmetric case. The result (left-middle panel in **Figure 2**) shows that although O+ (circle) has a much larger gyroradius compared to H+ (diamond), it is still much smaller than the KH wavelength. Thus, the transport rate is insensitive to the mass-to-charge ratio for Earth's typical magnetopause conditions. The left-bottom panel of **Figure 2** shows that with a much larger gyroradius, the mixed volume for O+ (dashed line) is much greater than the H+ (solid line). In the linear stage, the ratio between O+ and H+ mixed volume is close to the ratio of their gyroradii, with the oscillation in the dashed line caused by the O+ gyro-frequency. However, in the nonlinear stage the O+ and H+ mixed volumes have a similar mixing diffusion rate, and their ratio decreases to about two. This is because in the nonlinear stage the density boundary is highly twisted and folded by the KH instability, collapsing the original undulated boundary layer into a thick region, which limits the efficiency of the larger gyroradius on the increase of the mixed volume.

The large temperature and specific entropy difference between the magnetosheath and magnetospheric plasma leads to an important question of whether the plasma has been (nonadiabatically) heated when it is transported from the magnetosheath into the magnetosphere (Ma and Otto, 2014). It has been demonstrated that magnetic reconnection cannot provide sufficient adiabatic heating unless the plasma beta is much smaller than unity (Ma and Otto, 2014). However, the typical magnetosheath plasma beta is about one (Ma et al., 2020), leading to the speculation that the KH instability may be responsible for an additional nonadiabatic heating source (Moore et al., 2016; Moore et al., 2017; Nykyri et al., 2021a; Nykyri et al., 2021b). But, as an ideal instability (i.e., the onset of the instability does not break the "frozen-in" condition), the MHD description of the KH instability conserves specific entropy, meaning no nonadiabatic heating source. Nevertheless, the KH instability and the associated secondary instabilities are naturally associated with turbulence (Matsumoto and Hoshino, 2006; Stawarz et al., 2016; Nakamura et al., 2017; Nykyri et al., 2017; Dong et al., 2018; Nakamura et al., 2020), which has a long history of studies demonstrating that turbulent heating is a very effective mechanism for ion heating [e.g., Quataert (Quataert, 1998), Johnson and Cheng (Johnson and Cheng, 2001), Chandran et al. (Chandran et al., 2010), Told et al. (Told et al., 2015), Vasquez (Vasquez, 2015), Grošelj et al. (Grošelj et al., 2017), Arzamasskiy et al. (Arzamasskiy et al., 2019), Cerri et al. (Cerri et al., 2021)]. Delamere et al. (Delamere et al., 2021) estimated a turbulent ion heating rate density $\approx 10^{-15}$ W m^{-3} during the nonlinear stage of 3-D hybrid KH instability simulations based on the typical Saturn's magnetopause boundary condition, which is consistent with the Cassini data analysis (Burkholder et al., 2020). Such estimations should also apply to investigate Earth's magnetopause boundary both from numerical simulation and observational data analysis, which, however, is out of scope of this paper. Meanwhile, from the perspective of the particle description, there are two plausible hypotheses to increase the specific entropy. The first one is the free expansion of magnetosheath plasma into the newly reconnected magnetosphere flux tube (Johnson et al., 2014). The second one is that higher energy particles are preferentially transported from magnetosheath into the magnetosphere by the KH instability, which can be easily tested by using test particle simulation. Recently, MMS encountered trapped energetic particles within KH waves at the high-latitude magnetosphere (Nykyri et al., 2021a).

The top panel of **Figure 3** plots the energy distribution for the particles that moved from the magnetosheath into the magnetosphere (blue) and the particles that moved from the magnetosphere into the magnetosheath (red) at $t = 130$ for the symmetric case. As a reference, we also plot the energy distribution for those particles at $t = 0$ (dots), as well as the energy distribution for the particles remaining in the magnetosphere (black) and the magnetosheath (magenta). Here, the energy is v_d^2, where v_d is the particle velocity minus the MHD bulk velocity. The results show the energy distributions do not change with the time, indicating there is no heating source during the KH process, which is consistent with the MHD description. However, the mean energy (i.e., temperature) of the plasma transported from the magnetosheath into the magnetosphere is indeed higher than the plasma remaining in the magnetosheath, and particles transported from the magnetosphere to the magnetosheath are lower energy than those remaining in the magnetosphere. This appears to support that the KH instability filters higher energy particles from magnetosheath into the magnetosphere. However, the bottom panel of **Figure 3** plots the initial energy distribution (i.e., $t = 0$) for the particles that already crossed the boundary at $t = 130$ as a function of their initial location along the x-direction. The black line represents 1.5 times the initial temperature, T (i.e., kinetic energy), demonstrating that the higher energy (temperature) of the magnetosheath-originating particles is simply because they are from the hotter part of the preexisting boundary layer. Thus, the second hypothesis does not hold for the thermal population. The super-thermal population requires additional testing, which is out of the scope of this study.

The above results suggest that the zeroth order moment of the particle distribution in the whole simulation domain is mostly consistent with the density from the MHD simulation. It is of interest to examine the consistency of higher order moments between test particle and MHD simulation. The top panels of **Figure 4** plot the deviation between MHD bulk velocity, $\mathbf{v}_M$ and the first order moment from forward tracing ($\mathbf{v}_F$, left) and backward tracing ($\mathbf{v}_B$, right) in the equatorial plane $z = 0$ for the symmetric case at $t = 130$, while the bottom panels of **Figure 4** plot the logarithmic scale of the ratio between MHD temperature, T_M and the second order moment from forward tracing (T_F, left) and backward tracing (T_B, right). The red lines are the contour lines of $r_M = 0.5$. The results clearly illustrate that the region with large deviation between MHD simulation and test particle simulation are close to the high mixing rate, r_M region. In the nonlinear stage, although MHD can still well describe the region outside of the KH active region, the increase of the particle mixing due to the thin boundary layer generated by the KH vortex becomes more and more important, which may

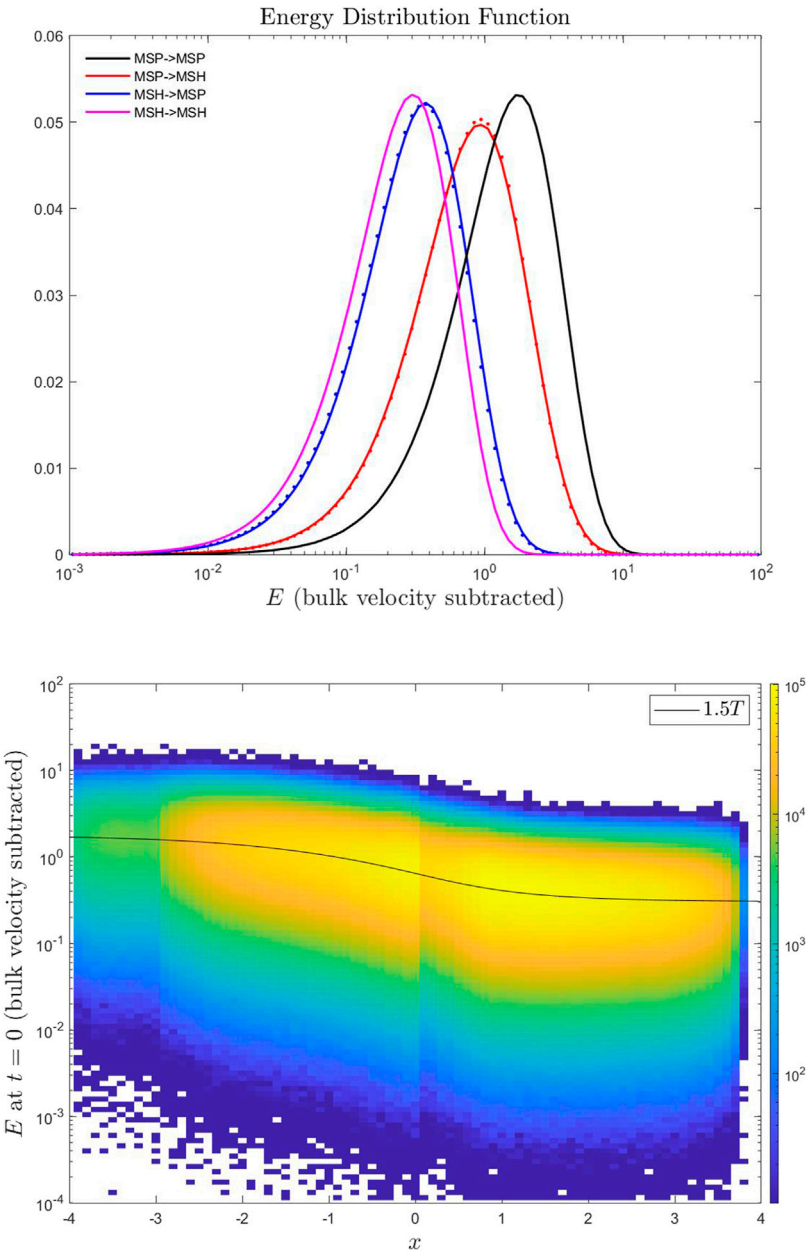

FIGURE 3 | The top panel shows the energy distribution (see text) for four different types of particles (see legend) from the symmetric case. The solid lines represent those particles' energy distribution at $t = 130$, while the dotted lines represent those particles' energy distribution at $t = 0$. The bottom panel shows the initial energy distribution as a function of their initial location (x-component) for the particles crossing between the magnetosphere and the magnetosheath. The black line shows the energy-associated with initial temperature $1.5T$.

eventually alter the MHD description. Therefore, simulations of the later stage of the nonlinear KH instability ultimately require including kinetic physics, that is hybrid simulation or even full kinetic simulation. The deviation of higher order moments between MHD and test particle simulations could be used as an indication of when the particle description becomes important. We also notice that fewer particles launched on the magnetosphere side due to the lower density in the forward tracing method leads to a higher statistical noise. As a comparison, although overall the forward tracing and backward tracing results are qualitatively consistent with each other, the backward tracing method indeed reduces the statistical noise outside of the KH active region even when compared with the magnetosheath region. Recall that a grid point contains about 150 particles on the magnetosheath side in the forward tracing, and 51^3 particles in the backward tracing. Thus, if we are interested in a specific region in the KH instability, the backward tracing method is a very useful

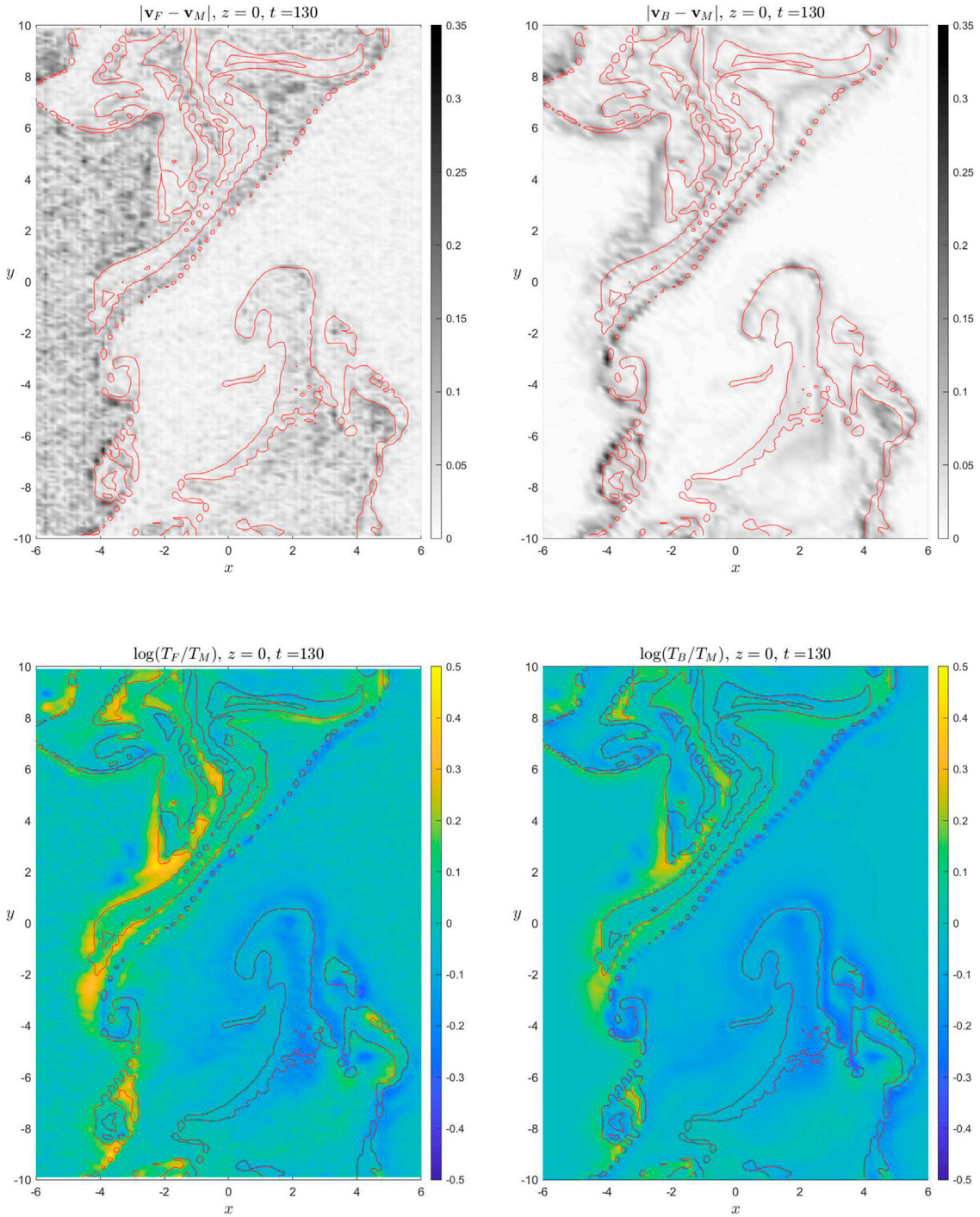

FIGURE 4 | The color index represents the deviation between the bulk velocity **(top)** and temperature **(bottom)** from MHD simulation and test particles for the symmetric case at t = 130. The left and right panels show the forward tracing and backward tracing, respectively. The red lines are the contour lines of r_M = 0.5.

method. However, if we are interested in the overall properties (e.g., mixing rate), then the forward tracing is a more practical approach.

Figure 5 plots the logarithmic scale of the anisotropic temperature $T_{\parallel}/T_{\perp}$ (color index) at t = 0 (left) t = 130 (middle) for the symmetric case by using forward tracing method. The right panel shows the results from the backward tracing method. The black arrows represent the x and y components of the bulk velocity from MHD simulation. The magenta line represents the magnetosheath-magnetosphere

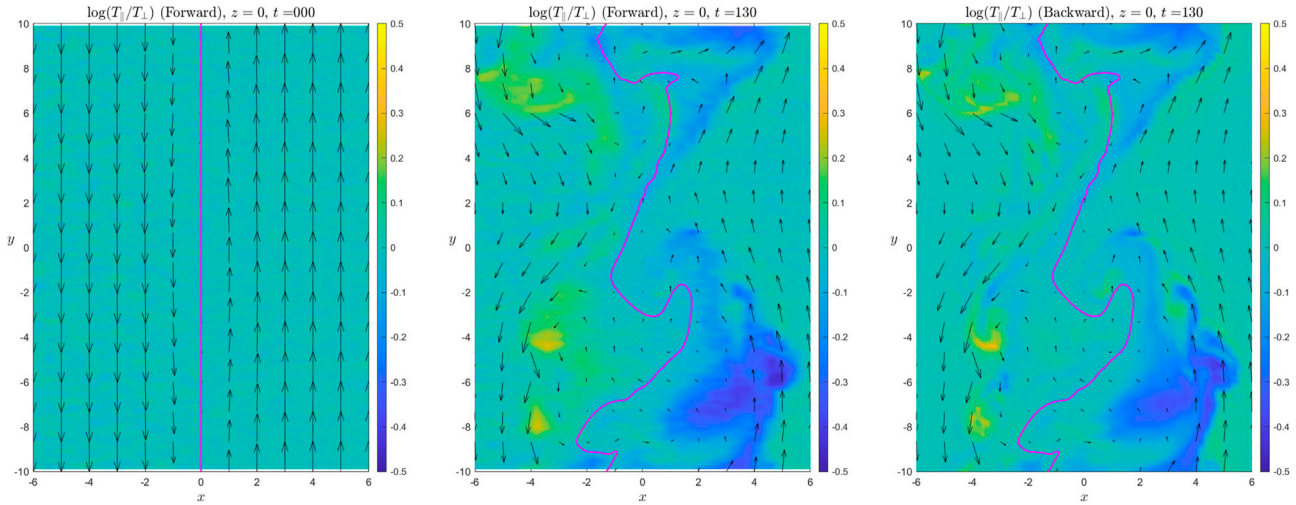

FIGURE 5 | The color index represents the temperature anisotropy $T_{\parallel}/T_{\perp}$ at $t = 0$ **(left)** $t = 130$ **(middle)** for the symmetric case by using forward tracing method. The right panel shows the results from backward tracing method. The black arrows represent the *x* and *y* components of the bulk velocity from MHD simulation. The magenta line represents the magnetosheath-magnetosphere boundary based on magnetic field topology.

boundary based on magnetic field topology. The particles were initialized isotropically (i.e., $T_{\parallel}/T_{\perp} = 1$) at $t = 0$ as shown in the left panel with small fluctuations due to the statistical noise. At $t =$ 130, anisotropic temperature regions appears around the edges of the KH vortex based on the forward tracing method, being quantitatively consistent with the results from backward tracing method, which suggests that KH instability can cause anisotropic temperature. It is interesting to note that $T_{\parallel} > T_{\perp}$ on the magnetospheric side, while $T_{\parallel} < T_{\perp}$ on the magnetosheath side. This can be easily explained by the DMLR process. For the newly reconnected magnetospheric closed magnetic field line, the magnetosheath-originating cold plasma (i.e., low parallel velocity) expand freely along the magnetic field line from low latitudes to high latitudes. Meanwhile, magnetosphere-originating hot plasma (i.e., high parallel velocity) expand freely along the magnetic field line from both high-latitude regions into low latitudes. Thus, on the low-latitude magnetospheric side, $T_{\parallel}$ becomes larger than $T_{\perp}$. Vice versa, on the magnetosheath side, the fast field-aligned expansion of the hot magnetosphere-originating plasma is replaced by the cold magnetosheath-originating plasma, which reduces $T_{\parallel}$. Notice, this type of anisotropic temperature generation mechanism only occurs when there is a large temperature asymmetry across the boundary, which is often satisfied at the Earth's magnetopause boundary. It also requires a relaxing time for particles from the two sides to fully mix. One should also keep in mind, a large anisotropic temperature or even a population with a two streaming beams (field-aligned and anti-field-aligned) often leads to different types of kinetic instabilities, which eventually leads to additional nonadiabatic heating sources to bring the particle distributions to local kinetic equilibrium. These

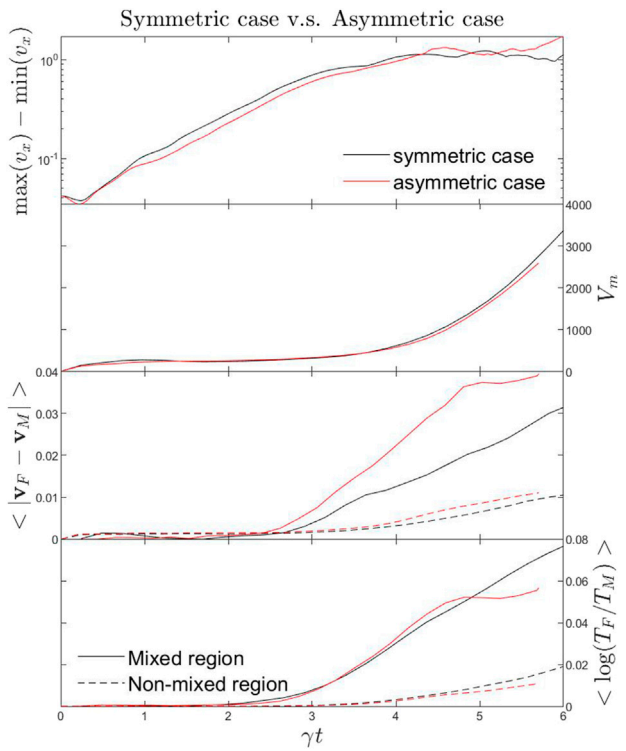

FIGURE 6 | The overall dynamical properties for the symmetric case (black lines) and the asymmetric case (red lines) in a normalized time scale (i.e., γt). The top to bottom panels show the growth of the KH instability (the range of the bulk velocity v_x component), the total mixed volume, V_m (based on H+), the change of $< |\mathbf{v}_F - \mathbf{v}_M| >$, and change of $< |\log(T_F/T_M)| >$ for mixed region (solid lines) and non-mixed region (dashed lines).

processes should also be resolved by the hybrid or PIC simulations. On the other hand, the mixing of plasma due to the finite gyroradius effect may also affect the temperature anisotropy, which is out of the scope of this study.

To systematically compare the symmetric case and the asymmetric case, we normalized the time, t, with the KH growth rate γt (Hasegawa et al., 2004; Henri et al., 2013). Here, the KH growth rate, γ, is obtained from the logarithmic fitting of t and $\max(\delta v_x) - \min(\delta v_x)$ during the interval of $5 < t < 70$, which gives $\gamma = 0.0487$ and 0.0439 for the symmetric and asymmetric cases, respectively. **Figure 6** plots four overall parameters as functions of normalized time for the symmetric case (black lines) and the asymmetric case (red lines) for comparison. The top panel shows the range of the normal bulk velocity component to indicate the linear and nonlinear stage, which is similar to the top-right panel of **Figure 2**. The second panel plots the total mixed volume, V_m (i.e., similar to bottom-right panel of **Figure 2**), showing these two lines are almost overlapped with each other, which demonstrates that the slower mixing rate in the asymmetric case is mainly due to the slower growth rate. The third and fourth panel of **Figure 6** plot the change of $< |\mathbf{v}_F - \mathbf{v}_M| >$, and $< |\log(T_F/T_M)| >$, respectively, to illustrate the deviation of bulk velocity, and temperature between the MHD and test particle (forward tracing method) as a function of the normalized time. Here, the average $<f>$ is weighted by the mixed rate r_M, (i.e., $<f>_M = \int f r_M dV / \int r_M dV$) for mixed region (solid lines) and $1 - r_M$, (i.e., $<f>_N = \int f(1 - r_M) dV / \int (1 - r_M) dV$) for non-mixed region (dashed lines), and the volume integration is taken within the volume $|x| < 6$ and $|z| < 35$, covering only the KH active region. For a better comparison between the symmetric case and the asymmetric case, we also subtracted the initial value of $<f>$, which can be considered as background statistical noise. It clearly shows that the deviation between the MHD and test particle simulations is almost constant in the non-mixed region, while the deviation significantly increases in the mixed region during the nonlinear stage. This again suggests that within certain deviation we can use fluid simulation with test particles to investigate the early nonlinear stage of the KH instability. However, eventually, during the later nonlinear stage the feedback from particles has to be taken into account for the system, requiring hybrid or full kinetic simulations. For both bulk velocity and temperature in the mixed region, the deviation in the asymmetric case increases a bit faster than the symmetric case, which could be partially due to the preexisting magnetic shear in the asymmetric case leading to a faster onset of magnetic reconnection with kinetic effects becoming important. However, the onset of kinetic physics is somewhat arbitrary during the KH instability. For instance, in a symmetric case, fast growth of KH instability could cause secondary KH instability which leads to a thin boundary layer without involving magnetic reconnection, where gyro-radius effects can cause deviation between MHD and test particle descriptions. Meanwhile, a large magnetic shear, B_y may stabilized the KH instability, which consequently delays the onset of magnetic reconnection. Thus, to draw a general conclusion whether the test particle simulation is less applicable for the asymmetric case or not requires a much wider and systematic comparison in future studies.

4 SUMMARY AND DISCUSSION

In this study, we carried out two 3-D KH instability MHD simulations accompanied by test particle simulations, in which the initial boundary condition is close to the MMS-observed KH event reported by Eriksson et al. (Eriksson et al., 2016). The simulation results suggests about 10^{25} particles/s mass is transported from the magnetosheath into the magnetosphere *via* the mid-latitude-double-reconnection process, and the mixing diffusion rate is about 10^{10} m^2 s^{-1}. The presence of the magnetic B_y component reduces the KH growth rate and also strongly reduces the mass increase rate on the magnetospheric side. For Earth's typical magnetopause boundary conditions, the finite gyroradius effect does not significantly increase the mass transport rate, even for O+. Although, a large gyroradius effect will bring a greater mixed volume, the mixing diffusion rate is insensitive to the charge-to-mass ratio in the nonlinear stage of the KH instability, partially because KH scale size is larger than gyro-radius of heavy ions (O+). However, this effect may play role in other planets (e.g., Mercury and Mars (Poh et al., 2021)). The DMLR process changes the magnetic field line topology which exchanges the low-latitude magnetic flux tubes between the magnetosheath side and the magnetosphere side. Thus, the plasma mixing can also occur through the DMLR process; however, it takes time for ion particles to undergo free expansion into the newly reconnected flux tube, which limits its effects on the mixing region.

During the KH instability process, an individual particle can be either accelerated or decelerated, however, the overall energy (subtracted by the bulk velocity) distributions do not vary with time, which indicates there is no additional heating source through this process. Although the average energy of particles moving from the magnetosheath into the magnetosphere is higher than the particles still remaining in the magnetosheath, this is simply because those transported particles were originally in a relatively higher temperature region of the initial transition layer. Thus, for the thermal particle population there is no energy filter effect for the KH instability. Nevertheless, it is still not clear whether the KH instability will select higher energy particles from the magnetosheath into the magnetosphere for the super-thermal population.

We also compared the zeroth, first, and second order moments of the particle velocity distributions from the test particle simulation with the density, bulk velocity, and temperature from the MHD simulation. It shows that the zeroth order moment is consistent with the MHD description, which also indicates the extended boundary condition along the z-direction for the test particles is consistent with the MHD boundary conditions. The first and second order moments remain consistent with the MHD bulk velocity and temperature, respectively, in the non-mixed region, but show clear deviation in the mixed region. This deviation between the particle description and the MHD description indicates that it is essential to use hybrid simulation or even PIC simulation to provide a self-consistent simulation of the later nonlinear stage of the KH instability.

Both the forward tracing method and the backward tracing method based on Liouville's theory suggest the KH instability can generate temperature anisotropy at the edge of the KH vortex, which is also observed by the MMS [(Eriksson et al., 2016), and our companion paper (Eriksson et al., 2021)]. In this case, the anisotropic temperature is caused by the reconnection of flux tubes with two different temperatures, which is interesting to compare with the results from a double-adiabatic MHD description. This condition also brings two important questions for future study. The first one is how long does it take for particles in the newly reconnected flux tube to become fully mixed? Recall that one of the plausible magnetosheath plasma specific entropy increase mechanisms is that the magnetosheath plasma expands freely in the newly reconnected flux tube. Thus, this question is directly related to this mechanism, and a related question is whether the free expansion happens during the KH instability at the magnetopause boundary or will it take a longer time while the newly reconnected flux moves radially earth-ward? This question likely can be addressed using test particle simulations in future studies. The second question is whether additional kinetic instabilities occur during the mixing process, bringing an additional nonadiabatic heating source? This is essentially a cross-scale problem, requiring hybrid or even PIC simulation.

The results from the forward tracing and the backward tracing methods are quantitatively comparable. The backward tracing can easily increase the resolution of the velocity space for a given point, which is suitable for investigating a certain region of interest. However, one should keep in mind, this method requires the whole process be reversible. For the 3-D KH instability, the DMLR process is an irreversible process. Thus, strictly speaking, the backward tracing method is not applicable. However, the mid-latitude reconnection sites are highly localized, and no parallel electric field is present during the particle tracing. Thus, the backward tracing method still works in our study. However, in principle, it cannot be used to investigate the possible nonadiabatic heating or acceleration mechanisms.

This study also highlights the importance of using hybrid or PIC simulation to resolve the later nonlinear stage of the KH instability. However, due to the high computational cost and complex boundary conditions, only a few hybrid and PIC simulations can investigate a 3-D KH instability with a non-periodic boundary condition along the third direction and with strong temperature asymmetry across the flow layer condition. This study provides a plausible approach for the non-periodic boundary condition. Meanwhile one can use MHD and test particle simulations to simulate the linear stage and early nonlinear stage of the KH instability, and switch to the hybrid simulation when the deviation between the first or second moments from the test particle and MHD simulation is greater than a critical value, which is another plausible scenario to save on computational cost.

In summary, the KH instability is a cross-scale process, which requires a spatial resolution of both meso-scale and kinetic scale processes. Although with the development of computational hardware, hybrid simulation and PIC simulation can investigate ever increasing regimes of cross-scale physical processes, MHD simulation with test particles is still a useful tool to address many suitable questions in the KH instability, as well as provide a helpful guide for the more computationally expensive simulations.

DATA AVAILABILITY STATEMENT

The simulation data and visualization tools in this paper can be accessed from https://commons.erau.edu/dm-ion-dynamics-meso-scale-3d-kelvin-helmholtz/

AUTHOR CONTRIBUTIONS

All the simulations are done by the first author, all co-authors provided critical discussions and comments.

FUNDING

This research is supported from NASA grants 80NSSC18K1108, 80NSSC18K1381, and NNX17AI50G.

ACKNOWLEDGMENTS

We appreciate both reviewers' helpful comments and suggestions. XM would like to thank Sheryl Nome and Ranka Lee for their encouragement during his writing.

REFERENCES

Arzamasskiy, L., Kunz, M. W., Chandran, B. D. G., and Quataert, E. (2019). Hybrid-kinetic Simulations of Ion Heating in Alfvénic Turbulence. *Astrophysical J.* 879, 53. doi:10.3847/1538-4357/ab20cc

Axford, W. I., and Hines, C. O. (1961). A Unifying Theory of High-Latitude Geophysical Phenomena and Geomagnetic Storms. *Can. J. Phys.* 39, 1433–1464. doi:10.1139/p61-172

Birn, J. (1976). "The Resistive Tearing Mode by a Two-Dimensional Finite Difference Method," in *Computing in Plasma Physics and Astrophysics*. Garching, West Germany.

Birn, J., Thomsen, M. F., Borovsky, J. E., Reeves, G. D., McComas, D. J., Belian, R. D., et al. (1998). Substorm Electron Injections: Geosynchronous Observations and Test Particle Simulations. *J. Geophys. Res.* 103, 9235–9248. doi:10.1029/97JA02635

Birn, J., Thomsen, M. F., Borovsky, J. E., Reeves, G. D., McComas, D. J., Belian, R. D., et al. (1997). Substorm Ion Injections: Geosynchronous Observations and Test Particle Orbits in Three-Dimensional Dynamic MHD fields. *J. Geophys. Res.* 102, 2325–2341. doi:10.1029/96JA03032

Boris, J. (1970). *The Acceleration Calculation from a Scalar Potential*. Princeton, New Jersey: Princeton University Plasma Physics Laboratory.

Burkholder, B., Delamere, P. A., Ma, X., Thomsen, M. F., Wilson, R. J., and Bagenal, F. (2017). Local Time Asymmetry of Saturn's Magnetosheath Flows. *Geophys. Res. Lett.* 44, 5877–5883. doi:10.1002/2017GL073031

Burkholder, B. L., Delamere, P. A., Johnson, J. R., and Ng, C. S. (2020). Identifying Active Kelvin-Helmholtz Vortices on Saturn's Magnetopause Boundary. *Geophys. Res. Lett.* 47, e2019GL084206. doi:10.1029/2019GL084206

Cerri, S. S., Arzamasskiy, L., and Kunz, M. W. (2021). On Stochastic Heating and its Phase-Space Signatures in Low-Beta Kinetic Turbulence. *Astrophysical J.* 916, 120. doi:10.3847/1538-4357/abfbde

Chandran, B. D. G., Li, B., Rogers, B. N., Quataert, E., and Germaschewski, K. (2010). Perpendicular Ion Heating by Low-Frequency Alfvén-Wave Turbulence in the Solar Wind. *Astrophysical J.* 720, 503–515. doi:10.1088/0004-637X/720/1/503

Chandrasekhar, S. (1961). "Hydrodynamic and Hydromagnetic Stability," in *The International Series of Monographs on Physics* (New York: Dover Publ.).

Cowee, M. M., Winske, D., and Gary, S. P. (2010). Hybrid Simulations of Plasma Transport by Kelvin-Helmholtz Instability at the Magnetopause: Density Variations and Magnetic Shear. *J. Geophys. Res.* 115, a–n. doi:10.1029/2009JA015011

Cowee, M. M., Winske, D., and Gary, S. P. (2009). Two-dimensional Hybrid Simulations of Superdiffusion at the Magnetopause Driven by Kelvin-Helmholtz Instability. *J. Geophys. Res.* 114, a–n. doi:10.1029/2009JA014222

Delamere, P. A., Ng, C. S., Damiano, P. A., Neupane, B. R., Johnson, J. R., Burkholder, B., et al. (2021). Kelvin-Helmholtz-Related Turbulent Heating at Saturn's Magnetopause Boundary. *J. Geophys. Res. Space Phys.* 126, e2020JA028479. doi:10.1029/2020JA028479

Delamere, P. A., Wilson, R. J., and Masters, A. (2011). Kelvin-Helmholtz Instability at Saturn's Magnetopause: Hybrid Simulations. *J. Geophys. Res.* 116, a–n. doi:10.1029/2011JA016724

Dong, C., Wang, L., Huang, Y.-M., Comisso, L., and Bhattacharjee, A. (2018). Role of the Plasmoid Instability in Magnetohydrodynamic Turbulence. *Phys. Rev. Lett.* 121, 165101. doi:10.1103/PhysRevLett.121.165101

Eriksson, S., Lavraud, B., Wilder, F. D., Stawarz, J. E., Giles, B. L., Burch, J. L., et al. (2016). Magnetospheric Multiscale Observations of Magnetic Reconnection Associated with Kelvin-Helmholtz Waves. *Geophys. Res. Lett.* 43, 5606–5615. doi:10.1002/2016GL068783

Eriksson, S., Ma, X., Burch, J. L., Otto, A., Elkington, S., and Delamere, P. A. (2021). MMS Observations of Double Mid-Latitude Reconnection Ion Beams in the Early Non-Linear Phase of the Kelvin-Helmholtz Instability. *Front. Astron. Space Sci.* 8, 760885. doi:10.3389/fspas.2021.760885

Faganello, M., and Califano, F. (2017). Magnetized Kelvin-Helmholtz Instability: Theory and Simulations in the Earth's Magnetosphere Context. *J. Plasma Phys.* 83, 535830601. doi:10.1017/S0022377817000770

Faganello, M., Califano, F., Pegoraro, F., Andreussi, T., and Benkadda, S. (2012). Magnetic Reconnection and Kelvin-Helmholtz Instabilities at the Earth's Magnetopause. *Plasma Phys. Control Fusion* 54, 124037. doi:10.1088/0741-3335/54/12/124037

Fairfield, D. H., Otto, A., Mukai, T., Kokubun, S., Lepping, R. P., Steinberg, J. T., et al. (2000). Geotail Observations of the Kelvin-Helmholtz Instability at the Equatorial Magnetotail Boundary for Parallel Northward fields. *J. Geophys. Res.* 105, 21159–21173. doi:10.1029/1999JA000316

Franci, L., Stawarz, J. E., Papini, E., Hellinger, P., Nakamura, T., Burgess, D., et al. (2020). Modeling MMS Observations at the Earth's Magnetopause with Hybrid Simulations of Alfvénic Turbulence. *Astrophysical J.* 898, 175. doi:10.3847/1538-4357/ab9a47

Grošelj, D., Cerri, S. S., Bañón Navarro, A., Willmott, C., Told, D., Loureiro, N. F., et al. (2017). Fully Kinetic versus Reduced-Kinetic Modeling of Collisionless Plasma Turbulence. *Astrophysical J.* 847, 28. doi:10.3847/1538-4357/aa894d

Hasegawa, H., Fujimoto, M., Phan, T.-D., Rème, H., Balogh, A., Dunlop, M. W., et al. (2004). Transport of Solar Wind into Earth's Magnetosphere through Rolled-Up Kelvin-Helmholtz Vortices. *Nature* 430, 755–758. doi:10.1038/nature02799

Henri, P., Cerri, S. S., Califano, F., Pegoraro, F., Rossi, C., Faganello, M., et al. (2013). Nonlinear Evolution of the Magnetized Kelvin-Helmholtz Instability: From Fluid to Kinetic Modeling. *Phys. Plasmas* 20, 102118. doi:10.1063/1.4826214

Henry, Z. W., Nykyri, K., Moore, T. W., Dimmock, A. P., and Ma, X. (2017). On the Dawn-Dusk Asymmetry of the Kelvin-Helmholtz Instability between 2007 and 2013. *J. Geophys. Res. Space Phys.* 122, 11,888–11,900. doi:10.1002/2017JA024548

Hwang, K. J., Goldstein, M. L., Kuznetsova, M. M., Wang, Y., ViñAs, A. F., and Sibeck, D. G. (2012). The First *In Situ* Observation of Kelvin-Helmholtz Waves at High-Latitude Magnetopause during Strongly Dawnward Interplanetary Magnetic Field Conditions. *J. Geophys. Res. (Space Physics)* 117, A08233. doi:10.1029/2011ja017256

Hwang, K. J., Kuznetsova, M. M., Sahraoui, F., Goldstein, M. L., Lee, E., and Parks, G. K. (2011). Kelvin-Helmholtz Waves under Southward Interplanetary Magnetic Field. *J. Geophys. Res. Space Phys.* 116. doi:10.1029/2011ja016596

Johnson, J. R., and Cheng, C. Z. (2001). Stochastic Ion Heating at the Magnetopause Due to Kinetic Alfvén Waves. *Geophys. Res. Lett.* 28, 4421–4424. doi:10.1029/2001gl013509

Johnson, J. R., Wing, S., and Delamere, P. A. (2014). Kelvin Helmholtz Instability in Planetary Magnetospheres. *Space Sci. Rev.* 184, 1–31. doi:10.1007/s11214-014-0085-z

Karimabadi, H., Roytershteyn, V., Wan, M., Matthaeus, W. H., Daughton, W., Wu, P., et al. (2013). Coherent Structures, Intermittent Turbulence, and Dissipation in High-Temperature Plasmas. *Phys. Plasmas* 20, 012303. doi:10.1063/1.4773205

Kavosi, S., and Raeder, J. (2015). Ubiquity of Kelvin-Helmholtz Waves at Earth's Magnetopause. *Nat. Commun.* 6. doi:10.1038/ncomms8019

Li, W., André, M., Khotyaintsev, Y. V., Vaivads, A., Graham, D. B., Toledo-Redondo, S., et al. (2016). Kinetic Evidence of Magnetic Reconnection Due to Kelvin-Helmholtz Waves. *Geophys. Res. Lett.* 43, 5635–5643. doi:10.1002/2016GL069192

Ma, X., Delamere, P., Otto, A., and Burkholder, B. (2017). Plasma Transport Driven by the Three-Dimensional Kelvin-Helmholtz Instability. *J. Geophys. Res. Space Phys.* 122, 10,382–10,395. doi:10.1002/2017ja024394

Ma, X., Nykyri, K., Dimmock, A., and Chu, C. (2020). Statistical Study of Solar Wind, Magnetosheath, and Magnetotail Plasma and Field Properties: 12+ Years of THEMIS Observations and MHD Simulations. *J. Geophys. Res. Space Phys.* 125, e2020JA028209. doi:10.1029/2020JA028209

Ma, X., Delamere, P. A., Nykyri, K., Burkholder, B., Neupane, B., and Rice, R. C. (2019). Comparison between Fluid Simulation with Test Particles and Hybrid Simulation for the Kelvin-Helmholtz Instability. *J. Geophys. Res. Space Phys.* 124, 6654–6668. doi:10.1029/2019JA026890

Ma, X., Otto, A., and Delamere, P. A. (2014). Interaction of Magnetic Reconnection and Kelvin-Helmholtz Modes for Large Magnetic Shear: 1. Kelvin-Helmholtz Trigger. *J. Geophys. Res. Space Phys.* 119, 781–797. doi:10.1002/2013JA019224

Ma, X., Otto, A., and Delamere, P. A. (2014). Interaction of Magnetic Reconnection and Kelvin-Helmholtz Modes for Large Magnetic Shear: 2. Reconnection Trigger. *J. Geophys. Res. Space Phys.* 119, 808–820. doi:10.1002/2013JA019225

Ma, X., Otto, A., Delamere, P. A., and Zhang, H. (2016). Interaction between Reconnection and Kelvin-Helmholtz at the High-Latitude Magnetopause. *Adv. Space Res.* 58, 231–239. doi:10.1016/j.asr.2016.02.025

Ma, X., and Otto, A. (2014). Nonadiabatic Heating in Magnetic Reconnection. *J. Geophys. Res. Space Phys.* 119, 5575–5588. doi:10.1002/2014JA019856

Ma, X., Stauffer, B., Delamere, P. A., and Otto, A. (2015). Asymmetric Kelvin-Helmholtz Propagation at Saturn's Dayside Magnetopause. *J. Geophys. Res. Space Phys.* 120, 1867–1875. doi:10.1002/2014JA020746

Masson, A., and Nykyri, K. (2018). Kelvin-Helmholtz Instability: Lessons Learned and Ways Forward. *Space Sci. Rev.* 214, 71. doi:10.1007/s11214-018-0505-6

Matsumoto, Y., and Hoshino, M. (2006). Turbulent Mixing and Transport of Collisionless Plasmas across a Stratified Velocity Shear Layer. *J. Geophys. Res.* 111, A05213. doi:10.1029/2004JA010988

Miura, A. (1984). Anomalous Transport by Magnetohydrodynamic Kelvin-Helmholtz Instabilities in the Solar Wind-Magnetosphere Interaction. *J. Geophys. Res.* 89, 801–818. doi:10.1029/ja089ia02p00801

Miura, A., and Pritchett, P. L. (1982). Nonlocal Stability Analysis of the MHD Kelvin-Helmholtz Instability in a Compressible Plasma. *J. Geophys. Res.* 87, 7431–7444. doi:10.1029/JA087iA09p07431

Moore, T. W., Nykyri, K., and Dimmock, A. P. (2016). Cross-scale Energy Transport in Space Plasmas. *Nat. Phys.* 12, 1164–1169. doi:10.1038/nphys3869

Moore, T. W., Nykyri, K., and Dimmock, A. P. (2017). Ion-Scale Wave Properties and Enhanced Ion Heating across the Low-Latitude Boundary Layer during Kelvin-Helmholtz Instability. *J. Geophys. Res. Space Phys.* 122, 11,128–11,153. doi:10.1002/2017JA024591

Nakamura, T. K. M., Hasegawa, H., Daughton, W., Eriksson, S., Li, W. Y., and Nakamura, R. (2017). Turbulent Mass Transfer Caused by Vortex Induced

Reconnection in Collisionless Magnetospheric Plasmas. *Nat. Commun.* 8, 1582. doi:10.1038/s41467-017-01579-0

Nakamura, T. K. M., Stawarz, J. E., Hasegawa, H., Narita, Y., Franci, L., Wilder, F. D., et al. (2020). Effects of Fluctuating Magnetic Field on the Growth of the Kelvin-Helmholtz Instability at the Earth's Magnetopause. *J. Geophys. Res. Space Phys.* 125, e2019JA027515. doi:10.1029/2019JA027515

Nakamura, T. K. M., and Fujimoto, M. (2008). Magnetic Effects on the Coalescence of Kelvin-Helmholtz Vortices. *Phys. Rev. Lett.* 101, 165002. doi:10.1103/physrevlett.101.165002

Nakamura, T. K. M., Fujimoto, M., and Otto, A. (2008). Structure of an MHD-Scale Kelvin-Helmholtz Vortex: Two-Dimensional Two-Fluid Simulations Including Finite Electron Inertial Effects. *J. Geophys. Res.* 113, a–n. doi:10.1029/2007JA012803

Nykyri, K., Ma, X., Burkholder, B., Rice, R., Johnson, J. R., Kim, E. K., et al. (2021). Mms Observations of the Multiscale Wave Structures and Parallel Electron Heating in the Vicinity of the Southern Exterior Cusp. *J. Geophys. Res. Space Phys.* 126, e2019JA027698. doi:10.1029/2019JA027698

Nykyri, K., Ma, X., Dimmock, A., Foullon, C., Otto, A., and Osmane, A. (2017). Influence of Velocity Fluctuations on the Kelvin-Helmholtz Instability and its Associated Mass Transport. *J. Geophys. Res. Space Phys.* 122, 9489–9512. doi:10.1002/2017JA024374

Nykyri, K., Ma, X., and Johnson, J. (2021). Cross-Scale Energy Transport in Space Plasmas. *Magnetospheres Solar Syst.* 7, 109–121. doi:10.1002/9781119815624.ch7

Nykyri, K., Otto, A., Adamson, E., Kronberg, E., and Daly, P. (2012). On the Origin of High-Energy Particles in the Cusp Diamagnetic Cavity. *J. Atmos. Solar-Terrestrial Phys.* 87-88, 70–81. doi:10.1016/j.jastp.2011.08.012

Nykyri, K., and Otto, A. (2004). Influence of the Hall Term on KH Instability and Reconnection inside KH Vortices. *Ann. Geophys.* 22, 935–949. doi:10.5194/angeo-22-935-2004

Nykyri, K., Otto, A., Lavraud, B., Mouikis, C., Kistler, L. M., Balogh, A., et al. (2006). Cluster Observations of Reconnection Due to the Kelvin-Helmholtz Instability at the Dawnside Magnetospheric Flank. *Ann. Geophys.* 24, 2619–2643. doi:10.5194/angeo-24-2619-2006

Nykyri, K., and Otto, A. (2001). Plasma Transport at the Magnetospheric Boundary Due to Reconnection in Kelvin-Helmholtz Vortices. *Geophys. Res. Lett.* 28, 3565–3568. doi:10.1029/2001GL013239

Otto, A. (2006). Mass Transport at the Magnetospheric Flanks Associated with Three-Dimensional Kelvin- Helmholtz Modes. *AGU Fall Meet. Abstr.* 2006, SM33B–0365.

Otto, A. (1990). 3d Resistive Mhd Computations of Magnetospheric Physics. *Comput. Phys. Commun.* 59, 185–195. doi:10.1016/0010-4655(90)90168-z

Otto, A., and Fairfield, D. H. (2000). Kelvin-Helmholtz Instability at the Magnetotail Boundary: MHD Simulation and Comparison with Geotail Observations. *J. Geophys. Res.* 105, 21175–21190. doi:10.1029/1999JA000312

Poh, G., Espley, J. R., Nykyri, K., Fowler, C. M., Ma, X., Xu, S., et al. (2021). On the Growth and Development of Non-Linear Kelvin-Helmholtz Instability at Mars: MAVEN Observations. *J. Geophys. Res. Space Phys.* 126, e2021JA029224. doi:10.1029/2021JA029224

Pu, Z.-Y., and Kivelson, M. G. (1983). Kelvin-Helmholtz Instability at the Magnetopause: Energy Flux into the Magnetosphere. *J. Geophys. Res.* 88, 853–861. doi:10.1029/JA088iA02p00853

Pu, Z.-Y., and Kivelson, M. G. (1983). Kelvin:Helmholtz Instability at the Magnetopause: Solution for Compressible Plasmas. *J. Geophys. Res.* 88, 841–852. doi:10.1029/JA088iA02p00841

Quataert, E. (1998). Particle Heating by Alfvenic Turbulence in Hot Accretion Flows. *Astrophysical J.* 500, 978–991. doi:10.1086/305770

Settino, A., Malara, F., Pezzi, O., Onofri, M., Perrone, D., and Valentini, F. (2020). Kelvin-Helmholtz Instability at Proton Scales with an Exact Kinetic Equilibrium. *Astrophysical J.* 901, 17. doi:10.3847/1538-4357/abada9

Sonnerup, B. U. Ö. (1980). Theory of the Low-Latitude Boundary Layer. *J. Geophys. Res.* 85, 2017–2026. doi:10.1029/ja085ia05p02017

Stawarz, J. E., Eriksson, S., Wilder, F. D., Ergun, R. E., Schwartz, S. J., Pouquet, A., et al. (2016). Observations of Turbulence in a Kelvin-Helmholtz Event on 8 September 2015 by the Magnetospheric Multiscale mission. *J. Geophys. Res. Space Phys.* 121, 11,021–11,034. doi:10.1002/2016JA023458

Terasawa, T., Fujimoto, M., Karimabadi, H., and Omidi, N. (1992). Anomalous Ion Mixing within a Kelvin-Helmholtz Vortex in a Collisionless Plasma. *Phys. Rev. Lett.* 68, 2778–2781. doi:10.1103/PhysRevLett.68.2778

Told, D., Jenko, F., TenBarge, J. M., Howes, G. G., and Hammett, G. W. (2015). Multiscale Nature of the Dissipation Range in Gyrokinetic Simulations of Alfvénic Turbulence. *Phys. Rev. Lett.* 115, 025003. doi:10.1103/PhysRevLett.115.025003

Vasquez, B. J. (2015). Heating Rate Scaling of Turbulence in the Proton Kinetic Regime. *Astrophysical J.* 806, 33. doi:10.1088/0004-637X/806/1/33

Conflict of Interest: The authors declare that the research was conducted in the absence of any commercial or financial relationships that could be construed as a potential conflict of interest.

Publisher's Note: All claims expressed in this article are solely those of the authors and do not necessarily represent those of their affiliated organizations, or those of the publisher, the editors and the reviewers. Any product that may be evaluated in this article, or claim that may be made by its manufacturer, is not guaranteed or endorsed by the publisher.

frontiers in Physics

ORIGINAL RESEARCH
published: 02 December 2021
doi: 10.3389/fphy.2021.738988

Kelvin-Helmholtz Instability Associated With Reconnection and Ultra Low Frequency Waves at the Ground: A Case Study

E. A. Kronberg[1], J. Gorman[1,2,3], K. Nykyri[4], A. G. Smirnov[5,6,1], J. W. Gjerloev[7,8], E. E. Grigorenko[9,10], L. V. Kozak[11,12], X. Ma[4], K. J. Trattner[13] and M. Friel[8]*

[1]Department of Earth and Environmental Sciences, Ludwig Maximilian University of Munich, Munich, Germany, [2]Max Planck Institute for Solar System Research, Göttingen, Germany, [3]The faculty of Civil, Geo and Environmental Engineering, Technical University of Munich, Munich, Germany, [4]Center for Space and Atmospheric Research, Physical Sciences Department, Embry-Riddle Aeronautical University, Daytona Beach, FL, United States, [5]Helmholtz-Centre Potsdam - GFZ German Research Centre for Geosciences, Potsdam, Germany, [6]Institute of Physics and Astronomy, University of Potsdam, Potsdam, Germany, [7]Department of Physics and Technology, University of Bergen, Bergen, Norway, [8]The Johns Hopkins University Applied Physics Laboratory, Laurel, MD, United States, [9]Space Research Institute, Russian Academy of Sciences, Moscow, Russia, [10]Moscow Institute of Physics and Technology, Moscow, Russia, [11]Faculty of Physics, Taras Shevchenko National University of Kyiv, Kyiv, Ukraine, [12]Space Research Institute of the National Academy of Sciences of Ukraine and State Space Agency of Ukraine, Kyiv, Ukraine, [13]Laboratory for Atmospheric and Space Physics, Boulder, CO, United States

OPEN ACCESS

Edited by:
Xochitl Blanco-Cano, National Autonomous University of Mexico, Mexico

Reviewed by:
Binbin Tang, National Space Science Center (CAS), China
Diana Rojas-Castillo, National Autonomous University of Mexico, Mexico

***Correspondence:**
E. A. Kronberg, kronberg@geophysik.uni-muenchen.de

Specialty section:
This article was submitted to Space Physics, a section of the journal Frontiers in Physics

Received: *09 July 2021*
Accepted: *05 November 2021*
Published: *02 December 2021*

Citation:
Kronberg EA, Gorman J, Nykyri K, Smirnov AG, Gjerloev J, Grigorenko EE, Kozak LV, Ma X, Trattner KJ and Friel M (2021) Kelvin-Helmholtz Instability Associated With Reconnection and Ultra Low Frequency Waves at the Ground: A Case Study. Front. Phys. 9:738988. doi: 10.3389/fphy.2021.738988

The Kelvin-Helmholtz instability (KHI) and its effects relating to the transfer of energy and mass from the solar wind into the magnetosphere remain an important focus of magnetospheric physics. One such effect is the generation of Pc4-Pc5 ultra low frequency (ULF) waves (periods of 45–600 s). On July 3, 2007 at ~ 0500 magnetic local time the Cluster space mission encountered Pc4 frequency Kelvin-Helmholtz waves (KHWs) at the high latitude magnetopause with signatures of persistent vortices. Such signatures included bipolar fluctuations of the magnetic field normal component associated with a total pressure increase and rapid change in density at vortex edges; oscillations of magnetosheath and magnetospheric plasma populations; existence of fast-moving, low-density, mixed plasma; quasi-periodic oscillations of the boundary normal and an anti-phase relation between the normal and parallel components of the boundary velocity. The event occurred during a period of southward polarity of the interplanetary magnetic field according to the OMNI data and THEMIS observations at the subsolar point. Several of the KHI vortices were associated with reconnection indicated by the Walén relation, the presence of deHoffman-Teller frames, field-aligned ion beams observed together with bipolar fluctuations in the normal magnetic field component, and crescent ion distributions. Global magnetohydrodynamic simulation of the event also resulted in KHWs at the magnetopause. The observed KHWs associated with reconnection coincided with recorded ULF waves at the ground whose properties suggest that they were driven by those waves. Such properties were the location of Cluster's magnetic foot point, the Pc4 frequency, and the solar wind conditions.

Keywords: kelvin-helmholtz instability, reconnection, magnetosheath, magnetopause, ULF waves at the ground, global magnetohydrodynamic simulation

1 INTRODUCTION

The Kelvin-Helmholtz instability (KHI) at the magnetopause has been noted for its role in the transport of mass and energy from the solar wind into the magnetosphere and down to the ground (e.g., [1–5]). The KHI has been found to occur fairly frequently under both southward and northward interplanetary magnetic field (IMF) configurations with no apparent low-speed cutoff [6,7]. When the IMF horizontal component is mostly in the Parker-Spiral orientation, the KHI has been shown to favor the dawn flank magnetopause [8].

One proposed manner in which energy transfer is achieved by the KHI is through the generation of ultra low frequency (ULF) waves. Hasegawa and Chen [9] and Southwood [1] showed theoretically that magnetic field line resonance oscillations can be caused by Kelvin-Helmholtz waves (KHWs) at the magnetopause. The observed dawnward asymmetry of Pc4-Pc5 range (frequencies of 2–22 mHz, periods of 47–600 s) ULF waves in the vicinity of the magnetopause [10] and enhanced heating of the cold-component ions at the dawn sector [11,12] are possibly related to the presence of KHI since the horizontal component of the IMF is most often in the Parker-Spiral orientation [13]. ULF waves have been shown to drive auroral arcs through magnetic field line resonance [14] and to efficiently accelerate energetic electrons in the outer radiation belt [15,16].

However, debate remains regarding whether or not the KHI is an actual, dominant driver for Pc4-Pc5 waves in the magnetosphere and at the ground [17]. Since other processes can externally drive ULF waves in the magnetosphere, it has been argued that it is likely these mechanisms that are the true drivers, occurring in conjunction with the KHI at the magnetopause. Such processes relate to high solar wind speeds and include dynamic pressure variations and foreshock fluctuation anisotropy instabilities [17]. Additionally, under southward IMF conditions other possible external drivers, such as flux transfer events, occur and interact with the KHI [18].

ULF pulsations at the magnetopause (believed to be KHWs but without explicit evidence) which were observed to propagate into the magnetosphere and down into the ionosphere in the dusk sector under fast solar wind speeds were investigated by Rae et al. [19]. Similarly, Agapitov et al. [20] presented THEMIS magnetic field observations at the dawn flank of magnetopause oscillations that coincided with ULF pulsations recorded deeper in the magnetosphere. The magnetopause surface waves were hypothesized to be KHWs based upon the critical velocity for KHI onset and wave growth [21]. Dougal et al. [22] modeled several instances of the KHI observed at the magnetospheric flanks under northward IMF to gain better insight into the resulting ionospheric signatures. Pc5 magnetic field oscillations within the ionospheric foot point ranges of some of these events were observed. Wang et al. [23] investigated magnetospheric Pc5 pulsations under steady solar wind conditions and made the case that ULF waves can not only be driven by field line resonance or waveguide modes [9], but also through the generation of inner and outer Kelvin-Helmholtz modes.

Presented herein is a Cluster-observed incidence of ULF waves in the Pc4 range observed at the magnetopause driven by the KHI associated with reconnection. The observed magnetospheric conditions were also modeled to further test if the magnetic field configuration was KHI-unstable. This event adds to the few previously published KHW-ULF linked events (e.g., [19,20,22]), but provides an even more comprehensive analysis of the magnetopause surface waves, investigating the magnetic field data in conjunction with plasma particle observations for KHI signatures at high latitudes.

Furthermore, as the present event occurs for the southward IMF orientation, according to the OMNI data and THEMIS observations at the subsolar point, both magnetic reconnection and KHI can start as a primary mode [23]. For southward IMF conditions, fast magnetic reconnection is driven and can be strongly modified by the nonlinear KH waves: MHD and Hall-MHD simulations have indicated that reconnection rates are comparable to Petschek reconnection even without the inclusion of Hall physics [24]. On the other hand, magnetic reconnection can seed the KH mode for KH unstable conditions [25]. We present evidence of north-south ULF magnetic field and plasma pressure fluctuations in the magnetosheath at the subsolar point observed by THEMIS satellites which may have modulated the KHW, and due to the additional plasma pressure compressions, may have driven the reconnection more strongly in KHI vortices. KHI vortices in our event are associated with reconnection signatures, making the case more comprehensive.

The event improves our understanding of under which conditions thin-current sheets, where reconnection can operate, are created. Identification of the processes that trigger ULF waves at the magnetospheric boundaries is important for the study of ion acceleration. Kronberg et al. [26] has demonstrated enhanced contamination of the XMM-Newton X-Ray telescope by soft protons at the flank high-latitude regions.

Finally, the satellite observed KHWs were compared with concurrent ULF pulsations measured at ground, indicating the connection between magnetic disturbances seen in space and those seen on Earth.

2 KHW OBSERVATIONS BY THE CLUSTER SPACECRAFT

2.1 Event Overview, its Location and the Solar Wind Conditions

On July 3, 2007 from 1,645 to 1720 UT, the Cluster spacecraft approached the high-latitude dawn side magnetopause at the border between the magnetosheath and closed magnetospheric field lines (the coordinates in Geocentric Solar Ecliptic (GSE) system were $X \approx -10\ R_E$, $Y \approx -15\ R_E$, $Z \approx -9.4\ R_E$). Observed plasma signatures of this event are shown in **Figure 1**. These measurements, which were obtained through the Cluster Science Archive [27], came from the Cluster Ion Spectrometry (CIS) experiment's [28] COmposition and DIstribution Function (CODIF) sensor and the Hot Ion Analyser

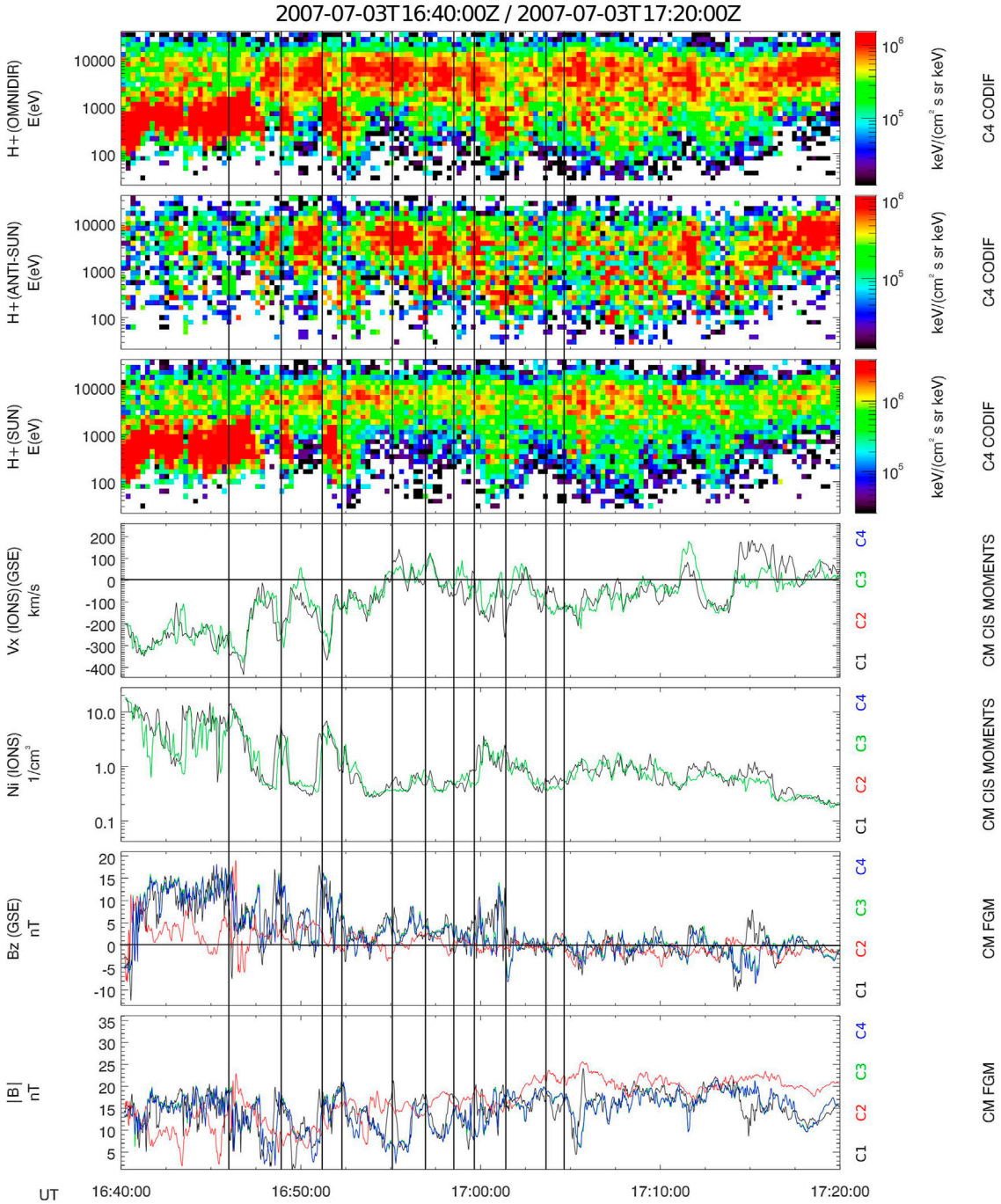

FIGURE 1 | Cluster CIS observations from July 3, 2007, 1640–1,720 UT. From top to bottom: CODIF energy-time spectrograms of proton energy flux: omnidirectional, measured by the anti-sunward sensors and by the sunward sensors, in keV cm^{-2} s^{-1} sr^{-1} keV^{-1}, from SC 4; ion density, cm^{-3}, from SC 1 & 3; X-component ion velocity, km s^{-1} (GSE), from SC 1 & 3; Z-component and the magnitude of the magnetic field, nT (GSE), from SC 1–4. The black vertical solid lines show the times of strong maxima in the total pressure profile defined in **Figure 3**.

(HIA). The magnetic field components were measured by Cluster's onboard fluxgate magnetometer (FGM) [29]. Further documentation regarding the Cluster mission can be found through Escoubet et al. [30].

The ion density and velocity profiles measured by the CIS/HIA instrument, in conjunction with the proton energy spectrograms measured by the CIS/CODIF instrument, showed the oscillation of plasma populations (see **Figure 1**). Velocity fluctuations from

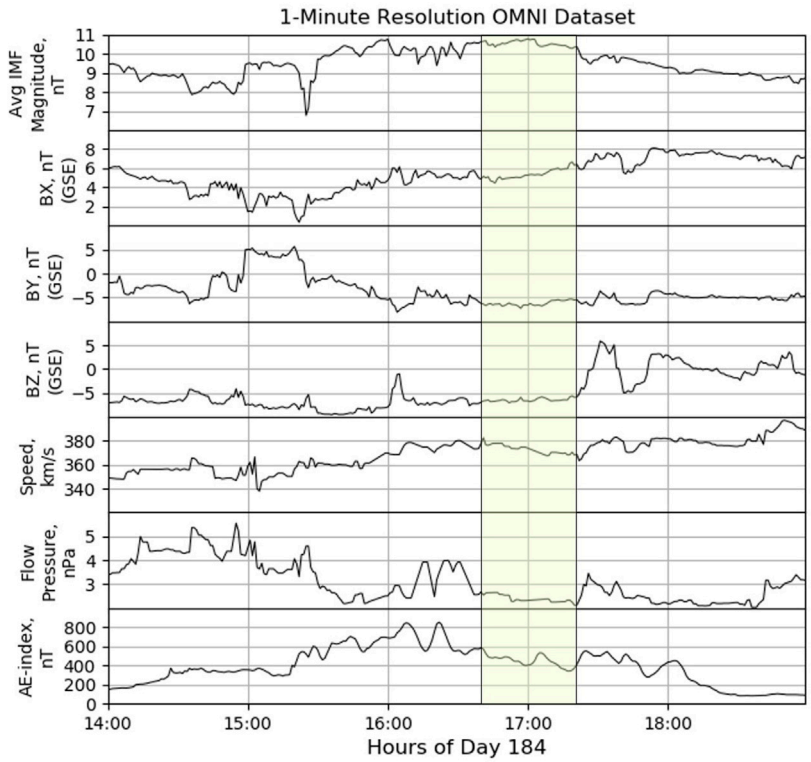

FIGURE 2 | OMNI derived solar wind parameters for July 3, 2007 from 1400 to 1900 UT. The highlighted portion represents the time frame of the observed KHI from 1640 to 1720. From top to bottom: average IMF magnitude, nT; B_X, nT; B_Y, nT; B_Z, nT; speed, km s^{-1}; flow pressure, nPa; and AE index, nT.

the strongly anti-sunward to the weakly anti-sunward or sunward direction were experienced by both Cluster spacecraft (SC) 1 and 3 starting after 1645 UT (HIA data were unavailable for SC 2 and 4 during the event). The proton energy spectrograms for SC 4 displayed similar alternations between high-energy (~ 5–10 keV) plasma typical for the magnetospheric environment and lower energy (~ 0.3 eV–1 keV) plasma typical for the magnetosheath. Those alternations corresponded with fluctuations in the SC 1 and 3 ion densities, n, from tenuous (<1 cm^{-3}) to dense (3–10 cm^{-3}), respectively. These fluctuations indicate that the spacecraft were observing alternating regimes between the magnetosheath and closed magnetospheric magnetic field lines[1] as expected within KHWs. The vertical, B_Z, magnetic field component is strongly northward in the magnetosheath region at SC 1, 3 and 4 from 1640 to ~1700 UT, see **Figure 1**. Also at these SC, the total magnetic field oscillates at the boundary between the two regimes, see discussion in **Section 2.2**. SC 2, which has the innermost location within the magnetosphere compared to the other SC, mainly shows higher values for the total magnetic field.

The OMNI-calculated solar wind parameters during this event can be found in **Figure 2**. There was a solar wind speed of ~375 km s^{-1}, nearly constant IMF of ~10.5 nT and the B_Z component of the IMF was southward. The wavelet analysis for wave power of the corresponding 3 s WIND data does not show any prominent spikes in the Pc4-Pc5 range (not shown). The horizontal component of the IMF was in Parker spiral orientation ($B_X \approx 5$ nT, $B_Y \approx -6$ nT). There were pressure fluctuations up until about 1635 UT which then ceased and remained rather stable throughout the event time frame. The Dst index (not shown) revealed that there wasn't a geomagnetic storm during the time of the event; however, the AE index indicated that a geomagnetic substorm had occurred.

The profiles of velocity; magnetic field, ion density and total pressure, including its magnetic and plasma components, using Cluster SC 1 data for the time interval from 1640 to 1705 UT are shown in **Figure 3**. The total pressure was calculated as the sum of the magnetic (p_{mag}) and plasma (p), calculated using observations from the CIS/HIA instrument) pressures.

The magnetic field and velocity data for this time interval were transformed to the (L, M, N) components which describe local

[1]The observation of closed magnetic field lines is indicated by the energy of maxima intensity in spectrograms of **Figure 1**, which is significantly higher than those typical for the plasma mantle, < 0.5 keV (the event is located at high latitude)[73]. The proton spectrograms in the anti-sunward and sunward direction show similar levels of particle fluxes for the time periods with the hot plasma implying that they bounce on the closed magnetic field lines in the plasma sheet. The location of Cluster for this event corresponds to the typical location of plasma sheet observations as derived by Kronberg et al. [74].

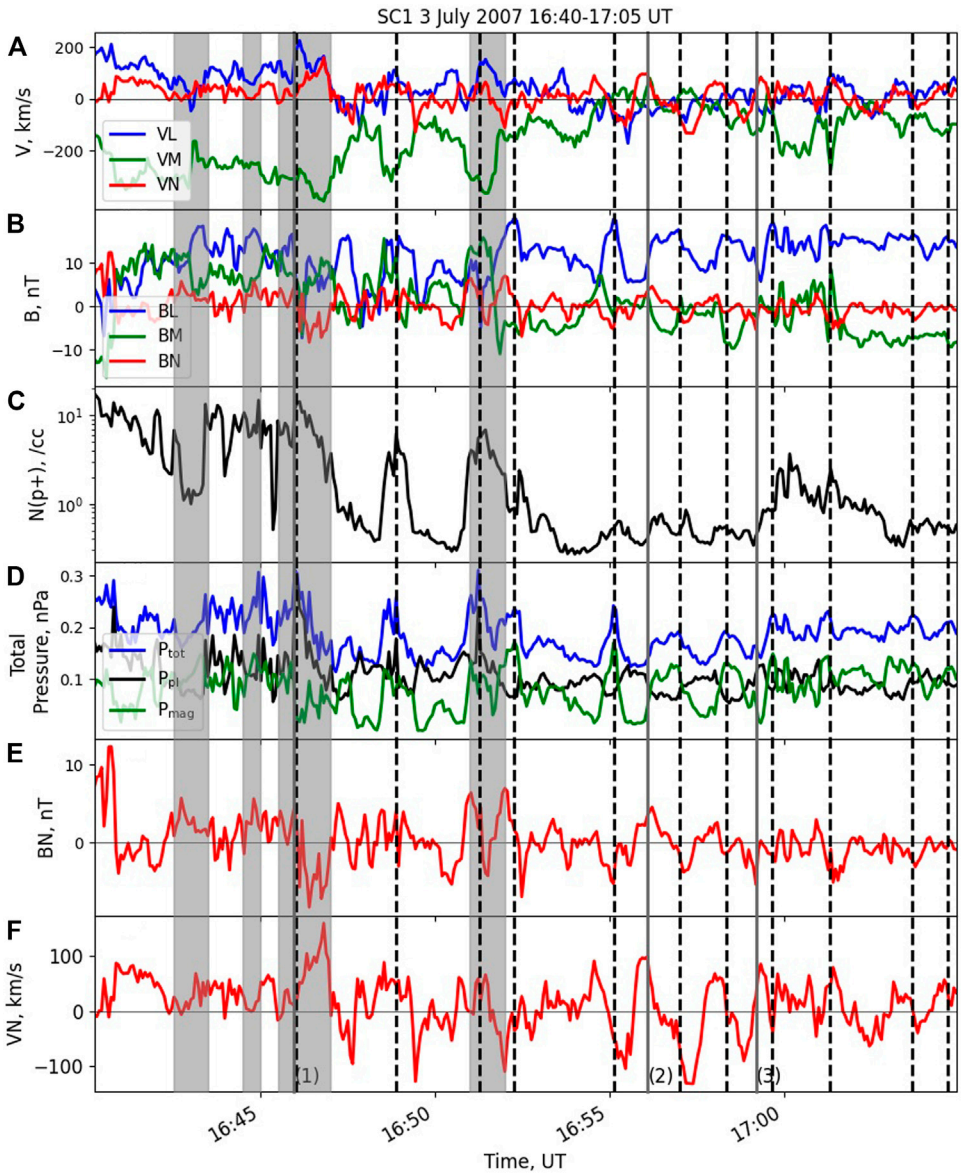

FIGURE 3 | SC 1 measured and derived parameter profiles for the KHI event on July 3, 2007 are shown for the time frame of 1640–1705 UT. From top to bottom within each graph: **(A)** transformed velocity components L (blue), M (green) and N (red), km s^{-1}; **(B)** transformed magnetic components L (blue), M (green) and N (red), nT; **(C)** ion density (black), cm^{-3}; **(D)** total/plasma/magnetic pressure (blue/black/green), nPa; **(E)** transformed magnetic normal component (red), nT; **(F)** transformed velocity normal component (red), km s^{-1}. The black vertical dashed lines indicate the times of strong maxima in the total pressure profile. The vertical shadowed bars show the locations of rotational discontinuities. The grey vertical solid lines denoted as (1), (2) and (3) indicate time intervals for which field-aligned beams were observed (see **Figure 8**).

boundary normal coordinate system. For this we used the Siscoe method [31]. The coordinate vectors L and M are mutually orthogonal and tangential to the boundary. N is the coordinate vector in the boundary normal direction. It is orthogonal to L and M, forming a right-handed coordinate system. The averaged values of (L, M, N) are as follows. L = [−0.62, −0.69, 0.37] and is directed mostly dawnward and tailward. M = [−0.67, 0.22, −0.71] and is directed mostly anti-sunward and southward. N = [−0.41, 0.69, 0.60] and is directed mostly duskward and northward. The eigenvalues of the system are [λ_1, λ_2, λ_3] = [149, 46, 8]. The ratio $\lambda_2/\lambda_3 = 5.6$, indicates that the normal direction is well-defined [32]. Also, L and M are reasonably defined because $\lambda_1/\lambda_2 = 3.2$. A well-defined Siscoe normal direction was also found for SC 4 during the event (not shown).

The three dimensionality of the boundary normal relative to the GSE coordinate system, produced by complex processes at the boundary, can lead to twisting of the magnetic field in the magnetosheath in the northward direction. This can also result

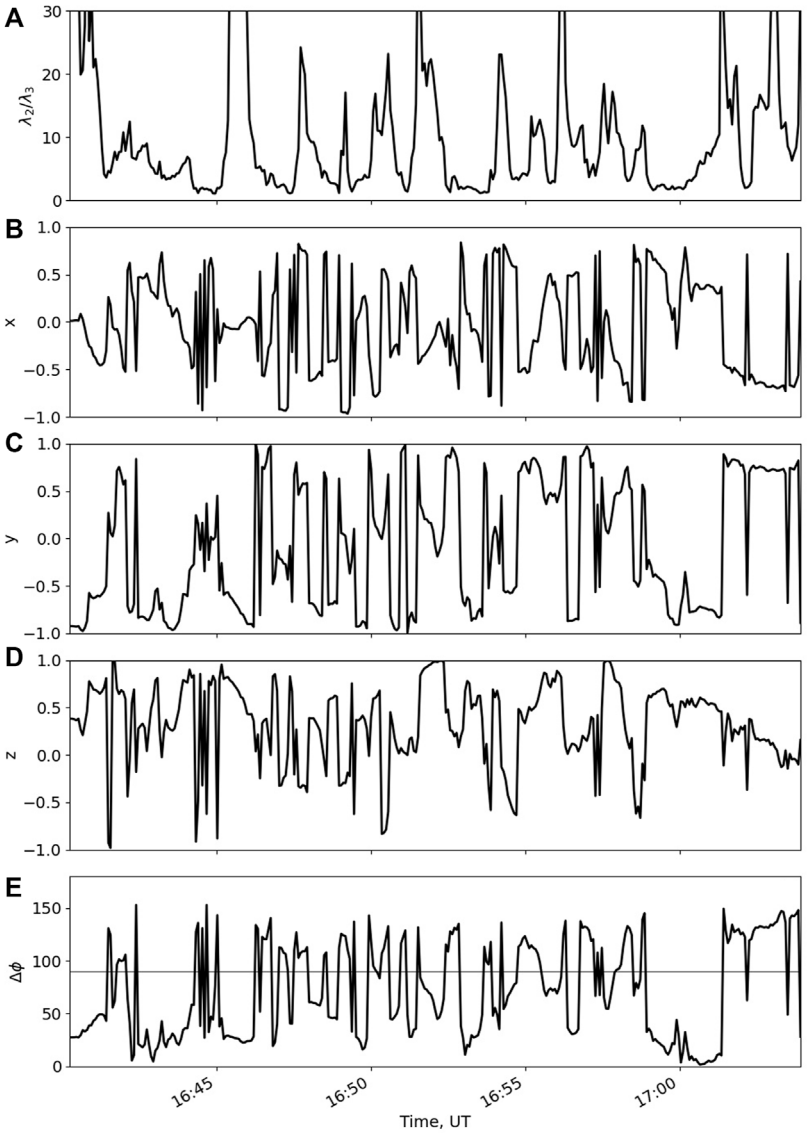

FIGURE 4 | SC 1 derived parameter profiles for the KHI event on July 3, 2007 are shown for the time frame of 1640–1705 UT. From top to bottom within each graph: **(A)** the ratio λ_2/λ_3; **(B–D)** *X*, *Y*, and *Z* components of boundary normals, respectively; **(E)** angle between average normal and individual normal. The average normal is calculated for the whole time interval using the Siscoe method. The individual normals were defined subsequently for each 1 min period of observations. The horizontal line is at 90°.

in a discrepancy between the southward direction as seen in the OMNI data and that observed by THEMIS-C and D at the subsolar point (not shown), see discussion in **Section 5.2**.

2.2 KHW Signatures

The vortex formations are indicated when the M and N coordinates are mainly in anti-phase for both the velocity and magnetic field, according to Yan et al. [33], see **Figure 3**. However, observations of B_M and B_N in anti-phase can also be associated with reconnection. As an indicator of KHI vortices, it is expected to observe anti-phase V_M and V_N oscillations.

In the vortex rest frame, centrifugal force moves plasma outwards from the central part of the rolled-up KHI vortices. This leads to the formation of a local minimum in total pressure at the center and a maximum at the hyperbolic point between vortices [17,34]. The hyperbolic point is also associated with the local absolute maxima of the normal magnetic field component and jumps in the density [17]. Bipolar fluctuations in the normal component of the magnetic field and flow reversals in the normal component of the velocity occurred throughout the entirety of the event, from 1645 to 1705 UT (see **Figure 3**). The ion density, total pressure, and other magnetic and velocity component profiles

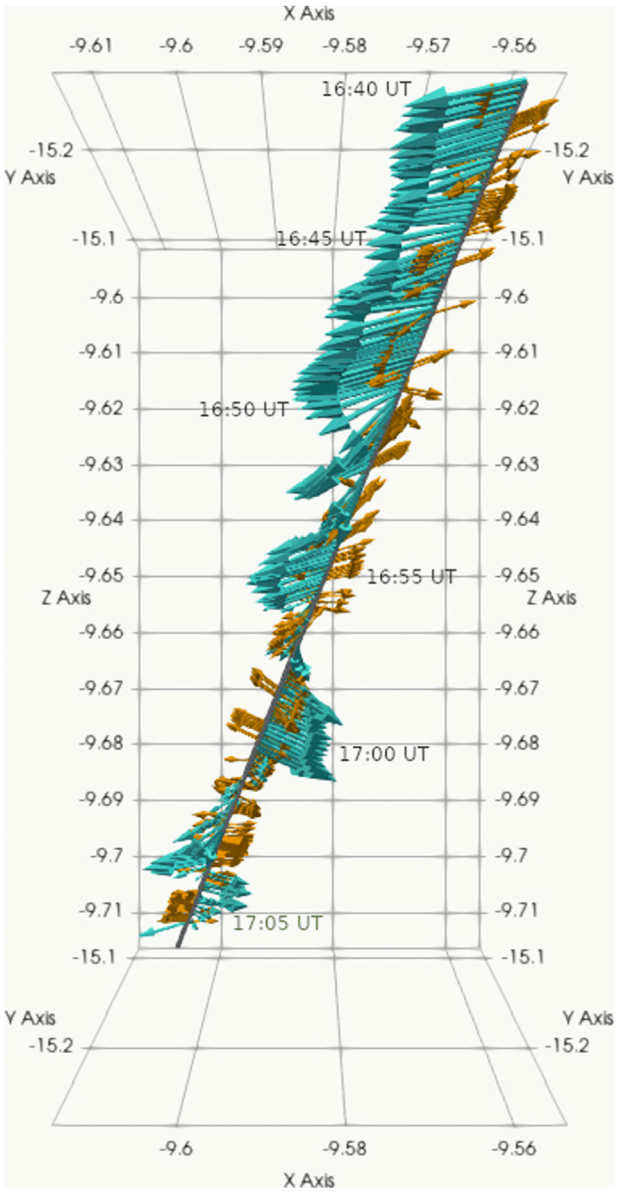

FIGURE 5 | SC 1 derived observations of the HT velocity vectors (cyan) and of the boundary normals (yellow) for the KHI event on July 3, 2007 are shown for the time frame of 1640–1705 UT.

were also highly oscillatory. The vertical dashed lines mark the local total pressure maxima that are mostly aligned with the local absolute maxima of B_N and with jumps in the density. This indicates the formation of the rolled-up KHI vortices (see also Discussion **5.1, (1)** below).

We calculated the individual (L, M, N) coordinates for subsequent 1 min windows centered on each point in the time series, between 1640 and 1705 UT. The first panel in **Figure 4** shows the values of the λ_2/λ_3 ratios, which are mostly well-defined throughout the event. The variation of the X, Y, and Z components of the boundary normals are also shown in **Figure 4**. One can see from the plot that the boundary normal is very dynamic. The angle between the averaged and individual boundary normals changes quasi-periodically in opposite directions indicating the oscillation of the boundary direction, as is typical for rolled-up KHWs.

We transformed the velocity into the deHoffmann-Teller (HT) frame, which is co-moving with the discontinuity [35]. The HT velocity, $\overrightarrow{V_{HT}}$, is determined by minimizing $|(\vec{V}_{HT} - \vec{V}) \times \vec{B}|^2$ to obtain the constant transformational velocity $\overrightarrow{V_{HT}}$ for a given dataset. Here $\vec{V}$ and $\vec{B}$ are the observed time series of the ion velocities and of the magnetic field. We calculated the

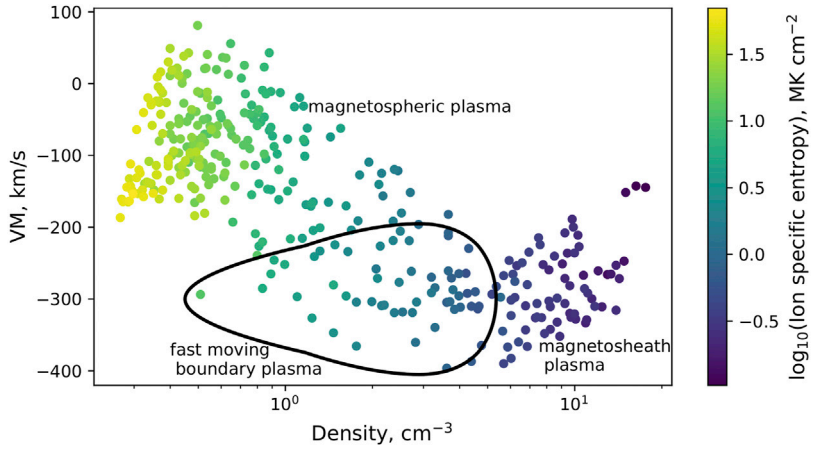

FIGURE 6 | SC 1 derived observations of the V_M velocity component versus ion density with colors indicating the ion specific entropy for the time frame of 1640–1705 UT.

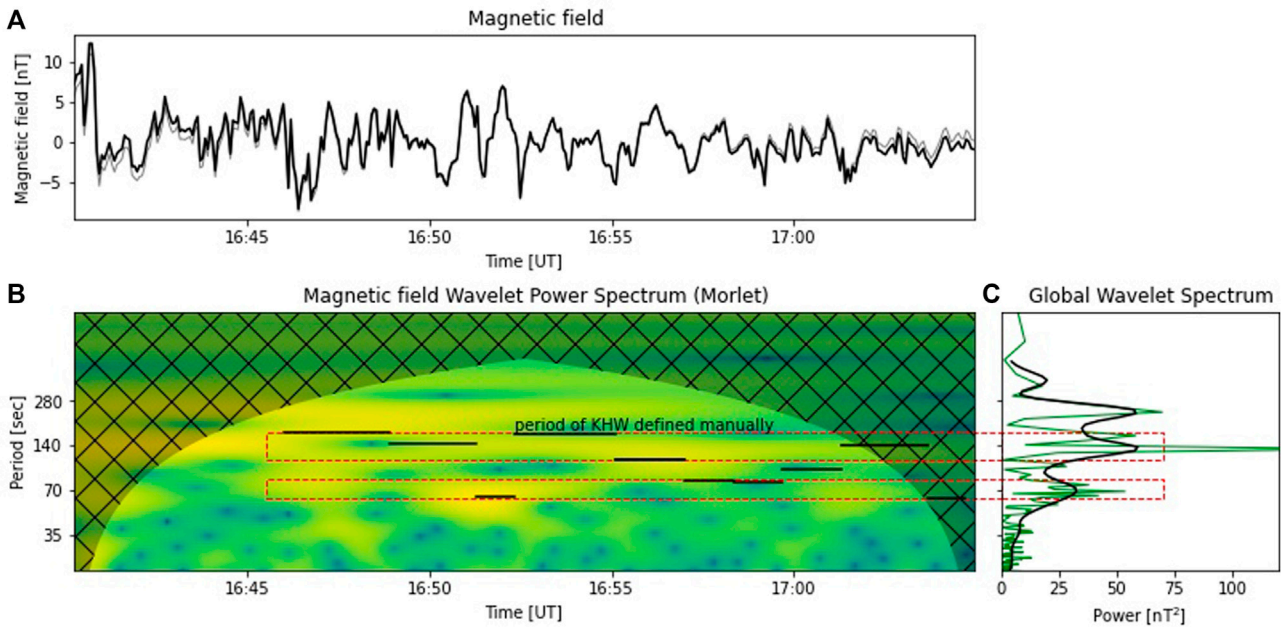

FIGURE 7 | Wavelet transform analysis of Siscoe-derived magnetic field normal component, nT, from Cluster SC 1 between 16:40 and 17:05 UT: **(A)** original series (black) and inverse (gray) wavelet transform; **(B)** the normalized wavelet power spectrum and cone of influence hatched and **(C)** the global wavelet for periods outside of the cone of influence (COI) (black) and Fourier power spectra (green). Note that the period scale is logarithmic. The horizontal lines in panel **(B)** indicate periods of KHW defined manually as the time between dashed lines for corresponding time intervals in **Figure 3**. The dashed red rectangles correspond to two period bands from 62 to 82 s and from 113 to 173 s.

HT velocity for every minute and plotted its vectors and the normal vectors, as determined above, along the Cluster trajectory for this event, see **Figure 5**. It shows that, after a solar wind period when HT velocity vectors were in the negative X_{GSE} direction, Cluster entered a region with rotating deHoffmann-Teller velocity vectors and normal vectors associated with the boundary direction oscillations.

The existence of fast-moving, low-density plasma is typical for the KHI associated with mixing of two plasma environments [36,37]. We demonstrate this existence by plotting V_M versus ion density in **Figure 6**. The color of each point indicates the ion specific entropy, S, calculated as

$$S = T/n^{2/3}. \quad (1)$$

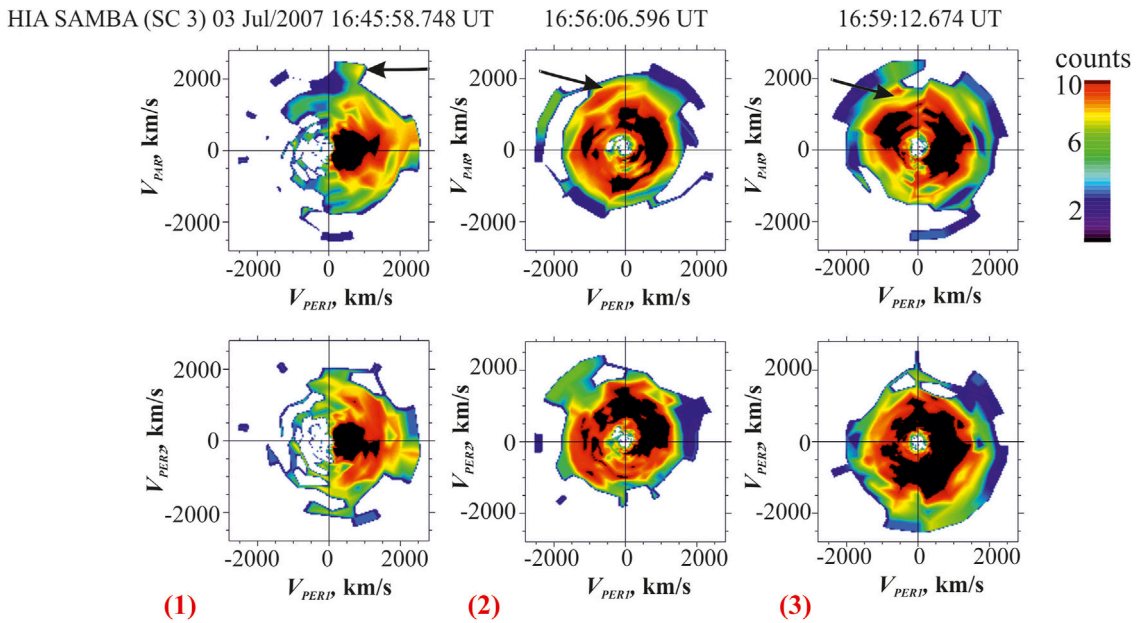

FIGURE 8 | Ion velocity distribution functions as measured by the HIA instrument onboard SC 3 at 16:45:58.748 UT **(left)**, 16:56:06.596 UT **(middle)** and 16:59:12.674 UT **(right)** during 12 s time-averaged ion velocity distribution functions. V_{PAR} is directed along B, V_{PER1} is directed along $-V \times B$ and V_{PER2} direction completes the orthogonal system. The black arrows indicate the field-aligned beams. The time of observation for distributions (1), (2), and (3) correspond to that similarly noted in **Figure 3**.

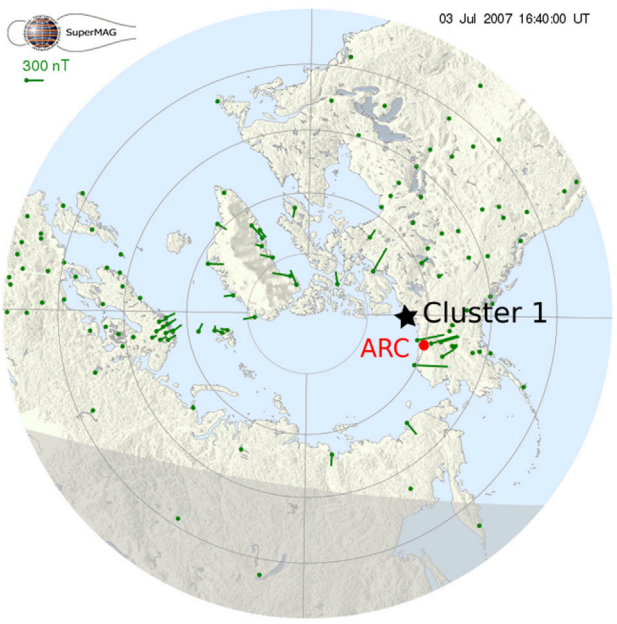

FIGURE 9 | The SuperMAG Polar Plot is shown for July 3, 2007 at 1640 UT. The field line foot point corresponding to Cluster SC 1 is shown by a black star. The green vectors represent the direction and magnitude of ground-based magnetic field disturbances. The approximate location of the Arctic Station (ARC) magnetometer is denoted by the red dot.

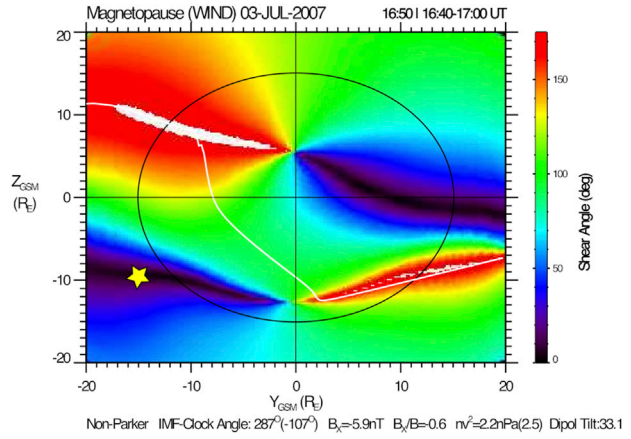

FIGURE 10 | The magnetopause shear angle for IMF values $B_Z < 0$, $B_Y < 0$ as seen from the Sun. Red areas represent magnetopause regions where the geomagnetic field and IMF are antiparallel within 150°–180°. White regions embedded in the red regions represent the line of maximum magnetic shear angles which are thought to be the most likely location for reconnection to occur. The black circle represents the location of the x = 0 plane. Earth's dayside and nightside magnetopause are shown inside and outside of the black circle, respectively. The yellow star marks the location of Cluster SC 1 ($X_{GSM} \approx -9.5\ R_E$, $Y_{GSM} \approx -15\ R_E$, $Z_{GSM} \approx -9.5\ R_E$).

The black line in the figure shows the fast-moving plasma population, with speeds in the range of −400 to −200 km s^{-1}, low ion density of < 5.5 cm^{-3}, and specific entropy values in the intermediate range between that of magnetospheric and magnetosheath ions [38].

2.3 Wavelet Analysis of the KHW

The spectral wavelet analysis of the magnetic field normal fluctuations as observed by Cluster is shown in **Figure 7**. The periods of KHWs were defined manually using pressure maxima criteria and are marked in **Figure 3** as the time between dashed lines. These periods were 173, 143, 64, 167, 113, 81, 79, 98, 142 and 62 s at ~ 16:46:00, 16:48:53, 16:51:16, 16:52:20, 16:55:07, 16:57:00, 16:58:21, 16:59:40, 17:01:18, 17:03:40 and 17:04:42 UT, respectively. We see that the KHW-associated periods mainly coincide with power spectra increases of the magnetic field (excluding the period at 98 s, which is approximate minimum of the Fourier power spectra, and the period at 113 s, which is at the boundary between the local maximum and minimum). Within the range of marked periods we observe two power peaks in the global wavelet spectrum for the magnetic fluctuations: at periods of about 133 s and 70 s, see panel (c). These are fluctuations within the Pc4 range [39]**.** It seems that we observe a primary wave mode with a period ~ 133 s and its submode at ~ 70 s.

2.4 Observations of Associated Reconnection

We also tested if reconnection was observed during this event. The Walén relation calculated in the HT frame shows the relation between the plasma velocity in the HT frame and the Alfvén velocity, $\overrightarrow{V_A} = \vec{B}/\sqrt{\mu_0 \rho}$ [35]. We found a 1 min deHoffmann-Teller interval from 16:45:58-16:47:01 UT (HT slope is one and correlation coefficient (CC) is 0.99) where the Walén relation is very well met (Walén slope = −0.99 and Walén CC = −0.87), see the **Supplementary Material S1**. The Walén slope was negative, which means the spacecraft crossed the rotational discontinuity (RD) tailward of the X-line [40]. The interval is marked by a gray shadowed bar in **Figure 3**. There were several other frames that met the "strict" HT (HT Slope = 0.9–1.1 and CC > 0.95) and RD (HT Slope = 0.7–1.1 and CC > 0.95) qualifications according to Nykyri et al. [41]. These were from 16:42:30–16:43:00 UT, 16:45:30–16:46:00 UT and 16:51:30–16:52:00UT. If the correlation requirements and slope requirements for the Walén relation are both relaxed (CC > 0.85, Walén slope > 0.5), then two RD intervals can be extended: 16:43:00–16:43:30 UT and 16:51:00–16:51:30 UT. Also an additional interval can be gained: 16:44:30–16:45:00 UT. All these RD intervals are marked by gray shadowed bars in **Figure 3**. In this figure we can see that the hyperbolic points of the rolled-up KHWs indicated by the dashed lines are in two cases accompanied by the RD likely associated with reconnection.

Field-aligned ion beams were observed at three instances during these marked intervals: 16:45:58.748 (V_{par} = 2,300 kms^{-1}, V_{perp} = 900 kms^{-1}), 16:56:06.596 (V_{par} = 1,400 kms^{-1}, V_{perp} = − 700 kms^{-1}) and 16:59:12.674 UT (V_{par} = 1,700 kms^{-1}, V_{perp} = − 500 kms^{-1}), see **Figure 8**. The field-aligned beams may be an indication of ions moving along a separatrix and further imply that reconnection may have occurred. In the distribution function 1) at 1645 UT one can also simultaneously observe a perpendicular beam. This can happen if Cluster was crossing different magnetic field lines during the same data accumulation interval. The perpendicular beam can indicate that there are demagnetized ions in the reconnection exhaust region. Additionally during this interval the crescent distribution is seen, see **Figure 8**. This is a sign that the ions are demagnetized and the satellite was crossing the diffusion region [42]. There are multiple observations of the crescent distributions from 1640 to 1650 UT (not shown).

3 GROUND-BASED OBSERVATIONS

During the same time period as the observed magnetopause fluctuations, large magnetic field disturbances were recorded at ground-based geomagnetic stations. These disturbances are shown in SuperMAG's Polar Plot (Gjerloev [43]; see **Figure 9**). Also shown in **Figure 9** is the estimated magnetic field line foot point from Cluster SC 1.

The magnetic foot point of the Cluster mission was mapped to the ionosphere by projecting the satellite location along the magnetic field lines to the altitude of 100 km, where the lower boundary of the ionosphere was assumed. Since the spacecraft was located at the magnetosheath boundary just outside the

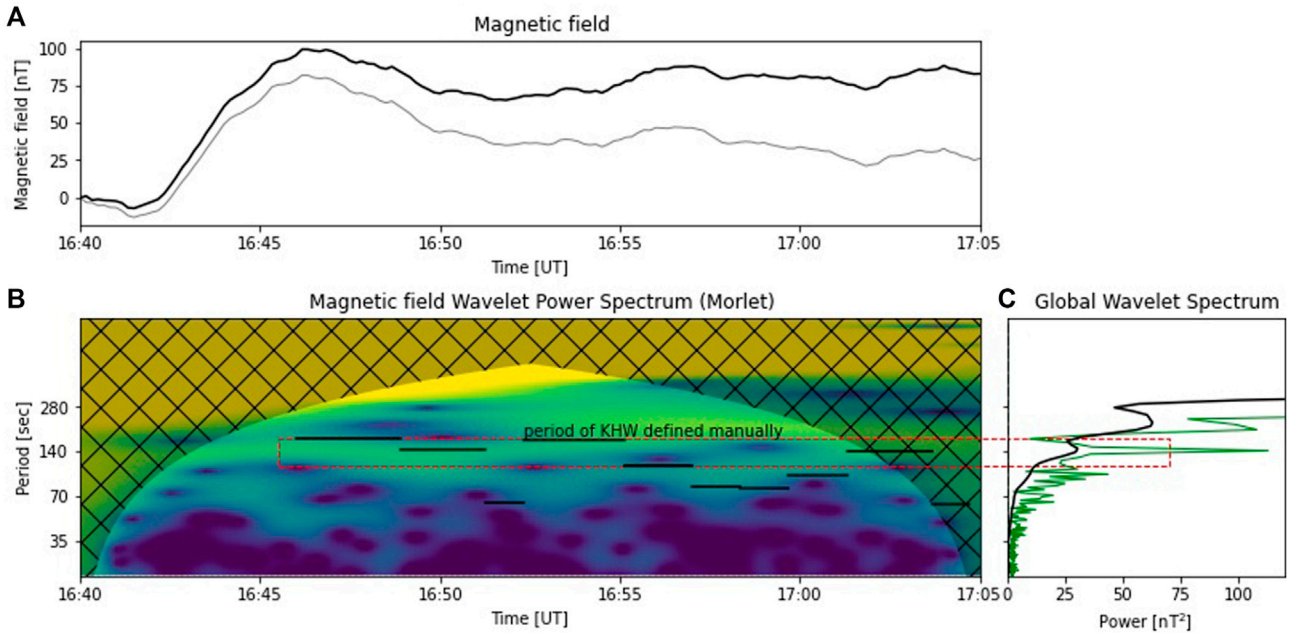

FIGURE 11 | Wavelet transform analysis of the geomagnetic field oscillations at Arctic Village, Alaska (ARC) for the E-component, nT, between 1640 and 1705 UT: **(A)** original (black) series and inverse wavelet transform (gray), each relative to their respective values at 1640 UT; **(B)** the normalized wavelet power spectrum and shaded COI and **(C)** the global wavelet for periods outside of the COI (black) and Fourier power spectra (green). Note that the period scale is logarithmic. The horizontal lines in panel (b) indicate periods of KHW defined manually in **Figure 3** as the time between dashed lines for corresponding time intervals. The dashed red rectangle corresponds to the period band from 113 to 173 s.

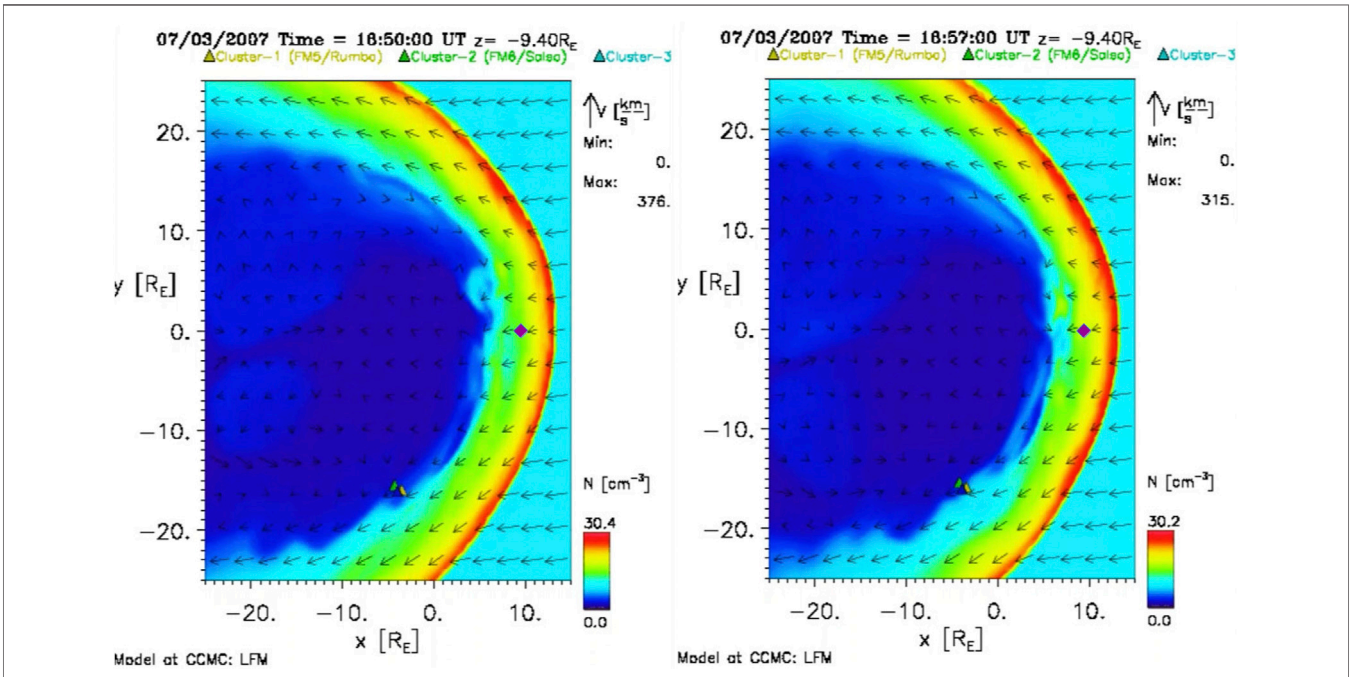

FIGURE 12 | Snapshot of the Global MHD (LFM-model) simulation in Solar Magnetic coordinates, driven with solar wind dynamic pressure variations, in the *XY*-plane with $Z = -9.4\ R_E$ (solar magnetic coordinates) for July 3, 2007 at 1650 (on the left) and 1657 UT (on the right). Colors represent plasma density (see color bar), arrows represent plasma velocity, and the triangles show the location of the four Cluster spacecraft. The purple diamond denotes the approximate (*X*, *Y*) location of the THEMIS-E spacecraft (with $Z_{GSE} \approx -2.4\ R_E$).

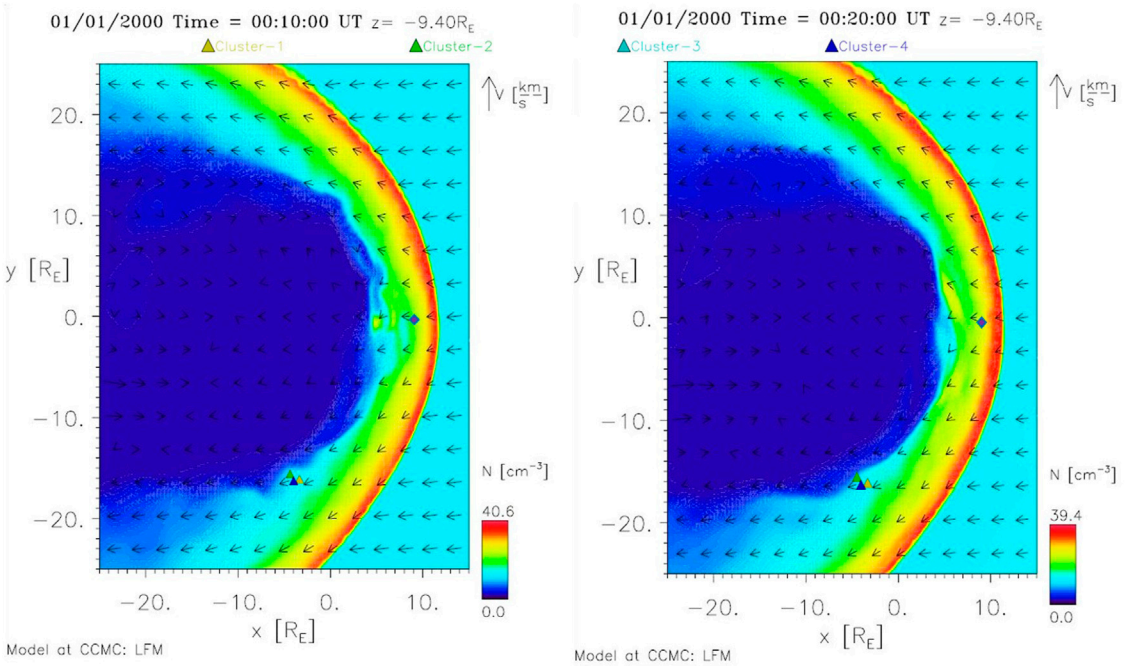

FIGURE 13 | Snapshot of the Global MHD (LFM-model) simulation in Solar Magnetic coordinates, driven with constant IMF orientation and without solar wind dynamic pressure variations, in the *XY*-plane with $Z = -9.4$ R_E (solar magnetic coordinates) for conditions characteristic of July 3, 2007 between 1600 and 1730 UT. The figure on the left shows a snapshot taken at 10 min into the simulation, and the figure on the right shows a snapshot taken at 20 min. Colors represent plasma density (see color bar), arrows represent plasma velocity, and the triangles show the location of the four Cluster spacecraft. The purple diamond denotes the approximate (*X*, *Y*) location of the THEMIS-E spacecraft (with $Z_{GSE} \approx -2.4$ R_E).

bounds of the magnetic field model, some adjustments were necessary in order to derive the magnetic foot point's location. In this case, the Z_{GSE}-coordinate of the spacecraft was assumed to be equal to −8.5 R_E instead of −9.6 R_E, **as it** was the closest point where mapping was possible. The location of the magnetic foot point was derived using the Tsyganenko-1989 model of the external magnetic field [44] with internal field given by IGRF (for K_P = 2.7), as implemented in the IRBEM library [45,46]. It is worth mentioning that magnetic foot point tracing is highly model dependent (as shown in Dunlop et al. [47]) and thus gives only an approximate indication of the spacecraft position with relation to the ionosphere.

The highest amplitude of ground-measured magnetic field disturbances in the SuperMAG Polar Plots were observed to be concentrated within the North Slope region of Alaska. While magnetic fluctuations were recorded at other geomagnetic stations around the polar cap, they were lower in amplitude. The magnetic field line foot point for Cluster SC 1 mapped to the northwest coast of Canada, in the vicinity of the highest magnitude magnetic field fluctuations. **Figure 10** shows the calculated magnetopause shear angle determined according to the event's specific solar wind parameters and geomagnetic field (calculated from the T96 model [48]). The white line depicts the maximum magnetic shear angle where magnetic reconnection had the highest probability of occurring [49,50], particularly at the dawn side of the northern hemisphere. Therefore, the magnetic field fluctuations were possibly at least partially triggered by flux transfer events (FTEs) in the northern hemisphere where they are likely to occur according to **Figure 10**. We note that location of reconnection in **Figure 10** is irrelevant to local reconnection occurring during the KHI observed by Cluster.

Our event showed magnetic field fluctuations at the magnetopause in the Pc4 frequency range. Therefore, to establish a link between the disturbances measured by Cluster in space and those recorded at ground-based magnetic field observatories, we needed to analyze those field measurements at a resolution of 1–10°s. The closest stations to the mapped Cluster location were Arctic Village (ARC) and Kaktovik, Alaska (KAV). To show that the ARC and KAV stations were located on the closed magnetic field lines and their observations are not directly affected by the solar wind, we launched the tracing described above, using a grid with 1° steps in latitude and longitude, see the **Supplementary Material S2**. If the corresponding magnetic field line was closed, IRBEM returned a position of its foot point, and if the field line was open, the output was "Not a Number". Using this information, the map of open and closed magnetic field lines was created. It can be seen from **Supplementary Material S2** that the KAV and ARC stations were on closed field lines.

The wavelet analysis for the magnetic field recorded at the magnetometer in ARC (selected for its better clarity) is shown in **Figure 11**. The analysis shows a wave power peak in the global wavelet spectrum for the N-component at 140˚s. This value approximately coincides with the main mode of the KHW. According to, for example, Hughes and Southwood [51]; Sciffer and Waters [52]; Paschmann et al. [53], not all ULF waves propagate from the magnetosphere down to the ground and the wave modes could be affected by complex wave mode conversions, modulation or damping. For instance, low ionospheric conductance during the summer could have prevented propagation of waves with periods of 70˚s observed by Cluster but not observed at the ground.

4 MODELING OF MAGNETOSPHERIC OBSERVATIONS

The Lyon-Fedder-Mobarry (LFM) global magnetosphere model, as hosted by the NASA Community Coordinated Modeling Center (CCMC), was used to further investigate the magnetopause configuration in the vicinity of the Cluster spacecraft during the event time frame. The LFM model solves the ideal magnetohydrodynamic (MHD) equations to simulate the 3D interaction between the solar wind and the Earth's magnetosphere. Further description of the simulation code and its numerical methods can be found in Lyon et al. [54] and Merkin and Lyon [55]. The LFM model can effectively resolve the KHI due to its low diffusion numerical scheme and has been used in previous studies of the KHI [56,57].

The simulation was driven by measured solar wind parameters provided by the virtual OMNI database King and Papitashvili [58] including plasma density, velocities, IMF vector and dipole tilt angle. The simulation was run from 1,600 to 1,730 UT and snapshots of its development at 1,650 and 1657 UT are shown in **Figure 12**. The background color represents plasma density and the arrows show the velocity vectors. The triangles show the actual location of the four Cluster spacecraft during the event. From the figure, it can be seen that the lower density magnetosphere (dark blue) has developed rolled-up waves at the border with the higher density magnetosheath (light blue). At both times the KH waves are not clearly visible on the dusk side. This is because the horizontal component of the IMF for this event is in the Parker Spiral orientation, making the dusk flank downstream of the quasi-perpendicular bow shock, where the stronger magnetic tension can stabilize the KHI. This is consistent with previous simulation studies of the KHI during Parker Spiral IMF [59] and observations from 6˚years of THEMIS data [8].

Figure 13 displays the simulation driven for constant solar wind and IMF conditions but without any solar wind dynamic pressure variations in order to check whether the ULF waves were caused by pressure driven surface waves or by KHI driven waves. Because the waves were formed in the simulation without any solar wind fluctuations, the non-linear waves seen by Cluster were most likely generated by the KHI. Note that for the unstable boundary conditions, the KHI can be seeded by any perturbation such as magnetic fluctuations [25], velocity fluctuations [60], pressure fluctuations, or any combination of these. The magnitude and frequency of the perturbation can affect the non-linear stage of the instability [60]. Based on the present simulation, the source region for the KHI appears to be on the dayside magnetopause where the magnetosheath flow first diverges dawnward. Note that this is a cut at $Z = -9.4$ R_E and low latitude reconnection is also likely to operate which can act as a seed perturbation for the KHI [25].

All the simulation results and more details on the settings of both runs can be found at https://ccmc.gsfc.nasa.gov/with run-name Katariina_Nykyri_111218_1 (real solar wind and IMF based run) and Katariina_Nykyri_070119_8 (synthetic run without solar wind dynamic pressure variations). A movie of the simulation can be found in the **Supplementary Materials, S3**. More detailed high-resolution 3D MHD simulations with test particles and Cluster data comparison is left for our future work.

5 DISCUSSION

5.1 Identification of KHW

Based on the Cluster observations, the Pc4 event shown here can be interpreted as the KHI because:

1) The magnetic field magnitude and normal component maxima were aligned with the pressure maxima, indicating that the spacecraft were traversing the rolled-up KHWs [5,17]. This differs from instances of observing either FTEs or persistent surface waves. In the case of FTE observation, the pressure maxima is expected at its core (the center of the bipolar B_N) and the bipolar B_N fluctuations are separated by repetitious quiet periods with periods longer than 4 min [6]. In the case of persistent surface waves, the pressure maxima would be associated with the bipolar $B_N = 0$ crossings. These KHW magnetic field and total pressure signatures occurred in conjunction with periodical observations of magnetospheric and magnetosheath plasma populations (jumps in the density at the hyperbolic points), indicating that the KHI had developed into the vortices necessary for energy transport across the magnetopause [61];
2) V_M and V_N and B_M and B_N are mainly in anti-phase, indicating that there are vortex formations according to Yan et al. [33]. In the case of FTEs, the velocity components will not show such anti-phase behavior;
3) The angle between the average boundary normal and the boundary normals, calculated for subsequent 1 min windows centered on each point in the time series, oscillates between opposite directions;
4) The HT velocity vectors show oscillations at the boundary region;
5) Fast-moving, low-density plasma populations associated with the mixing of two plasma environments are observed;
6) Pc4 is a typical KHW frequency.

The interpretation of the observations is also supported by the global modeling. The rolled-up vortices were clearly seen in LFM

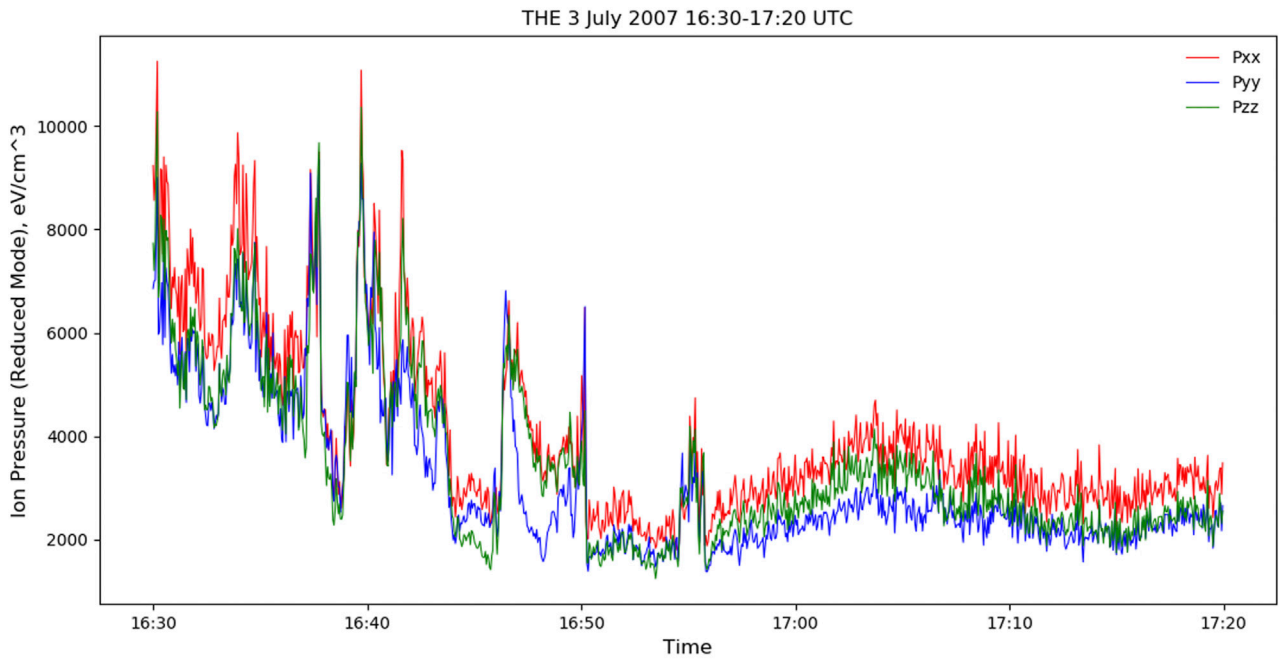

FIGURE 14 | THEMIS-E pressure tensor for the *xx* – (red), *yy* – (blue), and *zz* – components (green), eV cm^{-3}, recorded by the Electrostatic Analyzer (ESA). Reduced mode data are shown for July 3, 2007 from 1630 to 1720 UT.

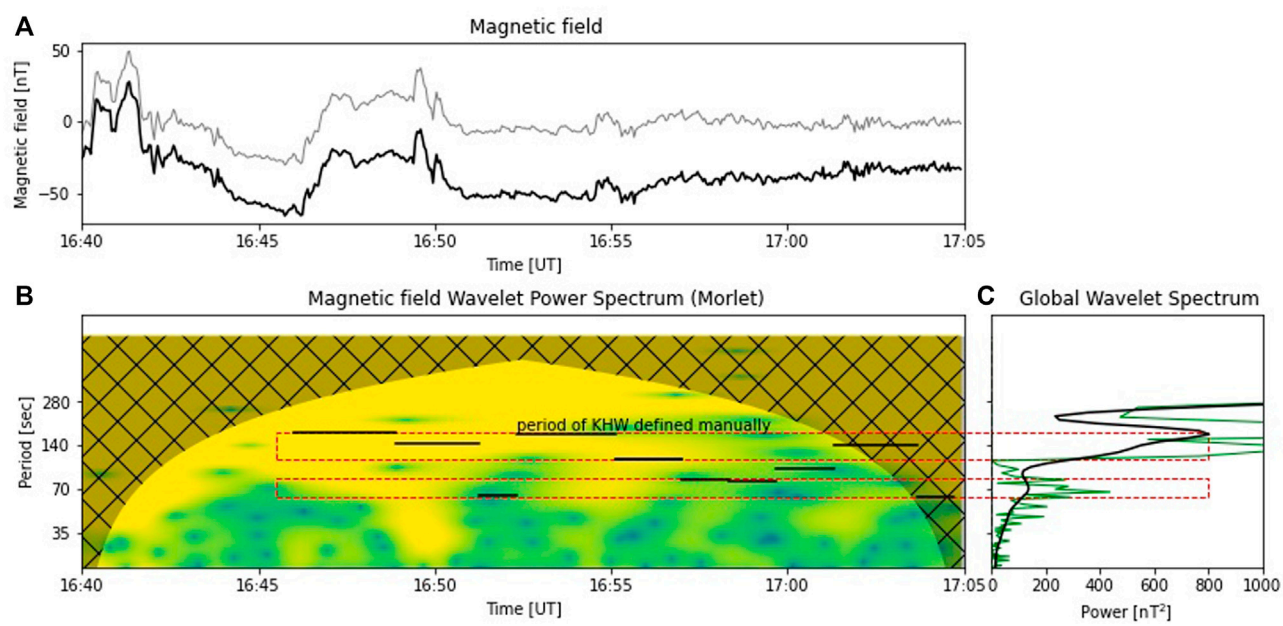

FIGURE 15 | Wavelet transform analysis of the magnetic field oscillations for the Z_{GSE}-component, nT, observed by THEMIS-E between 1640 and 1705 UT: **(A)** original (black) series and inverse (gray) wavelet transform; **(B)** the normalized wavelet power spectrum and shaded cone of influence and **(C)** the global wavelet for periods outside of the COI (black) and Fourier power spectra (green). Note that the period scale is logarithmic. The horizontal lines in panel (b) indicate periods of KHW defined manually in **Figure 3** as the time between dashed lines for corresponding time intervals. The dashed red rectangles correspond to two period bands from 62 to 82 s and from 113 to 173 s.

simulation results for the event, confirming that the solar wind conditions were favorable for KHW development. The favorable solar wind conditions are also supported by the analysis of the magnetopause shear angle. It has been shown that when the IMF has a strong Parker spiral component, the KHI can develop with tilted *k*-vectors with respect to the shear flow plane to maximize the onset condition [8,41,62], which could explain why KHWs were observed by Cluster at high latitudes.

5.2 Associated Reconnection

Several of the KHI vortices observed in this event were likely accompanied by reconnection events as indicated by the Walén relation, the presence of deHoffmann-Teller frames, field-aligned ion beams observed together with bipolar fluctuations in the normal magnetic field component, and crescent distributions. The relation between the KHI and reconnection is highly dependent upon the magnetic field direction with respect to the sheared flow.

For northward IMF conditions, Otto and Fairfield [3] demonstrated that as long as there is a KH wave vector component along the magnetic field, the nonlinear KH mode can twist the magnetic field line and consequently generate a strong anti-parallel component. This then triggers magnetic reconnection (even without an anti-parallel magnetic component in the initial condition). Later, Nakamura et al. [63] showed that if there is an anti-parallel magnetic component across the sheared flow, the spin region (trailing edge) of the KH wave can thin the current sheet, which also triggers magnetic reconnection. The above two KH driven reconnection mechanisms are described in a two-dimensional perspective. In three-dimensions, the KHI can strongly twist magnetic field lines in its active region, which triggers a pair of middle-latitude component reconnections (e.g., [64–66]).

For the southward IMF condition, as is namely the case in this paper according to the OMNI data and THEMIS observations at the subsolar point, there are pre-existing anti-parallel magnetic field components (mainly along the north-south direction) that are mostly perpendicular to the sheared flow (mainly along the Sun-Earth direction). This configuration is unstable for both magnetic reconnection and KHI. Thus, both KHI (mostly in XY_{GSE} plane) and reconnection (mostly in XZ_{GSE} plane) can operate simultaneously [23], One process can be initialized earlier or grow faster than the other. But it does not have to be that one triggers another. The onset of KHI can locally thin the current sheet which triggers reconnection, especially in the spine region (trailing edge) (see illustration of such coupling in **Figures 4**, **6**, **11** (at t = 124 s) in Ma et al. [24]). Note that the majority of open flux are connected through the spine region. In the vicinity of vortices, plasma flow strongly twists magnetic field lines which generates patchy reconnection and complex flux rope structures. Both strongly anti-parallel magnetic field and reconnection jets (i.e., along the *Z*-direction), may not be easily observed (see also [67]). In our study we observe field-aligned beams together with bipolar B_N magnetic field fluctuations as an indication of reconnection. The onset of magnetic reconnection can change the width of the sheared flow, and consequently changes the KH wavelength [25]. This event demonstrates the complexity of the instabilities generated at the magnetopause.

5.3 Source of KHI

Source regions for longer wavelengths and lower frequencies are expected farther down the magnetotail. For the present KHI associated with reconnection event, there are three possible source regions. The first is close to the subsolar point where magnetosheath flow first starts to diverge and where KHI growth may be enhanced by both dayside reconnection [25] and by solar wind velocity and pressure fluctuations [60]. The latter enhancement was also demonstrated by the LFM simulation of this event. The second source region is at the dawn sector of the southern cusp [68], and the third region is farther down the tail where flow from tail reconnection is moving Earthward and forms a shear layer. This velocity shear layer is observable in the LFM simulation, see, e.g., **Figure 12**. Most relevant for the present event are the first two source regions, and future work will need to address the possible KHI associated with reconnection interference from multiple sources.

ULF waves in the magnetosphere have been correlated with solar wind conditions. For example, dynamic pressure variations are known to generate pulsations [69]. However, the solar wind speed, IMF magnitude, Alfvénic Mach number (not shown), and flow dynamic pressure from the OMNI data all remained nearly constant during the event, ruling out the likelihood of the ULF waves observed by Cluster being driven directly by pressure perturbations.

There were solar wind ion pressure pulsations preceding the event which may have acted as seed perturbations at the subsolar point, providing for the propagation and development of the event KHWs seen farther down the flank [70]. In fact, three of the THEMIS spacecraft situated in the magnetosheath at the subsolar point during this event recorded signatures of significant boundary motion, including pressure perturbations, which further supports this hypothesis. **Figure 14** shows the pressure tensor for the *xx* –, *yy* –, and *zz* – components (red, blue, green, respectively) recorded by the Electrostatic Analyzer (ESA) onboard THEMIS-E (P4). The ion pressure moment data were obtained from reduced-mode data, which has a degraded angular resolution, but high time resolution (~ 3 s). Similar plots for THEMIS-C and THEMIS-D can be found in the **Supplementary Materials**, see **Supplementary Figures S4, S5**.

We did the wavelet analysis of the magnetic field $B_{Z,GSE}$ fluctuations observed by THEMIS-E, see **Figure 15**. We do observe spikes of the wave power at the periods of 140 and 70 s which is in agreement with the spikes observed by Cluster. Therefore, these fluctuations (via reconnection) may have further modulated the KHWs.

THEMIS-E also observes magnetosheath jets (see the plasma ram pressure pulsations in **Supplementary Figure S6** in the **Supplementary Materials**) with a periodicity of about 5 min, which would result in dayside magnetopause oscillations and/or magnetopause reconnection [71,72], and possibly also modulate the KHWs and associated reconnection. The origin and dynamics of these jets is beyond the scope of this paper and is left for a future study.

6 CONCLUSION

The current debate surrounding the extent of magnetospheric effects caused by KHWs at the magnetopause remains an exciting topic as more and more *in situ* observations become available for analysis. This process' role in the generation of ULF waves at the Earth's ground, in particular, continues to be uncertain since different potential drivers have been identified. The event scrutinized in this article suggests a relation between the KHI associated with reconnection and ground-based ULF waves.

On July 3, 2007 Cluster encountered KHWs at the high-latitude magnetopause. Signatures of these waves included bipolar fluctuations in the magnetic field normal component at the edge of total pressure maxima mostly coinciding with alternations of the low-density, low-speed and high-energy magnetospheric plasma with the high-density, high-speed, and low-energy magnetosheath plasma; existence of fast-moving, low-density mixed plasma; quasi-periodic oscillations of the boundary normal; and the boundary normal and parallel velocity components being in anti-phase. The KHWs exhibited frequency peaks in the Pc4 range which is typical for this instability. Several of the observed KHI vortices were accompanied by reconnection as indicated by the Walén relation, the presence of deHoffmann-Teller frames, field-aligned ion beams observed together with bipolar fluctuations in the normal magnetic field component, and crescent distributions. LFM simulations of the observed event conditions also resulted in KHWs at the magnetopause.

During the same time as the event at the magnetopause, there were Pc4 ULF perturbations recorded at ground-based geomagnetic stations. These pulsations were observed around the location of the foot point corresponding to the field line of the location of the spacecraft recordings. Solar wind conditions during the event were rather steady. The solar wind speed was low and the IMF magnitude was nearly constant. Only minimal pressure perturbations were recorded and the B_Z component of the IMF, according to the OMNI data, remained southward without strong fluctuations. However, the fluctuations in the southward IMF and plasma/ram pressure at the subsolar point may have triggered KHWs.

The conditions recorded during this case study provide evidence for the likelihood that Pc4 ULF waves can be generated by the KHI associated with reconnection at the magnetopause. This suggests that the KHI can play a role in the transfer of energy from the solar wind to the magnetosphere. However, further studies are needed before the ubiquity of such an event can be declared.

DATA AVAILABILITY STATEMENT

The datasets presented in this study can be found in online repositories. The names of the repository/repositories and accession number(s) can be found below: The Cluster data can be found in the Cluster Science Archive (https://csa.esac.esa.int). The SuperMAG data can be found at http://supermag.jhuapl.edu. We also used NASA/GSFC's Space Physics Data Facility's OMNIWeb (or CDAWeb or ftp - see https://cdaweb.sci.gsfc.nasa.gov/index.html) service, and OMNI data (https://omniweb.gsfc.nasa.gov). Data from the THEMIS Mission can be found at http://themis.igpp.ucla.edu/index.shtml). The results presented in this paper rely on the data collected at the Arctic Village and Kaktovik magnetometers, provided by the Geophysical Institute Magnetometer Array operated by the Geophysical Institute, University of Alaska (https://www.gi.alaska.edu/monitors/magnetometer/archive). Global LFM MHD simulations have been provided by the Community Coordinated Modeling Center at Goddard Space Flight Center through their public runs on request system (http://ccmc.gsfc.nasa.gov).

AUTHOR CONTRIBUTIONS

EK led the manuscript, did data analysis, produced figures, contributed to the text and wrote the Volkswagen proposal. JGo led the manuscript, did data analysis, produced figures and contributed to the text. KN led the MHD simulations, did data analysis, produced figures and contributed to the text. AS produced figures and contributed to the text. JGj and MF provided SuperMAG data and assisted in its use. EG did data analysis, produced a figure, contributed to the text and wrote the Volkswagen proposal. LK and KT produced figures. XM contributed to a figure and the text.

FUNDING

The work of JG, EG, LK, and EK is supported by the Volkswagen Foundation under grant Az 90 312, Az 90 312-1 and Az 97 742. Work by KN and XM is supported by the NASA grant ##NNX17AI50G. The work of EK is also supported by German Research Foundation (DFG) under number KR 4375/2-1 within SPP "Dynamic Earth".

ACKNOWLEDGMENTS

The authors would like to thank the Cluster Science Archive team for providing the data and assistance in obtaining the CIS plot. We acknowledge NASA contract NAS5-02099 and V. Angelopoulos for use of data from the THEMIS Mission, specifically, C. W. Carlson and J. P. McFadden for use of ESA data.

SUPPLEMENTARY MATERIAL

The Supplementary Material for this article can be found online at: https://www.frontiersin.org/articles/10.3389/fphy.2021.738988/full#supplementary-material

REFERENCES

1. Southwood DJ. Some Features of Field Line Resonances in the Magnetosphere. *Planet Space Sci* (1974) 22:483–91. doi:10.1016/0032-0633(74)90078-6
2. Fairfield DH, Otto A, Mukai T, Kokubun S, Lepping RP, Steinberg JT, et al. Geotail Observations of the Kelvin-Helmholtz Instability at the Equatorial Magnetotail Boundary for Parallel Northward fields. *J Geophys Res* (2000) 105: 21159–73. doi:10.1029/1999ja000316
3. Otto A, Fairfield DH. Kelvin-Helmholtz Instability at the Magnetotail Boundary: MHD Simulation and Comparison with Geotail Observations. *J Geophys Res* (2000) 105:21175–90. doi:10.1029/1999ja000312
4. Nykyri K, Otto A. Plasma Transport at the Magnetospheric Boundary Due to Reconnection in Kelvin-Helmholtz Vortices. *Geophys Res Lett* (2001) 28: 3565–8. doi:10.1029/2001gl013239
5. Hasegawa H, Fujimoto M, Phan T-D, Rème H, Balogh A, Dunlop MW, et al. Transport of Solar Wind into Earth's Magnetosphere through Rolled-Up Kelvin-Helmholtz Vortices. *Nature* (2004) 430:755–8. doi:10.1038/nature02799
6. Kavosi S, Raeder J. Ubiquity of Kelvin-Helmholtz Waves at Earth's Magnetopause. *Nat Commun* (2015) 6. doi:10.1038/ncomms8019
7. Yu Y, Ridley AJ. Exploring the Influence of Ionospheric O+ Outflow on Magnetospheric Dynamics: The Effect of Outflow Intensity. *J Geophys Res Space Phys* (2013) 118:5522–31. doi:10.1002/jgra.50528
8. Henry ZW, Nykyri K, Moore TW, Dimmock AP, Ma X. On the Dawn-Dusk Asymmetry of the Kelvin-Helmholtz Instability between 2007 and 2013. *J Geophys Res Space Phys* (2017) 122:888–11. doi:10.1002/2017JA024548
9. Hasegawa A, Chen L. Theory of Magnetic Pulsations. *Space Sci Rev* (1974) 16: 347–59. doi:10.1007/bf00171563
10. Nykyri K, Dimmock AP. Statistical Study of the ULF Pc4-Pc5 Range Fluctuations in the Vicinity of Earth's Magnetopause and Correlation with the Low Latitude Boundary Layer Thickness. *Adv Space Res* (2016) 58:257–67. doi:10.1016/j.asr.2015.12.046
11. Wing S, Johnson JR, Newell PT, Meng C-I. Dawn-dusk Asymmetries, Ion Spectra, and Sources in the Northward Interplanetary Magnetic Field Plasma Sheet. *J Geophys Res* (2005) 110. doi:10.1029/2005JA011086
12. Moore TW, Nykyri K, Dimmock AP. Ion-Scale Wave Properties and Enhanced Ion Heating across the Low-Latitude Boundary Layer during Kelvin-Helmholtz Instability. *J Geophys Res Space Phys* (2017) 122: 11128–11153. doi:10.1002/2017JA024591
13. Dimmock AP, Nykyri K. The Statistical Mapping of Magnetosheath Plasma Properties Based on THEMIS Measurements in the Magnetosheath Interplanetary Medium Reference Frame. *J Geophys Res Space Phys* (2013) 118:4963–76. doi:10.1002/jgra.50465
14. Lotko W, Streltsov AV, Carlson CW. Discrete Auroral Arc, Electrostatic Shock and Suprathermal Electrons Powered by Dispersive, Anomalously Resistive Field Line Resonance. *Geophys Res Lett* (1998) 25:4449–52. doi:10.1029/1998gl900200
15. Elkington SR, Hudson MK, Chan AA. Resonant Acceleration and Diffusion of Outer Zone Electrons in an Asymmetric Geomagnetic Field. *J Geophys Res* (2003) 108. doi:10.1029/2001JA009202
16. Kronberg EA, Grigorenko EE, Turner DL, Daly PW, Khotyaintsev Y, Kozak L. Comparing and Contrasting Dispersionless Injections at Geosynchronous Orbit during a Substorm Event. *J Geophys Res Space Phys* (2017) 122: 3055–72. doi:10.1002/2016JA023551
17. Hasegawa H. Structure and Dynamics of the Magnetopause and its Boundary Layers. *Monogr Environ Earth Planets* (2012) 1:71–119. doi:10.5047/meep.2012.00102.0071
18. Bentley SN, Watt CEJ, Owens MJ, Rae IJ. ULF Wave Activity in the Magnetosphere: Resolving Solar Wind Interdependencies to Identify Driving Mechanisms. *J Geophys Res Space Phys* (2018) 123:2745–71. doi:10.1002/2017JA024740
19. Rae IJ, Donovan EF, Mann IR, Fenrich FR, Watt CEJ, Milling DK, et al. Evolution and Characteristics of Global Pc5 ULF Waves during a High Solar Wind Speed Interval. *J Geophys Res* (2005) 110. doi:10.1029/2005JA011007
20. Agapitov O, Glassmeier K-H, Plaschke F, Auster H-U, Constantinescu D, Angelopoulos V, et al. Surface Waves and Field Line Resonances: A Themis Case Study. *J Geophys Res* (2009) 114:a–n. doi:10.1029/2008JA013553
21. Walker ADM. The Kelvin-Helmholtz Instability in the Low-Latitude Boundary Layer. *Planet Space Sci* (1981) 29:1119–33. doi:10.1016/0032-0633(81)90011-8
22. Dougal ER, Nykyri K, Moore TW. Mapping of the Quasi-Periodic Oscillations at the Flank Magnetopause into the Ionosphere. *Ann Geophys* (2013) 31: 1993–2011. doi:10.5194/angeo-31-1993-2013
23. Wang CP, Thorne R, Liu TZ, Hartinger MD, Nagai T, Angelopoulos V, et al. A Multispacecraft Event Study of Pc5 Ultralow-frequency Waves in the Magnetosphere and Their External Drivers. *J Geophys Res Space Phys* (2017) 122:5132–47. doi:10.1002/2016JA023610
24. Ma X, Otto A, Delamere PA. Interaction of Magnetic Reconnection and Kelvin-Helmholtz Modes for Large Magnetic Shear: 1. Kelvin-Helmholtz Trigger. *J Geophys Res Space Phys* (2014) 119:781–97. doi:10.1002/2013JA019224
25. Ma X, Otto A, Delamere PA. Interaction of Magnetic Reconnection and Kelvin-Helmholtz Modes for Large Magnetic Shear: 2. Reconnection Trigger. *J Geophys Res Space Phys* (2014) 119:808–20. doi:10.1002/2013JA019225
26. Kronberg EA, Gastaldello F, Haaland S, Smirnov A, Berrendorf M, Ghizzardi S, et al. Prediction and Understanding of Soft-Proton Contamination in XMM-Newton: A Machine Learning Approach. *ApJ* (2020) 903:89. doi:10.3847/1538-4357/abbb8f
27. Laakso H, Perry C, McCaffrey S, Herment D, Allen AJ, Harvey CC, et al. Cluster Active Archive: Overview. *Cluster Active Archive: Overview*. (2010). p. 3–37. doi:10.1007/978-90-481-3499-1_1
28. Rème H, Aoustin C, Bosqued JM, Dandouras I, Sauvaud JA, Barthe A, et al. First Multispacecraft Ion Measurements in and Near the Earth' S Magnetosphere with the Identical Cluster Ion Spectrometry (CIS) experiment. *Ann Geophysicae* (2001) 19:1303–54. doi:10.5194/angeo-19-1303-2001
29. Balogh A, Carr CM, Acuña MH, Dunlop MW, Beek TJ, Brown P, et al. The Cluster Magnetic Field Investigation: Overview of In-Flight Performance and Initial Results. *Ann Geophys* (2001) 19:1207–17. doi:10.5194/angeo-19-1207-2001
30. Escoubet CP, Schmidt R, Goldstein ML. Cluster—Science and mission Overview. *Space Sci Rev* (1997) 79:11–32. doi:10.1023/a:1004923124586
31. Siscoe GL, Davis L, Coleman PJ, Jones DE, Jones DE. Power Spectra and Discontinuities of the Interplanetary Magnetic Field: Mariner 4. *J Geophys Res* (1968) 73:61–82. doi:10.1029/JA073i001p00061
32. Dunlop MW, Woodward TI, Farrugia CJ. Minimum Variance Analysis: Cluster Themes. In: KH Glassmeier, U Motschmann, R Schmidt, editors. *Proceedings of the Cluster Workshops, Data Analysis Tools and Physical Measurements and Mission-Oriented Theory*, 371. Paris: ESA Special Publication (1995). p. 33.
33. Yan GQ, Mozer FS, Shen C, Chen T, Parks GK, Cai CL, et al. Kelvin-Helmholtz Vortices Observed by THEMIS at the Duskside of the Magnetopause under Southward Interplanetary Magnetic Field. *Geophys Res Lett* (2014) 41: 4427–34. doi:10.1002/2014GL060589
34. Miura A. Self-Organization in the Two-Dimensional Kelvin-Helmholtz Instability. *Phys Rev Lett* (1999) 83:1586–9. doi:10.1103/PhysRevLett.83.1586
35. Sonnerup BUÖ, Paschmann G, Phan T-D *Fluid Aspects of Reconnection at the Magnetopause*: In Situ *Observations*, 90. Washington DC. American Geophysical Union Geophysical Monograph Series (1995). p. 167–80. doi:10.1029/GM090p0167
36. Hasegawa H, Fujimoto M, Takagi K, Saito Y, Mukai T, Rème H. Single-spacecraft Detection of Rolled-Up Kelvin-Helmholtz Vortices at the Flank Magnetopause. *J Geophys Res* (2006) 111. doi:10.1029/2006JA011728
37. Taylor MGGT, Hasegawa H, Lavraud B, Phan T, Escoubet CP, Dunlop MW, et al. Spatial Distribution of Rolled up Kelvin-Helmholtz Vortices at Earth's Dayside and Flank Magnetopause. *Ann Geophys* (2012) 30:1025–35. doi:10.5194/angeo-30-1025-2012
38. Johnson JR, Wing S. Northward Interplanetary Magnetic Field Plasma Sheet Entropies. *J Geophys Res* (2009) 114:a–n. doi:10.1029/2008JA014017

39. Jacobs JA, Kato Y, Matsushita S, Troitskaya VA. Classification of Geomagnetic Micropulsations. *J Geophys Res* (1964) 69:180–1. doi:10.1029/JZ069i001p00180
40. Paschmann G, Haaland S, Sonnerup BUÖ, Hasegawa H, Georgescu E, Klecker B, et al. Characteristics of the Near-Tail Dawn Magnetopause and Boundary Layer. *Ann Geophys* (2005) 23:1481–97. doi:10.5194/angeo-23-1481-2005
41. Nykyri K, Otto A, Lavraud B, Mouikis C, Kistler LM, Balogh A, et al. Cluster Observations of Reconnection Due to the Kelvin-Helmholtz Instability at the Dawnside Magnetospheric Flank. *Ann Geophys* (2006) 24:2619–43. doi:10.5194/angeo-24-2619-2006
42. Torbert RB, Burch JL, Phan TD, Hesse M, Argall MR, Shuster J, et al. Electron-scale Dynamics of the Diffusion Region during Symmetric Magnetic Reconnection in Space. *Science* (2018) 362:1391–5. doi:10.1126/science.aat2998
43. Gjerloev JW. The SuperMAG Data Processing Technique. *J Geophys Res* (2012) 117:a–n. doi:10.1029/2012JA017683
44. Tsyganenko NA. A Magnetospheric Magnetic Field Model with a Warped Tail Current Sheet. *Planet Space Sci* (1989) 37:5–20. doi:10.1016/0032-0633(89)90066-4
45. Boscher D, Bourdarie S, O'Brien P, Guild T. Irbem-lib Library. (2012). Availableat: https://github.com/PRBEM (Accessed June 1, 2021).
46. Shumko M, Sample J, Johnson A, Blake B, Crew A, Spence H, et al. Microburst Scale Size Derived from Multiple Bounces of a Microburst Simultaneously Observed with the FIREBIRD-II CubeSats. *Geophys Res Lett* (2018) 45:8811–8. doi:10.1029/2018GL078925
47. Dunlop MW, Yang JY, Yang YY, Xiong C, Lühr H, Bogdanova YV, et al. Simultaneous Field-aligned Currents at Swarm and Cluster Satellites. *Geophys Res Lett* (2015) 42:3683–91. doi:10.1002/2015GL063738
48. Tsyganenko NA, Stern DP. Modeling the Global Magnetic Field of the Large-Scale Birkeland Current Systems. *J Geophys Res* (1996) 101:27187–98. doi:10.1029/96JA02735
49. Trattner KJ, Mulcock JS, Petrinec SM, Fuselier SA. Probing the Boundary between Anti-parallel and Component Reconnection during Southwards Interplanetary Magnetic Field Conditions. *J Geophys Res* (2007) 112. doi:10.1029/2007ja012270
50. Trattner KJ, Burch JL, Ergun R, Eriksson S, Fuselier SA, Giles BL, et al. The MMS Dayside Magnetic Reconnection Locations during Phase 1 and Their Relation to the Predictions of the Maximum Magnetic Shear Model. *J Geophys Res Space Phys* (2017) 122:991–12. doi:10.1002/2017JA024488
51. Hughes WJ, Southwood DJ. The Screening of Micropulsation Signals by the Atmosphere and Ionosphere. *J Geophys Res* (1976) 81:3234–40. doi:10.1029/JA081i019p03234
52. Sciffer MD, Waters CL. Propagation of ULF Waves through the Ionosphere: Analytic Solutions for Oblique Magnetic fields. *J Geophys Res* (2002) 107:1297. doi:10.1029/2001JA000184
53. Paschmann G, Haaland S, Treumann R. Auroral Plasma Physics. *Space Sci Rev* (2002) 103. doi:10.1023/A:1023030716698
54. Lyon JG, Fedder JA, Mobarry CM. The Lyon-Fedder-Mobarry (LFM) Global MHD Magnetospheric Simulation Code. *J Atmos Solar-Terrestrial Phys* (2004) 66. doi:10.1016/j.jastp.2004.03.020
55. Merkin VG, Lyon JG. Effects of the Low-Latitude Ionospheric Boundary Condition on the Global Magnetosphere. *J Geophys Res* (2010) 115:a–n. doi:10.1029/2010JA015461
56. Merkin VG, Lyon JG, Claudepierre SG. Kelvin-Helmholtz Instability of the Magnetospheric Boundary in a Three-Dimensional Global MHD Simulation during Northward IMF Conditions. *J Geophys Res Space Phys* (2013) 118:5478–96. doi:10.1002/jgra.50520
57. Sorathia KA, Merkin VG, Ukhorskiy AY, Allen RC, Nykyri K, Wing S. Solar Wind Ion Entry into the Magnetosphere during Northward IMF. *J Geophys Res Space Phys* (2019) 124:5461–81. doi:10.1029/2019JA026728
58. King JH, Papitashvili NE. Solar Wind Spatial Scales in and Comparisons of Hourly Wind and ACE Plasma and Magnetic Field Data. *J Geophys Res* (2005) 110. doi:10.1029/2004JA010649
59. Nykyri K. Impact of MHD Shock Physics on Magnetosheath Asymmetry and Kelvin-Helmholtz Instability. *J Geophys Res Space Phys* (2013) 118:5068–81. doi:10.1002/jgra.50499
60. Nykyri K, Ma X, Dimmock A, Foullon C, Otto A, Osmane A. Influence of Velocity Fluctuations on the Kelvin-Helmholtz Instability and its Associated Mass Transport. *J Geophys Res Space Phys* (2017) 122:9489–512. doi:10.1002/2017JA024374
61. Moore TW, Nykyri K, Dimmock AP. Cross-scale Energy Transport in Space Plasmas. *Nat Phys* (2016) 12:1164–9. doi:10.1038/NPHYS3869
62. Adamson E, Nykyri K, Otto A. The Kelvin-Helmholtz Instability under Parker-spiral Interplanetary Magnetic Field Conditions at the Magnetospheric Flanks. *Adv Space Res* (2016) 58:218–30. doi:10.1016/j.asr.2015.09.013
63. Nakamura TKM, Fujimoto M, Otto A. Magnetic Reconnection Induced by Weak Kelvin-Helmholtz Instability and the Formation of the Low-Latitude Boundary Layer. *Geophys Res Lett* (2006) 33:L14106. doi:10.1029/2006GL026318
64. Otto A. Mass Transport at the Magnetospheric Flanks Associated with Three-Dimensional Kelvin- Helmholtz Modes. *AGU Fall Meeting Abstracts*, 2006 (2006). p. SM33B–0365.
65. Faganello M, Califano F, Pegoraro F, Andreussi T. Double Mid-latitude Dynamical Reconnection at the Magnetopause: An Efficient Mechanism Allowing Solar Wind to Enter the Earth's Magnetosphere. *Epl* (2012) 100:69001. doi:10.1209/0295-5075/100/69001
66. Ma X, Delamere P, Otto A, Burkholder B. Plasma Transport Driven by the Three-Dimensional Kelvin-Helmholtz Instability. *J Geophys Res Space Phys* (2017) 122:10382. doi:10.1002/2017JA024394
67. Hwang K-J, Kuznetsova MM, Sahraoui F, Goldstein ML, Lee E, Parks GK. Kelvin-Helmholtz Waves under Southward Interplanetary Magnetic Field. *J Geophys Res* (2011) 116:a–n. doi:10.1029/2011JA016596
68. Nykyri K, Ma X, Burkholder B, Rice R, Johnson JR, Kim EK, et al. MMS Observations of the Multiscale Wave Structures and Parallel Electron Heating in the Vicinity of the Southern Exterior Cusp. *J Geophys Res Space Phys* (2021) 126:e27698. doi:10.1029/2019JA027698
69. Hwang K-J, Sibeck DG. *Role of Low-Frequency Boundary Waves in the Dynamics of the Dayside Magnetopause and the Inner Magnetosphere*. Hoboken, NJ: John Wiley (2016). p. 213–39. doi:10.1002/9781119055006.ch13
70. Hartinger MD, Plaschke F, Archer MO, Welling DT, Moldwin MB, Ridley A. The Global Structure and Time Evolution of Dayside Magnetopause Surface Eigenmodes. *Geophys Res Lett* (2015) 42:2594–602. doi:10.1002/2015GL063623
71. Hietala H, Phan TD, Angelopoulos V, Oieroset M, Archer MO, Karlsson T, Karlsson T, et al. *In Situ* Observations of a Magnetosheath High-Speed Jet Triggering Magnetopause Reconnection. *Geophys Res Lett* (2018) 45:1732–40. doi:10.1002/2017GL076525
72. Nykyri K, Bengtson M, Angelopoulos V, Nishimura Y, Wing S. Can Enhanced Flux Loading by High-Speed Jets Lead to a Substorm? Multipoint Detection of the Christmas Day Substorm Onset at 08:17 UT, 2015. *J Geophys Res Space Phys* (2019) 124:4314–40. doi:10.1029/2018JA026357
73. Wang C-P, Lyons LR, Angelopoulos V. Properties of Low-Latitude Mantle Plasma in the Earth's Magnetotail: ARTEMIS Observations and Global MHD Predictions. *J Geophys Res Space Phys* (2014) 119:7264–80. doi:10.1002/2014JA020060
74. Kronberg EA, Grigorenko EE, Haaland SE, Daly PW, Delcourt DC, Luo H, et al. Distribution of Energetic Oxygen and Hydrogen in the near-Earth Plasma Sheet. *J Geophys Res Space Phys* (2015) 120:3415–31. doi:10.1002/2014JA020882

Conflict of Interest: The authors declare that the research was conducted in the absence of any commercial or financial relationships that could be construed as a potential conflict of interest.

frontiers in Astronomy and Space Sciences

ORIGINAL RESEARCH
published: 09 December 2021
doi: 10.3389/fspas.2021.740560

Secondary Magnetic Reconnection at Earth's Flank Magnetopause

B. B. Tang[1], W. Y. Li[1]*, C. Wang[1,2], Yu. V. Khotyaintsev[3], D. B. Graham[3], Q. H. Zhang[4], T. R. Sun[1], H. Li[1], X. Y. Wang[4], K. J. Trattner[5], B. L. Giles[6], P. A. Lindqvist[7], R. E. Ergun[5] and J. L. Burch[8]*

[1]State Key Laboratory of Space Weather, National Space Science Center, Chinese Academy of Sciences, Beijing, China, [2]College of Earth and Planetary Sciences, University of Chinese Academy of Sciences, Beijing, China, [3]Swedish Institute of Space Physics, Uppsala, Sweden, [4]Shandong Provincial Key Laboratory of Optical Astronomy and Solar-Terrestrial Environment, Institute of Space Sciences, Shandong University, Weihai, China, [5]Laboratory of Atmospheric and Space Physics, University of Colorado Boulder, Boulder, CO, United States, [6]NASA Goddard Space Flight Center, Greenbelt, MD, United States, [7]KTH Royal Institute of Technology, Stockholm, Sweden, [8]Southwest Research Institute, San Antonio, TX, United States

OPEN ACCESS

Edited by:
Takuma Nakamura, Austrian Academy of Sciences (OeAW), Austria

Reviewed by:
Rungployphan Om Kieokaew, UMR5277 Institut de recherche en astrophysique et planétologie (IRAP), France
Tieyan Wang, Rutherford Appleton Laboratory, United Kingdom

***Correspondence:**
B. B. Tang
bbtang@spaceweather.ac.cn
W. Y. Li
wyli@spaceweather.ac.cn

Specialty section:
This article was submitted to Space Physics, a section of the journal Frontiers in Astronomy and Space Sciences

Received: *13 July 2021*
Accepted: *27 September 2021*
Published: *09 December 2021*

Citation:
Tang BB, Li WY, Wang C, Khotyaintsev YV, Graham DB, Zhang QH, Sun TR, Li H, Wang XY, Trattner KJ, Giles BL, Lindqvist PA, Ergun RE and Burch J (2021) Secondary Magnetic Reconnection at Earth's Flank Magnetopause. Front. Astron. Space Sci. 8:740560. doi: 10.3389/fspas.2021.740560

We report local secondary magnetic reconnection at Earth's flank magnetopause by using the Magnetospheric Multiscale observations. This reconnection is found at the magnetopause boundary with a large magnetic shear between closed magnetospheric field lines and the open field lines generated by the primary magnetopause reconnection at large scales. Evidence of this secondary reconnection are presented, which include a secondary ion jet and the encounter of the electron diffusion region. Thus the observed secondary reconnection indicates a cross-scale process from a global scale to an electron scale. As the aurora brightening is also observed at the morning ionosphere, the present secondary reconnection suggests a new pathway for the entry of the solar wind into geospace, providing an important modification to the classic Dungey cycle.

Keywords: magnetic reconnection, electron diffusion region, magnetopause, solar wind-magnetosphere coupling, solar wind entry

1 INTRODUCTION

The Earth's global magnetospheric plasma circulation, which is driven by the interaction between the magnetized solar wind and the magnetosphere, is known as the Dungey cycle (Dungey, 1961). When the interplanetary magnetic field (IMF) is southward, this cycle begins at the dayside magnetopause where magnetic reconnection opens previously closed magnetospheric magnetic lines. These open magnetic field lines are dragged anti-sunward by the solar wind flows to the magnetotail, where the nightside reconnection eventually re-closes the open field lines. The newly closed magnetic flux returns to the dayside where the cycle repeats (**Figure 1A**). Considering the modulation of the solar wind and the interplanetary magnetic field to this cycle (Cowley, 1973; Borovsky, 2008), the imbalance of the dayside and nightside magnetic reconnection (Milan et al., 2007), and the patchy/transient nature of reconnection (Khotyaintsev et al., 2004; Hasegawa et al., 2010), the Dungey cycle explains various space weather phenomena, such as geomagnetic storms, substorms and aurorae.

Magnetopause reconnection, the primary driver in the Dungey cycle, is locally determined by the magnetic shear, the plasma beta and the flow shear across the magnetopause (e.g., Swisdak et al., 2003; Phan et al., 2013; Doss et al., 2015). Therefore, its location and efficiency at macro scales varies significantly under different the solar wind conditions. In fact, magnetic reconnection is found to be most active when IMF is southward. In this situation, reconnection occurs at the low-latitude magnetopause, spanning from subsolar

magnetopause to the flanks (e.g., Fuselier et al., 2011; Trattner et al., 2012; Vines et al., 2015). Reconnection at the flank magnetopause can be affected by the local plasma shear flow, and thus presents some different features (e.g., Gomez et al., 2016; Haaland et al., 2020). As reconnection can change the toplogy of magnetic field lines and convert energy to plasmas, they act as a major process responsible for the solar wind entry into the magnetosphere, and the consequent global scale magnetospheric convection (Dungey, 1961; Fuselier and Lewis, 2011; Welling et al., 2015). Along with magnetic reconnection, other processes such as the Kelvin–Helmholtz instability at the flank region (Hasegawa et al., 2004) or the kinetic diffusive particle transport (Treumann et al., 1991) can also contribute to the mass and energy transfer across the magnetopause. Recently, magnetic reconnection, triggered by local plasma and magnetic field variations at the magnetopause, are also observed. For example, they are reported at the trailing edges of Kelvin–Helmholtz waves (Eriksson et al., 2016; Li et al., 2016), at the interface of interlinked magnetic flux tubes (Kacem et al., 2018; Øieroset et al., 2019) and at the boundary of two neighboring flux ropes (Wang et al., 2017; Zhou et al., 2017). The local secondary reconnection, which is basically taken as secondary effects of the primary reconnection are also reported (e.g., Daughton et al., 2011; Lapenta et al., 2015). These local reconnection are suggested to transfer plasma across the magnetopause (e.g., Nakamura et al., 2017), but whether they can result into magnetospheric consequences at large scales remains an open issue.

Here, we use observations from the Magnetospheric Multiscale (MMS) mission (Burch et al., 2016) to present local secondary magnetic reconnection at the flank magnetopause, which is identified by a secondary ion jet and the encounter of the electron diffusion region. This newly discovered secondary reconnection re-closes the open magnetic field lines previously generated by magnetopause reconnection, providing a new pathway for the entry of the solar wind into the magnetosphere.

2 OBSERVATIONS

On June 1, 2018, the four MMS spacecraft cross the flank magnetopause for several times approximately at (−15.6, −19.7, 2.2) Earth radii (R_E) in geocentric solar magnetospheric (GSM) coordinates, and the spacecraft are in a tetrahedron formation with ~36 km separation. We use ion and electron data from the fast plasma investigation (Pollock et al., 2016), magnetic field data from the fluxgate magnetometer (Russell et al., 2016), and electric field data from electric field double probes (Ergun et al., 2016; Lindqvist et al., 2016). During these multiple magnetopause crossings, the solar wind conditions are relatively stable (Both IMF B_Y and IMF B_Z are negative, seeing **Supplementary Figure S1**), and MMS do not observe quasi-periodic perturbations of the plasma and magnetic field parameters, suggesting Kelvin–Helmholtz waves are not active during this time interval.

Overview of one inbound magnetopause crossing between 01:01:20 UT and 01:02:55 UT is provided in **Figure 2**. The spacecraft are initially located in the magnetosheath, characterized by a high plasma density (**Figure 2B**) and large anti-sunward flows ($V_{i,x}$) at ~ −400 km s^{-1} (**Figures 2C,F**), corresponding to a typical energy of ~ 1 keV (**Figure 2D**). On the other side, the magnetosphere is characterized by a lower ion density, smaller ion speeds, and the appearance of high energy ions (~ 10 keV). During this magnetopause crossing, MMS observe a reversal of B_z (**Figure 2A**), a large northward ion flow ($V_{i,z}$) reaching ~ 300 km s^{-1} (**Figures 2C,G**), and a mixture of magnetosheath and magnetospheric ions (**Figure 2D**). Such observations indicate ongoing magnetopause reconnection between the shocked solar wind (i.e., magnetosheath plasma) and the magnetospheric plasmas (referred to as the primary reconnection hereafter) and the spacecraft are located northward of the reconnection X-line. These observations are in good agreement with the predictions of the maximum magnetic shear model shown in **Figure 3A** (Trattner et al., 2007, 2021). It presents large magnetic shear at the dawnside flanks, which is favorable for reconnection, and MMS is located at its north side, observing a northward reconnection jet. We also test the Walén relation by comparing two vectors $\Delta \boldsymbol{V_i} = \mathbf{V_i} - \mathbf{V_{i,MSH}}$ and $\Delta \boldsymbol{V_A} = \mathbf{V_A} - \mathbf{V_{A,MSH}}$, where $\mathbf{V_{A,MSH}}$, $\mathbf{V_{i,MSH}}$ are the reference plasma Alfven velocity and bulk velocity in the magnetosheath (Sonnerup et al., 1981). The result shows that the velocity change across the magnetosheath side of the primary reconnection is mostly Alfvenic (**Figure 3B**), indicating this boundary is a rotational discontinuity and open magnetic field lines are generated from reconnection. Moreover, in the reconnection exhaust, we find that the magnetic field has a significant positive B_x component (**Figure 2A**), and plasmas move anti-sunward ($V_{i,x}$ ~ −200 km s^{-1}, **Figure 2C**), indicating that these reconnected open field lines are draped along the magnetopause by the solar wind flows (**Figure 1A**).

It is interesting to note that an unexpected ion population flowing along the anti-sunward direction (**Figure 2H**) appears just seconds before the MMS crossing of the boundary between the primary reconnection exhaust and the magnetosphere, where a large local magnetic shear (~ 145°) is mainly due to the B_x component (**Figure 1A**). Here, we explain this ion population as the outflow of another ongoing reconnection at the boundary with large magnetic shear (referred to as secondary reconnection), since it is almost aligned in the -L direction in a local current sheet (LMN) coordinate [**Figure 4N**, (Russell and Elphic, 1978)], which is determined from minimum variance analysis of the magnetic field (L = [0.97, 0.09, −0.23] is the reconnecting field direction, M = [0.23, −0.61, 0.76] is the out-of-plane direction, and N = [−0.07, −0.77, −0.61] (GSM) is the normal direction). The eigenvalues of LMN vectors are [λ_1: λ_2: λ_3] = [200.3 : 5.5: 2.6]. The relative small ratio of λ_2: λ_3 (~2.1) is related to a local B_N enhancement around 01:02:49.8 UT, and this B_N enhancement can be explained by the magnetic flux pileup associated with the electron flow breaking (Genestreti et al.,

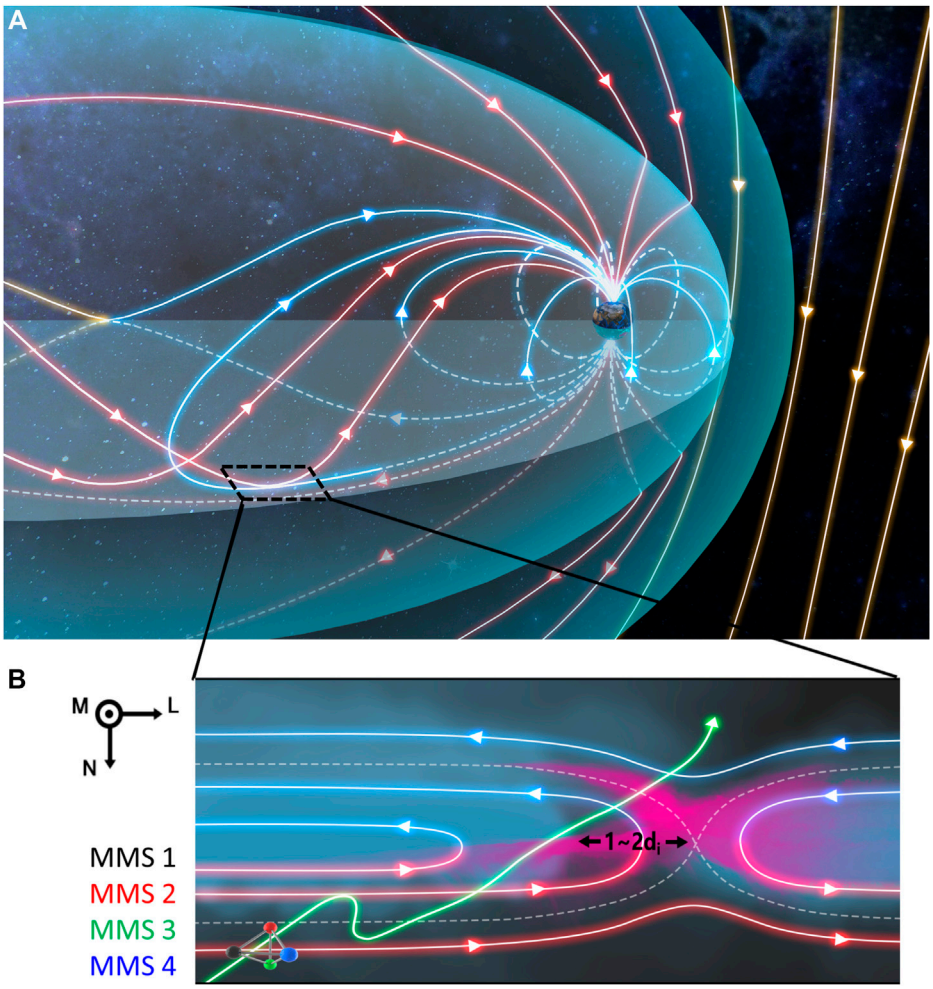

FIGURE 1 | Schematic illustration of the three-dimensional structure of Earth's magnetosphere and the secondary reconnection process at the flank magnetopause. **(A)** View of the magnetosphere, showing the opening of closed magnetospheric field lines through the magnetopause reconnection, and the re-closure of these open field lines by magnetotail reconnection. At the flank magnetopause, the reconnected open field lines can form a large magnetic shear with closed magnetospheric field lines, providing favorable conditions for the reported secondary reconnection. The closed magnetospheric field lines, open field lines and the solar wind field lines are presented in blue, red and yellow, respectively. **(B)** Two-dimensional schematic of the local secondary reconnection. The color of the magnetic field lines show their topology before secondary reconnection, and the magenta contours indicate the out-of-plane current density. The green line presents the MMS trajectory relative to the secondary reconnection, showing a short excursion into the reconnection exhaust and a full crossing anti-sunward of the X-line.

2020). We provide a zoom-in of this boundary with more signatures of the secondary reconnection in **Figure 4**. At the B_L reversal point (approximately 01:02:50.7 UT), MMS one observes a magnetic minimum at ($|\mathbf{B}|\sim$ 1.8 nT, **Figure 4F**), a large perpendicular electron flow in the L direction ($V_{e,L\perp} \sim -800\,\mathrm{km\,s^{-1}}$, **Figure 4H**), and nearly isotropic electron distributions (**Figure 4K**) with $T_{e,\perp} \approx T_{e,\parallel}$ (**Figure 4J**). At the two sides of the B_L reversal point, the electron temperature profile shows clear anisotropy ($T_{e,\perp} < T_{e,\parallel}$, **Figure 4I**), which is consistent with the magnetic field-aligned electrons from the inflow region (**Figure 4K**) (Egedal et al., 2011). These ion and electron signatures agree well with the scenario of reconnection.

We perform a detailed analysis of the observed secondary reconnection, which is embedded in the plasma flow imposed by the primary reconnection. The shear flow is negative in the reconnecting (L) direction and positive in the out-of-plane (M) direction (**Figures 4C,M**). The negative V_L shear flow can lead into the convection of the X-line, and a reduction of the outflow speed in the X-line frame (Doss et al., 2015). The predicted outflow density (ρ_{out}) (Cassak and Shay, 2007), the convection speed of the X-line (V_{drift}) and the outflow speed in the spacecraft frame (V_{out}) (Doss et al., 2015) are written as

$$\rho_{out} \sim \frac{\rho_1 B_2 + \rho_2 B_1}{B_1 + B_2} \quad (1)$$

$$v_{drift} \sim \frac{\rho_1 B_2 V_{L,1} + \rho_2 B_1 V_{L,2}}{\rho_1 B_2 + \rho_2 B_1} \quad (2)$$

$$v_{out} \sim \sqrt{c_{A,asym}^2 - (V_{L,1} - V_{L,2})^2 \frac{\rho_1 B_2 \rho_2 B_1}{(\rho_1 B_2 + \rho_2 B_1)^2}} \pm V_{drift}, \quad (3)$$

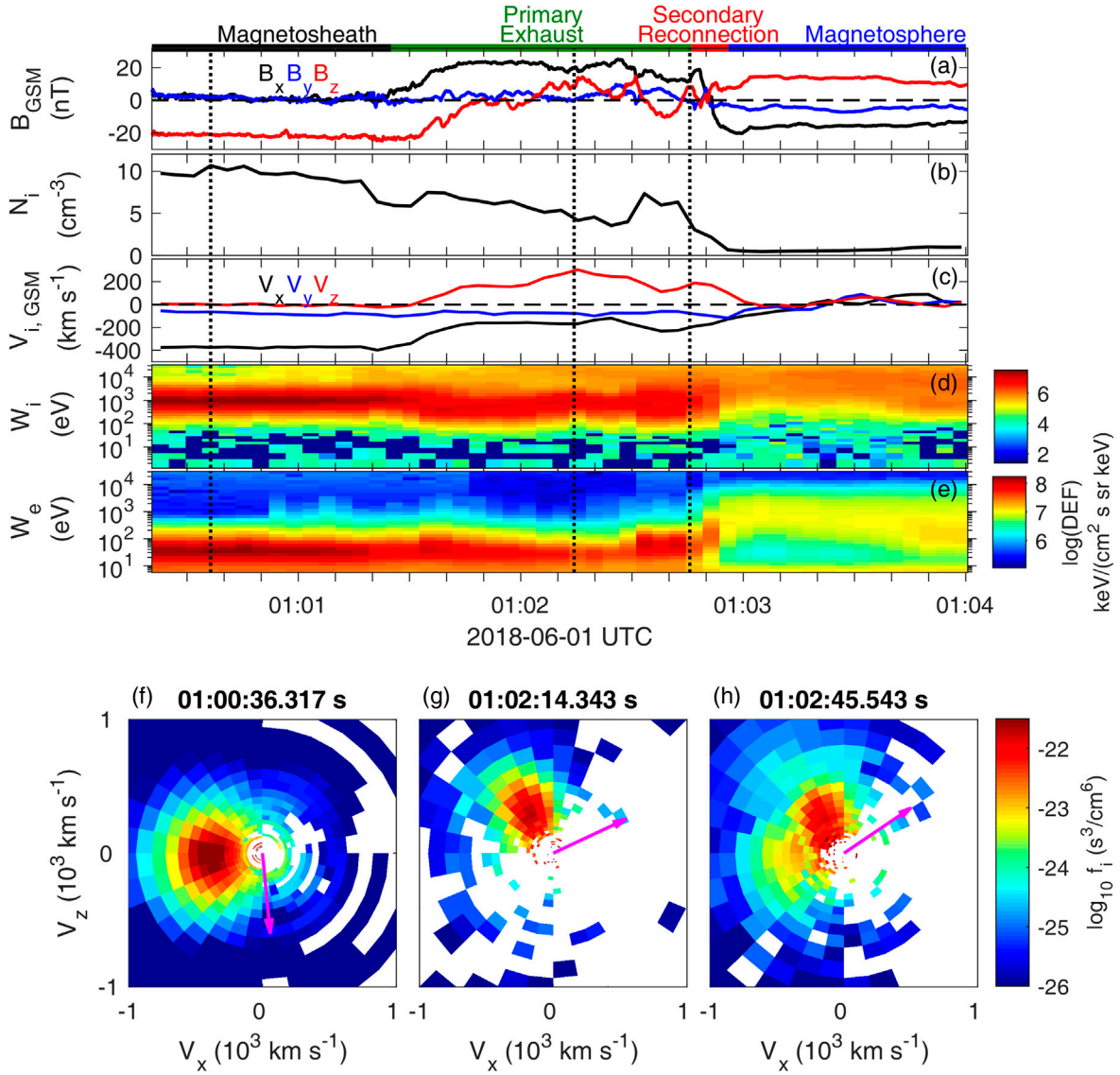

FIGURE 2 | Overview of the flank magnetopause crossing of MMS. MMS one observations of **(A)** Magnetic field (GSM), **(B)** Ion number density, **(C)** Ion bulk velocity (GSM), **(D)** Electron omnidirectional differential energy flux and **(E)** Ion omnidirectional differential energy flux. The color bars indicate the different regions during the magnetopause crossing. **(F–H)** Two dimensional cuts of ion velocity distribution functions in the plane of GSM-X and GSM-Z axis at 01:00:36.317 UT, 01:02:14.343 UT, and 01:02:45.543 UT as indicated by the dotted vertical lines. The overplotted magenta arrows show the projection of the local magnetic field.

where the "1", "2," and "out" subscripts refer to parameters in the primary reconnection exhaust, in the magnetospheric side and in the outflow region, respectively, and $c_{A,asym} = \sqrt{B_1 B_2/\mu_0 \rho_{out}}$ is the outflow speed of the secondary reconnection without a flow shear (Cassak and Shay, 2007). Using the values obtained from observations ($B_1 \sim 18.4$ nT, $\rho_1 \sim 1.48$ cm^{-3}, $V_{L,1} \sim -200$ km s^{-1}; $B_2 \sim 20.0$ nT, $\rho_2 \sim 0.43$ cm^{-3}, $V_{L,2} \sim 0$), we obtain $\rho_{out} \sim 0.98$ cm^{-3}, $V_{drift} \sim -160$ km s^{-1}, and the outflow speed at the anti-sunward side $V_{out} \sim -570$ km s^{-1}. Moreover, the shear flow in the M direction, which is larger than 100 km s^{-1} as shown in **Figure 4C**, can drag the reconnected magnetic field lines out of the reconnecting plane (**Figure 4L**), resulting into the B_M variation, and V_M reduction inside the reconnection exhaust. During the time interval from 01:02:32 UT to 01:02:46 UT, MMS observes negative B_M (**Figure 4A**), decreased V_M, slightly enhanced V_L (**Figure 4C**) and two ion populations (**Figure 4D**). The high energy ion population, which is almost aligned in the -L direction, travels at a speed of ~ 500 km s^{-1} (**Figure 4N**). These observations are consistent with the prediction of reconnection with a flow shear, suggesting a short excursion of MMS into the exhaust of the secondary reconnection. The secondary ion jet decreases its speed in **Figure 4O**, and is not easy to identify around the B_L reversal (**Figure 4P**), which indicates that MMS spacecraft moves closer to the central reconnection diffusion region (**Figure 4L**).

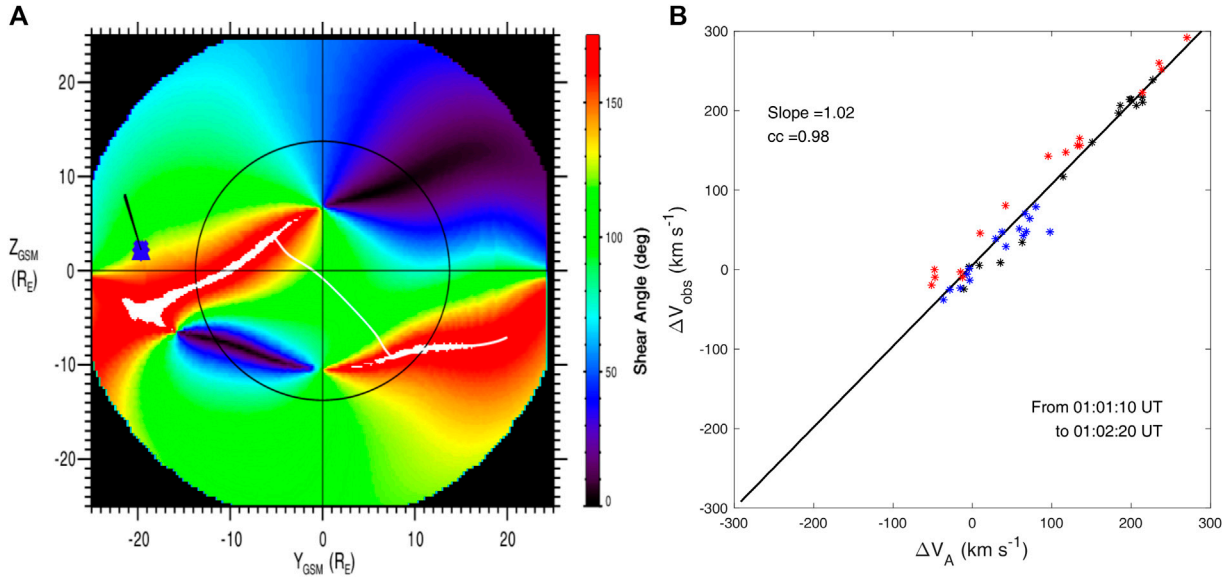

FIGURE 3 | (A) The predicted location of magnetopause reconnection from the maximum magnetic shear model. The color shows magnetic shear angle across the magnetopause. The circle represents the magnetopause shape at the terminator plane and the blue symbol marks the MMS position. **(B)** Wal\'en test for primary magnetic reconnection between 01:01:10 UT and 01:02:20 UT.

The topology of the magnetic field lines can be inferred from the pitch angle spectrum of high-energy magnetospheric electrons (**Figure 4E**), which has been extensively used in previous studies (e.g., Fuselier et al., 2011; Pu et al., 2013; Øieroset et al., 2015). In the primary reconnection exhaust with a northward ion jet, an anti-parallel streaming electron flow inside the primary exhaust suggests an open field line geometry connecting to the northern hemisphere (**Figure 3A**). While inside the magnetosphere, the electron flux is more intense, and mostly isotropic, indicating closed field lines. Therefore, we confirm that the secondary reconnection occurs between closed magnetospheric field lines and the open field lines previously generated by the primary magnetopause reconnection (**Figure 3B**), which is different from the primary magnetopause reconnection, occurring between the shocked solar wind magnetic field lines and the magnetospheric field lines.

Spatial structures of the secondary reconnection at the scale of MMS separations near the B_L reversal are further investigated (**Figure 5**). The reduced/enhanced B_M variations (**Figure 5C**), indicating a Hall pattern of reconnection (Øieroset et al., 2001) with a guide-field of ~ 5 nT, are consistent with the anti-sunward crossing of the X-line. During this crossing, the minimum magnetic field (|**B**|) at MMS two is obviously larger than that at other spacecraft (**Figure 5A**). Therefore, even though the "nominal" magnetic curvature radius (R_C) is comparable with the electron gyro-radius (ρ_e, $\kappa^2 = R_C/\rho_e$, **Figure 5G**) at the time interval of |**B**|, the expected electron pitch angle mixing due to the magnetic curvature scattering (Lavraud et al., 2016; Tang et al., 2019) is only found at MMS 1, 3 and 4, but not at MMS 2 (**Figure 5I1–I4**). The out-of-plane current density (J_M, **Figure 5F**) at MMS 1–MMS 4 are also different. In general, there are two main J_M peaks; one is at the centre of the B_L reversal and the other is near the magnetospheric side. The magnitude of the current density at these two current sheets observed at MMS two is about 200 nA m^{-2}, which is significantly weaker than that observed by other spacecraft. All these differences suggest dramatic changes of the electron dynamics at MMS separation scales, which can be explained by the spatial evolution of the reconnection structure along the outflow direction. MMS 2 then is the furthermost spacecraft in the outflow region (**Figure 1B**). The peak-to-peak separation of the two current sheets is approximately 0.8 s, corresponding to ~ 65 km or 0.33d_i (the ion inertial length $d_i \approx 200$ km). Note that the spatial separation is estimated using the magnetopause speed of 80 km s^{-1} along its normal direction estimated from the multi-spacecraft timing analysis of B_L. Such two strong current sheets are also found in the kinetic particle simulation with similar guide field strength and density asymmetry [see (Figure 3–7 of Montag, 2018)]. In his simulation, the two current sheets, with a separation less than 1d_i along the normal direction, extend from the X-line only up to several ion inertial lengths. These results, as well as the electron flow that is faster than predicted outflow speed (**Figure 4H**), demonstrate that MMS may cross in the vicinity of the electron diffusion region.

Agyrotropic electron distributions, which are an important indicator of the electron diffusion region (Burch et al., 2016; Webster et al., 2018), are also found during the secondary magnetic reconnection crossing, and measure of electron agyrotropy, $\sqrt{Q}$ (Swisdak, 2016) in **Figure 5G** presents several peaks. On the magnetosheath side, electrons with energies from

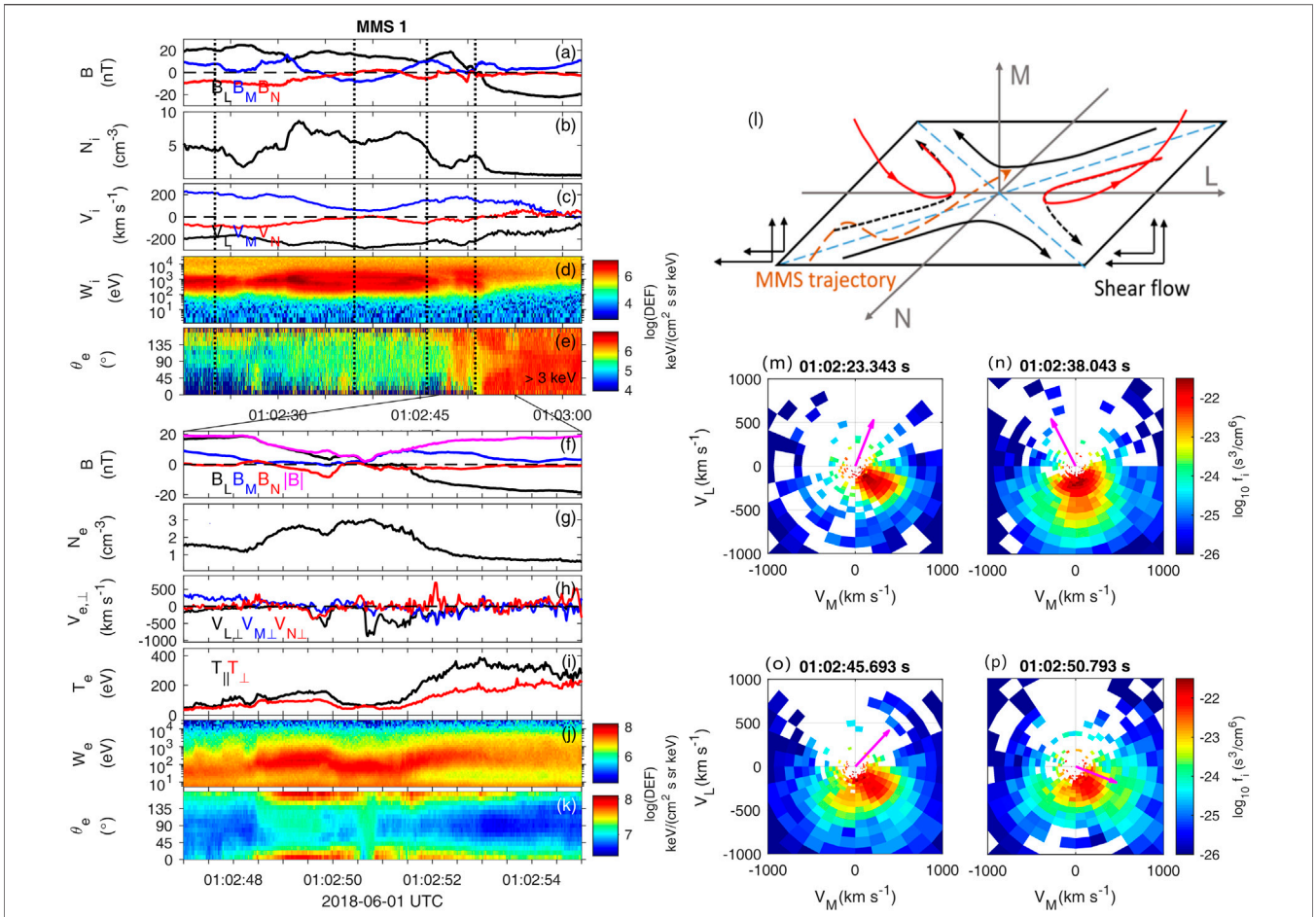

FIGURE 4 | Observations of secondary reconnection from MMS 1. MMS one observations of **(A)** Magnetic field (LMN), **(B)** Ion number density, **(C)** Ion bulk velocity (LMN), **(D)** Ion omnidirectional differential energy flux and **(E)** Electron pitch angle spectrum of energy larger than 3 keV. Zoom-in of the time interval at B_L reversal: **(F)** Magnetic field (LMN), **(G)** Electron number density, **(H)** Electron bulk velocity (LMN), **(I)** Electron temperature, **(J)** Electron omnidirectional differential energy flux, and **(K)** Electron pitch angle spectrum of all energies. The panels on the right show: **(L)** A schematic of MMS crossing of the secondary reconnection with a shear flow. The red reconnected field lines are dragged out of the reconnecting L-N plane due to the shear flow in M direction and the dashed brown line shows the MMS trajectory relative to the reconnection X-line **(M–P)** Two dimensional cuts of ion velocity distribution functions in the $\mathbf{v_L} - \mathbf{v_M}$ plane at times indicated by the black vertical lines in left panels. The projected local magnetic fields are shown by the magenta arrows.

approximately 150–300 eV are observed to be almost isotropic around 01:02:49.5 UT (**Figure 5**, panels (H1)–(H4)), and at its edge, agyrotropic crescent electron distributions in the plane perpendicular to the local magnetic field are found due to the finite gyro-radius effect (**Figure 5K**). The energy of these agyrotropic electrons is larger than that of typical sheath electrons (**Figure 2E**), which are energized sheath electrons and/or the electrons originated from the magnetosphere. At the boundary of the $|\mathbf{B}|_{\min}$ region, the gyration of the electrons after the magnetic curvature scattering forms crescent electron distributions as well (**Figure 5L**), and the energy of these electrons are similar to sheath electrons. Finally, agyrotropic electron distributions are found on the magnetospheric side (**Figure 5M**), where a density gradient is present. These observed agyrotropic electron distributions not only support the encounter of the electron diffusion region vicinity, but also indicate characteristic reconnection features with weak density and magnetic field asymmetry (**Figures 4F,G**).

The secondary reconnection re-closes the open magnetic field lines in the primary exhaust by reconnecting with closed magnetospheric field lines. The newly closed field lines can transport plasma in the solar wind into magnetosphere, which could populate the plasma sheet (e.g., Allen et al., 2017) and even precipitate in to the ionosphere. In this study, we present auroral observations in the northern hemisphere from Defense Meteorological Satellite Program (DMSP)/F18 satellite, and find some bright aurora in the morning sector (**Figures 6**) as observed by the on board Special Sensor Ultraviolet Spectrographic Imager (SSUSI) (Paxton et al., 2002). The magnetic footprint of MMS, marked by a white circle, is also located at one end of the bright auroral arc/streamer. The magnetic field used for the MMS footprint tracing includes an internal IGRF model (Thébault et al., 2015) and an external Tsyganenko-96 model (Tsyganenko, 1995). Unfortunately, the DMSP/F18 satellite does not fly over the bright aurora region (**Figures 6A**), which prevents direct observations of the particle

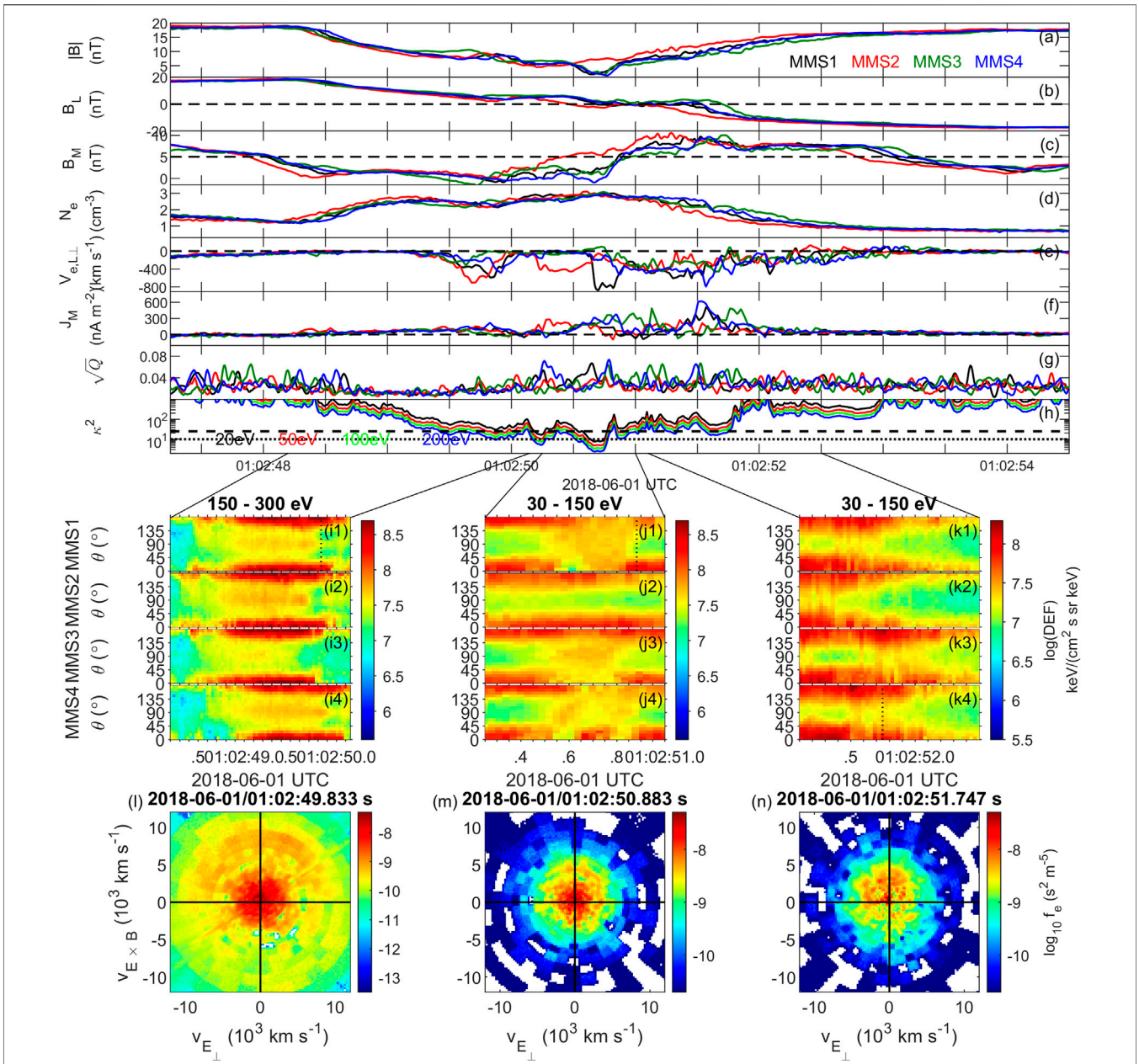

FIGURE 5 | Four MMS observations of the secondary magnetic reconnection. **(A)** |**B**|, **(B)** B_L, **(C)** B_M, **(D)** N_e, **(E)** $V_{e,L\perp}$, **(F)** J_M, **(G)** the agyrotropic measure $\sqrt{Q}$, **(H)** κ^2, defined by the ratio of magnetic curvature radius and the electron gyro-radius, **(I1–I4)**, **(J1–J4)** and **(K1–K4)** electron pitch angle spectrum at the magnetosheath side, the central current sheet and the magnetospheric side, **(L–N)** reduced electron distributions in the $\mathbf{v}_{\mathbf{E}\times\mathbf{B}} - \mathbf{v}_{\mathbf{E}_\perp}$ plane at 01:02:49.833 UT, 01:02:50.883 UT and 01:02:51.747 UT, respectively.

precipitation at the bright auroral emissions. Meanwhile, the dayside auroral intensity is much weaker (**Figures 6A**), and the related precipitating ions and electrons observed along the satellite track are possibly the solar wind origin, as inferred from their typical energies (**Figures 6B**). This indicates that the usual magnetopause reconnection cannot well explain the bright aurora in the morning ionosphere, and we suggest the secondary reconnection, which generates earthward propagating plasma flows in the magnetosphere, can be closely related to the bright aurora in the morning ionosphere. This relation is similar to that between the auroral streamer at the nightside ionosphere and the flow bursts in the magnetotail (Nakamura et al., 2001; Sergeev et al., 2004). Therefore the secondary reconnection reported in this study serves to transfer the mass and energy in the solar wind into geospace. Finally, it is addressed that the scanning of the bright aurora at the morning ionosphere is ~ 10 min prior to the flank magnetopause crossing of MMS, which could bring some errors to the relative locations between the footprint of MMS and aurora. Considering the solar wind is relatively stable during this period (**Supplementary Figure S1**),

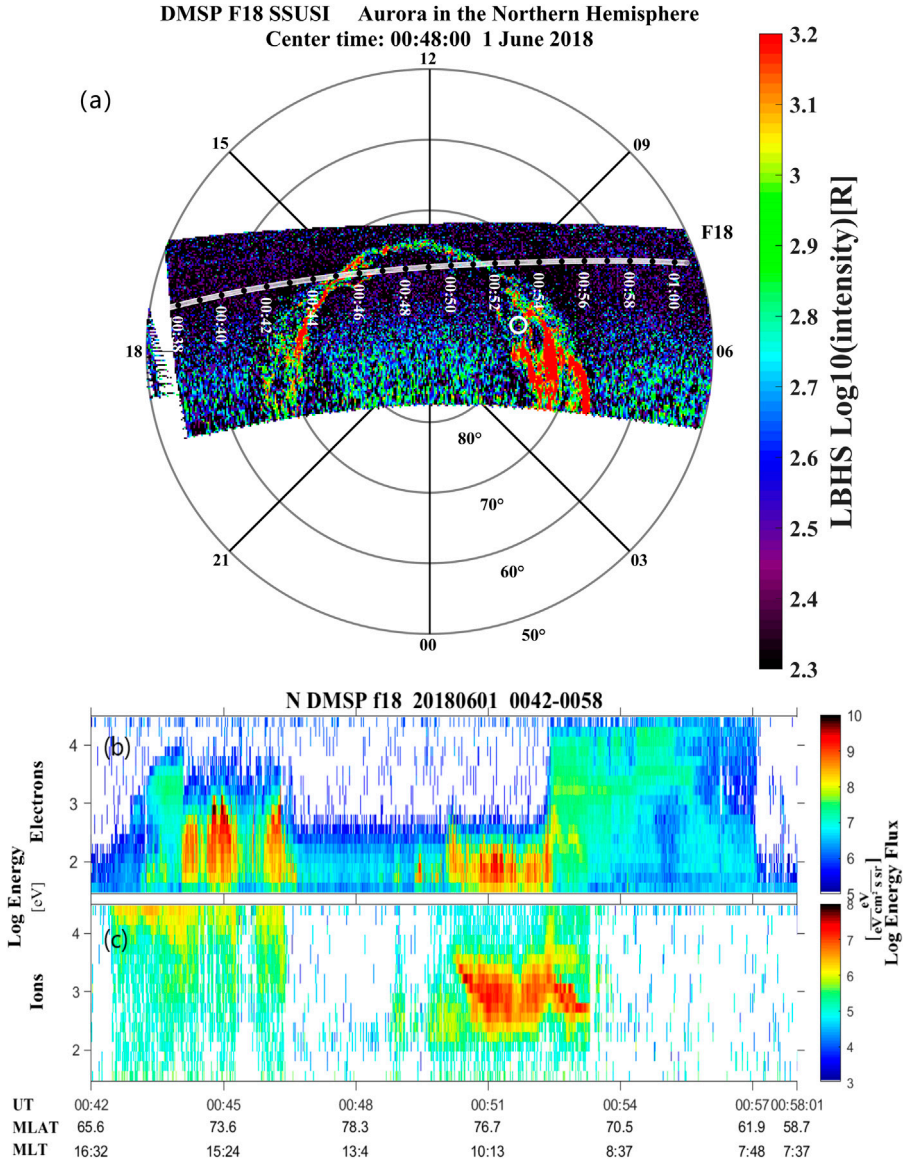

FIGURE 6 | Aurora and *in situ* plasma observations in the northern hemisphere from DMSP/F18 satellite. **(A)** Aurora in the Lyman-Birge-Hopfield band (LBHS) from the SSUSI instrument in the northern hemisphere on June 1, 2018. The data are shown in the geomagnetic coordinate with noon at the top of the panel. The white circle marks the magnetic footprint of MMS (MLT: 7.1 h and MLat: 76.8°) and the white dotted line shows the satellite track. **(B, C)** *in situ* electron and ion energy spectrum from the special sensor for precipitating particles (SSJ5) instrument.

this uncertainty for the MMS footprint is about 2° in latitude and 1 h in longitude according to the drift speed of the secondary X-line estimated above, which thus has not been taken into account here. Based on this point, more observational assessment should be performed in the future investigations.

3 DISCUSSION AND SUMMARY

In this study, we have presented newly revealed secondary magnetic reconnection at Earth's flank magnetopause from MMS observations. The observed secondary ion jet agrees well with predictions of magnetic reconnection with a flow shear, and the electron signatures indicate the encounter of the electron diffusion region. This secondary reconnection re-closes the open field lines generated by the primary magnetopause reconnection, so that it indicates a new pathway for the entry of the solar wind into the magnetosphere. The re-closure of open field lines by the reported secondary reconnection, rather than the nightside magnetotail reconnection, provides an important modification to the classic Dungey cycle.

The concept of secondary reconnection has been widely proposed in previous studies (e.g., Daughton et al., 2011; Lapenta et al., 2015; Fuselier et al., 2017, 2018), but there are some differences existing in these so-called secondary reconnection. For example, secondary reconnection can occur in the exhaust region of the primary

reconnection, behaving as an important feature of 3D magnetic reconnection (Daughton et al., 2011; Lapenta et al., 2015). Both the primary and secondary reconnection can be found between the magnetosheath and magnetospheric filed lines, or the magnetic field lines at two sides of the magnetopause, which can generate flux rope-like structures (Fuselier et al., 2017, 2018). In this study, secondary reconnection reconnects the previously reconnected open magnetic field lines with closed magnetospheric field lines (**Figure 1A**), resulting into the re-closure of the open field lines. Regarding this, the reported secondary reconnection, which is found at the flank magnetopause, is different from other secondary reconnection.

The secondary reconnection here is found at the flank magnetopause with a large magnetic B_x shear, which suggests that the primary X-line at the flank and the magnetotail current sheet should not be co-located at the magnetopause (**Figure 1A**). In this study, the magnetotail current sheet is twisted due to interplanetary B_y component (Tsyganenko, 1998; Tsyganenko and Fairfield, 2004), which leads a substantial offset of the magnetotail current sheet from the equatorial plane at the flank region (**Supplementary Figure S1**). Meanwhile, the location of the primary magnetopause reconnection is shifted southward of the equator plane (**Figure 3A**). This non-colocation of the primary X-line at the flank and the magnetotail current sheet produces favorable external conditions for a large magnetic shear, and also the secondary reconnection. A general description of this non-colocation should be investigated in the future.

Magnetic reconnection between the open and closed magnetic field lines is sometimes referred to as the interchange reconnection. It has been widely applied at the surface of the Sun, which is responsible for the acceleration of the slow solar wind (Abbo et al., 2016) and is suggested to play a role in the generation of magnetic switchbacks (Fisk and Kasper, 2020). The present finding shows that this type of reconnection also works in the Earth's magnetosphere, but behaves as secondary reconnection, as it relies on the generation of open field lines from the primary reconnection. Therefore the observed secondary reconnection essentially reflects a cross-scale process from the global magnetospheric scale to kinetic scales, and we suggest this reconnection process is applicable to other planets with similar magnetosphere structures, such as Mercury and Jupiter's moon, Ganymede.

DATA AVAILABILITY STATEMENT

The datasets presented in this study can be found in online repositories. The names of the repository/repositories and accession number(s) can be found below: MMS science data center (https://lasp.colorado.edu/mms/sdc/public/), the Johns Hopkins University Applied Physics Laboratory (https://ssusi.jhuapl.edu/data/_retriver) and NASA OMNIWeb (https://omniweb.gsfc.nasa.gov/form/omni/_min.html).

AUTHOR CONTRIBUTIONS

BBT, WL, and CW performed the data analysis, interpretation and manuscript preparation. YK, DG and KJT contributed to the data interpretation. QHZ and XYW contributed to the data interpretation of DMSP. TRS and HL contricuted to the MHD simulations. BG, PAL and RE contributed to the development and operation of MMS instruments. JB is the PI of MMS science and led the operation of the MMS mission.

FUNDING

This work was supported by the National Natural Science Foundation of China (grants 41731070, 41974196 and 41974170), the Chinese Academy of Sciences (QYZDJ-SSW-JSC028, XDA15052500, XDA17010301 and XDB 41000000) and the Specialized Research Fund for State Key Laboratories of China. BBT was supported by the Youth Innovation Promotion Association of the Chinese Academy of Sciences. WYL was also supported by the Youth Innovation Promotion Association, and the Young Elite Scientists Sponsorship Program by CAST and the Open Research Program of Key Laboratory of Geospace Environment CAS.

SUPPLEMENTARY MATERIAL

The Supplementary Material for this article can be found online at: https://www.frontiersin.org/articles/10.3389/fspas.2021.740560/full#supplementary-material

REFERENCES

Abbo, L., Ofman, L., Antiochos, S. K., Hansteen, V. H., Harra, L., Ko, Y.-K., et al. (2016). Slow solar wind: Observations and modeling. *Space Sci. Rev.* 201, 55–108. doi:10.1007/s11214-016-0264-1

Allen, R. C., Livi, S. A., Vines, S. K., Goldstein, J., Cohen, I., Fuselier, S. A., et al. (2017). Storm time empirical model of O+ and O6+ distributions in the magnetosphere. *J. Geophys. Res. Space Phys.* 122, 8353–8374. doi:10.1002/2017ja024245

Borovsky, J. E. (2008). The rudiments of a theory of solar wind/magnetosphere coupling derived from first principles. *J. Geophys. Res. Space Phys.* 113. doi:10.1029/2007ja012646

Burch, J. L., Torbert, R. B., Phan, T. D., Chen, L. J., Moore, T. E., Ergun, R. E., et al. (2016). Electron-scale measurements of magnetic reconnection in space. *Science* 352, aaf2939. doi:10.1126/science.aaf2939

Cassak, P. A., and Shay, M. A. (2007). Scaling of asymmetric magnetic reconnection: General theory and collisional simulations. *Phys. Plasmas* 14, 102114. doi:10.1063/1.2795630

Cowley, S. W. H. (1973). A qualitative study of the reconnection between the Earth's magnetic field and an interplanetary field of arbitrary orientation. *Radio Sci.* 8, 903–913. doi:10.1029/rs008i011p00903

Daughton, W., Roytershteyn, V., Karimabadi, H., Yin, L., Albright, B. J., Bergen, B., et al. (2011). Role of electron physics in the development of turbulent magnetic reconnection in collisionless plasmas. *Nat. Phys* 7, 539–542. doi:10.1038/nphys1965

Doss, C. E., Komar, C. M., Cassak, P. A., Wilder, F. D., Eriksson, S., and Drake, J. F. (2015). Asymmetric magnetic reconnection with a flow shear and applications to the magnetopause. *J. Geophys. Res. Space Phys.* 120, 7748–7763. doi:10.1002/2015ja021489

Dungey, J. W. (1961). Interplanetary magnetic field and the auroral zones. *Phys. Rev. Lett.* 6, 47–48. doi:10.1103/physrevlett.6.47

Egedal, J., Le, A., Pritchett, P. L., and Daughton, W. (2011). Electron dynamics in two-dimensional asymmetric anti-parallel reconnection. *Phys. Plasmas* 18, 102901. doi:10.1063/1.3646316

Ergun, R. E., Tucker, S., Westfall, J., Goodrich, K. A., Malaspina, D. M., Summers, D., et al. (2016). The axial double probe and fields signal processing for the MMS mission. *Space Sci. Rev.* 199, 167–188. doi:10.1007/s11214-014-0115-x

Eriksson, S., Lavraud, B., Wilder, F. D., Stawarz, J. E., Giles, B. L., Burch, J. L., et al. (2016). Magnetospheric Multiscale observations of magnetic reconnection associated with Kelvin-Helmholtz waves. *Geophys. Res. Lett.* 43, 5606–5615. doi:10.1002/2016gl068783

Fisk, L. A., and Kasper, J. C. (2020). Global circulation of the open magnetic flux of the Sun. *ApJ* 894, L4. doi:10.3847/2041-8213/ab8acd

Fuselier, S. A., and Lewis, W. S. (2011). Properties of near-Earth magnetic reconnection from *in-situ* observations. *Space Sci. Rev.* 160, 95–121. doi:10.1007/s11214-011-9820-x

Fuselier, S. A., Petrinec, S. M., Trattner, K. J., Broll, J. M., Burch, J. L., Giles, B. L., et al. (2018). Observational Evidence of Large-Scale Multiple Reconnection at the Earth's Dayside Magnetopause. *J. Geophys. Res. Space Phys.* 123, 8407–8421. doi:10.1029/2018ja025681

Fuselier, S. A., Vines, S. K., Burch, J. L., Petrinec, S. M., Trattner, K. J., Cassak, P. A., et al. (2017). Large-scale characteristics of reconnection diffusion regions and associated magnetopause crossings observed by MMS. *J. Geophys. Res. Space Phys.* 122, 5466–5486. doi:10.1002/2017ja024024

Fuselier, S., Trattner, K., and Petrinec, S. (2011). Antiparallel and component reconnection at the dayside magnetopause. *J. Geophys. Res. Space Phys.* 116. doi:10.1029/2011ja016888

Genestreti, K., Liu, Y.-H., Phan, T.-D., Denton, R., Torbert, R., Burch, J., et al. (2020). Multiscale coupling during magnetopause reconnection: Interface between the electron and ion diffusion regions. *J. Geophys. Res. Space Phys.* 125, e2020JA027985. doi:10.1029/2020ja027985

Gomez, R. G., Vines, S. K., Fuselier, S. A., Cassak, P. A., Strangeway, R. J., Petrinec, S. M., et al. (2016). Stable reconnection at the dusk flank magnetopause. *Geophys. Res. Lett.* 43, 9374–9382. doi:10.1002/2016gl069692

Haaland, S., Paschmann, G., Øieroset, M., Phan, T., Hasegawa, H., Fuselier, S., et al. (2020). Characteristics of the flank magnetopause: MMS results. *J. Geophys. Res. Space Phys.* 125, e2019JA027623. doi:10.1029/2019ja027623

Hasegawa, H., Fujimoto, M., Phan, T.-D., Rème, H., Balogh, A., Dunlop, M. W., et al. (2004). Transport of solar wind into Earth's magnetosphere through rolled-up Kelvin-Helmholtz vortices. *Nature* 430, 755–758. doi:10.1038/nature02799

Hasegawa, H., Wang, J., Dunlop, M., Pu, Z., Zhang, Q.-H., Lavraud, B., et al. (2010). Evidence for a flux transfer event generated by multiple x-line reconnection at the magnetopause. *Geophys. Res. Lett.* 37. doi:10.1029/2010gl044219

Kacem, I., Jacquey, C., Génot, V., Lavraud, B., Vernisse, Y., Marchaudon, A., et al. (2018). Magnetic reconnection at a thin current sheet separating two interlaced flux tubes at the Earth's magnetopause. *J. Geophys. Res. Space Phys.* 123, 1779–1793. doi:10.1002/2017ja024537

Khotyaintsev, Y., Buchert, S., Stasiewicz, K., Vaivads, A., Savin, S., Papitashvili, V., et al. (2004). Transient reconnection in the cusp during strongly negative IMF by. *J. Geophys. Res. Space Phys.* 109. doi:10.1029/2003ja009908

Lapenta, G., Markidis, S., Goldman, M. V., and Newman, D. L. (2015). Secondary reconnection sites in reconnection-generated flux ropes and reconnection fronts. *Nat. Phys* 11, 690–695. doi:10.1038/nphys3406

Lavraud, B., Zhang, Y. C., Vernisse, Y., Gershman, D. J., Dorelli, J., Cassak, P. A., et al. (2016). Currents and associated electron scattering and bouncing near the diffusion region at Earth's magnetopause. *Geophys. Res. Lett.* 43, 3042–3050. doi:10.1002/2016gl068359

Li, W., André, M., Khotyaintsev, Y. V., Vaivads, A., Graham, D. B., Toledo-Redondo, S., et al. (2016). Kinetic evidence of magnetic reconnection due to Kelvin-Helmholtz waves. *Geophys. Res. Lett.* 43, 5635–5643. doi:10.1002/2016gl069192

Lindqvist, P.-A., Olsson, G., Torbert, R. B., King, B., Granoff, M., Rau, D., et al. (2016). The spin-plane double probe electric field instrument for MMS. *Space Sci. Rev.* 199, 137–165. doi:10.1007/s11214-014-0116-9

Milan, S., Provan, G., and Hubert, B. (2007). Magnetic flux transport in the Dungey cycle: A survey of dayside and nightside reconnection rates. *J. Geophys. Res. Space Phys.* 112. doi:10.1029/2006ja011642

Montag, P. K. (2018). *Modeling the formation of current sheets in symmetric and asymmetric reconnection*. Massachusetts: Ph.D. thesis, Massachusetts Institute of Technology.

Nakamura, R., Baumjohann, W., Schödel, R., Brittnacher, M., Sergeev, V. A., Kubyshkina, M., et al. (2001). Earthward flow bursts, auroral streamers, and small expansions. *J. Geophys. Res.* 106, 10791–10802. doi:10.1029/2000ja000306

Nakamura, T. K. M., Hasegawa, H., Daughton, W., Eriksson, S., Li, W. Y., and Nakamura, R. (2017). Turbulent mass transfer caused by vortex induced reconnection in collisionless magnetospheric plasmas. *Nat. Commun.* 8, 1582–1588. doi:10.1038/s41467-017-01579-0

Øieroset, M., Phan, T. D., Drake, J. F., Eastwood, J. P., Fuselier, S. A., Strangeway, R. J., et al. (2019). Reconnection with magnetic flux pileup at the interface of converging jets at the magnetopause. *Geophys. Res. Lett.* 46, 1937–1946. doi:10.1029/2018gl080994

Øieroset, M., Phan, T. D., Fujimoto, M., Lin, R. P., and Lepping, R. P. (2001). *In situ* detection of collisionless reconnection in the Earth's magnetotail. *Nature* 412, 414–417. doi:10.1038/35086520

Øieroset, M., Phan, T. D., Gosling, J. T., Fujimoto, M., and Angelopoulos, V. (2015). Electron and ion edges and the associated magnetic topology of the reconnecting magnetopause. *J. Geophys. Res. Space Phys.* 120, 9294–9306. doi:10.1002/2015ja021580

Paxton, L. J., Morrison, D., Zhang, Y., Kil, H., Wolven, B., Ogorzalek, B. S., et al. (2002). "Validation of remote sensing products produced by the special sensor ultraviolet scanning imager (SSUSI): A far UV-imaging spectrograph on DMSP F-16," in *Optical spectroscopic techniques, remote sensing, and instrumentation for atmospheric and space research IV* (Massachusetts: International Society for Optics and Photonics), 4485, 338–348.

Phan, T. D., Paschmann, G., Gosling, J. T., Oieroset, M., Fujimoto, M., Drake, J. F., et al. (2013). The dependence of magnetic reconnection on plasmaβand magnetic shear: Evidence from magnetopause observations. *Geophys. Res. Lett.* 40, 11–16. doi:10.1029/2012gl054528

Pollock, C., Moore, T., Jacques, A., Burch, J., Gliese, U., Saito, Y., et al. (2016). Fast plasma investigation for magnetospheric multiscale. *Space Sci. Rev.* 199, 331–406.

Pu, Z. Y., Raeder, J., Zhong, J., Bogdanova, Y. V., Dunlop, M., Xiao, C. J., et al. (2013). Magnetic topologies of an *in vivo* FTE observed by Double Star/TC-1 at Earth's magnetopause. *Geophys. Res. Lett.* 40, 3502–3506. doi:10.1002/grl.50714

Russell, C. T., Anderson, B. J., Baumjohann, W., Bromund, K. R., Dearborn, D., Fischer, D., et al. (2016). The magnetospheric multiscale magnetometers. *Space Sci. Rev.* 199, 189–256. doi:10.1007/978-94-024-0861-4_8

Russell, C. T., and Elphic, R. (1978). Initial isee magnetometer results: Magnetopause observations. *Space Sci. Rev.* 22, 681–715. doi:10.1007/bf00212619

Sergeev, V. A., Liou, K., Newell, P. T., Ohtani, S.-I., Hairston, M. R., and Rich, F. (2004). Auroral streamers: characteristics of associated precipitation,convection and field-aligned currents. *Ann. Geophys.* 22, 537–548. doi:10.5194/angeo-22-537-2004

Sonnerup, B. U. Ö., Paschmann, G., Papamastorakis, I., Sckopke, N., Haerendel, G., Bame, S. J., et al. (1981). Evidence for magnetic field reconnection at the Earth's magnetopause. *J. Geophys. Res.* 86, 10049–10067. doi:10.1029/ja086ia12p10049

Swisdak, M. (2016). Quantifying gyrotropy in magnetic reconnection. *Geophys. Res. Lett.* 43, 43–49. doi:10.1002/2015gl066980

Swisdak, M., Rogers, B., Drake, J., and Shay, M. (2003). Diamagnetic suppression of component magnetic reconnection at the magnetopause. *J. Geophys. Res. Space Phys.* 108. doi:10.1029/2002ja009726

Tang, B. B., Li, W. Y., Graham, D. B., Rager, A. C., Wang, C., Khotyaintsev, Y. V., et al. (2019). Crescent-Shaped Electron Distributions at the Nonreconnecting Magnetopause: Magnetospheric Multiscale Observations. *Geophys. Res. Lett.* 46, 3024–3032. doi:10.1029/2019gl082231

Thébault, E., Finlay, C. C., Beggan, C. D., Alken, P., Aubert, J., Barrois, O., et al. (2015). International geomagnetic reference field: the 12th generation. *Earth, Planets and Space* 67, 1–19. doi:10.1186/s40623-015-0313-0

Trattner, K., Mulcock, J., Petrinec, S., and Fuselier, S. (2007). Location of the reconnection line at the magnetopause during southward imf conditions. *Geophys. Res. Lett.* 34. doi:10.1029/2006gl028397

Trattner, K., Petrinec, S., Fuselier, S., and Phan, T. (2012). The location of reconnection at the magnetopause: Testing the maximum magnetic shear model with themis observations. *J. Geophys. Res. Space Phys.* 117. doi:10.1029/2011ja016959

Trattner, K., Petrinec, S., and Fuselier, S. (2021). The location of magnetic reconnection at Earth's magnetopause. *Space Sci. Rev.* 217, 1–47. doi:10.1007/s11214-021-00817-8

Treumann, R. A., LaBelle, J., and Pottelette, R. (1991). Plasma diffusion at the magnetopause: The case of lower hybrid drift waves. *J. Geophys. Res.* 96, 16009–16013. doi:10.1029/91ja01671

Tsyganenko, N. A. (1998). Modeling of twisted/warped magnetospheric configurations using the general deformation method. *J. Geophys. Res.* 103, 23551–23563. doi:10.1029/98ja02292

Tsyganenko, N. A. (1995). Modeling the Earth's magnetospheric magnetic field confined within a realistic magnetopause. *J. Geophys. Res.* 100, 5599–5612. doi:10.1029/94ja03193

Tsyganenko, N., and Fairfield, D. (2004). Global shape of the magnetotail current sheet as derived from geotail and polar data. *J. Geophys. Res. Space Phys.* 109. doi:10.1029/2003ja010062

Vines, S. K., Fuselier, S. A., Trattner, K. J., Petrinec, S. M., and Drake, J. F. (2015). Ion acceleration dependence on magnetic shear angle in dayside magnetopause reconnection. *J. Geophys. Res. Space Phys.* 120, 7255–7269. doi:10.1002/2015ja021464

Wang, R., Lu, Q., Nakamura, R., Baumjohann, W., Russell, C., Burch, J., et al. (2017). Interaction of magnetic flux ropes via magnetic reconnection observed at the magnetopause. *J. Geophys. Res. Space Phys.* 122, 10–436. doi:10.1002/2017ja024482

Webster, J. M., Burch, J. L., Reiff, P. H., Daou, A. G., Genestreti, K. J., Graham, D. B., et al. (2018). Magnetospheric multiscale dayside reconnection electron diffusion region events. *J. Geophys. Res. Space Phys.* 123, 4858–4878. doi:10.1029/2018ja025245

Welling, D. T., André, M., Dandouras, I., Delcourt, D., Fazakerley, A., Fontaine, D., et al. (2015). The Earth: Plasma sources, losses, and transport processes. *Space Sci. Rev.* 192, 145–208. doi:10.1007/s11214-015-0187-2

Zhou, M., Berchem, J., Walker, R. J., El-Alaoui, M., Deng, X., Cazzola, E., et al. (2017). Coalescence of macroscopic flux ropes at the subsolar magnetopause: Magnetospheric multiscale observations. *Phys. Rev. Lett.* 119, 055101. doi:10.1103/PhysRevLett.119.055101

Conflict of Interest: The authors declare that the research was conducted in the absence of any commercial or financial relationships that could be construed as a potential conflict of interest.

Publisher's Note: All claims expressed in this article are solely those of the authors and do not necessarily represent those of their affiliated organizations, or those of the publisher, the editors and the reviewers. Any product that may be evaluated in this article, or claim that may be made by its manufacturer, is not guaranteed or endorsed by the publisher.

frontiers in Astronomy and Space Sciences

ORIGINAL RESEARCH
published: 13 December 2021
doi: 10.3389/fspas.2021.801824

The Kelvin-Helmholtz Instability From the Perspective of Hybrid Simulations

P. A. Delamere [1], N. P. Barnes [1], X. Ma [2] and J. R. Johnson [3]*

[1]University of Alaska Fairbanks, Fairbanks, AK, United States, [2]Embry-Riddle Aeronautical University, Daytona Beach, FL, United States, [3]Andrews University, Berrien Springs, MI, United States

The flow shear-driven Kelvin-Helmholtz (KH) instability is ubiquitous in planetary magnetospheres. At Earth these surface waves are important along the dawn and dusk flanks of the magnetopause boundary while at Jupiter and Saturn the entire dayside magnetopause boundary can exhibit KH activity due to corotational flows in the magnetosphere. Kelvin-Helmholtz waves can be a major ingredient in the so-called viscous-like interaction with the solar wind. In this paper, we review the KH instability from the perspective of hybrid (kinetic ions, fluid electrons) simulations. Many of the simulations are based on parameters typically found at Saturn's magnetopause boundary, but the results can be generally applied to any KH-unstable situation. The focus of the discussion is on the ion kinetic scale and implications for mass, momentum, and energy transport at the magnetopause boundary.

Keywords: kelvin-helmholtz, hybrid simulations, transport, ion kinetic scale, heavy ions, turbulence, heating

OPEN ACCESS

Edited by:
Takuma Nakamura, Austrian Academy of Sciences (OeAW), Austria

Reviewed by:
Matteo Faganello, UMR7345 Physique des interactions ioniques et moléculaires (P2IM), France
Misa Cowee, Los Alamos National Laboratory (DOE), United States

****Correspondence:***
P. A. Delamere
padelamere@alaska.edu

Specialty section:
This article was submitted to Space Physics, a section of the journal Frontiers in Astronomy and Space Sciences

Received: *25 October 2021*
Accepted: *03 November 2021*
Published: *13 December 2021*

Citation:
Delamere PA, Barnes NP, Ma X and Johnson JR (2021) The Kelvin-Helmholtz Instability From the Perspective of Hybrid Simulations. Front. Astron. Space Sci. 8:801824. doi: 10.3389/fspas.2021.801824

1 INTRODUCTION

From the perspective of hydrodynamics, any flow shear with a deformed interface develops pressure gradients following from the Bernoulli principle. A positive feedback yields further deformation leading to the Kelvin-Helmholtz (KH) instability where the boundary interface can be rolled up into a vortex structure. The planetary magnetopause boundary is a prime example of a potentially KH-unstable interface, provided that there is sufficient kinetic energy in the flow to overcome magnetic tension forces. Thus, the KH instability has generated considerable attention as a mechanism for facilitating a viscous-like interaction of the solar wind with planetary magnetospheres (review by Johnson et al. (2014) and references therein).

While magnetopause boundary processes garner much of the attention, it should be noted that a discontinuous flow shear with sufficient kinetic energy density to overcome magnetic tension will be KH unstable (Chandrasekhar, 1961). For the simple case of an incompressible plasma with a discontinuous flow shear, the condition for KH instability is

$$[\mathbf{k}\cdot(\mathbf{v}_1-\mathbf{v}_2)]^2 > \frac{\rho_1+\rho_2}{\mu_o\rho_1\rho_2}\left[(\mathbf{k}\cdot\mathbf{B}_1)^2+(\mathbf{k}\cdot\mathbf{B}_2)^2\right] \quad (1)$$

where $\mathbf{v}$ denotes velocity, ρ is the mass density, $\mathbf{B}$ is the magnetic field, $\mathbf{k}$ is the wave vector, and the indices refer to the two regions across the shear flow boundary. The corresponding linear growth rate of the wave is given by

$$\gamma = \left[\alpha_1\alpha_2[\mathbf{k}\cdot(\mathbf{v}_1-\mathbf{v}_2)]^2-\alpha_1(\mathbf{k}\cdot\mathbf{v}_{A1})^2-\alpha_2(\mathbf{k}\cdot\mathbf{v}_{A2})^2\right]^{1/2} \quad (2)$$

where $\alpha_i = \rho_i/(\rho_1+\rho_2)$. Further refinements were made by Miura and Pritchett (1982) by considering compressibility, demonstrating that for finite half width, L_o, of the initial shear flow layer, the growth

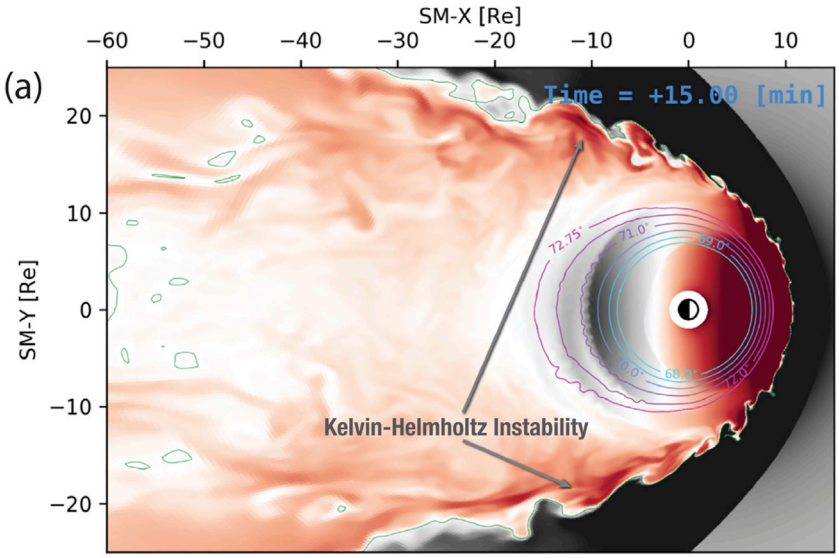

FIGURE 1 | GAMERA simulation of Earth's magnetosphere (Sorathia et al., 2020). The color depicts the residual magnetic field (with the dipole subtracted).

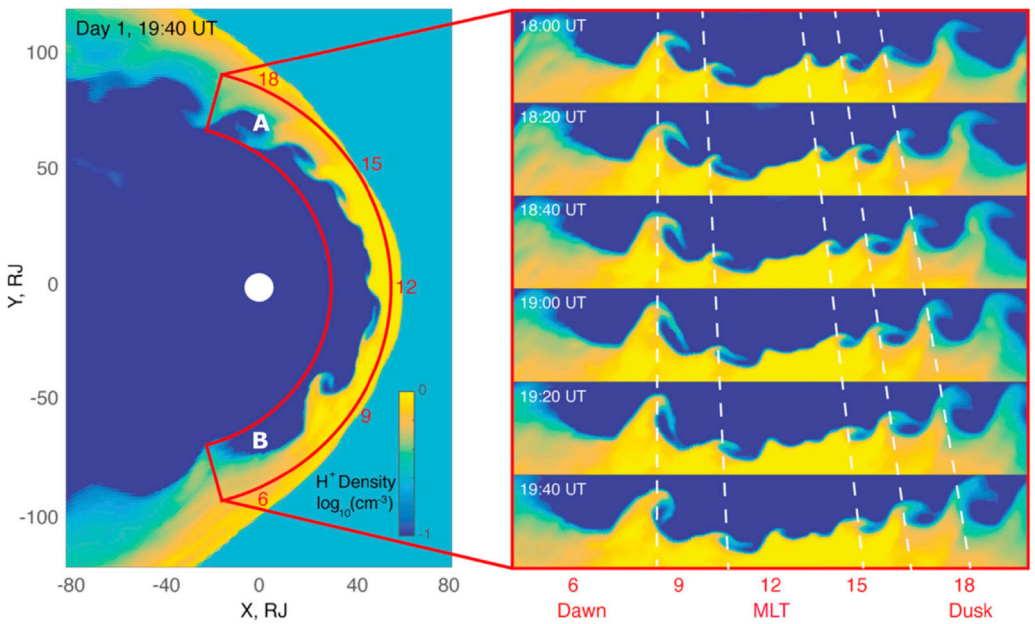

FIGURE 2 | Multifluid Lyon-Fedder-Mobarry simulation of Jupiter's magnetosphere showing KH waves on the dayside magnetopause boundary due to internal corotational flows (Zhang et al., 2018).

rates will be a function of the magnetosonic Mach number with most unstable modes occurring when the wavelength is comparable to the width of the shear layer, or $2kL_o \sim 1$.

The flow shear on the dawn and dusk flanks of the terrestrial magnetopause boundary are inherently KH unstable, leading to global-scale KH vortices advecting down the magnetotail (**Figure 1**). In the broader context of planetary magnetospheres, KH waves are ubiquitous and are thought to play an even more important role at the giant planet magnetospheres where the viscous-like processes are thought to play a critical role in the solar wind interaction (Delamere and Bagenal, 2010). **Figure 2**, from a multifluid Lyon-Fedder-Mobarry simulation of Jupiter's magnetosphere, shows KH waves on the dayside magnetpause boundary due to internal corotational flows (Zhang et al., 2018). It should be noted that KH waves are not found exclusively at the magnetopause

boundary. For example, secondary KH instabilities could occur at the boundaries of injection channels associated with, e.g., tail reconnection events.

The KH instability is rife with kinetic-scale physics. In fact, KH vortices could be considered as a microcosm for kinetic-scale plasma physics. This papers explores the wealth of KH-related plasma processes with specific application to planetary magnetospheres. While the goal is to explore implications for the terrestrial magnetosphere, numerous examples from the giant planet magnetospheres will be discussed to further understand the kinetic aspects of the KH instability. Specifically, we discuss KH growth characteristics, magnetic field topology, heavy ion effects, momentum transport, particle transport, energy tranport and heating, and electron energization due to parallel electric fields associated with driven KH reconnection.

2 HYBRID SIMULATIONS

The basis of our discussion will be hybrid (kinetic ions, fluid electrons) simulations of the KH instability (Delamere et al., 2011; Delamere et al., 2018; Delamere et al., 2021). Hybrid simulations push ions according to the Lorentz force equation using the Boris (1970) method. The electric and magnetic fields are ordered on a Yee grid to facilitate the correct field topology for curl operations (Yee, 1966) and to guarantee a divergence-free magnetic field. The magnetic field is updated with Faraday's law using a second-order, predictor-corrector method. The electric field is determined from the electron momentum equation (massless electrons) that contains an ion-electron collision term and an electron pressure term. The electron fluid is assumed to be isothermal in time and space for numerical simplicity. Ampere's law is used to calculate the electron bulk flow used in the electric field calculation.

With the addition of the electron pressure term, the hybrid simulation is capable of modeling kinetic Alfvén waves (KAW). The dispersion relation for the KAW is

$$\omega^2 \approx k_\parallel^2 v_A^2 \left[1 + (1 + T_e/T_i)k_\perp^2 \rho_i^2\right]$$

where ρ_i is the ion Larmor radius, v_A is the Alfvén speed. At ion inertial scales, KAW modes capture Alfvén and ion-ion hybrid resonances of the fast magnetosonic/whistler branch. In addition, mode conversion of the compressional fast mode waves to KAW will be captured in hybrid simulations (Lin et al., 2010; Lin et al., 2012).

To elucidate the ion kinetic effects, the simulations have been typically conducted for plasma $\beta \sim 1$ where both ion inertial and gyroradius effects are important. By expressing the plasma β as the ratio of thermal pressure to magnetic field pressure, it can be shown that $\beta/2 = \rho_i^2/\lambda_i^2$ where ρ_i is the thermal ion gyroradius and λ_i is the ion inertial length. For electron kinetics, we limit the studies to test particle simulations of electron motion along the magnetic field subject to parallel electric fields.

All simulations are based on typical conditions for Saturn's magnetopause boundary. The magnetospheric (corotational) flows are in the $+x$ direction, the $+z$ is normal to the magnetopause boundary from magnetosheath to magnetosphere, and $+y$ is the direction of the magnetic field. Protons are used by default and admixtures of heavy ions (where relevant) were added to the magnetospheric side of the boundary. The typical density is 0.4 cm^{-3} with an ion inertial length of 360 km. The magnetic field was of the order of 5 nT with a small (e.g., 2%) in-plane component included in the x direction. The velocity shear was of the form $\sim 0.8 v_A \tanh[(z - z_o)/L_0]$ where v_A is the Alfvén speed, and $L_o \sim \lambda_i$. The grid resolution was $\sim 0.5\lambda_i$. Boundary conditions perpendicular to the flow shear boundary were open while the remaining boundary conditions were periodic. We note that periodic boundary conditions are a limitation for understanding global scale evolution of the instability where field lines can be tied to the ionospheric boundary. Nevertheless, these local simulations should be considered valid during the initial non-linear evolution of the KH instability. Typical spatial domains spanned a few planetary radii.

3 KH GROWTH CHARACTERISTICS

The fastest growing wavelength of KH modes is typically at the ion kinetic scale. Boundaries in space plasma can be comparable to the ion inertial length (e.g., magnetopause boundary); therefore, the wavelength of fastest growing wavelength will be of the order of $4\pi\lambda_i$. Compared to magnetospheric scales, this is surprisingly small, i.e., a small fraction of the planet's radius. The slower growing, larger-scale modes can subsume the small-scale modes leading to an apparent inverse cascade. Eventually the KH waves can reach global scale with average KH wavelengths ~ 5 R_E on the flanks of Earth's magnetopause boundary (Otto and Fairfield, 2000).

In this paper we consider very simple configurations that promote an inverse cascade. But it is important to note that, e.g., density inhomogeneity can lead to secondary Rayleigh-Taylor instability that can disrupt vortex formation (Matsumoto and Hoshino, 2004). Faganello et al. (2008) showed that in the case where the magnetic field is strictly perpendicular to the flow, density inhomogeneity can lead to both inverse and direct cascades dominating the dynamics, though when an in-plane magnetic field component is added, the secondary instabilities can be stabilized (Cowee et al., 2010; Tenerani et al., 2010). For magnetospheric systems, the high latitude region is typically KH stable and the inverse cascade stops with the vortex scale is comparable to the height of the unstable region (Takagi et al., 2006).

One of the challenges for global-scale simulations is resolving the thin magnetopause boundary. With insufficient resolution and/or excessive numerical diffusion, the fastest growing mode could approach global-scale and the growth rates could be slower than the solar wind advection time scale, prohibiting the onset of KH waves. By using higher order numerics, the Lyon-Fedder-Mobarry model (and later incarnation as the Grid Agnostic MHD for Extended Research Applications or GAMERA simulation (Zhang et al., 2019)) has generated KH modes in both terrestrial (Merkin et al., 2013) and giant magnetosphere

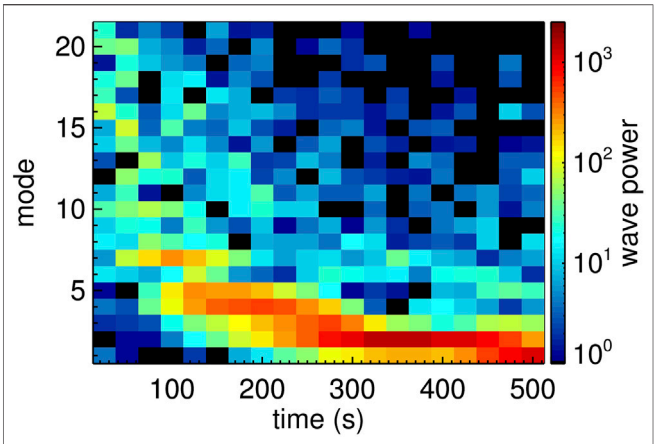

FIGURE 3 | Growth of KH, showing inverse cascade (Delamere et al., 2011).

simulations (Zhang et al., 2018). **Figure 1** shows a terrestrial GAMERA simulation with the KH waves reaching global-scale on the dawn and dusk flanks (Sorathia et al., 2020). Despite the success of global-scale simulations to model the KH instability, a three-dimensional, meso-scale simulation is required to capture the kinetic-scale processes to understand the interaction between the spectrum of modes that can be present. Typically, a meso-scale (few planetary radii) simulation will capture the inverse cascade and saturate at the $m = 1$ mode that is fixed by the spatial domain.

Figure 3 illustrates the inverse cascade from a two-dimensional hybrid simulation (Delamere et al., 2011). The cascade from an $m = 20$ (short wavelength) mode is apparent, with final state of the system in the $m = 1$ mode (longest wavelength supported by the simulation domain). An unresolved issue is the extent to which the slower-growing, smaller-m modes grow independently and subsume the larger m modes, or whether there is a true inverse cascade in which information is transferred from one scale to another. In **section 8** we note that in the presence of heavy ions, the protons can separately exhibit a forward cascade while the heavy ions participate in an inverse cascade. This is a topic for more detailed investigation in future studies.

4 MAGNETIC FIELD TOPOLOGY

Magnetic reconnection plays a critical role in the Kelvin-Helmholtz instability and requires a three dimensional treatment. We start with a discussion of strong guide field reconnection. The standard two-dimensional model (e.g., Sweet and Parker and/or Petschek) of a simple current sheet formed by strictly anti-parallel magnetic fields is misleading because these models neglect the more likely existence of a *guide magnetic field* in the ignorable, out-of-plane direction (**Figure 4**). Magnetic flux conservation in the two-dimensional configuration requires a constant out-of-plane electric field. But note that in the presence of an out-of-plane guide field, the electric field has a parallel component to the magnetic field in a small region of space near the X-line. Schindler et al. (1988) showed that magnetic reconnection occurs if and only if the integral of the parallel electric field is nonzero on a measurable set of field lines in the diffusion region. The parallel potential also gives the rate of reconnected flux (Hesse and Schindler, 1988).

Auroral acceleration in planetary magnetospheres occurs close to the planet on (highly) dipolar magnetic field lines. Extreme guide field reconnection can operate in this case and Seyler (1990)

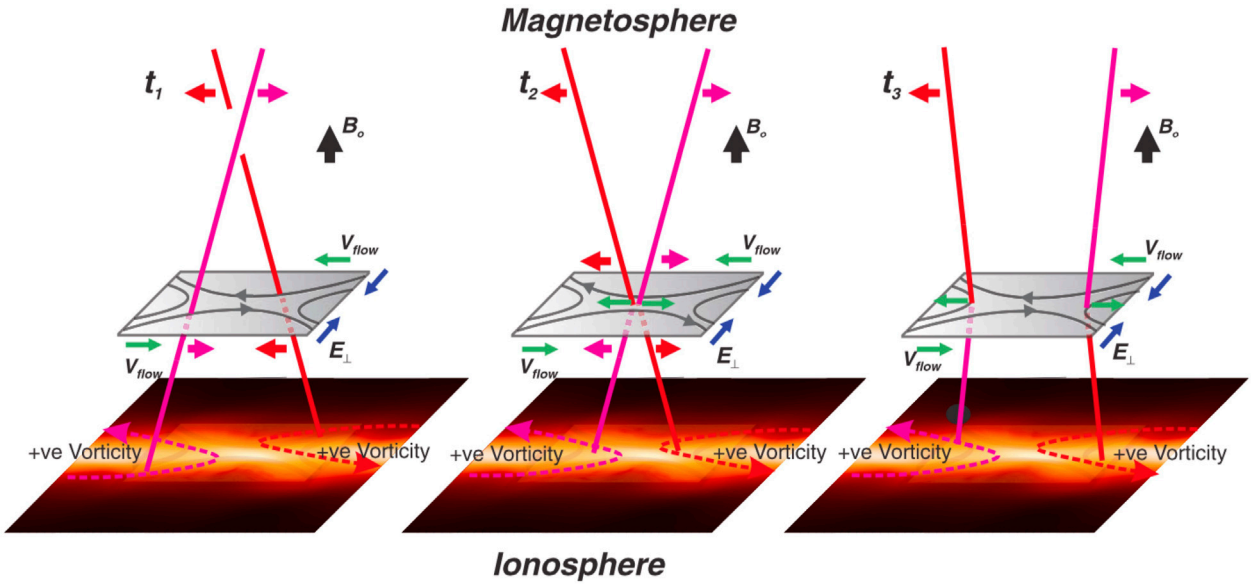

FIGURE 4 | Schematic of extreme guide field reconnection and its relation to discrete auroral arc structure (Chaston et al., 2015). Reconnection involves the horizontal magnetic field components.

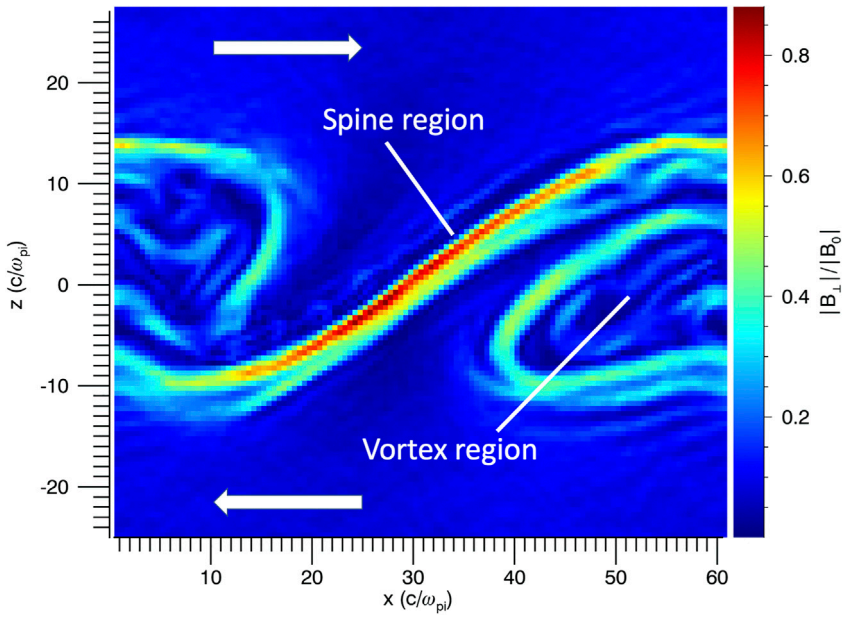

FIGURE 5 | Structure of a KH vortex as illustrated with the magnitude of the in-plane magnetic field. The spine region connects adjacent vortices and is a barrier to flow due to the accumulation of magnetic flux.

and Otto and Birk (1993) have suggested that thin, discrete aurora arcs are governed by magnetic reconnection with small magnetic shear. Chaston et al. (2015) recently presented the first experimental evidence of the role of extreme guide field reconnection in the auroral acceleration region. **Figure 4** summarizes the time sequence of the auroral reconnection process where red and magenta field lines reconnect, giving rise to islands of vorticity in thin auroral arcs (Chaston et al., 2015). Similar reconnection processes are expected to occur in KH vortices.

The magnetic field structure associated with KH vortices leads to intense currents due to the twisting of the magnetic field. The net result is driven reconnection which can lead to magnetic field line threading of the magnetopause boundary. In two-dimensions, the vortex structure can be defined by magnetic barriers. **Figure 5** shows the magnitude of the in-plane component [1] of the magnetic field in a 2-D hybrid simulation. As the surface wave develops, magnetic flux accumulates along the spine and vortex boundary. In the limiting case, $B^2_{in-plane}/2\mu_o = \frac{1}{2}\rho v^2_{sh}$ where v_{sh} is the flow shear. These magnetic barriers are consistent with the flow deflection that is required for a surface wave. The ongoing vortical motion can bring oppositely directed magnetic fields in close proximity, resulting in reconnection of the in-plane magnetic field components (Nykyri and Otto, 2001).

While a simple 2-D picture of KH illustrates general KH properties, many interesting aspects are revealed in three dimensions. When the antiparallel components of the magnetic field in the presence of flow shear are considered in a 2-D plane, KH and reconnection are mutually exclusive. If the flow shear is sub-Alfvénic, spontaneous reconnection can operate (and KH is stabilized), while if the flow is super-Alfvénic, KH is destabilized and spontaneous reconnection is suppressed as information transport along the magnetic field is truncated (La Belle-Hamer et al., 1995; Faganello et al., 2010). We note that during the KH growth, driven reconnection can occur as current layers are pinched during vortex rollup with a rate that is independent of prescribed mechanism (Knoll and Chacón, 2002; Nakamura and Fujimoto, 2006). In three dimensions, on the other hand, KH and reconnection can interact. Ma et al. (2014a) showed that for an initial KH driver, reconnection can be triggered along the spine region as the current layer thins and intensifies. On the other hand, Ma et al. (2014b) showed that reconnection flows for a preexisting current layer at the magnetopause boundary can trigger the KH instability. Ultimately, the twisting of the magnetic field can lead to strong guide field reconnection in pairs of reconnection sites (Otto, 2007; Faganello et al., 2012, 2014). Ma et al. (2017) showed that a KH-active magnetopause boundary, the reconnection sites form in the midlatitudes and asynchronous reconnection can lead to open flux generation. The double reconnection process can also effectively transport plasma across the magnetopause boundary.

During the non-linear rollup of KH vortices, multiple current sheets (and associated magnetic barriers and/or filaments) are folded together. Therefore, a transect of the vortex region yields a highly variable magnetic field with many bipolar signatures, typically in component pairs. Delamere et al. (2013) used these bipolar signatures to identify potential KH active regions near Saturn's magnetopause boundary, though any vortical flow

[1]Most 2-D simulations include an initial (but small) magnetic field component in the plane of the KH wave vector.

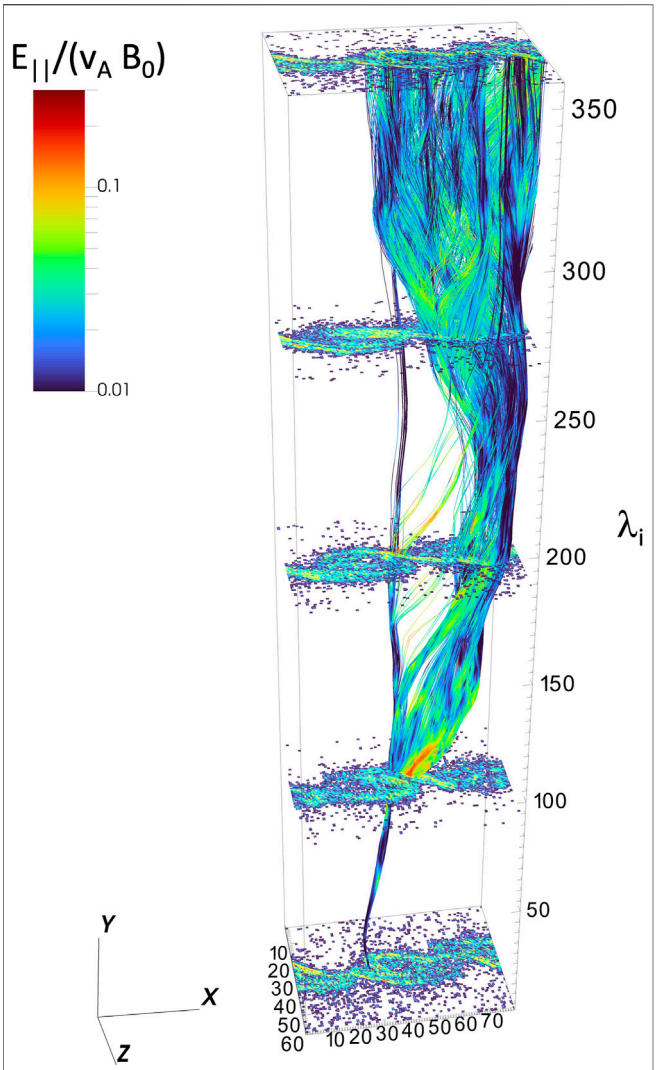

FIGURE 6 | Magnetic field line traces through KH active regions in a 3-D hybrid simulation. The magnitude of the parallel electric field ($E_{\parallel}/(v_A B_0)$) is indicated in color. Spatial units are in ion inertial length (λ_i).

associated with, e.g., radial transport can produce similar bipolar signatures (Stauffer et al., 2019).

In three-dimensional hybrid simulations, the complexity of the magnetic field topology is further enhanced during the inverse cascade. A key aspect of hybrid simulations is that the finite particle statistics provide the "stochastic" seed for surface wave formation. The phase of the surface wave at a given point along the magnetic field is therefore random. Provided that the simulation domain along the unperturbed magnetic field is sufficiently long (e.g., perpendicular to parallel spatial scale proportional to the Alfvén Mach number of the flow shear), then the phase of the surface waves can be a function of distance along the magnetic field. In other words, the system supports $k_{\parallel} \sim k_{\perp}$ where $k_{\perp}$ is the KH wavenumber of the fastest growing mode. As a result, twisted nodes form between out-of-phase surface waves, promoting strong guide field reconnection. At each stage of the inverse cascade, twisted node formation promotes reconnection. As a result, multiple reconnection sites can be identified on an instantaneous field line trace, adding further complexity to the magnetic field topology.

Figure 6 shows field line tracing from a 3-D hybrid simulation. The image slices and field line color show the magnitude of the parallel electric field, $E'_{\parallel} = E_{\parallel}/(v_A B_0)$, or the expected strong guide field reconnection rate for the case where the electron pressure term was neglected (i.e., $T_e = 0$). In a high Alfvén Mach number flow, the in-plane magnetic field perturbations can approach B_0, so the normalization uses B_0 as an upper limit (lower limit for the reconnection rate). The sample magnetic field lines originate from a localized region on the magnetosheath side of the boundary. The field lines trace to a region along the spine in the second slice ($y = \sim 100\ \lambda_i$) in a manner similar to that described by Otto and Birk (1993) in a current striation model for understanding formation of long thin auroral structures. Note the strong parallel electric field in this region ($E'_{\parallel} \sim 0.2$). Subsequent field lines continue to be altered by parallel electric fields until the mapping is spread over a significant portion of the KH vortex. In addition, the field lines thread the magnetopause boundary (defined by 50% mixing); therefore, momentum transport (i.e., Maxwell stress) across the magnetopause boundary occurs (Burkholder et al., 2017; Delamere et al., 2018). Future simulations should compare the mapping with field-line tying boundary conditions (i.e., to mimic the ionospheric boundaries) following Ma et al. (2017).

5 MOMENTUM TRANSPORT

Momentum transport at the magnetopause boundary occurs as a result of the KH instability. The classic Chapman-Ferraro magnetopause boundary is the idealized case where the normal component of the magnetic field is zero and $\mathbf{F} = \int \overleftrightarrow{\mathbf{T}} \cdot d\mathbf{a} = 0$, where $\overleftrightarrow{\mathbf{T}}$ is the Maxwell stress tensor with units of momentum flux. Due to the magnetic field line threading of the magnetopause boundary, momentum can be transported via Maxwell stresses ($\mathbf{BB}/\mu_o$). Reynolds stresses ($\rho\mathbf{uu}$) can also be generated as a result of the flow shear and the vortical motion.

Assuming an initial pressure balanced configuration, an estimate of the momentum transfer rates will be made by considering the steady flux conservative form of the momentum equation, i.e.,

$$\frac{\partial \rho \mathbf{u}}{\partial t} + \nabla \cdot \left[\rho \mathbf{uu} + \mathbf{P} + \frac{B^2}{2\mu_o}\mathbf{I} - \frac{\mathbf{BB}}{\mu_o} \right] = 0. \tag{3}$$

This equation will be integrated over any arbitrary volume and rewritten as a surface integral using the divergence theorem (i.e., $\int \nabla \cdot \overleftrightarrow{\mathbf{T}}\, dV = \oint \overleftrightarrow{\mathbf{T}} \cdot d\mathbf{a}$). If $+\hat{\mathbf{t}}$ is the tangential sheath flow (tailward) direction and $+\hat{\mathbf{n}}$ is the direction normal to the magnetopause boundary, then the sheath flow is modified (i.e., reduced) due to Maxwell shear stresses at the magnetopause boundary when $\mathbf{BB} \approx -B_t B_n \hat{\mathbf{t}}\hat{\mathbf{n}} \neq 0$. The Reynolds stress are $(\rho u_t u_n)\hat{\mathbf{t}}\hat{\mathbf{n}}$ and account for plasma source terms due to the direct

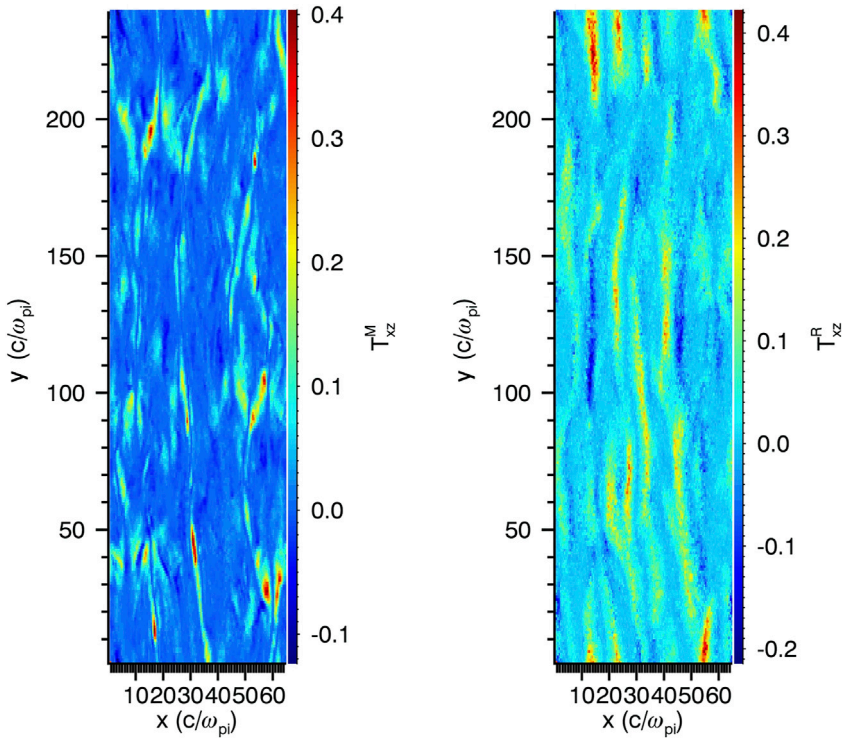

FIGURE 7 | Maxwell and Reynolds stresses (normalized) at the magnetopause boundary in a 3-D hybrid simulation.

transport of plasma across the magnetopause boundary. **Figure 7** shows an example of the (normalized) Maxwell and Reynolds stresses at the magnetopause boundary in a 3-D hybrid simulation where, e.g., Txz is x momentum transported in the z direction. Using the formalism of Miura (1984) and we can evaluate the "anomalous viscosity", $\nu_{ano} = \rho_0^{-1}\langle B_t B_n/\mu_o - \rho v_t v_n\rangle (d\langle v_t\rangle/dn)^{-1}$, to formally quantify KH contribution to the so-called "viscous-like" interaction.

Delamere et al. (2018) estimated the flow reduction in Saturn's dawnside magnetosheath due to Maxwell (T^M) and Reynolds stresses (T^R) from 3-D hybrid simulations. **Figure 7** shows the midplane of the simulation (i.e., magnetopause boundary) for both T^M and T^R where the color scale indicates relative momentum fluxes. The upper limit for combined stress is roughly 4×10^{-13} N/m^2 and this yields a flow reduction that is consistent with observations (Burkholder et al., 2019). Again, it should be emphasized that significant magnetic field line threading of the magnetopause boundary occurs and in general the Maxwell stresses (T^M_{xz}) were found to be larger than the Reynolds stresses.

6 PARTICLE TRANSPORT

There are two mechanisms that facilitate mass transport. In the magnetohydrodynamic limit, magnetic reconnection is required, involving the flow-aligned components in both 2-D and 3-D cases (Fadanelli et al., 2018; Sisti et al., 2019). Hybrid simulations, on the other hand, show both magnetic reconnection operating as well as diffusive transport due to large gyroradius effects and wave-particle interactions (Johnson and Cheng, 1997; Chen, 1999; Chaston et al., 2009). In a 2-D comparison of MHD + test particles vs. hybrid simulations with periodic boundary conditions, Ma et al. (2019) showed that both simulations produced similar transport rates, but that particle mixing by finite gyroradius is the dominant process in the hybrid simulations. The derived diffusion coefficients are typically $\sim 10^9$ to 1010 m^2/s (Cowee et al., 2009, 2010; Delamere et al., 2011), and Cowee et al. (2009) indicated that the time dependent diffusion coefficients can describe a non-classical "superdiffusion" process.

Hybrid simulations allow for a simple calculation of the diffusion coefficient. Initially, the particles are labeled as either magnetospheric or magnetosheath particles. During the evolution of the KH instability, the ions are mixed on the grid with fully mixed grid cells containing 50% of both populations, or a mixing of 0.5. The width of the mixed cell region is L_{mix} (t) where values above, e.g., 0.1 are considered mixed. The diffusion coefficient is D $(t) = dL_{mix}$ $(t)^2/dt$. **Figure 8** compares mixing/diffusion in 2-D and 3-D hybrid simulations. In both cases the mixing is very strong in the KH active region, but the 3-D simulations tend to produce a narrower diffused region (boundary layer) due to the magnetic tension generated by out-of-phase surface waves during the inverse cascade. Presumably when the KH modes reach global scale and periodic boundary conditions are no longer valid, the system will evolve with coherent vortical structure as seen in the global simulations.

Boundary layer formation can occur rapidly when growth rates exceed the solar wind/magnetospheric advection time. For an initial

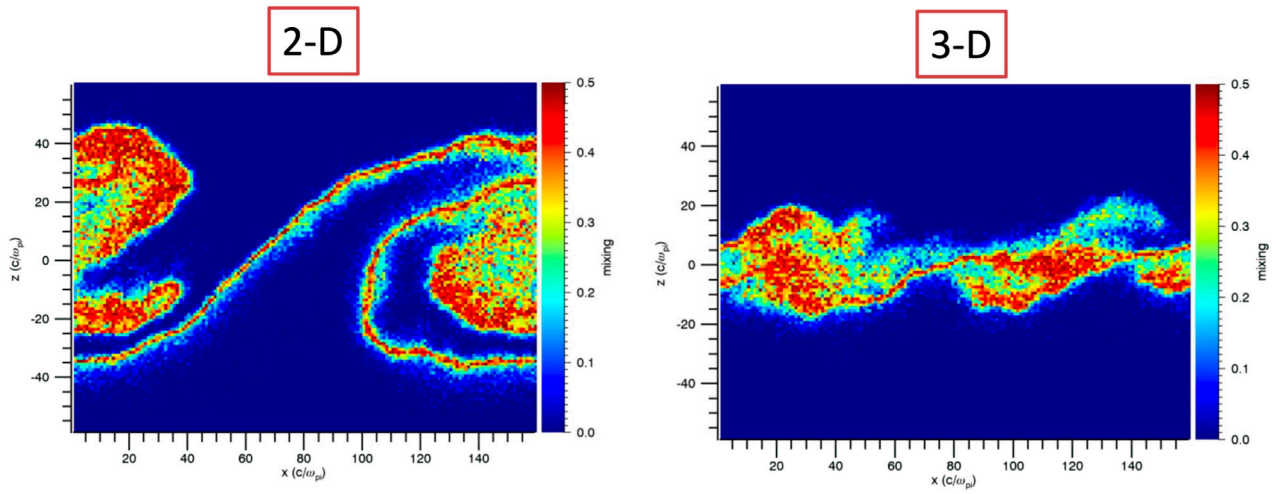

FIGURE 8 | Comparison of 2D and 3D hybrid simulations. The 2-D result shows a coherent m = 1 vortex structure while the 3-D case does not exhibit a coherent rolled up structure and at the same time appears as an m = 2 mode.

boundary width of the order of the ion inertial length, the growth rates can exceed $\gamma = 0.01\ s^{-1}$, or a growth time scale of minutes (Delamere et al., 2011). Eventually the boundary layer will thin such that the onset of KH waves is episodic. Burkholder et al. (2019) found an occurrence frequency ~ 18% of active KH waves in the 10–12 LT sector of Saturn's magnetopause boundary where KH activity is expected to be a maximum due to the strong flow shears. During this episodic activity, particle transport should be observed, particularly in the superthermal ion population. Indeed, Sergis et al. (2013) reported on water group (i.e., originating from Enceladus in Saturn's inner magnetosphere) "islands" in the Saturn's magnetosheath for particles > few keV. The observed pitch angle distribution of the W^+ ions was typically peaked away from 90° with a substantial field-aligned component (i.e., streaming distribution). While these energetic ions have large ion gyroradii and can likely escape across the magnetopause boundary, the transport could be modulated by KH waves. Similar distributions of iogenic ions have been observed by the Juno spacecraft at Jupiter (Mauk et al., 2019). At Earth, energetic oxygen ions tend to be entrained along the dayside magnetopause boundary during stable magnetospheric conditions and are less likely to be scattered compared to protons (Mauk et al., 2019). While much work remains regarding the dependence on mass/charge on energetic particle escape at Earth, Jupiter, and Saturn, we suggest here that KH waves could modulate the escape process, accounting for the episodic water group island observed in Saturn's dayside sheath.

As a preliminary test of KH-related transport of energetic ions, we conducted a proton-only, 3-D hybrid simulation that contained a small population (e.g., 1% of total mass density) of energetic protons ($4v_{th}$) on the magnetospheric side of the flow shear boundary. During the growth of the KH waves, these particles were found to be transported across the boundary (i.e., to regions dominated by magnetosheath plasma). The velocity distribution was often peaked well away from 90° pitch angle. **Figure 9** shows an example of such a streaming distribution with a peak near 130°, similar to the distributions reported by Sergis et al. (2013). We note that streaming distributions have also been measured by the magnetospheric multiscale mission at Earth. Vernisse et al. (2016) suggested that the streaming particles were generated by reconnection induced by KH instabilities. The Themis and Cluster missions have also observed streaming ion distributions far away from the vortex location (Bavassano Cattaneo et al., 2010; Faganello et al., 2014).

Figure 10 shows a sample field line trace taken through the KH active region. The top to bottom is the ion pitch angle distribution of the superthermal magnetospheric ions, the ion mixing, the normalized x component of flow, the normalized perpendicular magnetic field perturbations, the parallel electric field, and the integrated parallel electric field (field-aligned potential). In this example, the magnetic field samples a wide range of mixing values, plasma flows. We note that the pitch angle distribution is often not peaked near 90° as would be expected for an unperturbed Maxwellian distribution. The modification of the distribution function as a function of energy is a topic for future study; however, initial studies suggest that transport can be facilitated and/or modulated by KH activity.

7 ENERGY TRANSPORT AND HEATING

KH waves radiate compressional modes into the magnetospheric cavity. Pu and Kivelson (1983) and Delamere et al. (2011) showed that roughly 1% of the incident solar wind power can be radiated into the magnetosphere. As a result, magnetospheric resonant cavity modes can be excited and/or plasma heating can occur. The empirical estimate for the plasma heating rate at Saturn is 30–400 GW (Bagenal and Delamere, 2011), which compares favorably with Poynting flux in generated in hybrid simulations multiplied by the expected KH-active area of the dayside magnetopause boundary (Delamere et al., 2011). The internal energy transport via the magnetosonic fast mode can be comparable to or even shorter than the solar wind advection time past the magnetosphere (e.g., hours for the giant magnetospheres);

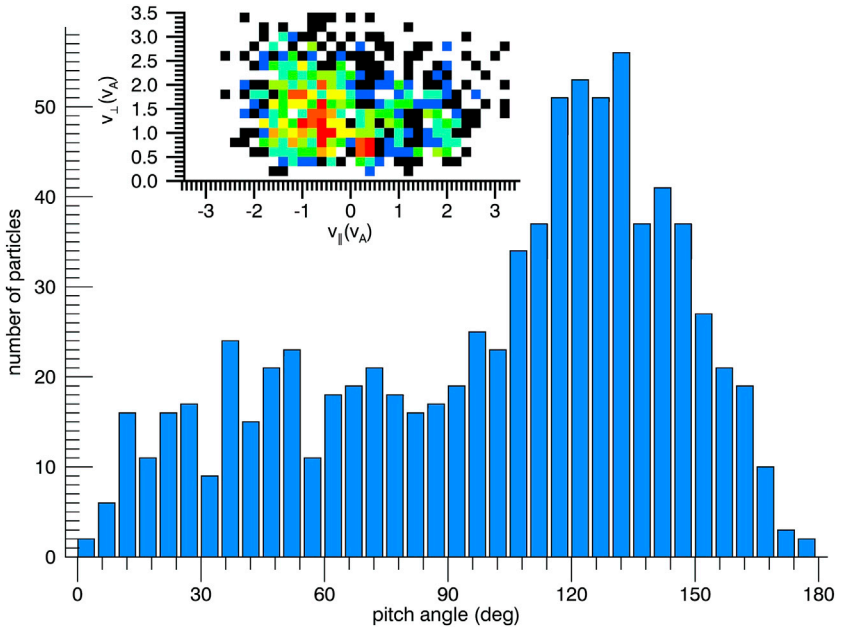

FIGURE 9 | Pitch angle distribution of energetic particles in the sheath from hybrid simulations.

therefore, prompt KH modulation of magnetospheric processes should be expected. Though, the details of energy flow partitioning in the magnetospheric system remains unresolved.

Within the KH vortex, on the other hand, significant plasma heating can be expected based on models for the non-linear interaction between counter-propagating Alfvén waves (Burkholder et al., 2020a). Delamere et al. (2021) examined the heating in 3-D KH simulations and found that indeed the ion heating is consistent with the turbulent heating mechanism (Saur, 2004). Assuming a turbulent spectrum of magnetic field fluctuations ($\delta B_\perp$), the heating rate density for the kinetic Alfvén wave (KAW) is

$$q_{KAW} \sim \frac{1}{2}\frac{\delta B_\perp^3 k_\perp}{\sqrt{\mu_0^3 \rho}}\left(1+k_\perp^2\rho_i^2\right)^{1/2}\left[1+\left(\frac{1}{1+k_\perp^2\rho_i^2}\right)\left(\frac{1}{1+1.25k_\perp^2\rho_i^2}\right)^2\right] \quad (4)$$

where ρ is the mass density and ρ_i is the thermal ion gyroradius. **Figure 11** shows the heating rate density for a 3-D hybrid simulation, showing the localization of regions with significant heating. The contours show the magnitude of the in-plane magnetic field. Future studies should investigate, in detail, the interaction of ions with kinetic Alfvén waves to fully understand the heating process.

8 HEAVY ION EFFECTS

Magnetospheric plasmas are rarely homogeneous and often contain multiple ion species. At Earth, ionospheric outflow can introduce heavy ions into the system (i.e., O^+) (Welling et al., 2015). Bouhram et al. (2005) showed that heavy ions are the dominant contributor to the mass density 30% of the time on the dusk flank and 5% of the time on the dawn flank. In the giant planet magnetospheres, heavy ions are sourced from the moons and play a significant role in magnetospheric dynamics. Magnetospheric heavy ions can also modify the growth rates of the KH instability and at kinetic-scale can significantly modify the structure of the KH modes. (Delamere et al., 2011) showed, using 2-D hybrid simulations, that: 1) growth rates tend to increase when protons (magnetosheath) are separated from the heavies (magnetosphere); 2) growth rates tend to decrease with equal mixtures of protons and heavies; and 3) decrease when only heavy ions are present on both sides of the boundary. In the latter case, it was suggested that inhibited growth was due to suppression of wavelengths less than the ion inertial length. The dawn/dusk asymmetry of heavy ions at Earth could have implications for KH-related plasma transport.

In the limiting case of magnetospheric heavy ions separated from the magnetosheath protons, the initial onset of the KH modes is distinctly different. **Figure 12** shows the results from a 2-D hybrid simulation during the onset of the KH instability for parameters based on Saturn's magnetopause boundary environment (i.e., heavy ions = 17 AMU for water group ions). The top region is the magnetosheath containing protons and the bottom region is the magnetosphere containing heavy ions. From left to right and top to bottom the figure shows 1) the magnetic field pressure, 2) plasma pressure, 3) total ion mass density, 4) proton density, 5) heavy ion density, and 6) normalized local entropy. Perhaps the most striking result is the absence of heavy ions in the magnetosheath. The onset of an $m \sim 6$–7 mode is clearly present, but the heavy ions do not participate in the fluid-scale wave motion because the wavelengths of the $m > 6$ modes are less than the heavy ion inertial length (e.g., cannot generate the compressional magnetosonic fast mode). Thus, the heavies cannot participate in the wave motion. On the other hand, the protons are affected by the surface wave and move in the vortical

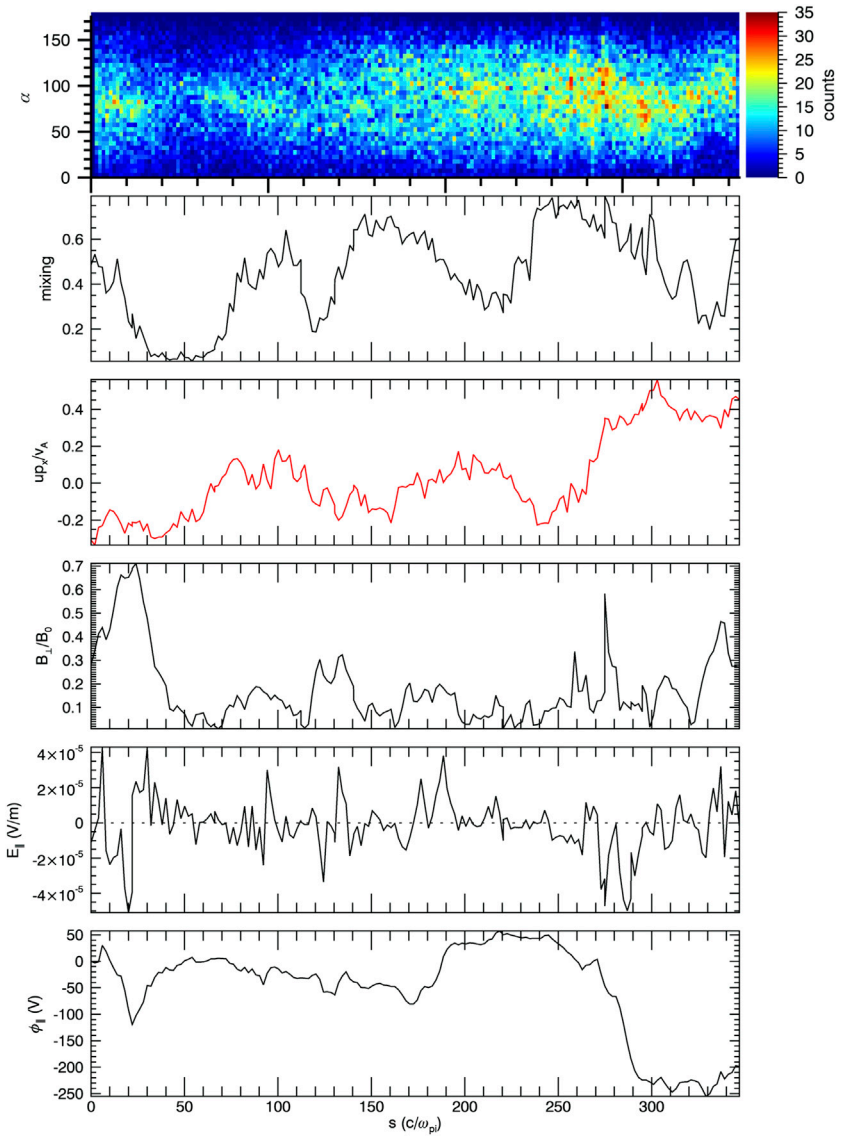

FIGURE 10 | Magnetic field line trace through KH active region in hybrid simulation, showing various properties. From top to bottom is "superthermal" ions, plasma mixing, plasma flow, in-plane magnetic field normalized to the background magnetic field, parallel electric field, and field-aligned potential.

flows. The appearance of protons on the magnetospheric side of the boundary is not balanced by heavy ions in the sheath, leaving voids in plasma pressure. The local entropy (p/ρ^{γ}) increases because of the apparent dominance of the inverse relation with plasma mass density (ρ). In terms of long-term wave evolution, the heavy ions exhibited the expected inverse cascade while the protons showed a forward cascade, saturating at $m = 5$ (**Figure 13**). These simulations are highly idealized but illustrate the potential importance of heavy ions in modifying the KH structure at kinetic scale. Future studies should examine the transfer entropy from conditional mutual information theory to further understand these forward and inverse cascades.

In a 2-D study of density asymmetry with heavy ions, Meier (2012) found that mixing was reduced by increasing the mass density across the magnetopause boundary. The heavy magnetospheric ion (16 amu) fraction was fixed at 25% (with a mixture of protons) while magnetosheath to magnetosphere number density ratio was varied between 2 and 8 (the corresponding mass density ratio varied between 0.5 and 2). Pressure balance was achieved by modifying the magnetospheric proton temperature accordingly. In addition to reduced mixing (presumably due to large gyroradius effects in the non-linear rollup phase), the vortices developed on the low density (magnetospheric) side of the boundary. Thus, the density asymmetry may expedite the formation of mixed boundary layers in the giant magnetosphere as these asymmetric density conditions are often found at Jupiter and Saturn.

Heavy ions can affect mass transport at the magnetopause due to wave-particle interactions. While we have not explicitly investigated these effects in KH hybrid simulations, we note that transport coefficients can be derived following standard methods from the

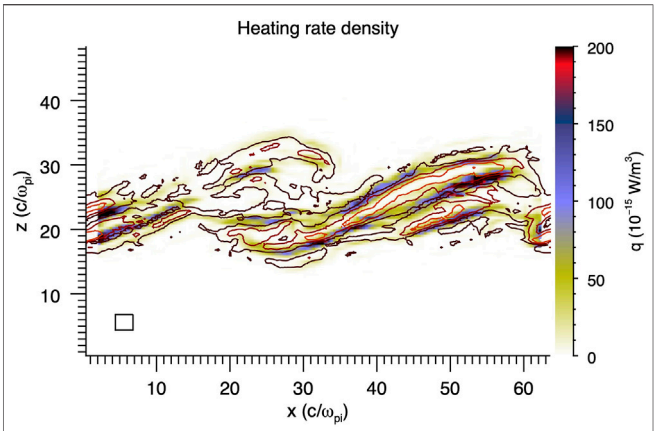

FIGURE 11 | Turbulent heating rate density (Delamere et al., 2021). Contours indicate the magnitude of the in-plane magnetic field.

drift-kinetic or the gyrokinetic equation (Johnson and Cheng, 1997; Chen, 1999; Chaston et al., 2009). In particular, some of the dominant mechanisms include contributions from Landau damping, magnetic field gradient drift, and transit time damping associated with KAW-related magnetic bottles. The presence of heavy ions affects the diffusion coefficients in two ways. First, increased ion mass leads to larger parallel electric fields. This effect is necessary because the ion polarization drift is larger for heavy ions, leading to increased charge separation and thus the parallel electric field required to maintain quasineutrality. Similarly, the ion density fluctuations associated with the polarization drift enhances the magnetic field compressions (particularly in a high β plasma), enhancing the transit time damping. Second, the heavy ions reduce the Alfvén speed which increases the fraction of resonant particles in the wave-particle interaction. Future studies should compare hybrid simulation results with theoretical expectations for the effects on heavy ions on transport.

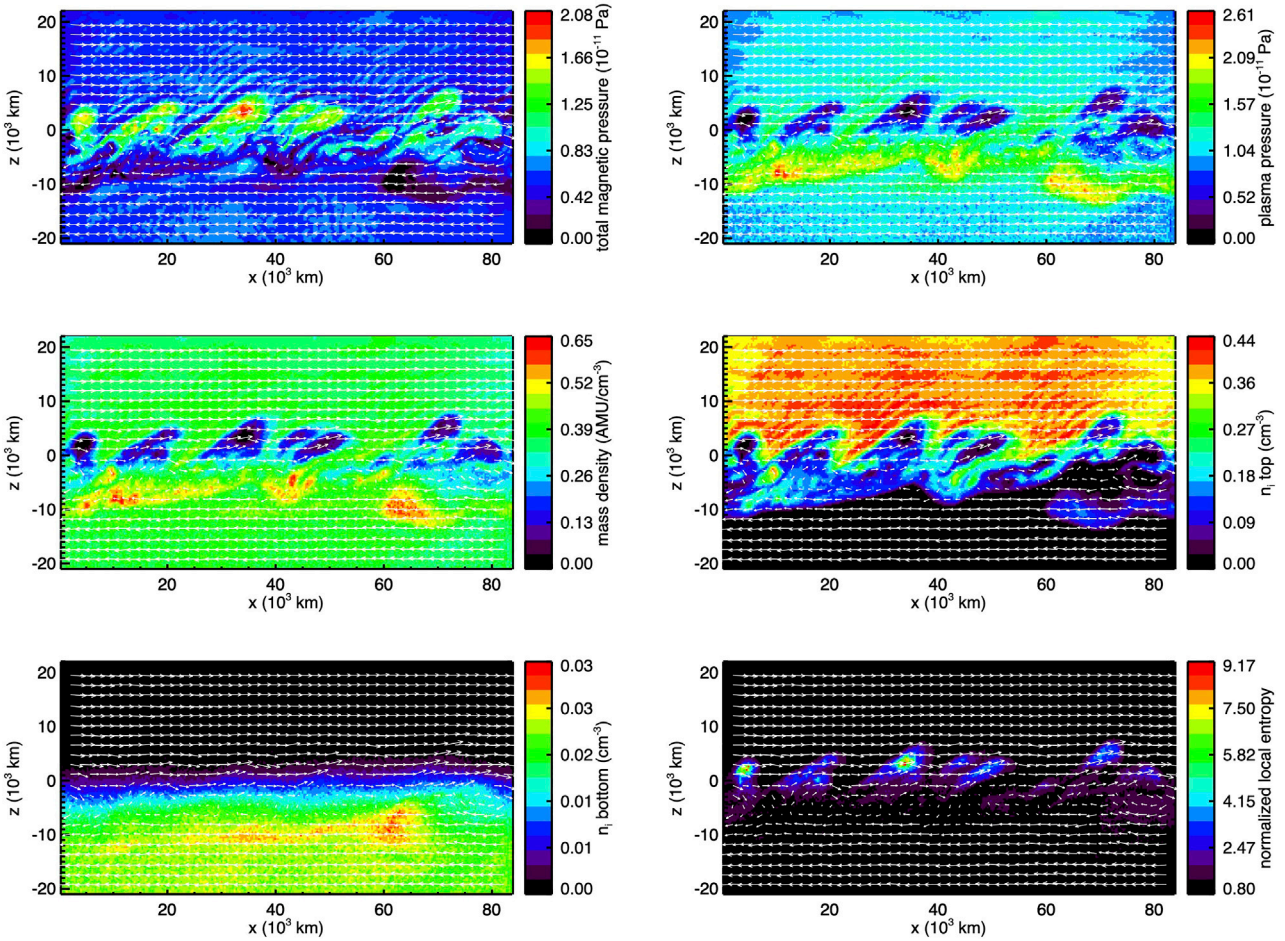

FIGURE 12 | KH waves with heavy ions. The protons are initialized in the top half and the heavies (17 amu) in the bottom half of the domain. From top to bottom and left to right: total magnetic pressure, plasma pressure, mass density, ion density for the top region (protons), ion density for the bottom region (heavies), normalized local entropy.

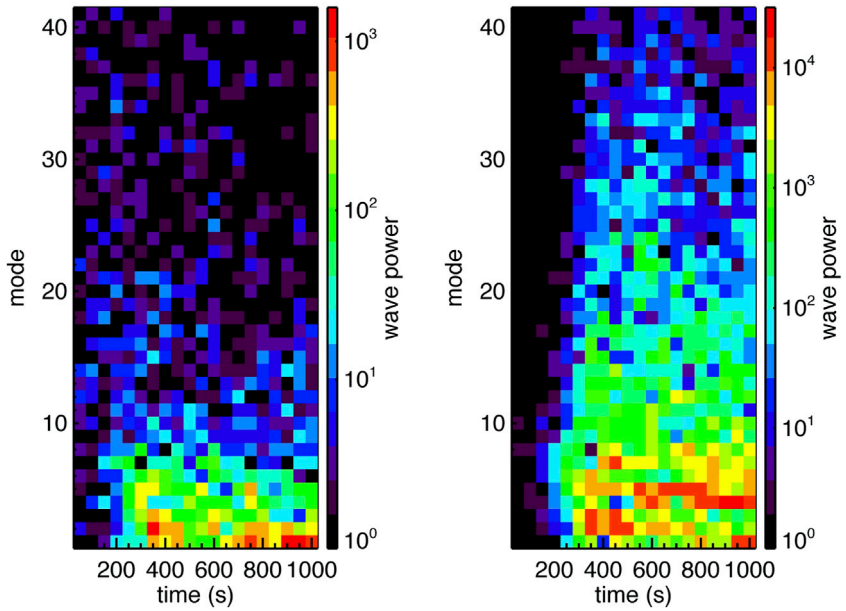

FIGURE 13 | KH wave mode cascade with heavy ions for the simulation shown in **Figure 12**. The heavy ions exhibit an inverse cascade to $m = 1$ while the protons show a forward cascade to $m \sim 5$.

9 ELECTRON ENERGIZATION

While electron kinetic effects cannot be addressed directly in hybrid simulations, it is possible to study the effects of parallel electric fields using electron test particle simulations. The parallel electric fields have been evaluated in both Rayleigh-Taylor (Stauffer et al., 2019) and KH simulations and are found to be independent of the specified resistivity. Estimates for the magnitude of the parallel electric fields (**Section 4**) based on local conditions in the simulations show that the reconnection rates approach or exceed 0.1, consistent with expectation for driven fast reconnection.

Using an ensemble of field line traces (i.e., similar to **Figure 6**), we conducted electron test particle simulations for parallel motion, i.e.,

$$m\frac{dv_{\parallel}}{dt} = qE_{\parallel} \tag{5}$$

We initialized a 20 eV Maxwellian distribution on the field line ensemble. **Figure 14** shows the phase space ($v_{\parallel}$ vs. y) at a snapshot in time for a sample field line, showing field-aligned streaming (acceleration) as well as trapped populations. Assuming that the evolution of the non-linear KH vortex modifies the parallel electric field configuration in time, we conducted an ensemble average to determine the likely steady state electron velocity distribution. For Saturn-like conditions, the final distribution was consistent with a 120 eV Maxwellian. Curiously, this is consistent with the thermal electron temperature in Saturn's outer magnetosphere (Neupane, 2021), but further study would be required to understand how internal radial transport could affect the thermal electron temperature. **Figure 15** shows the initial distribution (red) with a 20 eV Maxwellian fit and the final distribution (blue) with a 120 eV Maxwellian fit. A snapshot of any given field line would likely reveal bidirectional electron beams. Such beams are commonly observed in KH active regions of the terrestrial magnetopause boundary (Burkholder et al., 2020b). Nykyri et al. (2021) suggested that, among other mechanisms, magnetic reconnection could be a candidate for explaining the > 100 eV counter-streaming electrons observed by the Magnetosphere Multiscale mission. An example topic for further study is the role of oblique whistler waves in electron energization. Finally, the addition of heavy ions would enhance the parallel electric fields as noted in **Section 8**, leading to more effective electron energization.

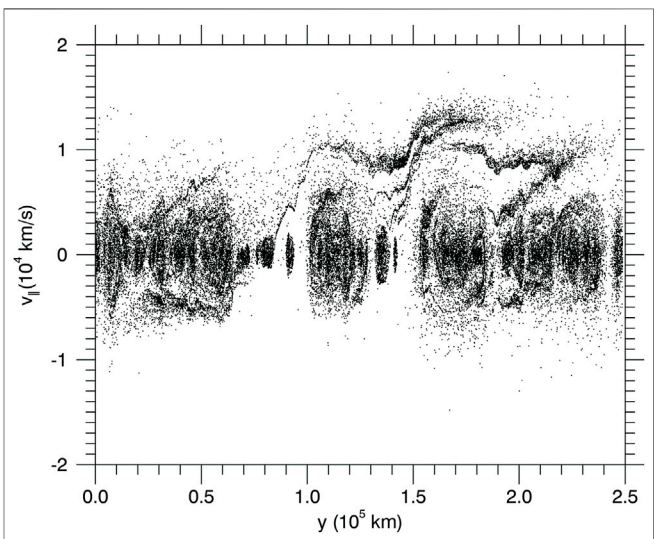

FIGURE 14 | Electron test particle simulations using the sample magnetic field line trace. The distribution in **Figure 15** is an ensemble average of many sample field lines taken from the KH active region.

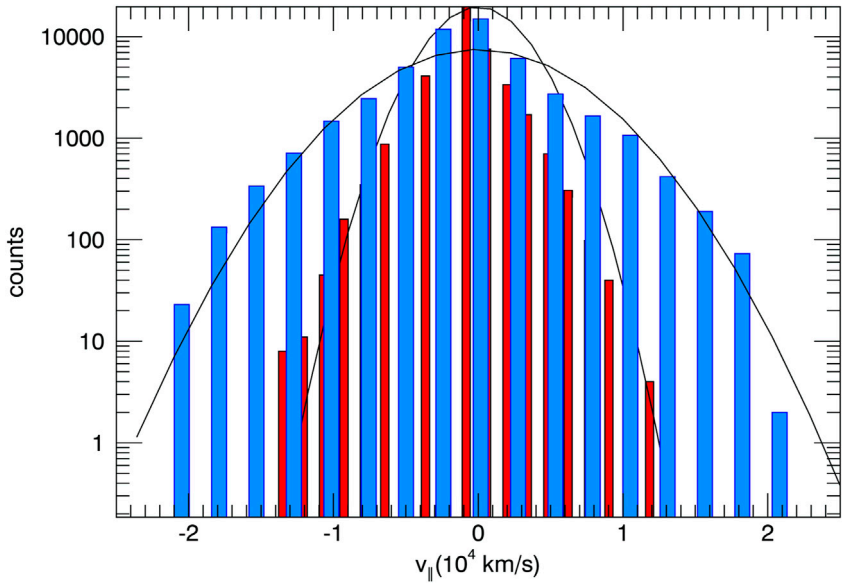

FIGURE 15 | The parallel velocity distribution from electron test particle simulations. Red is the initial 20 eV distribution. Blue is the ~120 eV ensemble-averaged distribution.

10 CONCLUSION

Considerable progress has been made with regard to ion kinetic-scale processes associated with the Kelvin-Helmholtz instability. Here we summarize the key advances in understanding and on directions for future studies.

- The growth of KH modes in our simulations can be described as a inverse cascade. For typical magnetopause boundary thickness (few ion inertial lengths), the fastest growing modes are relatively small scale (less than planetary radii) and, under certain conditions, could evolve to global scales (few planetary radii) as the structures advect down the tail flanks.
- The inverse cascade results in smaller scale structures being subsumed by larger scale structure, resulting in complex magnetic field topologies with a patchy network of strong guide field reconnection sites.
- Maxwell stresses associated with magnetic field line threading of the magnetopause boundary lead to substantial momentum transport and contribute to viscous-like tangential drag at the boundary.
- Plasma transport is facilitated by the patchy network of reconnection sites and diffusive transport is possible due, in part, to finite gyroradius effects. Energetic particles can be transported across the boundary with a strong field-aligned component to the velocity distribution.
- Turbulent magnetic field spectra can lead to substantial ion heating rates due to the non-linear interaction between counter propagating Alfvén waves. Future work should focus on the heating mechanism due to the interaction between particles and the kinetic Alfvén waves (Johnson and Cheng, 2001).
- Heavy ions can alter the growth rates, transport rates, and modify ion kinetic-scale structure due to competing ion scales during KH wave evolution. In the limiting case, heavy ions contained entirely on, e.g., the magnetospheric side of the boundary will be unaffected by KH wavelengths less than the heavy ion inertial length.
- Bidirectional electron beams can be expected from the parallel electric fields associated with the strong guide field reconnection.

DATA AVAILABILITY STATEMENT

The original contributions presented in the study are included in the article/Supplementary Material, further inquiries can be directed to the corresponding author.

AUTHOR CONTRIBUTIONS

PD contributed to all aspects of this article. Author NB provided the field line tracing analysis. XM contributed to the general discussion of the interaction between reconnection of KH modes in three dimensions. JJ contributed to the analysis of heavy ion effects and turbulent heating.

FUNDING

The authors acknowledge support from NASA grants 80NSSC20K1279 and 80NSSC19K0822.

REFERENCES

Bagenal, F., and Delamere, P. A. (2011). Flow of Mass and Energy in the Magnetospheres of Jupiter and Saturn. *J. Geophys. Res.* 116, A05209. doi:10.1029/2010JA016294

Bavassano Cattaneo, M. B., Marcucci, M. F., Bogdanova, Y. V., Rème, H., Dandouras, I., Kistler, L. M., et al. (2010). Global Reconnection Topology as Inferred from Plasma Observations inside Kelvin-Helmholtz Vortices. *Ann. Geophys.* 28, 893–906. doi:10.5194/angeo-28-893-2010

Boris, J. (1970). *The Acceleration Calculation from a Scalar Potential*. Plasma Physics LaboratoryPrinceton University. MATT-152.

Bouhram, M., Klecker, B., Paschmann, G., Haaland, S., Hasegawa, H., Blagau, A., et al. (2005). Survey of Energetic O+ Ions Near the Dayside Mid-latitude Magnetopause with Cluster. *Ann. Geophys.* 23, 1281–1294. doi:10.5194/angeo-23-1281-2005

Burkholder, B., Delamere, P. A., Ma, X., Thomsen, M. F., Wilson, R. J., and Bagenal, F. (2017). Local Time Asymmetry of Saturn's Magnetosheath Flows. *Geophys. Res. Lett.* 44, 5877–5883. doi:10.1002/2017GL073031

Burkholder, B. L., Delamere, P. A., Johnson, J. R., and Ng, C. S. (2020a). Identifying Active Kelvin-Helmholtz Vortices on Saturn's Magnetopause Boundary. *Geophys. Res. Lett.* 47, e84206. doi:10.1029/2019GL084206

Burkholder, B. L., Delamere, P. A., Johnson, J. R., and Ng, C. S. (2019). Identifying Active Kelvin-Helmholtz Vortices on Saturn's Magnetopause Boundary, submitted to Geophys. *Res. Lett*.

Burkholder, B. L., Nykyri, K., Ma, X., Rice, R., Fuselier, S. A., Trattner, K. J., et al. (2020b). Magnetospheric Multiscale Observation of an Electron Diffusion Region at High Latitudes. *Geophys. Res. Lett.* 47, e87268. doi:10.1029/2020GL087268

Chandrasekhar, S. (1961). Hydrodynamic and Hydromagnetic Stability.

Chaston, C. C., Johnson, J. R., Wilber, M., Acuna, M., Goldstein, M. L., and Reme, H. (2009). Kinetic Alfvén Wave Turbulence and Transport through a Reconnection Diffusion Region. *Phys. Rev. Lett.* 102, 015001. doi:10.1103/PhysRevLett.102.015001

Chaston, C. C. (2015). Magnetic Reconnection in the Auroral Acceleration Region. *Geophys. Res. Lett.* 42, 1646–1653. doi:10.1002/2015GL063164

Chen, L. (1999). Theory of Plasma Transport Induced by Low-Frequency Hydromagnetic Waves. *J. Geophys. Res.* 104, 2421–2427. doi:10.1029/1998JA900051

Cowee, M. M., Winske, D., and Gary, S. P. (2010). Hybrid Simulations of Plasma Transport by Kelvin-Helmholtz Instability at the Magnetopause: Density Variations and Magnetic Shear. *J. Geophys. Res.* 115. doi:10.1029/2009JA015011

Cowee, M. M., Winske, D., and Gary, S. P. (2009). Two-dimensional Hybrid Simulations of Superdiffusion at the Magnetopause Driven by Kelvin-Helmholtz Instability. *J. Geophys. Res.* 114. doi:10.1029/2009JA014222

Delamere, P. A., and Bagenal, F. (2010). Solar Wind Interaction with Jupiter's Magnetosphere. *J. Geophys. Res.* 115, a–n. doi:10.1029/2010JA015347

Delamere, P. A., Burkholder, B., and Ma, X. (2018). Three-Dimensional Hybrid Simulation of Viscous-Like Processes at Saturn's Magnetopause Boundary. *Geophys. Res. Lett.* 45, 7901–7908. doi:10.1029/2018GL078922

Delamere, P. A., Ng, C. S., Damiano, P. A., Neupane, B. R., Johnson, J. R., Burkholder, B., et al. (2021). Kelvin-Helmholtz-Related Turbulent Heating at Saturn's Magnetopause Boundary. *J. Geophys. Res. Space Phys.* 126, e28479. doi:10.1029/2020JA028479

Delamere, P. A., Wilson, R. J., Eriksson, S., and Bagenal, F. (2013). Magnetic Signatures of Kelvin-Helmholtz Vortices on Saturn's Magnetopause: Global Survey. *J. Geophys. Res. Space Phys.* 118, 393–404. doi:10.1029/2012ja018197

Delamere, P. A., Wilson, R. J., and Masters, A. (2011). Kelvin-Helmholtz Instability at Saturn's Magnetopause: Hybrid Simulations. *J. Geophys. Res.* 116, a–n. doi:10.1029/2011JA016724

Fadanelli, S., Faganello, M., Califano, F., Cerri, S. S., Pegoraro, F., and Lavraud, B. (2018). North-South Asymmetric Kelvin-Helmholtz Instability and Induced Reconnection at the Earth's Magnetospheric Flanks. *J. Geophys. Res. Space Phys.* 123, 9340–9356. doi:10.1029/2018JA025626

Faganello, M., Califano, F., Pegoraro, F., and Andreussi, T. (2012). Double Mid-latitude Dynamical Reconnection at the Magnetopause: An Efficient Mechanism Allowing Solar Wind to Enter the Earth's Magnetosphere. *Epl* 100, 69001. doi:10.1209/0295-5075/100/69001

Faganello, M., Califano, F., and Pegoraro, F. (2008). Competing Mechanisms of Plasma Transport in Inhomogeneous Configurations with Velocity Shear: The Solar-Wind Interaction with Earth's Magnetosphere. *Phys. Rev. Lett.* 100, 015001. doi:10.1103/PhysRevLett.100.015001

Faganello, M., Califano, F., Pegoraro, F., and Retinò, A. (2014). Kelvin-Helmholtz Vortices and Double Mid-latitude Reconnection at the Earth's Magnetopause: Comparison between Observations and Simulations. *Epl* 107, 19001. doi:10.1209/0295-5075/107/19001

Faganello, M., Pegoraro, F., Califano, F., and Marradi, L. (2010). Collisionless Magnetic Reconnection in the Presence of a Sheared Velocity Field. *Phys. Plasmas* 17, 062102. doi:10.1063/1.3430640

Hesse, M., and Schindler, K. (1988). A Theoretical Foundation of General Magnetic Reconnection. *J. Geophys. Res.* 93, 5559–5567. doi:10.1029/JA093iA06p05559

Johnson, J. R., and Cheng, C. Z. (1997). Kinetic Alfvén Waves and Plasma Transport at the Magnetopause. *Geophys. Res. Lett.* 24, 1423–1426. doi:10.1029/97GL01333

Johnson, J. R., and Cheng, C. Z. (2001). Stochastic Ion Heating at the Magnetopause Due to Kinetic Alfvã©n Waves. *Geophys. Res. Lett.* 28, 4421–4424. doi:10.1029/2001GL013509

Johnson, J. R., Wing, S., and Delamere, P. A. (2014). Kelvin Helmholtz Instability in Planetary Magnetospheres. *Space Sci. Rev.* 184, 1–31. doi:10.1007/s11214-014-0085-z

Kane Yee, K. (1966). Numerical Solution of Initial Boundary Value Problems Involving maxwell's Equations in Isotropic media. *IEEE Trans. Antennas Propagat.* 14, 302–307. doi:10.1109/TAP.1966.1138693

Knoll, D. A., and Chacón, L. (2002). Magnetic Reconnection in the Two-Dimensional Kelvin-Helmholtz Instability. *Phys. Rev. Lett.* 88, 215003. doi:10.1103/PhysRevLett.88.215003

La Belle-Hamer, A. L., Otto, A., and Lee, L. C. (1995). Magnetic Reconnection in the Presence of Sheared Flow and Density Asymmetry: Applications to the Earth's Magnetopause. *J. Geophys. Res.* 100, 11875–11890. doi:10.1029/94JA0096910.1029/95ja00969

Lin, Y., Johnson, J. R., and Wang, X. (2012). Three-Dimensional Mode Conversion Associated with Kinetic Alfvén Waves. *Phys. Rev. Lett.* 109. doi:10.1103/PhysRevLett.109.125003

Lin, Y., Johnson, J. R., and Wang, X. Y. (2010). Hybrid Simulation of Mode Conversion at the Magnetopause. *J. Geophys. Res.* 115, a–n. doi:10.1029/2009JA014524

Ma, X., Delamere, P. A., Nykyri, K., Burkholder, B., Neupane, B., and Rice, R. C. (2019). Comparison between Fluid Simulation with Test Particles and Hybrid Simulation for the Kelvin-Helmholtz Instability. *J. Geophys. Res. Space Phys.* 124, 6654–6668. doi:10.1029/2019JA026890

Ma, X., Delamere, P., Otto, A., and Burkholder, B. (2017). Plasma Transport Driven by the Three-Dimensional Kelvin-Helmholtz Instability. *J. Geophys. Res. Space Phys.* 122 (10), 10,382–10,395. doi:10.1002/2017JA024394

Ma, X., Otto, A., and Delamere, P. A. (2014a). Interaction of Magnetic Reconnection and Kelvin-Helmholtz Modes for Large Magnetic Shear: 1. Kelvin-Helmholtz Trigger. *J. Geophys. Res. Space Phys.* 119, 781–797. doi:10.1002/2013JA019224

Ma, X., Otto, A., and Delamere, P. A. (2014b). Interaction of Magnetic Reconnection and Kelvin-Helmholtz Modes for Large Magnetic Shear: 2. Reconnection Trigger. *J. Geophys. Res. Space Phys.* 119, 808–820. doi:10.1002/2013JA019225

Matsumoto, Y., and Hoshino, M. (2004). Onset of Turbulence Induced by a Kelvin-Helmholtz Vortex. *Geophys. Res. Lett.* 31, 2807. doi:10.1029/2003GL018195

Mauk, B. H., Cohen, I. J., Haggerty, D. K., Hospodarsky, G. B., Connerney, J. E. P., Anderson, B. J., et al. (2019). Investigation of Mass-/Charge-Dependent Escape of Energetic Ions across the Magnetopauses of Earth and Jupiter. *J. Geophys. Res. Space Phys.* 124, 5539–5567. doi:10.1029/2019JA026626

Meier, M. (2012). ProQuest Dissertations And Theses; Thesis (Ph.D.). *Dissertation Abstracts International* (Boulder, CO: University of Colorado) 74–05 (E), Section: B, 156.

Merkin, V. G., Lyon, J. G., and Claudepierre, S. G. (2013). Kelvin-Helmholtz Instability of the Magnetospheric Boundary in a Three-Dimensional Global MHD Simulation during Northward IMF Conditions. *J. Geophys. Res. Space Phys.* 118, 5478–5496. doi:10.1002/jgra.50520

Miura, A. (1984). Anomalous Transport by Magnetohydrodynamic Kelvin-Helmholtz Instabilities in the Solar Wind-Magnetosphere Interaction. *J. Geophys. Res.* 89, 801. doi:10.1029/ja089ia02p00801

Miura, A., and Pritchett, P. L. (1982). Nonlocal Stability Analysis of the MHD Kelvin-Helmholtz Instability in a Compressible Plasma. *J. Geophys. Res.* 87, 7431–7444. doi:10.1029/JA087iA09p07431

Nakamura, T. K. M., and Fujimoto, M. (2006). Magnetic Reconnection within MHD-Scale Kelvin-Helmholtz Vortices Triggered by Electron Inertial Effects. *Adv. Space Res.* 37, 522–526. Boundary Layers, Waves and Non-Linear Dynamical Processes. doi:10.1016/j.asr.2005.01.057

Neupane, B. R. (2021). *Plasma Transport and Magnetic Flux Circulation in Saturn's Magnetosphere*. Fairbanks, AK: Ph.D. thesis, University of Alaska Fairbanks.

Nykyri, K., Ma, X., Burkholder, B., Rice, R., Johnson, J. R., Kim, E. K., et al. (2021). MMS Observations of the Multiscale Wave Structures and Parallel Electron Heating in the Vicinity of the Southern Exterior Cusp. *J. Geophys. Res. Space Phys.* 126, e27698. doi:10.1029/2019JA027698

Nykyri, K., and Otto, A. (2001). Plasma Transport at the Magnetospheric Boundary Due to Reconnection in Kelvin-Helmholtz Vortices. *Geophys. Res. Lett.* 28, 3565–3568. doi:10.1029/2001GL013239

Otto, A., and Birk, G. T. (1993). Formation of Thin Auroral Arcs by Current Striation. *Geophys. Res. Lett.* 20, 2833–2836. doi:10.1029/93gl02492

Otto, A., and Fairfield, D. H. (2000). Kelvin-helmholtz Instability at the Magnetotail Boundary: MHD Simulation and Comparison with Geotail Observations. *J. Geophys. Res.* 105, 175. doi:10.1029/1999ja000312

Otto, A. (2007). Plasma Entry and Kelvin-Helmholtz Modes at the Flanks of the Magnetosphere. American Geophysical Union, Fall Meeting 2007, December 2007. abstract id.SM11B-07.

Pu, Z.-Y., and Kivelson, M. G. (1983). Kelvin-Helmholtz Instability at the Magnetopause: Energy Flux into the Magnetosphere. *J. Geophys. Res.* 88, 853–862. doi:10.1029/JA088iA02p00853

Saur, J. (2004). Turbulent Heating of Jupiter's Middle Magnetosphere. *ApJ* 602, L137–L140. doi:10.1086/382588

Schindler, K., Hesse, M., and Birn, J. (1988). General Magnetic Reconnection, Parallel Electric fields, and Helicity. *J. Geophys. Res.* 93, 5547–5557. doi:10.1029/JA093iA06p05547

Sergis, N., Jackman, C. M., Masters, A., Krimigis, S. M., Thomsen, M. F., Hamilton, D. C., et al. (2013). Particle and Magnetic Field Properties of the Saturnian Magnetosheath: Presence and Upstream Escape of Hot Magnetospheric Plasma. *J. Geophys. Res. Space Phys.* 118, 1620–1634. doi:10.1002/jgra.50164

Seyler, C. E. (1990). A Mathematical Model of the Structure and Evolution of Small-Scale Discrete Auroral Arcs. *J. Geophys. Res.* 95, 17199–17215. doi:10.1029/JA095iA10p17199

Sisti, M., Faganello, M., Califano, F., and Lavraud, B. (2019). Satellite Data-Based 3-D Simulation of Kelvin-Helmholtz Instability and Induced Magnetic Reconnection at the Earth's Magnetopause. *Geophys. Res. Lett.* 46, 11597–11605. doi:10.1029/2019GL083282

Sorathia, K. A., Merkin, V. G., Panov, E. V., Zhang, B., Lyon, J. G., Garretson, J., et al. (2020). Ballooning-Interchange Instability in the Near-Earth Plasma Sheet and Auroral Beads: Global Magnetospheric Modeling at the Limit of the MHD Approximation. *Geophys. Res. Lett.* 47, e88227. doi:10.1029/2020GL088227

Stauffer, B. H., Delamere, P. A., Ma, X., Neupane, B. R., and Burkholder, B. L. (2019). Hybrid Simulations of Magnetodisc Transport Driven by the Rayleigh-Taylor Instability. *J. Geophys. Res. Space Phys.* 124, 5107–5120. doi:10.1029/2018JA026420

Takagi, K., Hashimoto, C., Hasegawa, H., Fujimoto, M., and TanDokoro, R. (2006). Kelvin-helmholtz Instability in a Magnetotail Flank-like Geometry: Three-Dimensional Mhd Simulations. *J. Geophys. Res.* 111. doi:10.1029/2006JA011631

Tenerani, A., Faganello, M., Califano, F., and Pegoraro, F. (2010). Nonlinear Vortex Dynamics in an Inhomogeneous Magnetized Plasma with a Sheared Velocity Field. *Plasma Phys. Control Fusion* 53, 015003. doi:10.1088/0741-3335/53/1/015003

Vernisse, Y., Lavraud, B., Eriksson, S., Gershman, D. J., Dorelli, J., Pollock, C., et al. (2016). Signatures of Complex Magnetic Topologies from Multiple Reconnection Sites Induced by Kelvin-Helmholtz Instability. *J. Geophys. Res. Space Phys.* 121, 9926–9939. doi:10.1002/2016JA023051

Welling, D. T., André, M., Dandouras, I., Delcourt, D., Fazakerley, A., Fontaine, D., et al. (2015). The Earth: Plasma Sources, Losses, and Transport Processes. *Space Sci. Rev.* 192, 145–208. doi:10.1007/s11214-015-0187-2

Zhang, B., Delamere, P. A., Ma, X., Burkholder, B., Wiltberger, M., Lyon, J. G., et al. (2018). Asymmetric Kelvin-Helmholtz Instability at Jupiter's Magnetopause Boundary: Implications for Corotation-Dominated Systems. *Geophys. Res. Lett.* 45, 56–63. doi:10.1002/2017GL076315

Zhang, B., Sorathia, K. A., Lyon, J. G., Merkin, V. G., Garretson, J. S., and Wiltberger, M. (2019). GAMERA: A Three-Dimensional Finite-Volume MHD Solver for Non-orthogonal Curvilinear Geometries. *ApJS* 244, 20. doi:10.3847/1538-4365/ab3a4c

Conflict of Interest: The authors declare that the research was conducted in the absence of any commercial or financial relationships that could be construed as a potential conflict of interest.

Publisher's Note: All claims expressed in this article are solely those of the authors and do not necessarily represent those of their affiliated organizations, or those of the publisher, the editors and the reviewers. Any product that may be evaluated in this article, or claim that may be made by its manufacturer, is not guaranteed or endorsed by the publisher.

frontiers in Astronomy and Space Sciences

ORIGINAL RESEARCH
published: 20 December 2021
doi: 10.3389/fspas.2021.758241

Global MHD Simulation of the Weak Southward IMF Condition for Different Time Resolutions

Kyung Sun Park[1,2]*

[1]Department Astronomy and Space Science, Chungbuk National University, Cheongju, South Korea, [2]Basic Research Institute, Chungbuk National University, Cheongju, South Korea

We performed high-resolution three-dimensional global MHD simulations to determine the impact of weak southward interplanetary magnetic field (IMF) (Bz = −2 nT) and slow solar wind to the Earth's magnetosphere and ionosphere. We considered two cases of differing, uniform time resolution with the same grid spacing simulation to find any possible differences in the simulation results. The simulation results show that dayside magnetic reconnection and tail reconnection continuously occur even during the weak and steady southward IMF conditions. A plasmoid is generated on closed plasma sheet field lines. Vortices are formed in the inner side of the magnetopause due to the viscous-like interaction, which is strengthened by dayside magnetic reconnection. We estimated the dayside magnetic reconnection which occurred in relation to the electric field at the magnetopause and confirmed that the enhanced electric field is caused by the reconnection and the twisted structure of the electric field is due to the vortex. The simulation results of the magnetic field and the plasma properties show quasi-periodic variations with a period of 9–11 min between the appearances of vortices. Also the peak values of the cross-polar cap potential are both approximately 50 kV, the occurrence time of dayside reconnections are the same, and the polar cap potential patterns are the same in both cases. Thus, there are no significant differences in outcome between the two cases.

Keywords: global MHD simulation, reconnection, vortex, magnetopause, cross-polar cap potential

OPEN ACCESS

Edited by:
Kyoung-Joo Hwang, Southwest Research Institute (SwRI), United States

Reviewed by:
Steven Petrinec, Lockheed Martin Solar and Astrophysics Laboratory (LMSAL), United States
Xiaocheng Guo, National Space Science Center (CAS), China

***Correspondence:**
Kyung Sun Park
kspark@chungbuk.ac.kr

Specialty section:
This article was submitted to Space Physics, a section of the journal Frontiers in Astronomy and Space Sciences

Received: *13 August 2021*
Accepted: *22 November 2021*
Published: *20 December 2021*

Citation:
Park KS (2021) Global MHD Simulation of the Weak Southward IMF Condition for Different Time Resolutions. Front. Astron. Space Sci. 8:758241. doi: 10.3389/fspas.2021.758241

INTRODUCTION

Dayside magnetic reconnection between the geomagnetic field and the interplanetary magnetic field (IMF) is the most important for understanding the Earth's magnetosphere dynamics. There have been many observations, simulations and theory studies on the reconnection process of the magnetosphere. Dungey (1961) first examined magnetic reconnection for a purely southward IMF. The magnetic reconnection occurs efficiently in the dayside when IMF is southward and the rate is the largest where the magnetosheath magnetic field is antiparallel to the geomagnetic field (Sonnerup, 1974; Crooker, 1979; Luhmann et al., 1984; Park et al., 2006). Also, Park et al. (2010) found that antiparallel reconnection occurs dominantly on the magnetosphere outer boundary even in complicated cases where northward IMF, non-zero dipole tilt, and non-zero IMF B_y existed.

On the other hand, viscous-like interaction such as the Kelvin-Helmholtz (KH) instability (Dungey, 1955; Miura, 1984, 1995; Kivelson and Chen, 1995) is generally known to be driven by

the velocity shear with a rapid magnetosheath plasma at the boundary for northward IMF condition. There are MHD simulation studies that the KH vortices have properties with short time intervals of about 2–4 min (Otto and Fairfield, 2000; Guo, et al., 2010; Ogino, 2011). Merkin et al. (2013) also examined the double-vortex sheet with vortex trains propagating along the inner and outer edges of the boundary layer.

The magnetosphere boundary can also fluctuate in response to solar wind dynamic pressure pulse. In particular, observations of the magnetospheric magnetic field response showed quasi-periodic pulses with a period of 8 min (Sibeck et al., 1989; Sibeck 1990, 1992; Sibeck and Gosling, 1996). Sibeck (1990) reviewed that the pressure pulses mean large-amplitude solar wind dynamic pressure pulses recurring on time scales of 5–15 min that impact the Earth's bow shock. Lysak and Lee (1992) used a numerical model to show that field line resonances are dependent on the frequency of the driving pulse. Using a global MHD simulation, Claudepierre et al. (2010) found that the solar wind dynamic pressure fluctuations drive toroidal mode field line resonances on the dayside.

There have been few studies on the vortices in the magnetospheric boundary layer under southward IMF conditions. Claudepierre et al. (2008) performed high-resolution global MHD simulations to show that the pulsations of surface waves were generated by the KH instability at the magnetopause boundary for varying solar wind velocities under a southward IMF condition. Additionally, developed KH waves in the magnetopause have been reported using observational data and simulation under the southward IMF conditions (Hwang et al., 2011; Kavosi and Raeder 2015; Nakamura et al., 2020). Hwang et al. (2011) showed that the first *in situ* observation by Cluster of nonlinearly developed KH wave during ~17 min under southward IMF conditions. Kavosi and Raeder (2015) reported the relative KH waves occurrence rate as a function of solar wind parameters by 7 years of THEMIS(Time History of Events and Macro scale Interactions during Substorms) data. The statistical analysis showed that KH waves rate increase with solar wind speed, and Alfven Mach number and number density and also the KH waves occur about 10% for southward IMF. Park et al. (2020) found that the dayside reconnection leads to the quasi-periodic vortex with 8–10 min in the inner magnetopause boundary under the long duration of the solar wind and weak southward IMF.

However, it still needs to be understood what kind of factors of magnetopause boundary are more important depending on the solar wind and IMF conditions. There has been no previous study examining the significance of applying different grid spacing and time resolution to understand the magnetic field topology and magnetosphere and ionosphere response using MHD simulations, as attempted in this paper.

In *Simulation Model*, we briefly introduce the simulation model. In *Simulation Results*, we present the simulation results. In *Summary and Discussion*, a summary and discussion of the results are presented.

SIMULATION MODEL

The three-dimensional simulation is based on solving the normalized resistive MHD and Maxwell's equation as an initial value problem by using a modified leap-frog scheme. We provide only a brief review of the simulation model as it has been described in detail elsewhere (Ogino et al., 1992; Park et al., 2006). We used a quarter simulation box with -60 $R_E \leq X \leq$ 20 R_E, 0 $R_E \leq Y \leq$ 40 R_E, and 0 $R_E \leq Z \leq$ 40 R_E dimensions in Cartesian solar magnetospheric coordinates, assuming symmetry conditions are consistent with the dipole magnetic field. The number of grid points was (n_X, n_Y, n_Z) = (800, 400, 400), with a uniform grid spacing of 0.1 R_E. A mirror dipole field was applied to the solar wind at time t = 0, to form the shape of the magnetosphere. A smoothing function damps all perturbations near the ionosphere, including parallel currents. The parallel current does not close in the ionosphere, it partly closes above the ionospheric boundary. The internal ionospheric boundary conditions are set by forcing a static equilibrium at r = 2.5 R_E. A uniform solar wind conditions a velocity, V_{sw} = 300 km/s, a number density, n_{sw} = 5 cm^{-3} with a pure northward IMF B_z (= 5 nT) was held constant for up 2 h in order to obtain quasi-steady state of the magnetospheric configuration as the initial condition.

In the following three conditions, the weak and steady southward IMF of B_z = −2 nT entered the upstream boundary for 2 h. The beginning time of this simulation results are t = 0. The time resolutions are 1 min (Case 1), 30 s (Case 2), and 10 s (Case3) respectively in this simulation.

SIMULATION RESULTS

We demonstrate the response of the magnetospheric configuration of the 3D magnetic field lines in **Figure 1**. The Earth is located at the origin, closed field lines that connect to the Earth in both hemispheres are colored green, open field lines that connect to the ionospheres at one end and to the distant IMF at the other end are colored blue, and the twisted field lines in tail region are colored pink in **Figure 1**. The dayside reconnection initially and continuously occurs near the subsolar region (the magnetic equator) at t = 9 min during the simulation in the two cases of weak southward IMF. The dayside reconnection regions are located between the northern and southern hemispheres with highly kinked open field lines. The reconnected open field lines on the dayside move tailward through the dusk (dawn) side with a magnetosheath flow. The closed plasma sheet field line in tail is widely stretched tailward until the occurrence of tail reconnection. Plasmoids are generated near the midnight region (about ~14.5R_E) after precisely 85 min in Case 1 and after precisely 85 min and 30 s in Case 2.

Figure 2 shows the time evolutions with specific location at (X, Y, Z)= (−25, 0, 0) R_E the strength of magnetic field, $|\mathbf{B}|$, z-component of magnetic field, B_z, and the total velocity $|\mathbf{V}|$, x-component of velocity, V_x, the density (ρ) and the plasma (P) for two cases. The vertical dashed lines denote the center of the plasmoid. In a plasmoid the B_z component of the magnetic field has a bipolar signature and the B_y component is nearly zero in

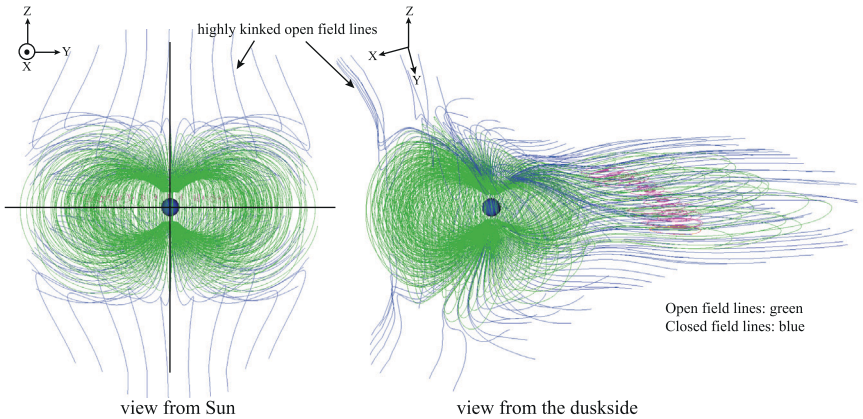

FIGURE 1 | 3D magnetic field line configuration at a specific time, t = 85 min (Case 1) in simulation. Closed field lines that connect to the Earth in both hemispheres are green, open field lines that connect to the ionospheres at one end and to the distant IMF at the other end are blue, and the twisted field lines in tail region refer to pink.

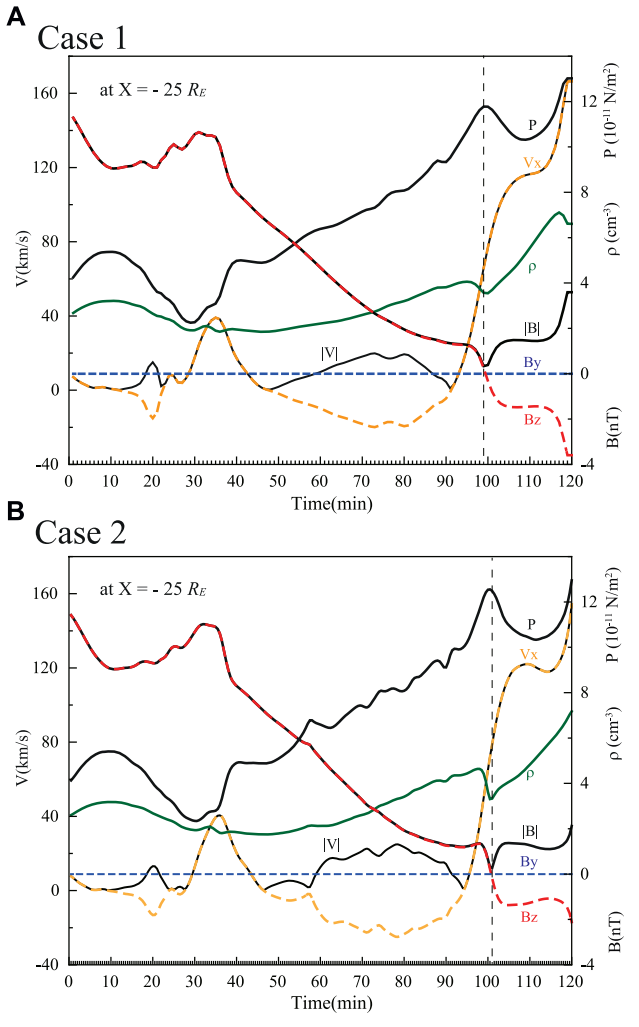

FIGURE 2 | The time evolutions of the strength of magnetic field, **|B|**, z-component of magnetic field, Bz, and the total velocity **|V|**, x-component of velocity, V_x, the density (ρ) and the plasma (*P*) for two cases.

both cases. The magnetic field strength of magnetic field decreases slightly when the plasma pressure reaches the maximum and the density decrease in the center of the plasmoid. These are typical feature for a plasmoid. In both cases, there was no helical magnetic field line in the center of plasmoid during the simulation for weak solar wind and southward IMF conditions. The plasmoid moves tailward with a velocity above 100 km/s as plasmasheet reconnection continues to involve lobe field lines.

Figure 3 shows the plasma flow vectors in the *XZ* (top) and *XY* planes (bottom) at time t = 90 min in Case 1 (A) and in Case 2 (B). The red curves refer to $B_Z = 0$ regions. The bow shock is located approximately at $X = 16\ R_E$ and the magnetopause is located approximately at $X = 12\ R_E$ at the nose throughout the simulation in both cases during the weak uniform southward IMF. The calculated convection electric fields, $Ec = |\eta \mathbf{Jc}| = \eta|\mathbf{B}\times\mathbf{J}|/|\mathbf{B}|$, are plotted with the color contour. The basic calculation method of the electric field has been described in detail by Park et al. (2006). The electric field becomes larger in the dayside and tail reconnection region in both cases. Also, the simulation results show that the high electric fields in the magnetopause are related to the vortex in **Figure 3**. The vortex-like structures are generated in the inner boundary of the magnetopause after t = 47 min after the steady weak southward IMF constantly impacts the magnetosphere. And the vortex propagates anti-sunward with a velocity 158 km/s in Case 1 (A) and 120 km/s for Case 2 (B). The vortices are counterclockwise in the duskside magnetopause in this simulation. The center of the region of vortex A is at (*X*, *Y*) = (9.0, 9.4) R_E in Case 1 (A) and (*X*, *Y*) = (6.0, 9.9) R_E in Case 2 (B) respectively. In Case 1, the size of the vortex changes from 3 R_E to 4.5 R_E during the move to the tail in **Figure 3A**. In Case 2, the size of vortex A is 2.3 R_E and increases to 3.5 R_E during the move to the tail.

Figure 4 shows 3D closed magnetic field lines indicated in green and tail reconnection field lines indicated in red at t = 120 min in Case1 (A) and in Case2 (B). The black arrow indicates the equatorial magnetospheric convection. The plasma flow in the near tail clearly moves earthward due to the tail reconnection.

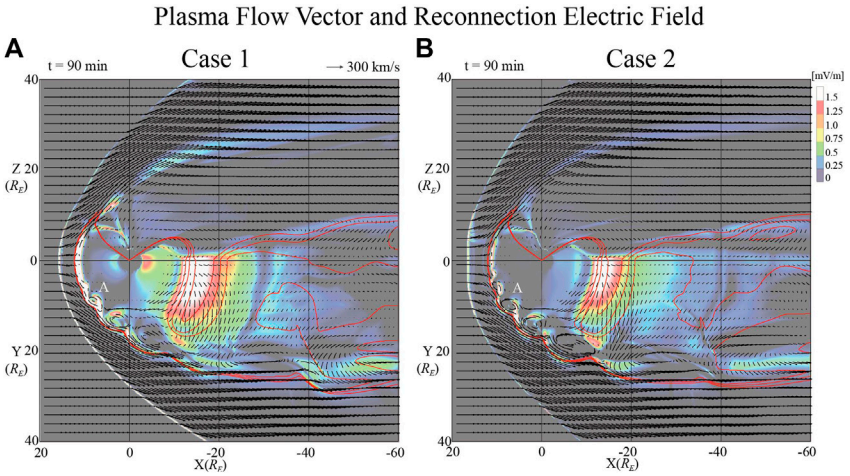

FIGURE 3 | The plasma flow vectors in the *XZ* **(top)** and *XY* planes **(bottom)** at time t = 90 min in simulation during the weak southward condition in Case 1 **(A)** and in Case 2 **(B)**. The red lines are contours of the B_z = 0 region. The color contour is convection electric field.

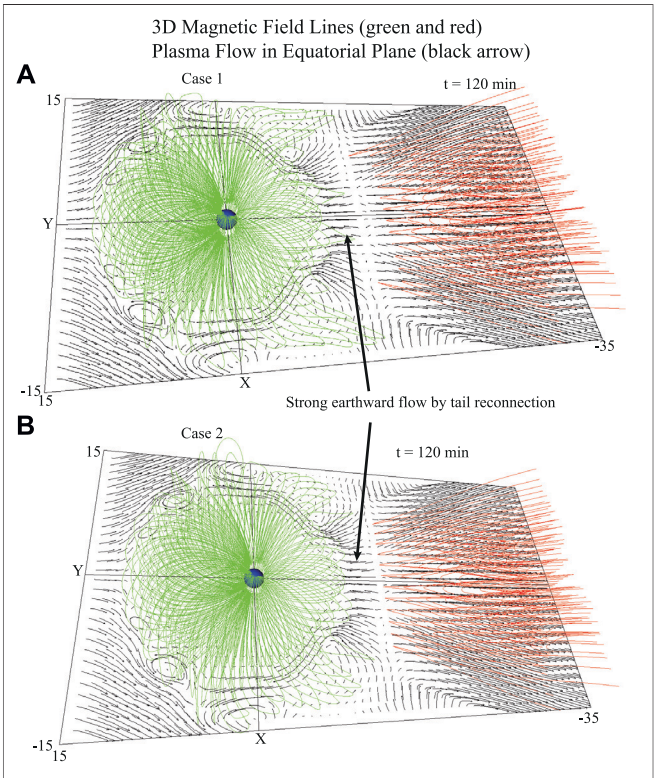

FIGURE 4 | 3D closed magnetic field lines that indicate green and tail reconnection field lines it indicate red at t = 120 min in Case1 **(A)** and in Case2 **(B)**. The black arrow indicate equatorial magnetospheric convection.

This is clearly shown in **Figure 4**. The tail reconnection region is at approximately $X = -14.2\ R_E$ where plasma flow diverges. A strong earthward plasma flow appears at the near-Earth line with a velocity of 40 km/s up to 194 km/s due to the tail reconnection in Case 1. In Case 2, the tail reconnection occurs at approximately $X = -13.4\ R_E$ and the peak value of velocity is about 200 km/s. Some closed field lines on the dusk (and dawn) are linked to the vortex and move duskward and then toward the tail.

Figure 5 shows the temporal variations of the magnetic field and plasma properties from t = 65–120 min in Case 1 (A), from t = 60–115 min in Case 2 (B) during the simulation. For the data, the following coordinates were designated to observe the movement of the vortices: $X = 6.9\ R_E$, $Y = 9.9\ R_E$ and $Z = 0\ R_E$ for Case 1, $X = 8.9\ R_E$, $Y = 8.1\ R_E$ and $Z = 0\ R_E$ for Case 2. The center of the vortices was indicated with dashed vertical lines. This figure clearly shows quasi-periodic behavior with an interval of 9–11 min. Observing the center of the vortices, the sizes of the bipolar magnetic field perturbation and the total magnetic field intense increase. The velocity is low at the center of the vortices and variations in the V_x and V_y components were roughly 90° out of phase. The density and the plasma pressure are low at the center of the vortices but the current is high. Some observation and model studies are related to KH waves under the southward IMF condition. It has been reported that the KH waves involve both with the magnetosheath and the magnetopause boundary. Hwang et al. (2011) examined by using a global MHD simulation under southward IMF condition that KH are well developed, but they quickly become unstable due to both subsolar fluctuations and external dynamics of FTEs. However, it is not clear whether these simulation results are a feature of KH waves. The vortices are generated in the inner boundary of the magnetopause and they exhibit stable, periodic fluctuations during the simulation Therefore, it is necessary to perform the simulations under various conditions.

The size, propagation speed and the intervals of the vortices in the two cases simulation results are similar to those obtained in our previous studies (Park et al., 2020). That study showed that the density and the plasma pressure are high, and the current is low at the center of the vortices at a 0.3 R_E grid spacing simulation. There are different simulation conditions with variances in the initial magnetosphere condition, simulation

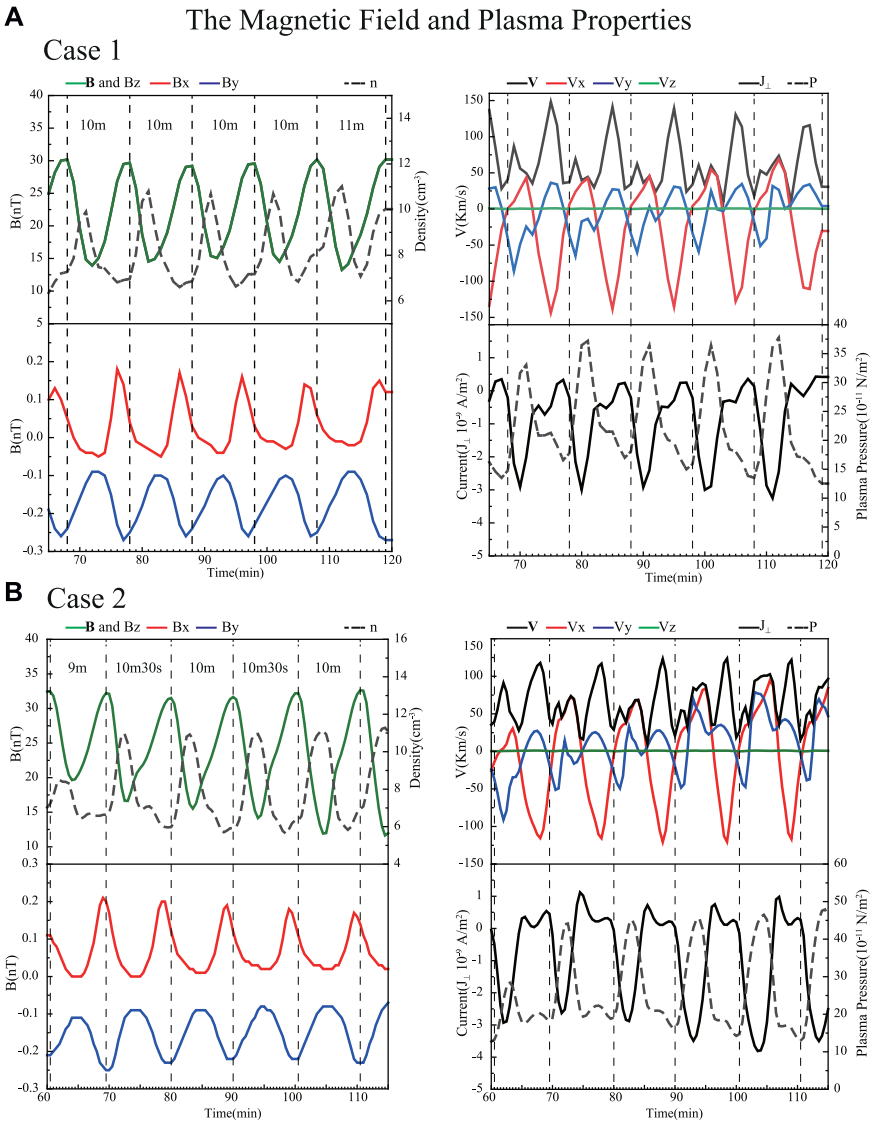

FIGURE 5 | The time evolution of the magnetic field and plasma density **(left)** and the plasma flow vector, current density and plasma pressure **(right)** from 65 to 120 min in Case 1 **(A)** and from 60 to 115 min in Case 2 **(B)**. The data were selected at the $X = 6.9\ R_E$, $Y = 9.9\ R_E$ and $Z = 0\ R_E$ in Case 1 and $X = 8.9\ R_E$, $Y = 8.1\ R_E$ and $Z = 0\ R_E$ in Case 2 across the vortex A in **Figure 3**.

grid spacing, and time resolution. However, further effects of other conditions should be investigated.

Figure 6 shows the simulation results of the evolution of the cross-polar cap potential mapped onto the polar region. The maximum value of the cross-polar cap potential reaches approximately 50 kV after 40–50 min with a strong dayside reconnection in both cases. Also, the cross-polar cap potential increased until t = 90 min as the tail reconnection persisted and intensified. In both cases, the cross-polar cap potential increase to more than 30 kV was observed during the simulation. Many studies suggested that the peak potential was substantial enough to set a growth phase condition for the later release of the energy such as substorm triggering (e.g., Milan, 2004; Lockwood et al., 2009; Liu et al., 2011; Andalsvik et al., 2012). Lockwood et al. (2009) determined the transpolar voltage as a function of the IMF B_z for quiet times and the growth phase of a substorm, reporting values of 10–60 kV for -10 nT < B_z < 10 nT. Liu et al. (2011) reported an increase in the cross-polar cap potential ranging from 16 to 29 kV associated with substorm occurrences. These results suggest that substorm energy storage and eventual release are possible as the cross-polar cap potential value exceed 30 kV even during the weak and long duration of southward IMF.

Figure 7 shows 2D electric potential patterns in the polar region at selected times. The blue and red contours indicate negative and positive potentials respectively. A double green line delimits the open-closed field lines boundary. The four-cell pattern is shown in the polar region due to the initial state

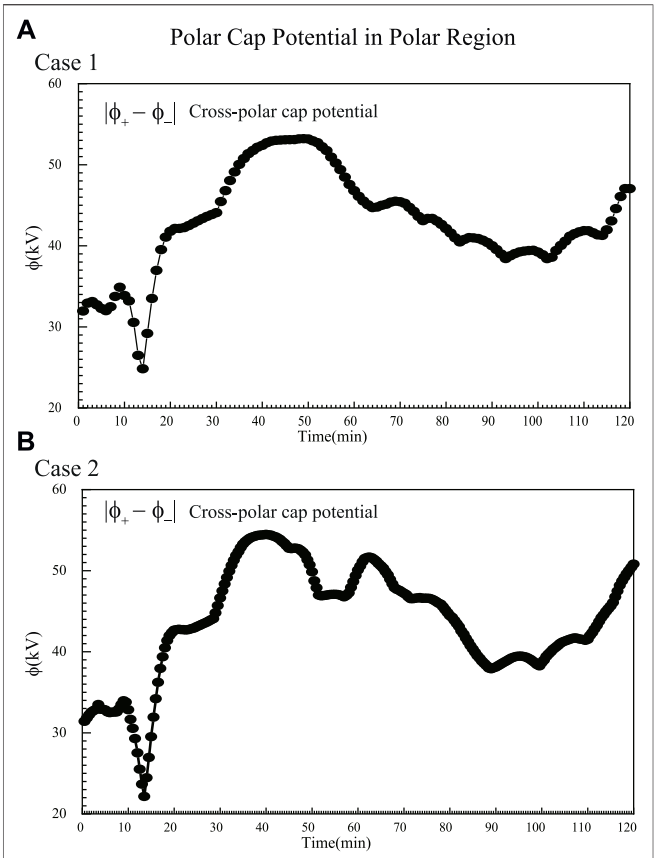

FIGURE 6 | The simulation results of the evolution over time of the cross-polar cap potential mapped onto the polar region for 1 min time resolution in Case 1 **(A)** and for 30 s time resolution in Case 2 **(B)**.

of the northward IMF condition simulation at **Figure 7** (top). A two-cell pattern appears after the weak southward IMF impacted with the magnetosphere in **Figure 7** (bottom panels). The open-closed boundary is located between 77° and 70° on the nightside, 83° and 78° on the dayside, and 79° and 74° on dawn and dusk regions during the simulation. The open-closed boundary extends close to 70° near midnight after the tail reconnection strengthened at t = 90 min while ionospheric convection is enhanced in the night side (plot not shown). The potential pattern and open-closed boundary in the polar region exhibit the same results during the simulation in both cases.

SUMMARY AND DISCUSSION

In this work, we studied the response of the magnetosphere and the ionosphere using a 3D global MHD simulation in high resolution grid spacing and time when the IMF is purely weak southward. The main features of the simulation results are summarized below;

(i) The magnetic reconnection starts in the subsolar region and magnetic equator region at t = 9 min during the weak southward IMF impacts. The vortices are generated in t = 47 min in the inner boundary of the magnetopause. The direction of motion of the reconnected open field line on the dayside changes from dusk (dawn) to tailward with the plasma flow. The stretched closed plasma sheet field lines in the tail led to a plasmoid formation near the midnight region (about 14.5 R_E) after approximately 85 min.

(ii) Vortices propagate anti-sunward with a quasi-periodicity of 9–11 min 30 s in the inner boundary of the magnetosphere. A strong convection electric field occurs in the magnetopause boundary which indicates that there is a dominant occurrence of a magnetic reconnection. Also, the twisted structure of the convection electric field in the magnetopause is the result of vortices.

(iii) The cross-polar cap potential reaches up to ~50 kV after 40–50 min with a strong dayside reconnection and then gradually decreased to 40 kV. Case 2 had a second peak different from Case 1. The cross-polar cap potential gradually increased until t = 90 min as the tail reconnection persisted and intensified in both cases.

(iv) The two-cell pattern appeared in the polar region during the weak southward IMF simulation. The location of the open-closed field boundary is 77°–70° at night (24:00 MLT), around 83°–78° at 12:00 MLT, and 79°–74° at 6:00 and 18:00 MLT.

The magnetic reconnection is the most important mechanism for magnetospheric phenomena even in the case of weak and steady southward IMF. The dayside reconnection first occurs and then vortices are generated near the inner magnetopause boundary. Park et al. (2020) showed that the velocity shear exists in the dayside magnetopause boundary because the plasma flows near the magnetic equator deformed by reconnection. They suggested that reconnection played a role in generating vortices with a periodicity in the dayside magnetopause boundary under a weak southward IMF in a simulation with a grid spacing of 0.3 R_E. These results are similar to those simulation results despite the different grid spacing of 0.1 R_E and different time resolution. Nakamura et al. (2020) reported using 3D full kinetic simulation of the KHI at the magnetopause under the southward IMF condition. They showed that the KH waves due to the enhanced reconnection rate are decay within the magnetopause boundary layer.

In addition, **Figure 8A** show the simulation results for 10 s time resolution of the plasma flow vector in XZ panel (upper) and in XY panel (bottom) at time t = 100 min. **Figure 8B** show the time evolution of the magnetic field and plasma properties from t = 60 to t = 120 min. The location of selected data is near the center of vortices at $X = 8.5\ R_E$, $Y = 8.1\ R_E$ and $Z = 0\ R_E$ (asterisked). This figure clearly shows quasi-periodic behavior with an interval of 9 min 20 s to 11 min 30 s for high resolution simulation. In **Figure 8A**, the vortex structure is also formed in the inner boundary magnetopause. The results of the simulation with a 10 s time resolution have no significant difference from either the 1 min or 30 s time resolution simulations. Details will be discussed in a future paper.

The observational study by Hwang et al. (2012) indicate that KH waves can occur at high-latitude magnetopause during

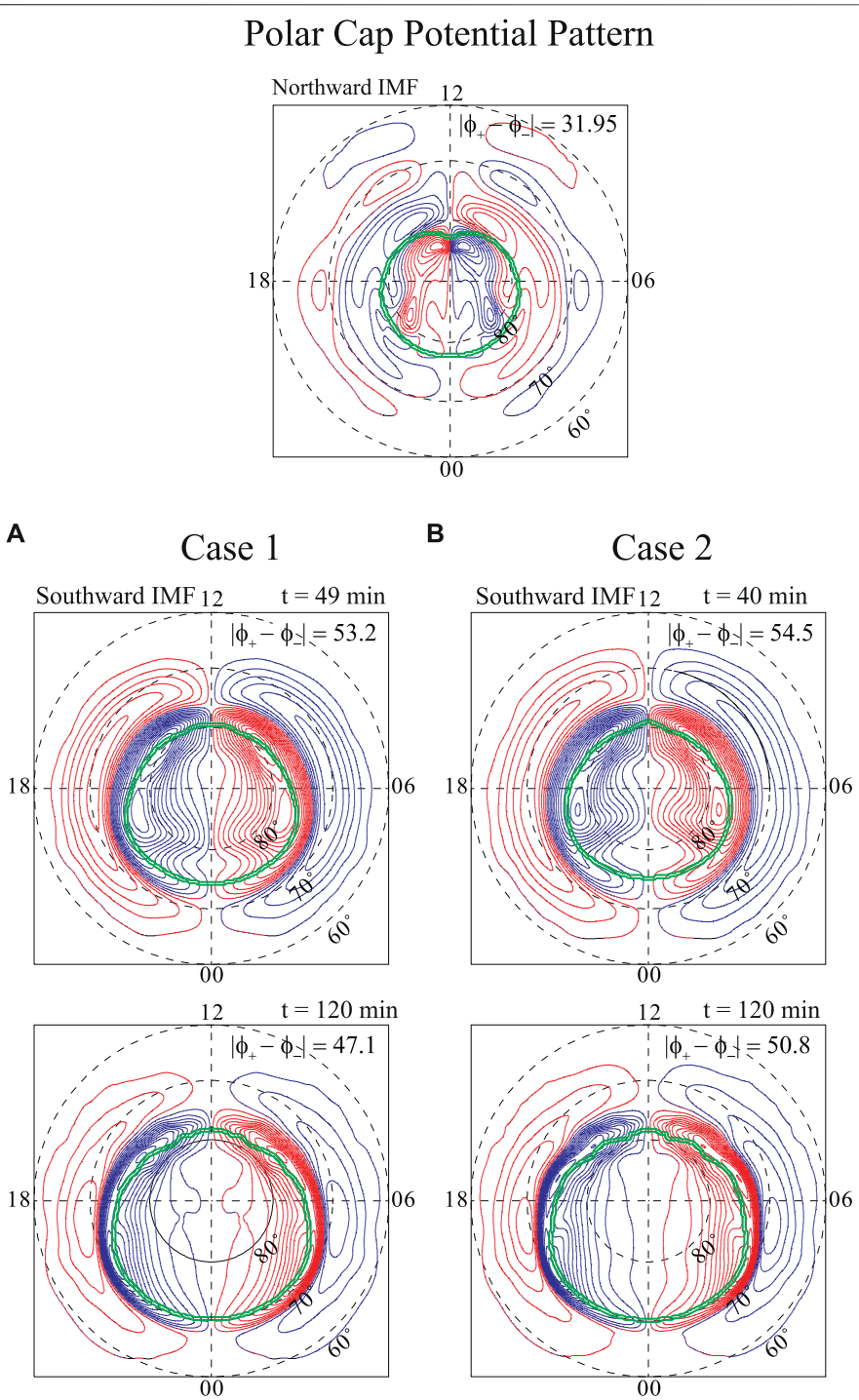

FIGURE 7 | 2D electric potential pattern in the polar region at selected times. The blue and red contours indicate negative and positive potentials, respectively. A double green lines delimit the open-closed field lines boundary.

strongly dawnward IMF conditions. When the IMF B_y is non-zero, the dayside reconnection occur at the high-latitude flanks to satisfy the antiparallel field conditions (Park et al., 2006). They examined using the global MHD simulation the direction of the plasma flow flowing the magnetic reconnection. It was showed that after the reconnection, open field lines easily move from dusk to dawn in the dayside polar region under the duskward IMF conditions. The fast transverse plasma flow moved dawnward simultaneously. The velocity shear could exist at high-latitude deformed plasma flow by the reconnected even high-speed

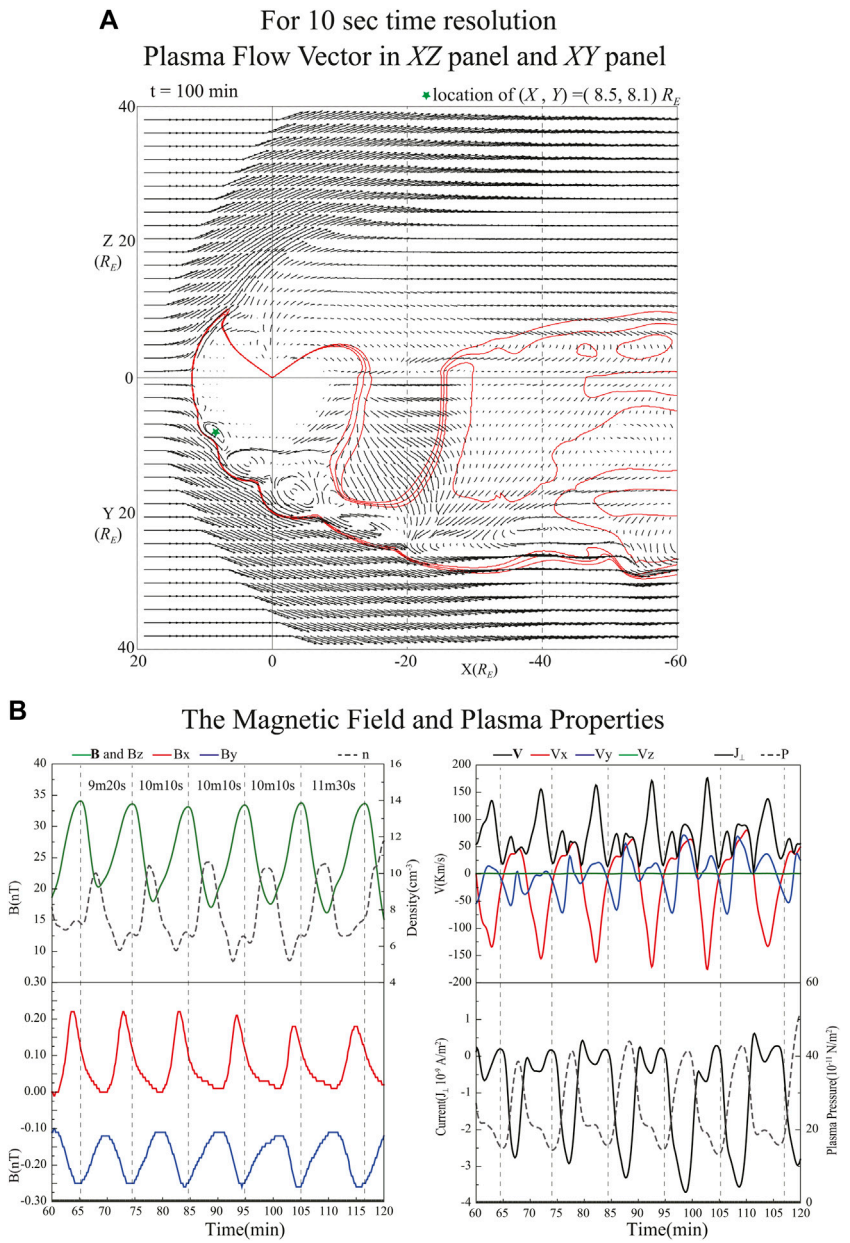

FIGURE 8 | The plasma flow vectors in the *XZ* **(top)** and *XY* planes **(bottom)** at time t = 100 min in simulation of 10 s time resolution for the weak southward condition in **(A)**. The red lines are contours of the B_z = 0 region. **(B)** show the time evolution of the magnetic field and plasm properties in the region of X = 8.5 R_E, Y = 8.1 R_E and Z = 0 R_E.

magnetosheath flow. It is necessary to further study the effects of IMF strength, direction, and variable solar wind parameter using global MHD simulation with different grid spacing and time resolution.

DATA AVAILABILITY STATEMENT

The simulation data supporting the conclusions of this paper will be made available by the authors, without undue reservation.

AUTHOR CONTRIBUTIONS

The author confirms being the sole contributor of this work and has approved it for publication.

FUNDING

This research was supported by Basic Science Research Program through the National Research Foundation of Korea (NRF)

funded by the Ministry of Education (No. NRF-2018R1D1A1B07043924) and by National Research Foundation of Korea (NFR) funded by Korea government (MSIP) (No. NRF-2019M1A3B2A04103464).

ACKNOWLEDGMENTS

I would like to thank the referees for their helpful comments. I am also grateful to Tatsuki Ogino.

REFERENCES

Andalsvik, Y., Sandholt, P. E., and Farrugia, C. J. (2012). Substorms and polar cap convection: the 10 January 2004 interplanetary CME case. *Ann. Geophys.* 30, 67–80. doi:10.5194/angeo-30-67-2012

Claudepierre, S. G., Elkington, S. R., and Wiltberger, M. (2008). Solar Wind Driving of Magnetospheric ULF Waves: Pulsations Driven by Velocity Shear at the Magnetopause. *J. Geophys. Res.* 113, a–n. doi:10.1029/2007JA012890

Claudepierre, S. G., Hudson, M. K., Lotko, W., Lyon, J. G., and Denton, R. E. (2010). Solar Wind Driving of Magnetospheric ULF Waves: Field Line Resonances Driven by Dynamic Pressure Fluctuations. *J. Geophys. Res.* 115, a–n. doi:10.1029/2010JA015399

Crooker, N. U. (1979). Dayside Merging and Cusp Geometry. *J. Geophys. Res.* 84, 951. doi:10.1029/ja084ia03p00951

Dungey, J. W. (1955). "Electrodynamics of the Outer Atmosphere," in Proceedings of the Ionosphere Conference. Phys. Soc. of London, London. 255p.

Dungey, J. W. (1961). Interplanetary Magnetic Field and the Auroral Zones. *Phys. Rev. Lett.* 6, 47–48. doi:10.1103/physrevlett.6.47

Guo, X. C., Wang, C., and Hu, Y. Q. (2010). Global MHD Simulation of the Kelvin-Helmholtz Instability at the Magnetopause for Northward Interplanetary Magnetic Field. *J. Geophys. Res.* 115, A10218. doi:10.1029/2009JA0115193

Hwang, K.-J., Goldstein, M. L., Kuznetsova, M. M., Wang, Y., Viñas, A. F., and Sibeck, D. G. (2012). The First *In Situ* Observation of Kelvin-Helmholtz Waves at High-Latitude Magnetopause during Strongly Dawnward Interplanetary Magnetic Field Conditions. *J. Geophys. Res.* 117, a–n. doi:10.1029/2011JA017256

Hwang, K.-J., Kuznetsova, M. M., Sahraoui, F., Goldstein, M. L., Lee, E., and Parks, G. K. (2011). Kelvin-Helmholtz Waves under Southward Interplanetary Magnetic Field. *J. Geophys. Res.* 116, a–n. doi:10.1029/2011JA016596

Kavosi, S., and Raeder, J. (2015). Ubiquity of Kelvin-Helmholtz Waves at Earth's Magnetopause. *Nat. Commun.* 6, 7019. doi:10.1038/ncomms8019

Kivelson, M. G., and Chen, S. H. (1995). "The Magnetopause: Surface Waves and Instabilities and Their Possible Dynamical Consequences," in *AGU Monograph 90, Physics of Magnetopause. Song and B. U. Ö. Sonnerup*. (Washington, D.C: AGU), 257.

Liu, J.-M., Zhang, B.-C., Kamide, Y., Wu, Z.-S., Hu, Z.-J., and Yang, H.-G. (2011). Spontaneous and Trigger-Associated Substorms Compared: Electrodynamic Parameters in the Polar Ionosphere. *J. Geophys. Res.* 116, a–n. doi:10.1029/2010JA015773

Lockwood, M., Hairston, M., Finch, I., and Rouillard, A. (2009). Transpolar Voltage and Polar Cap Flux during the Substorm Cycle and Steady Convection Events. *J. Geophys. Res.* 114, a–n. doi:10.1029/2008JA013697

Luhmann, J. G., Walker, R. J., Russell, C. T., Crooker, N. U., Spreiter, J. R., and Stahara, S. S. (1984). Patterns of Potential Magnetic Field Merging Sites on the Dayside Magnetopause. *J. Geophys. Res.* 89, 1739. doi:10.1029/ja089ia03p01739

Lysak, R. L., and Lee, D.-H. (1992). Response of the Dipole Magnetosphere to Pressure Pulse. *Geophys. Res. Lett.* 19, 97–940. doi:10.1029/92gl00625

Merkin, V. G., Lyon, J. G., and Claudepierre, S. G. (2013). Kelvin-Helmholtz Instability of the Magnetospheric Boundary in a Three-Dimensional Global MHD Simulation during Northward IMF Conditions. *J. Geophys. Res. Space Phys.* 118, 5478–5496. doi:10.1002/jgra.50520

Milan, S. E. (2004). Dayside and Nightside Contributions to the Cross Polar Cap Potential: Placing an Upper Limit on a Viscous-like Interaction. *Ann. Geophys.* 22, 3771–3777. doi:10.5194/angeo-22-3771-2004

Miura, A. (1984). Anomalous Transport by Magnetohydrodynamic Kelvin-Helmholtz Instabilities in the Solar Wind-Magnetosphere Interaction. *J. Geophys. Res.* 89, 801–818. doi:10.1029/ja089ia02p00801

Miura, A. (1995). "Kelvin-Helmholtz Instability at the Magnetopause: Computer Simulations," in *AGU Monograph 90, Physics of MagnetopauseP. Song and B. U. Ö. Sonnerup* (Washington, D.C: AGU), 285.

Nakamura, T. K. M., Plaschke, F., Hasegawa, H., Liu, Y. H., Hwang, K. J., Blasl, K. A., et al. (2020). Decay of Kelvin-Helmholtz Vortices at the Earth's Magnetopause under Pure Southward IMF Conditions. *Geophys. Res. Lett.* 47, e2020GL087574. doi:10.1029/2020GL087574

Ogino, T. (2011). "Magnetic Reconnection in the Magnetotail on Southward Turning of IMF, Proceeding of Conference on Earth-Sun System Exploration: Variability in Space Plasma Phenomena January," in 16-21. Hawaii, USA: Kona, 2011.

Ogino, T., Walker, R. J., and Ashour-Abdalla, M. (1992). A Global Magnetohydrodynamic Simulation of the Magnetosheath and Magnetosphere when the Interplanetary Magnetic Field Is Northward. *IEEE Trans. Plasma Sci.* 20 (6), 817–828. doi:10.1109/27.199534

Otto, A., and Fairfield, D. H. (2000). Kelvin-Helmholtz Instability at the Magnetotail Boundary: MHD Simulation and Comparison with Geotail Observation. *J. Geophys. Res. 105, NO. A9* 21, 21175–21190.

Park, K. S., Lee, D-Y., and Kim, K- H. (2020). Global MHD Simulation of a Prolonged Steady Weak Southward Interplanetary Magnetic Field Condition. *J. Astron. Space Sci.* 37 (2), 77–84. doi:10.5140/JASS.2020.37.2.77

Park, K. S., Ogino, T., and Kim, Y. H. (2010). Effects of the Dipole Tilt and Northward and Duskward IMF on Dayside Magnetic Reconnection in a Global MHD Simulation. *J. Geophys. Res.* 115, a–n. doi:10.1029/2009JA014212

Park, K. S., Ogino, T., and Walker, R. J. (2006). On the Importance of Antiparallel Reconnection when the Dipole Tilt and IMFByare Nonzero. *J. Geophys. Res.* 111, A05202. doi:10.1029/2004JA010972

Sibeck, D. G. (1990). A Model for the Transient Magnetospheric Response to Sudden Solar Wind Dynamic Pressure Variations. *J. Geophys. Res.* 95, 3735–3771. doi:10.1029/ja095ia04p03755

Sibeck, D. G., Baumjohann, W., Elphic, R. C., Fairfield, D. H., Fennell, J. F., Gail, W. B., et al. (1989). The Magnetospheric Response to 8-minute Period strong-amplitude Upstream Pressure Variations. *J. Geophys. Res.* 94, 2505–2519. doi:10.1029/ja094ia03p02505

Sibeck, D. G., and Gosling, J. T. (1996). Magnetosheath Density Fluctuations and Magnetopause Motion. *J. Geophys. Res.* 101, 31–40. doi:10.1029/95ja03141

Sibeck, D. G. (1992). Transient Events in the Outer Magnetosphere: Boundary Waves or Flux Transfer Events. *J. Geophys. Res.* 97, 4009–4026. doi:10.1029/91ja03017

Sonnerup, B. U. Ö. (1974). Magnetopause Reconnection Rate. *J. Geophys. Res.* 79, 1546–1549. doi:10.1029/ja079i010p01546

Conflict of Interest: The author declares that the research was conducted in the absence of any commercial or financial relationships that could be construed as a potential conflict of interest.

frontiers in Astronomy and Space Sciences

ORIGINAL RESEARCH
published: 14 January 2022
doi: 10.3389/fspas.2021.785413

Coupling Between Alfvén Wave and Kelvin–Helmholtz Waves in the Low Latitude Boundary Layer

E.-H. Kim[1]*, *J. R. Johnson*[2] *and K. Nykyri*[3]

[1]Princeton Plasma Physics Laboratory, Princeton University, Princeton, NJ, United States, [2]Andrews University, Berrien Springs, MI, United States, [3]Embry-Riddle Aeronautical University, Daytona Beach, FL, United States

The Kelvin–Helmholtz (KH) instability of magnetohydrodynamic surface waves at the low latitude boundary layer is examined using both an eigenfrequency analysis and a time-dependent wave simulation. The analysis includes the effects of sheared flow and Alfvén velocity gradient. When the magnetosheath flows are perpendicular to the ambient magnetic field direction, unstable KH waves that propagate obliquely to the sheared flow direction occur at the sheared flow surface when the Alfvén Mach number is higher than an instability threshold. Including a shear transition layer between the magnetosphere and magnetosheath leads to secondary KH waves (driven by the sheared flow) that are coupled to the resonant surface Alfvén wave. There are remarkable differences between the primary and the secondary KH waves, including wave frequency, the growth rate, and the ratio between the transverse and compressional components. The secondary KH wave energy is concentrated near the shear Alfvén wave frequency at the magnetosheath with a lower frequency than the primary KH waves. Although the growth rate of the secondary KH waves is lower than the primary KH waves, the threshold condition is lower, so it is expected that these types of waves will dominate at a lower Mach number. Because the transverse component of the secondary KH waves is stronger than that of the primary KH waves, more efficient wave energy transfer from the boundary layer to the inner magnetosphere is also predicted.

Keywords: Kelvin–Helmholtz instability, Alfvén wave, boundary layer, magnetopause, mode conversion, wave coupling

OPEN ACCESS

Edited by:
Olga V. Khabarova, Institute of Terrestrial Magnetism Ionosphere and Radio Wave Propagation (RAS), Russia

Reviewed by:
Elizaveta Antonova, Lomonosov Moscow State University, Russia
Namig Dzhalilov, Azerbaijan National Academy of Sciences (ANAS), Azerbaijan

***Correspondence:**
E.-H. Kim
ehkim@pppl.gov

Specialty section:
This article was submitted to Space Physics, a section of the journal Frontiers in Astronomy and Space Sciences

Received: *29 September 2021*
Accepted: *24 November 2021*
Published: *14 January 2022*

Citation:
Kim E-H, Johnson J and Nykyri K (2022) Coupling Between Alfvén Wave and Kelvin–Helmholtz Waves in the Low Latitude Boundary Layer. Front. Astron. Space Sci. 8:785413. doi: 10.3389/fspas.2021.785413

1 INTRODUCTION

The Kelvin–Helmholtz (KH) instability has been widely investigated in the Earth's magnetosphere (Johnson et al., 2014). Unstable KH waves generally occur at the interface between two fluids having different velocities and are fundamentally important for understanding dynamics within the boundary layer that develops between the flows. These waves can affect the exchange of mass, momentum, and energy across those boundaries (e.g., Miura, 1984; Thomas and Winske, 1993; Otto and Fairfield, 2000; Nykyri and Otto, 2001; Matsumoto and Hoshino, 2006; Cowee et al., 2010; Hwang et al., 2011; Nakamura et al., 2011; Moore et al., 2016; Nykyri et al., 2017; Johnson et al., 2021). Mass transport due to KH instability can result from diffusion through thin boundaries created by the instability (e.g., Nakamura et al., 2017) and/or as the result of secondary reconnection (e.g., Otto and Nykyri, 2003; Ma et al., 2017) which results in more effective transport (Ma et al., 2019). Cross-scale energy transport associated with the KH instability may result from the generation

of plasma waves leading to both ion and electron heating (Johnson and Cheng, 2001; Chaston et al., 2007; Moore et al., 2017; Nykyri et al., 2021a; Nykyri et al., 2021b; Delamere et al., 2021). The KH waves are also critical to the interaction between the solar wind and other planetary magnetospheres (McComas and Bagenal, 2008; Delamere and Bagenal, 2010; Delamere et al., 2021).

KH waves are surface waves because they are localized near the interface and exponentially decay away from the interface (e.g., Southwood, 1968; Pu and Kivelson, 1983). However, because the wave number is relatively small, the wave energy can still penetrate into the plasma sheet and/or the inner magnetosphere (e.g., Pu and Kivelson, 1983) and play a role in the generation of geomagnetic pulsations and mode conversion to the shear Alfvén waves (e.g., Chen and Hasegawa, 1974; Engebretson et al., 1998).

The magnetopause boundary is often assumed for simplicity to have zero thickness (Pu and Kivelson, 1983; Mills and Wright, 1999; Turkakin et al., 2013), and this assumption is valid for waves with wavelengths longer than the thickness of the boundary layer. When the shear velocity and the Alfvén speed jump at the zero-thickness interface, the linear dispersion relation of KH waves in a slab geometry for an incompressible plasma can be derived as follows (Chandrasekhar, 1961):

$$\omega = \frac{\mathbf{k}\cdot\left(\rho_{msh}\mathbf{V}_{msh}+\rho_{msp}\mathbf{V}_{msp}\right)}{\rho_{msp}+\rho_{msh}} \pm i\sqrt{\frac{\rho^*}{\rho_{msh}+\rho_{msp}}\left(\left[\mathbf{k}\cdot\left(\mathbf{V}_{msh}-\mathbf{V}_{msp}\right)\right]^2-\frac{(\mathbf{k}\cdot\mathbf{B}_{msh})^2+\left(\mathbf{k}\cdot\mathbf{B}_{msp}\right)^2}{\mu_0\rho^*}\right)}, \tag{1}$$

where ω and $\mathbf{k}$ are a wave frequency and vector, respectively, $\mathbf{V}$ and $\mathbf{B}$ are shear flow velocity and magnetic field, ρ and $\rho^* = \rho_{msh}\rho_{msp}/(\rho_{msh}+\rho_{msp})$ are a mass density and a mean mass density, respectively, μ_0 is the magnetic permeability of free space, and msp(msh) denotes the magnetosphere (magnetosheath). When $\mathbf{B}_{msp} = \mathbf{B}_{msh}$ and $\rho_{msp} = \rho_{msh}$, the KH wave frequency in **Equation 1** is reduced to $\omega = \omega_{KH0} = \frac{1}{2}\mathbf{k}\cdot\mathbf{V}_{msh}$. In **Equation 1**, the KH waves become unstable when

$$\left[\mathbf{k}\cdot\left(\mathbf{V}_{msh}-\mathbf{V}_{msp}\right)\right]^2 > \left[(\mathbf{k}\cdot\mathbf{B}_{msh})^2+\left(\mathbf{k}\cdot\mathbf{B}_{msp}\right)^2\right]\Big/\mu_0\rho^* \tag{2}$$

is satisfied; and the stability threshold condition (2) may be used to determine a critical Alfvén Mach number (M_{As}) above which the KH wave is unstable.

In addition to the velocity transition at the magnetopause boundary, there is also a large gradient in the Alfvén velocity, which is typically wider in extent than the velocity shear layer (Paschmann et al., 1993). When an Alfvén velocity (V_A) transition layer is included between the magnetosheath and magnetosphere, it can modify the KH wave properties. Strong coupling between the Alfvén surface wave and KH surface wave can result when the frequencies are comparable. This interaction between the two surface waves can lead to instability at a slower flow velocity. This new instability has been referred to as the resonant flow instability (RFI) as it results when Doppler-shifted compressional waves originating at the velocity interface have approximately the same frequency as the Alfvén resonance frequency (Taroyan and Erdélyi, 2003). The RFI includes a negative absorption of the magnetosonic waves, and it has been investigated for the solar corona (Tirry et al., 1998; Andries et al., 2000; Andries and Goossens, 2001; Taroyan and Ruderman, 2011; Antolin and Van Doorsselaere, 2019), magnetopause (Ruderman and Wright, 1998; Taroyan and Erdélyi, 2002, 2003), and magnetotail (Turkakin et al., 2014), respectively. While these works focused on shear in the velocity along the magnetic field direction, a similar instability can also result in velocity shear across the magnetic field or for discontinuous changes in the magnetic field direction at velocity interfaces. These modes can generally be referred to as secondary KH instabilities and are characterized by instability at a slower flow speed than the primary KH instability with growth occurring in a narrow range of propagation angle or Mach number (e.g., González and Gratton, 1994; Taroyan and Erdélyi, 2002; Turkakin et al., 2013). Turkakin et al. (2013) examined the primary and the secondary KH waves in the magnetopause and magnetotail when the magnetic fields in the magnetosheath and magnetosphere are perpendicular to each other. This mode may be particularly important during periods of low solar wind Alfvén Mach number (Lavraud and Borovsky, 2008; Lavraud et al., 2013; Génot and Lavraud, 2021) as it may be unstable even when the primary KH mode is stabilized. Although the (primary) KH wave is considered to be one source of the field-line resonances, the secondary KH instability is strongly coupled to the Alfvén waves. While it has been shown that the secondary KH instability is important in the solar corona, in this article, we show that the secondary KH waves also appear when the shear transition layer exists between the magnetosheath and magnetosphere. Using both eigenmode analysis and a newly developed time-dependent MHD wave model, detailed characteristics of the secondary waves are examined.

This article is structured as follows: in **Section 2**, the MHD wave equations are presented. **Section 3** describes the dispersion relation of the KH waves when the zero-thickness interfaces are assumed. The eigenmode frequency, growth rate, and the KH wave amplitude ratio are also shown. In **Section 4**, we introduce a new time-dependent MHD wave simulation code. The simulation results are compared with the eigenfrequency analysis from **Section 3**. We also discuss the wave coupling between KH and Alfvén waves. The last section contains a brief discussion and conclusions.

2 MHD WAVE EQUATIONS IN COLD PLASMA

In a cold plasma, basic equations of an ideal MHD plasma are

$$\rho\left[\frac{\partial}{\partial t}+\mathbf{V}\cdot\nabla\right]\mathbf{V}-\nu\mathbf{V} = \frac{1}{\mu_0}(\nabla\times\mathbf{B})\times\mathbf{B}, \tag{3}$$

$$\frac{\partial\mathbf{B}}{\partial t} = \nabla\times(\mathbf{V}\times\mathbf{B}), \tag{4}$$

where ν is a collisional frequency that is introduced to damp waves propagating outside the region of interest, which effectively imposes outgoing boundary conditions. It should be noted that collisional effects play no role in the stability of the primary or secondary KH instabilities that we analyze in the rest of this article.

We assume that a field variable consists of background equilibrium (0) and small perturbation (1) components ($\mathbf{B} = \mathbf{B}_0 + \mathbf{B}_1$, $\rho = \rho_0 + \rho_1$, and $\mathbf{V} = \mathbf{V}_0 + \mathbf{V}_1$), and a shear flow ($\mathbf{V}_0(x) = V_0(x)\hat{y}$) and a uniform background magnetic field ($\mathbf{B}_0 = B_0\hat{z}$) lie in the y- and z-directions, respectively. Then, the perturbed quantities can be Fourier analyzed in the y- and z-directions ($\partial/\partial y \rightarrow ik_y$ and $\partial/\partial z \rightarrow ik_\parallel$, where k_y and $k_\parallel$ are wavenumbers in the y and field-aligned (z) directions). Thus, the linearized MHD wave equations are

$$\rho_0\left(\frac{\partial}{\partial t} + ik_yV_0\right)V_{1x} + \nu V_{1x} = \frac{B_0}{\mu_0}\left(ik_\parallel B_{1x} - \frac{\partial B_{1z}}{\partial x}\right), \tag{5}$$

$$\rho_0\left(\frac{\partial}{\partial t} + ik_yV_0\right)V_{1y} + \nu V_{1y} = \frac{B_0}{\mu_0}\left(ik_\parallel B_{1y} - ik_yB_{1z}\right) - \rho_0 V_{1x}\frac{\partial V_0}{\partial x}, \tag{6}$$

$$\left(\frac{\partial}{\partial t} + ik_yV_0\right)B_{1x} = ik_\parallel B_0 V_{1x}, \tag{7}$$

$$\left(\frac{\partial}{\partial t} + ik_yV_0\right)B_{1y} = ik_\parallel B_0 V_{1y} + B_{1x}\frac{\partial V_0}{\partial x}, \tag{8}$$

$$\left(\frac{\partial}{\partial t} + ik_yV_0\right)B_{1z} = -ik_yB_0V_{1y} - B_0\frac{\partial V_{1x}}{\partial x}. \tag{9}$$

In **Section 3**, we solve the spectrum of eigenmodes of these equations in slab geometry, while in **Section 4**, we solve these equations using a finite-difference time-domain method.

To proceed with the spectral analysis, we define an auxiliary set of variables including the fluid displacement (ξ)

$$\mathbf{V}_1 \equiv \left(\frac{\partial}{\partial t} + \mathbf{V}_0\cdot\nabla\right)\xi, \tag{10}$$

the total pressure perturbation (p), and compressibility (ψ),

$$p \equiv B_0B_{1z}, \tag{11}$$

$$\psi \equiv \nabla\cdot V_1. \tag{12}$$

Taking the Fourier transform in time ($\frac{\partial}{\partial t} \rightarrow -i\omega$) and ignoring the collision term ($\nu \rightarrow 0$), **Equations 5–9** become

$$\mu_0\rho_0\tilde{\omega}^2\xi_x = -iB_0k_\parallel B_{1x} + \frac{\partial p}{\partial x}, \tag{13}$$

$$\mu_0\rho_0\tilde{\omega}^2\xi_y = -i\tilde{\omega}\mu_0\rho_0\xi_x\frac{\partial V_0}{\partial x} - iB_0k_\parallel B_{1y} + ik_yp, \tag{14}$$

$$\tilde{\omega}B_{1x} = i\tilde{\omega}B_0k_\parallel\xi_x, \tag{15}$$

$$\tilde{\omega}B_{1y} = i\tilde{\omega}B_0k_\parallel\xi_y + iB_{1x}\frac{\partial V_0}{\partial x}, \tag{16}$$

$$\tilde{\omega}B_{1z} = -iB_0\psi, \tag{17}$$

where $\tilde{\omega} = \omega - k_yV_0$.

Then, **Equations 11–17** can be reduced to two coupled first-order differential equations,

$$\frac{dp}{dx} = \mu_0\rho_0\left(\tilde{\omega}^2 - k_\parallel^2V_A^2\right)\xi_x, \tag{18}$$

$$\mu_0\rho_0\frac{d\xi_x}{dx} = -\left(\frac{\tilde{\omega}^2 - k_y^2V_A^2 + k_\parallel^2V_A^2}{\tilde{\omega}^2 - k_\parallel^2V_A^2}\right)\frac{p}{B_0^2}. \tag{19}$$

We solve **Equations 18** and **19** to analyze the eigenmode frequency in **Section 3**.

3 WAVE DISPERSION RELATION AT THE PLASMA INTERFACES

Eigenfrequency analysis is performed when the shear transition layer exists between magnetosheath and magnetosphere. For calculations, V_0 and V_A are assumed to vary only in the direction of the x-axis, as shown in **Figure 1A**,

$$V_0(x) = V_{0I}\Theta(x), \tag{20}$$

$$V_A(x) = V_{AI} + (V_{AIII} - V_{AI})\Theta(x-d), \tag{21}$$

where $\Theta(x) = 0(x<0)$ or $1(x\geq 0)$ is a Heaviside step function. **Figure 1A** illustrates the transition from magnetosheath (I) to magnetosphere (III). The flow is sheared between regions I and II, while the Alfvén velocity increases between regions II

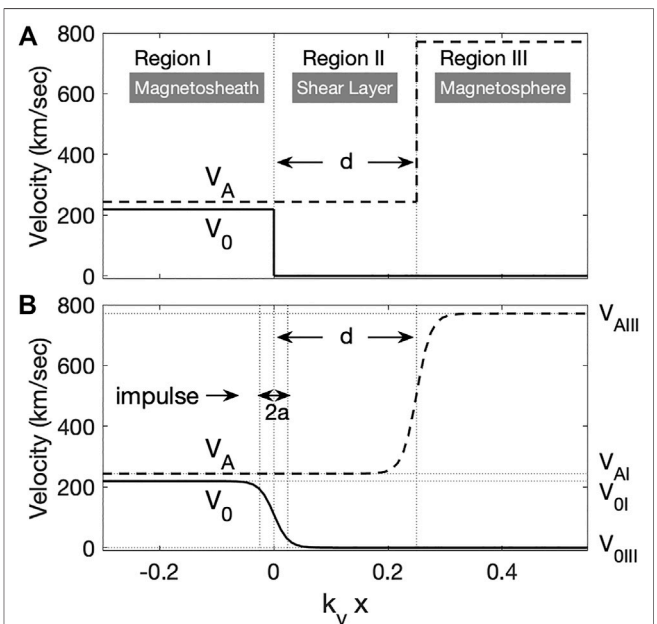

FIGURE 1 | Illustration of the adopted background plasma profile. We assume **(A)** zero and **(B)** finite boundary width for eigenfrequency analysis and the numerical simulation, respectively. Regions I and III correspond to the magnetosheath and magnetosphere, respectively, and region II is the shear transition layer.

and III. Region II is the shear layer, which divides the plasma into two semi-infinite homogeneous regions (I and III) separated with a width d. It is generally expected that velocity shear between layers I and II can drive a KH instability that is localized at this interface, while the jump in Alfvén velocity between regions II and III supports surface Alfvén waves satisfying the Alfvén resonance condition. In the following analysis, we show how these modes couple when the transitions occur in close proximity.

The eigenmodes of these equations are localized, so they must satisfy exponentially decaying boundary conditions in regions I and III. Moreover, it is also expected that in region II that the solution decays away from either boundary. As such, the analytical forms of the solutions in each region J are as follows:

$$p_J(x) = p_J^- \exp(-\kappa_J x) + p_J^+ \exp(\kappa_J x), \tag{22}$$

$$\xi_{xJ}(x) = \xi_{xJ}^- \exp(-\kappa_J x) + \xi_{xJ}^+ \exp(\kappa_J x), \tag{23}$$

where ± signs represent waves toward positive or negative directions in x.

For a surface wave, it is required that $p_I^- = p_{III}^+ = \xi_{xI}^- = \xi_{xIII}^+ = 0$, and ξ_x and p must be continuous at each interface; thus, at $x = 0$

$$p_I^+ = p_{II}^- + p_{II}^+, \tag{24}$$

$$\xi_{xI}^+ = \xi_{xII}^- + \xi_{xII}^+, \tag{25}$$

and at $x = d$,

$$p_{III}^- \exp(-\kappa_{III} x) = p_{II}^- \exp(-\kappa_{II} x) + p_{II}^+ \exp(\kappa_{II} x), \tag{26}$$

$$\xi_{xIII}^- \exp(-\kappa_{III} x) = \xi_{xII}^- \exp(-\kappa_{II} x) + \xi_{xII}^+ \exp(\kappa_{II} x). \tag{27}$$

The wave dispersion relation is obtained by inserting the solutions into **Equations 18** and **19** and noting that for solutions of the form $\exp(\pm\kappa x)$ that

$$\kappa p = \mp \mu_0 \rho_0 \left(\tilde{\omega}^2 - k_\parallel^2 V_A^2\right) \xi_x, \tag{28}$$

$$\kappa \mu_0 \rho_0 \xi_x = \pm \left(\frac{\tilde{\omega}^2 - k_y^2 V_A^2 + k_\parallel^2 V_A^2}{\tilde{\omega}^2 - k_\parallel^2 V_A^2} \right) \frac{p}{B_0^2}, \tag{29}$$

and the relationship between p and ξ_x in each region $J = I$, II, and III in **Figure 1A** becomes

$$H_J \xi_{xJ} = p_J, \tag{30}$$

where $H_J = \mu_0 \rho_{0J} (\tilde{\omega}^2 - k_\parallel^2 V_{AJ}^2)/\kappa_J$.

From **Equations 24–27** and **30**, the wave dispersion can be derived as

$$D\left(\omega, k_y, k_\parallel, V_0, V_A\right) = (H_I + H_{II})(H_{II} + H_{III}) - (H_I - H_{II})(H_{II} H_{II}) \exp(-2\kappa_{II} d) = 0. \tag{31}$$

The amplitude ratio (A_p) of the magnetic compressional component (p) between the two interfaces ($x = 0$ and d) can also be determined:

$$A_p \equiv \frac{p_{x=d}}{p_{x=0}} = \frac{p_{II}^+ \exp(\kappa_{II} d) + p_{II}^- \exp(-\kappa_{II} d)}{p_{II}^+ + p_{II}^-} = \frac{H_{III}}{H_I} \frac{H_I^2 - H_{II}^2}{H_{III}^2 - H_{II}^2}. \tag{32}$$

3.1 Primary and Secondary Kelvin–Helmholtz Waves

Using **Equations 31** and **32**, we calculate the eigenfrequency (ω), growth rate (γ), and amplitude ratio between magnetic compressional component (A_p) for various widths of the shear transition layer, $k_y d = 0$, 0.25, 0.75, and 2.0, as shown in **Figure 2**. For these plots, the plasma densities in region I and region III are assumed to be $N_{0I} = 5 \times 10^6/\mathrm{m}^3$ and $N_{0III} = 5 \times 10^5/\mathrm{m}^3$, and the background magnetic field strength is $B_0 = 25\mathrm{nT}$. We also specify an angle of propagation (ϕ) with respect to the ambient magnetic field, $\phi = \tan^{-1}(k_y/k_\parallel) = 80^\circ$ and $\sqrt{k_y^2 + k_\parallel^2} = \pi/(2R_E)$. For complete stability analysis, this angle would be varied to determine the maximum growth rate for a given Mach number. The upper panels of **Figure 2** are the calculated real (black and red) and imaginary (blue, growth rate γ) frequencies as functions of the Alfvén Mach number ($M_A \equiv V_{0I}/V_{AI}$), and the lower panels plot the amplitude ratio A_p of unstable wave modes.

In the absence of the shear transition layer ($k_y d = 0$) as shown in **Figure 2A**, forward and backward propagating fast waves, which have positive and negative frequencies at $M_A = 0$, occur when M_A is small (Taroyan and Erdélyi, 2002). These waves are stable until M_A reaches the threshold of the KH instability, $M_{As} = \tan^{-1}(\phi)\sqrt{2(1 + V_{AI}/V_{AIII})}$. For $M_A > M_{As}$ marked as a gray-shaded region in **Figure 2A**, the waves develop a complex frequency and become unstable. For the given range of M_A, ω and γ increase linearly with M_A. Because the characteristics of this wave mode are the same as the typical KH waves (e.g., Johnson et al., 2014), this wave corresponds to *primary* KH waves (hereafter PKHW). In this figure, we also found a shear Alfvén wave mode at $\omega = \omega_{AI} = k_\parallel V_{AI}$. The fast and shear Alfvén waves cross each other near $M_A \sim 0.45$, but the coupling of the two wave modes does not occur.

Introducing a finite width of the shear transition layer significantly changes the wave dispersion relations. In **Figure 2**, the PKHWs also occur for the cases of $k_y d \neq 0$. The M_A threshold decreases from 0.83 for $k_y d = 0$ to 0.35 for $k_y d = 2.0$. Overall, the wave frequency ω decreases, while the growth rate γ increases as $k_y d$ increases. For example, for $M_A = 0.85$, $\omega/\omega_{AI} = (4.35, 3.68, 2.95, 2.48)$ and $\gamma/\omega_{AI} = (0.35, 1.5, 1.85, 1.89)$ when $k_y d = (0.0, 0.25, 0.75, 2.0)$. Thus, when a shear transition layer is included, lower frequency PKHWs are excited with a stronger growth rate and lower M_A threshold.

For $k_y d = 0.25$ in **Figure 2B**, coupling between the backward propagating fast and shear Alfvén waves occurs near $\omega/\omega_{AI} \sim 1$, and unstable waves also appear for $0.355 \leq M_A \leq 0.47$ (shaded yellow in **Figure 2B**). These waves correspond to the *secondary* KH waves (hereafter SKHW) (Turkakin et al., 2013). In this case, the SKHWs are clearly separated from the PKHWs and have lower ω, lower γ, and lower M_A threshold than the PKHWs. The

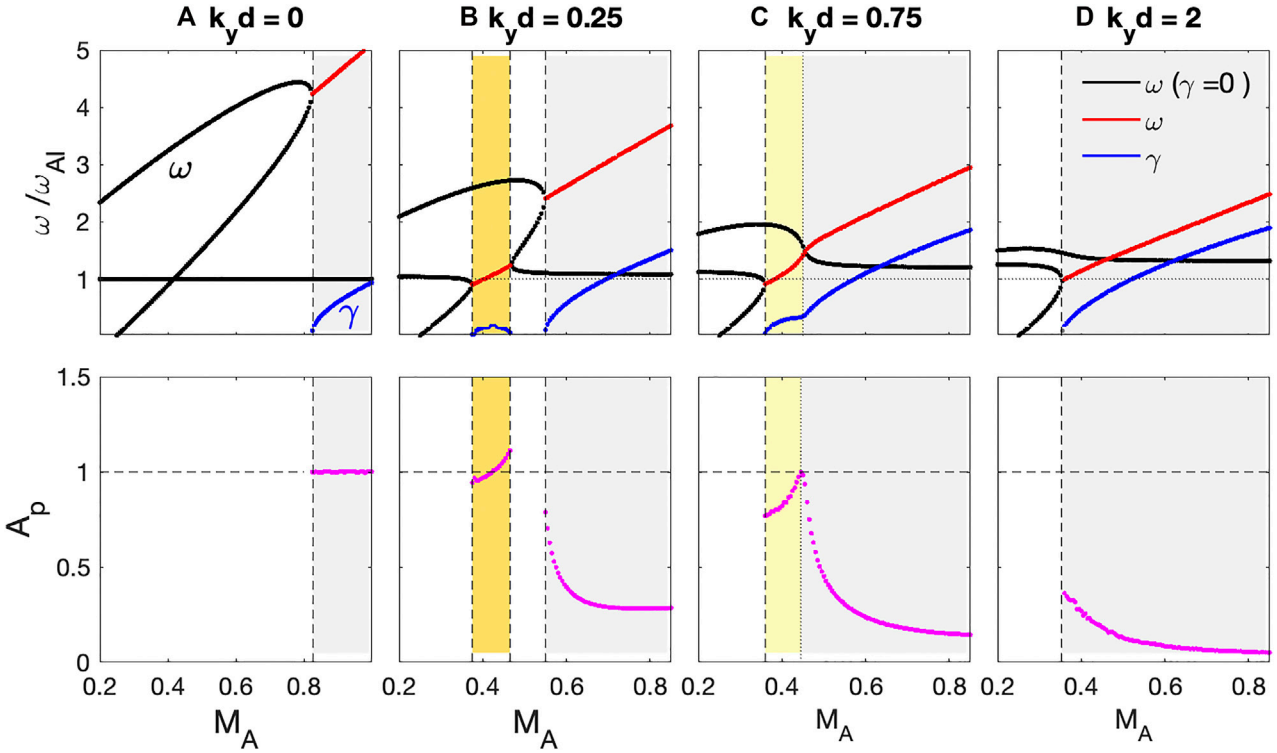

FIGURE 2 | (Upper) Normalized eigenfrequencies (ω) and wave growth rate (γ) to Alfvén wave frequency at the magnetosheath (ω_{AI}). **(Lower)** The amplitude ratio of the magnetic compressional component (A_p) at the two interfaces for $k_y d$ = 0, 0.25, 0.75, and 2.0, respectively.

compressional amplitude ratio (A_p) in the lower panel shows significant differences between PKHWs and SKHWs; $A_p \ll 1$ for the PKHWs and $A_p \sim 1$ for the SKHWs. Therefore, for SKHWs, the amplitude of the instability is similar at both the V_0 and V_A interfaces, indicating a spreading of wave power over a more extended region, while the PKHWs are localized about the V_0 interface. When the Mach number is low, it is expected that only the SKHWs would be excited.

When the V_A interface is further away from the V_0 interface ($k_y d$ = 0.75), as shown in **Figure 2C**, the PKHW and SKHW modes merge near $M_A \sim 0.47$. Although ω and γ monotonically increase as a function of M_A, the KH waves have similar behavior to the SKHW ($A_p \sim 1$ and $\omega \sim \omega_{AI}$) at smaller M_A and the PKHWs ($A_p < 1$ and $\omega \gg \omega_{AI}$) at larger M_A. Thus, the waves may still be divided into the semi-SKHW marked as a light yellow-shaded region and PKHW marked as a gray-shaded region in **Figure 2C**.

For $k_y d = 2$, as shown in **Figure 2D**, only a single unstable wave mode corresponding to the PKHWs occurs localized at the V_0 interface. The V_A profile can be treated as a constant at the V_0 interface and the M_A threshold becomes $M_{As} \sim 2\tan^{-1}(\phi) = 0.359$. The threshold occurs near $\omega/\omega_{AI} \sim 1$; thus, the wave frequencies are always higher than ω_{AI}.

It is also useful to examine how ω and A_p depend on M_A and $k_y d$. **Figure 3A,B** shows contour plots of ω normalized to 1) ω_{KH0} and 2) ω_{AI}, respectively. In this figure, two wave modes are clearly organized by ranges of M_A; the PKHW for $M_A > 0.47$ and the SKHW for $0.355 \leq M_A \leq 0.47$. Red and magenta lines in **Figure 3A** represent the M_A threshold for the PKHW and SKHW, respectively. The M_A threshold of the PKHWs decreases and the upper M_A limit of the SKHWs increases as $k_y d$ increases. The thresholds merge near $k_y d \sim 0.534$ and $M_A \sim 0.47$. Thus, for $M_A > 0.47$, a single wave mode appears (see **Figure 2C**); however, wave characteristics at lower and higher M_A are significantly different.

The PKHWs show that all parameters (ω/ω_{KH0}, ω/ω_{AI}, and A_p) have a strong dependence on $k_y d$, and they decrease as $k_y d$ increases. For most M_A, $\omega/\omega_{KH0} \sim 1$ and $1 < \omega/\omega_{KH0} < 2$. Because both ω and ω_{KH0} increase proportionally to M_A, ω/ω_{KH0} has less dependence on M_A. However, because ω_{AI} does not depend on k_y and ω increases as M_A increases, ω/ω_{AI} depends on both M_A and $k_y d$. For the given conditions, ω/ω_{AI} is maximized when $k_y d$ is small and M_A is large. **Figure 3C** shows $A_p < 1$ for $M_A \geq 0.47$, except $k_y d \to 0$. Thus, it shows that the PKHWs are almost always dominant at the V_0 interface. For $k_y d \to 0$, a strong amplitude of the pressure term occurs at the secondary interface. However, this increase in A_p is not an indicator of a separate instability, but rather it simply indicates that the decay of the wave power from the V_0 interface to the V_A interface reduced as the shear layer vanishes.

On the other hand, the eigenmode frequency of the SKHWs is comparable to ω_{KH0} and ω_{AI} ($0.9 \leq \omega/\omega_{KH0(AI)} \leq 1.2$) in the entire range of $k_y d$ and M_A because this wave mode appears due to the coupling between shear Alfvén mode and the fast compressional waves (thus, $\omega_{KH0(AI)} \sim \omega_{AI}$). For the entire range of $k_y d$, A_p is

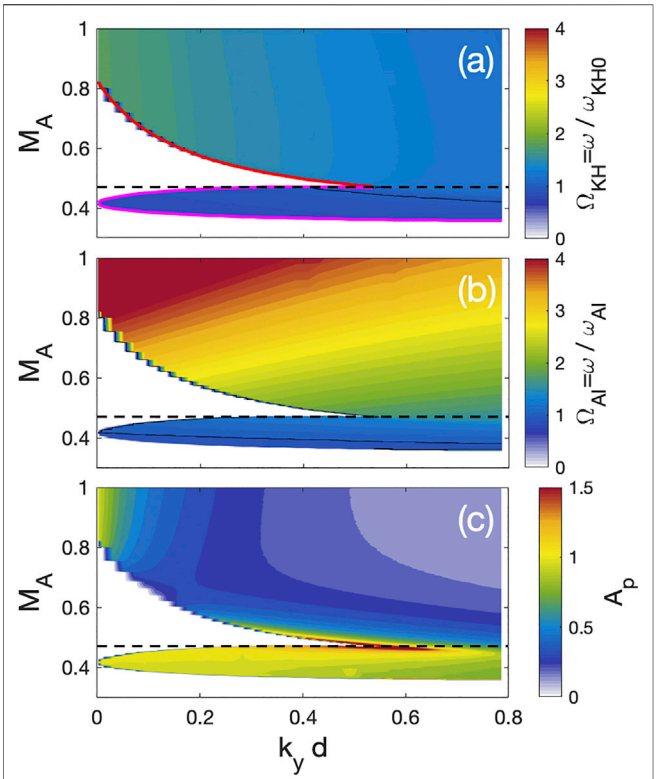

FIGURE 3 | (A,B) Normalized eigenfrequencies to $\omega_{KH0} = \frac{1}{2}k_y V_0$ and $\omega_{AI} = k_\parallel V_{AI}$. **(C)** The amplitude ratio of the compressional magnetic field component A_p. Here, the horizontal and vertical axes are normalized shear layer width ($k_y d$) and Alfvén Mach number (M_A).

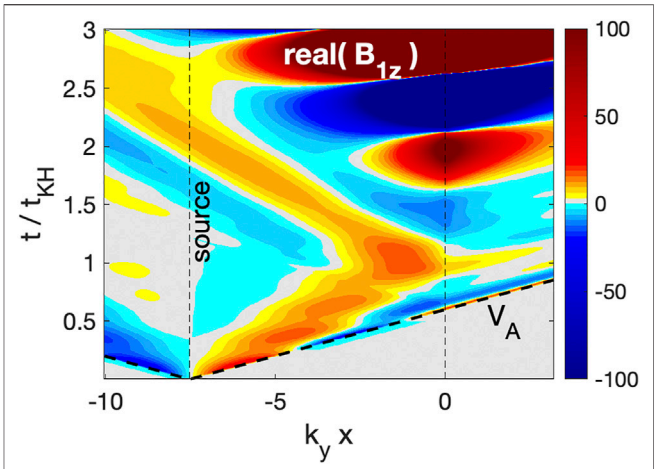

FIGURE 4 | The time evolution of the magnetic compressional component (B_{1z}) in the x-direction. The time and space are normalized to $t_{KH} = 2\pi/\omega_{KH0}$ and k_y, respectively. The interface is assumed to be located at $k_y x = 0$. It is noted that the wave power is saturated at a 100 in this figure.

always close to or even higher than 1. These results suggest that the KH instability occurs at both the V_0 and V_A interfaces with almost the same amplitude even though the interfaces are well separated.

The eigenmode calculations can be summarized as follows: the PKHWs are localized at the V_0 interface having a higher frequency than ω_A in the magnetosheath for faster shear flow velocity, while the SKHWs can be detected at both the V_0 and V_A interfaces with similar wave frequency to ω_{AI} in the magnetosheath for slower shear flow velocity.

4 MHD WAVE SIMULATIONS

In order to examine the PKHWs and SKHWs, we also developed an MHD wave simulation model. Similar to the previous fluid wave simulation codes (Kim and Lee, 2003; Kim et al., 2007), the finite-difference method is used in both time and space to solve the MHD **Equations 5–9** as an initial-valued problem. We adopt a box model in which B_0 is assumed to lie along the z-direction and inhomogeneity is introduced in the x-direction, while the boundary layer plasma flows in the y-direction with variation in the x-direction. Perfect reflecting boundaries are assumed and strong collisions are applied near the boundaries to describe semi-infinite space. Therefore, the total energy of traveling waves decreases once the initial waves reach the boundary. Seed perturbations in the simulation domain result in linear growth of unstable modes, and the growth rate can be calculated once the unstable waves exceed the amplitudes of the initial perturbation.

4.1 KH Waves in Uniform V_A Plasma

We first examine the KH waves in a plasma where V_A does not vary in space. In this simulation, a hyperbolic tangent V_0 profile along with constant V_A was adopted in the wave code:

$$V_0(x) = \frac{V_{0I}}{2}\left[1 - \tanh\left(\frac{x}{a}\right)\right], \tag{33}$$

where V_{0I} is the flow velocity in region I, and this profile characterizes the V_0 discontinuity in a scale length a, as shown in **Figure 1B**. One of the primary differences between the background profile used in the time-dependent analysis, and the previously discussed eigenmode analysis ($a \rightarrow 0$) is the fact that the discontinuous profile has been smoothed.

We assume that the length of the simulation box is $L_x \sim 45/k_y$. Since the KH surface wave is expected to not fully decay by the time it reaches the edge of the simulation domain in the x-direction, we add an absorption layer near the boundary ($\sim 30/k_y$) in the simulation box to prevent reflection. An initial perturbation is launched as a compressional component of V_{1x} at the source location ($k_y x_{source} \sim -7.5$) in region I (i.e., magnetosheath). This source is assumed to have a narrow spatial width ($k_y \delta_{source} = 0.093$) and to include broadband frequencies, $V_{1x}(x,t) = \exp(-1.5\frac{t^2}{t_{KH}^2})\exp(-\frac{(x-x_{source})^2}{\delta_{source}^2})$, where $k_{KH} = 2\pi/\omega_{KH0}$. The simulation is run from $t = 0$ to $t = 5.6t_{KH}$, and all components of B_1 and V_1 at each time step are stored during the simulation run time. The background densities in the magnetosheath (region I) and the magnetosphere (region III), the background magnetic field strength, k_y, and k_z are the same as in the eigenmode analysis of **Section 3**.

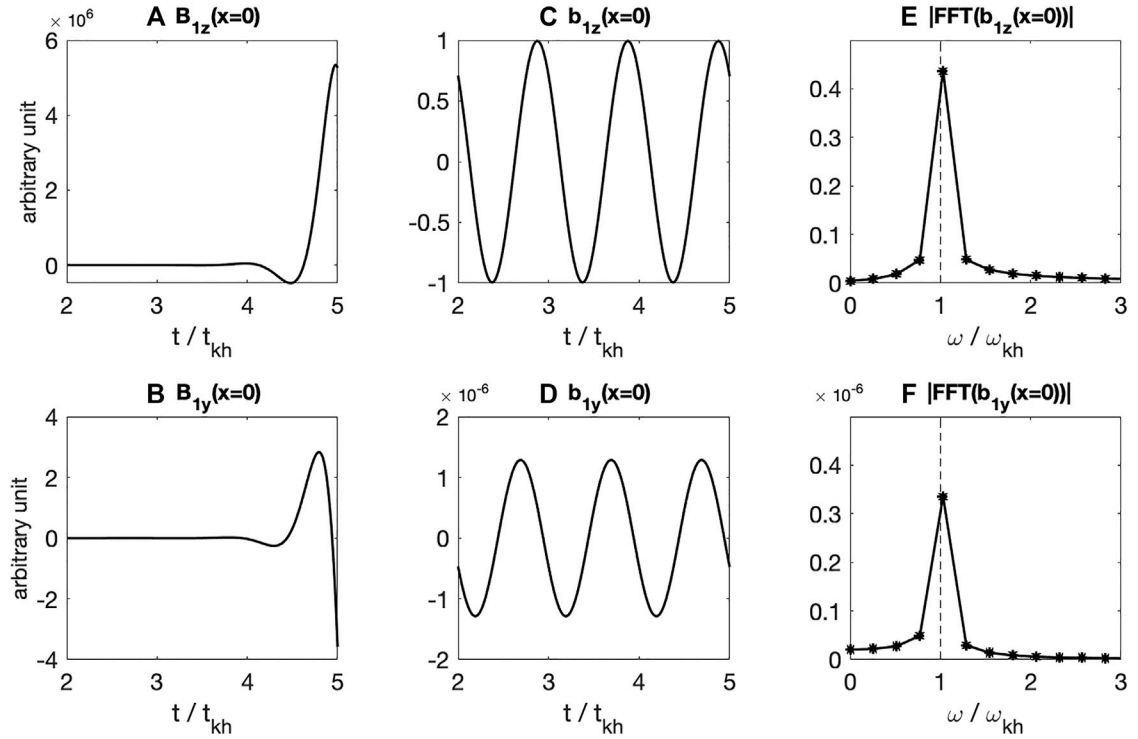

FIGURE 5 | (A,B) Time histories of magnetic compressional (B_{1z}) and transverse (B_{1y}) components, **(C,D)** time histories removing the growth rate of b_{1z} and b_{1y}, and **(E,F)** fast Fourier transform in time of b_{1z} and b_{1y} at the interface ($k_y x = 0$).

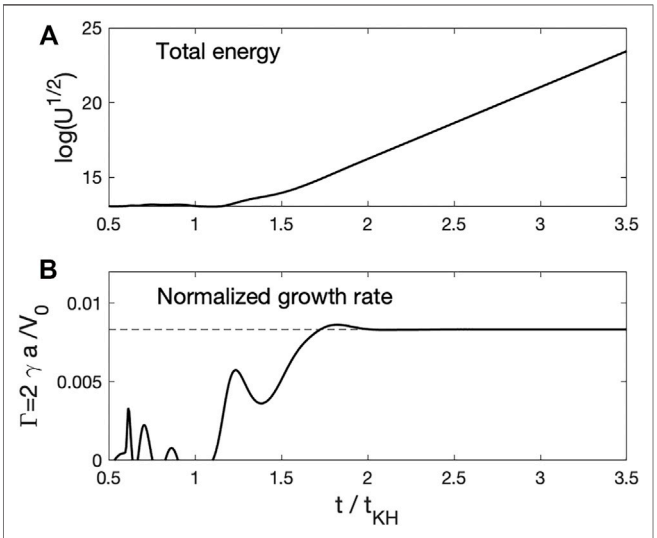

FIGURE 6 | (A) Time evolution of wave energy (U) and **(B)** normalized growth rate ($\Gamma = 2\gamma a/V_{0l}$) in time.

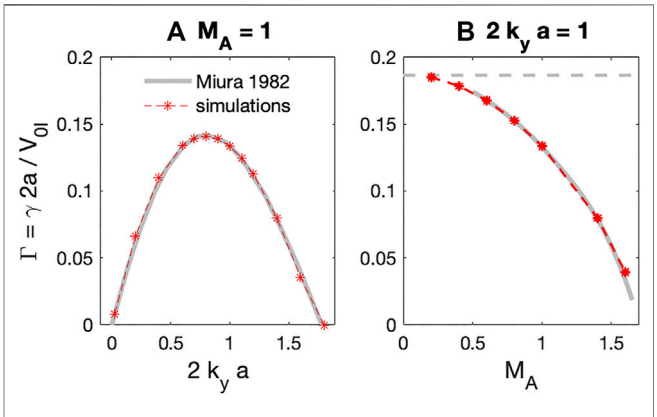

FIGURE 7 | Normalized growth rates ($\Gamma = 2\gamma a/V_{0l}$) of KH surface waves **(A)** as a function of normalized tangential wavenumber $2k_y a$ for $M_A = 1$ and **(B)** as a function of M_A for $2k_y a = 1$. Here, gray and red star dashed lines are from Miura and Pritchett (1982) and simulation results.

Figure 4 shows the time evolution of the magnetic compressional component (B_{1z}) in the x-direction for $M_A = 1$ and $k_y a = 0.025$. Two vertical lines represent the source location ($k_y a = -7.5$) and the V_0 interface ($k_y x = 0$), and thick dashed lines represent Alfvén speed (V_A). Since the initial wave packet includes broadband frequencies, the wave packet disperses in time and space. Leftward propagating waves reach a strong collisional layer near the boundary ($k_y x < -10.5$) and are totally absorbed. Rightward propagating waves reach the V_0 interface at $k_y x = 0$ around $t/t_{KH} = 0.7$, and they partially reflect from the interface due to a steepened density gradient. The rest of the waves penetrates the V_0 interface and reach the collisional layer ($k_y x > 3.0$). Once the magnetic field and velocities are perturbed near the interface, an unstable

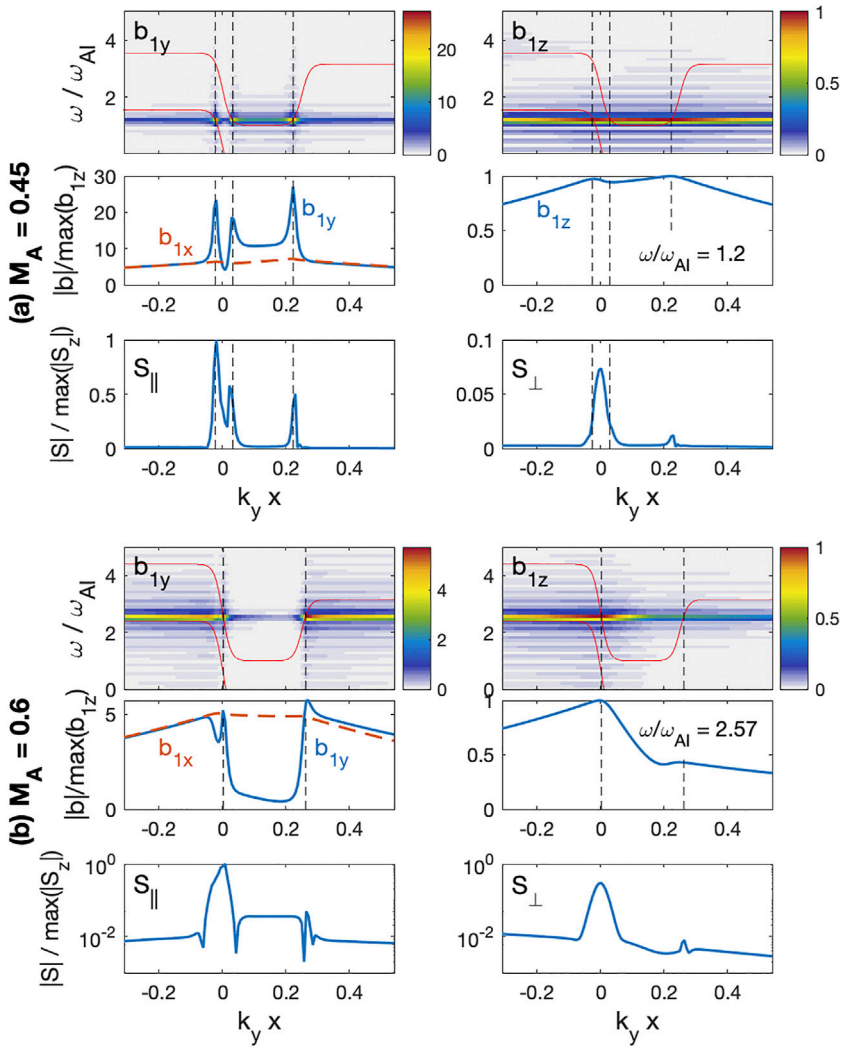

FIGURE 8 | Wave spatial distribution for $k_y d = 0.25$ **(A)** $M_A = 0.45$ and **(B)** $M_A = 0.6$. Upper panels are perturbed magnetic field compressional (b_{1z}) and transverse (b_{1y}) components, middle panels are the spatial structure of the peak frequency, and lower panels are the Poynting flux parallel ($S_\parallel$) and perpendicular ($S_\perp$) to B_0.

wave mode begins to grow at around $t/t_{KH} \sim 1.2$. Unlike the initial perturbation, these waves decay in the x-direction rather than propagate. The wave amplitude in **Figure 4** saturates at ± 100.

We focus on the surface waves at $k_y x = 0$ and determine the growth rate, wave frequency, and polarization. Time histories of B_{1z} and B_{1y} at $x = 0$ in **Figure 5A** rapidly grow in time; thus, the sinusoidal wave form is not clearly seen. However, the wave growth term can be removed from the time histories using the magnetic (U_B), kinetic energy (U_V), or total energy ($U = U_B + U_V$). We plot $U_{tot}(t) = \sum_x U(x, t)$ in the simulation box in **Figure 6A**. Early in the simulation period ($t/t_{KH} < 1.2$) U_{tot} is quasi-stable; however, once an unstable waves generated, it increases linearly. The wave magnetic field with a constant growth rate γ can be written as

$$B_1(x,t) \sim b_1(x,t)\exp[\gamma(x,t)t], \tag{34}$$

and because of the magnetic energy $U_B \propto |B|^2$, the wave growth rate γ in each grid point can be estimated from

$$\gamma(x,t) \sim \frac{\partial}{\partial t}\ln\left(\sqrt{U_B(x,t)}\right). \tag{35}$$

We also confirmed that γ calculated using either the magnetic (U_B) or kinetic energies (U_V) are identical; thus, $\gamma(x,t) = \frac{\partial}{\partial t}\ln\left(\sqrt{U(x,t)}\right) = \frac{\partial}{\partial t}\ln\left(\sqrt{U_B(x,t)}\right) = \frac{\partial}{\partial t}\ln\left(\sqrt{U_V(x,t)}\right)$. Furthermore, once the initial wave vanishes near the boundary, only the localized surface waves (such as KH waves) remain in the simulation domain; thus, γ also can be calculated using U_{tot}:

$$\gamma(t) = \frac{\partial}{\partial t}\ln\left(\sqrt{U_{tot}(t)}\right). \tag{36}$$

When a boundary has a finite thickness, the normalized growth rate ($\Gamma \equiv 2a\gamma/V_{0I}$) becomes a function of normalized

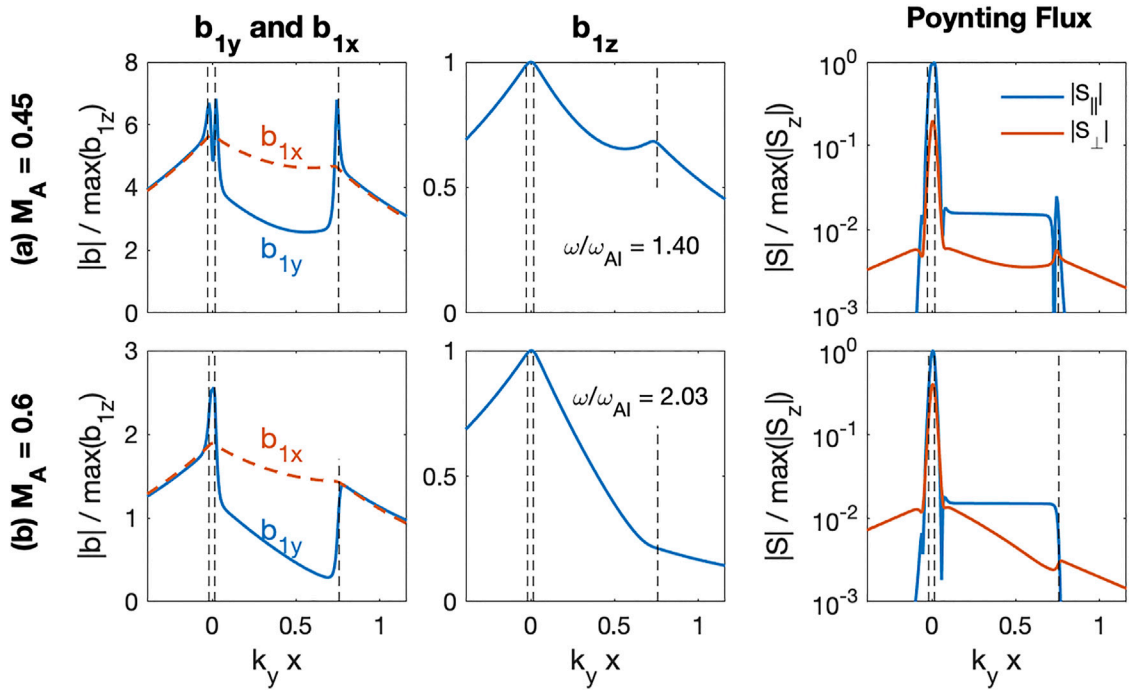

FIGURE 9 | Wave spatial distribution for $k_y d = 0.75$ **(A)** $M_A = 0.45$ and **(B)** $M_A = 0.6$.

boundary width ($2k_y a$) (Miura and Pritchett, 1982). To illustrate, the time evolution of $\Gamma(t)$ is plotted in **Figure 6B** for $k_y d = 0.025$ and $M_A = 1$, and it converges to ~ 0.0083. Therefore, for these parameters, the normalized growth rate can be estimated as $\Gamma = 0.0083$.

Once the growth rate is determined, the wave components (and polarization) can be obtained from

$$b_1(t) \sim B_1(t)/\exp(\gamma(t-t_0))\big|_{t>t_0}, \tag{37}$$

where t_0 is the time at which the wave growth begins. **Figures 5C,D** show that b_{1z} and b_{1y} have clear sinusoidal structures with a single frequency. The wave spectra of b_{1z} and b_{1y} in **Figures 5E,F** confirm that the single peak corresponds the KH wave frequency, $\omega_{KH0} = \frac{1}{2}k_y V_0$. In this manner, we can determine both the real and imaginary components of the frequency, which can be compared with the eigenmode analysis.

For code validation, we also compared the simulation results with prior analytical results in Miura and Pritchett (1982). **Figure 7** shows the growth rate, Γ, as a function of (a) $2k_y a$ for $M_A = 1$ and (b) as a function of M_A for $2k_y a = 1$. In this figure, the prior analytic results (gray lines) and our simulations (red stars) show excellent agreement with each other. For $M_A = 1$ in **Figure 7A**, wave growth only occurs for a limited value of the normalized boundary width $0 < 2k_y a < 1.8$ and maximizes near $2k_y a = 0.8$. For $2k_y a = 1$, the maximum Γ occurs for $M_A \to 0$ and has a value of 0.144, as predicted from Miura and Pritchett (1982). The growth rate decreases as M_A increases and no KH wave arises for $M_A > 1.6$. Therefore, the new MHD wave code successfully demonstrates KH waves and benchmarking comparisons of the simulations with previous analytical results validate the code accuracy.

4.2 Coupling Between KH and Alfvén Resonant Waves

In this section, the simulation results include the shear transition layer between the magnetosphere and the magnetosheath, as shown in **Figure 1B**. In contrast to the results of **Section 3**, we consider a finite width of the boundary layer. Similar to the V_0 profile in **Equation 33**, V_A is assumed to have a hyperbolic tangent profile:

$$V_A(x) = V_{AI} + \frac{V_{AI} + V_{AIII}}{2}\left[\tanh\left(\frac{x-d}{a}\right)\right]. \tag{38}$$

The two interfaces are separated with width d, although each interface has its own width, a. From the eigenfrequency calculations in **Figure 2**, we showed that the inclusion of a shear transition layer effectively generates the SKHWs when the shear flow velocity is slow; thus, we ran the simulations for $k_y d = 0.25$ and 0.75 and $M_A < 0.85$ to compare with the eigenmode calculation.

We used the time histories of b_1, which does not include the exponential growth, in order to analyze the real frequency and relative strength of the field components. **Figure 8** presents wave spectra of perturbed magnetic field and the Poynting flux for $k_y d = 0.25$. For $M_A = 0.45$ in **Figure 8A**, only the waves at $\omega/\omega_{AI} \sim 1.2$ have strong amplitude. This frequency is close to the eigenmode frequency of $\omega/\omega_{AI} = 1.17$ in **Figure 2**. The

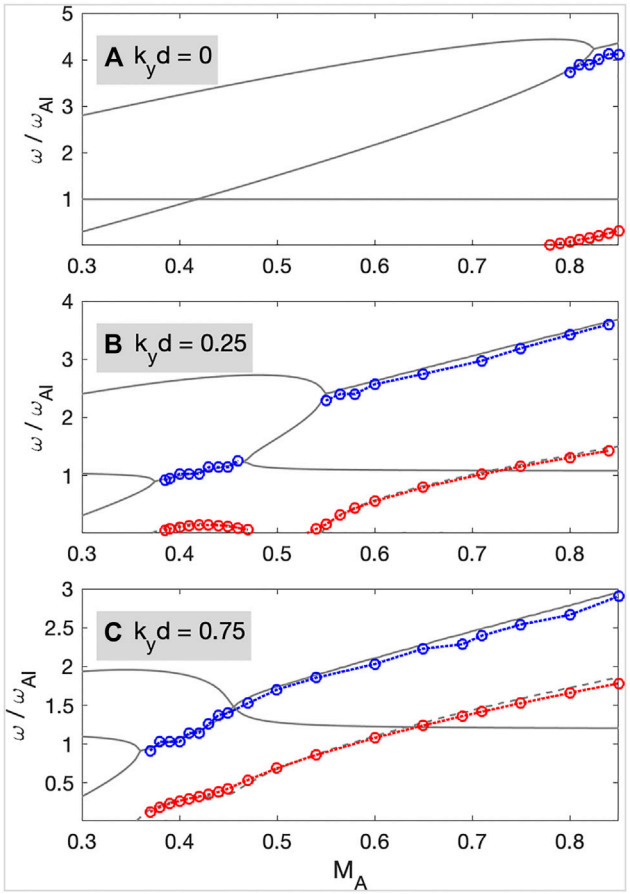

FIGURE 10 | Calculated wave frequency (blue circles) and growth rate (red circles) from time-dependent simulations and eigenmode analysis (gray lines) for $k_y d$ = 0.25 and 0.75.

estimated growth rate near the V_0 and V_A interfaces are identical with γ/ω_{AI} = 0.128. This growth rate is also in good agreement with the analytical results of γ/ω_{AI} = 0.142 in **Section 3**.

In order to examine the detailed wave properties, we plot spatial structures of the fluctuating magnetic field (b_{1x}, b_{1y}, and b_{1z}) at ω/ω_{AI} = 1.2 in the middle row of **Figure 8A**. In this case, the compressional components (b_{1x} and b_{1z}) maximize at the V_A and V_0 interfaces and decay in the x-direction away from the interfaces. The b_{1z} and b_{1x} amplitudes at the two interfaces are comparable; thus, $b_{1z}(x = d)/b_{1z}(x = 0)$ = 1.025. This ratio is almost identical to the amplitude ratio of the pressure A_p = 1.06 from **Figure 2B**.

On the other hand, the transverse component b_{1y} is enhanced at three different locations near V_0 ($k_y x$ = −0.022 and 0.033) and V_A interfaces (k_y = 0.22), where the wave frequency matches the Alfvén resonance condition (ω_{AR}):

$$\omega = \omega_{AR}^{\pm} \equiv k_y V_0 \pm k_{\parallel} V_A.$$

Due to the finite width of the V_0 interface near x = 0, ω_{AR}^{-} can be positive at the V_0 interface; thus, two separate regions of enhanced wave power can occur corresponding to Doppler-shifted resonance with both Alfvén resonances. In this case, b_{1y} is significantly stronger than b_{1z} or b_{1x}, and $b_{1y}/\max(b_{1z})$ ~ 28 at the V_A interface. Furthermore, strong field-aligned Poynting flux occurs at the interfaces, as shown in the lower panels of **Figure 8A**. The Poynting flux parallel ($S_{\parallel}$) and perpendicular ($S_{\perp}$) to B_0 show that the wave energy predominantly flows along the magnetic field line at both interfaces. Since we launch compressional waves (with V_{1x}) in the magnetosheath, and the growing KH waves are compressional waves, the amplitude enhancement of the magnetic transverse component and intense field-aligned Poynting flux at the interfaces are clear evidences of the mode conversion from the surface KH waves to the surface Alfvén waves.

For the higher M_A case in **Figure 8B**, the amplitude is maximized at ω = 2.57ω_{AI}, which is similar to the analytical value of ω = 2.6ω_{AI} in **Section 3**. The b_{1z} component maximizes near x = 0 and the secondary peak near $k_y x$ = 0.25 becomes weaker. The b_{1z} amplitude ratio between the two interfaces is 0.64, which is in good agreement with the analytical value of A_p = 0.4. The b_{1y} component shows strong amplitude near $k_y x$ = 0 and $k_y x$ = 0.26. In this case, because the eigenmode frequency is higher than ω_{AR}^{-}, b_{1y} enhanced only at $\omega = \omega_{AR}^{+}$. The amplitude ratio between b_{1y} and b_{1z} is much lower than that for the case with M_A = 0.45 in **Figure 8A**, having $b_{1y}/\max(b_{1z})$ ~ 6 at $x \sim d$. Strong field-aligned flux $S_{\parallel}$ appears at the V_0 interface in the bottom panels, but $S_{\perp}$ becomes stronger than the case of M_A = 0.45. The analytic eigenmode calculations predict that the PKHWs occur under ($k_y d$, M_A) = (0.25, 0.75). The simulation results show that the mode conversion from the PKHWs to the surface Alfvén wave still occurs at each interface, but this process is less effective than that from the SKHWs.

For $k_y d$ = 0.75, the waves have a strong amplitude peak near ω/ω_{AI} = 1.4 and 2.03 for M_A = 0.45 and 0.6, respectively, and the spatial structures of these waves are presented in **Figure 9**. In this case, the PKHWs and SKHWs are not separated anymore (See **Figure 2**) and we define the KH waves in the lower M_A as semi-SKHWs in **Section 3**. For M_A = 0.45 in **Figure 9A**, b_{1z} maximizes near x = 0 and a weak secondary peak appears near $x = d$. On the other hand, three amplitude peaks near $k_y x$ = − 0.025 4, 0.018, and 0.754 appear in b_{1y}. The power ratio $|b_{1y}/\max(b_{1z})|$ at the V_0 interface is reduced to $|b_{1y}/\max(b_{1z})|$ ~ 7 from 23 for ($k_y d$, M_A) = (0.25, 0.45) in **Figure 8A**. The enhancement of $S_{\parallel}$ is also seen at both interfaces and relatively strong $S_{\perp}$ also appears. Near x = 0 at the V_0 interface, $|S_{\perp}/S_{\parallel}|_{x=0}$ is about 0.39, which is almost twice as large as $|S_{\perp}/S_{\parallel}|_{x=0}$ = 0.195 for ($k_y d$, M_A) = (0.25, 0.45). Therefore, even though the compressional wave behavior of the semi-SKHWs is similar to the SKHWs, the mode conversion from semi-SKHWs becomes much weaker than that from the SKHWs.

For M_A = 0.6 in **Figure 9B**, b_{1z} decays along the x-direction from the V_0 interface and no amplitude bump occurs at the V_A interface. The b_{1y} component shows a discontinuity at the V_A interface following the compressional Alfvén wave dispersion relation. Therefore, $S_{\perp}$ becomes comparable to $S_{\parallel}$ for $k_y x$ > 0.75. In this case, the mode conversion at the V_A interface does not occur, but energy still flows along the magnetic field line at the V_0 interface.

We also analyzed the cases for M_A for $k_y d$ = 0, 0.25, and 0.75 at various M_A. **Figure 10** shows the extracted eigenmode frequency and growth rate from the simulations. In this figure, the red and

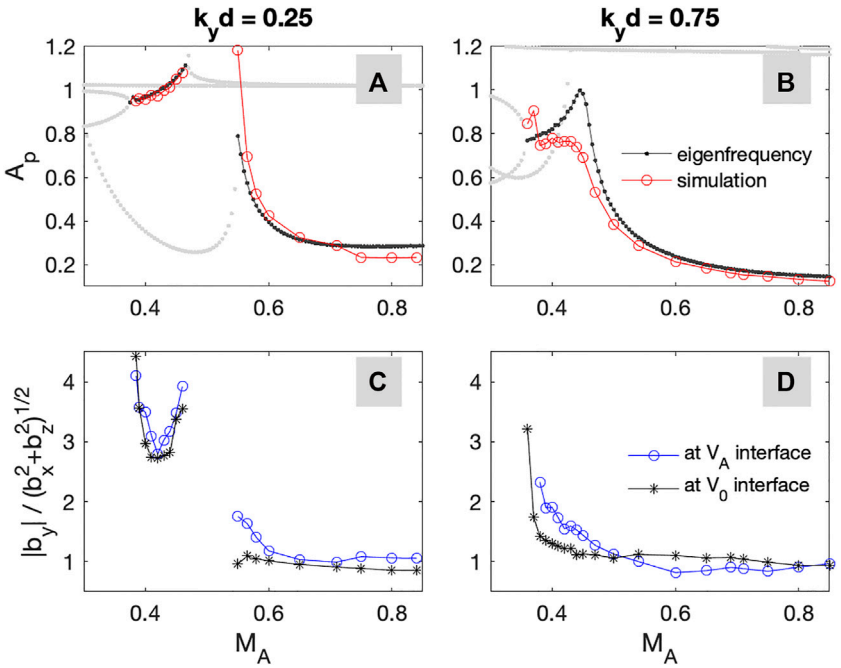

FIGURE 11 | (A,B) A_p from the simulations (red circles) eigenfrequency calculations (black dots) for $k_y d$ = 0.25 and 0.75. **(C,D)** The amplitude ratio between the transverse and compressional components at the V_0 interface (black stars) and the V_A interface (blue circles), respectively.

blue circled lines represent simulations, and the gray lines are taken from the eigenfrequency analysis from **Figure 2** in **Section 3**. Although the boundary thicknesses used in **Section 2** (slab) and **Section 3** (width a) are different because the inhomogeneity scale length for the numerical simulation is much shorter than the wavelength, the eigenmode analytical and simulation results in ω and γ show excellent agreement.

We also calculate the amplitude ratios between the compressional component at the two interfaces (A_p) and between transverse (b_{1y}) and compressional ($\sqrt{b_{1x}^2 + b_{1z}^2}$) components at each interface. Due to the finite thickness of the boundary, two wave amplitude peaks can occur within the V_0 interface as shown in **Figures 8**, **9**, so we average the amplitude near $x = 0$, if $\omega = \omega_{AR}^{\pm} = k_y V_0 \pm k_z V_A$. The simulated A_p and eigenfrequency calculations show good agreement with each other in **Figure 11A,B**. In particular, A_p of the SKHWs in **Figure 11A** are almost identical to the analytic calculations. Thus, these results confirm that the SKHWs occur with nearly the same amplitude at both interfaces, while the PKHWs only happen at the V_0 interface. The amplitude ratio between the transverse and compressional components in **Figure 11C,D** suggests that the transverse magnetic component of the SKHWs is dominant. In other words, the mode conversion to the shear Alfvén wave from the SKHWs effectively occurs at the interfaces. The PKHWs in **Figure 11C** and semi-SKHWs and PKHWs in **Figure 11D** show that the transverse mode amplitudes are comparable to the compressional mode amplitude; therefore, weaker or no mode conversion occurs under given conditions at the V_A interface.

5 CONCLUSION AND DISCUSSION

This article investigates the coupling between KH and Alfvén waves when a shear transition layer exists between the magnetosheath and magnetosphere. Using the eigenfrequency analysis and time-dependent wave simulations, we showed that the SKHWs are generated when the shear velocity is slower than the typical threshold value for the onset of the KH instability.

The SKHWs occur with a frequency comparable to both KH wave frequency ($\omega_{KH0} = \frac{1}{2} k_y V_0$) and the Alfvén frequency at the magnetosheath ($\omega_{AI} = k_{\parallel} V_{AI}$), while the PKHWs have a much higher frequency than ω_{AI}. These results suggest that PKHWs and SKHWs can be identified using the frequency ratio to ω_{KH0} and ω_{AI} from *in situ* observations. The SKHWs appear at both the V_0 and V_A interfaces with nearly the same amplitude, while the PKHWs appear only at the V_0 interface. Since V_0 is uniform at the V_A interface, no KH waves can be generated at the V_A interface without coupling between the KH and Alfvén waves. For the given conditions of $0 < k_y d \leq 0.5$, where the SKHWs are well separated from the PKHWs in **Figure 3** and the shear transition layer width is $0 < d \leq 0.3 R_E$; thus, if the thickness of each boundary (a) is much shorter than the width of the transition layer (d), the SKHWs can be detected at the V_A interface.

The simulation results in **Figures 8**, **9** show that the magnetic transverse component is dominant at the interface and a strong

field-aligned Poynting flux appears. Therefore, the energy transfer from the boundary layer to the Earth via mode-converted shear Alfvén waves occurs, which is similar to observations (Chaston et al., 2007). The wave simulations predict that a stronger mode conversion occurs from the SKHWs than from the PKHWs. However, the wave growth rate should be considered as well. Even though the mode conversion efficiency from the PKHWs is weaker than the SKHWs, the PKHWs amplitude can be strong enough due to the higher growth rate. Thus, a strong transverse component also can be detected from the PKHWs, but the compressional components are still comparable to the transverse components.

Although we clearly show the characteristics of PKHWs and SKHWs, this article only considers that the magnetic field is perpendicular to the flow velocity, and the magnetic field is assumed to be a constant. Indeed, the magnetic field in the magnetosheath and magnetosphere can be perpendicular in the magnetopause, and also the magnetic field and the flow velocity can be parallel in space, such as the solar corona and magnetotail. The secondary KH instability or resonant flow instability can occur under such conditions (Taroyan and Erdélyi, 2002, 2003; Turkakin et al., 2013). Furthermore, compressional waves bounded in the inner magnetosphere can contribute to the generation of the secondary KH instability (Turkakin et al., 2013) and also mode conversion to the shear Alfvén wave (Taroyan and Erdélyi, 2002). The total length of our numerical simulation model, including the collisional layer in **Section 4**, is somewhat comparable to $\sim 10R_E$; thus, the *bounded* plasma effect should be considered in the future.

We also used a cold plasma approximation in the magnetosheath. The inclusion of thermal effects leads to an additional KH wave branch (Taroyan and Erdélyi, 2003). In warm plasmas, the Alfvén waves propagate as kinetic Alfvén waves (KAW). The KAW can have a larger wavenumber across the magnetic field line and field-aligned electric field and velocity components (Lin et al., 2010, 2012). Similar to Alfvén waves, KAW also transfers the energy away from the mode conversion location along the magnetic field line; thus, it is expected that a strong transverse component at each interface would also be detected with thermal effect.

In addition, a high level of turbulent fluctuations in the magnetosheath is observed in multiple satellites (e.g., Rakhmanova et al., 2021); however, nonlinear effects are not included in our analysis. It is possible that if these modes grow to sufficient amplitude, vortices will form and nonlinear interactions may become important, leading to plasma heating and transport. These nonlinear effects are left for future studies.

DATA AVAILABILITY STATEMENT

The raw data supporting the conclusions of this article will be made available by the authors, without undue reservation. Digital data can be found in the DataSpace of Princeton University http://arks.princeton.edu/ark:/88435/dsp013r074z09k

AUTHOR CONTRIBUTIONS

E-HK developed the real-time simulation code and ran both eigenfrequency calculation and simulation code, JRJ solved the dispersion relation of the KH waves and built the eigenfrequency calculation code, and KN discussed the observational background.

FUNDING

This material is based upon work supported by the United States Department of Energy, Office of Science, Office of Fusion Energy Sciences under contract DE-AC02-09CH11466. Work at Princeton University is under National Science Foundation (NSF) grant AGS1602855 and National Aeronautics and Space Administration (NASA) grants 80HQTR18T0066, 80HQTR19T0076, and NNX17AI50G. Work at Andrews University is supported by NASA grants NNX16AQ87G, 80NSSC19K0270, 80NSSC19K0843, 80NSSC18K0835, 80NSSC20K0355, NNX17AI50G, NNX17AI47G, 80HQTR18T0066, 80NSSC20K0704, and 80NSSC18K1578 and NSF grants AGS1832207 and AGS1602855. Work at Embry-Riddle Aeronautical University is under NASA grant NNX17AI50G.

REFERENCES

Andries, J., and Goossens, M. (2001). Kelvin-Helmholtz Instabilities and Resonant Flow Instabilities for a Coronal Plume Model with Plasma Pressure. *A&A* 368, 1083–1094. doi:10.1051/0004-6361:20010050

Andries, J., Tirry, W. J., and Goossens, M. (2000). Modified Kelvin-Helmholtz Instabilities and Resonant Flow Instabilities in a One-dimensional Coronal Plume Model: Results for Plasma \documentclass{aastex} \usepackage{amsbsy} \usepackage{amsfonts} \usepackage{amssymb} \usepackage{bm} \usepackage{mathrsfs} \usepackage{pifont} \usepackage{stmaryrd} \usepackage{textcomp} \usepackage{portland,xspace} \usepackage{amsmath,amsxtra} \usepackage[OT2,OT1]{fontenc} \newcommand\cyr{ \renewcommand\rmdefault{wncyr} \renewcommand\sfdefault{wncyss} \renewcommand\encodingdefault{OT2} \normalfont \selectfont} \DeclareTextFontCommand{\textcyr}{\cyr} \pagestyle{empty} \DeclareMathSizes{10}{9}{7}{6} \begin{document} \landscape $\beta =0$ \end{document}. *ApJ* 531, 561–570. doi:10.1086/308430

Antolin, P., and Van Doorsselaere, T. (2019). Influence of Resonant Absorption on the Generation of the Kelvin-Helmholtz Instability. *Front. Phys.* 7, 85. doi:10.3389/fphy.2019.00085

Chandrasekhar, S. (1961). *Hydrodynamic and Hydromagnetic Stability*. Oxford, U.K.: Oxford University Press.

Chaston, C. C., Wilber, M., Mozer, F. S., Fujimoto, M., Goldstein, M. L., Acuna, M., et al. (2007). Mode Conversion and Anomalous Transport in Kelvin-Helmholtz Vortices and Kinetic Alfvén Waves at the Earth's Magnetopause. *Phys. Rev. Lett.* 99, 175004. doi:10.1103/PhysRevLett.99.175004

Chen, L., and Hasegawa, A. (1974). Plasma Heating by Spatial Resonance of Alfve´n Wave. *Phys. Fluids* 17, 1399–1403. doi:10.1063/1.1694904

Cowee, M. M., Winske, D., and Gary, S. P. (2010). Hybrid Simulations of Plasma Transport by Kelvin-Helmholtz Instability at the Magnetopause: Density Variations and Magnetic Shear. *J. Geophys. Res.* 115, A06214. doi:10.1029/2009JA015011

Delamere, P. A., and Bagenal, F. (2010). Solar Wind Interaction with Jupiter's Magnetosphere. *J. Geophys. Res.* 115, A10201. doi:10.1029/2010JA015347

Delamere, P. A., Ng, C. S., Damiano, P. A., Neupane, B. R., Johnson, J. R., Burkholder, B., et al. (2021). Kelvin-Helmholtz-Related Turbulent Heating at Saturn's Magnetopause Boundary. *J. Geophys. Res. Space Phys.* 126, e2020JA028479. doi:10.1029/2020JA028479

Engebretson, M., Glassmeier, K.-H., Stellmacher, M., Hughes, W. J., and Lühr, H. (1998). The Dependence of High-Latitude Pcs Wave Power on Solar Wind Velocity and on the Phase of High-Speed Solar Wind Streams. *J. Geophys. Res.* 103, 26271–26283. doi:10.1029/97JA03143

Génot, V., and Lavraud, B. (2021). Solar Wind Plasma Properties during Ortho-parker Imf Conditions and Associated Magnetosheath Mirror Instability Response. *Front. Astron. Space Sci.* 8, 153. doi:10.3389/fspas.2021.710851

González, A. G., and Gratton, J. (1994). The Role of a Density Jump in the Kelvin-Helmholtz Instability of Compressible Plasma. *J. Plasma Phys.* 52, 223–244. doi:10.1017/S0022377800017888

Hwang, K.-J., Kuznetsova, M. M., Sahraoui, F., Goldstein, M. L., Lee, E., and Parks, G. K. (2011). Kelvin-Helmholtz Waves under Southward Interplanetary Magnetic Field. *J. Geophys. Res.* 116, A08210. doi:10.1029/2011JA016596

Johnson, J. R., and Cheng, C. Z. (2001). Stochastic Ion Heating at the Magnetopause Due to Kinetic Alfvén Waves. *Geophys. Res. Lett.* 28, 4421–4424. doi:10.1029/2001gl013509

Johnson, J. R., Wing, S., and Delamere, P. A. (2014). Kelvin Helmholtz Instability in Planetary Magnetospheres. *Space Sci. Rev.* 184, 1–31. doi:10.1007/s11214-014-0085-z

Johnson, J. R., Wing, S., Delamere, P., Petrinec, S., and Kavosi, S. (2021). Field-Aligned Currents in Auroral Vortices. *J. Geophys. Res. Space Phys.* 126, e28583. doi:10.1029/2020JA028583

Kim, E.-H., Cairns, I. H., and Robinson, P. A. (2007). Extraordinary-Mode Radiation Produced by Linear-Mode Conversion of Langmuir Waves. *Phys. Rev. Lett.* 99, 015003. doi:10.1103/physrevlett.99.015003

Kim, E.-H., and Lee, D.-H. (2003). Resonant Absorption of Ulf Waves Near the Ion Cyclotron Frequency: A Simulation Study. *Geophys. Res. Lett.* 30, 2240. doi:10.1029/2003gl017918

Lavraud, B., and Borovsky, J. E. (2008). Altered Solar Wind-Magnetosphere Interaction at Low Mach Numbers: Coronal Mass Ejections. *J. Geophys. Res.* 113, A00B08. doi:10.1029/2008JA013192

Lavraud, B., Larroque, E., Budnik, E., Génot, V., Borovsky, J. E., Dunlop, M. W., et al. (2013). Asymmetry of Magnetosheath Flows and Magnetopause Shape during Low Alfvén Mach Number Solar Wind. *J. Geophys. Res. Space Phys.* 118, 1089–1100. doi:10.1002/jgra.50145

Lin, Y., Johnson, J. R., and Wang, X. (2012). Three-Dimensional Mode Conversion Associated with Kinetic Alfvén Waves. *Phys. Rev. Lett.* 109, 125003. doi:10.1103/PhysRevLett.109.125003

Lin, Y., Johnson, J. R., and Wang, X. Y. (2010). Hybrid Simulation of Mode Conversion at the Magnetopause. *J. Geophys. Res.* 115, A04208. doi:10.1029/2009JA014524

Ma, X., Delamere, P. A., Nykyri, K., Burkholder, B., Neupane, B., and Rice, R. C. (2019). Comparison between Fluid Simulation with Test Particles and Hybrid Simulation for the Kelvin-Helmholtz Instability. *J. Geophys. Res. Space Phys.* 124, 6654–6668. doi:10.1029/2019JA026890

Ma, X., Delamere, P., Otto, A., and Burkholder, B. (2017). Plasma Transport Driven by the Three-Dimensional Kelvin-Helmholtz Instability. *J. Geophys. Res. Atmos.* 122, 10,382–10,395. doi:10.1002/2017JA024394

Matsumoto, Y., and Hoshino, M. (2006). Turbulent Mixing and Transport of Collisionless Plasmas across a Stratified Velocity Shear Layer. *J. Geophys. Res.* 111, A05213. doi:10.1029/2004JA010988

McComas, D. J., and Bagenal, F. (2008). Reply to comment by s. w. h. cowley et al. on "jupiter: A fundamentally different magnetospheric interaction with the solar wind". *Geophys. Res. Lett.* 35, L10103. doi:10.1029/2008GL034351

Mills, K. J., and Wright, A. N. (1999). Azimuthal Phase Speeds of Field Line Resonances Driven by Kelvin-Helmholtz Unstable Waveguide Modes. *J. Geophys. Res.* 104, 22667–22677. doi:10.1029/1999JA900280

Miura, A. (1984). Anomalous Transport by Magnetohydrodynamic Kelvin-Helmholtz Instabilities in the Solar Wind-Magnetosphere Interaction. *J. Geophys. Res.* 89, 801–818. doi:10.1029/JA089iA02p00801

Miura, A., and Pritchett, P. L. (1982). Nonlocal Stability Analysis of the MHD Kelvin-Helmholtz Instability in a Compressible Plasma. *J. Geophys. Res.* 87, 7431–7444. doi:10.1029/JA087iA09p07431

Moore, T. W., Nykyri, K., and Dimmock, A. P. (2016). Cross-scale Energy Transport in Space Plasmas. *Nat. Phys* 12, 1164–1169. doi:10.1038/NPHYS3869

Moore, T. W., Nykyri, K., and Dimmock, A. P. (2017). Ion-Scale Wave Properties and Enhanced Ion Heating across the Low-Latitude Boundary Layer during Kelvin-Helmholtz Instability. *J. Geophys. Res. Space Phys.* 122, 11128–11153. doi:10.1002/2017JA024591

Nakamura, T. K. M., Hasegawa, H., Daughton, W., Eriksson, S., Li, W. Y., and Nakamura, R. (2017). Turbulent Mass Transfer Caused by Vortex Induced Reconnection in Collisionless Magnetospheric Plasmas. *Nat. Commun.* 8, 1582. doi:10.1038/s41467-017-01579-0

Nakamura, T. K. M., Hasegawa, H., Shinohara, I., and Fujimoto, M. (2011). Evolution of an MHD-Scale Kelvin-Helmholtz Vortex Accompanied by Magnetic Reconnection: Two-Dimensional Particle Simulations. *J. Geophys. Res.* 116, A03227. doi:10.1029/2010JA016046

Nykyri, K., Ma, X., Burkholder, B., Rice, R., Johnson, J. R., Kim, E.-K., et al. (2021a). Mms Observations of the Multiscale Wave Structures and Parallel Electron Heating in the Vicinity of the Southern Exterior Cusp. *J. Geophys. Res. Space Phys.* 126, e2019JA027698. doi:10.1029/2019JA027698

Nykyri, K., Ma, X., Dimmock, A., Foullon, C., Otto, A., and Osmane, A. (2017). Influence of Velocity Fluctuations on the Kelvin-Helmholtz Instability and its Associated Mass Transport. *J. Geophys. Res. Space Phys.* 122, 9489–9512. doi:10.1002/2017JA024374

Nykyri, K., Ma, X., and Johnson, J. (2021b). *Cross-Scale Energy Transport in Space Plasmas*. Washington, D.C., United States: American Geophysical Union, 109–121. chap. 7. doi:10.1002/9781119815624.ch7

Nykyri, K., and Otto, A. (2001). Plasma Transport at the Magnetospheric Boundary Due to Reconnection in Kelvin-Helmholtz Vortices. *Geophys. Res. Lett.* 28, 3565–3568. doi:10.1029/2001GL013239

Otto, A., and Fairfield, D. H. (2000). Kelvin-Helmholtz Instability at the Magnetotail Boundary: MHD Simulation and Comparison with Geotail Observations. *J. Geophys. Res.* 105, 21175–21190. doi:10.1029/1999JA000312

Otto, A., and Nykyri, K. (2003). "Kelvin-Helmholtz Instability and Magnetic Reconnection: Mass Transport at the LLBL," in *Geophysical Monograph Series*. Editors P. T. Newell and T. Onsager (Washington DC: American Geophysical Union), 133, 53–62. doi:10.1029/133GM05

Paschmann, G., Baumjohann, W., Sckopke, N., Phan, T.-D., and Lühr, H. (1993). Structure of the Dayside Magnetopause for Low Magnetic Shear. *J. Geophys. Res.* 98, 13409–13422. doi:10.1029/93JA00646

Pu, Z.-Y., and Kivelson, M. G. (1983). Kelvin:Helmholtz Instability at the Magnetopause: Solution for Compressible Plasmas. *J. Geophys. Res.* 88, 841–852. doi:10.1029/JA088iA02p00841

Rakhmanova, L., Riazantseva, M., and Zastenker, G. (2021). Plasma and Magnetic Field Turbulence in the Earth's Magnetosheath at Ion Scales. *Front. Astron. Space Sci.* 7, 115. doi:10.3389/fspas.2020.616635

Ruderman, M. S., and Wright, A. N. (1998). Excitation of Resonant Alfvén Waves in the Magnetosphere by Negative Energy Surface Waves on the Magnetopause. *J. Geophys. Res.* 103, 26573–26584. doi:10.1029/98JA02296

Southwood, D. J. (1968). The Hydromagnetic Stability of the Magnetospheric Boundary. *Planet. Space Sci.* 16, 587–605. doi:10.1016/0032-0633(68)90100-1

Taroyan, Y., and Erdélyi, R. (2002). Resonant and Kelvin-Helmholtz Instabilities on the Magnetopause. *Phys. Plasmas* 9, 3121–3129. doi:10.1063/1.1481746

Taroyan, Y., and Erdélyi, R. (2003). Resonant Surface Waves and Instabilities in Finite β Plasmas. *Phys. Plasmas* 10, 266–276. doi:10.1063/1.1532741

Taroyan, Y., and Ruderman, M. S. (2011). MHD Waves and Instabilities in Space Plasma Flows. *Space Sci. Rev.* 158, 505–523. doi:10.1007/s11214-010-9737-9

Thomas, V. A., and Winske, D. (1993). Kinetic Simulations of the Kelvin-Helmholtz Instability at the Magnetopause. *J. Geophys. Res.* 98, 11425–11438. doi:10.1029/93JA00604

Tirry, W. J., Cadez, V. M., Erdelyi, R., and Goossens, M. (1998). Resonant Flow Instability of MHD Surface Waves. *Astron. Astrophysics* 332, 786–794.

Turkakin, H., Mann, I. R., and Rankin, R. (2014). Kelvin-Helmholtz Unstable Magnetotail Flow Channels: Deceleration and Radiation of MHD Waves. *Geophys. Res. Lett.* 41, 3691–3697. doi:10.1002/2014GL060450

Turkakin, H., Rankin, R., and Mann, I. R. (2013). Primary and Secondary Compressible Kelvin-Helmholtz Surface Wave Instabilities on the Earth's Magnetopause. *J. Geophys. Res. Space Phys.* 118, 4161–4175. doi:10.1002/jgra.50394

Conflict of Interest: The authors declare that the research was conducted in the absence of any commercial or financial relationships that could be construed as a potential conflict of interest.

Publisher's Note: All claims expressed in this article are solely those of the authors and do not necessarily represent those of their affiliated organizations, or those of the publisher, the editors, and the reviewers. Any product that may be evaluated in this article, or claim that may be made by its manufacturer, is not guaranteed or endorsed by the publisher.

frontiers in Astronomy and Space Sciences

BRIEF RESEARCH REPORT
published: 25 January 2022
doi: 10.3389/fspas.2021.809045

Diffusive Plasma Transport by the Magnetopause Kelvin-Helmholtz Instability During Southward IMF

T. K. M. Nakamura[1,2]*, *K. A. Blasl*[1,2], *Y. -H. Liu*[3] *and S. A. Peery*[3]

[1]Institute of Physics, University of Graz, Graz, Austria, [2]Space Research Institute, Austrian Academy of Sciences, Graz, Austria, [3]Department of Physics and Astronomy, Dartmouth College, Hanover, NH, United States

At the Earth's low-latitude magnetopause, the Kelvin-Helmholtz (KH) waves, which are driven by the super-Alfvénic velocity shear across the magnetopause, have been frequently observed during periods of northward interplanetary-magnetic-field (IMF) and believed to contribute to efficiently transporting the solar wind plasmas into the magnetosphere. On the other hand, during southward IMF periods, the signatures of the KH waves are much less frequently observed and how the KH waves contribute to the solar wind transport has not been well explored. Recently, the Magnetospheric Multiscale (MMS) mission successfully detected signatures of the KH waves near the dusk-flank of the magnetopause during southward IMF. In this study, we analyzed a series of two- and three-dimensional fully kinetic simulations modeling this MMS event. The results show that a turbulent evolution of the lower-hybrid drift instability (LHDI) near the low-density (magnetospheric) side of the edge layer of the KH waves rapidly disturbs the structure of the layer and causes an effective transport of plasmas across the layer. The obtained transport rate is comparable to or even larger than that predicted for the northward IMF. These results indicate that the diffusive solar wind transport induced by the KH waves may be active at the flank-to-tail magnetopause during southward IMF.

Keywords: Kelvin-Helmholtz instability, earth's magnetosphere, solar wind-magnetosphere interaction, lower-hybrid drift instability, plasma mixing, magnetic reconnection, plasma turbulence

OPEN ACCESS

Edited by:
Marian Lazar,
Ruhr University Bochum, Germany

Reviewed by:
Jim Burch,
Southwest Research Institute (SwRI), United States
Francesco Pegoraro,
University of Pisa, Italy

***Correspondence:**
T. K. M. Nakamura
takuma.tkm.nakamura@gmail.com

Specialty section:
This article was submitted to Space Physics, a section of the journal Frontiers in Astronomy and Space Sciences

Received: *04 November 2021*
Accepted: *10 December 2021*
Published: *25 January 2022*

Citation:
Nakamura TKM, Blasl KA, Liu Y-H and Peery SA (2022) Diffusive Plasma Transport by the Magnetopause Kelvin-Helmholtz Instability During Southward IMF. Front. Astron. Space Sci. 8:809045. doi: 10.3389/fspas.2021.809045

INTRODUCTION

The Kelvin-Helmholtz instability (KHI) becomes unstable when the plasma shear flow is super-Alfvénic with respect to the Alfvén speed based on the magnetic field component parallel to the shear flow (Chandrasekhar, 1961). At the Earth's low-latitude magnetopause, this condition is easily satisfied when the interplanetary-magnetic-field (IMF) is strongly northward or southward. Indeed, clear signatures of surface waves and flow vortices, which could be generated by the KHI, have been frequently observed around the magnetopause during periods of strongly northward IMF (e.g., Sckopke et al., 1981; Kokubun et al., 1994; Kivelson and Chen, 1995; Fairfield et al., 2000; Slinker et al., 2003; Hasegawa et al., 2004; Hasegawa et al., 2006; Foullon et al., 2008; Kavosi and Raeder, 2015; Moore et al., 2016). High-time-resolution fields and plasma data collected by the recently-launched Magnetospheric Multiscale (MMS) mission (Burch et al., 2016) further demonstrated the evolution of small-scale processes within the observed KH waves and vortices, such as the vortex-induced reconnection (VIR), during strong northward IMF (Eriksson et al., 2016a; Eriksson et al., 2016b; Li et al., 2016; Vernisse et al., 2016; Stawarz et al., 2016; Tang et al., 2018; Hasegawa et al., 2020; Hwang et al., 2020; Kieokaew et al., 2020). 2-D and 3-D fully kinetic simulations of these

northward IMF MMS events showed that the VIR can cause very efficient solar wind transport into the magnetosphere along the low-latitude magnetopause (e.g., Nakamura et al., 2017a; Nakamura et al., 2017b, Nakamura et al., 2020, Nakamura, 2021). Given that the simulated VIR signatures are reasonably consistent with many of the observation signatures, these studies indicated that the KHI and subsequent occurrence of the VIR would indeed contribute to efficient solar wind transport across the magnetopause during northward IMF.

On the other hand, the signatures of the magnetopause KH waves and vortices have been much less frequently observed during southward IMF (Kavosi and Raeder, 2015). Hwang et al. (2011) reported a Cluster observation event of non-linear KH vortices during a strong southward IMF period. In this Cluster event, observed plasma and field variations were irregular and temporally intermittent, indicating that the structure of the KH vortices was being distorted during this event. More recently, Blasl et al. (2022) (hereafter referred to as B22) reported the first MMS observation of the KH waves during southward IMF. In this MMS event, the observed surface waves, which can be interpreted as being formed by the KHI, also consisted of the intermittent and irregular variations as seen in the above Cluster event. Although clear VIR signatures as reported for the northward IMF were not found in this southward IMF event, the high-time-resolution MMS measurements detected small-scale fluctuations, which can be interpreted as being generated by the lower-hybrid drift instability (LHDI), near the edge of the surface waves (B22).

To investigate this southward IMF MMS event in more detail, in Nakamura et al. (2022) (hereafter referred to as N22), we performed a series of 2-D and 3-D fully kinetic simulations with parameters matched to this event. The simulation results are consistent with the observations in terms of both large-scale surface wave signatures and small-scale LHDI fluctuations. The simulations also demonstrated that reconnection locally occurs within the LHDI turbulence, but does not develop at the larger-scale that coherently changes the connectivity of the magnetic field lines on the two sides across the magnetopause, as seen in the simulations of the VIR for the above northward IMF cases. The simulations further demonstrated that the primary KH waves induce the secondary Rayleigh-Taylor instability (RTI) at the surface bent by the KHI. The RTI forms high-density arms penetrating into the low-density (magnetospheric) side. This arm penetration quickly distorts the primary KH wave structures and produces intermittent and irregular variations of the surface waves, leading to a reduction in the observational probability of the primary KH waves. Interestingly, this RTI-related reduction of the observational probability of the KH waves proceeds faster than the VIR-related reduction in the aforementioned northward IMF cases, indicating that the secondary RTI may be a key process that makes it more difficult to detect the KH waves during southward IMF (see B22 and N22 for more details of these initial results of this MMS event).

Based on these previous studies, in this paper, we revisited the 2-D and 3-D simulations of the southward IMF MMS event shown in B22 and N22, with a special focus on the mass and energy transfer process caused by the LHDI turbulence and additional, microscopic magnetic reconnection induced within the turbulence. The obtained mixing and transport rates are comparable to or even larger than the ones previously obtained in the northward IMF cases, indicating that the KHI and the resulting LHDI turbulence may actively contribute to the solar wind transport into the Earth's magnetosphere during southward IMF.

METHODS

We analyze the simulations that were initially presented by N22, which model the southward IMF MMS event introduced in B22. The simulations were performed on MareNostrum, using the fully kinetic particle-in-cell code VPIC (Bowers et al., 2008; Bowers et al., 2009). The x, y and z coordinates in the simulations correspond to the directions along the velocity shear (~the magnetosheath flow), the boundary normal (~magnetosheath-to-magnetosphere), and the out-of-the-vortex-plane (~south-to-north), respectively. The initial density, magnetic field and bulk velocities across the magnetopause are set to the values obtained from the observations near the KH vortex-like interval 15:33-15:35 UT (see B22 for more details of this interval). Denoting the magnetosheath and magnetospheric sides as 1 and 2, respectively, we first selected the parameters on the two sides from the observations, as $n_{10}/n_{20} = 8.0$, $(B_{x10},B_{z10})=(0.17B_0, -B_0)$, $(B_{x20},B_{z20})=(0.17B_0, B_0)$, $U_{x10} = V_0/2$, and $U_{x20} = -V_0/2$, where $n_{10} = 8\mathrm{cm}^{-3}$, $B_0 = 12$nT, $|V_0| = 290$ km/s $= 3.0V_A$ (V_A: Alfvén speed based on $n_0 = n_{10}$ and B_0). Note that the system is set to be in the frame with half the velocity of the magnetosheath flow. We then set the initial components by connecting these values using a $\tanh(y/L_0)$ function (Nakamura and Daughton, 2014), where $L_0 = 1.5d_i$ is the initial half thickness of the shear layer and $d_i = c/\omega_{pi}$ is the ion inertial length based on n_0. To satisfy the force balance, the temperatures for the magnetospheric components are set to be higher than the magnetosheath components, where the ion-to-electron temperature ratio is fixed as $T_{i0}/T_{e0} = 5.0$. The initial plasma beta on the magnetosheath side is $\beta_1 = 1.5$, the ratio between the electron plasma frequency and the gyrofrequency is $\omega_{pe}/\Omega_e = 2.0$ and the ion-to-electron mass ratio is $m_i/m_e = 100$. The system is periodic in x (and in z for 3-D), and y boundaries are modeled as perfect conductors for the fields and reflecting for the particles. Further details of the initial setup are given in N22.

In this paper, we will show a 3-D and a corresponding 2-D run, whose system sizes are $L_x \times L_y \times L_z = 15d_i \times 30d_i \times 10.4d_i = 864 \times 1728 \times 600$ cells with a total of 3.6×10^{11} particles for 3-D, and $L_xxL_y = 15d_ix30d_i = 864 \times 1728$ cells with a total of 6.0×10^9 particles for 2-D. To investigate the effects of the in-plane magnetic field, we will also show an additional 2-D run in which the in-plane field (B_x) is initially set to be zero.

RESULTS

Overviews

Figure 1 shows the time evolutions of the electron mixing measure $F_e=(n_{e1}-n_{e2})/(n_{e1}+n_{e2})$ for the three runs. The simulation time is normalized by $\alpha^{-1} = \lambda_{KH}/V_0$ which is the

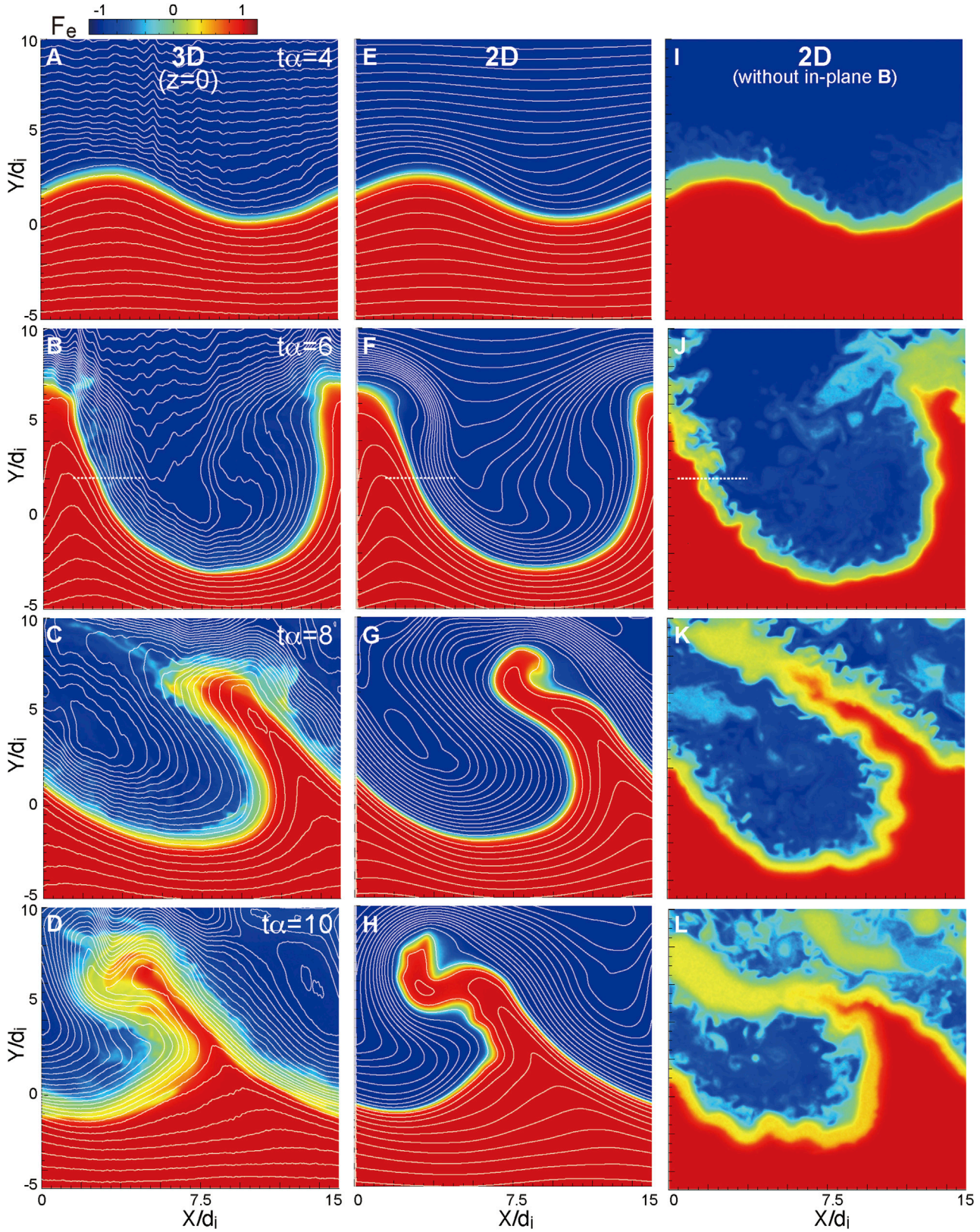

FIGURE 1 | Time evolution of the mixing measure $F_e=(n_{e1}-n_{e2})/(n_{e1}+n_{e2})$ in the x-y plane ($z = 0$ for the 3-D run) for the 3-D **(A–D)**, the corresponding 2-D **(E–H)**, and 2-D without initial in-plane fields **(I–L)** runs. The white curves for the 3-D and corresponding 2-D runs show the surfaces of the z-component of the vector potential, which corresponds to the in-plane magnetic field lines in 2-D.

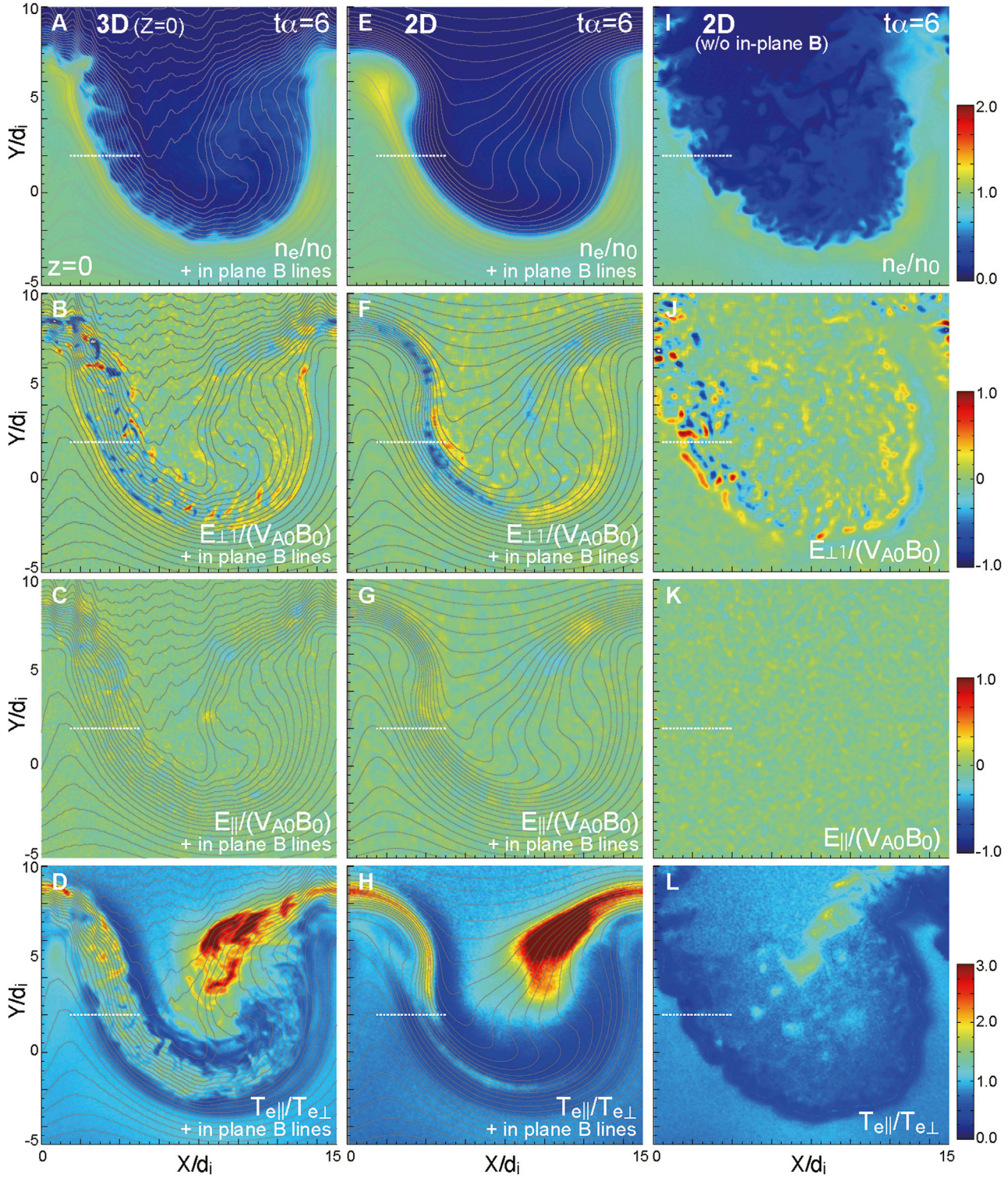

FIGURE 2 | Color contours in the x-y plane (z = 0 for the 3-D run) of n_e, the perpendicular and parallel components of **E**, and the ratio of the parallel and perpendicular electron temperatures $T_{e\|}/T_{e\perp}$ at $t = 6\alpha^{-1}$ for the 3-D **(A–D)**, the corresponding 2-D **(E–H)**, and 2-D without initial in-plane fields **(I–L)** runs. The gray curves for the 3-D and corresponding 2-D runs show the surfaces of the z-component of the vector potential.

time unit for the growth phase of the KHI (Nakamura et al., 2013). In the non-linear growth phase of the primary KHI ($t > 4\alpha^{-1}$), the high-density vortex arm penetrates deep into the low-density (upper) side for all runs. As shown in N22, this is because the ion current in the direction nearly parallel to the shear flow, which is associated with the anti-parallel (south-north) magnetic field across the boundary, is bent by the primary KHI and drives the secondary RTI growing in the boundary normal (y) direction from the high-density to low-density sides. See N22 for the details of the evolution of the secondary RTI. As also shown in N22, the density jump across the edge of the primary KH wave and vortex further causes the LHDI, resulting in small-scale field and plasma fluctuations on the low-density side of the edge layer. Note that the LHDI-induced fluctuations are seen in the 3-D run and the 2-D run without initial in-plane fields (see left and right panels in **Figure 1**) but not seen in the 2-D run that has initial in-plane fields (see middle panels in **Figure 1**). This is because the in-plane field, which is locally compressed and enhanced along the edge of the surface wave (see white curves in **Figure 1**), prevents the small-scale fluctuations from growing in the 2-D run. For the 3-D run, a similar enhancement of the in-plane field is seen but the LHDI can still grow obliquely in the direction nearly perpendicular to the magnetic field. See N22 for the details of the onset conditions of the LHDI and the related linear analysis based on a dispersion relation solver in the fully kinetic regime (Umeda and Nakamura, 2018). As a result of the LHDI turbulence, plasmas near the edge layer are mixed and the layer is diffused (compare **Figures 1D,H,L**). In this paper, we will further investigate how the LHDI turbulence diffuses the layer and causes the mass and energy transfer across the layer.

The first three panels from the top in **Figure 2** shows the electron density, the perpendicular and parallel components of the electric field at $t = 6\alpha^{-1}$ for all three runs. We see the strong fluctuations caused by the LHDI near the vortex edge mainly in the density and perpendicular electric field (see panels in the first and second rows from the top). Note that in addition to the small-scale fluctuations of the LHDI, a pair of negative-positive electric field layer is seen for all runs near the edge of the vortex, whose half thickness is less than the ion gyro-radius (~ion inertial length) (see panels in the second row from the top). The LHDI-induced fluctuations and the polarized field are seen mainly in the perpendicular component of the electric field, and we see no significant enhancement of the parallel electric field in the 2-D runs (see **Figures 2G,K**). On the other hand, for the 3-D run, we see some small-scale negative and positive peaks even in the parallel electric field within the LHDI turbulence (see **Figure 2C**). This is caused by local, microscopic magnetic reconnection as partially shown in N22.

The bottom panels in **Figure 2** show $T_{e\parallel}/T_{e\perp}$. We here focus on the edge layer of the vortex including the region near the horizontal white dashed lines, where the strong fluctuations of the LHDI are produced as seen in **Figures 2B,J**. Note that the region near the head of the vortex arm, where the strong parallel anisotropy is produced by the adiabatic heating with concentrated magnetic field lines, are not our focus. Past kinetic studies showed that the LHDI heats electrons in the perpendicular direction (e.g., Daughton, 2004), and we indeed see the perpendicular temperature anisotropy widely within the LHDI turbulence for the 2-D run without in-plane field (**Figure 2L**). However, for the 3-D run in which the LHDI turbulence also appears near the vortex edge, a wide band of parallel anisotropy develops within the turbulence (**Figure 2D**). This additional electron heating in the parallel direction can arise from the parallel electric field associated with reconnection as hinted in **Figure 2C**. Similar parallel electron heating processes were seen in past kinetic studies of reconnection accompanied by the LHDI turbulence (e.g., Shinohara and Hoshino, 1999; Li et al., 2016).

Mass and Energy Transfer

The top panels in **Figure 3** show a cut of crossing of the edge of the vortex arm (along the horizontal dashed lines in **Figure 2**) at $t = 6\alpha^{-1}$ of B_z, U_{ix}, and n_e for all three runs. As seen in **Figures 3A,E** (i.e., the cases with the LHDI turbulence), the initially sharp density and magnetic gradients are diffused by the LHDI turbulence, forming humps that contain mixed plasmas on the low-density side of the boundary layer. As seen in **Figure 4A**, which shows the time evolution of the thickness of the mixing region, the expanding speed of this mixing region $d(L_{mix})/dt$ in the cases with the LHDI turbulence (red and blue curves) is nearly a quarter of the velocity shear ($\sim V_0/4$), which is comparable to the rotating plasma flow speed within the vortex layer. That is, the time-scale in which the mixing region expands within the vortex layer in this run is comparable to the evolution time-scale of the primary KH vortex. Interestingly, this expanding speed of the mixing region is comparable to or even slightly faster than that in a 3-D run of the northward IMF event (Nakamura et al., 2017a; Nakamura et al., 2017b), in which the LHDI does not occur and the mixing is caused by the vortex-induced reconnection (VIR) across the magnetopause (black dashed curve in **Figure 4A**). This quick expansion of the mixing region in the present runs with the LHDI turbulence leads to a large mass flux across the mixing surface F_m and a large diffusion coefficient D_{diff} estimated from the Fick's law $F_m/D_{diff} = d(m_e n_e)/dx \sim m_e n_0/L_{mix}$ (red and blue curves in **Figures 4B,C**), both of which are comparable to the ones for the 3-D run of the northward IMF event (black dashed curve). Note that there is no significant difference in these mixing measures between the two cases with the LHDI turbulence (red versus blue curves in **Figure 4**), indicating that microscopic reconnection, which appears only in the 3-D case, does not play a significant role in the plasma transport across the magnetopause.

The expansion of the mixing region on the low-density side of the edge layer also plays a role in preventing the plasma in the low-density region from entering the high-density region and inhibiting the development of a larger-scale reconnection across the magnetopause current layer (i.e., between the high- and low-density sides). In **Figure 3C** (2-D), U_{ix} in the low-density region ($x > 4$), which corresponds to the flow component in the direction nearly perpendicular to the vortex edge, is smaller than that in the high-density region ($x < 3$), indicating the compression of the layer. In contrast, in **Figure 3A** (3-D), U_{ix} in the low-density side within the mixing region ($x > 3.5$) is not smaller than that in the high-density region ($x < 2.5$), indicating that the inflowing flux is diffused by the turbulence. As shown in N22, the global reconnection rate measured from the inflowing flux across the mixing surfaces (Figure 8 in N22) indeed suggested that reconnection occurs

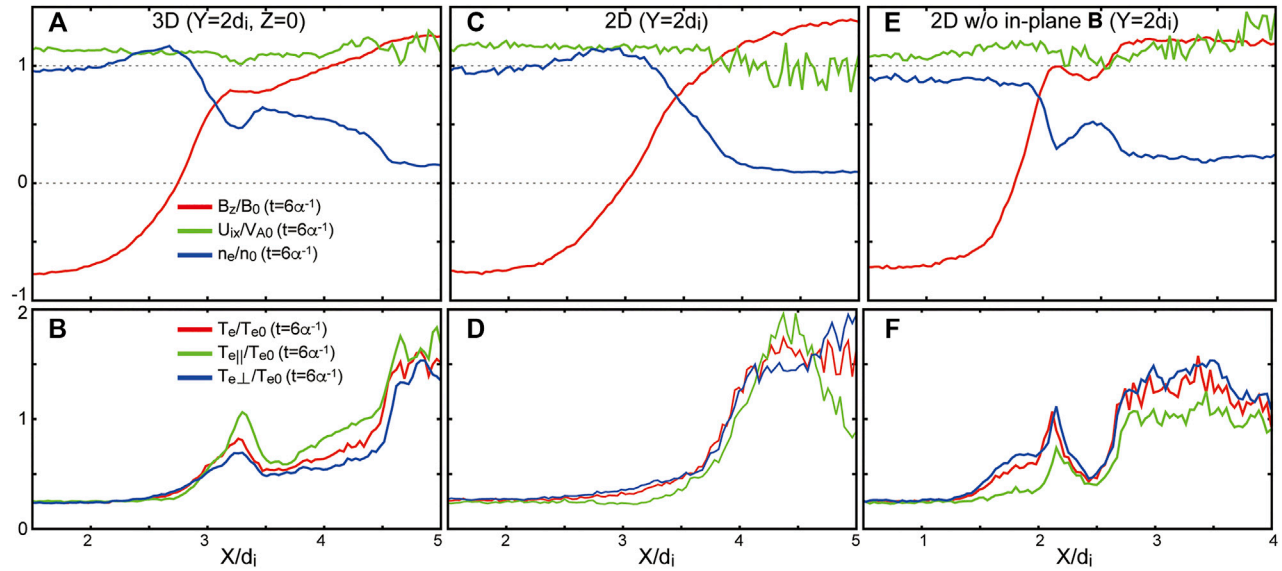

FIGURE 3 | Quantities of the same three runs at $t = 6\alpha^{-1}$ along the dashed lines marked in **Figure 2** (the same lines in panels of the second row from the top in **Figure 1**). The top panels show the out-of-plane magnetic field (B_z), the *x*-component of the ion bulk velocity (U_{ix}), and the electron density (n_e). The bottom panels show the total, parallel and perpendicular temperatures of electrons (T_e, $T_{e\parallel}$, and $T_{e\perp}$).

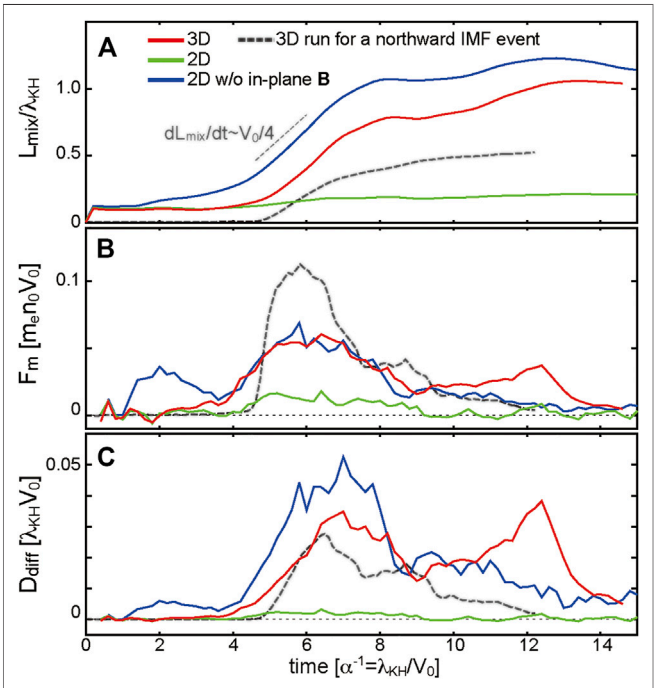

FIGURE 4 | Time evolution of **(A)** the y-averaged thickness L_{mix} of the mixing region defined using $|F_e|<0.99$, **(B)** the electron mass flux F_m across the mixing surfaces defined as $|F_e| = 0.99$ and **(C)** the diffusion coefficient D_{diff} estimated from the Fick's law $F_m/D_{diff} = d(m_e n_e)/dx \sim m_e n_0/L_{mix}$, for the three runs and the 3-D run of the September 8 2015 event employed in Nakamura (2021) (black dashed curves), in which the KH waves were observed during northward IMF. Red, green and blue curves in **Figure 4** are the same ones shown in Figure 9B in N22.

almost only within the mixing region on the low-density side and does not directly couple the two sides.

The bottom panels in **Figure 3** use the same cut as the top panels but show the electron temperature components. The perpendicular and parallel temperatures are nearly identical near the edge layer of the vortex in the 2-D run with initial in-plane field (middle panels), while the perpendicular anisotropy caused by the LHDI turbulence is seen near the edge layer in the 2-D run without initial in-plane field (right panels). On the other hand, for the 3-D run, the parallel anisotropy is seen near the edge layer (left panels). The anisotropy is enhanced especially in the low-density side of the layer, where the layer is diffused as seen in the density profile in **Figure 3A**, and this enhancement is likely due to reconnection within the LHDI turbulence (discussed in *Overviews Section*). A similar parallel anisotropy is seen in the MMS observation of the present southward IMF event (see Figure 10 in B22), suggesting that the parallel electron heating within the LHDI turbulence as seen in the present 3-D simulation may occur in this MMS event.

SUMMARY AND DISCUSSIONS

In this paper, we analyzed data from 2-D and 3-D fully kinetic simulations designed for an MMS observation event of the KH waves at the dusk-flank magnetopause during southward IMF, with a special focus on quantifying the mass and energy transfer efficiency. The results showed that the LHDI and the resulting small-scale field and plasma fluctuations strongly diffuse the edge layer of the primary KH vortex and cause efficient plasma mixing within the vortex. We find that the mixing measures, such as the diffusion coefficient D_{diff}, are comparable to those obtained in the

previous 3-D simulation of the KH waves during northward IMF (Nakamura et al., 2017b). Here, considering the observed values of the primary KH wavekength $\lambda_{KH} \sim 4 \times 10^4$ km and the velocity shear amplitude V_0~290 km/s (see B22 for the estimation of λ_{KH} and V_0 in the observations), the estimated D_{diff}~(0.01-0.02)$\lambda_{KH}V_0$ corresponds to (1-4)×10^{11} m^2/s, which is comparable to that in the northward IMF simulation (~1 × 10^{11} m^2/s). This D_{diff} value is more than one order of magnitude larger than past predictions for the formation of the low-latitude boundary layer (LLBL) where plasmas are mixed across the magnetopause (Sonnerup 1980; Nykyri and Otto, 2001; Wing et al., 2006; Nakamura and Daughton, 2014). The 3-D simulation further demonstrates the parallel electron anisotropy within the diffused turbulent layer. Given that both the mixing and the parallel electron anisotropy are typical observational features of the LLBL (e.g., Nakamura, 2021 and references therein), this current work strongly suggests that the KH waves and the subsequent LHDI turbulence, where microscopic reconnection potentially takes place, may play an important role in the mass and energy transfer across the low-latitude magnetopause even during southward IMF.

Past simulation studies under northward IMF conditions suggested that the VIR across the edge layer of the KH vortex causes effective plasma mixing and transport across the layer (e.g., Nakamura and Daughton, 2014; Nakamura et al., 2017b). In comparison, the present simulation under a southward IMF condition shows that the diffusion of the edge layer by the LHDI turbulence prevents the VIR from fully developing across the layer. Instead, microscopic reconnection occurs within the turbulence on the lower-density (magnetospheric) side of the edge layer. This process does not significantly affect the mass transport across the layer, but leads to the parallel electron heating within the turbulence. This local, microscopic reconnection process may also change the magnetic field topology near the turbulent layer and lead to a global transport (leak) of the mixed plasma within the turbulence across the flank-to-tail magnetopause. Although the other dayside processes, such as the dayside low-latitude reconnection and the associated flux transfer events (FTEs), have been considered as primary processes that globally transport the solar wind plasmas into the magnetosphere during southward IMF (Fuselier, 2021 and references therein), investigating how the KHI-driven LHDI turbulence, as seen in the present simulation, contribute to the solar wind transport and affect (and/or be affected by) the other processes remains important to understand the global solar wind transport system during southward IMF.

This LHDI turbulence was not seen in the previous northward IMF case (Nakamura et al., 2017a; Nakamura et al., 2017b; Nakamura, 2021), probably due to the lower density ratio across the magnetopause (n_1/n_2 = 3.3) than that in the present southward IMF case (n_1/n_2 = 8). Since the pre-existing boundary layer formed by reconnection at the high-latitude magnetopause, which frequently occurs during northward IMF, can easily reduce the density ratio during northward IMF (Hasegawa et al., 2009; Nakamura et al., 2017b), the KHI-induced LHDI turbulence as seen in the present simulations may be more active during southward IMF. Nevertheless, of course, the LHDI turbulence would occur even during northward IMF as long as the instability conditions for the LHDI are satisfied. Indeed, the enhanced LHD waves were observed within the KH waves in an MMS observation event during northward IMF (Tang et al., 2018). A systematic study of the LHDI effects on the magnetopause KH waves under different IMF and other background conditions would also be an important next step to achieve a comprehensive understanding of the diffusive processes at the Earth's magnetopause.

DATA AVAILABILITY STATEMENT

The simulation data shown in this paper are made available upon request by the corresponding author.

AUTHOR CONTRIBUTIONS

TN conducted the analyses of the diagnostics and wrote the paper. KB supported the diagnostics from the spacecraft observations. All listed authors discussed the simulation results.

FUNDING

This work was supported by the Austrian Research Fund (FWF): P32175-N27. Y-HL and SAP are grateful for support from grants NSF-DoE 1902867 and NASA MMS 80NSSC18K0289.

ACKNOWLEDGMENTS

For the simulations analyzed in this paper, we acknowledge PRACE for awarding us access to MareNostrum at Barcelona Supercomputing Center (BSC), Spain. A part of the simulation data was analyzed with resources at the Space Research Institute of Austrian Academy of Sciences.

REFERENCES

Blasl, K. A., Nakamura, T. K. M., Plaschke, F., Nakamura, R., Hasegawa, H., Stawarz, J. E., et al. (2022). Multi-Scale Observations of the Magnetopause Kelvin-Helmholtz Waves during Southward IM. *Phys. Plasmas* 29, 012101. doi:10.1063/5.0067370

Bowers, K. J., Albright, B. J., Yin, L., Bergen, B., and Kwan, T. J. T. (2008). Ultrahigh Performance Three-Dimensional Electromagnetic Relativistic Kinetic Plasma Simulation. *Phys. Plasmas* 15, 055703. doi:10.1063/1.2840133

Bowers, K. J., Albright, B. J., Yin, L., Daughton, W., Roytershteyn, V., Bergen, B., et al. (2009). Advances in Petascale Kinetic Plasma Simulation with VPIC and Roadrunner. *J. Phys. Conf. Ser.* 180, 012055. doi:10.1088/1742-6596/180/1/012055

Burch, J. L., Moore, T. E., Torbert, R. B., and Giles, B. L. (2016). Magnetospheric Multiscale Overview and Science Objectives. *Space Sci. Rev.* 199, 5–21. doi:10.1007/s11214-015-0164-9

Chandrasekhar, S. (1961). *Hydrodynamic and Hydromagnetic Stability*. New York: Oxford University Press.

Daughton, W., Lapenta, G., and Ricci, P. (2004). Nonlinear Evolution of the Lower-Hybrid Drift Instability in a Current Sheet. *Phys. Rev. Lett.* 93 (10), 105004. doi:10.1103/PhysRevLett.93.105004

Eriksson, S., Wilder, F. D., Ergun, R. E., Schwartz, S. J., Cassak, P. A., Burch, J. L., et al. (2016b). Magnetospheric Multiscale Observations of the Electron Diffusion Region of Large Guide Field Magnetic Reconnection. *Phys. Rev. Lett.* 117, 015001. doi:10.1103/PhysRevLett.117.015001

Eriksson, S., Lavraud, B., Wilder, F. D., Stawarz, J. E., Giles, B. L., Burch, J. L., et al. (2016a). Magnetospheric Multiscale Observations of Magnetic Reconnection Associated with Kelvin-Helmholtz Waves. *Geophys. Res. Lett.* 43, 5606–5615. doi:10.1002/2016GL068783

Fairfield, D. H., Otto, A., Mukai, T., Kokubun, S., Lepping, R. P., Steinberg, J. T., et al. (2000). Geotail Observations of the Kelvin-Helmholtz Instability at the Equatorial Magnetotail Boundary for Parallel Northward fields. *J. Geophys. Res.* 105, 21159–21173. doi:10.1029/1999JA000316

Foullon, C., Farrugia, C. J., Fazakerley, A. N., Owen, C. J., Gratton, F. T., and Torbert, R. B. (2008). Evolution of Kelvin-Helmholtz Activity on the Dusk Flank Magnetopause. *J. Geophys. Res.* 113. doi:10.1029/2008JA013175

Fuselier, S. A. (2021). "Dayside Magnetopause Processes," in *Magnetospheres in the Solar System*Editors R. Maggiolo, N. André, H. Hasegawa, D. T. Welling, Y. Zhang, and L. J. Paxton (Hoboken: Wiley). doi:10.1002/9781119815624.ch10

Hasegawa, H., Fujimoto, M., Phan, T.-D., Rème, H., Balogh, A., Dunlop, M. W., et al. (2004). Transport of Solar Wind into Earth's Magnetosphere through Rolled-Up Kelvin-Helmholtz Vortices. *Nature* 430, 755–758. doi:10.1038/nature02799

Hasegawa, H., Fujimoto, M., Takagi, K., Saito, Y., Mukai, T., and Rème, H. (2006). Single-spacecraft Detection of Rolled-Up Kelvin-Helmholtz Vortices at the Flank Magnetopause. *J. Geophys. Res.* 111, A09203. doi:10.1029/2006JA011728

Hasegawa, H., Nakamura, T. K. M., Gershman, D. J., Nariyuki, Y., Viñas, A. F., Giles, B. L., et al. (2020). Generation of Turbulence in Kelvin-Helmholtz Vortices at the Earth's Magnetopause: Magnetospheric Multiscale Observations. *J. Geophys. Res. Space Phys.* 125, e2019JA027595. doi:10.1029/2019JA027595

Hasegawa, H., Retinò, A., Vaivads, A., Khotyaintsev, Y., André, M., Nakamura, T. K. M., et al. (2009). Kelvin-Helmholtz Waves at the Earth's Magnetopause: Multiscale Development and Associated Reconnection. *J. Geophys. Res.* 114, A12207. doi:10.1029/2009JA014042

Hwang, K.-J., Kuznetsova, M. M., Sahraoui, F., Goldstein, M. L., Lee, E., and Parks, G. K. (2011). Kelvin-Helmholtz Waves under Southward Interplanetary Magnetic Field. *J. Geophys. Res.* 116, A08210. doi:10.1029/2011JA016596

Hwang, K. J., Dokgo, K., Choi, E., Burch, J. L., Sibeck, D. G., Giles, B. L., et al. (2020). Magnetic Reconnection inside a Flux Rope Induced by Kelvin-Helmholtz Vortices. *J. Geophys. Res. Space Phys.* 125, e2019JA027665. doi:10.1029/2019JA027665

Kavosi, S., and Raeder, J. (2015). Ubiquity of Kelvin-Helmholtz Waves at Earth's Magnetopause. *Nat. Commun.* 6, 7019. doi:10.1038/ncomms8019

Kieokaew, R., Lavraud, B., Foullon, C., Toledo-Redondo, S., Fargette, N., Hwang, K. J., et al. (2020). Magnetic Reconnection inside a Flux Transfer Event-Like Structure in Magnetopause Kelvin-Helmholtz Waves. *J. Geophys. Res. Space Phys.* 125, e2019JA027527. doi:10.1029/2019JA027527

Kivelson, M. G., and Chen, S.-H. (1995). "The Magnetopause: Surface Waves and Instabilities and Their Possible Dynamic Consequences," in *Physics of the Magnetopause* (Washington, DC: AGU), 90, 257.

Kokubun, S., Kawano, H., Nakamura, M., Yamamoto, T., Tsuruda, K., Hayakawa, H., et al. (1994). Quasi-periodic Oscillations of the Magnetopause during Northward Sheath Magnetic Field. *Geophys. Res. Lett.* 21, 2883–2886. doi:10.1029/94gl02103

Li, W., André, M., Khotyaintsev, Y. V., Vaivads, A., Graham, D. B., Toledo-Redondo, S., et al. (2016). Kinetic Evidence of Magnetic Reconnection Due to Kelvin-Helmholtz Waves. *Geophys. Res. Lett.* 43, 5635–5643. doi:10.1002/2016GL069192

Moore, T. W., Nykyri, K., and Dimmock, A. P. (2016). Cross-scale Energy Transport in Space Plasmas. *Nat. Phys* 12, 1164–1169. doi:10.1038/nphys3869

Nakamura, T. K. M., and Daughton, W. (2014). Turbulent Plasma Transport across the Earth's Low-latitude Boundary Layer. *Geophys. Res. Lett.* 41, 8704–8712. doi:10.1002/2014GL061952

Nakamura, T. K. M., Blasl, K. A., Hasegawa, H., Umeda, T., Liu, Y. -H., Peery, S. A., et al. (2022). Multi-Scale Evolution of Kelvin-Helmholtz Waves at the Earth's Magnetopause during Southward IMF Periods. *Phys. Plasmas*29, 012901. doi:10.1063/5.0067391

Nakamura, T. K. M., Daughton, W., Karimabadi, H., and Eriksson, S. (2013). Three-dimensional Dynamics of Vortex-Induced Reconnection and Comparison with THEMIS Observations. *J. Geophys. Res. Space Phys.* 118, 5742–5757. doi:10.1002/jgra.50547

Nakamura, T. K. M., Eriksson, S., Hasegawa, H., Zenitani, S., Li, W. Y., Genestreti, K. J., et al. (2017b). Mass and Energy Transfer across the Earth's Magnetopause Caused by Vortex-Induced Reconnection. *J. Geophys. Res. Space Phys.* 122, 11505–11522. doi:10.1002/2017JA024346

Nakamura, T. K. M., Hasegawa, H., Daughton, W., Eriksson, S., Li, W. Y., and Nakamura, R. (2017a). Turbulent Mass Transfer Caused by Vortex Induced Reconnection in Collisionless Magnetospheric Plasmas. *Nat. Commun.* 8, 1582. doi:10.1038/s41467-017-01579-0

Nakamura, T. K. M., Stawarz, J. E., Hasegawa, H., Narita, Y., Franci, L., Wilder, F. D., et al. (2020). Effects of Fluctuating Magnetic Field on the Growth of the Kelvin-Helmholtz Instability at the Earth's Magnetopause. *J. Geophys. Res. Space Phys.* 125, e2019JA027515. doi:10.1029/2019ja027515

Nakamura, T. K. M. (2021). "The Earth's Low-Latitude Boundary Layer," in *Magnetospheres in the Solar System*. Editors R. Maggiolo, N. André, H. Hasegawa, D. T. Welling, Y. Zhang, and L. J. Paxton (Hoboken: Wiley), 177–191. doi:10.1002/9781119815624.ch12

Nykyri, K., and Otto, A. (2001). Plasma Transport at the Magnetospheric Boundary Due to Reconnection in Kelvin-Helmholtz Vortices. *Geophys. Res. Lett.* 28 (18), 3565–3568. doi:10.1029/2001GL013239

Sckopke, N., Paschmann, G., Haerendel, G., Sonnerup, B. U. Ö., Bame, S. J., Forbes, T. G., et al. (1981). Structure of the Low-Latitude Boundary Layer. *J. Geophys. Res.* 86, 2099–2110. doi:10.1029/ja086ia04p02099

Shinohara, I., and Hoshino, M. (1999). Electron Heating Process of the Lower Hybrid Drift Instability. *Adv. Space Res.* 24, 43–46. doi:10.1016/S0273-1177(99)00420-2

Slinker, S. P., Fedder, J. A., Sibeck, D. G., Lyon, J. G., Frank, L. A., and Mukai, T. (2003). Simulation of Magnetopause Oscillations Observed January 9, 1996. *Geophys. Res. Lett.* 30 (11), 1569. doi:10.1029/2003gl017063

Sonnerup, B. U. Ö. (1980). Theory of the Low-Latitude Boundary Layer. *J. Geophys. Res.* 85, 2017–2026. doi:10.1029/JA085iA05p02017

Stawarz, J. E., Eriksson, S., Wilder, F. D., Ergun, R. E., Schwartz, S. J., Pouquet, A., et al. (2016). Observations of Turbulence in a Kelvin-Helmholtz Event on 8 September 2015 by the Magnetospheric Multiscale mission. *J. Geophys. Res. Space Phys.* 121 (11), 021–111. doi:10.1002/2016JA023458

Tang, B., Li, W., Wang, C., Dai, L., Khotyaintsev, Y., Lindqvist, P.-A., et al. (2018). Magnetic Depression and Electron Transport in an Ion-Scale Flux Rope Associated with Kelvin-Helmholtz Waves. *Ann. Geophys.* 36, 879–889. doi:10.5194/angeo-36-879-2018

Umeda, T., and Nakamura, T. K. M. (2018). Electromagnetic Linear Dispersion Relation for Plasma with a Drift across Magnetic Field Revisited. *Phys. Plasmas* 25, 102109. doi:10.1063/1.5050542

Vernisse, Y., Lavraud, B., Eriksson, S., Gershman, D. J., Dorelli, J., Pollock, C., et al. (2016). Signatures of Complex Magnetic Topologies from Multiple Reconnection Sites Induced by Kelvin-Helmholtz Instability. *J. Geophys. Res. Space Phys.* 121, 9926–9939. doi:10.1002/2016JA023051

Wing, S., Johnson, J. R., and Fujimoto, M. (2006). Timescale for the Formation of the Cold-Dense Plasma Sheet: A Case Study. *Geophys. Res. Lett.* 33, L23106. doi:10.1029/2006GL027110

Conflict of Interest: The authors declare that the research was conducted in the absence of any commercial or financial relationships that could be construed as a potential conflict of interest.

frontiers in Astronomy and Space Sciences

ORIGINAL RESEARCH
published: 18 February 2022
doi: 10.3389/fspas.2022.827612

Multi-Spacecraft Observations of Fluctuations Occurring Along the Dusk Flank Magnetopause, and Testing the Connection to an Observed Ionospheric Bead

Steven M. Petrinec[1]*, *Simon Wing*[2], *Jay R. Johnson*[3] and *Yongliang Zhang*[2]

[1]Lockheed Martin Advanced Technology Center, Palo Alto, CA, United States, [2]Applied Physics Laboratory, Johns Hopkins University, Laurel, MD, United States, [3]Department of Engineering and Computer Science, Andrews University, Berrien Springs, MI, United States

During 2018 November 06, 11:30—18:00 UT, the MMS constellation, the Cluster set of spacecraft, and the Geotail spacecraft were all situated near the dusk flank magnetopause. Large scale fluctuations were observed by the available and operating science instruments at these various spacecraft (i.e., magnetic field, plasma moment, and energy flux measurements). Similar fluctuations were not observed by upstream solar wind monitors, suggesting that the waves were initiated at the magnetopause. A localized emission 'bead' from the post-noon ionosphere was also observed from low Earth orbit. The nature and relation of the fluctuations observed at all of these spacecraft at the magnetosphere boundary and the connection to the post-noon high-latitude ionosphere are investigated in this study.

Keywords: magnetopause, kelvin-helmholtz instability, ionospheric bead, ULF waves, boundary layer

OPEN ACCESS

Edited by:
Luca Sorriso-Valvo,
Institute for Space Physics (Uppsala), Sweden

Reviewed by:
Alla V. Suvorova,
National Central University, Taiwan
Tommaso Alberti,
Institute for Space Astrophysics and Planetology (INAF), Italy

***Correspondence:**
Steven M. Petrinec
petrinec@lmsal.com

Specialty section:
This article was submitted to Space Physics, a section of the journal Frontiers in Astronomy and Space Sciences

Received: *02 December 2021*
Accepted: *25 January 2022*
Published: *18 February 2022*

Citation:
Petrinec SM, Wing S, Johnson JR and Zhang Y (2022) Multi-Spacecraft Observations of Fluctuations Occurring Along the Dusk Flank Magnetopause, and Testing the Connection to an Observed Ionospheric Bead. Front. Astron. Space Sci. 9:827612. doi: 10.3389/fspas.2022.827612

INTRODUCTION

Large-scale motions of the magnetopause have long been observed by spacecraft (e.g., Holzer et al., 1966; Kaufmann and Konradi, 1969; Howe and Siscoe, 1972; Song et al., 1988, 1994; Sibeck and Croley, 1991; Sibeck, 1992; Phan and Paschmann, 1996; Sibeck and Gosling, 1996; Russell et al., 1997; Plaschke et al., 2016). Such fluctuations of the magnetopause location can be caused by variations in the convected solar wind, or by magnetosheath fluctuations initiated by processes at the bow shock (Schwartz et al., 1996; Omidi et al., 2010; Dmitriev and Suvorova (2012, 2015); Li et al., 2020; and references therein). Such fluctuations in the solar wind or magnetosheath can be either coherent or incoherent. Instabilities at the magnetopause surface can also be caused by the interaction of the magnetosheath and magnetosphere plasmas. For example, the initiation and evolution of the Kelvin-Helmholtz Instability (KHI) along the magnetopause surface are due primarily to a significant velocity shear across the boundary. The resulting Kelvin-Helmholtz waves evolve into quasi-periodic vortices traveling anti-sunward along the magnetopause flanks, and have been observed by various spacecraft sampling the *in situ* plasma and/or fields (e.g., Southwood, 1979; Chen et al., 1993; Chen and Kivelson, 1993; Kivelson and Chen, 1995; Miura, 1995; Fairfield et al., 2000; Hasegawa et al., 2004, 2006, 2009; Nykyri, 2013; Hwang, 2015; Nykyri and Dimmock, 2015; Plaschke, 2016). Kelvin-Helmholtz waves occurring at the magnetopause have also been studied in association with waves generated interior to the magnetopause. Lee et al. (1981) described two KH modes: one occurring at

the magnetopause, and one occurring at the inner edge of the magnetopause boundary layer. The associations between these phenomena have been explored in several investigations (e.g., Hones et al., 1981; Pu and Kivelson, 1983; Kivelson and Pu, 1984; Couzens et al., 1985; Claudepierre et al., 2008).

The Kelvin-Helmholtz Instability has also been conjectured to be coupled via field-aligned currents to periodic dayside high-latitude ionosphere bright spots observed in ultraviolet emissions by the Viking spacecraft (Lui et al., 1989), and by Defense Meteorological Satellite Program (DMSP) spacecraft (Johnson et al., 2021).

The interval described in this paper was observed by several spacecraft at a time when they were all aligned near the dusk flank magnetopause. Specifically, the NASA Magnetospheric Multiscale (MMS) constellation of spacecraft, the ESA Cluster set of spacecraft, and the JAXA Geotail spacecraft were all situated tailward of the dusk terminator, at locations between X_{GSM} of −2 R_E and −14 R_E, Y_{GSM} between +13 R_E and +18 R_E, and Z_{GSM} between −12 R_E and +4 R_E (i.e., at mid-to-low latitudes). Multiple plasma and field fluctuations over an extended period of time were observed at all of these spacecraft.

Finally, the DMSP F17 spacecraft at low-Earth orbit observed far ultraviolet (FUV) ionospheric auroral zone emissions during this time. Of particular interest for this investigation is a post-noon "bead" that was observed in the northern hemisphere by the SSUSI package on board DMSP F17, and how the "bead" is related to the spacecraft observations along the dusk flank magnetopause.

INSTRUMENTATION

Observations of the solar wind during this interval were made by several spacecraft. The ARTEMIS 1 and 2 spacecraft were upstream of the Earth's bow shock, but closer than the solar wind monitors stationed near L1. The solar wind plasma and magnetic field observations were provided by the Electrostatic Analyzer (ESA) (McFadden et al., 2008a, McFadden et al., 2008b) and the FluxGate Magnetometer (FGM) (Auster et al., 2008), respectively. These observations have been convected to the bow shock nose. Additional convection time from the bow shock nose (BSN) to the observing spacecraft (sc) along the flank magnetopause is estimated as $\Delta X(BSN—sc)/(V_{sw}/2)$.

The MMS instrument observations used in this paper are from the Fluxgate Magnetometer (FGM) (Russell et al., 2016; Torbert et al., 2016) and the Fast Plasma Instrument (FPI) (Pollock et al., 2016). The FPI instrument provides rapid ion measurements over the energy range 10 eV/e—30 keV/e at a temporal resolution of 150 msec ("burst" mode data rate for ions) and 4 s (slower "survey" mode data rate for ions). Magnetic field observations are from the Fluxgate Magnetometer (FGM) experiments on board each of the Cluster spacecraft (Balogh et al., 1997). Geotail magnetic field experiment (MGF) observations of the vector magnetic field (Kokubun et al., 1994) are also used in the study, as well as proton and electron observations from the Low Energy Particle (LEP) instrument on board the Geotail spacecraft (Mukai et al., 1994).

DMSP F17 Special Sensor Ultraviolet Spectrographic Imager (SSUSI) imager (Paxton et al., 1992, 1993, 2002; Paxton and Zhang, 2016; Paxton et al., 2017) is used to record Far-ultraviolet (115–180 nm) emissions from the high-latitude regions. In particular, the presence/absence of compact vortex-like structures in the dayside ionosphere (beads) are described and related to observations along the dusk flank magnetopause in this investigation, using the Lyman–Birge–Hopfield short-band (LBHS) emissions (140—150 nm).

ANALYSIS OF INTERVAL

Solar Wind Observations and Geomagnetic Activity

Figure 1 shows the solar wind as observed by the ARTEMIS 1 spacecraft almost directly upstream, and convected to the bow shock nose (an additional time of 7–12 min accounts for the convection of the solar wind from the bow shock nose to the locations of MMS to Geotail, respectively). ARTEMIS 2 provides very similar solar wind observations, and is not shown here. A 5-h interval (11–16 UT) is displayed, spanning the MMS encounters with and passage across the flank magnetopause between ~12 and ~14 UT. The interplanetary magnetic field (IMF) in **Figure 1A** was slightly southward during most of the 5-h interval, The $B_{x\text{-}GSM}$ component was also negative during this interval. The $B_{y\text{-}GSM}$ component was positive during most of the interval, with the notable exception of a reversal in sign between ~11:40 and ~12:25 UT. The IMF cone angle is displayed in **Figure 1B**. During this interval, the subsolar region was rather evenly divided between being downstream of the quasi-parallel bow shock (cone angle <45°) and being downstream of the quasi-perpendicular bow shock (cone angle >45°). The solar wind bulk density (**Figure 1C**) and solar wind bulk flow (**Figure 1D**) were steady during this time interval.

There was no significant geomagnetic activity during this interval. The Kp index was <2 throughout the interval (**Figure 1E**), and the Dst index was > −40 nT during this time (**Figure 1F**). The SME U/L indices are SuperMAG derived indices (based on all available ground magnetometer stations at geomagnetic latitudes between +40° and +80°), provided in **Figure 1G** for context only, and are not officially authorized by the International Association of Geomagnetism and Aeronomy (IAGA). The SME U/L data products are similar to the traditional auroral electrojet indices (AE U/L) (Davis and Sugiura, 1966), as described in detail by Newell and Gjerloev (2011a,b). Based on these records, some modest auroral activity was present early during this interval of interest; but was not of great significance.

Locations of Sampling Spacecraft

Figure 2 shows the projected locations of multiple plasma and field sampling spacecraft during this time interval, in the GSM coordinate system. **Figure 2A** shows the projection into the XY (GSM equatorial) plane; **Figure 2B** shows the projection into the XZ (GSM noon-midnight meridian) plane. The magnetopause (Shue et al., 1997) and bow shock (Chao et al.,

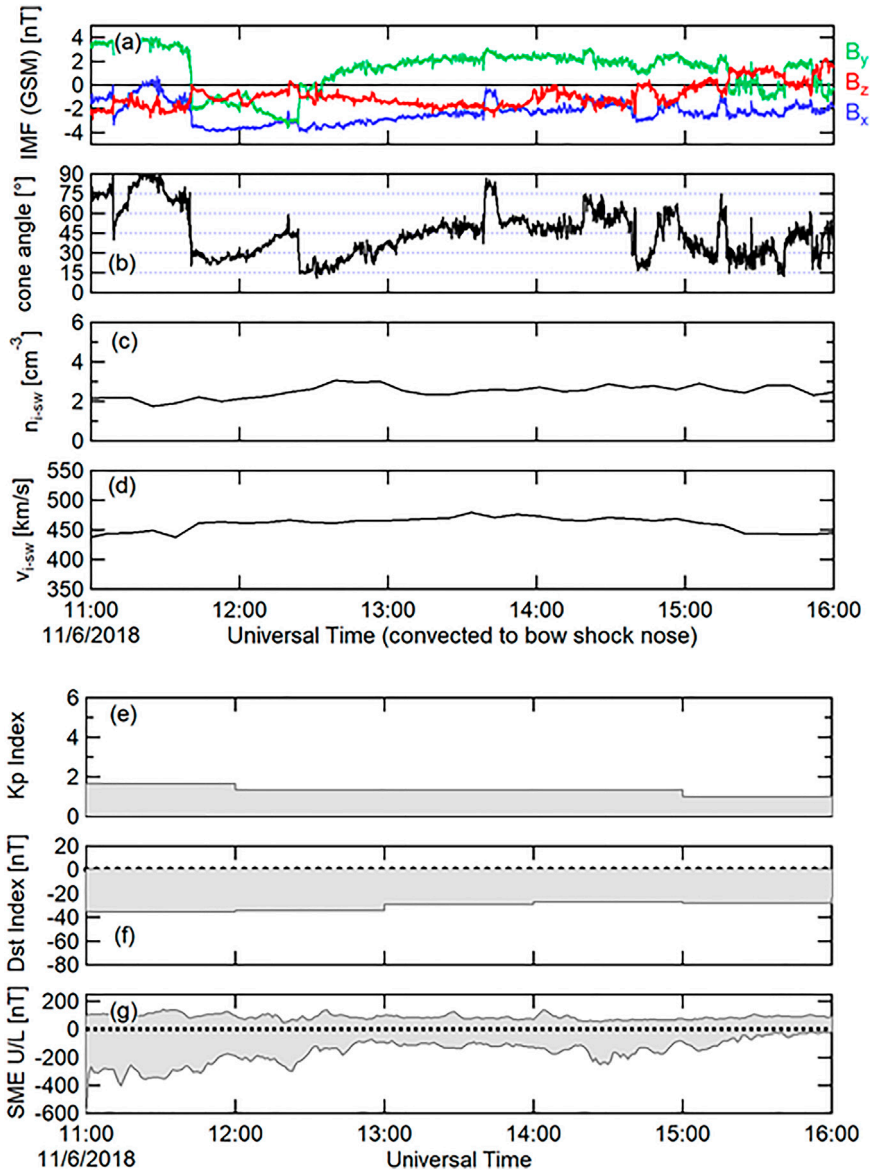

FIGURE 1 | Observations of the solar wind by the ARTEMIS 1 spacecraft, convected in time by 11.2 min to the bow shock nose. **(A)** IMF components in GSM coordinates; **(B)** IMF cone angle; **(C)** Solar wind ion density; **(D)** Solar wind bulk speed; **(E)** Kp index; **(F)** Dst index; **(G)** SME U/L index (similar to the AE index).

2002)–parameterized by the solar wind and including a small (4°) rotation to account for aberration of the solar wind - are provided for context. The Time History of Events and Macroscale Interactions during Substorms (THEMIS) A, D, and E spacecraft were all located in the dayside magnetosheath, north of the GSM equatorial plane at this time. These spacecraft did not observe any long period fluctuations in either the fields or plasma moments during this interval, and are not discussed further. The MMS constellation was at the dusk flank magnetopause, just past the terminator plane (i.e., X_{GSM} = 0), and was situated a couple R_E below the equatorial plane. The MMS spacecraft were on the inbound portion of the orbit, traveling normal to the magnetopause surface. Although it might at first appear that this is an unfortunate "angle of attack" of the magnetopause for studying KH, it actually provides for a relatively clean pass and sampling of the boundary, along with the plasma and magnetic fields of the magnetosheath proper and magnetosphere proper, which are also sampled relatively close in time to the observance of KH vortices. The Cluster set of spacecraft was also along the dusk flank; somewhat earthward of the magnetopause, and had crossed the GSM equatorial plane, moving from the southern magnetotail lobe to the northern lobe over the span of several hours. The Geotail spacecraft was also situated at the dusk flank magnetopause; a bit further downtail (X_{GSM} = ~−12 R_E), but at higher southern latitude than any of the other spacecraft. The

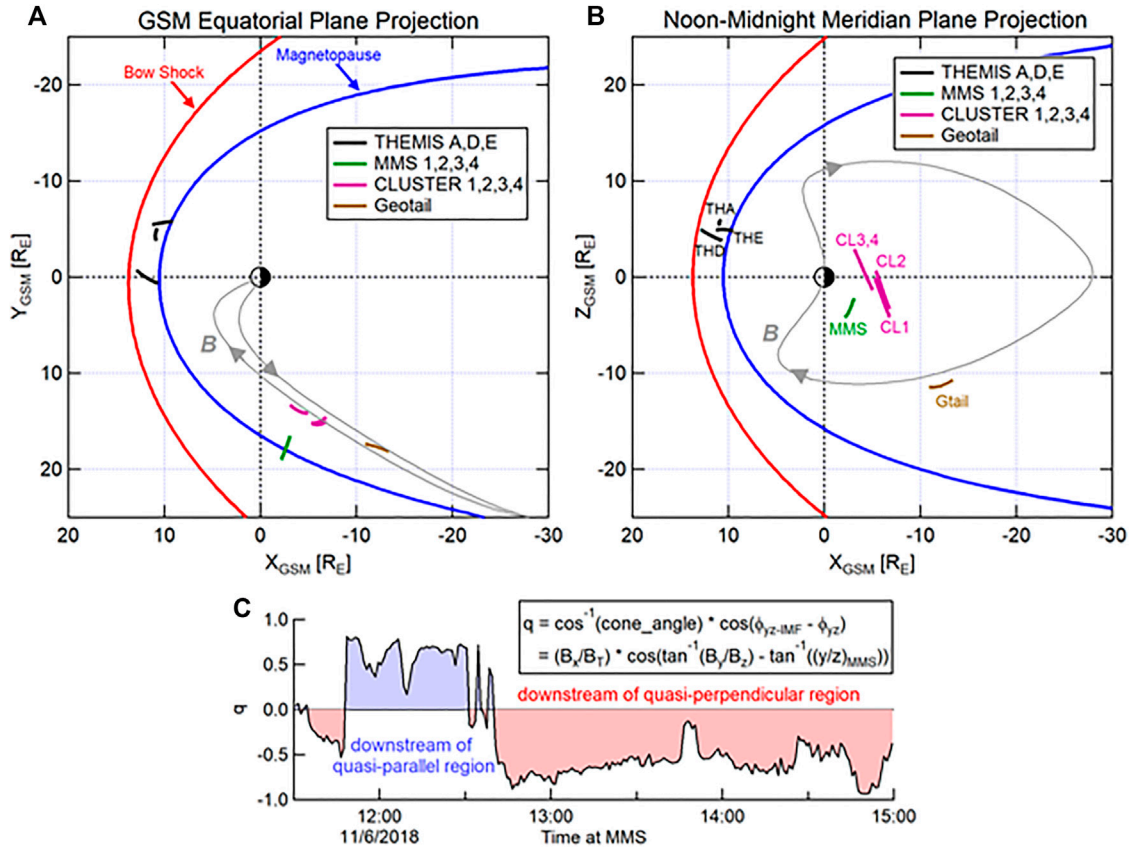

FIGURE 2 | Spacecraft locations in GSM coordinates during the interval 2018-11-06, 11:30–15:00 UT. **(A)** Equatorial plane projection; **(B)** Meridian plane projection. The red trace demarks the parameterized bow shock shape and location; while the blue trace demarks the parameterized magnetopause shape and location. A magnetospheric magnetic field line (grey) is traced from the center location of the ionospheric bead in the northern ionosphere into the magnetotail and ending in the southern ionosphere. **(C)** Time series of parameter "*q*". This parameter uses the ARTEMIS 1 IMF components (convected to the bow shock, plus an additional convection time of 7 mins) in conjunction with the MMS Y/Z location to determine whether the region local to MMS was downstream of the quasi-parallel bow shock (q > 0, in blue), or was downstream of the quasi-perpendicular bow shock (q < 0, in red).

projection of a single magnetospheric magnetic field line is also shown, and will be discussed in further detail in *Magnetic Field Mapping of Ionospheric "Bead"*. **Figure 2C** uses the IMF cone angle and "clock angle" (convected to the bow shock, and then to the location of MMS) in conjunction with the YZ coordinates of the MMS spacecraft (a spatial "clock angle") to construct a parameter "q". This single parameter provides an assessment as to whether the magnetosheath region in the vicinity of MMS is downstream of the quasi-parallel bow shock (q > 0), or is downstream of the quasi-perpendicular bow shock (q < 0). Using this parameter, during the interval of ~11:50—~12:40 UT, the magnetosheath region near MMS was downstream of the quasi-parallel bow shock. Otherwise, the magnetosheath region near MMS is surmised to have been downstream of the quasi-perpendicular bow shock.

MMS Observations

Figure 3 shows the plasma and magnetic field observations from the MMS1 spacecraft for a 3.5-h interval, as the spacecraft traveled from the magnetosheath into the magnetosphere. The four spacecraft of the MMS constellation were very close to one another (a few tens of km separation) at this time, and differences are negligible when viewed over larger time scales (hours). Therefore, the observations from MMS1 represent the observations from each of the spacecraft. The first panel of **Figure 3** shows the GSE components of the magnetic field, and the magnetic field intensity is shown in the second panel. The third panel displays the overlaid time series of the ion (blue) and electron (red) number densities. The next three panels show the GSE components of the ion bulk velocity. The ion and electron temperatures parallel and perpendicular to the magnetic field are presented in the next two panels of **Figure 3**. The bottom panel shows the static pressure ($P_{\mathrm{Tot}} = n_i k_B(T_{\mathrm{i\text{-}para}} + 2\ T_{\mathrm{i\text{-}perp}})/3 + n_e k_B(T_{\mathrm{e\text{-}para}} + 2\ T_{\mathrm{e\text{-}perp}})/3 + B^2/2\mu_0$).

Significant fluctuations were observed in all parameters as the MMS spacecraft passed from the magnetosheath into the magnetosphere, as displayed in **Figure 3**. As described earlier, the IMF orientation at the time suggests that the MMS spacecraft were downstream of the quasi-perpendicular bow shock. Therefore, it is not likely that these fluctuations were due to convected foreshock wave activity from the quasi-parallel bow shock. It was also noted that the solar wind bulk flow speed was

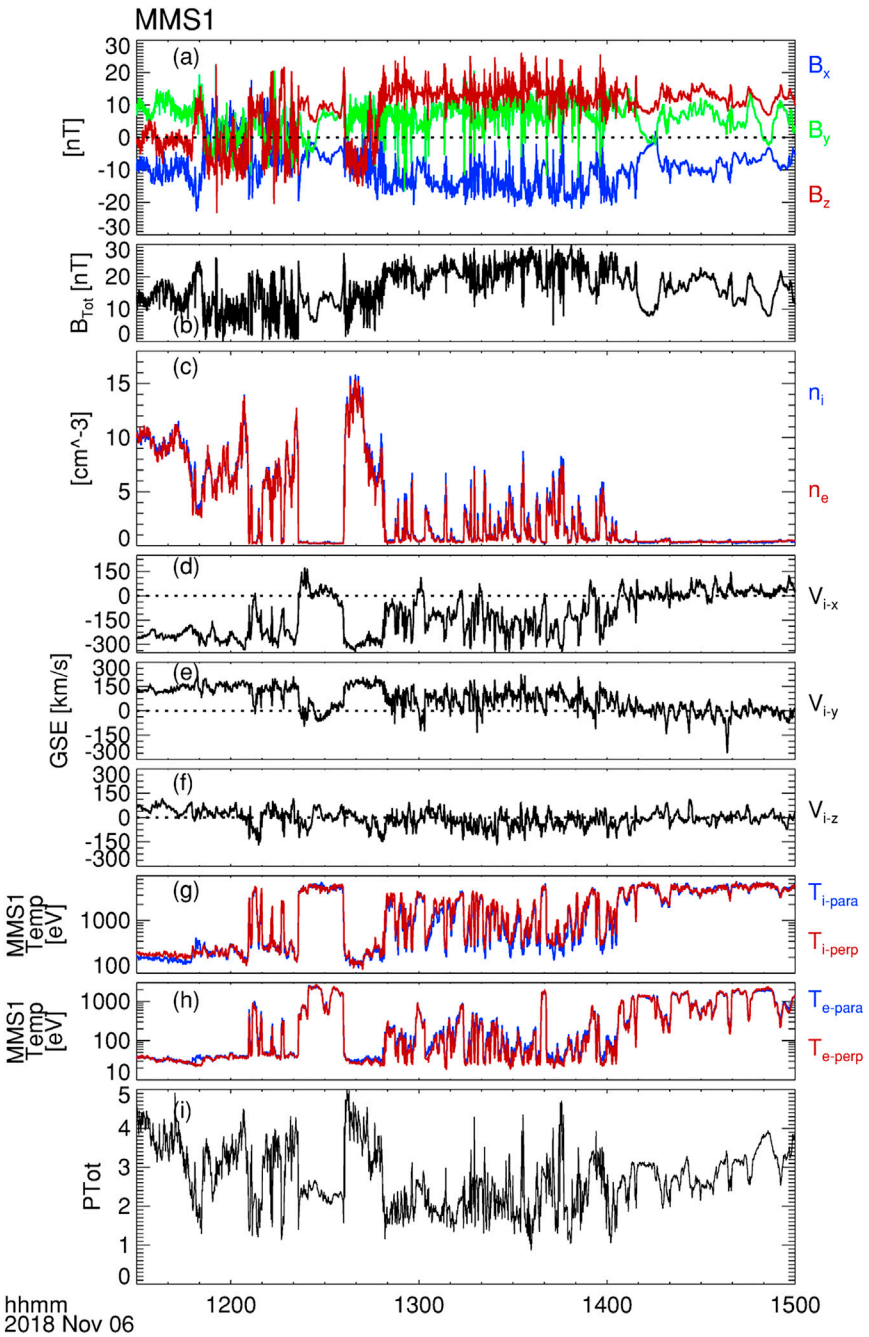

FIGURE 3 | MMS observations of the magnetic field and plasma moments during the inbound traversal from the magnetosheath across the flank dusk magnetopause and into the magnetosphere. **(A)** Magnetic field components in GSE coordinates; **(B)** Magnetic field intensity; **(C)** Number densities of ions (blue) and electrons (red); **(D)** Ion bulk velocity component V_{xGSE}; **(E)** Ion bulk velocity components V_{yGSE}; **(F)** Ion bulk velocity components V_{zGSE}; **(G)** Perpendicular temperatures of ions (blue) and electrons (red); **(H)** Parallel temperatures of ions (blue) and electrons (red); and **(I)** Total static pressure (Sum of magnetic and thermal pressures).

considerably higher than average during this time. Higher solar wind speed has been shown to be statistically more conducive to initiate Kelvin-Helmholtz waves along the magnetopause, due to a larger velocity shear (e.g., Kavosi and Raeder, 2015). **Figure 4** shows a 70-min expanded view focused on the fluctuations at the magnetopause, displaying the same set of panels as was shown in **Figure 3**. Variations in the ion number density are observed and exhibit the common and well-known feature of sharp increases followed by more gradual decreases associated with observations of rolled-up KH vortices at the magnetopause (cf., Chen et al., 1993; Hasegawa et al., 2004; Hasegawa et al., 2006; Hasegawa et al., 2009).

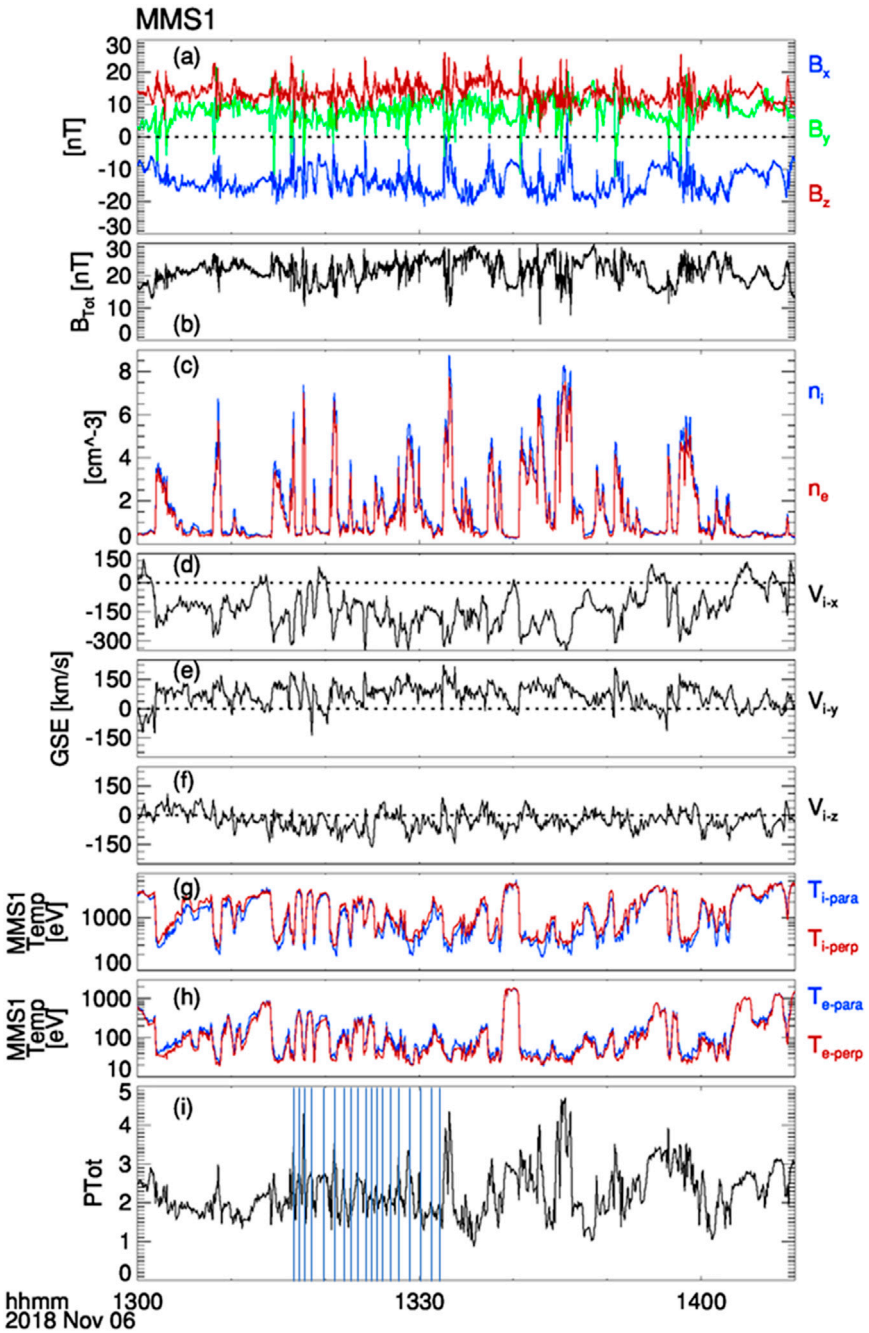

FIGURE 4 | Expanded view of sub-interval from **Figure 3**. This sub-interval lies between the magnetosheath proper and magnetosphere proper, and shows several brief crossings of the magnetopause boundary. Panel format is the same as that of **Figure 3**. Blue vertical lines in the bottom panel demark peaks of the static pressure.

An often-used test for the onset of the KHI for an ideal, incompressible plasma across a thin velocity shear layer satisfies the following inequality (Chandrasekhar, 1961; Henry et al., 2017):

$$[\boldsymbol{k}\cdot(\boldsymbol{v_1}-\boldsymbol{v_2})]^2 \geq \frac{\boldsymbol{n_1}+\boldsymbol{n_2}}{4\pi \boldsymbol{m_0 n_1 n_2}}\left[(\boldsymbol{k}\cdot\boldsymbol{B_1})^2+(\boldsymbol{k}\cdot\boldsymbol{B_2})^2\right] \quad (1)$$

and is tested across the flank magnetopause. The subscript "1" refers to the magnetosheath proper, and subscript "2" refers to the magnetosphere proper. The methodology for determining these regions is based on the description of Henry et al., 2017. The average of the highest and lowest quartiles of the ratio n_i/T_i are used to determine "the magnetopause" value of n_i/T_i. Larger values are designated to "the magnetosheath"; lower values are designated to "the magnetosphere". The top one-third of the ranked n_i/T_i ratio of "the magnetosheath" population is used to determine the mean vector and scalar components for the

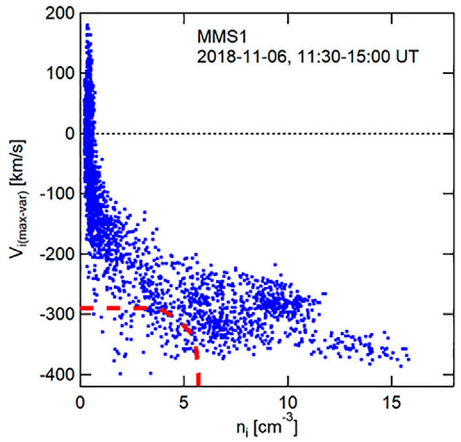

FIGURE 5 | MMS ion bulk velocity along maximum variance direction during this interval, as a function of the ion number density. Positive velocities are in the sunward direction. Low density, larger anti-sunward speeds (below the red dashed curve) are indicative of Kelvin-Helmholtz activity, with plasma mixing within well-developed vortices.

magnetosheath proper. Similarly, the lowest one-third of "the magnetosphere" population is used to determine the mean vector and scalar components for the magnetosphere proper. The mean vector (GSE) components and ion number density values are thus as follows: $\mathbf{B_1}$ = {−7.738, 6.977, −2.593} nT; $\mathbf{B_2}$ = {−5.925, 3.965, 10.009} nT; $\mathbf{V_1}$ = {−261.563, 145.446, 29.466} km/s; $\mathbf{V_2}$ = {13.953, 0.189, −0.215} km/s; n_1 = 10.336 cm^{-3}; n_2 = 0.290 cm^{-3}. Using these mean plasma moment and magnetic field vector values for the magnetosheath proper and for the magnetosphere proper, the unit *k*-vector corresponding to maximum wave growth is: {−0.736, −0.668, −0.114}. With this unit *k*-vector, the ratio of the left hand side to the right hand side of the inequality of **Eq. 1** is 2.95; easily satisfying this test for the presence of a Kelvin-Helmholtz instability. As shown in **Figure 1**, the IMF was steady and slightly southward during most of this time interval. Although the Kelvin-Helmholtz instability commonly occurs along Earth's low-latitude magnetopause flanks during sustained intervals of northward IMF (e.g., *Kavosi and Raeder,* 2015), it is occasionally observed during intervals of southward IMF. About 10% of all KH intervals occurred during southward IMF as reported in the statistical study by Kavosi and Raeder, (2015), while a larger percentage of KH intervals were reported to occur during southward IMF by Henry et al. (2017). Individual cases of flank magnetopause Kelvin-Helmholtz occurring during southward IMF were investigated by Hwang et al. (2011); Nakamura et al. (2020); Kronberg et al. (2021).

A second diagnostic to test for the presence of Kelvin-Helmholtz observed by the MMS spacecraft at the magnetopause is to plot the bulk velocity as a function of the ion density. The presence of low ion density at high tailward velocity is suggestive of the mixing of plasmas and the occurrence of well-developed rolled-up vortices, as described by both models and observations (Hasegawa et al., 2004, 2006; Takagi et al., 2006; Taylor et al., 2012). The maximum variance of the magnetosheath electric field (-**vxB**) is estimated via the MVA-E method (Sonnerup and Scheible, 1998), and provides the bulk velocity tangential to the magnetopause, which is displayed in **Figure 5**. The data points in the region below the red dashed curve provide evidence for the presence of rolled-up vortices, and is consistent with the results of the first diagnostic test. It is therefore concluded from the results of these diagnostic tests that KH waves were observed along the dusk flank magnetopause by MMS.

Cluster Observations

As described above (and shown in **Figure 2**), the four Cluster spacecraft were relatively close to the MMS constellation during this interval; but were located slightly further within the magnetotail. The four Cluster spacecraft were traveling northward from south of the GSM equator along their respective orbits during this interval, and all four observed clear oscillations in the magnetic field components and intensity. Although it is not proven here that the KH waves along the dusk flank magnetopause drove the magnetic field oscillations observed at Cluster, past observational studies have established an observations-based connection between KH waves along the magnetopause and the excitation of ULF waves observed within the magnetosphere and on the ground (e.g., Mann et al., 2002; Rae et al., 2005). The Lyon-Fedder-Mobarry (LFM) global, three-dimensional magnetohydrodynamic (MHD) single-fluid simulations has also been shown that ULF pulsations can be generated near the flank magnetopause in response to the magnetopause KH instability (Claudepierre et al., 2008). A recent study by Kim et al. (2021) also shows how KH waves may couple to Alfvén waves in the magnetosphere. In contrast to the MMS observations of fluctuations at the magnetopause, the magnetic field transverse and compressional fluctuations observed at Cluster are of a more sinusoidal nature.

Wave periods are determined during the interval of greatest observed wave activity in the maximum variance direction of the Cluster magnetic field; i.e., from estimates of peak-to-peak times during 12:30 to 15:41 UT. The Cluster 3 and 4 spacecraft were very close to one another during this time interval, with a separation distance of ~13.5 km at 10:30 UT, decreasing to ~11.0 km at 16:00 UT. As would be expected from spacecraft in such proximity, the observed magnetic field variations are nearly identical (**Figure 6**): with a correlation coefficient of $r >$ +0.999. The average and standard deviation of the wave period was 7.5 ± 2.9 min (frequencies of 1.6—5.7 mHz). In comparison (**Figure 7**), the Cluster 1 and 2 pair of spacecraft were further separated from one another than the Cluster 3,4 pair: from ~6,000 km at 10:30 UT, decreasing to ~5,300 km at 16:00 UT. The average and standard deviation of the wave period was 7.6 ± 3.2 min (frequencies of 1.5—3.8 mHz), with a high correlation coefficient (r = +0.92); though not quite as high as the correlation between Cluster 3 and 4. The Cluster 1 and 2 pair of spacecraft were significantly distant from the Cluster 3 and 4 spacecraft (~3.1–4.5 R_E distant).

The frequency range of the Cluster magnetic field fluctuations overlaps substantially with the ULF frequency range found in the LFM simulations by Claudepierre et al. (2008) within the magnetosphere (0.5—3 mHz). The magnetic field oscillations

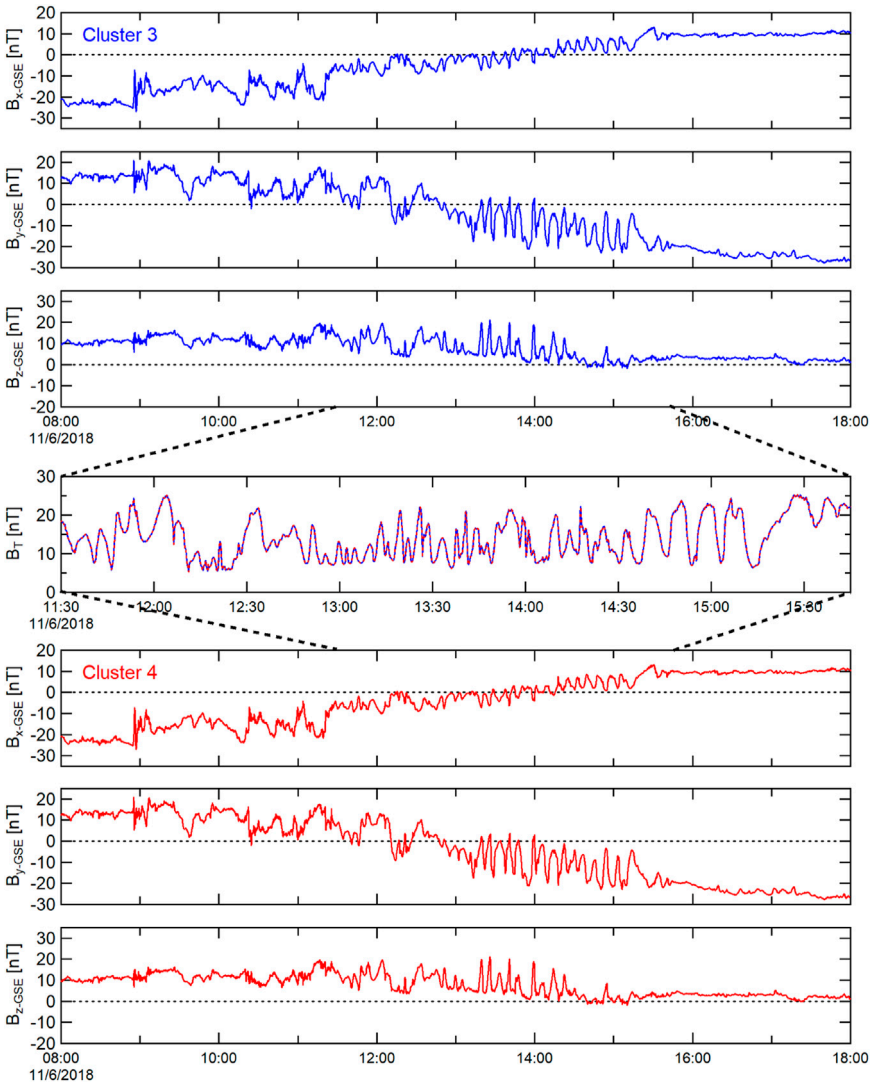

FIGURE 6 | Magnetic field observations from Cluster 3 and Cluster 4, in GSE coordinates. These spacecraft were initially in the southern lobe (strong and rather steady negative B_x), and ended in the northern magnetotail lobe (strong and rather steady positive B_x). During the time spent near the magnetopause and flank neutral sheet, coherent transverse and compressional waves were observed in the magnetic field. Magnetic field intensity (and compressional waves) from the two spacecraft are overlaid in the fourth (middle) panel, and are essentially identical in amplitude, frequency, and phase. Highest frequency waves are closest to the neutral sheet (B_x near zero).

were also of similar frequency to long-period ULF waves in the plasma sheet as described by Tian et al. (2012) (1.7—2.0 and 3.0—3.2 mHz). The location of the spacecraft is consistent with being near the magnetopause edge of the magnetotail plasma sheet. Cluster Ion Spectrometry (CIS) plasma moment data were available during this time. However, the observed plasma moments showed no significant variations; in contrast to the magnetic field. The observed proton density remained relatively constant; between ~0.1 and ~0.3 cm^{-3} throughout this entire interval (not shown).

Geotail Observations

The Geotail magnetic field, electron and proton energy flux spectrograms are shown in **Figure 8**, plotted over a 6-h interval (12:00—18:00 UT). A >1-h data gap occurred between ~15:30—16:25 UT. The components and intensity of the magnetic field were fairly steady during the first few hours of this interval, and are consistent with the expectations of the Geotail spacecraft being located within the magnetotail, south of the neutral sheet. Small oscillations of the magnetic field (a few nT) were observed after ~14:25 UT. The magnetic field fluctuations did not exhibit any significant linear or circular polarization. The diminished magnetic field fluctuations relative to those observed at Cluster is consistent with the LFM numerical simulations of Claudepierre et al. (2008); which suggests that the ULF integrated wave power as driven by KH decreases markedly with distance downtail, and with distance away from the GSM equator.

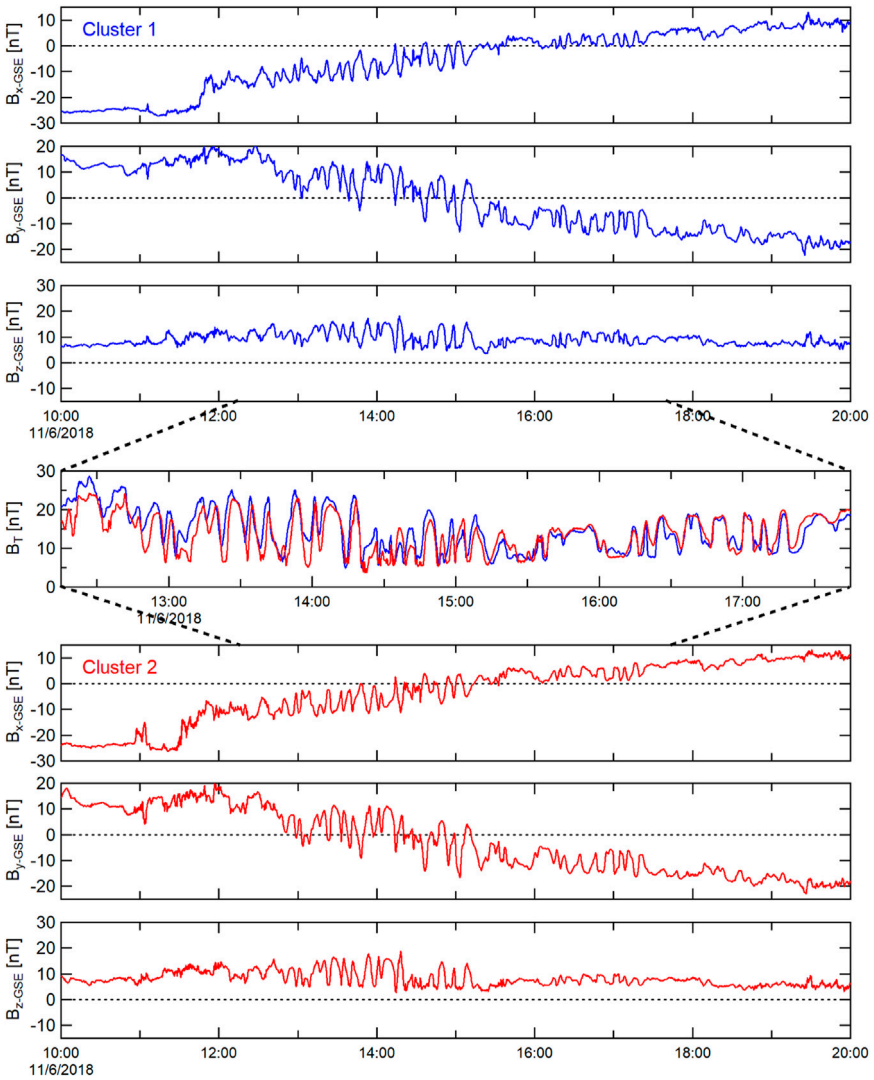

FIGURE 7 | Magnetic field observations from Cluster 1 and Cluster 2, in GSE coordinates. Panel format is the same as that of **Figure 6**.

The electron and proton energy flux spectrograms from the Geotail LEP instrument during this interval are also shown in **Figure 8**, segregated into four distinct sectors designating plasma flow directions: Sunward, duskward, tailward, and dawnward. For the electron energy flux spectrograms, equal flux was observed in all directions, with an energy of ~100 eV. For the proton energy flux spectrograms, significant flux was only observed moving towards dusk and downtail, with an energy of several hundred eV. These observations are consistent with the spacecraft sampling the plasma mantle (cf., Rosenbauer et al., 1975; Haaland et al., 2008).

Starting just prior to 14:30 UT, enhancements in the electron flux appear in all directions; while the peak energy remains at ~100 eV. Coincident with the electron flux enhancements, proton flux enhancements are also observed. The proton flux enhancements are also seen in all directions, and are at higher energy (peaked at a few to several keV). An expanded (90-min) view of these flux enhancements (along with the magnetic field) is shown in **Figure 9**. The enhancements are likely due to brief excursions into the plasma sheet boundary layer. The enhancements are somewhat periodic, with eight enhancements occurring within the span of about hour (period of ~7 min; or frequency of ~2.4 mHz). This frequency is within the frequency band observed by the Cluster magnetometers, and suggests that the flux enhancements observed at Geotail are related to the ULF wave activity observed by Cluster.

DMSP Observations of a Dayside Ionosphere "Bead"

DMSP satellites imaged significant portions of the auroral oval several times during this KH event. **Figure 10A** presents an example of an auroral oval in the northern hemisphere imaged DMSP SSUSI at ~11:40–12:00 UT. This time is near the start of the larger time interval when fluctuations were observed by the various spacecraft, as

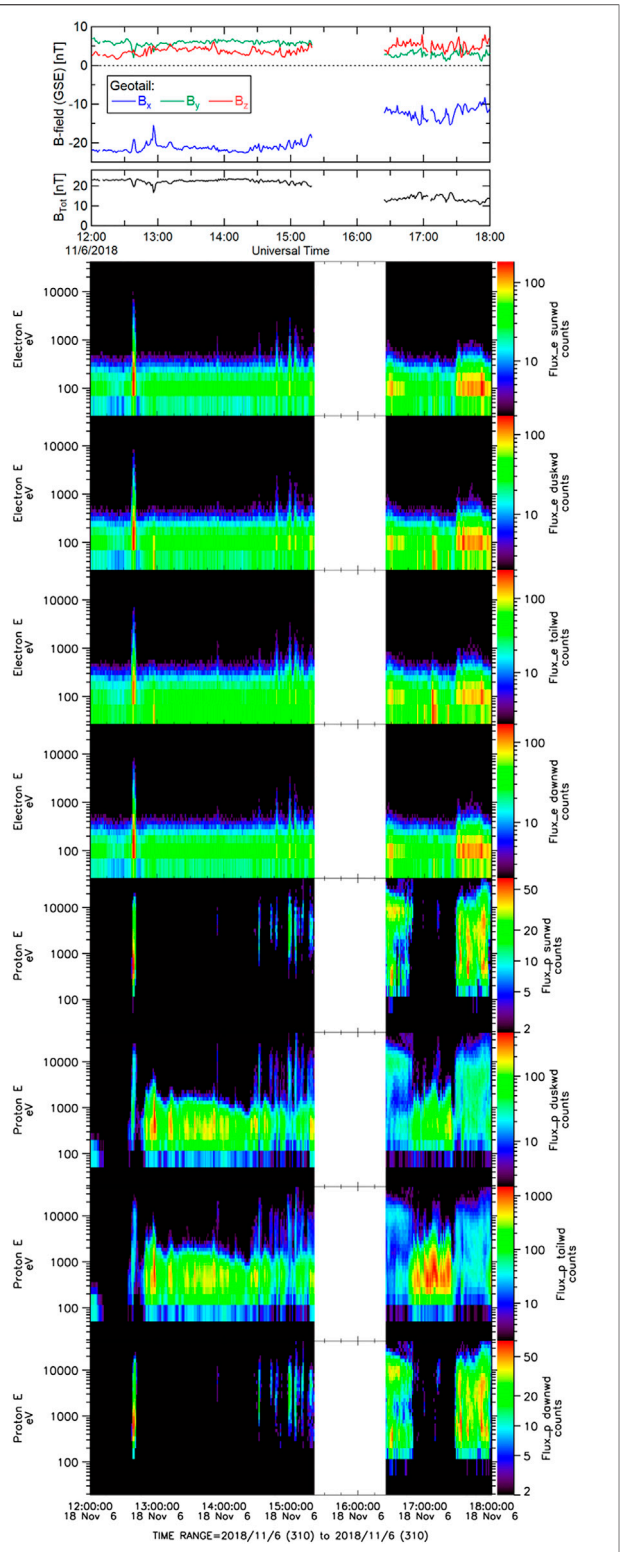

FIGURE 8 | Geotail observations of the magnetic field, electron energy flux spectrograms, and proton energy flux spectrograms observed in four directions. Color scale of flux min/max values are auto-scaled within each panel.

described above. The image reveals several bead structures can be seen more clearly in the zoomed in image presented in **Figure 10B**. Although the DMSP satellite re-visited and images the northern auroral region every ~101 min, due to the precession of the magnetic dipole, subsequent passes did not provide image coverage of the same auroral region near local noon. Although this particular DMSP SSUSI observation occurred just prior to the MMS spacecraft encountering the flank magnetopause, this interval does coincide with the Cluster 3 and 4 observations of ULF pulsations just inside the flank magnetopause (starting ~11:30 UT). As described above, these pulsations are believed to occur in response to KH activity (Claudepierre et al., 2008).

Recently, Johnson et al. (2021) developed a theory for mesoscale field-aligned currents generated by the KH vortices at the magnetopause boundary layer. The theory predicts that the mapping of the KH vortex to the ionosphere is optimal when $\Lambda/L = 2.8$, where Λ = width of the vortex field-aligned current, L = the auroral electrostatic scale length = $\sqrt{\Sigma_p/\kappa}$, Σ_p = Pedersen conductivity, and κ = Knight κ (Knight, 1973). The assumption of the linear approximation to the Knight current-voltage relation is used: $j = \kappa\Phi$, and $\kappa = e^2 n_e/(2\pi m_e T_e)^{1/2}$; where j and Φ represent the field-aligned current density and field-aligned potential, respectively. Moreover, they demonstrated that the theory can predict the KH vortex size at the magnetopause boundary layer from DMSP and THEMIS observations in one event.

A theory–observation comparison using DMSP and MMS observations is conducted here, as was done in Johnson et al. (2021). For the analysis, the focus is on a bead pointed to by the red arrow in **Figure 10B**. The bead is centered at (Mlat, MLT) = (76.5°, 14.1) and Λ = 93 km. Using the solar zenith angle at this location ($\chi \sim 6°$) and F10.7 solar flux density = 68 W m^{-2} Hz^{-1}, the Pedersen conductivity due to the ionizing solar extreme ultraviolet (EUV) radiation is $\Sigma_{p,s}$ = 7 S (Robinson and Vondrak, 1984). Inside the bead, the mean energy is estimated to be 8 keV and the mean energy flux to be 18 erg s^{-1} cm^{-2} based on N_2 LBHS (140–150 nm) and LBHL (165–180 nm) radiances (Zhang and Paxton, 2008 and references therein) observed by DMSP SSUSI (Paxton et al., 1993). Using these values, the Pedersen conductivity due to electron precipitation is estimated as $\Sigma_{p,e}$ = 17 S (Robinson et al., 1987). The total $\Sigma_p = \sqrt{\Sigma_{p,e}^2 + \Sigma_{p,s}^2} \sim 18$ S (Wallis and Budzinski, 1981).

MMS provides observations of T_e = 39.7 eV, n_e = 2.9 cm^{-3}, $|B|_{MMS}$ = 20.5 nT near the center of the KH vortex at the boundary layer. Using the Knight κ calculated from MMS T_e and n_e and Σ_p calculated from DMSP observations, values of L = 39 km and $\Lambda/L = 2.4$ are obtained, which is close to the Johnson et al. (2021) theoretical optimal value for mapping the vortex to the ionosphere: $\Lambda/L = 2.8$.

The predicted KH vortex spatial scale is calculated from Λ, L, B_i, and B_m where $B_m = |B|_{MMS}$, and $B_i = |B|_{DMSP}$ = 39,759 nT. Johnson et al. (2021) derived an expression for $\Delta_i = 2\,\alpha\,L = 49$ km, where Δ_i = the vortex radius mapped to the ionosphere and α = a mapping parameter obtained from Λ/L ($|x|/L = 2\,\Lambda/L$) as

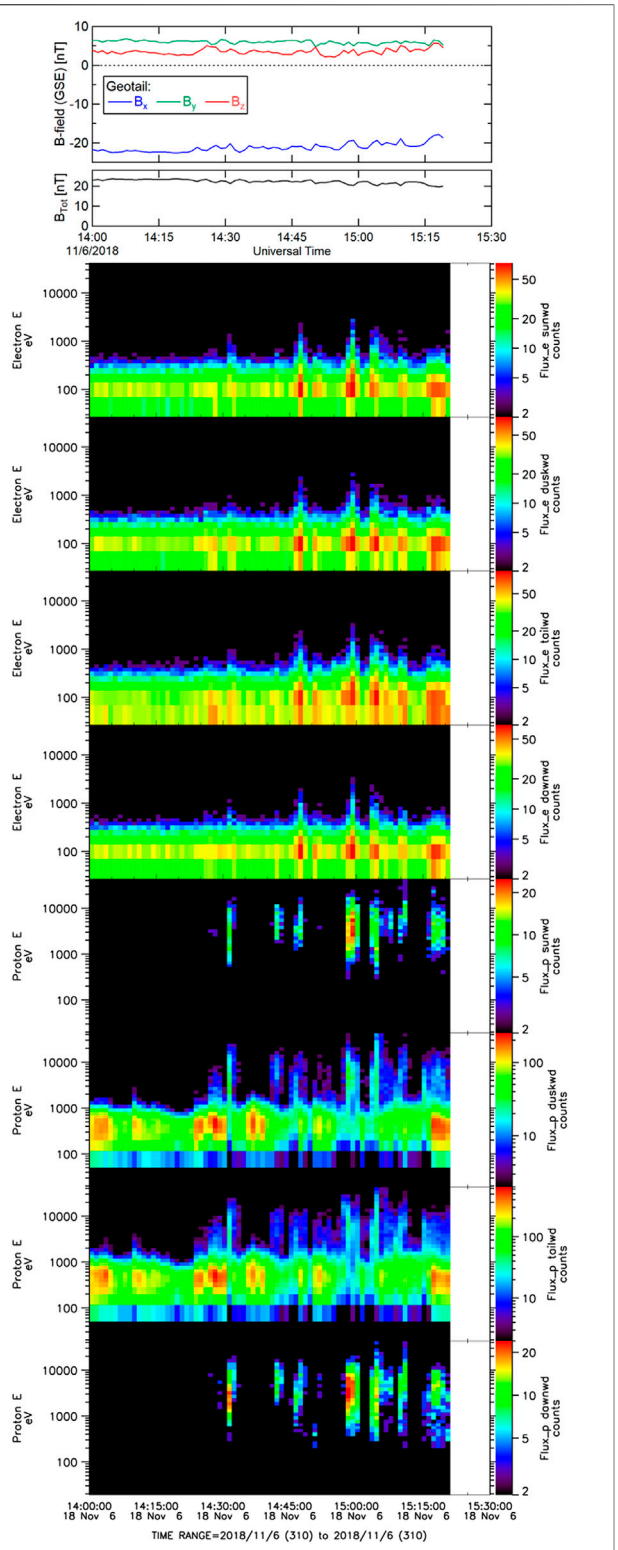

FIGURE 9 | Expanded view of the Geotail magnetic field and electron and proton energy flux spectrograms. Layout is the same as **Figure 8**.

described in **Figure 3** in Johnson et al. (2021). The radius of the KH vortex at the boundary layer $\Delta_m = b\,\Delta_i$ = 2,162 km, where $b = (B_i/B_m)^{1/2}$. The diameter of the KH vortex = 4325 km (0.68 RE), where R_E = radius of the Earth = 6,372 km. This size is compared with that estimated from the MMS observation. The estimate from **Figure 3** is that the KH wavelength = 1.5 R_E, using the number of identified static pressure peaks between 13:17 and 13:32 UT to estimate the wave period, and using the bulk speed at the center of the vortex (at 13:25:18 UT, identified from the local minima observed in the $|V_{i\text{-}N}|$, $|V_{i\text{-}M}|$, and $|B_N|$ components, where the GSE–> LMN coordinate transformation was determined from the MVA-E method mentioned earlier, and used in the diagnostic test of **Figure 5**). Otto and Fairfield (2000) found that KH vortex size is about one-half the wavelength. Using this ratio of KH wavelength to diameter, the estimate of the observed KH diameter = 0.75 R_E, which is close to the predicted value of 0.68 R_E. Using the peak value ε_{max} from **Figure 7** of Johnson et al. (2021), the predicted maximum current density using observed KH vortex parameters is $j_{||,max}$ = 45 $\mu A/m^2$.

In the above calculation, $\Sigma_{p,e}$ was estimated from the precipitating electron energy flux (J_e) and mean energy (E_e) inside the bead from DMSP SSUSI LBHS and LBHL emissions using the method described in Zhang and Paxton (2008). The estimated J_e and E_e have relatively large statistical errors due to limited counts in the LBHS and LBHL channels. The estimated values of J_e = 18 erg s^{-1} cm^{-2} and E_e = 7 keV are probably too high, which leads to a rather high estimated value of $\Sigma_{p,e}$ = 17 S (Robinson et al., 1987; Johnson and Wing, 2015; Wing and Johnson, 2015). If a value of $\Sigma_{p,e}$ = 5 S is used (resulting in total Σ_p = 8.6 S), then a value of Λ/L = 3.5 would have been obtained, with a predicted KH vortex diameter = 0.72 R_E. It is interesting to note that the predicted KH diameter of 0.72 R_E would be closer to the observed value of 0.75 R_E, although the value of Λ/L = 3.5 would represent a larger deviation from the theoretical optimal value of 2.8. It is also interesting to note that in this particular event, changing Σ_p from 17 to 8.6 S would result in only a small change of the predicted KH diameter; from 0.68 R_E to 0.72 R_E. Using the peak ε_{max} from Johnson et al. (2021), the predicted maximum parallel current density is then significantly reduced ($j_{||,max}$ = 21 $\mu A/m^2$).

Magnetic Field Mapping of Ionospheric "Bead"

The Tsyganenko 1996 magnetospheric magnetic field model (Tsyganenko, 1995) has been used to trace the magnetic field from the center location of the ionospheric bead out into the magnetosphere. The traced magnetic field line extends from the post-noon high-latitude ionosphere to the deep magnetotail, to X_{GSM} = ~−28 R_E downtail (shown in gray in **Figure 2**). This field line trace is also close to the dusk flank magnetopause, in the same general region as the sampling spacecraft previously discussed. Continuing the trace to the southern hemisphere, the magnetic field line associated with the ionospheric bead passed very close to the location of Geotail.

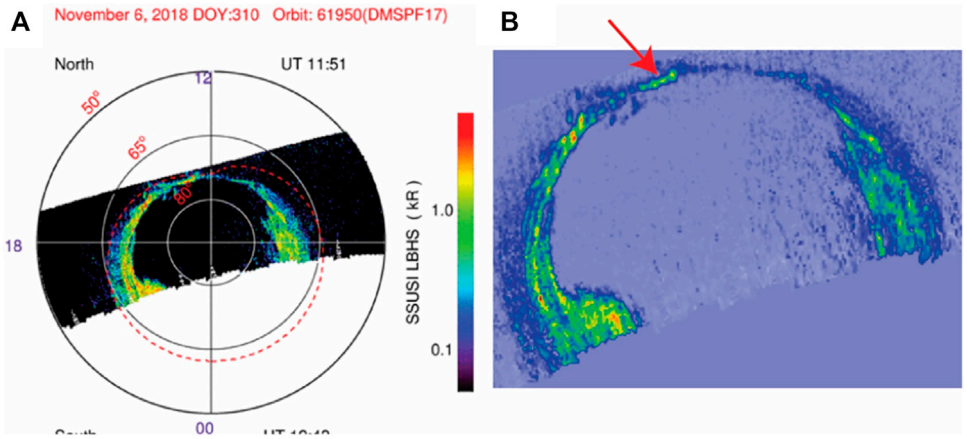

FIGURE 10 | (A) DMSP SSUSI LBHS image of the auroral bead on 2018-11-06 11:40–12:00 UT. **(B)** A zoomed in version of auroral emissions shown in panel **(A)**. The red arrow shows the bead that is analyzed in *DMSP Observations of a Dayside Ionosphere "Bead"*.

CONCLUSIONS AND SUMMARY

During an extended interval on 2018 November 06, Kelvin-Helmholtz wave activity was observed by multiple instruments on board the MMS spacecraft at the dusk flank magnetopause. The solar wind during this time was slightly faster than the nominal solar wind; but was steady with a slightly southward $B_{z\text{-}GSM}$ component. Additional spacecraft (Cluster at low latitudes; Geotail at mid-latitude) within the dusk flank magnetotail near the magnetopause also observed wave activity in the magnetic field and plasma fluxes. However, this wave activity was more coherent than that observed at MMS, consistent with ULF waves driven by the Kelvin-Helmholtz wave activity at the magnetopause. The observed magnetic field ULF wave activity is consistent in location and in frequency range with the global MHD simulation results described by Claudepierre et al. (2008). Fluctuations in ion and electron fluxes were also observed further downtail within the plasma mantle close to the duskside magnetopause by Geotail; with a periodicity similar to that of the ULF magnetic field waves observed by the Cluster spacecraft.

DMSP SSUSI LBHS observations of an ionospheric bead structure in the post-noon high-latitude region along with observed properties of the KH vortices along the flank magnetopause have been used to successfully test a theory of mesoscale field-aligned currents generated by KH vortices. This theory (Johnson et al., 2021) predicts that the optimal mapping of the KH vortex to the ionosphere occurs when Λ/L (= 2.8). Observations have provided a value of close to the optimal value. This theoretical treatment has also been used to show that ionospheric observations along with a mapping relation can provide an estimate of the KH vortex size, which is very similar to the size determined from the *in situ* observations of KH vortices (d = ~0.7 R_E).

To summarize, an extended, seredipitous interval of multi-spacecraft observations along the dusk flank magnetopause and at low Earth orbit has been investigated. KH vortices observed at the magnetopause boundary layer are associated with ULF waves observed just inside of the flank magnetopause, along with a successful testing of parameters associating an observed pre-noon high-latitude ionospheric "bead" with the KH vortices along the flank magnetopause.

DATA AVAILABILITY STATEMENT

Publicly available datasets were analyzed in this study. This data can be found here: http://cdaweb.gsfc.nasa.gov/istp_public/, https://lasp.colorado.edu/mms/sdc/public/about/, https://ssusi.jhuapl.edu/gal_edr-aur_cs, https://ccmc.gsfc.nasa.gov/modelweb/magnetos/tsygan.html.

AUTHOR CONTRIBUTIONS

SP plotted and analyzed the solar wind, geomagnetic, and magnetopause flank spacecraft data sets. He also traced the magnetic field line from the ionosphere into the magnetotail. SW identified the ionospheric bead and provided estimates of the conductivity. SW and JJ provided estimates of the energy flux, and scale sizes of the bead and vortex, and comparisons with a theory of mesoscale field-aligned currents generated by KH vortices and optimal mapping criterion. YZ created the DMSP SSUSI map of auroral emissions.

FUNDING

Research at Lockheed Martin was performed on Contracts 499935Q, 80NSSC18K1379, and 80NSSC17K0643 (sub-contract 18-027). SW acknowledges the support of NASA Grants 80NSSC20K0704, 80NSSC19K0843, 80NSSC19K0822, 80NSSC20K0188, 80NSSC20K1279, and 80NSSC21K1678. JJ

acknowledges support from NASA grants NNX15AJ01G, NNX16AQ87G, 80NSSC19K0843, NNX17AI50G, and 80NSSC20K0704. YZ acknowledges the support of USAF Contract N00024-13-D-6400.

ACKNOWLEDGMENTS

The women and men that worked and continue to work on these missions share in their successes.

REFERENCES

Auster, H. U., Glassmeier, K. H., Magnes, W., Aydogar, O., Baumjohann, W., Constantinescu, D., et al. (2008). The THEMIS Fluxgate Magnetometer. *Space Sci. Rev.* 141, 235–264. doi:10.1007/s11214-008-9365-9

Balogh, A., Dunlop, M. W., Dunlop, M. W., Cowley, S. W. H., Southwood, D. J., Thomlinson, J. G., et al. (1997). The Cluster Magnetic Field Investigation. *Space Sci. Rev.* 79, 65–91. doi:10.1023/A:1004970907748 10.1007/978-94-011-5666-0_3

Chandrasekhar, S. (1961). *Hydrodynamic and Hydromagnetic Stability*. New York: Oxford University Press.

Chao, J. K., Wu, D. J., Lin, C.-H., Yang, Y.-H., Wang, X. Y., Kessel, M., et al. (2002). "Models for the Size and Shape of the Earth's Magnetopause and bow Shock," in *Space Weather Study Using Multipoint Techniques, COSPAR Colloq. Ser.* Editor L.-H. Lyu (Oxford: Pergamon), Vol. 12, 127–135. doi:10.1016/s0964-2749(02)80212-8

Chen, S.-H., Kivelson, M. G., Gosling, J. T., Walker, R. J., and Lazarus, A. J. (1993). Anomalous Aspects of Magnetosheath Flow and of the Shape and Oscillations of the Magnetopause during an Interval of Strongly Northward Interplanetary Magnetic Field. *J. Geophys. Res.* 98, 5727–5742. doi:10.1029/92JA02263

Chen, S.-H., and Kivelson, M. G. (1993). On Nonsinusoidal Waves at the Earth·s Magnetopause. *Geophys. Res. Lett.* 20, 2699–2702. doi:10.1029/93GL02622

Claudepierre, S. G., Elkington, S. R., and Wiltberger, M. (2008). Solar Wind Driving of Magnetospheric ULF Waves: Pulsations Driven by Velocity Shear at the Magnetopause. *J. Geophys. Res.* 113, a–n. doi:10.1029/2007JA012890

Couzens, D., Parks, G. K., Anderson, K. A., Lin, R. P., and Reme, H. (1985). ISEE Particle Observations of Surface Waves at the Magnetopause Boundary Layer. *J. Geophys. Res.* 90, 6343–6353. doi:10.1029/JA090iA07p06343

Davis, T. N., and Sugiura, M. (1966). Auroral Electrojet Activity indexAEand its Universal Time Variations. *J. Geophys. Res.* 71, 785–801. doi:10.1029/JZ071i003p00785

Dmitriev, A. V., and Suvorova, A. V. (2015). Large-scale Jets in the Magnetosheath and Plasma Penetration across the Magnetopause: THEMIS Observations. *J. Geophys. Res. Space Phys.* 120 (6), 4423–4437. doi:10.1002/2014JA020953

Dmitriev, A. V., and Suvorova, A. V. (2012). Traveling Magnetopause Distortion Related to a Large-Scale Magnetosheath Plasma Jet: THEMIS and Ground-Based Observations. *J. Geophys. Res.* 117, a–n. doi:10.1029/2011JA016861

Fairfield, D. H., Otto, A., Mukai, T., Kokubun, S., Lepping, R. P., Steinberg, J. T., et al. (2000). Geotail Observations of the Kelvin-Helmholtz Instability at the Equatorial Magnetotail Boundary for Parallel Northward fields. *J. Geophys. Res.* 105 (A9), 21159–21173. doi:10.1029/1999JA000316

Haaland, S., Paschmann, G., Förster, M., Quinn, J., Torbert, R., Vaith, H., et al. (2008). Plasma Convection in the Magnetotail Lobes: Statistical Results from Cluster EDI Measurements. *Ann. Geophys.* 26, 2371–2382. doi:10.5194/angeo-26-2371-2008

Hasegawa, H., Fujimoto, M., Phan, T.-D., Rème, H., Balogh, A., Dunlop, M. W., et al. (2004). Transport of Solar Wind into Earth's Magnetosphere through Rolled-Up Kelvin-Helmholtz Vortices. *Nature* 430, 755–758. doi:10.1038/nature02799

Hasegawa, H., Fujimoto, M., Takagi, K., Saito, Y., Mukai, T., and Rème, H. (2006). Single-spacecraft Detection of Rolled-Up Kelvin-Helmholtz Vortices at the Flank Magnetopause. *J. Geophys. Res.* 111, A09203. doi:10.1029/2006JA011728

Hasegawa, H., Retinò, A., Vaivads, A., Khotyaintsev, Y., André, M., Nakamura, T. K. M., et al. (2009). Kelvin-Helmholtz Waves at the Earth's Magnetopause: Multiscale Development and Associated Reconnection. *J. Geophys. Res.* 114, a–n. doi:10.1029/2009JA014042

Henry, Z. W., Nykyri, K., Moore, T. W., Dimmock, A. P., and Ma, X. (2017). On the Dawn-Dusk Asymmetry of the Kelvin-Helmholtz Instability between 2007 and 2013. *J. Geophys. Res. Space Phys.* 122, 888–911. doi:10.1002/2017JA024548

Holzer, R. E., McLeod, M. G., and Smith, E. J. (1966). Preliminary Results from the Ogo 1 Search Coil Magnetometer: Boundary Positions and Magnetic Noise Spectra. *J. Geophys. Res.* 71, 1481–1486. doi:10.1029/JZ071i005p01481

Hones, E. W., Jr., BirnAsbridge, J. J. R., BamePaschmannSckopke, S. J. G. N., Asbridge, J. R., Paschmann, G., Sckopke, N., et al. (1981). Further Determination of the Characteristics of Magnetospheric Plasma Vortices with ISEE 1 and 2. *J. Geophys. Res.* 86, 814–820. doi:10.1029/ja086ia02p00814

Howe, H. C., and Siscoe, G. L. (1972). Magnetopause Motions at Lunar Distance Determined from the Explorer 35 Plasma experiment. *J. Geophys. Res.* 77, 6071–6086. doi:10.1029/JA077i031p06071

Hwang, K.-J., Kuznetsova, M. M., Sahraoui, F., Goldstein, M. L., Lee, E., and Parks, G. K. (2011). Kelvin-Helmholtz Waves under Southward Interplanetary Magnetic Field. *J. Geophys. Res.* 116, a–n. doi:10.1029/2011JA016596

Hwang, K.-J. (2015). Magnetopause Waves Controlling the Dynamics of Earth's Magnetosphere. *J. Astron. Space Sci.* 32 (1), 1–11. doi:10.5140/JASS.2015.32.1.1

Johnson, J. R., Wing, S., Delamere, P., Petrinec, S., and Kavosi, S. (2021). Field-Aligned Currents in Auroral Vortices. *J. Geophys. Res. Space Phys.* 126, e2020JA028583. doi:10.1029/2020JA028583

Johnson, J. R., and Wing, S. (2015). The Dependence of the Strength and Thickness of Field-aligned Currents on Solar Wind and Ionospheric Parameters. *J. Geophys. Res. Space Phys.* 120, 3987–4008. doi:10.1002/2014JA020312

Kaufmann, R. L., and Konradi, A. (1969). Explorer 12 Magnetopause Observations: Large-Scale Nonuniform Motion. *J. Geophys. Res.* 74, 3609–3627. doi:10.1029/JA074i014p03609

Kavosi, S., and Raeder, J. (2015). Ubiquity of Kelvin-Helmholtz Waves at Earth's Magnetopause. *Nat. Commun.* 6, 7019. doi:10.1038/ncomms8019

Kim, E.-H., Johnson, J. R., and Nykyri, K. (2021). Coupling between Alfven Wave and Kelvin-Helmholtz Waves in the Low Latitude Boundary Layer. *Front. Phys.* doi:10.3389/fphy.2021.785413

Kivelson, M. G., and Chen, S.-H. (1995). "The Magnetopause: Surface Waves and Instabilities and Their Possible Dynamic Consequences," in *Physics of the Magnetopause, Geophys. Monogr. Ser.* Editors P. Song, B. U. Ö. Sonnerup, and M. F. Thomsen (Washington D.C.: AGU), Vol. 90, 257–268.

Kivelson, M. G., and Zu-Yin, P. (1984). The Kelvin-Helmholtz Instability on the Magnetopause. *Planet. Space Sci.* 32, 1335–1341. doi:10.1016/0032-0633(84)90077-1

Knight, S. (1973). Parallel Electric fields. *Planet. Space Sci.* 21 (5), 741–750. doi:10.1016/0032-0633(73)90093-7

Kokubun, S., Yamamoto, T., Acuña, M. H., Hayashi, K., Shiokawa, K., and Kawano, H. (1994). The GEOTAIL Magnetic Field experiment. *J. Geomagn. Geoelec* 46, 7–21. doi:10.5636/jgg.46.7

Kronberg, E. A., Gorman, J., Nykyri, K., Smirnov, A. G., Gjerloev, J. W., Grigorenko, E. E., et al. (2021). Kelvin-Helmholtz Instability Associated with Reconnection and Ultra Low Frequency Waves at the Ground: A Case Study. *Front. Phys.* 9. doi:10.3389/fphy.2021.738988

Lee, L. C., Albano, R. K., and Kan, J. R. (1981). Kelvin-Helmholtz Instability in the Magnetopause-Boundary Layer Region. *J. Geophys. Res.* 86, 54–58. doi:10.1029/JA086iA01p00054

Li, H., Jiang, W., Wang, C., Verscharen, D., Zeng, C., Russell, C. T., et al. (2020). Evolution of the Earth's Magnetosheath Turbulence: A Statistical Study Based on MMS Observations. *ApJ* 898 (2), L43. doi:10.3847/2041-8213/aba531

Lui, A. T. Y., Venkatesan, D., and Murphree, J. S. (1989). Auroral Bright Spots on the Dayside Oval. *J. Geophys. Res.* 94, 5515–5522. doi:10.1029/JA094iA05p05515

Mann, I. R., Voronkov, I., Dunlop, M., Donovan, E., Yeoman, T. K., Milling, D. K., et al. (2002). Coordinated Ground-Based and Cluster Observations of Large Amplitude Global Magnetospheric Oscillations during a Fast Solar Wind Speed Interval. *Ann. Geophys.* 20, 405–426. doi:10.5194/angeo-20-405-2002

McFadden, J. P., Carlson, C. W., Larson, D., Bonnell, J., Mozer, F., Angelopoulos, V., et al. (2008b). THEMIS ESA First Science Results and Performance Issues. *Space Sci. Rev.* 141, 477–508. doi:10.1007/s11214-008-9433-1

McFadden, J. P., Carlson, C. W., Larson, D., Ludlam, M., Abiad, R., Elliott, B., et al. (2008a). The THEMIS ESA Plasma Instrument and In-Flight Calibration. *Space Sci. Rev.* 141, 277–302. doi:10.1007/s11214-008-9440-2

Miura, A. (1995). Dependence of the Magnetopause Kelvin-Helmholtz Instability on the Orientation of the Magnetosheath Magnetic Field. *Geophys. Res. Lett.* 22, 2993–2996. doi:10.1029/95GL02793

Mukai, T., Machida, S., Saito, Y., Hirahara, M., Terasawa, T., Kaya, N., et al. (1994). The Low Energy Particle (LEP) Experlment Onboard the GEOTAIL Satellite. *J. Geomagn. Geoelec* 46, 669–692. doi:10.5636/jgg.46.669

Nakamura, T. K. M., Plaschke, F., Hasegawa, H., Liu, Y. H., Hwang, K. J., Blasl, K. A., et al. (2020). Decay of Kelvin-Helmholtz Vortices at the Earth's Magnetopause under Pure Southward IMF Conditions. *Geophys. Res. Lett.* 47, e2020GL087574. doi:10.1029/2020GL087574

Newell, P. T., and Gjerloev, J. W. (2011a). Evaluation of SuperMAG Auroral Electrojet Indices as Indicators of Substorms and Auroral Power. *J. Geophys. Res.* 116, a–n. doi:10.1029/2011JA016779

Newell, P. T., and Gjerloev, J. W. (2011b). Substorm and Magnetosphere Characteristic Scales Inferred from the SuperMAG Auroral Electrojet Indices. *J. Geophys. Res.* 116, a–n. doi:10.1029/2011JA016936

Nykyri, K., and Dimmock, A. P. (2016). Statistical Study of the ULF Pc4-Pc5 Range Fluctuations in the Vicinity of Earth's Magnetopause and Correlation with the Low Latitude Boundary Layer Thickness. *Adv. Space Res.* 58, 257–267. doi:10.1016/j.asr.2015.12.046

Nykyri, K. (2013). Impact of MHD Shock Physics on Magnetosheath Asymmetry and Kelvin-Helmholtz Instability. *J. Geophys. Res. Space Phys.* 118, 5068–5081. doi:10.1002/jgra.50499

Omidi, N., Eastwood, J. P., and Sibeck, D. G. (2010). Foreshock Bubbles and Their Global Magnetospheric Impacts. *J. Geophys. Res.* 115. doi:10.1029/2009JA1482810.1029/2009ja014828

Otto, A., and Fairfield, D. H. (2000). Kelvin-Helmholtz Instability at the Magnetotail Boundary: MHD Simulation and Comparison with Geotail Observations. *J. Geophys. Res.* 105, 21175–21190. doi:10.1029/1999JA000312

Paxton, L. J., Meng, C.-I., Fountain, G. H., Ogorzalek, B. S., Darlington, E. H., Gary, S. A., et al. (1992). "Special Sensor Ultraviolet Spectrographic Imager: an Instrument Description," in *Proc. SPIE 1745, Instrumentation for Planetary and Terrestrial Atmospheric Remote Sensing*. Editors S. Chakrabarti and A. B. Christensen (Bellingham, WA: Society of Photo-Optical Instrumentation Engineers, SPIE, 2–15. doi:10.1117/12.60595

Paxton, L. J., Meng, C.-I., Fountain, G. H., Ogorzalek, B. S., Darlington, E. H., Gary, S. A., et al. (1993). "SSUSI - Horizon-To-Horizon and Limb-Viewing Spectrographic Imager for Remote Sensing of Environmental Parameters," in *Proc. SPIE 1764, Ultraviolet Technology IV*. Editor R. E. Huffman (Bellingham, WA: Society of Photo-Optical Instrumentation Engineers, SPIE). doi:10.1117/12.140846

Paxton, L. J., Morrison, D., Zhang, Y., Kil, H., Wolven, B., Ogorzalek, B. S., et al. (2002). "Validation of Remote Sensing Products Produced by the Special Sensor Ultraviolet Scanning Imager (SSUSI): a Far UV-Imaging Spectrograph on DMSP F-16," in *Proc. SPIE 4485, Optical Spectroscopic Techniques, Remote Sensing, and Instrumentation for Atmospheric and Space Research IV*. Editors A. M. Larar and M. G. Mlynczak (Bellingham, WA: International Society for Optics and Photonics, SPIE, 338–348. doi:10.1117/12.454268

Paxton, L. J., Schaefer, R. K., Zhang, Y., and Kil, H. (2017). Far Ultraviolet Instrument Technology. *J. Geophys. Res. Space Phys.* 122, 2706–2733. doi:10.1002/2016ja023578

Paxton, L. J., and Zhang, Y. (2016). "Far Ultraviolet Imaging of the aurora," in *Space Weather Fundamentals*. Editor G. V. Khazanov (Laurel, MD, USA: CRC Press), 213–244. doi:10.1201/9781315368474-14

Phan, T. D., and Paschmann, G. (1996). Low-latitude Dayside Magnetopause and Boundary Layer for High Magnetic Shear: 1. Structure and Motion. *J. Geophys. Res.* 101 (A4), 7801–7815. doi:10.1029/95JA03752

Plaschke, F., Kahr, N., Fischer, D., Nakamura, R., Baumjohann, W., Magnes, W., et al. (2016). Steepening of Waves at the Duskside Magnetopause. *Geophys. Res. Lett.* 43, 7373–7380. doi:10.1002/2016GL070003

Plaschke, F. (2016). "ULF Waves at the Magnetopause,"in *Low-Frequency Waves in Space Plasmas, Geophys. Monogr. Ser*. Editors A. Keiling, D.-H. Lee, and V. Nakariakov (Washington DC and Hoboken, New Jersey: AGU and John Wiley & Sons, Inc., Vol. 216, 193–212. doi:10.1002/9781119055006.ch12

Pollock, C., Moore, T., Jacques, A., Burch, J., Gliese, U., Saito, Y., et al. (2016). Fast Plasma Investigation for Magnetospheric Multiscale. *Space Sci. Rev.* 199, 331–406. doi:10.1007/s11214-016-0245-4

Pu, Z.-Y., and Kivelson, M. G. (1983). Kelvin-Helmholtz Instability at the Magnetopause: Energy Flux into the Magnetosphere. *J. Geophys. Res.* 88, 853–861. doi:10.1029/JA088iA02p00853

Rae, I. J., Donovan, E. F., Mann, I. R., Fenrich, F. R., Watt, C. E. J., Milling, D. K., et al. (2005). Evolution and Characteristics of Global Pc5 ULF Waves during a High Solar Wind Speed Interval. *J. Geophys. Res.* 110, A12211. doi:10.1029/2005JA011007

Robinson, R. M., and Vondrak, R. R. (1984). Measurements ofEregion Ionization and Conductivity Produced by Solar Illumination at High Latitudes. *J. Geophys. Res.* 89, 3951–3956. doi:10.1029/JA089iA06p03951

Robinson, R. M., Vondrak, R. R., Miller, K., Dabbs, T., and Hardy, D. (1987). On Calculating Ionospheric Conductances from the Flux and Energy of Precipitating Electrons. *J. Geophys. Res.* 92, 2565–2569. doi:10.1029/JA092iA03p02565

Rosenbauer, H., Grünwaldt, H., Montgomery, M. D., Paschmann, G., and Sckopke, N. (1975). Heos 2 Plasma Observations in the Distant Polar Magnetosphere: The Plasma Mantle. *J. Geophys. Res.* 80, 2723–2737. doi:10.1029/JA080I019P02723

Russell, C. T., Anderson, B. J., Baumjohann, W., Bromund, K. R., Dearborn, D., Fischer, D., et al. (2016). The Magnetospheric Multiscale Magnetometers. *Space Sci. Rev.* 199, 189–256. doi:10.1007/s11214-014-0057-3

Russell, C. T., Petrinec, S. M., Zhang, T. L., Song, P., and Kawano, H. (1997). The Effect of Foreshock on the Motion of the Dayside Magnetopause. *Geophys. Res. Lett.* 24, 1439–1441. doi:10.1029/97GL01408

Schwartz, S. J., Burgess, D., and Moses, J. J. (1996). Low-frequency Waves in the Earth's Magnetosheath: Present Status. *Ann. Geophys.* 14, 1134–1150. doi:10.1007/s00585-996-1134-z

Shue, J.-H., Chao, J. K., Fu, H. C., Russell, C. T., Song, P., Khurana, K. K., et al. (1997). A New Functional Form to Study the Solar Wind Control of the Magnetopause Size and Shape. *J. Geophys. Res.* 102, 9497–9511. doi:10.1029/97JA00196

Sibeck, D. G., and Croley, D. J., Jr. (1991). Solar Wind Dynamic Pressure Variations and Possible Ground Signatures of Flux Transfer Events. *J. Geophys. Res.* 96, 1669–1683. doi:10.1029/90JA02357

Sibeck, D. G., and Gosling, J. T. (1996). Magnetosheath Density Fluctuations and Magnetopause Motion. *J. Geophys. Res.* 101, 31–40. doi:10.1029/95JA03141

Sibeck, D. G. (1992). Transient Events in the Outer Magnetosphere: Boundary Waves or Flux Transfer Events. *J. Geophys. Res.* 97, 4009–4026. doi:10.1029/91JA03017

Song, P., Elphic, R. C., and Russell, C. T. (1988). ISEE 1 & 2 Observations of the Oscillating Magnetopause. *Geophys. Res. Lett.* 15, 744–747. doi:10.1029/GL015i008p00744

Song, P., Le, G., and Russell, C. T. (1994). Observational Differences between Flux Transfer Events and Surface Waves at the Magnetopause. *J. Geophys. Res.* 99, 2309–2320. doi:10.1029/93JA02852

Sonnerup, B. U. Ö., and Scheible, M. (1998). "Minimum and Maximum Variance Analysis," in *Analysis Methods for Multi-Spacecraft Data, ISSI Scientific Report SR-001*. Editors G. Paschmann and P. W. Daly (Noordwijk (Netherlands: ESA Pub. Division

Southwood, D. J. (1979). Magnetopause Kelvin-Helmholtz Instability."in Proceedings of Magnetospheric Boundary Layers Conference, Vol. 148. Netherlands: NoordwijkEuropean Space Agency Publ., Scientific and Technical Publications Branch, 357–364.

Takagi, K., Hashimoto, C., Hasegawa, H., Fujimoto, M., and TanDokoro, R. (2006). Kelvin-Helmholtz Instability in a Magnetotail Flank-like Geometry: Three-Dimensional MHD Simulations. *J. Geophys. Res.* 111, A08202. doi:10.1029/2006JA011631

Taylor, M. G. G. T., Hasegawa, H., Lavraud, B., Phan, T., Escoubet, C. P., Dunlop, M. W., et al. (2012). Spatial Distribution of Rolled up Kelvin-Helmholtz Vortices at Earth's Dayside and Flank Magnetopause. *Ann. Geophys.* 30, 1025–1035. doi:10.5194/angeo-30-1025-2012

Tian, A. M., Zong, Q. G., Zhang, T. L., Nakamura, R., Du, A. M., Baumjohann, W., et al. (2012). Dynamics of Long-Period ULF Waves in the Plasma Sheet:

Coordinated Space and Ground Observations. *J. Geophys. Res.* 117, a–n. doi:10.1029/2011JA016551

Torbert, R. B., Russell, C. T., Magnes, W., Ergun, R. E., Lindqvist, P.-A., LeContel, O., et al. (2016). The FIELDS Instrument Suite on MMS: Scientific Objectives, Measurements, and Data Products. *Space Sci. Rev.* 199 (1-4), 105–135. doi:10.1007/s11214-014-0109-8

Tsyganenko, N. A. (1995). Modeling the Earth's Magnetospheric Magnetic Field Confined within a Realistic Magnetopause. *J. Geophys. Res.* 100, 5599–5612. doi:10.1029/94JA03193

Wallis, D. D., and Budzinski, E. E. (1981). Empirical Models of Height Integrated Conductivities. *J. Geophys. Res.* 86 (A1), 125–137. doi:10.1029/ja086ia01p00125

Wing, S., and Johnson, J. R. (2015). Theory and Observations of Upward Field-aligned Currents at the Magnetopause Boundary Layer. *Geophys. Res. Lett.* 42, 9149–9155. doi:10.1002/2015GL065464

Zhang, Y., and Paxton, L. J. (2008). An Empirical Kp-dependent Global Auroral Model Based on TIMED/GUVI FUV Data. *J. Atmos. Solar-Terrestrial Phys.* 70, 1231–1242. doi:10.1016/j.jastp.2008.03.008

Conflict of Interest: The authors declare that the research was conducted in the absence of any commercial or financial relationships that could be construed as a potential conflict of interest.

Advantages of publishing in Frontiers

OPEN ACCESS
Articles are free to read for greatest visibility and readership

FAST PUBLICATION
Around 90 days from submission to decision

HIGH QUALITY PEER-REVIEW
Rigorous, collaborative, and constructive peer-review

TRANSPARENT PEER-REVIEW
Editors and reviewers acknowledged by name on published articles

Frontiers
Avenue du Tribunal-Fédéral 34
1005 Lausanne | Switzerland

Visit us: www.frontiersin.org
Contact us: frontiersin.org/about/contact

REPRODUCIBILITY OF RESEARCH
Support open data and methods to enhance research reproducibility

DIGITAL PUBLISHING
Articles designed for optimal readership across devices

FOLLOW US
@frontiersin

IMPACT METRICS
Advanced article metrics track visibility across digital media

EXTENSIVE PROMOTION
Marketing and promotion of impactful research

LOOP RESEARCH NETWORK
Our network increases your article's readership